# HANDBOOK ON THE PHYSICS AND CHEMISTRY OF RARE EARTHS

For information on all North-Holland publications
visit our website at http://store.elsevier.com/

# Contributors

*Numbers in Parentheses indicate the pages on which the author's contributions begin.*

**Christopher L. Cahill** (147), Department of Chemistry, The George Washington University, Washington, District of Columbia, USA

**John A. Capobianco** (273), Department of Chemistry and Biochemistry and Centre for NanoScience Research, Concordia University, Montreal, Quebec, Canada

**Korey P. Carter** (147), Department of Chemistry, The George Washington University, Washington, District of Columbia, USA

**William P. Gillin** (1), Materials Research Institute and School of Physics and Astronomy, Queen Mary University of London, London, United Kingdom, and College of Physical Science and Technology, Sichuan University, Chengdu, People's Republic of China

**Yasuchika Hasegawa** (101), Division of Materials Chemistry, Faculty of Engineering, Hokkaido University, Sapporo, Hokkaido, Japan

**Ignacio Hernández** (1), Dpto. CITIMAC, Facultad de Ciencias, Universidad de Cantabria, Santander, Spain

**Rafik Naccache** (273), Institut National de la Recherche Scientifique—Énergie, Matériaux et Télécommunications, Université du Québec, Varennes, Quebec, Canada

**Takayuki Nakanishi** (101), Division of Materials Chemistry, Faculty of Engineering, Hokkaido University, Sapporo, Hokkaido, Japan

**Claude Piguet** (209), Department of Inorganic and Analytical Chemistry, University of Geneva, Geneva, Switzerland

**Diana C. Rodriguez Burbano** (273), Department of Chemistry and Biochemistry and Centre for NanoScience Research, Concordia University, Montreal, Quebec, Canada

# Preface

*These elements perplex us in our reaches [sic], baffle us in our speculations, and haunt us in our very dreams. They stretch like an unknown sea before us – mocking, mystifying, and murmuring strange revelations and possibilities.*

<div align="right">Sir William Crookes (February 16, 1887)</div>

Volume 47 of the *Handbook on the Physics and Chemistry of Rare Earths* adds five chapters to the series, covering quite different, yet exciting subjects ranging from fundamental to applied sciences. Featured themes encompass lanthanide-organic chromophores for telecommunications, semiconductor nanoparticles, inorganic–organic hybrid materials, microscopic thermodynamic descriptors in complexation processes, and upconversion nanoparticles for bioimaging, medical diagnosis, and therapy.

The first chapter (Chapter 269) is devoted to infrared emitters based on materials containing trivalent lanthanide ions such as $Nd^{3+}$, $Er^{3+}$, or $Yb^{3+}$. These materials are of great interest for lasers, telecommunications, and other photonic applications due to their high monochromaticity at the silica transparency windows. Their use for amplifying optical signals traveling through fibers in the so-called erbium-doped fiber amplifiers is widespread in long-distance broadband data transmission. However due to poor light-absorption properties, purely inorganic amplifying materials require high excitation power. A remedy to this situation could be to turn to organic complexes. Yet the presence of high-energy vibrations in the surroundings of the emitting ions has detrimental consequences on the emission lifetimes and efficiencies that offset the advantage earned by the antenna effect, i.e., excitation in the ligand electronic levels. Replacement of hydrogen atoms with halogen groups has been therefore suggested to enhance emission properties of organic-based lanthanide optical materials. The review describes fundamentals and recent progress while paying particular attention to the implication of this strategy on the design of such materials; perspectives for enhanced and/or novel photonic applications such as on-chip telecommunication devices are discussed.

Intrinsic magnetic semiconductor nanoparticles containing europium chalcogenides EuX (X=O, S, Se, and Te) are the subject of Chapter 270. These materials are being investigated from the viewpoints of fundamental condensed matter science and also of practical applications, for instance, in spintronics and magneto-optic devices. The quantum-size and

quantum-confinement effects found in europium chalcogenides are especially remarkable and engender new photophysics arising from both ferro- and antiferromagnetic spin configurations. The review first focuses on preparation methods that largely depend on the progress achieved in nanotechnology. In particular, high-quality nanoscale EuO, EuS, and EuSe materials can be successfully prepared by the reaction of a Eu(III) complex used as single-source precursor. As far as properties are concerned, nano-sized structures of magnetic semiconductor europium chalcogenides lead to the formation of single-domain nanocrystals, while aggregates of sphere-shaped EuX nanoparticles exhibit superparamagnetic and superantiferromagnetic behaviors. Moreover, enhancement of ferromagnetic properties for aggregates of cube-shaped EuS nanoparticles has been observed. These observations make magnetic semiconductor nanocrystals containing Eu(II) ions promising materials for next-generation photonic components such as optical isolators and spintronic devices.

Chapter 271 deals with crystalline hybrid materials. These materials combine a substrate (organic or inorganic) with active metal ions or complexes that are blended on the molecular scale. They are found in a number of systems and can be broadly divided into sol–gel (glasses, silica, organically modified xerogels), porous (metal-organic frameworks), mesoporous (silicates, zeolites), polymeric, intercalation (layered double hydroxides), and nanocomposite (nanoparticles) materials. The review explores polymeric and molecular lanthanide hybrid materials with special emphasis on covalent and noncovalent means of assembly. The chapter first takes a detailed look at the structures and properties of Ln hybrids featuring various linkers accompanied by chelating N-donor ligands as well as at molecular lanthanide materials. Structural trends and common building units are highlighted along with assembly processes via noncovalent interactions. The chapter culminates with an insight into where the field of crystalline lanthanide hybrid materials will be heading next. New synthesis methods are needed for gaining precise control over $Ln^{3+}$ nuclearity and for optimizing the properties of hybrid materials. Deepening our understanding of the material properties and subsequently delineating structure/property relationships and manifestations thereof are the next challenges to tackle.

Importance of coordination chemistry is reflected in the 20 or so chapters devoted so far to the subject in the Handbook series. Chapter 272 brings a new insight into the field by focusing on thermodynamic models for rationalizing the complexation mechanisms. The review first puts the matter into historical perspective, showing how interest for lanthanide complexes stemmed from needs generated by extraction and separation of the rare earths and resulted in showing how the coordination chemistry of rare-earth ions differs considerably from that of d-transition metal ions. The lanthanide series features a

homogeneous set of elements with properties varying smoothly with the atomic number, an ideal situation for developing models aiming at rationalizing the numerous stability constants collected. Initial efforts concentrated on macroscopic aspects, with Choppin's two-step desolvation/complexation mechanism and Ford's model for entropy/enthalpy compensation. The advent of supramolecular chemistry then added a whole new dimension to the problem and novel concepts were proposed including the site-binding model, the principle of maximum occupancy, and microscopic thermodynamic descriptors. This contribution reports on the most important innovation brought by these novel ideas for the design, the stability, and the rationalization of rare earth complex formation.

The final chapter (Chapter 273) discusses the role of upconverting nanoparticles (UCNPs) in biology and medicine. Lanthanide-doped UCNPs have large anti-Stokes shifts, sharp emission bands, and are not subject to photobleaching. Furthermore, when they are used as bioprobes in an NIR(excitation)–NIR(emission) mode, high penetration depths can be attained in biological tissues and autofluorescence from the sample is minimized. UCNPs can also be conveniently stabilized in biological media and bioconjugated. Therefore, they appear as being strong alternatives to existing organic bioprobes despite low quantum yields and some unknowns about their cytotoxicity. The authors first put UCNPs in perspective with respect to other types of bioprobes and give an overview of upconversion processes before concentrating on the synthesis and surface modification of these nanoparticles. A careful choice of host and dopants is essential and depends on the targeted application. Increasing upconversion efficiency is a real challenge but several possibilities are at hand and start to yield interesting results. The last two sections are devoted to biosensing, imaging, and drug delivery: sensing cell temperature, immunoassays, *in vitro* and *in vivo* bioimaging, and photodynamic and photothermal therapy of cancer are some of the current applications of UCNPs.

## CHAPTER 269: ORGANIC CHROMOPHORES-BASED SENSITIZATION OF NIR-EMITTING LANTHANIDES: TOWARD HIGHLY EFFICIENT HALOGENATED ENVIRONMENTS

Ignacio Hernandez* and William P. Gillin[†,‡]

*Dpto. CITIMAC, Universidad de Cantabria, Facultad de Ciencias, Santander, Spain

[†]Materials Research Institute and School of Physics and Astronomy, Queen Mary University of London, Mile End Road, London, United Kingdom

[‡]College of Physical Science and Technology, Sichuan University, Chengdu, People's Republic of China
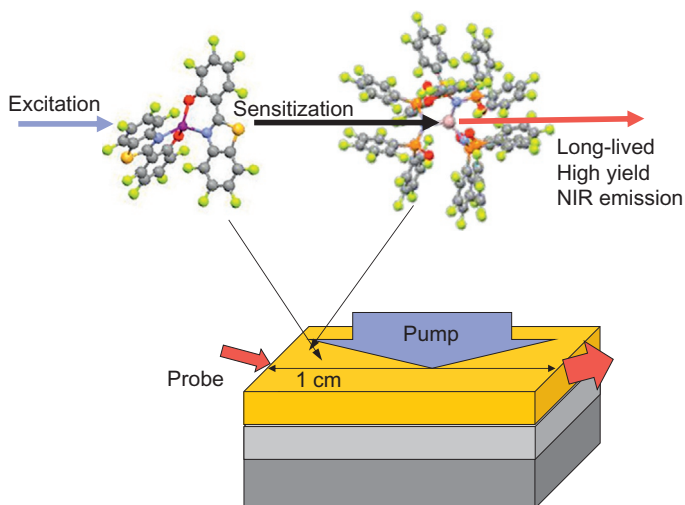
Infrared emitters based on materials with lanthanides, and especially those containing $Yb^{3+}$, $Nd^{3+}$, and $Er^{3+}$, are of great interest for laser, telecommunication, photonic and biological applications due to the high monochromaticity, and potential long emission lifetimes at the silica transparency windows around 1, 1.3, and 1.5 μm. In particular, their use for amplifying optical signals traveling through fibers in the so-called erbium-doped fiber amplifiers is widespread and has had important consequences for long-distance broadband data transmission. Nevertheless, due to the poor light-absorbing properties of these ions and the low solubility in most matrixes, devices based on inorganic compounds require high excitation power. Organic complexes of these rare earth ions offer the possibility of indirect excitation (sensitization) through highly absorbing organic-based chromophores, fine tuning of the concentrations, and enhanced processability. These properties, coupled with electric pumping capability, open up new approaches for integrating organic materials into silicon substrates and developing optoelectronic devices. However, the presence of O–H, N–H, and C–H bonds in the surroundings of these ions quenches the excited states. The use of halogenated compounds has therefore been suggested and the chapter reviews the fundamentals and recent progresses in the field. The strategic choice of organics and lanthanides determines the working wavelengths and conditions to allow for effective pumping of the lanthanides with the challenge of keeping high quantum yields. Focus is made on $Nd^{3+}$, $Er^{3+}$, and $Yb^{3+}$ emitters and a number of organic chromophores and ligands to illustrate the physical mechanisms and implications in the performance. The possibilities for enhanced operations offer exciting prospects for novel photonic and biological applications, especially for on-chip telecommunication and laser devices.

## CHAPTER 270: EUROPIUM CHALCOGENIDE NANOPARTICLES

Yasuchika Hasegawa and Takayuki Nakanishi

Division of Materials Chemistry, Faculty of Engineering, Hokkaido University, Japan
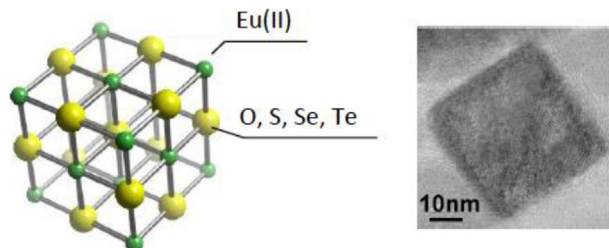


Magnetic semiconductor nanoparticles containing europium chalcogenides EuX (X=O, S, Se, and Te) are being targeted from the viewpoints of fundamental condensed matter science and of practical application for spintronics and magneto-optic devices. Until now, various types of magnetic dopants in II–VI or III–V semiconductor nanoparticles have been investigated and it turns out that the quantum-size and quantum-confinement effects found in europium chalcogenide materials are providing new photophysics arising from both ferro- and antiferromagnetic spin configurations. Therefore, magnetic semiconductor nanocrystals containing Eu(II) chalcogenides are promising materials for designing next-generation photonic devices.

The review begins with a brief history of divalent europium semiconductors and their nanoparticles, the properties of which have come into focus since the 1960s and 1990s, respectively. The chapter then describes the various preparation methods of europium chalcogenide nanoparticles that have been dramatically improved during the past decade thanks to progress in nanoscience and technology: liquid ammonia method, photochemical reactions, single-source precursor, electrochemical deposition, and vapor-phase conversion. In particular, high-quality nanoscale EuO, EuS, and EuSe materials can be successfully prepared by the reaction of a Eu(III) complex used as single-source precursor. The synthesis of polymeric and silica glass materials is also described. As far as physical properties are concerned, nanosized structures of semiconductor europium chalcogenides lead to the formation of single-domain nanocrystals. Further, aggregates of sphere-shaped nanoparticles exhibit superparamagnetic and superantiferromagnetic behaviors, while those of cube-shaped EuS nanoparticles display enhancement of ferromagnetic properties. EuX nanoparticles with giant magneto-optical efficiency are expected to be useful in applications such as optical isolators and spintronic devices. The last part of the chapter concentrates on characteristic structures and nanostructures.

## CHAPTER 271: HYBRID MATERIALS OF THE f-ELEMENTS PART I: THE LANTHANIDES

Korey P. Carter and Christopher L. Cahill
  The George Washington University, Washington, DC, USA
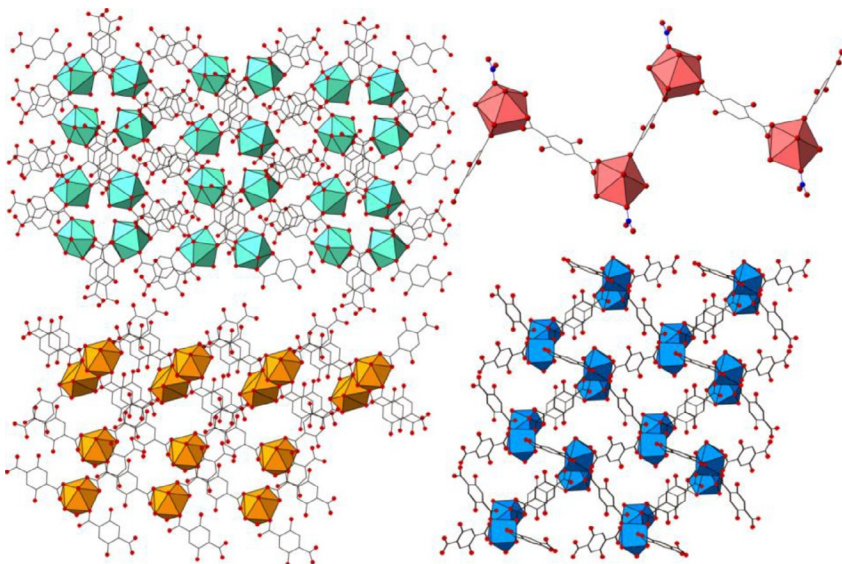


Hybrid materials combine a substrate (organic or inorganic) with active metal ions or complexes that are blended on the molecular scale. Lanthanide-containing hybrid materials have garnered significant interest due to their rich structural diversity, as well as owing to the unique magnetic and spectroscopic properties of these ions. They have proven particularly attractive for a wide array of applications including gas storage, heterogeneous catalysis, magnetism, luminescence, and bioanalyses. In this review, polymeric and molecular lanthanide hybrid materials are explored with a specific focus on both covalent and noncovalent means of assembly. The review is restricted to compounds for which an X-ray crystal structure could be established. Challenges remain with these materials regarding control over $Ln^{3+}$ nuclearity and the resulting secondary building units in hydro/solvothermally synthesized systems. Subsequently, the delineation of structure/property relationships and manifestations thereof remains ripe for exploration.

After a general introduction of lanthanide hybrid materials, the chapter takes a deeper look at the structures and properties of lanthanide hybrids featuring aliphatic and aromatic carboxylic acid linkers, phosphonate linkers, carboxylic acid linkers accompanied by chelating N-donor ligands, and finally molecular lanthanide materials. Where possible, structural trends and common building units are highlighted and in the molecular lanthanide section a

detailed look at assembly via noncovalent interactions (i.e., hydrogen and halogen bonding) is provided. The chapter concludes with an outlook at where the field of crystalline lanthanide hybrid materials may go next considering new synthesis techniques and optimization and enhanced understanding of material properties. Work on these materials has now moved beyond the serendipitous discoveries to a more crystal engineering centric approach where efforts to rationally design materials with specific topologies and properties are being realized.

## CHAPTER 272: MICROSCOPIC THERMODYNAMIC DESCRIPTORS FOR RATIONALIZING LANTHANIDE COMPLEXATION PROCESSES

Claude Piguet

Department of Inorganic and Analytical Chemistry, University of Geneva, Geneva, Switzerland



$$[R_4(\mathbf{L})_4]^{12+}$$
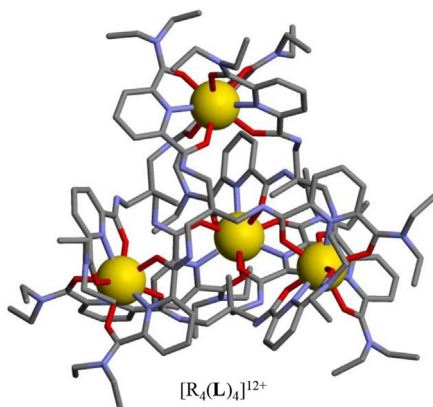
$$\beta_{4,4}^{R,L} = 6.48 \times 10^6 \left( f_{inter}^{R,L} \right)^{12} \left( EM^{R,L} \right)^5 \left( u^{L,L} \right)^{12} \left( u^{R,R} \right)^5$$

While some transition d-block elements are known and used since millenniums, the first f-block analogues were discovered after the French revolution. Their reluctance toward reduction forced the early chemists to develop separation techniques relevant to what will become coordination chemistry at the turn of the nineteenth century. In absence of satisfying model for rationalizing the trends in the associated thermodynamic complexation processes, the coordination chemistry of trivalent rare earth remained exploratory and empirical for a long period. In a seminal review published in the first set of four volumes of the Handbook, Thompson elegantly highlighted the gap between the demanding requirements of separation processes and the limited understanding of simple lanthanide–ligand interactions (Thompson, L.C., 1979. Complexes. In: Gschneidner Jr., K.A., Eyring L. (Eds.), Handbook on the Physics and Chemistry of Rare Earths, vol. 3. North-Holland Publishing

Company, pp. 209–297). During the past 35 years, the well-established main stream approach focused on the systematic characterization and isolation of rare earth complexes with myriads of novel ligands benefited from the parallel development of enthalpy/entropy correlations and of supramolecular chemistry.

The chapter starts with a short historical overview of rare-earth coordination chemistry and its first landmarks. It then describes the thermodynamics parameters governing complexation with monodentate and multidentate ligands, in relationship with extraction/separation processes and with solvation and hydrolysis. These first sets of systematic data triggered interest; models were proposed to rationalize them, including Choppin's two-step mechanism and Ford's model for entropy/enthalpy compensation during complexation. The review then focuses on metallosupramolecular chemistry that opened a new dimension in coordination chemistry. The concepts of intermolecular affinity, allosteric cooperativity, chelate cooperativity, and interannular cooperativity are rationalized within the frame of the principle of maximum occupancy and using microscopic thermodynamic descriptors.

## CHAPTER 273: NEAR-IR-TRIGGERED PHOTON UPCONVERSION: IMAGING, DETECTION, AND THERAPY

Diana C. Rodriguez-Burbano*, Rafik Naccache[†], and John A. Capobianco*

*Department of Chemistry and Biochemistry and Centre for NanoScience Research, Concordia University, Montreal, Canada

[†]Institut National de la Recherche Scientifique—Énergie, Matériaux et Télécommunications, Université du Quebec, Varennes, Quebec, Canada
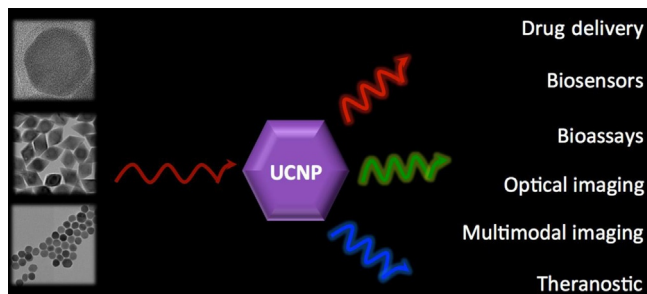
Upconversion is a multiphoton process that converts NIR light to higher energy light such as UV, visible, or even NIR (with a wavelength shorter than the excitation source). Several lanthanide ions are ideal for designing compounds featuring this phenomenon because they have numerous electronic levels some of them equally spaced. This is in particular the case of $Er^{3+}$ entering in the composition of the ubiquitous $NaYF_4$:Yb,Er upconversion phosphor and the corresponding nanoparticles (UCNPs). The review first presents lanthanide-doped upconverting nanoparticles with a focus on the

mechanisms of upconversion and the various synthetic approaches for their preparation: thermal decomposition, hydrothermal method, coprecipitation, sol–gel method, combustion method, and flame synthesis. The choice of the host material and of the lanthanide dopant ions is crucial to the targeted application. The authors then describe the different strategies to achieve surface modifications for rendering the nanoparticles hydrophilic and for bioconjugating them as required for targeting specific biological markers. The two subsequent sections are devoted to applications in bioanalysis, medical imaging, and drug release. Lanthanide-doped upconverting nanoparticles have indeed found widespread use for the sensing of cell temperature and as optical probes for metal ions analysis as well as in immunoassays. More recently, they have been part of the strategy for developing cell and small organism/ animal imaging, including multimodal bioimaging. Finally, beacons based on upconverting nanoparticles have been constructed with the aim of inducing *in situ* drug release or energy transfer for triggering the formation of singlet oxygen. This is of interest in photodynamic and photothermal therapy of cancer. The last section provides the reader with clues on the challenges faced in order to turn lanthanide-doped upconverting nanomaterials into versatile platforms for the generation of the nanotheranostic agents needed in nanomedicine.

**Jean-Claude G. Bünzli**
**Vitalij K. Pecharsky**

# Contents of Volumes 1–46

# Index of Contents of Volumes 1–47

Chapter 269

# Organic Chromophores-Based Sensitization of NIR-Emitting Lanthanides: Toward Highly Efficient Halogenated Environments

**Ignacio Hernández\* and William P. Gillin[†,‡]**

*\*Dpto. CITIMAC, Facultad de Ciencias, Universidad de Cantabria, Santander, Spain*
*†Materials Research Institute and School of Physics and Astronomy, Queen Mary University of London, London, United Kingdom*
*‡College of Physical Science and Technology, Sichuan University, Chengdu, People's Republic of China*

## Chapter Outline

# 1    INTRODUCTION

## 1.1    Motivation and Background

Infrared emitters based on materials with lanthanides, and especially those containing $Nd^{3+}$, $Er^{3+}$, and $Yb^{3+}$, are of great interest for telecommunications, photonic, optoelectronic, and biological applications due to the high monochromaticity and potential long emission lifetimes in the near infrared (NIR) range, and in particular in the biological media and silica low-loss windows. A strong effort has been devoted to the research of compounds based on these emitters, particularly for potential use in lasers and amplifiers. At the current time, the success of infrared lasers and amplifiers based on these emitters is proved in fields such as manufacturing and telecommunications, but extending their potential is still a very active field involving multidisciplinary research.

Most fibers used in photonic devices, conventional fiber lasers, and modern optical telecommunications are typically made of silica ($SiO_2$) glass. Economic and historic reasons based on the performance of available lasers and detectors, together with its advantageous properties, have motivated this. Silica is extraordinarily transparent in the visible and NIR range which favors its generalized use in fiber applications, but losses are even smaller in a number of so-called windows in the infrared range (Fig. 1).

The first NIR transparency window for silica fibers is 800–900 nm and was originally used taking advantage of GaAs/AlGaAs-based laser diodes and light-emitting diodes (LEDs) and silicon photodiodes. However, due to the fact that the absorption losses are still relatively high and the lack for suitable optical amplifiers, this window is only employed for short-distance fibers and telecommunications.

The silica losses are greatly reduced at around 1–1.3 μm and the fibers' chromatic dispersion is at a minimum. This minimizes dispersive broadening and facilitates high data rates. This second window was originally employed for long-distance telecommunications.

Modern silica fibers show an enhanced transparency in the third window at around 1.5 μm with the lowest losses in the so-called C-band and the closest sub-bands S, L and U. Low losses, together with the high performance and the development of erbium-doped amplifiers, have contributed to its extensive use in telecommunications.

Despite the phenomenally low losses obtained at these wavelengths ($\sim$0.3 dB/km) with modern manufacturing techniques, regeneration of the
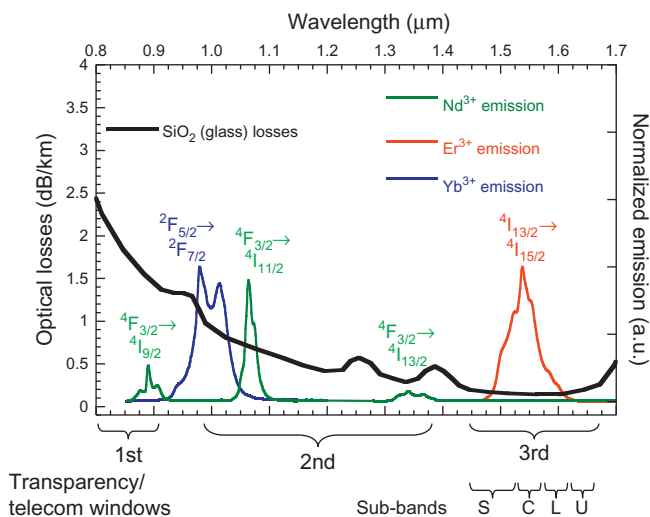
**FIGURE 1** Absorption of commercial silica ($SiO_2$) fiber (thick line), overlapped with the typical emission spectra of $Nd^{3+}$, $Er^{3+}$, and $Yb^{3+}$. The labels identify the bands with the associated f–f transitions of the corresponding ion (see figure 2).

optical signal is still required every 100 km or so. In addition to these intrinsic absorption losses, there are other situations such as fiber splices and optical splitters, which reduce signal intensity and hence require amplification of the optical signal. In early telecommunication systems, this regeneration required the translation of the optical signal back to an electrical signal before pulse shaping and retransmission by a new laser. However, all optical amplifiers (and in particular erbium and lanthanide fiber amplifiers) were introduced resulting in a considerably better performance in terms of speed and signal/noise.

The variety of narrow intraconfigurational (f–f) transitions of the trivalent ions of the lanthanides, whose energies show little dependence on the host matrix, and the long lifetimes for spontaneous recombination have favored the use of some of them, such as $Nd^{3+}$, $Er^{3+}$, $Yb^{3+}$ (Figs. 1 and 2), $Pr^{3+}$, $Tm^{3+}$, and $Ho^{3+}$ in optical amplifiers for the NIR windows relying on stimulated transitions between levels in excited ions within a length of optical fiber. 1.06 μm $Nd^{3+}$ lasers and amplifiers were proposed in the 1960s (Koester and Snitzer, 1964); they initially captured the attention of researchers (Becker et al., 1999) and are still being used, mainly for laser applications. It was the development of the $Er^{3+}$-doped fiber and the idoneity of transmission in the third band that favored the triumph of the technology of the erbium-doped fiber amplifier after 1987 (Meats et al., 1987), which has allowed for the rapid proliferation of long-distance fiber-optic telecommunications operating at a wavelength of 1.5 μm of erbium. Importantly, $Yb^{3+}$ also was found to show
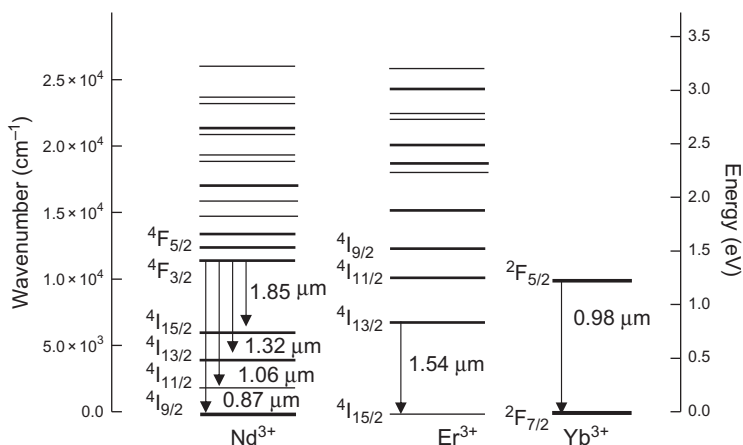
**FIGURE 2**   Generic electronic configuration of $Er^{3+}$, $Nd^{3+}$, and $Yb^{3+}$. *After Dieke and Crosswhite (1963)*.

amplification and laser action at ~1.0 μm (Hanna et al., 1988; Lacovara et al., 1991) and thus widely used in diverse high power-related (mainly laser) applications.

Amplification of the optical signal, and similarly laser action, occurs when the stimulated emission from the emitter's states is induced by the incoming photons (signal), resulting in a coherent (in phase) replication of the optical signal (Fig. 3). Apart from optical considerations regarding the cavity (material medium in which the photons are produced), a population inversion of the emitting centers is required for the amplification, meaning that a majority of the emitters must be in the emitting excited state to allow for the subsequent resonant emission of photons identical to the signal present in the cavity. The stimulated emission probability, given by the corresponding *B* Einstein coefficient, is proportional to the spontaneous radiative decay of the emitting state (given by *A* Einstein coefficient), depending mainly on (material) parameters describing the excited and ground states and their coupling to the radiation (see below (Section 3) for a more elaborate description of the emission processes). Importantly, the inversion is achieved upon sufficient population of the excited state via absorption of the pump, and therefore very much dependent on the absorption cross-section, $\sigma_{Abs}$, related to the absorption coefficient, $\varepsilon$, as $\sigma_{Abs} = \varepsilon \times N$, with $N$ the density of absorbing centers. The potentially long-lived, relatively narrow-band intraconfigurational f–f transitions of lanthanides are ideal excited states for producing the population inversion and stimulated emission in the presence of a pump and signal, and these have been successfully employed in lasers and amplifiers for a long time. Commercial devices based on the amplifying properties of many lanthanide systems (and particularly $Nd^{3+}$, $Er^{3+}$, and $Yb^{3+}$) are exploited not only in
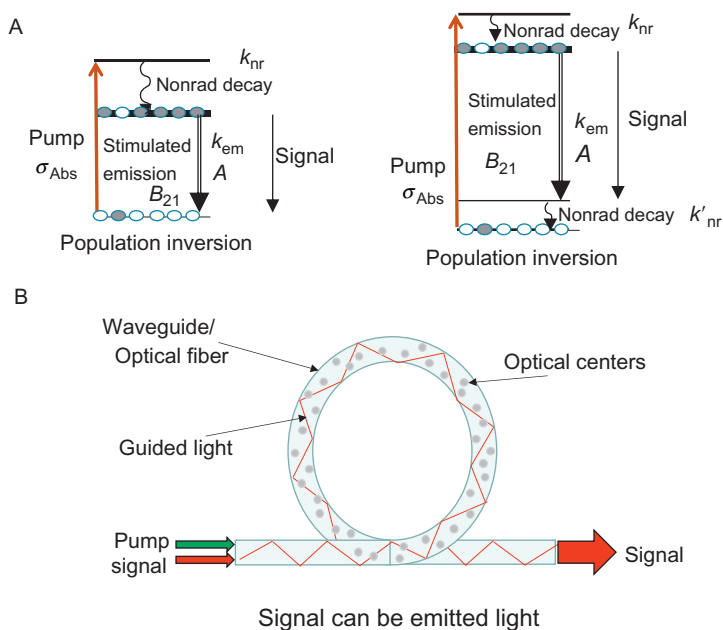
**FIGURE 3** (A) Three- and four-level laser scheme and some related processes and magnitudes, including the absorption (and corresponding cross-section, $\sigma_{Abs}$), nonradiative decays (with associated rate constants $k_{nr}$), and probability of stimulated emission, given by the corresponding Einstein coefficient $B$ (which is proportional to the spontaneous emission probability, $k_{em}$, given by the Einstein coefficient $A$). Note that the stimulated emission involves a different level than the absorption. (B) Schematic representation of an optical amplifier or fiber laser.

communications but in other fields like, for instance, lasers for manufacturing or sensor applications.

Other interesting prospective applications of NIR-lanthanide (organic) materials due to their low-energy excitation and emission properties (including potential visible emission, via upconversion) include luminescence-related applications in biological media, for instance in imaging, such as markers, probes, for therapy, etc. (Bünzli, 2004; Bünzli and Eliseeva, 2013; Faulkner et al., 2005). Due to the nature of the surrounding medium and common strategies for sensitization, high-efficiency (long lifetime) phenomena, and even upconversion of radiation, much of the phenomenology of organics-based NIR-lanthanide emitters described in this chapter applies to NIR-lanthanide emitters for biological applications, too.

Novel secret-ink-related applications have been proposed (White et al., 2009b) for NIR emitters, which add to those of upconverting materials with NIR-absorbing and/or emitting lanthanides (Meruga et al., 2012). Besides the biological applications (Chatterjee et al., 2008; Nyk et al., 2008), NIR-based upconverters have been thought to be of interest for photonic purposes

(Lenth and Macfarlane, 1992), illumination (Milliez et al., 2006), and solar power conversion for photovoltaic applications (Trupke et al., 2002). A dedicated chapter for solar energy applications of lanthanide-based materials exists in this series of books, which reviews properties of NIR-emitting lanthanides for optical downshifting, upshifting, and other solar energy-related uses (Bünzli and Chauvin, 2014).

The lanthanide atoms show a general electronic configuration given by [Xe] $4f^{n-1}5d^16s^2$ or $[Xe]4f^n5d^06s^2$. In the trivalent ions, the 4f orbitals, mainly determining their optical properties, are occupied from $4f^1$ to $4f^{14}$ and the outer shells $5s^25p^6$ are fully filled. In a free lanthanide ion, the 4f electrons are only affected by the nuclear attraction, interelectronic repulsion and weak spin–orbit coupling. It is complicated to describe rigorously the electronic configuration of the lanthanides, particularly in solids and molecules, considering the interactions between the many electrons, and subjected to the symmetric external interactions. However, since the screening of 4f electrons by the outer levels is significant, we observe that the relative energies of the multiplets are always within given ranges and show little dependence when doped in different matrixes (Fig. 2). The electronic fingerprint of the f–f electronic transition allows for a relatively easy assignment, on the bases of previous measurements, such as the Dieke diagram or measurements in other matrixes (Dieke and Crosswhite, 1963). Upon given electronic excitations of the lanthanides, a number of (partially forbidden) f–f emissions (radiative decay) can occur in the infrared range, not only from excited to ground state but also from a excited state to a lower-lying excited state, as can be observed in Fig. 2.

An innumerable amount of lanthanide-doped inorganic crystalline and glassy matrixes, from silica and alumina to other oxides and fluorides, chlorides, phosphates, borates, tungstates, etc., have been proposed and successfully employed to attain enhanced lanthanide luminescence properties, laser and amplification action, more and more tending toward an on-chip solution (waveguide amplifier or laser) (van den Hoven et al., 1996), which can be of interest in areas such as optoelectronics, biology and sensing. The search for a suitable matrix is not only a matter of improved optical properties of the lanthanide dopants but, importantly, related to the concentrations of these ions, as it can be observed that for the characteristic low absorption coefficients ($\varepsilon \sim 1$ cm$^{-1}$), higher concentrations (in principle) result in better optical performance (see Fig. 4). Thus, in principle, it would be desirable to obtain high concentrations of optically active lanthanide ions, but (a) they are relatively insoluble in most matrixes, and (b) segregation at increased concentrations causes a decrease in their optical properties, even in defect-free compounds due to energy transfer between the ions (ion–ion interactions) resulting in strong cross-relaxation and the extinction of excitations. The concentration of the lanthanides in inorganic matrixes is, in fact, a critical issue in the sense that concentrations in the order of $\sim 10^{20}$ ions/cm$^3$ coupled with the typically low absorption cross-sections arising from the parity and spin
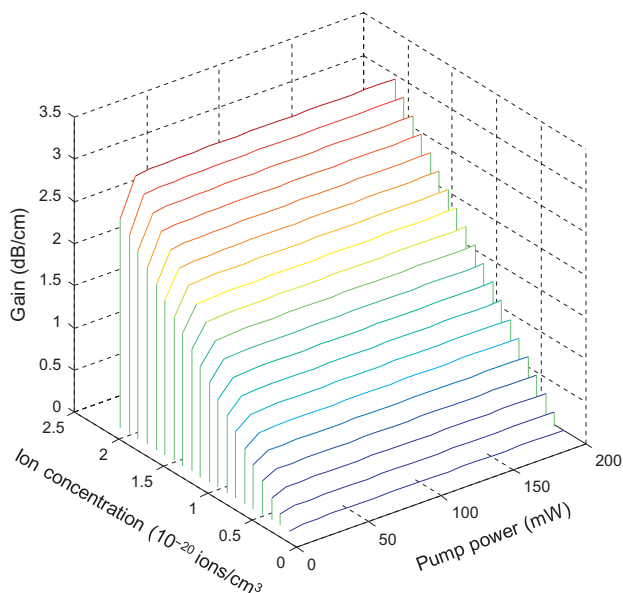
**FIGURE 4** Estimate of gain as a function of $Er^{3+}$ concentration and pumping power for a typical inorganic compound with pumping at 1.48 μm and emission at 1.54 μm. Realistic values (fiber core radius: 2 μm, lifetime of the excited state: 11 ms, absorption cross-sections: $3 \times 10^{21}$ $cm^2$ (stimulated), $1.5 \times 10^{21}$ $cm^2$ (stimulated); emission cross-sections: $1.5 \times 10^{21}$ $cm^2$ (stimulated), $0.5 \times 10^{21}$ $cm^2$ (stimulated), spectral overlap 1) were employed for characterizing the medium. Calculation are based on the simple model (Xia et al., 1998) for the gain of an erbium amplifier derived from the dynamic equations describing the population and depopulation of the emitting $Er^{3+}$ state upon pumping. Only one-photon interactions have been included for simplicity. The inclusion of other processes like excited state absorption, or energy transfer would result in a decreased value for the given pumping power, mainly at the higher pumping powers.

forbidden f–f transitions ($10^{-21}$ $cm^2$) would require relatively long working distances and high pumping powers in order for the amplifier to produce the desired stimulated emission and amplification (Fig. 4).

YAG (yttrium aluminum garnet) and ZBLAN (Zr–Ba–La–Al–Na fluoride glass) are canonical matrixes for enhanced performance of $Nd^{3+}$, $Er^{3+}$, and $Yb^{3+}$, with extended commercial uses. However, currently the record amplification to our knowledge is held by the $KGdLu(WO_4)_2$ matrix lattice-matched doped with 47.5% $Yb^{3+}$, with values up to nearly 1000 dB/cm at 981 nm (excitation 932 nm), which underlines the importance of good dispersion and heavy doping in lanthanide-doped systems (Geskus et al., 2012).

Interestingly, some of the studied inorganic matrixes show remarkable NIR luminescence properties in the bulk and also as nanoparticles. The improved understanding and quality of production of NIR-emitting lanthanide-doped materials, and particularly nanoparticles, have also benefited the range of possibilities for amplification, and particularly in organic environments, by

means of the incorporation of lanthanides into polymer waveguides (Zhang et al., 2007a). The lanthanide-doped nanoparticles activate the polymers, and despite the necessary cautions for transparency, they offer the possibility of synergizing some of the organics' and lanthanides' properties (efficiency, control, processing, integration, mechanical and thermal properties, etc.). Still, this approach is out of the scope of this review which focuses on the *intrinsic* advantages of the NIR lanthanides in organic environments, and mainly those derived from the organic-lanthanide interaction. Importantly, nanoscale NIR lanthanide-based materials allow for enhanced properties toward biological applications too. Lanthanide-doped nanosized phosphates and fluorides are among the most used materials (typically with organic functionalization and coatings to enhance solubility), with $NaYF_4$ being one of the most promising and employed matrix (Heer et al., 2004), due to its high efficiency and synthetic control (size, structure, morphology, doping, and coating), and the interplay between visible and NIR states, including upconversion. Despite maybe in organic environments, these purely inorganic nanosystems are not the subject of this chapter save when an organic–inorganic sensitizing interaction exists, conforming hybrid systems.

A possibility for overcoming the deficiencies of inorganic materials involves the use of lanthanides in combination with organics. The advantages of organics-based lanthanide materials for optical applications are twofold. On the one hand, organic ligands can chelate the lanthanide ions and polymers dissolve them, thus allowing a fine control of the concentration, either by making pure lanthanide compounds and controlling the distance and architecture by engineering the chemical nature of the ligands or by diluting the lanthanide complexes with optically inactive complexes or in polymer matrixes. This strategy increases the solubility of the lanthanides, solves the problem of aggregation/segregation, and provides very interesting possibilities based on NIR-lanthanide complexes and pseudo-ions for biological applications. A number of interesting polymer matrixes have been proposed for fibers and waveguides (Ma et al., 2002). On the other hand, and even more importantly, lanthanides in organic environments allow indirect excitation of the lanthanide ion through the organics, involving energy transfer to the lanthanides' states from allowed excitations in the ligands and providing orders of magnitude higher excitation rates, a phenomenon called sensitization from the organics. This is also beneficial for optical applications of enhanced NIR-based lanthanides in biological systems. The main drawbacks of lanthanides in organic media include the fact that in general the lanthanides' states can be relatively sensitive to vibrational quenching, which becomes important in the case of states in the infrared range and in an organic environment or matrix. This phenomenon is a consequence of the so-called gap law (see Section 3.2) which relates the vibrational quenching probability with the number of overtones of the vibrational modes needed to bridge the gap to lower-lying states. In NIR-emitting lanthanides in organic environments, it is typical that few overtones are required due to the high

energy of hydrogenated vibrational modes and the reduced energy gap. This results in a considerable decrease of the lanthanide emission efficiency and life-time, due to this predominant quenching channel. The use of heavier ligands, in which hydrogen atoms are substituted by deuterium or heavier atoms such as fluorine, has been proposed as strategy to improve the lanthanide performance in organic media (see Section 4).

## 1.2 Organic-Based NIR-Emitting Lanthanide Photonic Devices

Despite the difficulties in keeping the long lifetimes, amplifier and lasers based on $Nd^{3+}$ and $Er^{3+}$ emitters in organic material environments have been produced, although at present none of them take advantage of sensitization. Apart from the ones that include nanoparticles in organic matrixes, all of them incorporate $Er^{3+}$ or $Nd^{3+}$ complexes in organic polymer matrixes, to allow for increased solubility and concentrations higher than $10^{20}$ ions/cm$^3$ conferring them with gain and laser activity in devices that are a few centimeter in length. Importantly, the optical features of the host polymer are critical to confine the light and minimize the losses in the desired range. A number of polymers have been proposed as hosts (Ma et al., 2002). The first amplifiers based on $Nd^{3+}$ involved high concentration Nd(III) chloride-doped polymers (Chen et al., 1993; Karve et al., 2000) allowing for amplification in channel waveguides upon high power 800 nm excitation. Relative control of the vibrational quench-ing via fluorination or deuteration (see below) allowed for gain in systems based on the fluorinated β-diketonate $Nd^{3+}$ complex [Nd(hfa)$_3$] (hfa = hexafluoroacetylacetonate) in polyimide matrix and the deuterated [Nd(hfa-$d$)$_3$] in perdeuterated PMMA (polymethyl methacrylate) matrixes (Fig. 5) for $Nd^{3+}$ direct excitation (Kuriki et al., 2000). More recently, the β-diketonate [Nd(tta)$_3$phen] complex (tta = thenoyl-trifluoroacetonate, phen = 1,10 phenanthroline) in the partially fluorinated cross-polymer of 4,4-(hexafluoroisopropylidine) diphthalic anhydride (6FDA) and 3,4-epoxycyclo-hexylmethyl-3-4-epoxycyclohexane carboxylate (UVR) showed an enhanced behavior with limited quenching capable of producing 1.4 dB/cm gain at 1.06 and 0.5 dB/cm gain at 0.87 μm in channel waveguides with cycloaliphatic epoxy prepolymer as side cladding (Yang et al., 2009, 2010). The same material allowed for the implementation of an integrated continuous wave solid-state Nd-polymer laser above a threshold of 50 mW of absorbed pump power at 800 nm direct excitation (Grivas et al., 2010). Similarly, Nd(III) trifluoroacetate [Nd(CF$_3$COO)$_3$] in DMA (*N,N*-dimethylacetamide) also produced laser action in a 13-mm-long liquid laser cavity with a threshold of 86.4 W, which has been considerably reduced by employing polymer poly(hexamethylene *p*-phenylenediacryl amide) as the host (Yoshioka et al., 2011, 2012).

$Er^{3+}$-based organic amplifiers have also been proposed, as late as 2005, based on $Er^{3+}$ β-diketonates (Fig. 5) dissolved in polymers such as epoxy Novolac resin SU8. The low performance upon direct excitation of $Er^{3+}$ at
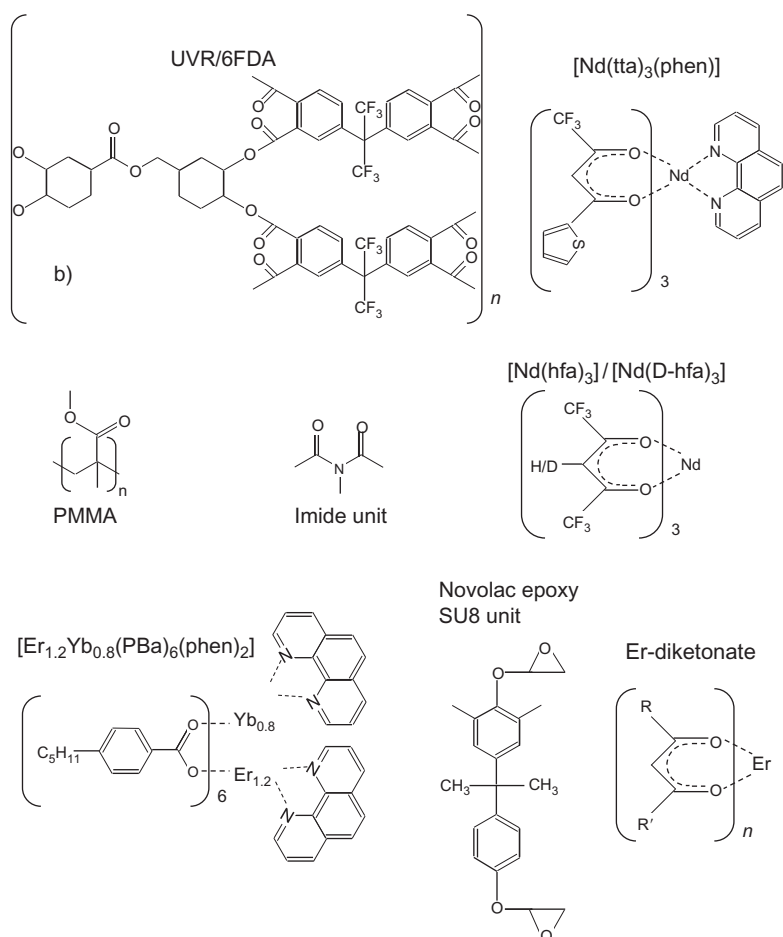
**FIGURE 5** Schemes of some polymer matrixes and coordination complexes with organic ligands of $Nd^{3+}$ and $Er^{3+}$, which have been employed for organics-based amplifying waveguides and lasers upon direct excitation on the lanthanides' states.

1450 and 980 nm has promoted the use of $Yb^{3+}/Er^{3+}$ codoping to enhance the pump due to the larger absorption cross-section of the $Yb^{3+}$ and by exploiting $Yb^{3+}$-to-$Er^{3+}$ energy transfer (see below), a strategy which is also used in inorganic matrixes. With $Er^{3+}$ concentrations of 1% and 10% $Yb^{3+}$, 1.6 dB/cm gains have been obtained at 180 mW pumping (Wong et al., 2004, 2005b). PMMA doped with QB-Er, erbium(III) tris-nitrato-tris-[4-[4-(3-triethoxysilylpropoxy)-phenylazo-oxyide]-phenyl-diphenylphosphine, shows 1.34 dB gain for 1.6 cm length (Le Quang et al., 2006). Interestingly, $Er^{3+}$–$Yb^{3+}$–pure organic polymeric medium $[Er_{1.2}Yb_{0.8}(PBa)_6(phen)_2]$, PBa = 4-pentylbenzoate, 1.2 cm waveguides with SU8, and PMMA-GMA

(GMA = glycyl-methacrylate) cladding yield gains of 5.2 and 6.5 dB, when pumped at 976 nm (Chen et al., 2009).

As we have previously commented, this report emphasizes on the prospective of NIR-based organic materials incorporating the lanthanides as constituents, and particularly including chromophores to take advantage of enhanced indirect excitation. In the following sections, we therefore develop the bases and progress of the field of organics-based NIR-emitting containing lanthanides with the focus on sensitization and creation of an efficient lanthanide environment, together with other related relevant processes that may contribute to the enhanced optical performance.

## 2 SENSITIZATION OF NIR-EMITTING LANTHANIDES

Sensitization of infrared-emitting lanthanide ions (and particularly $Er^{3+}$) for optical amplification has been pursued in inorganic materials by a number of strategies, particularly lanthanide doping in semiconductors, with the aim of exciting the lanthanides' luminescence properties upon pumping involving the enhanced optical transitions in the semiconductor bands (Daldosso et al., 2005; Han et al., 2001; Wojdak et al., 2004). However, lanthanides' solubility in most inorganic semiconductors is very poor, which makes synthesis of the doped materials challenging, often requiring ion implantation. Furthermore, importantly, the extremely short spontaneous recombination time of the excitons in semiconductors causes severe difficulties in sensitization, this mechanism being extremely favored in the competition with the sensitization deactivation channel. Alternatives include controlled codoping of the optically active lanthanides with other ions, acting like (longer lived or more energetically favored) intermediating excitation traps to excite the lanthanides (Fukushima et al., 2005; Xiao et al., 2012).

Importantly, organic sensitization has emerged as an interesting strategy for enhancing indirect excitation of NIR emitting lanthanides. Organic chromophores-mediated sensitization of lanthanides shows a number of advantages (see below) which we discuss in this chapter and has been studied for more than 70 years, when it was first observed in UV-excited $Eu^{3+}$ chelates, in which the lanthanide was encapsulated and excited indirectly via β-diketonate organic ligands (Weissman, 1942). However, the organics-based sensitization of NIR-emitting lanthanides involves a number of challenges, mainly derived from the presence of the lanthanide in an organic environment, but also due to the coupling of the chromophore and lanthanide states.

## 2.1 Electronic Configuration of Organic Molecules and Semiconductors

Typically, either considered molecularly or extendedly, organic compounds or coordination complexes with organic ligands present a diamagnetic

ground-state configuration arising from the discrete $HOMO^{2n}$–$LUMO^0$ configuration in which typically all the individual spins are paired, resulting in a total spin 0, $S = 0$, singlet state, $S_0$. Thus, the first electronic excitation leading to the $HOMO^{2n-1}$–$LUMO^1$ constitutes the first excited state with $S = 1$, a triplet state $T_1$. The second excitation results typically in a singlet $S_1$ with paired electrons, and it is the allowed $S_0 \rightarrow S_1$ the first intense absorption that should be observed in the optical absorption spectrum. This is due to the fact that to a first approximation, only transitions between states with the same spin quantum number are allowed, $S_0 \rightarrow T_1$ being spin forbidden. Reciprocally, the emission spectrum typically occurs from the $S_1 \rightarrow S_0$ (fluorescence) process. The molar extinction coefficients for these allowed transitions are considerably high, in the order of $10^4 \, cm^{-1}$, and thus, the spontaneous decay times are in the order of nanoseconds. Employing these high oscillator strengths, one can potentially substantially enhance the absorptivity of lanthanides toward photoluminescence (PL) applications (and particularly for NIR, in the case of $Yb^{3+}$, $Er^{3+}$, $Nd^{3+}$).

Importantly, it is usual that the fluorescence spectrum of the organics occurs at longer wavelengths with respect to the absorption spectrum. This is called the Stokes shift and it is a consequence of the redistribution of electrons and resulting rearrangement of atoms in the electronic excited state in a vibrating molecular environment (Atkins, 1976; Di Bartolo, 1968). The energies and dynamic properties of electronic states of color centers in a vibrating environment are contributed by the matrix's vibrations. This causes the consideration of vibronic (electronic, together with vibrational) states for a complete description of the dynamic system. In the so-called Born–Oppenheimer approximation, the electronic rearrangement times are orders of magnitude faster than the nuclear rearrangement times, and the electrons immediately follow the moving nuclei. Under this condition, it can be shown that the vibrational part of the wave-function, $\chi$, can be separated (Di Bartolo, 1968). As a consequence, the electronic state, $\psi$, can be considered as split in a set of vibrational replicas, associated to the corresponding levels of the quantum states of the different symmetry oscillations (modes) of the environment (Fig. 6). Thus, the vibronic states can be considered as a quasicontinuous set due to the rich vibrational density of states. The vibrational levels are populated according to the temperature and the electronic transitions can involve the creation and destruction of vibrational modes, which results in broad bands, of typically more than a hundred nanometers ($\sim 3500 \, cm^{-1}$, $\sim 0.4 \, eV$) when measuring the absorption and emission spectra. This is the appearance of the envelope curve that involves all possible vibronic transitions at the given temperature.

Importantly, the coupling between structure and electronic cloud in the molecule may be such that the electronic excitation can cause an intrinsic structural rearrangement (represented by the horizontal (mode coordinate) displacement of the excited states, $\psi_{ex}$, and the ground state, $\psi_{gr}$, in Fig. 6). This occurs as a
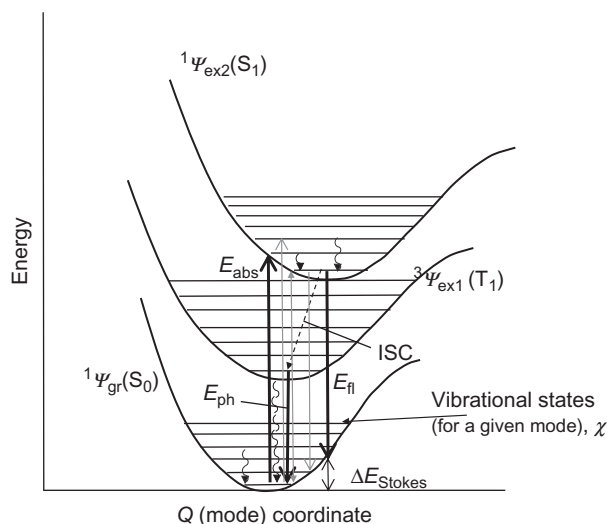
**FIGURE 6** Schematic representation of the electronic configuration of an arbitrary organic chromophore and potential optical processes within it. The vertical axis represents the energy and the abscissa axis is the distortion in the mode coordinate (only one vibrational mode is represented, for simplicity). Absorption, fluorescence, and phosphorescence vibronic transitions are represented by solid vertical arrows. The predominance of the vertical vibronic transitions (without change in the coordinate $Q$, from the electronic equilibrium state (corresponding curve minima)) causes the Stokes shift, $\Delta E_{Stokes}$, implying the emission at lower energies than absorbed (notwithstanding this, other transitions from/to different vibrational states involving the creation or destruction of a different number of overtones of the given mode are possible (some of them represented in gray)). From the graph, it is observable that larger displacements of the excited electronic state, $\psi_{ex}$, configurational curve, implying larger electron–phonon coupling, cause larger Stokes shift. Nonradiative transitions can be vibrational (represented by curly arrows), even involving changes between electronic states, or intersystem crossing (ISC, dotted arrow, between the electronic states).

consequence of the change in the electronic distribution for the reaccommodation of the new hole/electron configuration in the molecular orbitals upon this electronic excitation, which causes a different electrostatic potential for the charged nuclei. These geometric differences between the ground and excited states, together with the most likely occurrence of the vertical transitions (in which the structure is "frozen" at departing state equilibrium coordinate and only the electron initially changes state) for a minimal creation or destruction of vibrational overtones (see Figure 6) causes the absorption and emission at different energies (Stokes shift) (Atkins, 1976; Di Bartolo, 1968).

In this vibronic scheme for the description of the optical processes, the change of energy along vibrational deexcitation within an electronic state, or by changing the electronic state, is possible in the absence of light interactions (curly arrows in Fig. 6). Electronic relaxations along vibrational states (Fig. 6) are rapid and efficient at ambient and low temperatures, so the process can be as short as $10^{-13}$ to $10^{-11}$ s for allowed relaxations within

the same electronic states, and somewhat longer if a quantum forbidden transition or a connection between different nature electronic states must be taken into account (for example, multiphonon nonradiative relaxation from a excited state to a lower-lying electronic state or ground state (Fig. 6)). Importantly, it is found that for this type of nonradiative quenching, the rates are exponentially dependent on the effective number of phonons of given energies necessary to bridge the electronic energy gap (see below for a more explicit derivation in the case of a lanthanide state, which is also subjected to these rules).

The $T_1$ state (first excited state) may not be completely transparent, and in some cases, it can be photoexcited and subsequently decay radiatively (phosphorescence) through the relaxed spin forbidden transition from/to ground state. Nonetheless, due to the (in principle) spin forbidden nature of the transition, the lifetime of a triplet state is long (approx. in the $10^{-4}$–10 s range), which is considerably longer than the typical lifetime of fluorescence processes (typically nanoseconds). (Note that phosphorescence is a different phenomenon to delayed fluorescence, which occurs at the $S_1 \to S_0$ energy, but with delayed dynamics.) In organic semiconductors, $T_1$ can typically be more efficiently excited by the injection of charges (electrons and holes) in organic diodes, and in general by an enhanced interaction mixing spin states, including external fields, for instance, which allows the creation of triplets upon singlet excitation. The process of creation of triplets from singlets is called intersystem crossing (ISC). This involves an electron spin interaction mixing the singlet and triplet states that allows that a number of (optically) excited singlets decay nonradiatively to triplets. The ISC requires approximately $10^{-8}$ to $10^{-7}$ s for such a nonradiative spin forbidden transition, which is the same order of magnitude as the typical lifetime of an excited singlet state. Therefore, ISC can be completed to a certain degree in the timescale of fluorescence. In general, the triplet's low emission probability and its relatively low-energy gap with respect to the ground state in comparison with the singlet cause a considerable higher probability of nonradiative quenching, either by multiphonon radiationless phenomena or by cross-relaxation mechanisms such as triplet–triplet annihilation resulting in singlet repopulation. Phosphorescent processes, derived from direct emission from the triplet are thus typically limited in organic semiconductors unless ISC, resulting in a large population, and subsequent increase of $T_1 \to S_0$ radiative decay, is enhanced. A number of triplet emitters, some of them incorporating heavy transition metal ions that can favor ISC through large spin-orbit coupling, have been proposed.

In the case of metal complexes with organic ligands, and depending where in the space defined by the molecule the ground and electronic state's wavefunction lies, the nature of the singlet and triplet transitions can involve metal-to-ligand charge transfer (MLCT), ligand-to-metal charge transfer (LMCT), ligand-to-ligand charge transfer (LLCT), or being simply intraligand transitions. In general, it is possible that several of these processes lie within a

similar energy range, as a consequence of the small energy differences between the corresponding molecular orbitals and multielectron states, and multiple states with singlet and/or triplet character may overlap (in terms of electronic energies alone or, in general, in vibronic terms) for a given molecule. This rich structure and possible interactions between the states may complicate very much the electronic configuration of the chromophores. Interestingly, if the states involved in the excitation or deexcitation of the metal complex encompass a wave-function lying on or nearby the metal, the ISC or singlet–triplet mixing may be enhanced due to the heavy metal ion effect. Higher atomic numbers provide increased spin–orbit interaction, capable of relaxing the pure $S=1/S=3$ character of the electronic states.

Importantly when the lanthanide is coordinated to the organic ligands or organic moieties, the interactions arising from the ligand-lanthanide bond or the change in geometry with respect to the isolated state may affect the electronic levels and result in a different overall electronic configuration of the metal-ligand complex itself with respect to that of the organic ligand alone. This is particularly important in general in organo-metallic or coordination complexes, and if the presence of the lanthanide determines that the transitions between states involve MLCT or vice versa, but can also be the case in LLCT states. The electronic configuration of the complex itself and the differences when unbound can be measured by comparing the optical properties of the ligand alone and the metal complex. Trivalent lanthanide f levels are typically internal and independent of the bond. The complex's absorption is in general not very dependent of the lanthanide and an optically inactive (rare earth) ion such as $Gd^{3+}$, $La^{3+}$, $Lu^{3+}$, or $Y^{3+}$, not providing states in the optical range are typically employed to gain access to the magnitudes relating to the purely organic transitions without new intermediate states, but in a realistic configuration for the chromophore. The energies of the chromophores may depend on the packing or environment as a consequence of $\pi$–$\pi$ or other aggregation-dependent molecular interactions (Hernández and Gillin, 2009), and thus it is usual that solutions, different conformations (isomers), or different polymorphs show different energies and associated spectra.

## 2.2 Electronic Configuration of Lanthanides in Material Environments

As we have previously said, the relative energies of lanthanides' multiplet states arising from the f–f electronic configuration are not significantly dependent on the host matrix. These states are typically described in the Russell–Saunders scheme for coupling, focusing on the overall angular momenta (see for instance Ronda, 2007). Strictly speaking, the Russell–Saunders model is not fully adequate for the lanthanides since in heavy atoms the interaction between electrons is strong but it is largely used in the lanthanides in the view of simplicity. In the Russell–Saunders coupling scheme, $L$ is the quantum

number that accounts for the total orbital angular momentum that defines the energy state for a system of electrons in the presence of orbit–orbit coupling. $L = 0, 1, 2, 3, 4, 5$, and 6 correspond to the term letters S, P, D, F, G, and H, respectively, as the atomic states. The total spin is $S$ and the total angular momentum is $J$, with the spin–orbit coupling determining the condition $|L - S| \leq J \leq L + S$. When the 4f orbitals are less than half filled, $J = |L - S|$, and otherwise, $J = L + S$. The electronic states arising from the 4f configurations are described by the Russell–Saunders symbols $^{2S+1}L_J$ ($^{2S+1}\Gamma_J$, $L \sim \Gamma$ when in a material medium). Each $^{2S+1}\Gamma_J$ term is split further into a $(2J + 1)$ multiplicity. For instance, the ground term of $Yb^{3+}$ is split into $^2F_{7/2}$ and $^2F_{5/2}$ (in increasing order of energy). Moreover, the $J$ of the ground level is given by $J = J_{\min}$ if $n < (2l + 1)$ or $J = J_{\max}$ if $n > (2l + 1)$, with $n$ being the number of electrons in the orbital l and thus if $n < (2l + 1)$, the energy of the levels increases with increasing values of $J$, while if $n > (2l + 1)$, the opposite is observed. For instance, the ground $Nd^{3+}$ ($4f^3$) term is split into $^4I_{9/2}$, $^4I_{11/2}$, $^4I_{13/2}$, and $^4I_{15/2}$, and for $Er^{3+}$ ($4f^{11}$) into $^4I_{15/2}$, $^4I_{13/2}$, $^4I_{11/2}$, and $^4I_{9/2}$, both in increasing order of energy.

When a lanthanide ion is inserted into a fixed ligand environment, the spherical symmetry of its electronic structure is broken and the remaining $(2J + 1)$ degeneracy of its electronic states is partially lifted depending on the symmetry for the ion site or the shape of the coordination polyhedron (Görller-Walrand et al., 1998). Due to the shielding of the outer electrons, the $4f^n$ electronic wave-function observes a weak influence of the outer fields and a weaker mixture with the surrounding orbitals, resulting in a minor influence of the $^{2S+1}\Gamma_J$ state splitting (a few hundreds of $cm^{-1}$) as a consequence of the ligand coordination. This perturbation of the ligand environment is still responsible for observable fine spectral structures. In a simplified ligand-field model, the ligand-field term in the electronic Hamiltonian can be expressed as

$$\sum_{k,q,j} B_{kq} C_{kq} \tag{1}$$

where the summation involves $j$, for all 4f electrons, $B_{kq}$ represents each of the ligand-field parameters (commonly treated as phenomenological parameters) and $C_{kq}$ represents the corresponding component of the tensor operators transforming like spherical harmonics. The $B_{kq}$ parameters depend on the characteristics of 32 crystallographic symmetry groups, which can be evaluated by $k$ and $q$ with $q \leq k$ in any case.

Although the splitting caused by the ligand field in the f states is relatively small in comparison to the splitting of less screened electrons like, typically, d-block ions, it can be measured. In fact, this splitting can be used to build a three-level laser or amplifying system, by using field states $^{2S+1}\Gamma_{JM}$ as pumping levels for the corresponding emissions from lower-lying levels, $^{2S+1}\Gamma_{JM'}$ (typically with $E(^{2S+1}\Gamma_J < ^{2S+1}\Gamma_{JM'})$), for instance in $Yb^{3+}$ (excitation at

980 nm for emission at 1050 nm) or in $Er^{3+}$ (excitation at 1480 nm for emission at 1540 nm).

$J$-mixing in the ligand field means that $J$ can no longer considered a pure valid quantum number, and relaxes transition rules relying on conditions about $J$. This fact, together with the limitations of the Russell–Saunders coupling scheme, causes that $J$ is considered an "approximate" quantum number or label, which describes phenomenologically field states.

The accurate measurement of the crystal field parameters can be difficult in a solid environment because it is often the case that upon high concentrations, lanthanides occupy various positions in the matrix, or slightly distorted sites in the case of softer materials. Thus, different coordination polyhedra caused by the presence of these multisites or tensions result in an inhomogeneous broadening that often masks the ligand-field structure in the optical spectra. Importantly, this different field experienced by NIR-emitting lanthanides in the matrix can affect the corresponding emission probability.

It is important to remark that the energies of the f states of the lanthanides are described above as relative to the corresponding lanthanides' ground-state energy, analogously to the case of an isolated ion if it were in vacuum. However, in a semiconductor material environment, we must consider that the ground state may be at a different energy than the top of the valence band (Dorenbos, 2003). Equivalently, in an organic environment understood as an extended organic semiconductor or a molecular chromophore, the lanthanides' ground states are not in general aligned with the $S_0$ ground state of the organics, which in turn may be affected by the presence of the lanthanide ion. In other words, considered in absolute terms with respect to vacuum or in relative terms with respect to the ground-state energy of the organics, they may appear shifted to higher or lower energies depending on the nature of the organics and the lanthanide ion. This has been thoroughly studied in the case of lanthanide impurities in inorganic matrixes where despite the fact that many of the states can be considered intra-gap due to their relative energy, the absolute energetic position relative to the valence and conduction band will significantly affect many of the sensitization and back-transfer properties (Dorenbos and van der Korlk, 2008). This phenomenon is illustrated in Fig. 7A. However, to represent the electronic configuration and consider more simply energy exchanges, these states are typically represented in relative terms to the ground state in the so-called Jablonski diagrams (Fig. 7B).

While, as we have previously stated, the molecular chromophore states are typically strongly coupled to vibrations and broad bands and large Stokes shifts occur, the shielding of the f levels of the lanthanides prevents a large energetic dependence with the solid or molecular (or complex) vibrations. Thus, although vibrational broadening of the absorption and emission bands is observed, the lanthanides' states show significantly smaller Stokes shift (weak vibrational couplings). Notwithstanding this, it is also observed that lanthanides in molecular/organic environments show a considerably more
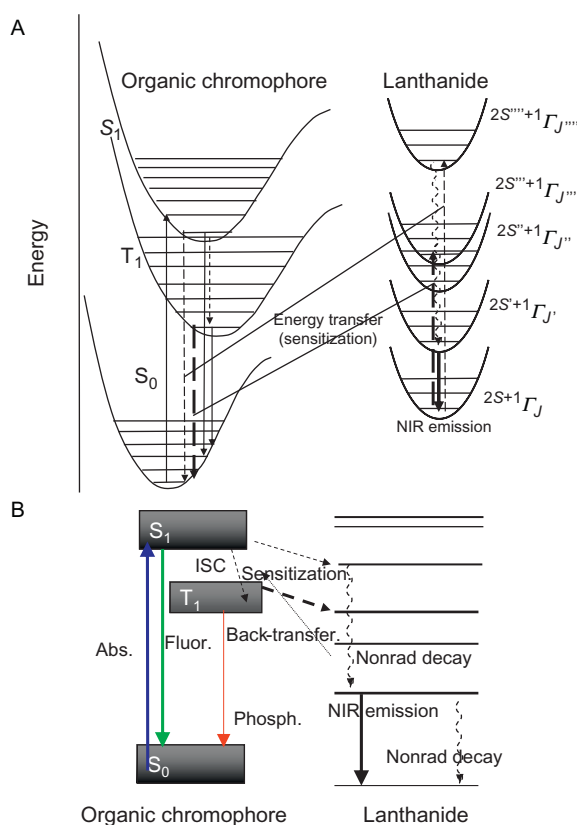
**FIGURE 7** (A) Representation of the electronic configuration of an NIR-emitting lanthanide in an arbitrary organic environment with the corresponding organic chromophore configuration, as given by Fig. 6. The corresponding electronic states $^{2S+1}\Gamma_J$ are slightly split due to crystal field, although not represented. (B) Jablonski diagram showing some radiative and nonradiative processes, including the energy transfer from the organic states to the lanthanide states (sensitization). The represented energy transfers result in the excitation and subsequent NIR emission of the lanthanide upon absorption in the organic chromophore.

stretched and rich vibrational contributions than in inorganic matrixes, in which the contribution of few phonons or specific complex vibrations causes a well-delimited vibronic progression of the lanthanides' states, sometimes appreciable, particularly at low temperatures. Relaxations are also possible along the corresponding vibrational sublevels of the electronic states of the lanthanides in the (organic) environment, which are produced by the creation or destruction of vibrational modes (overtones), and importantly, vibrational relaxations can occur between different electronic states.

## 2.3 Sensitization of NIR-Emitting Lanthanides through Organic Chromophores

Sensitization of a lanthanide (acceptor, A) via organic chromophore (donor, D) states occurs when a nonradiative electronic interaction $H_{int}$ connecting the lanthanide and the organic-based states results in an excitation of the lanthanide to an excited state at expenses of the organic's electronic energy, which relaxes to the ground state. We must bear in mind that a radiative reabsorption of an organic chromophore emission by the lanthanide could also occur, resulting in the corresponding lanthanide emission, but this is not the subject of this consideration of sensitization. Such a radiative process could be treated independently and modeled in a way in which the radiative and nonradiative dynamics of the absorbent and emitter states are not affected (Di Bartolo, 1968).

A first mathematical approximation to describe sensitization may be reached through Fermi's golden rule, expressing the probability (per time unit), $k_{ET}$, of such a nonradiative electronic transition from the organics' (donor) states into the lanthanides' (acceptor) ones, and explicitly representing the physical/dynamic connection between acceptor and donor:

$$
\begin{aligned}
k_{ET} &= \frac{2\pi}{\hbar} \left| \langle D, A^* | \hat{H}_{int} | D^*, A \rangle \right|^2 \int_E g_D(E) g_A(E) \, dE \\
&= \frac{2\pi}{\hbar} \left| \langle Chr, Ln^* | \hat{H}_{int} | Chr^*, Ln \rangle \right|^2 \int_E g_{Chr}(E) g_{Ln}(E) \, dE
\end{aligned}
\tag{2}
$$

where $\hbar$ is the reduced Planck constant ($h/2\pi$), the asterisk denotes that the subsystem is in an excited state, and $g_{Chr}(E)$ and $g_{Ln}(E)$ are the spectral lineshapes for the chromophore (donor) and lanthanide (acceptor) transitions. It must also be considered that, in principle, organic sensitization from the lanthanide excitation should also be possible. If the final subject of an excitation is the organic chromophore, this is called back transfer. This can be considered similarly to this development, but reversing the roles of the acceptor and donor correspondingly.

The nature of the electronic interaction, $H_{int}$, must be such to mix the organic chromophore-based states, $|Chr\rangle$, and the lanthanides' ones, $|Ln\rangle$. The bracket captures all the symmetry and quantum number conditions necessary for the overlap of the projected state $H_{int} |Chr^*, Ln\rangle$ on the final state $|Chr, Ln^*\rangle$, but there is also an energy resonance condition given by the overlap of the spectral lineshapes, arising from the energy conservation laws. Importantly, the energy overlap must be considered in terms of the vibronic wave-function; thus, vibrational assistance can be important.

Dipolar/multipolar energy transfer (Förster type) and exchange-based mechanisms (Dexter type) have been proposed as the connecting $H_{int}$ interactions allowing for sensitization. For energy transfer from an excited singlet or

triplet state to the $^{2S+1}\Gamma_J$ levels of lanthanide ions the selection rules for energy transfer are:

$|\Delta J| = 0, 1$ ($J = J' = 0$ excluded) for a Dexter mechanism or
$|\Delta J| = 2, 4, 6$ for a Förster mechanism.

Importantly, to theoretically analyze the transfer from the organic chromophore to the lanthanides, the transfer to all possible vibronic states in a lanthanide multiplet from the corresponding vibronic states of the chromophore should be considered (which allows a large span of the density of states). For an analytical formulation of the Dexter- or Förster-type interaction Hamiltonians, $H_{int}$, a general text book can be sought (Henderson and Imbusch, 1989). Importantly, it must be taken into account that due to the undefinition of the $J$ quantum number in a real environment as a consequence of limited validity of Russell–Saunders approach, or $J$-mixing in a ligand field, for instance, these rules may be relaxed and apparent prohibitions can be overcome (Lazarides et al., 2008).

Dexter mechanism is strongly dependent on the spatial overlap between the donor and acceptor's wave-function and decreases exponentially with the distance between the optical centers. Consequently, the interactive distances are very small and Dexter mechanism operates in a short distance <3 nm. Förster's multipolar interactions extend over longer distances and a corresponding power law with the inverse of the distance is employed for describing the magnitude, the exponent depending on the multipolar nature of the interaction (dipole–dipole varying as $R^{-6}$, and higher order interactions involving higher exponents).

The dominant specific transfer interactions may vary with the materials, and also the dominating states involved in the transfer. It has been demonstrated that singlet and triplet states of an organic chromophore may be involved and Dexter and Förster interactions may occur (Hebbink et al., 2002; Klink et al., 1999; Lazarides et al., 2008; Reinhard and Güdel, 2002). However, in a number of examples transfer occurs mainly from the triplets and the commonly accepted picture is that the majority of sensitizations occur via organic excited states with $S = 1$ (Crosby et al., 1961), either by Dexter or by Förster transfer. This is because not only they can take up the major probability constant due to electronic (interaction) reasons, but also because the transfer rates in the case of singlets may not be sufficiently significant to compete with other decay mechanisms (including radiative and nonradiative deexcitations; Klink et al., 1999).

Besides the (electronic) symmetry, the energetic overlap between donating and accepting states is also a considerable modulation of the energy transfer probability, as represented by the integral factor in Eq. (2). Importantly, we must remark that the overlap involves the energy of the relaxed organic state and that of the lanthanide's excited state which correspond, respectively, to the chromophore's emission density of states and the lanthanide's absorption

density of states. Due to the small crystal field and vibrational coupling leading to the small Stokes shift, the lanthanides' absorption density of states is similar to the emission profile. The resonance condition is critical to the extent that often sensitization is considered a resonance energy transfer process. However, we must bear in mind that the overlap is considered over vibronic states, and therefore, vibrational assistance can occur. In vibrationally assisted energy transfer, it is possible to bridge the energy gap between the donor's and acceptor's states by the involvement of vibrations. In other words, the nonradiative electronic transitions may occur at a high vibrational state in the accepting ion, which subsequently relaxes. This probability depends on the vibrational density of states, as contained in the integral factor, and thus, importantly, on the temperature. This factors are critical for back transfer from the lanthanide's states to the chromophore's ones.

In summary, for efficient sensitization, it is typically assumed that the lanthanides and organic chromophores must be spatially close, and that must present high ISC, and the triplet energies typically in the order of 1200–2000 cm$^{-1}$ higher in energy than the lowest accepting level of the lanthanide ion. This is to avoid back energy transfer, which is typically a thermal/vibrationally assisted process.

Importantly, accepting states of the trivalent lanthanide with lower reduction potential (like $Yb^{3+}$) may involve charge transfer (CT) from soft donor ligands (Horrocks et al., 1997), the sensitization involving a photo-redox process. Thus, an $L^X$-$Yb^{3+}$ (L=organic ligand including a ligand-based chromophore) may be photoexcited via a ligand-based transition to $L^{X*}$-$Yb^{3+}$ (where the asterisk represents being in an excited electronic state) and the energy subsequently transferred involving transitory ligand-to-metal CT, $L^{(X-1)}$-$Yb^{2+}$, decaying to $L^X$-$Yb^{3+*}$, which then decays radiatively to produce sensitized lanthanide-based NIR emission. For this to happen, the localization of the CT states of the $L^X$-$Yb^{3+}$ system, $E[L^{(X-1)}$-$Yb^{2+}]$ must be in the range of the gap between the ground state of the $Yb^{2+}$ ion in the complex and the top of the ligand-based valence band (Dorenbos, 2003; Liu et al., 2006). Since $Yb^{3+}$ has only the possibility of accepting at $^2F_{5/2}$, with an energy $\sim$1.26 eV (10,200 cm$^{-1}$), the energy mismatch between the chromophore's donating state and the $Yb^{3+}$ excitation energy may be large. This makes the previously described mechanism a competing one with conventional vibrationally assisted for sensitization of the $Yb^{3+}$ from high energy chromophores, if the ligand, $Yb^{3+}$ and CT energies fulfill the described conditions (Gonçalves e Silva et al., 2002; Reinhard and Güdel, 2002; Fig. 8).

The sensitization of the NIR-emitting lanthanide ion can be assessed from the excitation spectrum of the corresponding f–f transition. While in the absence of sensitization mechanisms, the absorption bands of the lanthanide (typically above the emitting state) are the only ones yielding the IR transition, in a sensitized process, new broad bands, originating in organic-related transitions, will be observed. To prove sensitization, the excitation spectrum
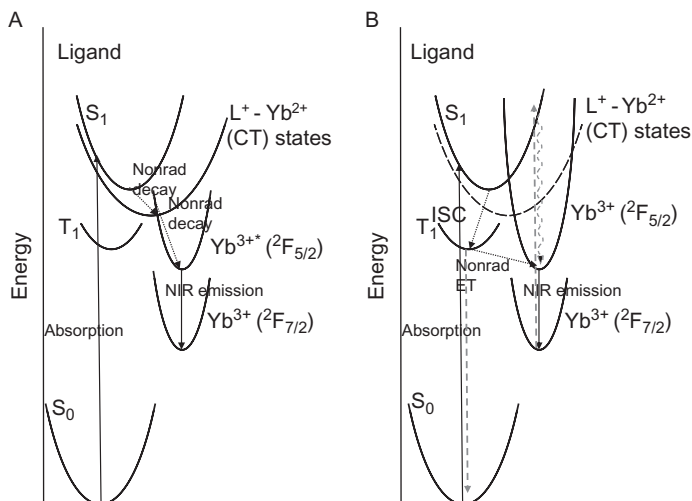
**FIGURE 8** (A) Schematic configurational diagram showing photo-redox excitation of $Yb^{3+}$ from a soft donor, in which the charge transfer (CT) states occur at the energy range allowing excitation of $Yb^{3+}$ after temporary photo-oxidation/reduction of the ligand to $L^+$ $Yb^{3+}$ to $Yb^{2+}$. The nonradiative transitions from ligand, complex, and Yb-based states occur via (vibrationally assisted, when necessary) tunneling between the parabolae. (B) Conventional, vibrationally assisted energy transfer mechanism involving excitation on a ligand-based chromophore to sensitize $Yb^{3+}$ NIR emission. The nonradiative energy transfer causing the $Yb^{3+}$ sensitization is represented with a diagonal dashed arrow. The curly gray arrow represents vibrational intrastate decay.

(recorded in nonoptical saturation conditions) of a lanthanide material should be compared with the absorption spectrum of the coordinated organic chromophore, due to the predominance of the organic state-based transitions. The magnitude of the organics-related excitation bands with respect to the lanthanides' transitions (which should still occur in the spectrum) and their comparison with the absorption spectra yields information on the participating states and degree of sensitization.

Energy transfer to an oxygen ($O_2$) molecule (oxygen sensitization) is an important channel of triplet deactivation that must be taken into account for some chromophores. It is known that dioxygen is a paramagnetic molecule with a fundamental triplet state $^3\Sigma_g$, and the first excited state at $\sim 0.1$ eV (7882 cm$^{-1}$) corresponds to a $^1\Delta_g$ singlet. $^3\Sigma_g$ can accept the excitation from organic dyes acting as sensitizers from transfer through the chromophore's triplet state [$(^3T_1, \, ^3\Sigma_g) \rightarrow (^1S_0, \, ^1\Delta_g)$]. This results in the quenching of the phosphorescence and can be measured. This process must be taken into account in the presence of the lanthanide: not only is it a competing mechanism to lanthanide sensitization, but it can be employed to assess the magnitude of the transfer to the NIR-emitting lanthanide from the chromophores' triplets (Klink et al., 1999; Werts et al., 1997). Besides, oxygen singlets are

extremely long lived ($\tau \sim 72$ min in gas phase) and, chemically very active, thus can diffuse and result in a degradation (burning) of the organics. In fact, they are deliberately produced in photodynamic therapy to kill cancer cells. Importantly, oxygen singlets can also be produced by the lanthanides through upconversion in a sort of reverse process to that described above. This is interesting for (biomedical) applications involving photodynamic therapy applications (Zhang et al., 2007d).

## 2.4 Sensitized NIR-Emitting Lanthanides in Organic Environments

From the point of view of the functionalities, the possibilities offered by organic sensitization of the lanthanides are the following:

- The organics can be chemically tailored in order for their excited states to be matched to the NIR-emitting ions allowing for much higher absorption coefficients and broader absorption bands to be used to excite the lanthanides. This is particularly interesting in applications oriented to low concentration of lanthanides or solutions. Moreover, this involves a control of the optical excitation energy range, to match the emission of low power lasers and LEDs.
- Broader emissions as a consequence of the organics' vibrational environments could result in broader bandwidth (typically larger than 50–60 nm).
- A high concentration of active ions ($>10^{21}$ ions/cm$^3$) in the solids which, together with their enhanced absorption in the presence of sensitization, could allow improved performance in applications like optical amplifiers in the order of centimeter length scales, or smaller.
- Processability via wet and relatively low-temperature vacuum methods allows for cheap and versatile production methods, in phosphor, optoelectronic, and on-chip applications. Moreover, molecular or functionalized sensitized lanthanides may find new or improved applications in liquid phases for instance in biology as a consequence of solubility or compatibility.
- The charge transport properties of conjugated organic semiconductors potentially permit the fabrication of electrically pumped devices. This couples with the advantage of greater creation of triplets via electrical pumping which should favor enhanced sensitization.

In principle, for infrared applications such as optical amplifiers in telecommunications, the desired sensitization energy range should be related to the existing technologies for high-power LEDs and lasers (as well as conventional optics) which would be employed as pumps, typically in the visible range and below. From the point of view of energy losses, the longest possible wavelengths would be desirable. An optimum match of the organic with the useful emitting states of the lanthanides (Nd$^{3+}$, Er$^{3+}$, and Yb$^{3+}$) should minimize losses of energies in nonradiative (multiphonon) processes, avoiding

other relaxations such as those mentioned above. This is not only interesting from the point of view of the energy efficiency but also avoiding the associated residual heating on the device. It is common that the intrinsic performances of the lanthanides are diminished upon temperature increases. For other applications, such as biological labels, dyes, and probes, low-energy excitations are also in principle desired, due to the increased transparency ranges. A sensitization range at lower wavelengths also favors the chemical stability of the organic part of the material as a consequence of minimization of the photodegradation of the organics (although the creation of oxygen singlets must not be forgotten).

A vast literature of sensitizing agents and configurations has been produced over the years reporting innumerable instances of infrared-emitting lanthanides in organic environments, particularly for $Nd^{3+}$, $Er^{3+}$, and $Yb^{3+}$ in molecular mononuclear coordination complexes-based architectures. Indeed, some of the most studied chromophore–lanthanide arrangements include coordinating and chelating ligand–lanthanide complexes in which sensitization is achieved from the organic ligands-based excitations. Sometimes, it is possible to include the chromophores as functionalizations of the chelating ligands, in order to keep them in close interaction with the lanthanide (which is critical, as the energy transfer is very dependent on the chromophore–lanthanide distance). Some configurations include polynuclear species, either with lanthanides or with other metals, in which other energy transfer pathways, like ion–ion or ligand–metal–lanthanide interactions, are involved.

Some of these lanthanide complexes have been also implemented as lanthanide-based NIR-emitting layers in organic LEDs (OLEDs), with the suitable electric operation providing electroluminescence (EL). Considerations about the influence of the energies and dynamics of the chromophores' states (in relation to the lanthanides') are critical. One of the main aims is to quantify or estimate the efficiency of the sensitization, $\eta_{sens}$, and the overall efficiency of the NIR emission, $\eta_{tot}$:

$$\eta_{tot} = \eta_{sens}\eta_{Ln} = (\eta_{S\text{-}Ln} + \eta_{ISC}\eta_{T\text{-}Ln})\eta_{Ln} \sim \eta_{ISC}\eta_{T\text{-}Ln}\eta_{Ln} \qquad (3)$$

where $\eta_{Ln}$ represents the lanthanide NIR emission efficiency, $\eta_{ISC}$ the ISC efficiency, and $\eta_{S\text{-}Ln}$ and $\eta_{T\text{-}Ln}$ are the efficiencies of the transfer from singlet and triplet to the lanthanide (efficiency is understood as fractional number of excitations undergoing the given process).

Optical absorption measurements can easily grant access to the energies of the excited state configurations of the singlets (if ISC is significant and there is a considerable singlet–triplet mixing, depending on the intensity and sensitivity, the triplet absorption can also be measured). Luminescence spectroscopy allows access to the relaxed singlet and triplet configuration, and time-resolved techniques, to their dynamic behavior, and in particular, the ISC and nonradiative quenching probabilities, quantities of interest for

considering the magnitude and mechanisms of organic-to-lanthanide energy transfer. Although it is expected to occur at lower energies, the separation of the phosphorescence component of the chromophore can be difficult if it overlaps significantly with the spectral region of the singlet emission. Since singlet to ground-state transitions are spin allowed and triplet to ground-state transitions are, in principle, spin forbidden, it will be masked and the singlet will dominate if ISC is limited. However, different radiative and overall lifetimes are expected for each component (microseconds to milliseconds or seconds, for phosphorescence, vs. nanoseconds, for fluorescence). Thus, a natural way to separate the singlet and triplet in the spectrum can be the measurement at different times after the illumination period in time-resolved emission spectroscopy experiments. Luminescence spectroscopy in the visible and NIR range also grants access to the lanthanide efficiency $\eta_{Ln}$ (as explained below).

The efficiency of the lanthanide sensitization from the chromophore, $\eta_{sens}$, is a critical magnitude for applications because it is the one that can compensate for the typically low $\eta_{Ln}$ that is usually achieved in organic environments. Its exact derivation may be difficult, but it can be estimated by the change in the materials properties in the absence and the presence of the sensitized lanthanide. Particularly if new NIR emissions corresponding to the lanthanide appear at the expense of the fluorescence or phosphorescence of the organic, the existence of sensitization can be inferred. To demonstrate unambiguously that this is the case, it is recommended to observe new, organics-based excitation bands of the lanthanides' emission which can match the organics states' energy. The lifetime of the singlet and triplet will provide information of the sensitization probability and efficiency. If a singlet and triplet decay with given time constants $\tau_S$ and $\tau_T$, respectively, in the absence of a lanthanide and the inclusion of a lanthanide provides different lifetimes $\tau_{S\text{-}Ln}$ and $\tau_{T\text{-}Ln}$, it can be inferred that the change of the inverse lifetimes is due to the inclusion of the nonradiative decay channel that implies sensitization of the lanthanide and from the given states, and thus numerical value of the sensitization from each level, $\eta_{s\text{-}Ln}$ and $\eta_{T\text{-}Ln}$. The enhancement of this nonradiative probability explains the associated reduction of fluorescence or phosphorescence and, actually, can be quantified from it.

Ideally, the measurements should be done in the same configuration (solid, solution, dispersion, etc.) and in the presence of a transparent trivalent rare earth, like $Y^{3+}$, $Gd^{3+}$, $La^{3+}$, $Lu^{3+}$, …, with no electronic states capable of accepting excitation or interfering with the states associated with the organic, both for the measurement of the energies of the organics' singlet and triplet states and the dynamic regime, but providing a similar geometry and physical–chemical conditions, incorporating heavy atom and intermolecular effects, for instance. The measurements in the presence of a transparent, nonemitting lanthanide, compared with the measurements of the sensitized lanthanide, and in particular those of the singlet and triplet intensities and lifetimes, carry qualitative and quantitative information on the states participating in the

sensitization process, and the corresponding efficiencies. Together with the structural information (distances and geometries), information about the sensitization mechanisms can be inferred. However, inferring directly from compounds with no lanthanides may hamper the accurate determination due to changes in geometry, masses, distances, and maybe other interactions, such as magnetic interactions or spin–orbit coupling which can affect the dynamic processes, such as ISC. For instance, in azulene-based lanthanide complexes, it has been observed that the inclusion of $Gd^{3+}$ activates organics-based phosphorescence, while in the free ligand it is undetectable. Thus, although triplet-lanthanide sensitization may be an important sensitization channel, it could have been concealed in the comparison of the dye and the NIR-active complex (Zhang and Petoud, 2008).

Moreover, in an extended solid or concentrated solution, it is possible that long-lived states such as triplets are transferred from a molecule to a nearby molecule in the ground state (similar to sensitization of the lanthanide center), which allows for diffusion of the excitation that may favor reaching relatively distant regions or color centers (Ern et al., 1971; Pope and Swnberg, 1982; Sternlicht et al., 1963). This route may affect the efficiency of the sensitization, which in principle could be limited by the interactions between lanthanide and nearest chromophores (Quochi et al., 2010). However, it can also cause triplet–triplet interactions, cross-relaxations, and quenching in nonradiative traps, resulting in an overall loss of excitation and, thus, a diminished efficiency.

### 2.4.1 Representative Ligands and Chromophores

Chemical considerations about lanthanide complexes with organic ligands include the consequences of low participation of the valence levels of the lanthanides determining an essentially ionic character of the bond (extremely polar), with no significant covalency (although the outer 5 and 6 level orbitals may somewhat participate in the bond) leading to the fact that coordination is mainly determined by packing and steric hindrance considerations. Thus, the number of atoms in the first coordination sphere of the lanthanide depends on the lanthanide radius and ligand nature, typically in the range 6–12, with 8 or 9 being among the most common. Trivalent lanthanides are generally considered relatively hard Lewis acids, and while in inorganic environments typically bind oxygen and halogen ions, in relation with organic moieties these will bind with Lewis bases with oxygen or nitrogen donors, preferentially, over softer donors such as sulfur or phosphorous which can also come in the coordination. The binding is thus done through "donating" sites or "dents" of the ligands or deprotonated acids (conjugate bases). Importantly, ligand functionalizations reducing the basicity of the corresponding conjugate base of a potential chemical to be used as a ligand (like fluorination) may reduce the binding potential to the lanthanides. Although neutral ligands can be employed, the charge balance of the trivalent lanthanide should be

provided by at least three negatively charged ligands in stoichiometric relation, although nonstoichiometric configurations of binding charged ligands can be produced, by the use of corresponding counterions, for overall neutral charge (these counterions could be atoms or charged molecular species).

Classical chelating ligands like polyaminocarboxylates can be employed for complexating the lanthanides although, by themselves, they do not offer the possibility of sensitization from organic chromophores (Aime et al., 1997). However, aminocarboxylate units can be tailored in more intricate units with chromophores in which the carboxylates provide the chelation of NIR-emitting lanthanides.

Among chelating ligands, β-diketonate (1,3-diketonate) ligands have been classically employed since the discovery of lanthanide sensitization in 1942. An exhaustive review of the chemical implications, properties, and applications of lanthanide β-diketonates, including those of NIR-emitting lanthanides such as $Nd^{3+}$, $Er^{3+}$, and $Yb^{3+}$, exists in this series of books (Binnemans, 2005). β-Diketonates (Fig. 9A) are good, oxygen donor, chelating ligands, chemically stable and allowing for a rich chemistry at the nonbinding positions (Fig. 9B). They allow a considerable degree of fluorination in many of the constituting groups, which provides them with relatively high efficiencies. However, the simpler ones usually only show absorption wavelengths in the UV region of the spectrum. Simple diketonate ligands employed in combination with other ancillary Lewis (typically nitrogenated) bases-based ligands (Fig. 9C) providing higher delocalization of the electron over distributed π-orbitals, or more elaborate diketonates, including cyclic diketonates (like 9-hydroxyphenalen-1-one) (Van Deun et al., 2006) (Fig. 10) or incorporating aromatic functional groups and dyes (like anthracene) (Nah et al., 2006) to provide redshifted absorptions have been proposed as sensitizers. It is possibly the versatility, together with the well-known chemistry that has allowed for myriads of configurations, including mononuclear and polynuclear complexes. Moreover, the organic semiconducting properties of lanthanides with β-diketonate ligands have favored their use in OLEDs. Diketonates allow a fine control of the incorporation of the lanthanide-emitting centers in host polymer and inorganic matrixes, providing an easy way to avoid aggregation and thus achieving high concentrations, which also make them potentially attractive in applications from the point of view of direct absorption at the lanthanides' states or in NIR-emitting lanthanides complexes-doped polymer-based OLEDs.

Tropolone (cycloheptatriene) can be considered a particular case of a cyclic diketone. Either alone, functionalized or within azulene-derivatives, cycloheptatriene-based ligands have also succeeded in sensitizing NIR lanthanides from the absorptions in the chromophore states around 300–450 nm (Zhang and Petoud, 2008; Zhang et al., 2005). Mononuclear and polynuclear tropolonato complexes can be made. The tris-mononuclear forms do not fully chelate the lanthanide (Fig. 10) and could allow for the inclusion of other
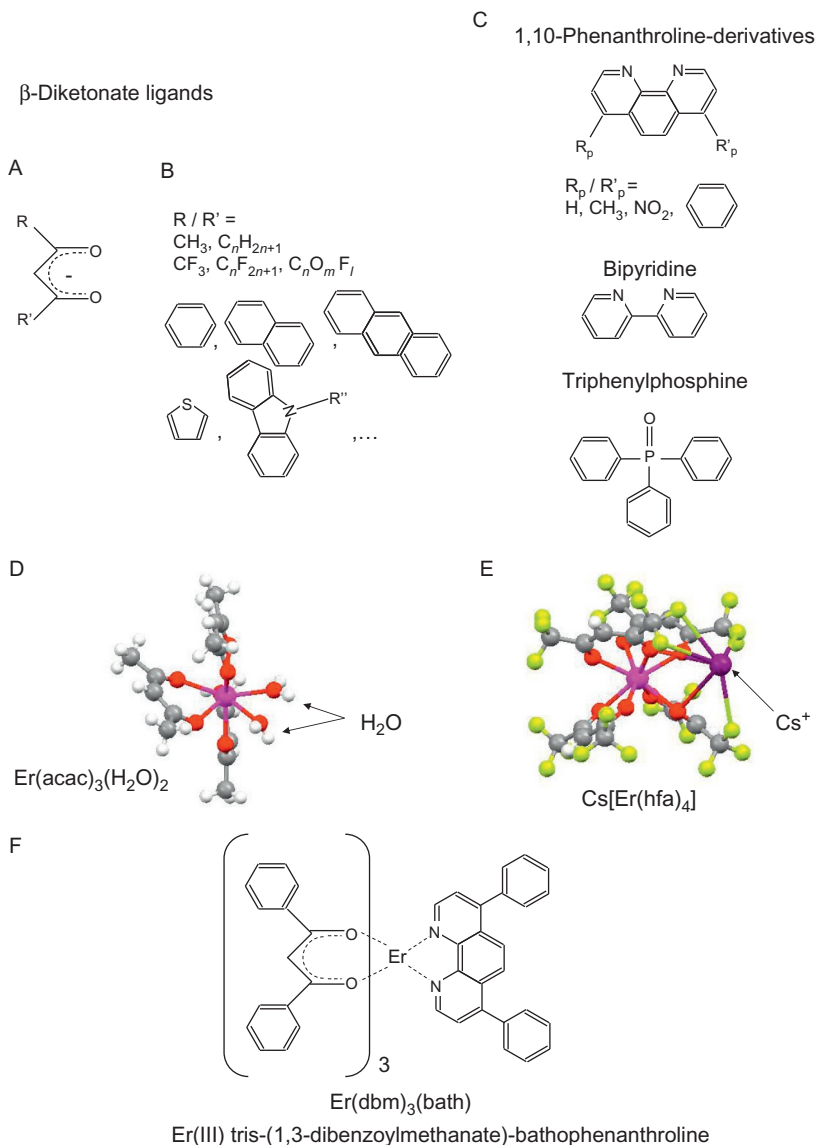
**FIGURE 9** (A) Generic scheme of an acyclic β-diketonate ligand. (B) Some simple functionalizations of the β-diketonate, some of them showing sensitization upon the ligand chromophores. (C) Other ancillary ligands employed for sensitization in combination with diketonate and other ligands. (D) Structure of a simple tris-NIR-emitting lanthanide complex $[Er(acac)_3(H_2O)_2]$ showing the incomplete encapsulation of the $Er^{3+}$ ion, which allows for the incorporating ancillary ligands. (E) Tetrakis lanthanide complex $[CsEr(hfa)_4]$ showing full coordination of the lanthanide. A corresponding counterion, $Cs^+$ for charge balance of the complex is then needed. (F) Scheme of a tris-lanthanide complex incorporating the neutral bidentate ligand bathophenanthroline.
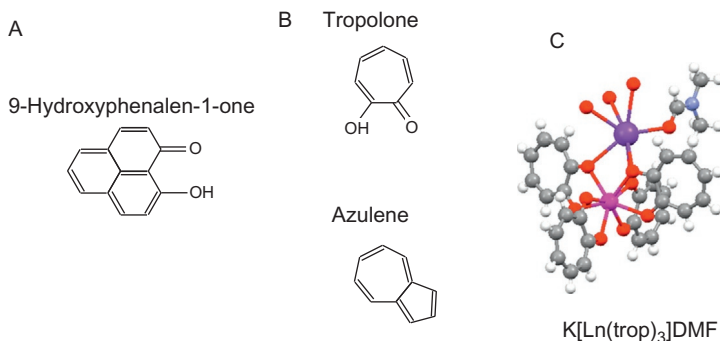
**FIGURE 10** (A) 9-Hydroxyphenalen-1-one ligand. (B) Tropolonate and azulene (cycloheptatriene-based ligand and chromophores). (C) Structure of a lanthanide tetrakis compound with corresponding charge-balancing counterion, K$^+$, and a neutral DMF molecule. *Redrawn from Zhang et al. (2005).*

neutral ligands and chromophores, including solvent DMF (4,4′-dimethylformamide) and tetrakis and other multinuclear forms require corresponding counterions to provide charge balance, and typically trap (DMF) solvent molecules in the structure (Zhang et al., 2007b). The presence of the heavy lanthanide ion is thought to stimulate ISC and enhance transfer from the triplet bands in the red-NIR region of the spectrum (Zhang and Petoud, 2008).

Other chelating, sensitizing ligands with typically redshifted states include quinolinates and derivatives. Similar to Alq$_3$ (q=tris-8-hydroxyquinolinate) which allowed for the first OLED, Erq$_3$ allowed for the first Er-based NIR OLED (Gillin and Curry, 1999), showing a corresponding 1.5 μm transition in the NIR region of the spectrum, apart of the ligand-based yellow-green emission at 520 nm. Nd$^{3+}$ and Yb$^{3+}$ analogues have been shown to provide the corresponding NIR bands (Khreis et al., 2000, 2001). The electric excitation of the lanthanide involves as a first step the creation of excitons in the emitting material, either by the application of an electric field or by injection of electrons or holes (extraction of electrons) via assisting layers with suitable band structures (see Section 2.5). Excitons correspond to localized hole–electron pairs and, depending on their electronic nature, have a singlet and triplet nature, similar to the equivalent photoexcitation. Excitons can produce the sensitization of the NIR-emitting lanthanide via energy transfer, as described above. This technique can be exploited in other organic semiconductors with lanthanides, the lanthanide complex being either a dopant or the major constituent of the emissive layer (see Section 2.5). Traditionally, these chelants have attracted the attention of researchers, and numerous configurations and functionalizations of the basic 8-hydroxyquinoline ligand have been produced: hydrated, anhydrous, halogenation of the quinolone (Albrecht et al., 2007; Artizzu et al., 2011; van Deun et al., 2003), introduction of carboxamides to yield tridentate ligands, benzidimidazoles, and more complex

variations including those based on aminopropyl-ethyleneamines, amidoqui-nolinates, etc. (Albrecht et al., 2008; Artizzu et al., 2011) some of them result-ing a so-called helicate structure (Albrecht et al., 2008). Polynuclear complexes have been observed of some of the combinations ligand–lanthanide (Albrecht et al., 2008; Artizzu et al., 2005, 2011), as well as tris and tetrakis configurations (Artizzu et al., 2011; van Deun et al., 2004; Fig. 11).

Macrocyclic ligands are attractive as chelating agents with sensitization possibilities. Since the beginning of macrocyclic chemistry, cryptands- and coronands-based lanthanide complexes have received particular attention for chemical and transport reasons and soon were studied from the point of view of sensitization properties. Macrocyclic ligands like phthalocyanines and por-phyrins are among the ones showing a particular interest due to the fact that their extended delocalized π orbitals provide low-energy absorptions to sensi-tize the IR-emitting lanthanides. In particular, these systems show the so-called S and Q bands (of singlet nature), the latter in the lower energy region of the visible ∼600 nm to the NIR up to ∼800 nm. However, because of this, it has been challenging to avoid back transfer, particularly because IR levels of the lanthanides occur at close energies. Phthalocyanines can encap-sulate the lanthanide ions in homoleptic bis(phthalocyaninato) configuration as double-decker sandwich mononuclear complexes by direct combination of two rings to the lanthanide or, in heteroleptic monophthalocyaninates, in combination with other ligands, and halogens to complete the coordination; dinuclear triple-decker compounds have also been reported (Bo et al., 2008; Smola et al., 2012). Some of the compounds in this family have been observed to produce lanthanide $Er^{3+}$ and $Yb^{3+}$ NIR emission when sensitized
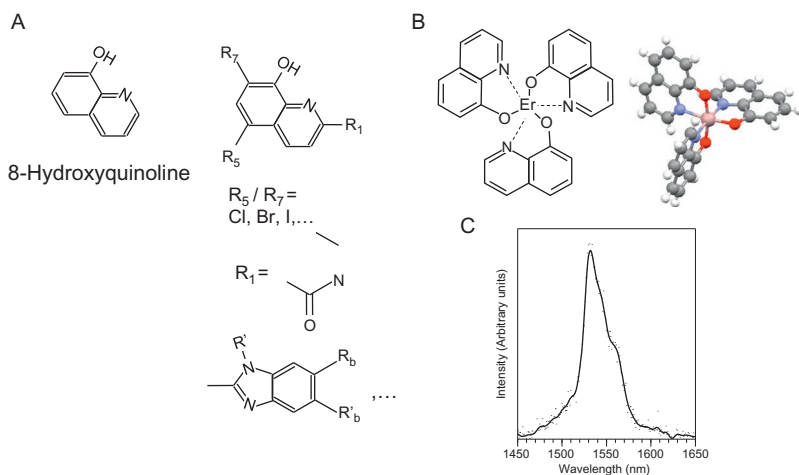


**FIGURE 11** (A) 8-Hydroxyquinoline (q) ligand and (B) some derivatives. (C) $Erq_3$ formula and corresponding EL in a $TPD/Erq_3$ OLED with ITO and Al contacts.

through the phthalocyanine ligands. But it has been observed that the mono-phthalocyaninato complexes show higher PL properties than the double-decker ones. A number of NIR-emitting lanthanide-based porphyrins have also shown successful in sensitizing NIR-emitting lanthanides in similar homoleptic and heteroleptic architectures (Bulach et al., 2012; Zhu et al., 2011). The very rich chemistry of these and other macrocyclic architectures such as cryptands, calixarenes, crown ethers, and azacrowns allow for chelation of the lanthanides and incorporation of classic and metal-based chromophores to sensitize NIR emission (Comby and Bünzli, 2007; Zhu et al., 2011). Many of the chelants do offer the possibility of halogenation at different positions (Fig. 12).

Acyclic and cyclic *m*-terphenyl trivalent ligands (Fig. 13) have also been extensively studied and known to complex the lanthanides (Wolbers et al., 1998) in a number of configurations (typically coordination 7–10, for 1:1 L-Ln$^{3+}$ stoichiometry, through the three carboxylate units and nearby oxygen). Variations allow for the inclusion of several chromophores incorporated typically as functionalization of the ligands in diverse positions (Klink et al., 1999). This is a strategy that has also been used in polyaminocarboxylates and other podands to bring classic dyes in close contact with the lanthanide in a molecular unit for sensitization through a number of wavelengths. Dendrimer ligands and architectures based on branched organic moieties and capable of incorporating chromophores within their structures are also a possibility
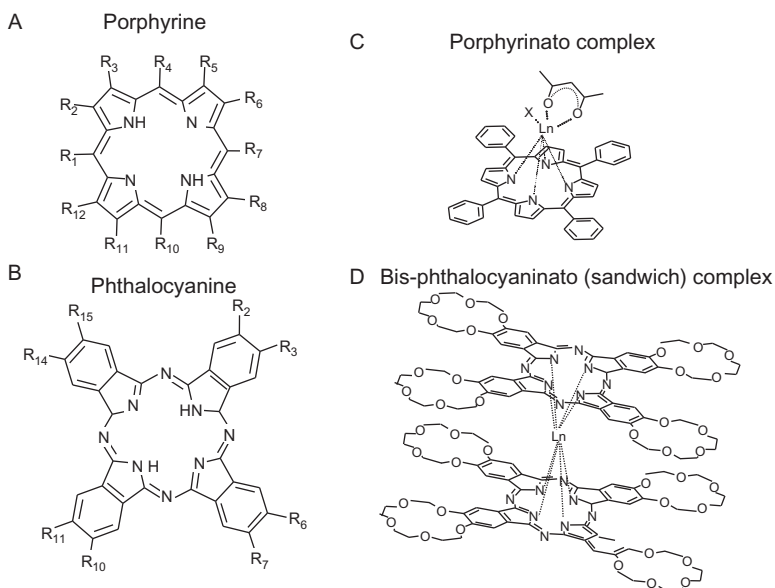


**FIGURE 12** (A) Porphyrin ring and (B) phthalocyanine ring. (C) Yb$^{3+}$ porphyrinato and (D) bis-phthalocyaninato complexes showing NIR-emitting lanthanide sensitization.

employed to sensitize the lanthanides in molecular environments (Comby and Bünzli, 2007).

In general, direct coordination of the lanthanide to functionalized chromophore units by corresponding deprotonated hydroxides and carboxylic, phosphonic, or sulfonic acid versions of many organic dyes is possible. However, most frequently derivatives of classic dyes are employed either in functionalization of chelating ligands such as polyaminocarboxylates, macrocyclic ligands, and terphenyl ligands or as extra monodentate or polydentate units to coordinate in the presence of inorganic (Ziessel et al., 2006) or organic chelating ligands such as those above or diketonates, tropolonates, and nitrogenated organic bases. In all cases, the idea is to fill the coordination of the lanthanide and provide close contact of the lanthanide with the light-harvesting unit to produce energy transfer upon absorption in the desired energy range. Sometimes, the optical properties of the dye are affected by the coordination to the functional groups, to the ligand or by the lanthanide itself, which may result in changes in the electronic configuration (energies) or dynamics (radiative and nonradiative processes (including ISC), etc.). Innumerable classic dyes have been employed in NIR-emitting lanthanide sensitization, including polyaromatic dyes; xylenol derivatives; anthracene, anthraquinone, xanthene, and coumarin derivatives; azo-dyes; pyrazo- and pyridine derivatives; phenanthroline derivatives, etc. Interestingly, the important application of NIR-emitting lanthanides as luminescent (and magnetic) probes and markers for biological applications has motivated a considerable research of functionalization and chelates of NIR-emitting lanthanides with protein derivatives. In fact, lanthanides have been shown to bind directly at
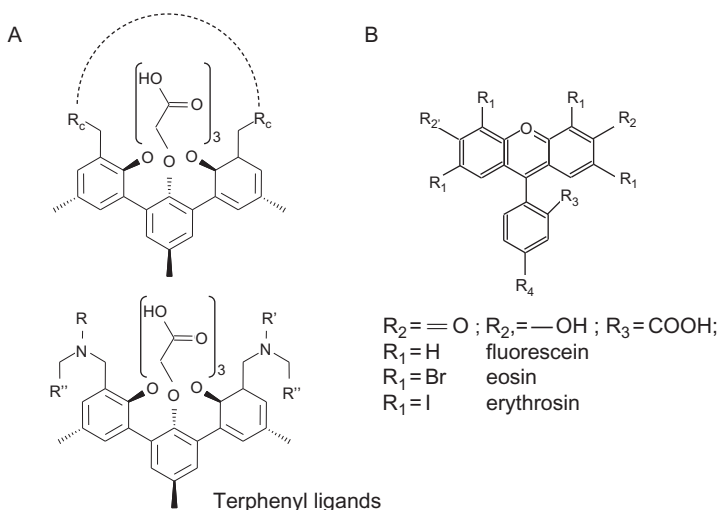


**FIGURE 13** (A) Cyclic and acyclic terphenyl ligands, and (B) some xanthene dyes used as sensitizers.

$Ca^{2+}$-binding sites of natural proteins and the tryptophan amino acid has also been shown to serve as a chromophore of visible and NIR-emitting lanthanides (Horrocks et al., 1997).

A thorough review of results concerning multiple chromophores and dyes in relation with NIR-emitting lanthanides, together with an extensive review of ligands and strategies for functional molecular lanthanide edifices, is included in the Comby and Bünzli (2007) review in this series.

Metal organic frameworks (MOFs) are polymeric hybrid material networks with different dimensionalities, typically porous and allowing for a precise tuning of the nature of the network and small pores through the adequate choice of metal ions, organic and inorganic linkers. Depending on the chemical nature and structure, MOFs can be used for a number of optical, magnetic, catalytic, gas storage, sensing applications, etc. NIR-emitting lanthanide ions can be included in the framework and in the pores and exhibit direct excitation emission, if the $Ln^{3+}$ absorption bands are excited, or sensitized emission from surrounding chromophores. Typically, these chromophores are aromatic-based, organometallic, or organic and inorganic metal complexes. Many $Nd^{3+}$, $Er^{3+}$, and $Yb^{3+}$-based MOFs have been produced. However, NIR emitters in MOFs are mostly inefficient, due to the abundant presence of highly quenching groups (typically, $H_2O$ and various hydrogenated solvent molecules), and visible emitters or magnetic lanthanides-based MOFs are more attractive than those for optical applications in the NIR range. Desolvated MOFs show considerably better emissions, for example, in Yb-BPT (BPT = biphenyl-3,4′,6-tricarboxylate) (Guo et al., 2011), which shows a considerably more efficient sensitized emission. However, often desolvation implies a break of the framework structure as grown desolvated materials are difficult to obtain. Nevertheless, exceptional behaviors based on rigid carboxylate units such as $Yb^{3+}$ with 4,4′-[(2,5-dimethoxy-1,4-phenylene)di-2,1-ethenedyyl]--bisbenzoate, which shows a network of oxalate-spaced $Yb^{3+}$ ions along chains, have shown favorable luminescence properties, including relatively high efficiency and (relatively) redshifted excitation wavelengths (White et al., 2009a).

Although maybe not strictly an organic environment, sensitized NIR emission can be obtained from visible and NIR excited endohedral erbium fullerenes $C_{82}$ or $C_{84}$ (in Er@$C_{8x}$ and carbide, $Er_2C_2$@$C_{8x}$, configurations (Ito et al., 2007)) and $Er_{3-x}Sc_xN$@$C_{80}$ systems (Xiaoya et al., 1997; Hoffman et al.; 1995). The performance is however poor, involving very low efficiencies, although a higher intensity from $Er_2C_2$@$C_{82}$, isomer III (Ito et al., 2007), is observed with respect to other isomers and configurations, due to the wider gap in the fullerene cage, reducing back transfer. The $Er^{3+}$ quantum yield in the $C_{80}$-Er/Sc caged is also poor, in the order of $10^{-4}$.

### 2.4.2 Organic Chromophores Based on Transition Metal Complexes

Direct absorptions on (much more sensible to material environment) transition metal ions are typically more allowed than in the lanthanides. Interestingly,

direct sensitization from nearby transition metal ion-centered states of NIR-emitting lanthanides is possible. This strategy has been employed in inorganic environments by codoping of lanthanides and transition metal ions and in organic environments, in molecules or compounds with both kind of metals (Fig. 14). However, it is frequent that transition metal ion complexes show strong transitions associated with the presence of organic ligands, which can be exploited for sensitization of the lanthanides. Transition metal ion coordination complexes can be strongly colored due to MLCT transitions and, also LMCT or ligand-centered charge transfer (LLCT, and intraligand (ILCT)), depending on the nature of the metal and the ligands. Importantly, the d-metal provides a strong spin–orbit coupling that favors ISC, which can also favor sensitization. In fact, numerous transition metal ion complexes have been employed in OLEDs for taking advantage of the triplets, either as triplet emitters or as triplet harvesters. Transition metal ion organometallics and coordination complexes have been used in combination with NIR-emitting lanthanides to produce sensitization, benefiting of the combined high ISC rates and low-lying triplets in the visible-red region of the spectrum, energetically favorable for the accepting states of $Nd^{3+}$, $Er^{3+}$, and $Yb^{3+}$. A varied chemical architecture has been employed, focused mainly in molecular bimetallic/polymetallic complexes or extended polymeric frameworks. A commonly employed strategy involves the use of functionalized
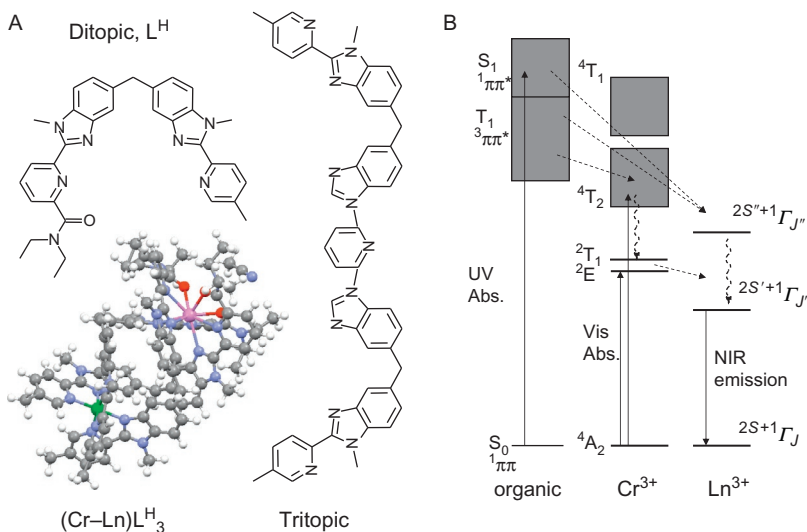


**FIGURE 14** (A) ditopic and tritopic ligands for building triple-stranded heterometallic helicates, usually employed with $CF_3SOO^-$ counterions, and $Cr^{3+}$–Ln bimetallic helicate structure. (B) Sensitization scheme of a generic NIR-emitting lanthanide showing the routes through the ligand (UV excitation) and through the corresponding $Cr^{3+}$ crystal field states (visible and NIR). *Panel (A): Redrawn from Imbert et al. (2003).*

nitrogenated bases like 2,2′-bipyridine (bpy), 1,10-phenanthroline (phen), bipyrimidine, and terpyridine (tpy) to coordinate the metal complexes as ancillary ligands in β-diketonates or other chelated lanthanide complexes. This structure involving ligands that can complex a metal from different sites has also been employed in producing dinuclear lanthanide complexes. Additionally, the transition metal complexes can be tailored as functionalization acting as chromophores in other ligands chelating the complexes (Fig. 15). Many of the metal complexes include or can include fluorination or halogenation at many sites, very often near the lanthanide complex.

$Cr^{3+}$ states allow sensitization from the metal states to $Nd^{3+}$, $Er^{3+}$, and $Yb^{3+}$ in various bimetallic and trimetallic complexes, typically through the ligand and through the doublet states of the $Cr^{3+}$ ion, which act as reservoirs, and can be populated upon excitation of the more allowed transitions at higher energies. Among the possible architectures, the (multicharged) $Nd^{3+}$-, $Yb^{3+}$-, and $Er^{3+}$-based dinuclear and trinuclear helicates with $Cr^{3+}$ (Fig. 14) and highly fluorinated counterions can be highlighted (Cantuel et al., 2006; Imbert et al., 2003). These double- and triple-stranded helicates allow not only the sensitization but, interestingly, the increase in the PL lifetime caused in the lanthanide-based NIR emission as a consequence of the modulation of the lanthanide decay by the energy transfer from the $Cr^{3+}$ states (Imbert et al., 2003). These helicates-based architectures have also been employed in $Ru^{2+}$–$Ln^{3+}$ combinations with no changes in the lifetime (Torelli et al., 2005).
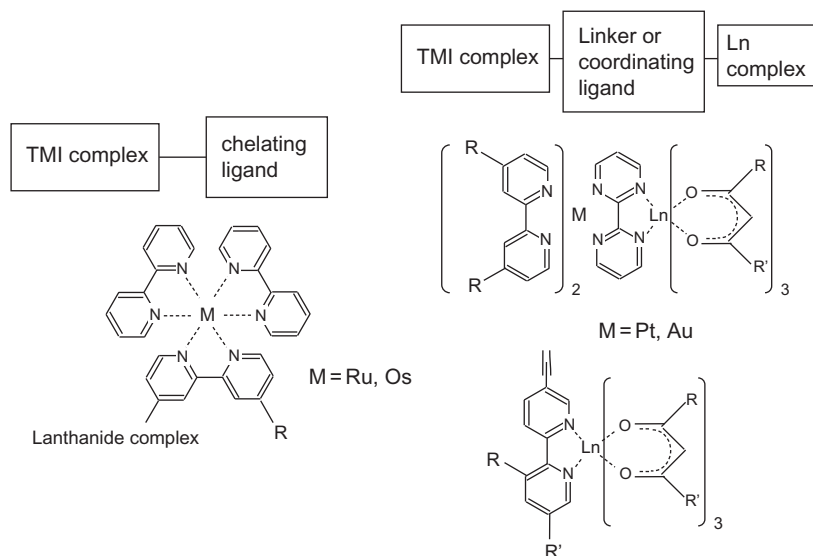


FIGURE 15  Typical architectures for coordinating transition metal ion complexes with lanthanide complexes. Examples of some transition metal ion complexes used as light-harvesting units for NIR-emitting lanthanide through metal-to-ligand charge transfer states.

Ruthenium(II) tris(2,2′-bipyridine (Ru[(bpy)$_3$]$^{2+}$) and ferrocene (iron(II) bis-cyclopentadiene, (C$_5$H$_5$)$_2$Fe) were first employed as functionalizations of the *m*-terphenyl ligands at the amide position and showed sensitization of Nd$^{3+}$ and Yb$^{3+}$ (Klink et al., 2000). In the case of the Ru(bpy)$_3$ chromophore, it was demonstrated that the sensitization occurred via $^3$MLCT triplet states. Ferrocene was also been introduced as a functionalization in 1,10-phenanthroline and in thenoyl-trifluoroacetonate for Nd$^{3+}$ and Yb$^{3+}$ complexes with the corresponding inclusion in the phenanthroline or diketonate ligand (Yuan et al., 2007). Ru(bpy)$_3$ units have also been incorporated in calixarenes and Ru(bpy) and Ru(bpy)$_2$ and in other architectures, including bridging configurations in which a linker based on a modified nitrogenated base like 4,4-bipyridine or bipyrimidine allows for incorporation to lanthanide complexes with other ligands (Beer et al., 2004; Pope et al., 2005). Thus, the inclusion of the metal complex as ancillary ligand in β-diketonates (hfa, tta, for instance) is done taking advantage of the affinity for the nitrogenated bases and corresponding N-donors. These units can retain the electronic properties of the metal complex at its site, which can be employed to modulate the NIR-emitting properties (Lazarides et al., 2008). For instance, a Ru$^{2+}$ acetylide-bipyridine heterodinuclear complex with Yb$^{3+}$ allows redox-modulated sensitization of the NIR Yb$^{3+}$ emission: it occurs normally via excitation into the Ru$^{2+}$-MLCT band at 450 nm, but it can be canceled through reversible electrochemical or chemical oxidation to Ru$^{3+}$, the band disappearing in the higher oxidation state (Wei et al., 2012). Another strategy involves the production of mononuclear, dinuclear, and trinuclear Ru$^{2+}$ complexes with CN ligands and nitrogenated bases, L$^{xp}$, xp = bpy, phen, bipyrimidine, etc., in which the lanthanides are incorporated in a range of coordination polymers or MOFs, through Ru$^{2+}$–CN–Ln$^{3+}$ architectures. Ru(L$^{xp}$)(CN)$_4$ units show sensitization of Nd$^{3+}$ and Yb$^{3+}$ (Herrera et al., 2006, 2007).

Osmium(II) complexes analogous to the modified [Ru(bpy)$_3$]$^{2+}$ ones have also been employed in 1,4,7,10-tetraazacyclododecane-1,4,7-triacetate (DO3A), showing sensitization for Nd$^{3+}$ and Yb$^{3+}$ (although minor for Er$^{3+}$) (Pope et al., 2004), and in the trimetallic complex with an amine-based open ring modification of the ligand, dtpa (diethylene triamine pentaacetic acid), as in the case of Ru$^{2+}$, but showing better sensitization properties (Pope et al., 2005). Similar to other metals, it is postulated that $^3$MLCT deactivation is involved in the transfer mechanism to the NIR-emitting lanthanides. Os$^{2+}$ bipyridimine–bipyridine modifications analogous to the Ru$^{2+}$ ones have also been employed in lanthanide β-diketonate configuration (see Fig. 15).

Re$^+$ and Pt$^{2+}$ transition metal ion chromophores have also been employed in combination with NIR-emitting lanthanide β-diketonates, typically through nitrogenated bases, bpy, phen, tpy (tpy = terpyridine) configurations (sometimes including ClCO$_3$ as additional ligands) (Kennedy et al., 2007; Shavaleev et al., 2003). Some of the compounds have allowed different distances to the fluorinated lanthanide (tta/hfa/bta (benzoyltrifluoroacetonate))

β-diketonate complexes, thus studying the distance-dependent energy transfer from the $^3$MLCT states to the NIR-emitting lanthanides $Er^{3+}$, $Nd^{3+}$, and $Yb^{3+}$ (Xu et al., 2008). Some of the $Pt^{2+}$-functionalized bases, like tpy, allow for coordination to dtpa to form trinuclear complexes (Glover et al., 2003), and acetylide-functionalized phen, bpy, or pyridine also allow for multinuclear complexes or extended networks (Ronson et al., 2006).

Iridium(III) tris(2-phenylpyridinato), $Ir(ppy)_3$, and modifications are classically employed as phosphorescent emitters in OLEDs (Yersin, 2008). Derivatives and particularly those with difluorinated ppy have been widely used with $Eu^{3+}$ for white emission combining the iridium blue and $Eu^{3+}$ red emissions (Coppo et al., 2005), including high fluorination dinuclear complexes (Chen et al., 2008). A 2-(5-phenyl-4H-[1,2,4]triazol-3-yl)-based carboxylic acid modification incorporating $Ir(ppy)_2$ was used to sensitize $Yb^{3+}$ in tris-tetranuclear complexes (Mehlstäubl et al., 2008). Interestingly, using a 1,4-phenylene spaced bis-bpy functionalization and 1,10-phenanthroline modifications allows for the incorporation of β-diketonates for forming dinuclear complexes (Fig. 16A–C) showing NIR-sensitized emission in the visible range, in solution and solid forms. This strategy has been employed for attaining different spacings and thus study the distance-dependent energy transfer (Tart et al., 2010). Pyrimidine-imidazole-based ligands can be employed to link bis-difluoro-ppy $Ir^{3+}$ complex and tris-diketonate- or other ligands-based lanthanide complexes, like the $Nd^{3+}$ tris(1-phenyl-3-methyl-4-isobutyryl-5-pyrazolone) complex (Fig. 16D), resulting in the effective sensitization of the $Nd^{3+}$, and that has been used in OLED configurations (see below) (Chen et al., 2010a,b).

$Pd^{2+}$ chromophores based on porphyrins have been employed with NIR-emitting lanthanides in dtpa, cyclene, and dtpy (pyridine-thiol) ligands. This strategy is based on using the metal porphyrins as light harvesting units and
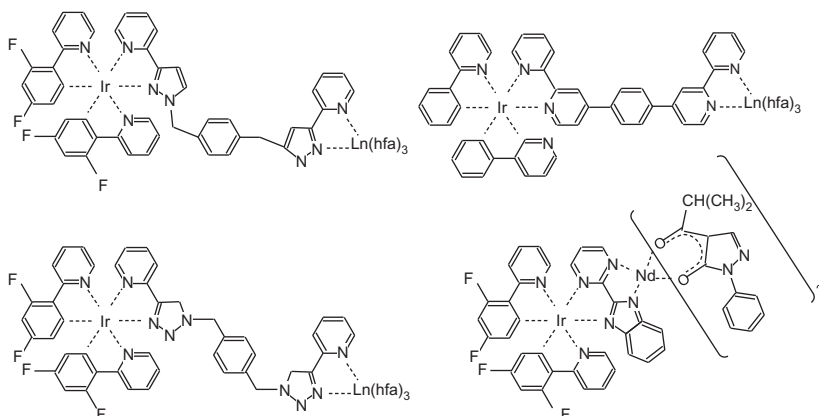


**FIGURE 16** $Ir(ppy)_x$ derivatives used in coordination with lanthanide diketonate-based complexes to obtain visible excitation-sensitized NIR emission.

binding the lanthanides off the center via functionalization of the ligand. This allowed for sensitization upon excitation in the visible range via triplet related with metal-ligand states of the prophyrin complex (Beeby et al., 2000). Interestingly, the $Nd^{3+}$ ion can be also placed on top of the center of the porphyrin center (Eckes et al., 2010) with four chelating hydroxyquinolinyl monoanionic units. Transfer is reported to occur from excitation of the Soret (S) band. $Au^+$ has been used to sensitize $Yb^{3+}$ through Au-organic-based transitions in architectures based on macrocyclic tetragold complexes with acetylide-functionalized modified bpy units and involving two $[Yb(hfa)_3]$ complexes, and in similar open versions with digold architecture with acetylide-modified bpy or tpy linking to $[Yb(hfa)_3]$ (Fig. 15) (Li et al., 2010, 2012).

$Zn^{2+}$ has been used as a stabilizer in lanthanide structures (particularly including Schiff bases) (Comby et al., 2012; Wong et al., 2002). Typically, $Nd^{3+}$, $Er^{3+}$, and $Yb^{3+}$ dinuclear complexes with quinolone derivatives showed NIR emission and some intense sensitization upon visible excitation, but ligand-based ($\pi$-based) states (Albrecht et al., 2008) are mostly involved. Interestingly, $[(Znq_2)](\mu\text{-}CH_3COO)][Ln(hfa)_2]$ (q = 8-hydroxyquinolinato) trinuclear complexes with $Ln^{3+} = Nd^{3+}$, $Er^{3+}$, and $Yb^{3+}$ show typical NIR emission upon corresponding excitation in the light-harvesting unit (which showed quenched visible emission in comparison with $Znq_2$) (Xu et al., 2010a) (Fig. 17). A similar behavior has been observed in the 2-methyl-8-hydroxyquinoline (Mq) tetranuclear analogues with terpyridin-4-phenol, which employs a similar approach to a successful one used exploiting the $Al(Mq)_3$ units as chromophores (Xu et al., 2010b). $(Znq_2)_4$, similar to $Alq_3$, are promising high luminance OLED materials. Sensitization wavelengths up to 440 nm of the NIR-emitting ions involve the $Zn^{2+}$ quinolinate units as the color centers, although not involving $Zn^{2+}$-based states (Xu et al., 2010a,b). However, it is important that these states are different than those in the q ligand alone, as the $\pi$–$\pi$-stacking interactions produce a considerable



$\{(Znq_2)_2(\mu\text{-}CH_3COO)[Ln(hfa)_2]\}$        $\{[Zn_2(Mq)_2(tpyO)_2][(Ln(hfa)_3]_2\}$

Hq = 8-hydroxyquinoline              HMq = 2-methyl-8-hydroxyquinoline
hfa = hexafluoroacetylacetonate      tpyOH = [2,2':6'2'']terpyridin-4'-ol
                                     hfa = hexafluoroacetylacetonate
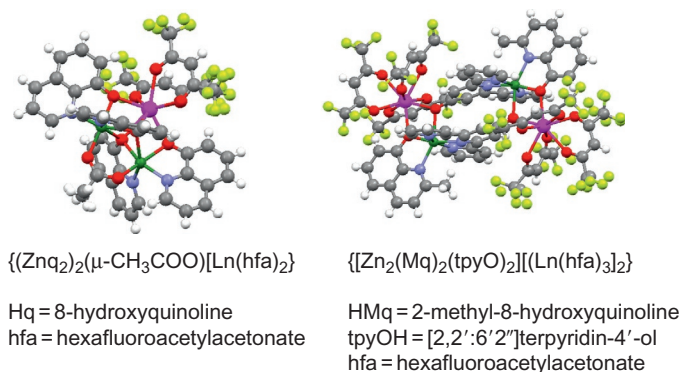
**FIGURE 17**  $Zn^{2+}$-8-hydroxyquinoline derivatives-based multinuclear complexes with NIR-emitting lanthanide hexafluoroacetylacetonato diketonates. *Redrawn from Xu et al. (2010a,b).*

variation (redshift) with respect to the isolated ligand. Other configurations including these and other transition metal ions (like $Co^{3+}$) exist, mostly following the general rules of direct coordination of the metal complex to a chelating ligand or to a charged or neutral ligand in coordination with the NIR-emitting lanthanide (Fig. 15), and sometimes employing the transition metal a stabilizer of the multinuclear edifices (Chen et al., 2010a,b; Comby and Bünzli, 2007).

## 2.5 NIR-Emitting Lanthanides OLEDs

OLEDs exploit EL of organic molecules in diode-layered structures favoring injection of excitons in the luminescent materials. The field of OLEDs has quickly developed after the creation of the first small-molecule OLED in 1987 (Tang and VanSlyke, 1987) based on the aluminum(III) 8-hydroxyquinolinate complex, $Alq_3$, as an emitter, and the alternative polymer-based OLEDs in 1990 (Burroughes et al., 1990). The incorporation of NIR-emitting lanthanides to OLEDs to exploit the metal-based f–f transitions was exploited as early as 1999 with the production of $Erq_3$-based OLEDs, similar to $Alq_3$ devices, showing 1540 nm emission (Gillin and Curry, 1999), and $Nd^{3+}$ β-diketonate, $[Nd(dbm)_3bath]$ (dbm = dibenzoylmethanato, bath = bathophenanthroline) (Kawamura et al., 1999), showing the characteristic 870, 1060, and 1300 nm emissions. Lanthanide-based OLEDs (and in NIR-emitting ones, containing $Nd^{3+}$, $Er^{3+}$, and $Yb^{3+}$) are advantageous to overcome the lanthanides' poor solubility and sensitization in inorganic LEDs. Besides, other advantages include the high monochromaticity of the f–f transitions together with the ease of processability of organics (by low-temperature evaporation in vacuum and wet methods). However, it must be noted that, mainly due to the low emission efficiencies of the NIR-emitting lanthanides in organic environments, the performances obtained for NIR-emitting lanthanide-based OLEDs are significantly poorer than those measured in visible-emitting lanthanide-based OLEDs such as those containing $Eu^{3+}$.

A general structure of an OLED is represented in Fig. 18A. Some of the organic materials employed as emitters in OLEDs may not have very good carrier injection or transport properties. In this case, a single layer is not enough and a multilayer structure is needed, with each layer having a specific role so that the emissive material is only used as the emissive layer where electrons and holes are injected and transported from other materials. The need for transport layers is the usual case in OLEDs, and in the more general case, sometimes a hole (or electron)-blocking layers (Fig. 18B) is also needed between the emissive layer and the electron transport layer (or hole transport layer) to confine the excitons to the emitting material (as represented in Fig. 18A). Figure 19A shows the band structure for a three-layer OLED involving electron and transport layers apart from the emitting layer. The energy difference between the Fermi levels of the electrodes in the OLED
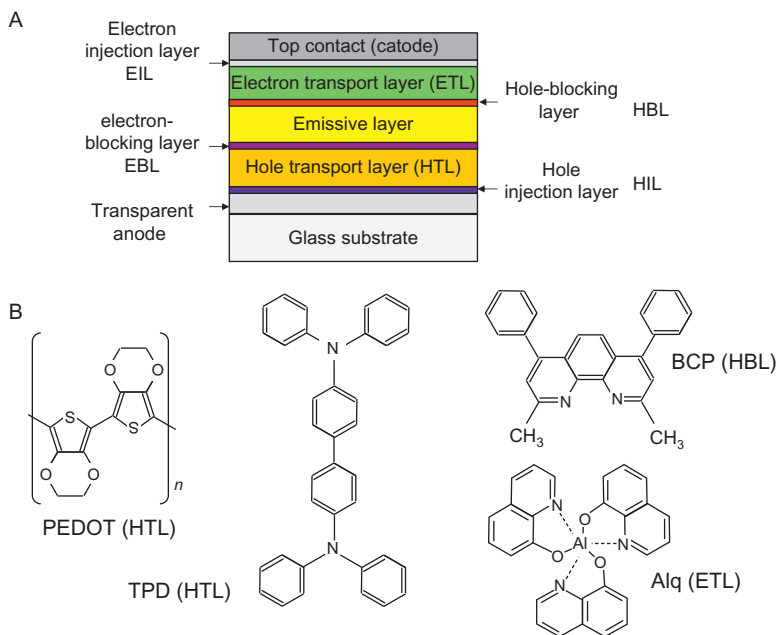
**FIGURE 18** (A) General structure of an OLED. (B) Some materials used as assisting layers for injection, transport, or blockage of holes and electrons.

determines the built-in potential of the device, representing the barrier for charge injection into the organic layer, electrons in the LUMO or holes in the HOMO (electron extraction). In the short circuit (Fig. 19B), the Fermi levels of the electrodes readjust, relative to the vacuum level, and become equal which causes the creation of a potential gradient across the OLED. The application of a forward bias allows the reduction of the barrier, and when the applied voltage reaches the built-in potential, a flat band structure occurs, the low work-function cathode can inject electrons into the LUMO, and the high work-function anode may inject holes into the HOMO. Charge diffuses along the potential gradient toward the opposite electrode, creating excitons (bound electron–hole pairs on a molecule) in the organic layer, which in turn can deactivate radiatively from the corresponding multielectron states. Figure 19C represents the charge injection and formation of excitons in a multilayer OLED. In the NIR-emitting lanthanide-based OLEDs, the emission occurs for recombination of the excitons in the lanthanide-centered states, yielding NIR f–f emission (Fig. 19D). In general, the interplay between layers' chemical nature and thicknesses is critical for the efficient injection of the OLED and, in turn, for good working conditions (turn-on voltage, efficiency, etc.). These layers and thickness need to be carefully selected as a function of the emissive layer electrical properties. Importantly, the optical
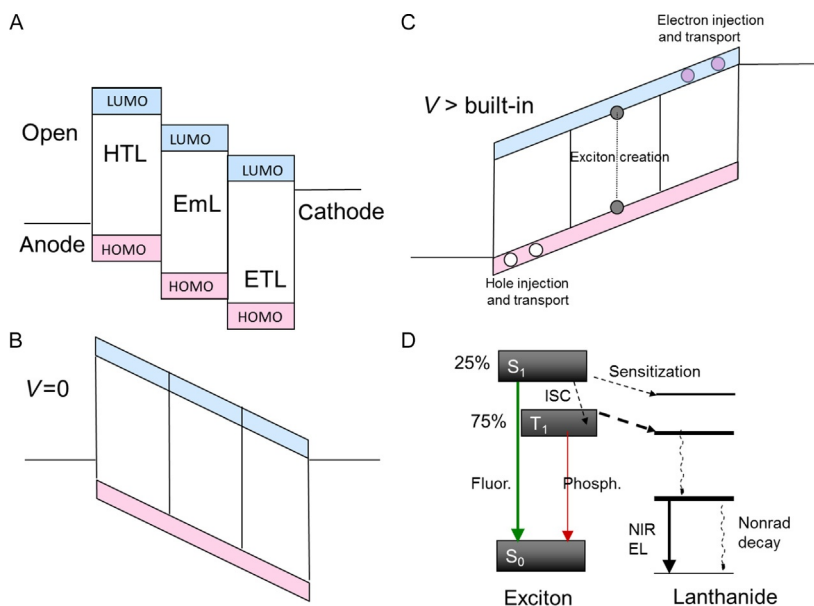
**FIGURE 19** (A–C) Representation of the band structure of an OLED as a function in the open circuit and at different applied voltages, showing the injection of carriers above the built-in potential, resulting in the creation of excitons in the emitting layer. (D) Schematic representation of the electroluminescent processes in the NIR-emitting lanthanide containing organic layer.

transmission of the layers must be selected for the corresponding emission range, so light can travel across the multiple heterolayered structure. Typically, a transparent electrode (usually the anode) made of a transparent metal like ITO (indium tin oxide), AZO (aluminum-zinc-oxide), fluorine-tin-oxide (FTO), and polyaniline is used. This is to be taken into account as some of the compositions which are employed in visible-emitting OLEDs present a loss transparency toward the infrared range.

Since the first devices, NIR OLEDs based on NIR-emitting lanthanides in the emissive layer have been predominantly explored with $Nd^{3+}$, $Er^{3+}$, and $Yb^{3+}$ quinolinates and $\beta$-diketonates-based chelates. Chemical variations include configurations involving functionalization of the ligands in both the quinolinates and diketonates and the incorporation of ancillary ligands (such as triphenylphosphine, TPP, or bathophenanthroline, bath), mainly in the latter case. Other lanthanide complexes incorporated as emitting units in NIR OLEDs include terphenyl-based chelates, pyrazolone derivatives, porphyrinates, and benzoxyazole/benzoxythiazole-phenolates (see Table 1). As in the case of photosensitization, the organic chromophores present in these materials can act as exciton traps to subsequently transfer the excitation to the lanthanide emitters. Interestingly, NIR-emitting lanthanide complexes can be used either as the emissive layers in depositions made by wet or vapor

**TABLE 1** Some Representative NIR-Emitting Lanthanides-Based OLED Configurations and Corresponding Compositions of the Anode, Hole Transport Layer (HTL), NIR Emissive Layer, Hole-Blocking Layer (HBL), Electron Transport Layer (ETL), Electron Injection Layer (EIL), and Cathode (for Other Abbreviations, see Abbreviations List)

| Anode | HTL | Emissive Layer | HBL | ETL | EIL | Cathode | References |
|---|---|---|---|---|---|---|---|
| ITO | TPD | Erq$_3$ | | | | Al | Gillin and Curry (1999) |
| ITO | TPD | Ndq$_3$ | | | | Al | Khreis et al. (2000) |
| ITO | TPD | Ybq$_3$ | | | | Al | Khreis et al. (2001) |
| ITO | TPD | Er(dbm)$_3$(bath) | BCP | | MgAg | Ag | Kawamura et al. (1999) |
| ITO | TPD | Nd(dbm)$_3$(bath) | BCP | | | MgAg | Kawamura et al. (2000) |
| ITO | TPD | Yb(dbm)$_3$(bath) | BCP | | MgAg | Ag | Kawamura et al. (2001) |
| ITO | NPB | Er-pyrazolone-deriv./TPP | BCP | Alq | LiF | Al | Li et al. (2008) |
| ITO | PEDOT | F8VBt:Nd(lissamine-terphenyl) | | | | CaAl | Slooff et al. (2001) |
| ITO | | PVK:Er(acac)$_3$(phen) | | | LiAl | Ag | Sun et al. (2000) |
| ITO | PEDOT | PVK:Nd(9hydroxyphenalen1one)$_3$ | | | | CaAl | O'Riordan et al. (2006) |
| ITO | PEDOT | PVK:Nd(dichloroquinolinate)$_4$ | | | | CaAl | O'Riordan et al. (2008) |
| ITO | PEDOT:PSS | PPP-OR11:Yb/porph/acac | | | | CaAl | Harrison et al. (2001) |
| ITO | NPB | Ir(Fppy)$_2$Nd(pyrazolone-deriv.)$_3$ | BCP | Alq | MgAg | Ag | Chen et al. (2010a,b) |
| ITO | TPD | Nd/Er/Yb(benzoxyazol/thiol-phenolate)$_6$ | | bath | | Yb | Katkova et al. (2011) |

methods, or in guest–host systems, in which they are doped in polymers, which is often favorable in terms of processability, but worse in terms of efficiency.

Interestingly, spin statistics considerations about the injection of carriers imply that the ratio of excitons created with a singlet and triplet character should be near 25–75%. The large number of triplets could, in principle, favor lanthanide sensitization, and the singlets could be converted or transfer directly. The field of triplet-based OLEDs is gaining relevance, and the NIR emitters can benefit from the conversion properties of common materials employed as phosphorescent emitters or triplet harvesters (Yersin, 2008).

Transition metal ions in combination with lanthanides have been employed for enhanced EL performance in the NIR. Interestingly, mixtures of [Ir(ppy)$_3$] with [Er(dbm)$_3$(bath)] produced a considerable increase in both the PL and EL (Zhang et al., 2008). Also, bimetallic complexes have been employed for EL from Ir$^{3+}$ fluorinated phenylpyridine (Chen et al., 2010a,b). These materials benefit from the sensitization caused by the Ir$^{3+}$ phosphorescent species, involving the intermolecular/interspecies energy transfer.

## 3 THE NIR-EMITTING EFFICIENCY OF LUMINESCENT LANTHANIDES

As we have previously implied, quantification of the lanthanides' emission efficiencies is critical for describing the performance of the lanthanide in the given organic environment. Once the NIR-emitting lanthanide is excited, the system can relax in a number of ways, apart from back transfer, which we have previously commented, and is described in similar terms to the sensitization process. These include radiative deexcitation (emission of NIR photons), nonradiative vibrational quenching (vibrational relaxation), and nonradiative energy transfer (which involves other lanthanides present in the material and thus is strongly concentration dependent, or backtransfer to the organic).

### 3.1 The NIR-Emitting Lanthanides' Radiative Probability and Judd–Ofelt Formalism

Quantifying the radiative transition probabilities for f–f transitions of the lanthanide, referring the probability of the emission of a photon from an excited state, is extremely important for optical applications and for determining the lanthanide and overall efficiencies. It is known that in a luminescent (spontaneous) process, an electromagnetic interaction acting on the excited state may result in a deactivation to the ground state (or in fact to other low-lying state), the excess of electromagnetic energy being carried by a photon. The transition probability for this process, $k^{\mathrm{rad}}$, is given by

$$k_{\text{ex}\to\text{gr}}^{\text{rad}} = \frac{2\pi}{\hbar} \left| \langle \Psi_{\text{ex}} | \hat{H}_{\text{int}}^{\text{rad}} | \Psi_{\text{gr}} \rangle \right|^2 \rho(E) = A_{\text{ex}\to\text{gr}}\rho(E) \tag{4}$$

with $\rho(E)$ being the density of states (number of overlapping states at the transition energy per energy unit), $A$ representing the Einstein coefficient for spontaneous emission transition, and $H_{\text{int}}$ is the interaction Hamiltonian. When the interaction mechanism is expanded through multipolar expansion, the major component is expected to be the electric dipole. We have previously commented that f–f optical transitions are spin and Laporte (parity) forbidden, and mechanisms mixing the initial or final states with suitable other parity, $J$, or spin components, typically crystal field components, or vibrational states, are usually small due to the strong shielding. Thus, oscillator strengths are typically small. The radiative probabilities for electronic transitions to the ground state can be measured directly from the absorption spectrum given that the emission transition probability is proportional to the stimulated absorption probability, which is the reciprocal process, $k_{\text{gr}\to\text{ex}}=B_{\text{gr}\to\text{ex}}\rho(E)$ with $B_{\text{gr}\to\text{ex}}$ the Einstein coefficient for stimulated absorption,

$$B_{\text{gr}\to\text{ex}} = A_{\text{ex}\to\text{gr}}\frac{1}{16\pi\hbar}\lambda^3 \tag{5}$$

This is the easiest way to characterize the radiative properties of lanthanide such as $Yb^{3+}$, with only one absorption band. If the line strength, $S$, for a $^{2S+1}\Gamma_J \to {}^{2S'+1}\Gamma'_{J'}$ transition is given by

$$S(J \to J') = \frac{3cn\hbar(2J+1)}{4\pi e^2\bar{\lambda}} \left[ \frac{9}{(n^2+2)^2} \right] \int_{\text{band}} \varepsilon(\lambda)\mathrm{d}\lambda \tag{6}$$

where $c$ is the speed of light, $n$ refractive index, $e$ the electron charge, $\lambda$ the transition wavelength (barred meaning, average), and $\varepsilon$ the absorption coefficient ($\varepsilon = N \times \sigma$, with $\sigma$ the absorption cross-section and $N$ the ion density), and the decay probability can be estimated (Görller-Walrand et al., 1998) as

$$A(J \to J') = \frac{32\pi^3 e^3 cn}{3\hbar(2J+1)\bar{\lambda}} \left[ \frac{(n^2+2)^2}{9} \right] S(J \to J') \tag{7}$$

In the general case, a large number of radiative transitions are possible with different probabilities and energies, not all of them accessible in conventional spectroscopic experiments: for instance, in $Nd^{3+}$, typically only the ground state $^4I_{9/2}$ to the $^4F_{3/2}$ at 0.87 μm is accessible through absorption, while other lines are observed in the emission apart from the reciprocal $^4F_{3/2}$ to $^4I_{9/2}$, such as the $^4F_{3/2}$ to $^4I_{11/2}$ (1.1 μm), $^4F_{3/2}$ to $^4I_{13/2}$ (1.3 μm), or $^4F_{3/2}$ to $^4I_{13/2}$ (1.8 μm). Moreover, the sample or the environment might prevent good accessibility to these transitions, due to lack of crystallinity, providing spurious absorptions.

Although a general description of the line strengths is usually complicated, independently Judd (1963) and Ofelt (1962) proposed a theoretical model

framework for the calculation of induced electric dipole transitions (also extended to magnetic dipole). The basic idea of Judd–Ofelt theory is that the admixture of states of opposite parity can relax the Laporte forbidden 4f electric dipole transitions. The odd part of the ligand-field potential is considered as the perturbation mixing states of different parity. The line strength, which in turn depends the probability of a transition, is parametrized in a number of elements relating to the transitioning lanthanide configuration and thus, depending on the chemical nature of the lanthanide and ligands, the geometrical arrangement.

It is firstly considered a single spectral line in an oriented (field) system. Given an initial state and final states in the l configuration of wave-functions:

$$\langle \Psi_{\mathrm{gr}}| = \langle l^n\psi JM|, \quad |\Psi_{\mathrm{exc}}\rangle = |l^n\psi'JM'\rangle \tag{8}$$

where $\psi$, $\psi'$ are the additional quantum numbers defining uniquely the state (in the Russell–Saunders coupling scheme, they represent $L$ or $S$) and $M$ is the quantum number of the projection $J_z$ of the total quantum momenta $J$ [$l^n$ denotes that the transition occurs between the levels of the same configuration, $l = 3$ for f–f transitions], and dipole transitions are driven by the electric dipole operator through the corresponding induced dipole matrix elements

$$\langle \Psi_{\mathrm{gr}}|\hat{\mu}_{\mathrm{ED}}|\Psi_{\mathrm{exc}}\rangle \tag{9}$$

with

$$\hat{\mu}_{\mathrm{ED}} = -e\sum_j \hat{r}_j = -e\sum_j r\hat{C}_j \tag{10}$$

where $r$ is the position vector of the electron $j$ and $\hat{C}_j$ represents the irreducible tensor operator (in the ligand field) containing the angular coordinates of the electron $j$.

The wave-function of the initial state can be described as a linear combination of all components of the ground levels of the $l^n$ configuration:

$$\langle \Psi| = \sum_M \langle l^n\psi JM|a_M \tag{11}$$

in which $\psi$ is a ligand-field state and $a_M$ represents the corresponding weight arising from the ligand-field mixing. Similarly, the final state is given by

$$|\Psi'\rangle = \sum_{M'} |l^n\psi'J'M'\rangle a'_M \tag{12}$$

As we have previously discussed, according to Laporte's selection rule, the electric dipole transition is only allowed between two states of the opposite parity; thus, no intraconfigurational 4f transition could occur through the electric dipole as given in Eqs. (4) and (9) since there is no change in the dipole moment of ion at the same $l^n$ configuration. However, they can occur (and are denominated induced electric dipole transition) as a consequence of the perturbing admixture of $\Psi$ and $\Psi'$ with available states (typically of higher

energy) from the configurations of the opposite parity to the $l^n$ due to nonsymmetrical ligand-field components. In the case of the lanthanides, the $4f^{n-1}5d$ configuration is typically considered (so-called f–d mixing). Upon mixing with $\Psi''$ states given by $l^{n-1}$ and quantum numbers represented by $\psi''$, $J''$, and $M''$, the resulting (perturbed) $\Psi$ and $\Psi'$ states must be considered, respectively

$$\langle\Psi| = \sum_M \langle l^n\psi JM|a_M + \sum \langle l^{n-1}\psi''J''M''|b$$
$$|\Psi'\rangle = \sum_{M'} a'_M|l^n\psi'J'M'\rangle + \sum b'\langle l^{n-1}\psi''J''M''| \tag{13}$$

where

$$b = \frac{\displaystyle\sum_{M'} a_M \langle l^n\psi JM|\hat{V}_{\mathrm{odd}}|l^{n-1}\psi''J''M''\rangle}{E(\psi J) - E(\psi''J'')}$$
$$b' = \frac{\displaystyle\sum_{M'} a'_{M'} \langle l^n\psi''J''M''|V_{\mathrm{odd}}|l^{n-1}\psi'J'M'\rangle}{E(\psi'J') - E(\psi''J'')} \tag{14}$$

and where the operator $V_{\mathrm{odd}}$ represents the odd symmetry part of the ligand-field Hamiltonian, Eq. (1) ($k=$ odd) (Görller-Walrand et al., 1998).

Then, the matrix elements in the electric dipole transition operator given by expression (9), for the mixed states $\Psi$ and $\Psi'$, may now be different from zero.

Solving exactly the matrix elements in expression (9) for calculating the line strength is challenging and several approximations are considered, the validity of which will depend on lanthanide and field configuration.

- First approximation: No ligand-filed splitting of the perturbing configuration $\Psi''$ ($|l^{n-1}\psi''J''M''\rangle$) is considered so $J''$ and $M''$ are degenerate. This is the case when the splitting of $^{S+1}\Gamma_{J''}$ within one scheme of the perturbation level can be negligible compared to the energy difference between the energy of the perturbation level and ground level. Also, the spin–orbit coupling is neglected in this perturbation level.
- Second approximation: The energy of the level $E(\psi'J')$ is set to the mean energy of the corresponding configuration so that it assumes that the band of each transition is symmetric. Also, it is considered invariant with respect to the $\psi''$ and $J''$, which means that the lanthanide ion that has a very broad energy level of the $4f^{n-1}5d$ configuration might not be described perfectly by Judd–Ofelt theory.
- Third approximation: The perturbing configurations lie far above the states for the 4f transitions. If the highest levels of the $4f^n$ configuration are close to the average energy of the perturbing configuration, the mixing of the perturbing configuration and $4f^n$ configuration is canceled.

More elaborate versions of the Judd–Ofelt theory including $J$-mixing, spin–orbit, and vibronic corrections exist to describe more accurately the microscopic behavior of the system in cases where the basic approximations fail.

In all, the final expression of the line strength of the induced electric dipole transition between states $\psi$ and $\psi'$ is given by

$$
\begin{aligned}
S_{ED} &= \sum_{\lambda=2,4,6} \Omega_\lambda \big| \langle \Psi | U^{(\lambda)} | \Psi \rangle \big| \\
S_{ED}(J \to J') &= \sum_{\lambda=2,4,6} \Omega_\lambda \big| \langle S,L,J \| U^{(\lambda)} \| S',L',J' \rangle \big|^2
\end{aligned}
\tag{15}
$$

where the term $\lambda$ ($\lambda$ even and $0 < \lambda \le 6$) is introduced during the calculation of the matrix elements following selection rules for electric dipole transitions regarding $S$, $L$, and $J$ quantum numbers:

$$
|\Delta L| \le 6; \quad |\Delta J| \le 6; \quad |\Delta J| = 2,4,6 \text{ if } J = 0 \text{ or } J' = 0; \quad |\Delta S| = 0
$$

It is noteworthy that the selection rules of $\Delta L$ and $\Delta S$ are only applicable in the Russell–Saunders coupling scheme. If $J$ remains a relatively good quantum number (the $J$-mixing is weak), the selection rule for $\Delta J$ is harder to be broken than in the opposite case (Görller-Walrand et al., 1998; Hatanaka and Yabushita, 2009).

In the above expression, $U^{(\lambda)}$ represents the corresponding irreducible tensor form of the electric dipole operator and the $\Omega_\lambda$ parameters are the phenomenological Judd–Ofelt parameters. The reduced $\langle S, L, J \| U^{(\lambda)} \| S', L', J' \rangle$ values can be considered as essentially geometric for the corresponding configurations given by the $S$, $J$, $L$ numbers in the field geometry, while the Judd–Ofelt parameters can be interpreted as carrying all the physics of the lanthanide–matrix interaction. The solutions of the (lanthanide in ligand field) electric dipole matrix elements $[U^{(\lambda)}] = \langle \Psi \| U^{(\lambda)} \| \Psi' \rangle$ are crucial to estimate the Judd-Ofelt parameters through experimental methods, but complicated. The reduced matrix elements $\langle S, L, J \| U^{(\lambda)} \| S', L', J' \rangle$ for lanthanide ions in both aqueous solution and $LaF_3$ crystals are typically employed to account for these factors.

Given the reduced matrix elements $[U^{(\lambda)}]^2$ and the phenomenological Judd–Ofelt parameters, the whole set of optical transitions can be then analyzed, including the radiative probabilities and branching ratios even if the transitions are not accessible in the spectra. Judd–Ofelt parameters can be obtained from fitting the experimentally measured line strengths to the theoretically calculated line strengths. Typically, this is done from the absorption spectrum, although it can be done with reflectivity measurements or other techniques, including combination with luminescence data if direct access to a reasonable estimate of the radiative lifetime can be achieved in, for instance, cases in which we know low nonradiative quenching rates are expected (Cantelar et al., 2014) or at low-temperature experiments.

If a suitable energy range is employed, the measured line strengths from absorption spectroscopy can provide the three Judd–Ofelt parameters. The

$\Omega_\lambda$ values are determined by minimizing the deviation between the calculated line strength (Eq. 15) as a function of the $\Omega$s and the measured line strength, $S_{\mathrm{me}}$ (from the corresponding absorption coefficient of the electronic transition, Eq. 6) via a standard least-squares method:

$$\Delta^{|\mathrm{calc-meas}|} = \sum_{i=1}^{n} \left( S_{\mathrm{me}}^{(i)} - S_{\mathrm{calc}}^{(i)} \right)^2 \tag{16}$$

with $i$ representing every $^{2S+1}\Gamma_J \to {}^{2S'+1}\Gamma'_{J'}$.

Leading in practical terms to the linear set of equations that can be written in a matrix form:

$$
\begin{pmatrix}
\sum_{i=1}^{n}\left[U_i^{(2)}\right]^4 & \sum_{i=1}^{n}\left[U_i^{(2)}\right]^2\left[U_i^{(4)}\right]^2 & \sum_{i=1}^{n}\left[U_i^{(6)}\right]^2\left[U_i^{(2)}\right]^2 \\
\sum_{i=1}^{n}\left[U_i^{(2)}\right]^2\left[U_i^{(4)}\right]^2 & \sum_{i=1}^{n}\left[U_i^{(4)}\right]^4 & \sum_{i=1}^{n}\left[U_i^{(4)}\right]^2\left[U_i^{(6)}\right]^2 \\
\sum_{i=1}^{n}\left[U_i^{(2)}\right]^2\left[U_i^{(6)}\right]^2 & \sum_{i=1}^{n}\left[U_i^{(4)}\right]^2\left[U_i^{(6)}\right]^2 & \sum_{i=1}^{n}\left[U_i^{(6)}\right]^2
\end{pmatrix}
\begin{pmatrix}
\Omega_2 \\
\Omega_4 \\
\Omega_6
\end{pmatrix}
$$

$$
= \begin{pmatrix}
\sum_{i=1}^{n}\left[U_i^{(2)}\right]^2 S_{\mathrm{me}}^{(i)} \\
\sum_{i=1}^{n}\left[U_i^{(4)}\right]^2 S_{\mathrm{me}}^{(i)} \\
\sum_{i=1}^{n}\left[U_i^{(6)}\right]^2 S_{\mathrm{me}}^{(i)}
\end{pmatrix}
\tag{17}
$$

Importantly, the more bands the fit/comparison includes, the more representative Judd–Ofelt parameters are obtained. However, Eq. (17), together with Table 2, shows that the tensor $U^{(\lambda)}$ components in the corresponding irreducible form provide, in fact, a weighing of the corresponding $\Omega_\lambda$ for the corresponding transitions. So reciprocally, for determining the given parameters, some bands are more representative than others.

The relation of the phenomenological Judd–Ofelt parameters with the lanthanides and ligands nature (including systematic changes like halogenation) and structure has been the subject of numerous studies (Görller-Walrand et al., 1998; Koeppen et al., 1997; Kuriki et al., 2002), mainly in inorganic matrixes (Hehlen et al., 2013; Reid and Richardson, 1984). And several relations have been studied. For instance, it is well established that $\Omega_2$ is intimately related to the radiative probabilities of the so-called hypersensitive transitions of the $Ln^{3+}$, which are the lanthanides' f–f transitions most dependent on the environment ($^4I_{15/2} \to {}^2H_{11/2}$ (520 nm) and $^4I_{15/2} \to {}^4G_{11/2}$ (378 nm) for $Er^{3+}$ and $^4I_{9/2} \to {}^4G_{5/2}$ (580 nm) for $Nd^{3+}$). It and the corresponding line strength for those transitions decrease considerably when the lanthanide is immersed in a more symmetrical environment, representing

**TABLE 2** Squared Reduced Matrix Elements $[U^{(\lambda)}]^2$ for the Given Transitions of $Er^{3+}$ and $Nd^{3+}$ in the Range of Wavelengths up to 375 nm, for the Given Transitions from the Ground States ($^4I_{15/2}$ for $Er^{3+}$; $^4I_{9/2}$ for $Nd^{3+}$) to the Corresponding Excited State $^{2S'+1}\Gamma_{J'}$ $(S'J'L')$

| $Er^{3+}$ | | | |
|---|---|---|---|
| $^4I_{15/2} \rightarrow {}^{2S'+1}\Gamma'_{J'}$ | $[U^{(2)}]^2$ | $[U^{(4)}]^2$ | $[U^{(6)}]^2$ |
| $^4I_{13/2}$ | 0.0195 | 0.1173 | 1.4316 |
| $^4I_{11/2}$ | 0.0282 | 0.0003 | 0.3953 |
| $^4I_{9/2}$ | 0 | 0.1733 | 0.0099 |
| $^4F_{9/2}$ | 0 | 0.5354 | 0.461 |
| $^4S_{3/2}$ | 0 | 0 | 0.2211 |
| $^2H_{11/2}$ | 0.7125 | 0.4125 | 0.0925 |
| $^4F_{7/2}$ | 0 | 0.1469 | 0.6266 |
| $^4F_{5/2}$ | 0 | 0 | 0.2232 |
| $^4F_{3/2}$ | 0 | 0 | 0.1272 |
| $^2G_{9/2}$ | 0 | 0.0189 | 0.2256 |
| $^4G_{11/2}$ | 0.9183 | 0.5262 | 0.1172 |
| $Nd^{3+}$ | | | |
| $^4I_{9/2} \rightarrow {}^{2S'+1}\Gamma'_{J'}$ | $[U^{(2)}]^2$ | $[U^{(4)}]^2$ | $[U^{(6)}]^2$ |
| $^4I_{11/2}$ | 0.0194 | 0.1073 | 1.1652 |
| $^4I_{13/2}$ | 0.0001 | 0.0136 | 0.4557 |
| $^4I_{15/2}$ | 0 | 0.0001 | 0.0452 |
| $^4F_{3/2}$ | 0 | 0.2293 | 0.0549 |
| $^4F_{5/2}$ | 0.0010 | 0.2371 | 0.3970 |
| $^2H_{9/2}$ | 0.0092 | 0.0080 | 0.1154 |
| $^4F_{7/2}$ | 0 | 0.0027 | 0.2352 |
| $^4S_{3/2}$ | 0.0010 | 0.0422 | 0.4245 |
| $^4F_{9/2}$ | 0.0009 | 0.0092 | 0.0417 |
| $^2H_{11/2}$ | 0.0001 | 0.0027 | 0.0104 |
| $^4G_{5/2}$ | 0.8979 | 0.4093 | 0.0359 |
| $^2G_{7/2}$ | 0.0757 | 0.1848 | 0.0314 |

*Continued*

**TABLE 2** Squared Reduced Matrix Elements $[U^{(\lambda)}]^2$ for the Given Transitions of $Er^{3+}$ and $Nd^{3+}$ in the Range of Wavelengths up to 375 nm, for the Given Transitions from the Ground States ($^4I_{15/2}$ for $Er^{3+}$; $^4I_{9/2}$ for $Nd^{3+}$) to the Corresponding Excited State $^{2S' + 1}\Gamma_{J'}$ $(S'J'L')$—Cont'd

**Nd$^{3+}$**

| $^4I_{9/2} \rightarrow {}^{2S'+1}\Gamma'_{J'}$ | $[U^{(2)}]^2$ | $[U^{(4)}]^2$ | $[U^{(6)}]^2$ |
| --- | --- | --- | --- |
| $^2K_{13/2}$ | 0.0068 | 0.0002 | 0.0312 |
| $^4G_{7/2}$ | 0.0550 | 0.1570 | 0.0553 |
| $^4G_{9/2}$ | 0.0046 | 0.0608 | 0.0406 |
| $^2K_{15/2}$ | 0 | 0.0052 | 0.0143 |
| $^2G_{9/2}$ | 0.0010 | 0.0148 | 0.0139 |
| $^2D_{3/2}$ | 0 | 0.0188 | 0.0002 |
| $^4G_{11/2}$ | $\sim$0 | 0.0053 | 0.0080 |
| $^2P_{1/2}$ | 0 | 0.0367 | 0 |
| $^2D_{5/2}$ | $\sim$0 | 0.0002 | 0.0021 |

After Carnall et al. (1968).

the stronger forbidden character of the transitions when a very symmetric environment disfavors Laporte relaxation. Besides, it is usually called the covalency parameter to emphasize that its value is also strongly dependent on the covalency as determined by the polarizability of the electronic cloud of the ligands binding the lanthanide. Due to these reasons, the change in $\Omega_2$ can be employed to elucidate changes in coordination of the lanthanide, for instance, ligand displacements, nonsubstitutive or different sites within the matrix, etc. (Jørgensen and Reisfeld, 1983; Karraker, 1967). Also, it can be observed from Table 2 and Eq. (15) that the radiative probability of the 1.5 μm emission depends mainly on $\Omega_6$, so the determination of this parameter is critical for characterizing the radiative probability of this level.

The determination of the Judd–Ofelt parameters in the presence of organic ligands may be challenging. The parameters are representative of the geometry, so in principle, it would be desirable to obtain them in the working geometry, in the presence of all the ligands and chromophores. However, the absorption of colored ligands may considerably mask the absorption of the lanthanides' states. In the case of characterizing the lower levels of NIR-emitting lanthanides, this is less of a problem, given that the optical transitions of the lanthanide ligand will occur under the gap of the organics, but in NIR-emitting lanthanides showing emissions from the excited state occurring at higher energies than the organic environment, this could be a problem. In general, even in

$Er^{3+}$ and $Nd^{3+}$, an overall characterization involving the upper states would be desired, to account for energy transfer and sensitization probabilities.

Interestingly, the framework of the Judd–Ofelt theory can be employed in describing the sensitization process from the organic chromophore. The energy exchange rate, Eq. (2), can be written as a function of the corresponding $\Omega$ parameters in the case of an electric dipole interaction (and the corresponding reduced tensor operators, $U^{(\lambda)}$ for the interaction); however, the previous remarks on the validity of the approximations are still in force, and the other nondipole mechanisms must be taken into account (Görller-Walrand et al., 1998).

The most important parameter for characterizing the emission properties of NIR-emitting lanthanides is possibly the radiative probability of the emitting state or its reciprocal quantity, the radiative lifetime, $\tau_{rad} = 1/k_{rad}$, which, together with the nonradiative probability, yields the lanthanide efficiency.

Note that $Yb^{3+}$, involving an $f^{13}$ configurations, shows a single possible excited state, $^2F_{5/2}$ (which, in turn, shows relatively large crystal field coupling) at 1.26 eV (1020 cm$^{-1}$) and, therefore, the radiative characterization of the $^2F_{5/2} \rightarrow {}^2F_{7/2}$ transition just requires the measurement of the corresponding reciprocal absorption band $^2F_{7/2} \rightarrow {}^2F_{5/2}$, so the Judd–Ofelt formalism is typically not employed with this ion. However, $Nd^{3+}$ requires the characterization of the branching parameters for the possible decays from the $^4F_{3/2}$ state (see Fig. 2), and thus the Judd–Ofelt formalism becomes very important.

It is important to remark that ideally, the absorption experiments leading to a characterization of radiative processes should be done in similar conditions to the emission conditions. Often, lanthanide complexes' absorption spectra are measured in the solution phase, even for solid-state applications, which may lead to inaccurate measurements. Two factors may affect the reliability of the so obtained radiative deexcitation probabilities. On the one hand, in the solution phase, it is possible that solvent molecules solvate the lanthanide complex, even coordinating directly to the lanthanide by displacing partially or totally one or various ligands. In this case, the molecule geometry and forces may be affected and thus the measured line strengths and Judd–Ofelt parameters may be influenced, leading to inaccurate description of radiative processes. On the other hand, most of the common solvents present strong absorptions in the NIR range, which impede measuring the lanthanide's absorptions in the range (particularly for $Er^{3+}$). This way, Judd–Ofelt parameters $\Omega_\lambda$ determined from the absorption spectrum available in the visible or NIR range can lack representativity for specific NIR transitions, and thus the oscillator strengths inferred from them for the given NIR transitions through Eq. (17) may not be accurate to describe the corresponding emissions.

The difficulty in measuring the line strengths or $k_{rad}$ through absorption spectroscopy experiments, particularly in the infrared range, has motivated an extensive use of generic, approximate $\tau_{rad}$ values around 250–500 μs for $Nd^{3+}$, 8–14 ms for $Er^{3+}$, and ~2 ms for $Yb^{3+}$. The use of these values or

approximate values as derived from the optical absorption in the visible range may mask the absolute values of the efficiencies. Thus, particular attention and care must be employed in the direct comparison of the values obtained in real measurements and in estimates through different measurements as published in the literature, especially when radiative lifetimes, line strengths and Judd–Ofelt parameters have been shown to strongly depend on geometry and composition specially in the case of changes of ligand and environment (Hasegawa et al., 1998). This is so for the $Nd^{3+}$ and $Er^{3+}$ even only changing the ancillary ligand (Wang et al., 2012), and slight changes in functional groups, particularly for fluorinated materials (Iwamuro et al., 2000; Ye et al., 2013b).

## 3.2 The NIR-Emitting Lanthanides' Nonradiative Vibrational Quenching

Similar to nonradiative vibrational quenching of organic states mentioned above, the lanthanides' states are sensitive to radiationless phenomena associated to multiphonon deexcitation. The nonradiative probability for a given vibronic level of the lanthanide is given in terms of the nonradiative electronic interaction Hamiltonian,

$$
\begin{aligned}
w_{\mathrm{ex}\to\mathrm{gr}}^{n,m}(\mathrm{nr}) &= \frac{2\pi}{\hbar}\left\langle \Psi_{\mathrm{ex}}^{m}\middle|\hat{H}_{\mathrm{int}}^{\mathrm{nr}}\middle|\Psi_{\mathrm{gr}}^{\mathrm{n}}\right\rangle\rho(E) = \frac{2\pi}{\hbar}\left\langle \psi_{\mathrm{ex}}\chi_{m}^{(\mathrm{ex})}\middle|\hat{H}_{\mathrm{int}}^{\mathrm{nr}}\middle|\psi_{\mathrm{gr}}\chi_{n}^{(g)}\right\rangle\rho(E) \\
&= \frac{2\pi}{\hbar}\left\langle \psi_{\mathrm{ex}}\middle|\hat{H}_{\mathrm{int}}^{\mathrm{nr}}\middle|\psi_{\mathrm{gr}}\right\rangle\left\langle \chi_{m}^{(\mathrm{ex})}\middle|\chi_{\mathrm{n}}^{(g)}\right\rangle\rho(E) = P_{\mathrm{electronic}}^{\mathrm{nr}}\left\langle \chi_{m}^{(\mathrm{ex})}\middle|\chi_{n}^{(g)}\right\rangle
\end{aligned}
\tag{18}
$$

where $\Psi$ represents the corresponding vibronic state, decomposable in the electronic and vibrational part under the Born–Oppenheimer approximation, $\psi_i$ and $\chi_i$, respectively, where $\psi_i$ represents the lanthanide $^{2S+1}\Gamma_J$ multiplet electronic wave-function and $\chi_{m,n}^{i}$ represents the vibrational part corresponding to the given mode at levels $n$ and $m$ (overtones), and $\rho(E)$ the corresponding density of states (Henderson and Imbusch, 1989).

The partial probabilities thus relate through an electronic coefficient (accounting for the involved electronic interaction) to the corresponding Frank–Condon factors, $\langle\chi_m|\chi_n\rangle$, representing the tunneling probability between the corresponding vibrational states $n$, $m$ in different electronic states. At finite temperature, this is modulated by the partition function, accounting for the thermal population of the vibrational levels. The energy conservation introduces the condition $n=p+m$ for the correspondence of the vibrational levels in the excited and ground states, $p$ being the number of overtones required for the bridging the electronic energy gap, $p=(E_{\mathrm{exc}}-E_{\mathrm{gr}})/\hbar\omega$, with $\omega$ the mode fundamental frequency. For the small vibrational coupling, which is characteristic of the lanthanides, the overall Franck–Condon factors are smaller for larger overtones; thus, it can be demonstrated that the nonradiative multiphonon transition at $0\,\mathrm{K}$ for a mode corresponds to a

negative exponential with the number of overtones of the given mode required for bridging the gap between the excited state and the final state, which in turn is known as the gap law. Sometimes, a slightly modified law applies, when only some vibrations intervene in the deexcitation (van Dijk and Schuurmans, 1983). Moreover, anharmonic effects can be important and have significant consequences on the Franck–Condon factors and thus in the vibrational relaxation probability (Doffek et al., 2012a). It has been shown that gaps smaller than $p = 3$–$5$ overtones for the highest fundamental energy phonon result in a predominant nonradiative deexcitation of the lanthanide (Henderson and Imbusch, 1989; Weber, 1968). This can be particularly important in NIR-emitting lanthanides, in which the gap to lower-lying levels is necessarily small.

The small mass of hydrogen atoms confers the stretching vibrational modes of hydrogen-containing groups a high vibrational energy. In the graph (Fig. 20), the energies of the corresponding overtones of O–H, N–H, and C–H oscillators are represented compared to the gaps of the emitting states for $Nd^{3+}$, $Er^{3+}$, and $Yb^{3+}$. Thus, the abundant presence of hydrogen-containing groups determines that nonradiative processes are dominant for NIR-emitting lanthanides in organic environment. The magnitude to derive the importance of nonradiative quenching is typically the lanthanide quantum yield, or lanthanide emission efficiency $\eta_{Ln}$, ultimately representing the number of emitted photons upon nominal excitation of the lanthanide. It can be demonstrated that for an emitting process described by a lifetime $\tau$,

$$\eta_{Ln} = \tau / \tau_{rad} \tag{19}$$

where $\tau$ is the overall decay time, which relates to the partial radiative and nonradiative probability:

$$\tau^{-1} = \tau_{rad}^{-1} + \tau_{nr}^{-1} = \tau_{rad}^{-1} + \tau_{mp\,nr}^{-1} + \tau_{nr'}^{-1} \tag{20}$$
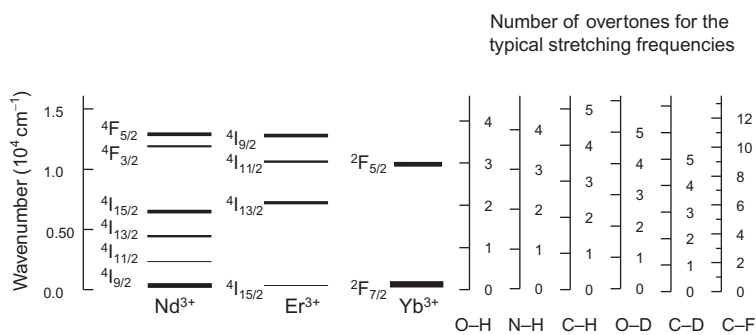


**FIGURE 20** NIR-emitting diagram and representation of the number of overtones of typical frequencies of the O–H, N–H, C–H, O–D, C–D, and C–F groups necessary to bridge the corresponding gaps.

where $\tau_{nr'}^{-1}$ represents other nonradiative mechanisms (like back transfer, or transfer to other lanthanides or quenching centers, etc.). The predominance of the multiphonon decays causes a large value of $\tau_{mprnr}^{-1}$ in comparison to $\tau_{rad}^{-1}$ resulting in typically low efficiencies, in the order of lower than a percent for the majority of the NIR-emitting lanthanides in organic environments. As Eqs. (19) and (20) represent, the competition between the radiative and nonradiative mechanisms determines how luminescent (or efficient) an NIR lanthanide is in the given molecular/organic environment.

The most important challenge for the development of NIR-emitting lanthanides in organic environments has been (and probably still is) the development of environments in which the lanthanides do not suffer from multiphonon quenching. Thus, the magnitude of the quenching has been studied as a function of the structure and chemical nature of lanthanide complexes, and new strategies for minimizing the quenching have been proposed. Typically, the overall contribution of the multiple oscillators can be modeled by a quasicontinuous medium (Quochi et al., 2006). The electronic interactions involved in the purely electronic part of nonradiative vibrational deexcitations are typically distance dependent, and thus, the importance of the presence of the hydrogen-containing oscillators will be affected by a number of electronic interaction issues, including the distance to the lanthanide center. General rules explored (Hasegawa et al., 2004) to minimize the quenching produced by vibrating nearby groups include:

– Filling the coordination sphere of the lanthanide with multidentate ligands, so no hydrogen-rich solvent molecules are in the first coordination sphere of the lanthanide. This is particularly important for organic ligand-based complexes in solutions or produced by wet methods. Sometimes, this requires employing additional neutral or charged ligands than in a purely stoichiometric charge neutralization configuration. The creation of a "caged" ligand in a lipophilic bulky environment contributes to a decrease of the nonradiative quenching rates.
– Eliminating O–H groups in the immediacies of the complex. O–H groups are the most efficient quenchers for lanthanides, typically above other common groups in organic moieties such as C–H and N–H groups; thus, the avoidance of O–H containing solvents or ligands is going to be critical. O–H groups provide important multiphonon quenching channels, even for visible-emitting lanthanides showing a large gap, such as $Eu^{3+}$ or $Tb^{3+}$. It has been observed that the nonradiative decay constant of aqueous-derived quenching of lanthanide ions (measured by comparison of substitution of water for heavy water) is proportional to the number of water molecules in the first coordination sphere of the lanthanide, $q$:

$$q = A(k_H - k_D) - B \tag{21}$$

where $k_H = 1/\tau_H$ is the inverse of the lifetime in hydrogenated medium and $k_D$ is $1/\tau_D$, in deuterated medium and $A$ is a constant depending on the ion, with values $\sim$0.29 or $\sim$2 µs (for $Nd^{3+}$ and $Yb^{3+}$) (Beeby et al., 1999, 2002; Davies et al., 2005).

– Eliminating the presence of C–H and, in general, hydrogenated groups in the successive coordinating spheres of the lanthanide. Although the effect of C–H oscillators is in general smaller than O–H oscillators, which is also contributed by the narrower band profile, their presence (and also that of N–H oscillators and other hydrogenated groups) in the surroundings of the lanthanide, either as a constituent of the solvent or the ligands, is frequent in organics environments. In particular, as we have previously discussed, it has been shown that in general, a closer distance to the lanthanide center bears stronger quenching effects, but relatively long-distance interactions have also shown to quench NIR-emitting lanthanides' excitation.

Figure 20 represents the energies of the O–H, N–H, C–H, O–D, C–D, and C–F overtones in comparison to the energies of the NIR-emitting lanthanides' multiplets, to illustrate the considerable quenching capability of most of them, in terms of the few overtones that can bridge the corresponding gaps to lower-lying states.

## 4 STRATEGIES TO DECREASE MULTIPHONON-QUENCHING OF THE NIR-EMITTING LANTHANIDES

### 4.1 Deuteration

Possibly the easiest way to systematically suppress hydrogen-containing groups without, in principle, requiring significant changes in the chemical processes involves the use of deuterated or perdeuterated species. This has extensively been done for solvents and also for ligands coordinating to the NIR-emitting lanthanides, and it is a simple way of preserving the electronic properties of the involved chromophores. The substitution of hydrogen for deuterium decreases the energy of the oscillators due to the increased mass, and therefore, higher overtones are needed to bridge the gap, resulting in a decrease of multiphonon decay probability.

The effects of deuteration at different positions of hydrogenated chelating ligands have been studied. Interestingly, when multiple oscillating groups occur in the vicinity of the ligand, it is sometimes possible to describe the global effect by a superposition of deactivation mechanisms based on each vibrating group. Through progressive deuteration, partial deactivation rates can be determined from the actual change in the total quenching rate, and thus study the influence the influence of the geometric factors (including distance), and even nonharmonic effects in the nonradiative deexcitation probability of

NIR lanthanides (Bischof et al., 2010; Doffek et al., 2012a,b; Hebbink et al., 2001; Tan et al., 2006; Winkless et al., 2006).

In general, as expected, it has been observed that the effect of deuteration in closer positions to the ligand contributes more to enhance the lifetime, and higher degrees of deuteration provide longer lifetimes, which is ascribed to the decrease of the vibrational energy, and cause an increase of the emission efficiency of the lanthanide.

Although the vibrational energies of the O–H, C–H, and N–H oscillators decrease and thus a larger number of vibrational quanta are needed to bridge the gap between a lower-lying and an NIR-emitting excited state (see Fig. 20), the vibrational quenching caused by O–D, C–D, and N–D is still significant, particularly for $Er^{3+}$ complexes or in organic environments, even upon perdeuteration.

## 4.2 Fluorination

A more efficient way to increase the efficiency through the systematic elimination of hydrogenated oscillators (particularly C–H) in the surroundings of the lanthanide is by including halogens instead of hydrogen in the organic environment of the lanthanide, mainly by the use of halogenated ligands which can often be halogenated versions of previously existing ligands. Inclusion of halogens substituting hydrogen or the design and use of halogenated ligands may require some complex chemistry and may have other consequences apart from the decrease in energy of the vibrational levels.

Fluorination has been particularly studied and rendered significant increases of the lanthanide emission quantum yields. In β-diketonates, which allow for a simple environment to produce a significant change of the degree of hydrogenation near the lanthanide, the inclusion of fluorine has been done through functionalization with fluorinated groups. High degrees of fluorination can be introduced (Binnemans, 2005). In general lines, it has been observed that a larger degree of fluorination contributes more to an enhancement of the lanthanide lifetime with respect to the hydrogenated counterparts, and that large fluorinated groups create a more favorable shell around the lanthanide resulting in protective effects with respect to quenching caused by residual hydrogens in the environment, or in solutions. The success of the partial fluorination strategy to increase the lifetime of NIR-emitting lanthanides allows the remarkable PL lifetime of 130 μs (radiative lifetime 473 μs in PMMA; Wang et al., 2012) that has been obtained for the NIR (1060 nm) emission of the Nd chelate [Nd(tta)$_3$phen], when diluted in a fluorinated polymer 6FDA/epoxy matrix (6-fluorinated-dianhydride) (Yang et al., 2009). The favorable properties of this complex have allowed amplification and laser action of the $Nd^{3+}$ ions in the system upon direct excitation at 0.8 μm (Grivas et al., 2010; Yang et al., 2010).

Fluorination of MOFs has also proved as a good strategy to enhance the NIR-emitting lanthanide properties in extended systems (Chen et al., 2006).

Interestingly, a combined use of deuteration and fluorination can produce advantageous physical effects in the lifetime and somewhat simplify the chemistry, and a number of instances have employed it to increase the NIR lifetimes or quantum efficiencies of lanthanides in organic environments (Kuriki et al., 2002). Quantification of the role of C–H vibrational oscillators on the emission of $Nd^{3+}$, $Yb^{3+}$, and $Er^{3+}$ has been made by using the simple tetrakis lanthanide diketonates $CsLn(hfa)_4$ and the corresponding totally and partially deuterated analogues (when a variable number of ligands are deuterated (at position 3) and the rest are not). The deuterated ligands produce nearly two orders of magnitude increase in the $Er^{3+}$ lifetime to 0.1 ms, 6-fold in the $Nd^{3+}$ and 14-fold in the $Yb^{3+}$ analogues (Tan et al., 2006). Calculations of the effective rate constant for erbium deexcitation due to a single C–H bond as a function of the distance from the emitting ion in the deuterated environment demonstrate that any hydrogen within at least 20 Å of an $Er^{3+}$ ion will produce sufficient quenching to discourage its use as an optical gain medium (Winkless et al., 2006) and similarly in the $Nd^{3+}$ case (Tan et al., 2006).

In these conditions, while deuteration/perdeuteration or partial fluorination may produce significant enhancement of the optical properties of NIR-emitting lanthanides, perfluorination of the organic species surrounding the lanthanide offers possibly the best conditions to achieve a significant quantum efficiency for NIR emission of lanthanides in organic ligand-based complexes and materials, and particularly for $Er^{3+}$-based emitters at 1.5 μm toward optical amplifier applications.

## 4.3 Perfluorination

### 4.3.1 Perfluorinated Ligands and Lanthanide Environments

Possibly due to the considerable chemical difficulties, including the reduced acidity of the binding precursors, and consequent difficulties to coordinate to the lanthanides, few perfluorinated ligands have been proposed. Nearly in all cases, they have been shown to provide remarkably long PL lifetimes, although sometimes not as good as expected by comparison to partially fluorinated complexes.

Perfluoroalkyl carboxylic acid ligands partially complex the $Er^{3+}$ and $Nd^{3+}$ ions, in mono-, di-, and trinuclear structures, and with ancillary ligands (Gao et al., 2009; She et al., 2008; Ye et al., 2013b). In comparison with the hydrogenated alkylcarboxylates, it has been observed that the perfluoro-octane $Er^{3+}$ carboxylate yields a considerably longer NIR luminescence lifetime (up to hundreds of μs) than the $Er^{3+}$ alkylcarboxylates (in the order of μs) (Li et al., 2005). Interestingly, laser action upon 800 nm excitation of a $Nd(tfa)_3$ (tfa = trifluoroacetate) complex in liquid and polymer solution has been observed despite the considerable amount of remaining quenching

oscillators (Yoshioka et al., 2011, 2012). Benzoate and pentafluorobenzoate ligands do not fully chelate the $Er^{3+}$ complexes, but compounds based on the latter ligands also show an enhancement of the optical properties of the $Er^{3+}$ ion (Roh et al., 2004). Similar to these acids, the perfluorohydroxy-monodentate ligand also can be employed to bind to NIR-emitting lanthanides. Interestingly, recently, a series of $Ln^{3+}$, including $Nd^{3+}$, $Er^{3+}$, and $Yb^{3+}$, pentafluorophenolates with phenanthroline (Pushkarev et al., 2014) have been produced and implemented in OLEDs, showing organic-based visible EL and lanthanide-centered NIR-EL in the case of $Nd^{3+}$ and $Yb^{3+}$.

Fluorinated dendrimers based on the pentafluorophenyl carboxylic acid (zero generation) have also been employed to produce NIR-emitting lanthanides in the various generations (increased branching though acetate) (Pitois et al., 2003, 2005) although no data about efficiency are presented. The perfluoroaryl moiety can excite the lanthanides in generations 2 and 3.

The perfluorinated (hepta-fluoro-) version of the acetylacetonate β-diketonate ligand (Fig. 21) in which all the hydrogens, including the one remaining for the hexafluoro-acetylacetonate ligand binds to the $Er^{3+}$ ion to form the tris-diketonate, bis-perfluorotriphenylphosphine perfluorinated complex in which the coordination sphere of the lanthanide is full. This compound shows a relatively with extended NIR emission lifetime (∼17 μs) (Monguzzi et al., 2008).

A series of fluorinated and perfluorinated bis-perfluoroalkylsulfonylaminates, perfluoroalkylsulfonyl-perfluoroalkylaminates, and perfluoroalkyl sulfonates (Hasegawa et al., 2000, 2004) have been studied as ligands for $Nd^{3+}$ and compared to deuterated perfluorofluoroalkyl-diketonates. These materials provide considerably long lifetimes, even in solutions as a consequence of the protection
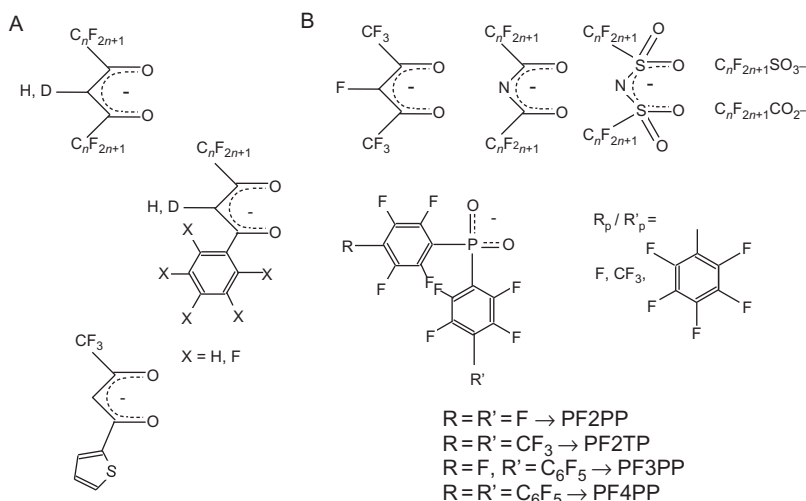


**FIGURE 21** (A) Some fluorinated and (B) perfluorinated ligands for NIR-emitting lanthanides. These ligands show no visible sensitization.

against oscillators in the solvent molecules around the coordination sphere, particularly in the anhydrous compounds. It has been observed that the tris complexes of lanthanides with chelating bis(perfluoroalkylsulfonylaminate) ligands with longer chains are anhydrous and provide good efficiencies as a consequence of the absence of water and the protection against the hydrogenated and deuterated solvents.

Lanthanide perfluoroalkylsulfonates are highly hygroscopic, which severely affects their lifetimes in solid phase. However, dry version of the as-grown solids can yield extremely high luminescence lifetimes. Er(triflate)$_3$ has an stretched exponential lifetime of $\sim$50–150 µs depending on the drying conditions. The butane and octane derivatives show even longer lifetimes (see Section 5.1), up to 1.4 and 2.6 ms for the dry Er(PFBS)$_3$ (perfluorobutanesulfonate) and Er(PFOS)$_3$ (perfluorooctanesulfonate) compound even when the drying conditions are kept mild (120 °C, $10^{-4}$ mbar) to avoid degradation. These waxy materials are highly soluble in water and allow simple processing (via spin-coating, for instance).

Interestingly, a polymeric form of Nafion with perfluoalkylsulfonic acid terminations can be employed to bind Er$^{3+}$ and allow for long-lived lifetimes higher than 100 µs, upon heating at 300 °C for some hours (Song et al., 2010). These polymers are also processable by wet methods in dimethylacetamide solvent.

Another family of perfluorinated ligands include perfluorobisphenylphosphinates (Fig. 21B, bottom). Similar to the hydrogenated analogues, tris complexes of perfluorobis(phenylphosphinate) (PF2PP) of Yb$^{3+}$, Er$^{3+}$, and Nd$^{3+}$ (Song et al., 2008; Zheng et al., 2009) and those composed with functionalized ligands at the p-position of the perfluorophenyl ring (Tan, 2008) arrange in insoluble coordination polymers, apparently along long fibers (Hernández et al., 2009; Tan, 2008). The strong hydrophobic character of the ligands allows for a very efficient elimination of solvent molecules in the fiber structure, leading to long luminescence lifetime, even in the hydrogenated case. So they allow for the longest PL lifetime for an as-grown (nonprocessed) Er$^{3+}$ perfluorinated environment (Hernández et al., 2009). The family has been studied in Yb$^{3+}$–Er$^{3+}$ and other NIR-emitting lanthanides mixed with Y$^{3+}$ (codoping) (Hernández et al., 2009; Song et al., 2008; Tan, 2008). Functionalizations at the p-position of the ligand include perfluoromethyl and perfluorophenyl groups, resulting in perfluorobis-p-tolyl-phosphinate (PF2TP) (Tan et al., 2008), perfluoro-p-phenyldiphenylphosphinate (three rings, PF3PP), and perfluorobis-p-diphenylphosphinate (four rings, PF4PP) (Tan, 2008; see Fig. 21B). Nearly all of the complexes show NIR emissions with nonexponential decay curves involving extremely long average lifetimes and/or components, in the range of 220–780 µs for Er$^{3+}$, 200 µs to 1.8 ms for Yb$^{3+}$, and 20–150 µs for Nd$^{3+}$, increasing when the NIR-emitting lanthanide complex is diluted with the analogue Y$^{3+}$ complex, which proves energy transfer (see below). The hydrogenated analogue bis(phenylphosphinate) compounds are also similarly structured and present considerably smaller lifetimes (5.3 µs for Er$^{3+}$) (Tan, 2008).

A

X = H → tpip          X = F → F-tpip

B

Ln(tpip)₃          Ln(F-tpip)₃
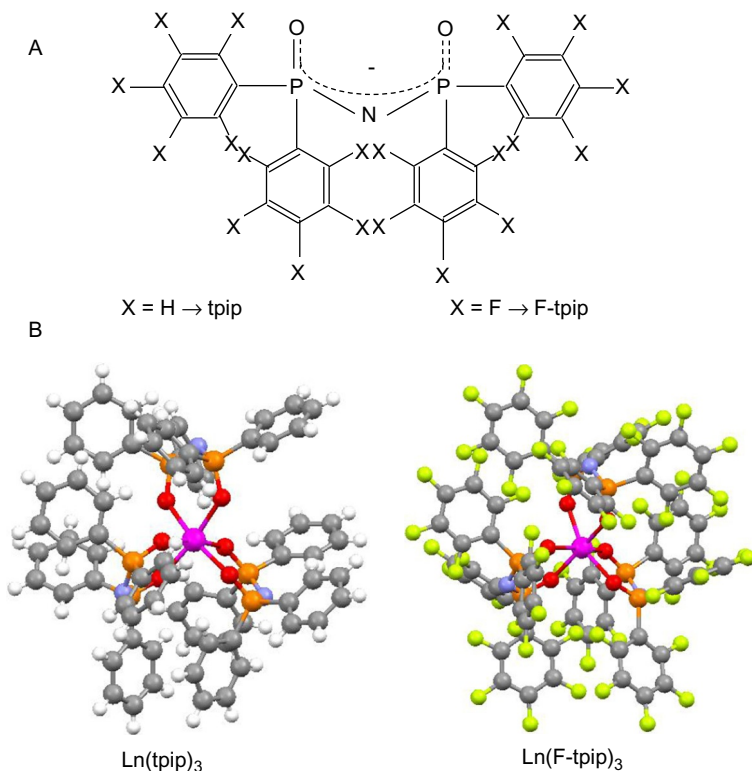
**FIGURE 22** (A) Tetrakis(phenylimidodiphosphinate) ligand and (B) tris complexes of erbium(III) with the hydrogenated (tpip) and perfluorinated (F-tpip) ligands.

Perfluoro-tetrakisphenyl-imidodiphosphinates, F-tpip, $[(C_6F_5)_2P(O)_2]_2N^-$ (Fig. 22), are also extremely favorable ligands for NIR luminescence of lanthanides. Even in the hydrogenated form (tpip = tetrakisphenyl-imidodiphosphinate, $[(C_6H_5)_2P(O)]_2N^-$), Ln(tpip)₃ complexes show remarkable luminescence lifetimes (Bassett et al., 2005) due to the protective shell of 12 phenyl rings around the lanthanide and even though the total coordination of the lanthanide is $z = 6$ (Fig. 22). The lanthanide structure resembles that of the bis(alkylsulfonylamides) and the bis(arylphosphinates) and produces a strong steric hindrance, preventing that even relatively small hydrogenated molecules come in close contact with the lanthanide. OLEDs were tried for the NIR-emitting lanthanides, but no lanthanide-based NIR emission was observed (Katkova et al., 2009).

When three perfluorinated F-tpip ligands form a tris-lanthanide complex, providing 12 perfluorophenyl rings, the lifetime is even more dramatically increased ($\tau \sim 40 \, \mu s$ for $Nd^{3+}$, 150–750 $\mu s$ for $Er^{3+}$, 580 $\mu s$ to 1.1 ms for $Yb^{3+}$) (Glover et al., 2007; Mancino et al., 2005). It is important, however, to remark that while as-grown solid samples offer various component

lifetimes resulting in an average lifetime in the order of 100–200 μs for the $Er^{3+}$, a considerable increase is produced by high temperature, vacuum subli- mation of the complexes at 260 °C (Mancino et al., 2005). Thus, the com- pound results in a very pure form with nearly no volatile hydrogenated species which could be otherwise residually trapped in the structure. The total elimination of hydrogenated oscillators following this process provides a con- siderably reduced multiphonon quenching of the central NIR-emitting lantha- nide and lifetimes higher than 200–300 μs for the $Er(F\text{-tpip})_3$ compounds. The energy transfer between lanthanides in the as-grown and pure compounds (see Section 5.1) is also responsible for the multiple different lifetimes reported as well as for the enhancement upon dilution in dry and deuterated solvents.

From instances published in the literature, it is observed that perfluori- nated complexes in which binding to the lanthanide is done through $RPO^-$ or $RSO_n^-$ units show longer lifetimes than those binding at $RCO^-$ or RCN units. Besides other possible causes, including electronic effects, hydrogen affinity and rigidity, the higher efficiency may be associated to an increase of the mass in the first coordination sphere of the lanthanide and that of the ligand, favoring the decrease in the corresponding mode frequencies. Thus, the overall probability of vibrational tunneling between excited and ground levels is diminished, which favors an overall dominance of radiative deexcita- tion. Also, in general, more massive (highly fluorinated) complexes show a trend to provide an enhanced behavior, maybe due to increased hydrophobi- city and protection against nearby hydrogenated species, but also to this phe- nomenon (even in the case of partial fluorination, such as is the case of the thenoyl-trifluoroacetonate ligand).

Regarding the optical properties of fluorinated lanthanide complexes, and particularly sensitization, it is important to mention that the strongly withdrawing properties of fluorine can cause changes in the electronic levels of the organic chromophore (Babudri et al., 2007). Interestingly, fluorination of aromatic ligands can cause both the negative inductive effect (electron withdrawing) and the positive mesomeric effect (electron releasing). In $Alq_3$, for example, substitu- tion at the C-6 position does not have conjugation effect, but only negative induc- tive effect occurs, which decreases the HOMO and yields an increased band gap and a blue-shifted emission. When F substitution is made at the C-5 position which is far from the large electron density at O atom, the positive mesomeric effect is dominating and thus results in an increased HOMO and redshift com- pared to the parent $Alq_3$ (Shi et al., 2006). When F substitution is made at the C-7 position which is *ortho-* to the O atom, both negative inductive effect and positive mesomeric effect are contributing to the electron density, so the HOMO does not change substantially (Shi et al., 2006), see Fig. 23. Fluorination has also been applied on phosphorescent materials, such as $Ir^{3+}$ complexes. Fluorinated phenylpyridine-type ligands (Ragni et al., 2006) utilize the electron-withdrawing property of fluorine atoms to decrease the HOMO energy level and increase the HOMO–LUMO energy gap, thus obtaining blue phosphorescent complexes, $[Ir(2Fppy)_3]$, $(2Fppy = 2\text{-}[2,4\text{-bis(fluorophenylpyridine)}])$.
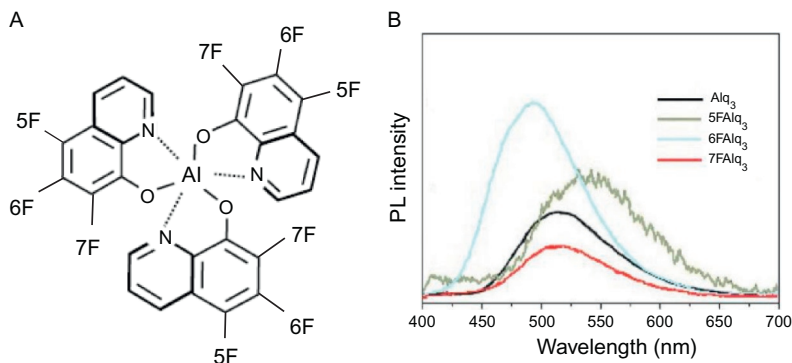
**FIGURE 23** (A) Partially fluorinated AlXFq$_3$ (XFq$=$F-substituted (at position X) 8-hydroxyquinolinato ligand) and (B) corresponding changes in the emission spectrum as a consequence of the changes in the HOMO and LUMO position. *Reproduced with permission Shi et al. (2006)* © *Royal Society of Chemistry.*

Most of the proposed perfluorinated ligands show no sensitization properties in the visible range even though some of them do show sensitization by ligands through the UV-based perfluorophenyl chromophores, at ~300–350 nm (Glover et al., 2007). Although providing a PL lifetime of several hundreds of microseconds up to nearly 1 ms for NIR-emitting lanthanides, perfluoroaromatic and polyaromatic ligands such as perfluoro-phenylphosphinates, perfluoro-polyphenylphosphinate ligands, perfluoro-tolylphosphinates, and tetrakis(phenil imidodiphosphinates) only show sensitization for wavelengths shorter than 350 nm. Fluorination can be thus disadvantageous in terms of the sensitization of NIR-emitting lanthanides for visible or low energy-based excitation applications. To the best of our knowledge, few colored perfluorinated chromophores have been produced.

Pentakis complexes of bidentate tetrafluoro-2-nitro phenoxide (CF$_4$NO$_2$)$^-$ and Yb$^{3+}$, Nd$^{3+}$, and Yb$^{3+}$ with two Cs$^+$ counterions are shown to provide NIR luminescence with poor sensitization from lower-lying states from the ligand in the 400–570 nm range (Zheng et al., 2008). The lifetimes are in the order of 20 μs.

Perfluorinated nitrosopyrazolone (Fig. 24A) is the perfluorinated analogue of nitrosopyrazolone, which has been proved to chelate and sensitize the Er$^{3+}$ ions. The N—O—, C═O groups chelate the lanthanide, and the rest of the ligand conform a more extended conjugated structure providing a long tail to perfluoro-phenyl absorption which reaches up to 560 nm. Corresponding complexes of the ligand in various configurations, including heteroligand ternary complexes completing the coordinating sphere with perfluorotriphenylphosphine (FTPPO) monodentate ligands, allow for solution-processable NIR-emitting (1.5 μm) compounds (Beverina et al., 2009). The authors explain that the absence of visible PL is due to sensitization, causing the presence of NIR luminescence at 1520 upon 355 nm excitation. The lifetime in these systems,
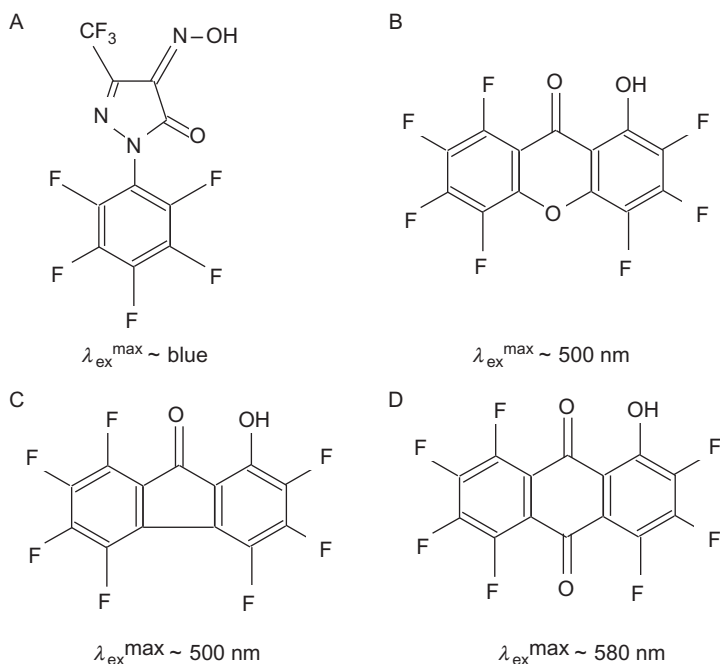
**FIGURE 24** Some colored perfluorinated ligands for NIR-emitting lanthanides and the indicative excitation wavelength for sensitization. A: perflorinated nitriosopyrazolone, B: 8-hydroxy-perfluoroxanthene-9-one, C: 8-hydroxy-perfluoronen-9-one, D: 8-hydroxy-perfloroanthracene-9,10-dione, 2-hydroxy-perfloroanthraquinone.

reaching from 5 to 14–16 μs, is considerable in comparison with hydrogenated samples, but still limited with respect to the potential of fluorination, possibly due to water and residual hydrogens and/or lack of postprocessing to eliminate these.

Bidentate 2-acylphenoxide complexes are structurally somewhat comparable to β-diketonates. Acylated and polycyclic ligands have been produced and homoleptic tetrakis complexes of $Er^{3+}$ and $Yb^{3+}$ based on these ligands with $Cs^{+}$ counterions show a certain degree sensitization in the visible range, as derived from the PL excitation spectrum. Acylated ligands show relatively low sensitization, at ~475 nm, but extending up to 540 nm (Peng et al., 2014). Estimating the sensitization by the rate of chromophore-based excitation with respect to the $Er^{3+}$ direct excitation from the quotient of the areas in the excitation spectrum, values of up to 19% are obtained. Tricyclic ligands (Fig. 24B–D) show an enhanced sensitization, with values in the order of 50% for the areas quotient, and extending at higher wavelengths in the visible, reaching excitation wavelengths longer than 550 nm, up to 650 nm, in the case of the 2-hydroxy-perfluoroanthraquinone ligand (Peng et al., 2014). The decay curves of erbium emission at 1.54 μm of the as-grown samples are considerably nonexponential for this family of compounds, with average decay times

varying in the range of 7–16 μs. Similar to previous cases, the unexpectedly low value for a perfluorinated compound is ascribed to residuals of hydrogen either in the structure or in the trapped solvent molecules.

### 4.3.2 Other Effects of Highly Fluorinated and Perfluorinated Ligands and Environments

Perfluorination, and in general fluorination, may strongly affect the processability of the materials, due to changes in the noncovalent forces and the competition of stabilization forces within the material and the solvent, as a consequence of the fluorine extreme electronegativity. For instance, although the C–H…F forces and F…F interactions are small, the electropositive center of a perfluorinated ring tends to have an electrostatic attraction $\pi_F$-F with electronegative fluorine atoms (Schwarzer and Weber, 2008).

Fluorination causes a significant decrease of the solubility in most of the common solvents. It also typically increases stability and resilience of materials to external perturbations, making them more difficult to melt. Also, if the interactions are important (depending on the packing, if insulated units or polymers are favored), heating may result in degradation instead of evaporation (Berger et al., 2011).

The changes in the HOMO and LUMO and the stacking of the materials as a consequence of fluorination may also produce changes in the charge transport properties, and thus, the electronic properties of the materials for OLED applications (Gurge et al., 1997; Katz et al., 2000; Milián Medina et al., 2007; Sakamoto et al., 2004). Also, the typical downshift of the states caused by fluorination may have favorable effects on the stability of the organic parts through the enhancement of photoreduction potentials.

It has been shown that fluorination has also consequences in the radiative behavior of lanthanides (Ye et al., 2013a). Fluorination in organic environments may affect the geometry as a consequence of noncovalent interactions or steric hindrances. Changes in geometry of the surroundings of the lanthanide cause differences in the corresponding line strengths for the lanthanide states and thus the f–f deexcitation probabilities. This can be particularly significant in the so-called hypersensitive transitions. This phenomenon can be analyzed in terms of the Judd–Ofelt parameters that are employed for phenomenologically describing the radiative behavior. In particular, $\Omega_2$ has been shown to be strongly dependent on the geometry and covalency (Hehlen et al., 2013; Jørgensen and Reisfeld, 1983; Karraker, 1967). Even if the changes in geometry of complexes upon fluorination may be relatively small, due to its extraordinary electronegativity, fluorine may have a strong electron withdrawal effect which may be a considerable perturbation in the covalent components. Judd–Ofelt analysis in the fluorinated and perfluorinated analogues of $Nd^{3+}$ and $Er^{3+}$ complexes shows changes in $\Omega_2$ upon fluorination for analogue ligands (Hasegawa et al., 1998; Ye et al., 2013a).

Also, importantly, reported measurements of $\Omega_2$ for organic complexes of lanthanides show a strong dependence for $Er^{3+}$ and $Nd^{3+}$ with the solvent, which represents an important proof of the interaction of the solvating molecules with the lanthanide geometry.

The measurements of $\Omega_6$ and the line strength of the NIR emission at 1.54 μm, which is strongly dependent on it, show a considerable enhancement upon fluorination and perfluorination with respect to the hydrogenated analogues, as observed for $Er(acac)_3/Er(hfa)_3$ and $Er(tpip)_3/Er(F-tpip)_3$ (hfa = hexafluoroacetylacetonate; acac = acetylacetonate) in crystals. This is interpreted as a consequence of the withdrawal of electrons at the donor site, allowing for an expansion and mixing of the lanthanide states for enhanced overcoming of Laporte's rule. The radiative lifetimes, either as calculated from the Judd–Ofelt analysis or as measured from the absorption of the crystals, are strongly reduced upon fluorination or perfluorination with values nearly halved for the fluorinated compounds with respect to the hydrogenated analogues (Ye et al., 2013a). Thus, fluorinated compound $Er(F-tpip)_3$ yields a radiative lifetime ~12 ms, while the hydrogenated compound $Er(tpip)_3$ shows a value up to 18 ms. If partial or total fluorination implies changes in geometry or coordination changes, the radiative lifetime may also show significant variations for the different configurations. The values of radiative lifetime range from 23 ms in the mostly centrosymmetric fluorinated environment for $Er^{3+}$, $Cs[Er(hfa)_4]$ in which the erbium shows a very symmetric octacoordinated environment with four hfa ligands to values of ~10 ms in the more distorted coordination sphere in fluorinated structure $Er(hfa)_3$, which also shows a considerable reduction with respect to the hydrogenated analogue. The difference in radiative lifetimes must be taken into account when estimating the PL quantum yield of the lanthanide complex in the fluorinated environment. The decrease in radiative lifetime causes an additional increase in the overall efficiency calculated as $\tau/\tau_{rad}$ and which can be ascribed to the effect of fluorination (Table 3).

**TABLE 3** Radiative Decay Rate for $Cs[Er(hfa)_4]$, $[Er(acac)_3(H_2O)_2]$, $[Er(hfa)_3(H_2O)_2]$, $[Er(tpip)_3]$, and $[Er(F-tpip)_3]$ (Ye et al., 2013a)

| Material (Solid Form) | $\langle\tau\rangle$ (Measured) | $\tau^{rad}$ (Measured) | $\eta_{Ln}$ (%) |
|---|---|---|---|
| $CsEr(hfa)_4$ | 1.8 μs | 23.4 ms | 0.0086 |
| $Er(hfa)_3(H_2O)_2$ | 1.8 μs | 9.5 ms | 0.0190 |
| $Er(acac)_3(H_2O)_2$ | 60 ns | 16.9 ms | 0.0004 |
| $Er(tpip)_3$ | 5 μs | 18.4 ms | 0.026 |
| $Er(F-tpip)_3$ | 200 μs | 12.6 ms | 1.5 |

Importantly, the inclusion of heavier atoms such as fluorine and/or other halogens can also have an effect on the ISC, affecting the fluorescence, phosphorescence, and energy transfer properties from the organic chromophores to the lanthanides (Zheng et al., 2008).

## 4.4 Other Halogens

Besides fluorination, the replacement of hydrogen for other halogens such as chlorine or bromine may also contribute to the decrease of multiphonon nonradiative properties as a consequence of the mass effect. However, it has been shown that the reduction of multiphonon quenching through chlorination might be potentially less effective than through fluorination, due to the anharmonicity of the oscillators involving the softer chlorine atoms (Doffek et al., 2012a; Monguzzi et al., 2009).

Bromination of porphyrin-derivative ligands in erbium complexes shows that the lifetime increases from 1.5 μs in the hydrogenated [Er(acac)(TPPor)] (TPPor = 5,10,15,20-tetraphenylporphyrin) complex to 2.5 μs in the fluorinated version [Er(acac)$_3$(FTPPor)] (FTPPor = 5,10,15,20-tetrakis-(pentafluorophenyl)-porphyrin) and to 3.5 μs in the brominated version in which all the remaining hydrogen atoms in the porphyrin rings were replaced for bromine (Pizzoferrato et al., 2003). 5,7-Dihalo-8-hydroxyquinolinates (halo = chloro, bromo, or iodo) have shown to provide more favorable environments for $Nd^{3+}$, $Er^{3+}$, and $Yb^{3+}$ (van Deun et al., 2003). However, mononuclear and polynuclear complexes have been observed for this family of compounds, so further considerations may be required to analyze the effects (Artizzu et al., 2011). In the case of carboxamide functionalization in the 2-position to produce the tridentate ligand, it is observed that higher degree of bromination shows enhanced quantum efficiency (Albrecht et al., 2007). Eosin and erythrosine are tetra-brominated and tetra-iodinated analogues of the fluorescein chromophore which have been used in terphenyl-based ligands (Hebbink et al., 2003) and polyaminocarboxylates (dtpa) (Werts et al., 1997). In the case of dtpa, bromination offers an increase of the lifetimes for all three ions. In the terphenyl-based complex, halogenation results in a slight increase in the $Yb^{3+}$ lifetimes but no improvement in the other cases. However, the halogenation from fluorescein to erythrosine redshifts significantly the chromophore states, which disfavors sensitization for $Nd^{3+}$, $Er^{3+}$, and $Yb^{3+}$ in the case of the terphenyl complex (Hebbink et al., 2003), while no significant changes occur for the dtpa complexes. Interestingly, the iodinated (at position 3) version of the BODIPY (4,4-difluoro-4-bora-3$a$,4$a$-diaza-$s$-indacene) chromophore sensitizing the $Yb^{3+}$ NIR luminescence when functionalizing quinolinate-based ligands (6-iodo-8-hydroxyquinolinate, for the iodinated BODiPY) also shows an excitation redshift with respect to the perhydrogenated version. In this case, the iodinated compound enhances ISC (Section 4.5) and provides longer lifetimes than the noniodinated analogues

(note that the BODIPY is difluorinated, and the quinoline ligand is also iodinated in this work). In this case, DFT calculations relate the redshift with iodine-enhanced stacking interactions (He et al., 2012).

The highly brominated (but highly hydrated) dimetallic compound of $Nd^{3+}$ with tetrabromoterephthalic acid $[Nd_2(TBTA)_3(H_2O)_{10}]$ has been recently produced (Wei et al., 2014) and shows the characteristic $Nd^{3+}$ NIR emission upon excitation at 356 nm.

Perchlorinated tropolonates (Fig. 25) are the perchlorinated analogues of the well-known tropolonates, which include the tropolone chromophore to sensitizing NIR-emitting lanthanides in the 300–420 nm range (see above). Tetrakis tropolonates of $Er^{3+}$, $Yb^{3+}$, and $Nd^{3+}$ show lifetimes of up to ~5, 12, and 1 μs, respectively, in solutions of the potassium salt $K[Ln(trop)_4]$ in deuterated DMSO (Zhang et al., 2005, 2007c). Some of the perchlorotropolonate (pctrop)-based complexes, such as $Cs[Ln(pctrop)_4]$, have been produced.
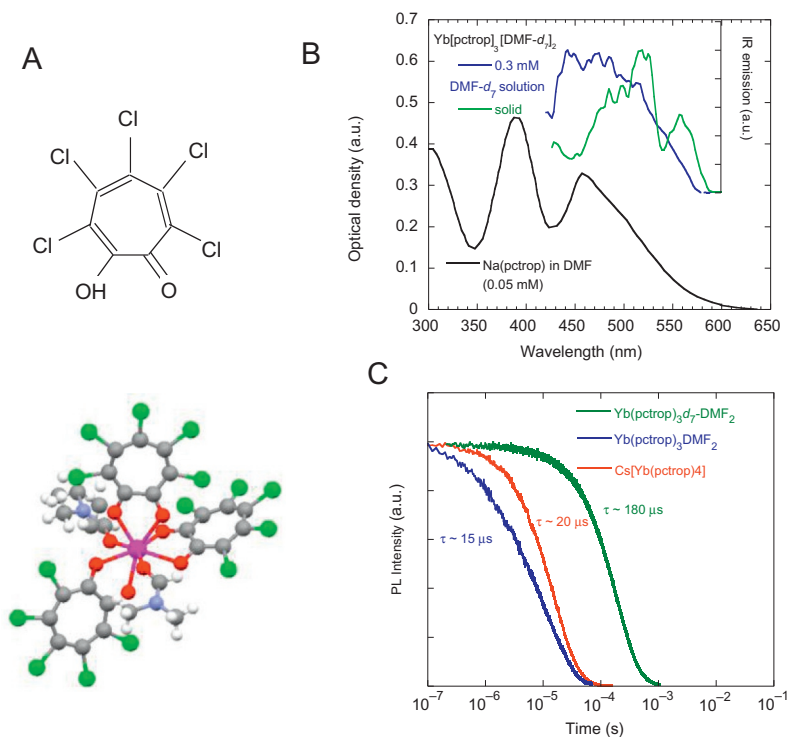


**FIGURE 25** (A) Perchlorotropolone (H-pctrop) and $[Yb(pctrop)_3(DMF)_2]$ complex (Hernández et al., 2013). (B) Inset: Excitation spectrum of the 980 nm emission of the corresponding $Yb^{3+}$ tris complexes and absorption of the sodium tropolonate complex in solution. (C) Decay curves and lifetimes of the tris and tetrakis complexes and the deuterated version of the $[Yb(pctrop)_3(DMF)_2]$, $[Yb(pctrop)_3(d_7$-DMF$)_2]$ in the solids.

The as-grown solid compounds of the tetrakis $Yb^{3+}$ (Fig. 25C) and $Er^{3+}$ complexes provide a PL lifetime in the order of 20 μs, which is still reduced for a perhalogenated sample, and may include the effects of surrounding hydrogen atoms or solvent molecules. Interestingly, the tris-perchlorotropolonate $Yb^{3+}$ and $Er^{3+}$ complexes, in which the coordination sphere is completed by two DMF molecules (Fig. 25), have been studied in solid phase and in solutions incorporating DMF as a solvent (Hernández et al., 2013). The lifetimes of the solids are similar to the tetrakis case for the $Er^{3+}$ complex. Solutions of [Yb(pctrop)$_3$(DMF)$_2$] in deuterated DMF feature a lifetime $\tau \sim 10$ μs, which is smaller than the observations of the detuerated DMSO solutions of the tetrakis hydrogenated compound. This smaller value is possibly associated to the smaller quenching effect of the deuterated oscillators in the DMSO solvent when measured for the tropolonate sample. However, the solid form incorporating the deuterated DMF as a ligand shows a dramatic increase of the NIR PL lifetime to values up to 180 μs, representing a 15% lanthanide quantum yield and thus, the most efficient nonfluorinated complex of an organic ligand (Hernández et al., 2013). All of the tetrakis and tris-perchlorotropolonate complexes show sensitization in the UV–Vis range. The perchlorotropolone ligand absorption is very similar to that of the $Yb^{3+}$ tris complex in DMF and peaks at around 450 nm, with a tail extending over 580 nm (Fig. 25B); the visible absorption of the solid materials experiences a redshift with respect to the solutions, reaching longer than 620 nm (Hernández et al., 2013). Excitation of the $Yb^{3+}$ NIR emission in these compounds reproduces the corresponding organics-based absorption. Although an important increase of the PL intensity is observed upon organics-based excitation in the solutions and in the solid, a visible luminescence at the same wavelength as the one present in the $Y^{3+}$ analogue is also observable, with lifetime in the order of nanoseconds, showing that the sensitization is not 100% efficient (Hernández et al., 2013). Similar tris complexes with only one perchlotropolonate, two $C_6Cl_5CO_2^-$ and three DMF in coordination with the trivalent lanthanide show comparable sensitization and lifetime properties.

## 4.5 Other Effects of Halogenation

We have already mentioned (particularly in the case of the fluorination) the effect on the HOMO and LUMO of the chromophore. For the other halogens, this can occur too, which may affect strongly the stabilization of the complexes (Plata-Iglesias et al., 2000) and sensitization of the lanthanides (as, for instance, observed in the fluorescein, eosin, and erythrosine series; Hebbink et al., 2003). Moreover, the inclusion of heavy atoms like halogens may have an important effect on the organics states' energies and dynamics with consequences on the sensitization mechanisms and efficiencies, including ISC (as in iodinated BODIPY (He et al., 2012; Yogo et al., 2005)).

As we have said, changes in the composition may cause the energy shift of the HOMO and LUMO orbitals with respect to the hydrogenated analogues resulting in a change of the singlet and triplet energies. Thus, the energy resonance conditions with the lanthanides' states may become altered with respect to the hydrogenated analogue. This phenomenon can be employed to elucidate the main sensitization mechanisms as well as donating states of the chromophore and accepting states of the NIR-emitting lanthanide. For instance, the enhanced fluorescein sensitization of $Er^{3+}$ with respect to the heavier atom analogues implies an excitation transfer to higher-lying levels (Hebbink et al., 2003). But halogenation may also have an effect on the dynamics and thus the excited state lifetimes, which can also affect the overall sensitization process, for instance, regarding the vibrational quenching of the singlet and triplet states themselves after the changes in mass and harmonicity.

Importantly, halogenation can affect the ISC rates, which should change the corresponding chromophore's states lifetimes and also the sensitization channels. As we have previously commented in Section 2, the long lifetime and quantum numbers of the triplet mean that very often much of the sensitization from the organics states is produced through the triplet states, lying at lower energy than the singlet states and populated via nonradiative transitions changing spin and known as ISC. First, if the gap between singlet and triplet states is affected, the ISC rates may be affected as a consequence of the changes in the energy barrier. Second, ISC involves a magnetic interaction mixing the spin singlet and spin triplet states so that the nonradiative transition from a state with eminently total spin number $S=0$ to a state with eminently triplet spin state is possible. The enhancement of magnetic interactions such as spin–orbit coupling, $\xi$, has been proved to strongly influence ISC processes. It is well known that heavier atoms provide enhanced spin–orbit interaction as consequence of the increased total spin of the heavier nucleus; thus, the spin–orbit interaction shows a monotonous increasing dependence with $Z$ ranging from $\xi \sim Z$ to $\xi \sim Z^2$ and higher dependences (Dehmer, 1973; Landau and Lifshitz, 1977; Montalti et al., 2006). The influence of a high $Z$ atom due to the inclusion of the lanthanide or transition metal ions in the chromophore does increase the ISC. The influence of the heavy ion over the ISC depends on its distance to the valence electron. Therefore, spin–orbit coupling due to lanthanides or metal ions will be important in the chromophore if the electronic states involve MLCT or LMCT, or if the electronic wave-function has a significant spatial distribution over the metal. If the organic states involve LLCT or ILCT, the electronic wave-function mainly based on given organic-based fragment or ligands, the heavy metal ions will have less influence on the ISC, but heavy-atom substitutions on the ligands are expected to have more consequences. Thus, the use of halogenated ligands in organic chromophores can provide an enhanced singlet–triplet mixing. Enhanced singlet–triplet mixing can increment the total number of triplets at

expenses of the singlets via nonradiative transition (or vice versa, if the energy barrier can be overcome) which should cause an increase of the phosphorescence at expenses of the fluorescence and an overall decrease of the corresponding lifetimes. But importantly, in the presence of mixing interactions, spin quantum number can no longer be considered an accurately describing number, and spin rules allowing and permitting radiative transitions are relaxed. Thus, less pure singlet and triplet character of the excited states of the organic will provide increased oscillator strength to the ground-state to first excited-state radiative transition. This way, the corresponding band in the absorption spectrum may be enhanced and, if transfer to the lanthanide is predominantly done through the lower lying or more triplet-character states, it will be even more significant in the PL excitation spectrum. This is the model that is consistent with observations in lanthanide complexes of perchlorinated and perfluorinated ligands which show unexpected bands below the main organic-based absorption peaks (Hernández et al., 2013; Zheng et al. 2008).

Also interestingly, the enhancement of the triplet absorption can be used to extend the sensitization energy range. The inclusion of sensitization from optically excited triplets can downshift the photoexcitation wavelengths considerably (up to 150 nm). Also, if an electronic method is employed for exciting the lanthanide in NIR OLED configurations, in which an initially 25–75% singlet-to-triplet ratio is expected, the enhanced ISC interactions in halogenated compounds with respect to the hydrogenated analogues must be taken into consideration to correctly describe the system.

The efficient lanthanide complexes obtained by (per)fluorination or halogenation allow sometimes to observe PL (even sensitized, upon chromophore excitation), from the higher-lying levels of some NIR-emitting lanthanides. This is unusual in the general case of $Er^{3+}$ or $Nd^{3+}$ in organic environments because the potential blue/green/red or NIR-emitting transitions occur from levels showing small gaps with respect to the lower-lying ones (see Fig. 2) and thus are strongly quenched by molecular vibrations. Due to the decrease in the quenching probability as a result of the substitution of hydrogenated oscillators (particularly by fluorination), emissions may be observable. Green/red/980 nm emissions from the $^4S_{3/2}$, $^4F_{9/2}$, and $^4I_{11/2}$ states, respectively, can be measured in $Er^{3+}$ (and also some visible emissions for $Nd^{3+}$, although more difficultly) at very high excitation powers and high concentrations (either in the solid or in very concentrated solutions in solvents), particularly in the case of highly fluorinated and perfluorinated compounds. The visible emissions of NIR-emitting lanthanides can be also masked by the visible luminescence of the organic chromophores. It is well known that NIR-emitting lanthanides are poor visible emitters in organics, and visible lanthanide emission research is typically focused on $Eu^{3+}$ and $Tb^{3+}$. Other lanthanides like $Sm^{3+}$, $Pr^{3+}$, and $Dy^{3+}$ may also emit in the NIR and visible ranges (although with relatively low yields, due to similar reasons to $Nd^{3+}$ and $Er^{3+}$), so could also benefit from the ligands and environments showing high efficiency as described above.

## 5 ENERGY TRANSFER BETWEEN LANTHANIDES

Similar to the energy transfer between the organics-based states and the lanthanides, energy exchanges can occur between lanthanides if the multiple competing mechanisms and interactions between ions allow for them. The exchange of energy between an excited lanthanide ion and another lanthanide ion (which may be identical or of a different nature, in the ground or in an excited state) is described similar to the sensitization processes referred in Section 2.3. In this case, the sensitizer is the excited lanthanide which is transferring part or all of its energy to another lanthanide, and the acceptor is the one being promoted to the (higher) excited state.

Energy transfer phenomena between lanthanides are generally termed cross-relaxation, if partial energy transfer between ions or energy transfer to an excited state. [special cases include sensitization (energy transfer from a lanthanide to a different nature lanthanide in the ground state) and energy transfer upconversion (ETU) if the acceptor is in an excited state and the new excitation promotes it to an even higher state resulting in emission at higher energies than excitation] and excitation hopping or energy migration (when the total excited energy is transferred to an identical ion in the ground state to the same excited state as the original). Figure 26 represents these energy transfer processes in pairs of NIR-emitting lanthanides of the same or different nature. As in the general case, a number of (more or less relaxed) quantum rules apply, and the energy transfer is importantly dependent on the distance between the lanthanides, and the resonance conditions are very important, although nonresonant and vibrationally assisted energy transfers are known to occur (Reinhard and Güdel, 2002). The times for the occurrence
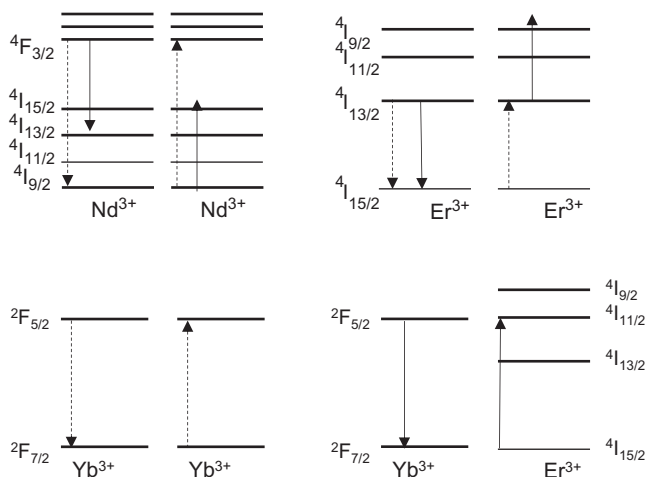


**FIGURE 26** Cross-relaxations resulting in a loss of the excitation, excitation migration processes (dotted lines) and sensitization in pairs of NIR-emitting lanthanides, $Nd^{3+}$, $Er^{3+}$, and $Yb^{3+}$.

of energy transfer, as derived from the inverse probabilities per unit time, are generally in the order of some nanoseconds to microseconds and depend considerably on the transfer mechanism and distances between centers. Therefore, these processes will be observable when their probabilities or associated times are comparable to other dynamic processes, mainly in the case of the long-lived states. Given that higher thermal factors typically increase the quenching probability due to the enhancement of the population of higher vibrational states and the consequent effect in the vibronic tunneling probability (see Section 3.2), emission of NIR-emitting lanthanide from higher-lying states has a better chance to be observed at lower temperatures.

## 5.1 Cross-Relaxation and Energy Migration

Very often, the occurrence of energy migration and cross-relaxations results in a loss of excitations and thus a decrease of the efficiency of NIR-emitting materials. This can be either a consequence of excitation of upper levels—resulting either in ETU or energy losses in subsequent nonradiative deexcitations in the acceptor- or, in the case of energy migration, because the excitation is led to nonradiative impurities in the material. However, sensitization of NIR-emitting lanthanides from other lanthanides has been exploited in inorganic matrixes for enhancing the desired emission (and also exploited for upconversion (UC), see Section 5.2). Particularly, the high oscillator strength of the $^2F_{7/2} \rightarrow {}^2F_{5/2}$ of the $Yb^{3+}$ ion at 0.98 μm provides efficient pumping which, with subsequent energy transfer to an unexcited $Er^{3+}$ $^4I_{15/2}$ ion, results in the promotion to the resonant $Er^{3+}(^4I_{11/2})$ and then emission from $Er^{3+}(^4I_{13/2})$ at 1.5 μm.

Lanthanide–lanthanide energy transfer has been observed for various lanthanides (mainly $Er^{3+}$ toward NIR emission) in inorganic complexes and in directly excited NIR lanthanides in polymers (Chen et al., 2009; Wong et al., 2004) and frameworks (White et al., 2009a), as well as in directly and indirectly excited polynuclear complexes. With the objective of enhancing NIR emission, sensitization from other lanthanides has been done mostly by $Yb^{3+}$–$Er^{3+}$ transfer (Artizzu et al., 2013; Tanaka and Ishibashi, 1996; Zhong et al., 2006) but also for $Tb^{3+}$–$Yb^{3+}$ (Faulkner and Pope, 2003) and in hybrids for $Eu^{3+}$–$Er^{3+}$ and $Eu^{3+}$–$Yb^{3+}$ (Biju et al., 2013). Even though lifetimes are small in a highly hydrogenated environment, hetero-trinuclear hydroxyquinoline complexes containing $Yb^{3+}$ and $Er^{3+}$ ions in DMSO reported considerable sensitization. The proximity of the ions and the strong resonance condition between $Er^{3+}$ and $Yb^{3+}$ causes a strong energy transfer, upon direct excitation and excitation on the ligands.

When the PL lifetimes of the NIR lanthanides in organic environments are enhanced, long-distance cross-relaxation and energy transfer processes can be important. Highly fluorinated $[Yb(hfa)_3(TPPO)_2]$, TPPO = triphenylphosphine oxide, shows a 89 μs lifetime for the 0.98 μm emission, and the cocrystalline $[Er_{1/2}Yb_{1/2}(hfa)_3(TPPO)_2]$ shows a 84 μs lifetime for the same emission. This,

together with the considerably enhanced $Er^{3+}$ emission either under ligand or IR excitation, demonstrates the occurrence of strong $Er^{3+}$ sensitization from the long-lived $Yb^{3+}$ ions (Zhong et al., 2006).

Sensitization of the $Er^{3+}$ 1.54 μm emission from excitation in the $Yb^{3+}$ 0.98 μm absorption has been employed in "transparent" perfluorinated phenyl-phosphinate compounds showing no organic-mediated visible or infrared sensitization (Song et al., 2008). When the $Yb^{3+}$ lifetime is of the order of 400 μs in the pure compound, $Yb^{3+}$-to-$Er^{3+}$ energy transfer allows for a considerable increase of the emission at the telecommunication line. The decrease of cross-relaxation mechanisms also explains the enhancement of the lifetime of the $Er^{3+}$ emission in the codoped $0.5Yb^{3+}$–$0.5Er^{3+}$ systems (Song et al., 2008).

A study of the lifetime of $Er^{3+}$, $Nd^{3+}$, and $Yb^{3+}$ perfluorobis($p$-phenylphosphinates), perfluorobis($p$-tolylphosphinates) (PF2TP), and other PFXPP of the same family (Fig. 21B, bottom) upon dilution of the NIR-emitting lanthanide with $Y^{3+}$ in $[Ln_xY_{1-x}[PF2PP]_3]$ and $[Ln_xY_{1-x}[PF2TP]_3]$ shows that energy transfer is responsible for the decrease of the lifetime for upon increasing the $Ln^{3+}/Y^{3+}$ content from 0.1% to 100% (Hernández et al., 2009; Tan, 2008; Tan et al., 2008; see Table 4). The behavior of the decay curves has been found to be strongly nonexponential for most of the lanthanides, especially at high concentrations. It has been described by a modified exponential function (Lindsey and Patterson, 1980)

$$I(t) = I_0 \ \exp\left[-(t/\tau)^{\beta}\right] \tag{22}$$

The function is referred to as William–Watt or stretched exponential distribution, where $I_0$ is the initial intensity and $0 < \beta \leq 1$ is the stretching function. Using this stretched exponential function, it is possible to define a lifetime distribution function and calculate an average relaxation time in which different decay constants are accounted for, on the basis of the continuous distribution of lanthanide ions transferring and decaying with different probabilities. Interestingly, in parallel to the increase of the $Ln^{3+}$ average lifetime upon dilution, the decay becomes more exponential, to finally turn into monoexponential ($\beta = 1$) at low NIR-emitting lanthanide concentrations. The distribution of lifetimes has also been found to depend on the fiber morphology (Hernández et al., 2009).

For the $Er^{3+}$ compounds, it has been possible to demonstrate that the decrease in the lifetime is due to hopping and cross-relaxations between the lowest-lying excited states. Donating $Er^{3+}$ ions in the $^4I_{13/2}$ state are capable of transferring their energy to neighboring $Er^{3+}$ ions in the ground state or to excited erbium atoms in the $I_{13/2}$ state, thus promoting the latter to the $I_{11/2}$ state. The subsequent nonradiative deactivation of this short-lived state as a consequence of the vibrational decay to the lowest-lying state ($I_{13/2}$) results in the loss of a photon (Hernández et al., 2009), which has been established through experiments varying temperature and pressure.

**TABLE 4** Summary of Nd/Er $(PF2PP)_3/(PF2TP)$ Average Lifetimes (in microseconds) as a Function of Ion Concentration, $x$ (Tan, 2008)

| Material | Ion Concentration ($x$) | | | | | | | | | |
|---|---|---|---|---|---|---|---|---|---|---|
| | *100%* | *97%* | *93%* | *90%* | *85%* | *80%* | *70%* | *50%* | *30%* | *10%* |
| $Er_xY_{(1-x)}(PF2PP)_3$ | 343 | 437 | 540 | 606 | 556 | 597 | 629 | 659 | 717 | 707 |
| $Er_xY_{(1-x)}(PF2TP)_3$ | 222 | 187 | 230 | 312 | 393 | 434 | 496 | 576 | 677 | 669 |
| $Nd_xY_{(1-x)}(PF2PP)_3$ | 38 | 42 | 46 | 49 | 46 | 53 | 63 | 67 | 68 | 85 |
| $Nd_xY_{(1-x)}(PF2TP)_3$ | 76 | 81 | 91 | 99 | 103 | 101 | 117 | 132 | 132 | 154 |

A comparable increase of lifetime upon dilution of the NIR-emitting lanthanide compound with the $Y^{3+}$ analogue has been observed for $Nd^{3+}$ and $Yb^{3+}$. However, it must be noted that quenching of $Yb^{3+}$ compounds does not involve cross-relaxation but only hopping and transfer to excitation killing (nonradiative) sites. This results in a different thermal behavior (Hernández et al., 2009).

Dry $Er^{3+}$ tris-perfluoromethanesulfonate (triflate, PFMS), $Er(PFMS)_3$, $Er(PFBS)_3$ (PFBS = perfluorobutane sulfonate), and $Er(PFOS)_3$ (PFOS = perfluorooctanesulfonate) show longer lifetimes as the perfluoroalkyl chain is increased: from ~60 μs to 1.4 ms and 2.6 ms, respectively. This alone could be a consequence of the increased hydrophobicity; however, dilution of the $Er^{3+}$ content with $Y^{3+}$, to form the $[Er_xY_{1-x}(PFXS)_3]$, X = M (methane), B (butane), O (octane) compounds, shows an extraordinary increase of the 1.5 μm lifetime for the same chain length (Fig. 27), along with an increase of the intensity for the same excitation conditions. This is as a consequence of the increase of the average distance between the lanthanides in the polymer which decreases the importance of energy transfer mechanisms.

This section demonstrates that enhancement of the lifetime of NIR-emitting states causes an increase in energy transfer mechanisms, so efficient organic environments are not free from the occurrence of these mechanisms, which are in principle undesired for NIR applications, as is the case in inorganic environments. However, the enhanced concentration of excited states in the lower-lying levels of the NIR-emitting lanthanides due to the enhanced
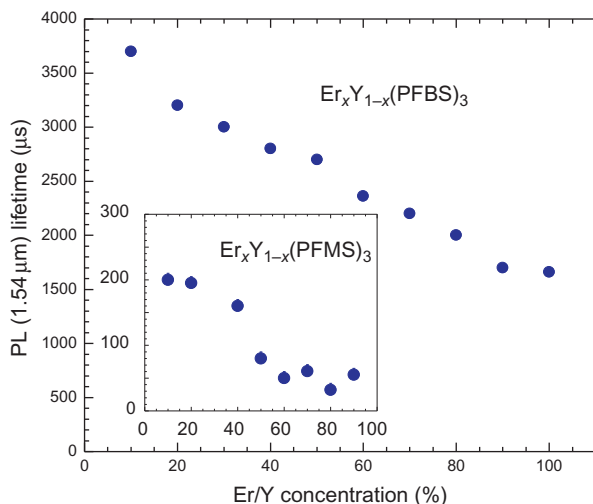


**FIGURE 27** Evolution of the average decay time (as obtained from a stretched exponential function) for dry $Er^{3+}$ perfluoroalkane sulfonates as a function of the Er/Yb content along $[Y_{1-x}Er_x(PFXS)_3]$, X = M (methane), B (butane). The decrease of the lifetime upon increase of the $Er^{3+}$ concentration is ascribed to cross-relaxation and hopping processes involving excited levels in the $Er^{3+}$ (Fig. 26).

cascade deexcitation from higher-lying cases favors a smaller number of energy transfer-related quenching routes. Besides, they offer an enhanced possibility to control the aggregation, lanthanide concentrations, and geometries so that energy transfer mechanisms in solid-state or high concentration applications are minimized.

## 5.2 Energy Transfer Upconversion

Cross-relaxations resulting in UC in long-lived NIR-emitting materials may be undesirable for infrared applications as it represents a loss of NIR emission. Therefore, optimization of the concentrations may be important to guarantee a reduction of such a nonradiative quenching resulting in a smaller efficiency. However, NIR-to-visible UC applications may be pursued and constitute, indeed a considerable field of research. UC finds its use in biological applications, such as labeling, imaging, and therapy, and in photonic and phosphor applications including lasers, lighting, solar conversion for photovoltaics, photocatalysis, etc.

Conversion of infrared photons into visible can occur though a number of mechanisms. The most relevant processes for such light conversion are summarized in Fig. 28. In a simplified view, in all processes, two incident low-energy photons (typically in the NIR range) are converted into an emitted photon of higher energy (typically in the visible). These processes include, in order of increasing efficiency, second harmonic generation (SHG), two-photon absorption (TPA), excited state absorption (ESA), and ETU. TPA and SHG are nonlinear processes (the interaction Hamiltonian depending quadratically on the electric field of the incident radiation) and including
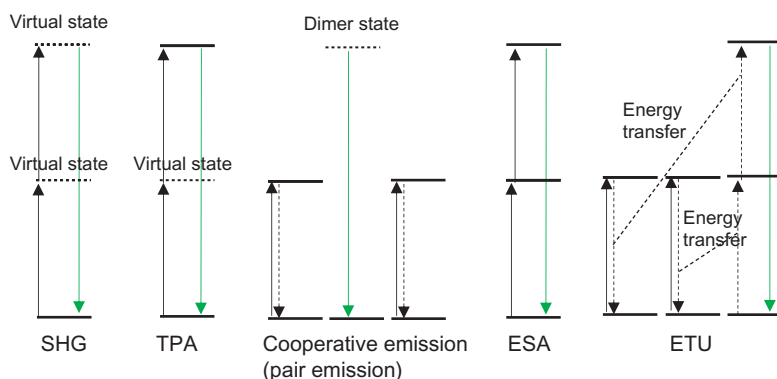


**FIGURE 28** Most relevant processes to convert low-energy incident radiation into higher energy emitted radiation, in inverse probability order (equivalently, in decreasing excitation powers needed), namely second harmonic generation (SHG), two-photon absorption (TPA), emission of pairs through a virtual (dimer) state (this process is favored if the emitting centers are preferably arranged in pairs), excited state absorption (ESA), and energy transfer upconversion (ETU).

virtual intermediate levels, being proportional to the squared pumping power. This implies that the two excitation photons must coincide (and also be coherent for SHG, since the emitting level is also virtual), which makes these processes very unlikely, and high-power thresholds are required.

Pair emission, ESA, and ETU are linear processes with the radiation, in the sense that the depend only on the first power of the electric field and thus involve only creation or destruction of one photon at a time, although they are nonlinear with the number of excited states required for populating the emitting state, given that UC depends on a real intermediate state. This state must have a finite lifetime that is long enough for an excitation to be stored there, for such a time as to allow a second photon to further excite the phosphor into a higher-lying excited state (Auzel, 2004). Since UC only involves real energy levels, very high excitation powers are no longer necessary. The excitation power thresholds for UC are typically about 6–11 orders of magnitude lower than those required for SHG or TPA, depending on the absorption coefficients and optical properties of the color centers (Suijver, 2008). It is also worth mentioning that no coherent excitation source is required for UC (Fig. 28). An analysis of the population and depopulation mechanisms yields that the emission intensities also result in a power law with the pump power, with exponent 2, if the linear emission from the reservoir states dominates. If the UC rate dominates, however, and the reservoir is comparatively quickly fed, a linear dependence with the pumping power is observed (Pollnau et al., 2000). Higher exponents can also observed in the case of so-called avalanche effects, in which absorption is nonresonant, but resonant cross-relaxations populating intermediate states are in place (Auzel, 2004; Joubert, 1999) or changes of UC routes are in place (Sivakumar et al., 2007).

In lanthanides in organic environments, conversion of NIR radiation to visible has been mainly produced by means of TPA processes. These processes take advantage of the highly delocalized electrons in the chromophores and the sensitization of visible lanthanide emitters such as $Tb^{3+}$ or $Eu^{3+}$ (Fu et al., 2005; Wong et al., 2005a).

In inorganic compounds, ETU is mainly produced by 980 nm excitation in $Yb^{3+}/Er^{3+}$ pairs or trimers by the resonant energy transfer from $Yb^{3+}(^2F_{5/2})$ to photoexcited $Er^{3+}(^4I_{11/2})$ or, due to the enhanced oscillator of the $Yb^{3+}$, most likely by two consecutive energy transfers from $Yb^{3+}(^2F_{5/2}) \rightarrow Er^{3+}(^4I_{15/2})$ and $Yb^{3+}(^2F_{5/2}) \rightarrow Er^{3+}(^4I_{11/2})$ and/or the nonresonant but significant $Yb^{3+}(^2F_{5/2}) \rightarrow Er^{3+}(^4I_{13/2})$, resulting in the population and green luminescence from the $^2H_{11/2}$, $^2S_{3/2}$, or red luminescence from $^2F_{9/2}$, respectively, directly or after multiphonon relaxation (Auzel, 2004).

The main drawback of lanthanides with NIR-emitting levels in organic environments toward UC applications resides not only in the relatively short lifetimes of the NIR-based levels but mainly in the high quenching rates for the visible emission levels, as explained above in preceeding sections. Visible emission from $Nd^{3+}$ and $Er^{3+}$ in organic environments upon infrared excitation

may be detected at sufficiently high powers, due to ESA (Xiao et al., 2005) and ETU, but even for excitation at higher energies (downconversion configuration) is expected to be unlikely and inefficient due to the enhanced probability of multiphonon deexcitations (Reinhard and Güdel, 2002), particularly in hydrogenated environments as caused by the small gap between visible-emitting states and the lower-lying IR-emitting states (see Section 3.2). Visible emission has been observed through ETU upon 980 nm excitation in rigid $Yb^{3+}/Er^{3+}$-codoped frameworks (Ma et al., 2013; Sun et al., 2009) and (moderately intense) in perfluorinated polymers of the perfluorophosphinate families, by our group. Low temperatures favour these emissions, as a consequence of the corresponding decrease in multiphonon quenching. Even Transition metal ion-mediated ETU has been measured at very low temperature in efficient Cr–Er–Cr trinuclear helicate complexes in which highly fluorinated species are used as counterions, by taking advantage of the NIR $Cr^{3+}$–$Er^{3+}$ sensitization upon NIR excitation (Aboshyan-Sorgho et al., 2011).

$Tb^{3+}$ and $Eu^{3+}$ are the main lanthanide emitters in the visible used in organic environments, for blue/green and red luminescence, respectively. Due to their wide gaps from the $^5D_4$ and $^5D_0$ states to the lower-lying state, correspondingly, the visible emission is significant even in the presence of hydrogen-based oscillators. However, the lack of intermediate levels in the IR range discourages their use in UC applications. Notwithstanding this, the use of highly efficient NIR-based $Yb^{3+}$ dry perfluorobutanesulfonates in combination with the analogue $Tb^{3+}$ and $Eu^{3+}$ complexes has allowed intense 980 nm to visible and UV range UC, in $[Yb_{1-x}Tb_x(PFBS)_3]$ and $[Yb_{1-x-y}Y_yTb_x(PFBS)_3]$ coordination polymers, which is observable to the naked eye (Fig. 29B) for $[Yb_{0.7}Tb_{0.3}(PFBS)_3]$, $[Yb_{0.8}Tb_{0.2}(PFBS)_3]$, and $[Yb_{0.9}Tb_{0.1}(PFBS)_3]$ (Hernández et al., 2010). The mechanism of cooperative energy transfer visible UC, in which two excited $Yb^{3+}$ ions simultaneously transfer the excitation to the $Tb^{3+}$ or (nonresonantly) $Eu^{3+}$, has allowed for the observation of the UC phenomenon when the lifetime of the $Yb^{3+}$ complexes is large (Fig. 29A). Importantly, this cooperative energy transfer steps are considerably more likely processes than pair emissions, even in the nonresonant case, since it is a real accepting state of the lanthanide emitter in the $Yb^{3+}$–$Tb^{3+}$–$Yb^{3+}$ trimer or $Yb^{3+}$–$Eu^{3+}$–$Yb^{3+}$ trimer the one which is responsible for the visible emission. Due to the long lifetime of the $Tb^{3+}$, higher than 3 ms, a third ETU step can occur to yield even UV emission (Hernández et al., 2010). Moreover, the high concentration of $Yb^{3+}$ complexes allows for long-distance diffusion of the excitation via hopping and thus the possibility for reaching the corresponding emitting sites. Similar observations have taken place with other complexes of perfluorinated ligands, based on PFXPP (perfluoro-*p*-poly-phenyl phosphinate), $[Yb_{1-x}Tb_x(PFXPP)_3]$, and perfluoro-di-*p*-tolyl phosphinate ligands, $[Yb_{1-x}Tb_x(PF2TP)_3]$ and in some of the $Eu^{3+}$ analogues. Processing (drying) is not needed for these series the UC being observable in the as-grown samples, although considerably less intense than in the PFBSs. In this case, we believe that the polymer structure prevents a full three-dimensional diffusion of the
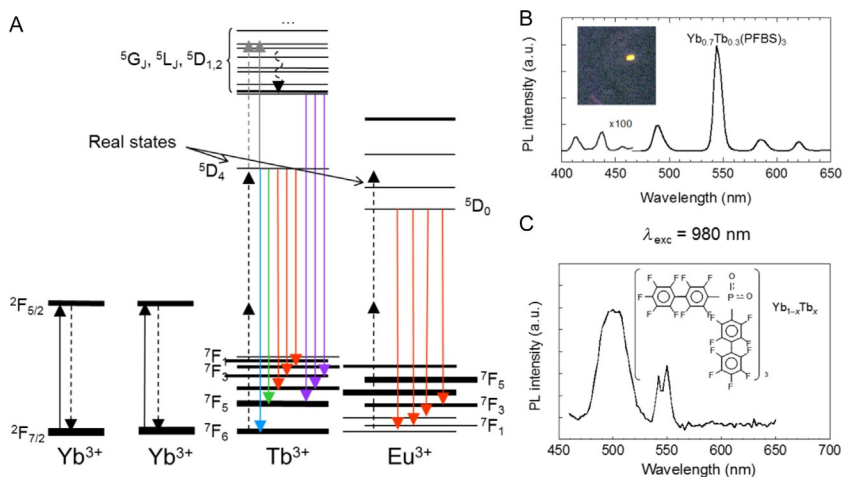
FIGURE 29   (A) Cooperative energy transfer upconversion processes resulting in visible emission of $Tb^{3+}$ and $Eu^{3+}$ with efficient $Yb^{3+}$ sensitization in coordination polymers (Hernández et al., 2010). (B) Emission spectra of the corresponding $[Yb_{0.7}Tb_{0.3}(PFBS)_3]$ and (C) $[Yb_{0.7}Tb_{0.3}(PF4PP)_3]$ compounds. The inset in (B) represents the image through a filter cutting at 520 nm. *Panel (B): Redrawn from Hernández et al. (2010).*

excitation which, despite the comparable lifetimes with respect to the PFBS compounds, results in the difficulty in the excitation to simultaneously reach the acceptor in the span of the reservoir ($Yb^{3+}$, $^2F_{5/2}$) lifetime. The increase of the blue band at (490 nm) assigned to pair emission (Fig. 28C) arising from the statistically significant number of close-lying $Yb^{3+}$ ions supports this interpretation which suggests that geometry and dimensionality play a very important role in the UC mechanisms.

For NIR-emitting applications, UC mechanisms should ideally be suppressed. The corresponding energy transfer rates should therefore be minimized, which could be done by means of engineering the optimum concentration and geometries, particularly in the presence of sensitizers.

# 6   COMPOSITE MATERIALS WITH IR-BASED LANTHANIDE SENSITIZATIONS THROUGH ORGANIC CHROMOPHORES

The complicated chemistry of highly fluorinated compounds makes it difficult to pursue efficient optical properties and quantum yields in NIR-emitting lanthanides by the classical approach of incorporating sensitizers in lanthanide complexes for infrared applications. Two novel strategies have been recently suggested to produce highly efficient sensitized NIR-lanthanide emitters, based on composite materials[1] in which one component provides a high

---

1. As referred to in discussion with Prof. J.C.G. Bünzli, private communication.

emission efficiency environment for the lanthanide and the other one sensitization. One involves the use of hybrid environments in which the lanthanide is present in an inorganic compound and organic chromophores allow for the sensitization, and the other one involves a use of a very efficient perfluorinated ligands-based molecular environment for the $Er^{3+}$, and the juxtaposition of a perfluorinated molecular chromophore.

## 6.1  Hybrid Organic–Inorganic Materials

The use of hybrid organic–inorganic frames for incorporation of lanthanides in a controlled environment from sol–gel and their comparably easy synthetic routes have been discussed over the past few years and applied in a number of visible-emitting lanthanides (mainly $Tb^{3+}$ and $Eu^{3+}$, which do not suffer from the strong quenching by residual hydrogen) and also in NIR-emitting-based lanthanides. The resultant materials could be implemented in potential device applications, such as planar waveguides, directly or incorporated into polymers (Binnemans, 2009; Escribano et al., 2008).

Zeolites are inorganic aluminosilicate frameworks of typically alkaline metals with a periodic porous structure of diverse size and geometry, often with channels interconnecting the whole framework. Incorporation of lanthanides in the zeolite frame is easily done by exchange of the metals at mild wet conditions after growth (Fig. 30). It has been shown that incorporation of lanthanides by wet methods involving exchange with framework atoms and (often) "ship in a bottle" functionalization with organic ligands (or complexation) is possible as well as introduction of the lanthanide complexes during or after growth for a number of lanthanides, although mainly visible-based
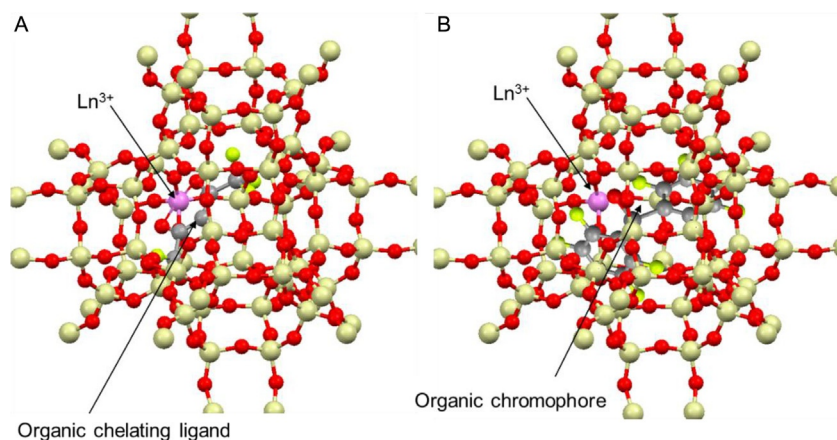


**FIGURE 30**  Schematic representation of an inorganic zeolite, with an exchanged NIR-emitting lanthanide in a pore, either (A) chelated by an organic ligand or (B) in the presence of a decafluorobenzophenone chromophore.

emission is sought (Binnemans, 2009). Regarding NIR-emitting lanthanides, $Nd^{3+}$ has been introduced in the large pores (12 Å) of faujasite (Zeolite-Y) at high exchange by wet methods and the small bidentate bis(perfluoromethyl-sulfonyl)aminate functionalization leads to relatively long PL lifetimes, 100 μs, in the presence of the organic, which is extremely high, but the organic does not produce sensitization (Wada et al., 2000). It has been also shown that $Nd^{3+}$–$Nd^{3+}$ energy transfer is possible in this high loading configuration. Sensitization of lanthanide-exchange zeolites with perfluorinated chromophores has been more recently demonstrated. Zeolite-L incorporating 5% $Er^{3+}$ was thoroughly dried at high temperatures in vacuum and annealed to remove the maximum possible hydrogenated groups, and decafluorobenzophenone was loaded in its pores. Excitation in the absorption band of the perfluorinated chromophore at 370 nm yields sensitized 1.5 μm Er-based emission with no chromophore emission (Mech et al., 2010).

Another organic–inorganic hybrid alternative for exploiting organic chromophores for lanthanide sensitization includes the surface functionalization of lanthanide-doped inorganic nanoparticles with organic chromophore-containing ligands (Fig. 31). The incorporation of photoluminescent NIR-emitting lanthanides in inorganic matrixes at various sizes nanoparticle morphology is relatively well known. In particular, a great effort has been done in the control of the polymorphism and size distribution of a number of hosts in
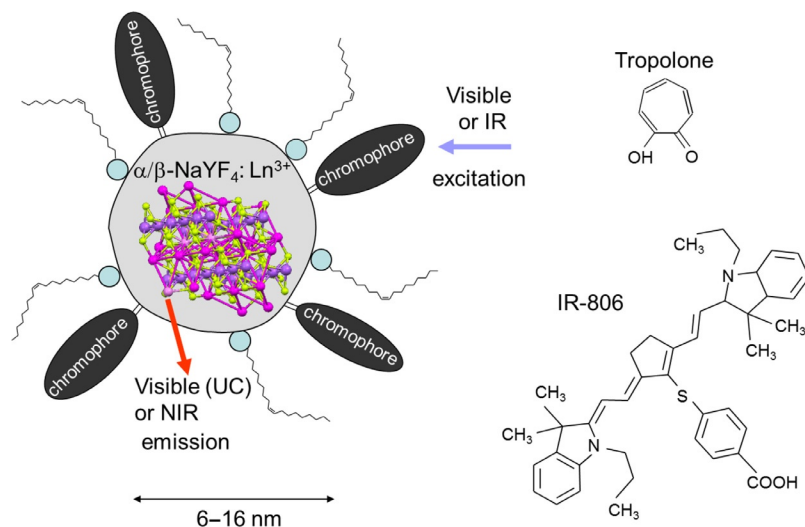


**FIGURE 31** Schematic representation of an inorganic ($NaYF_4$) nanoparticle doped with NIR-emitting lanthanides with external organic functionalization including chromophores. Typically, these nanoparticles have small sizes <20 nm and are oleylamine and/or oleic acid-functionalized for dispersion and solubilization, as represented. Tropolone and IR-806 chromophores employed for sensitization of $Nd^{3+}$, $Yb^{3+}$, and $Er^{3+}$ NIR luminescence (and upconversion, for $Yb^{3+}$, $Er^{3+}$ codoping, in the second case), in cubic and hexagonal $NaYF_4$.

the presence of various concentrations of $Yb^{3+}$, $Er^{3+}$, $Nd^{3+}$, etc. Among them, β (hexagonal)-$NaYF_4$ is one of the most studied because upon 20% Yb and 10% Er, it shows the highest measured upconversion efficiency (Heer et al., 2004), which has made it attractive for a number of phosphors and biological applications. The α (cubic) polymorph is somewhat easier to obtain, especially at the nanoscale, and allos for efficient optical properties too. The incorporation of tropolonate chromophores on the outside of small (∼6 nm) α-$NaYF_4$ nanoparticles doped with 20% Yb or 20% Nd allows the ($^2F_{5/2} \to {}^2F_{7/2}$) 980 nm emission of the $Yb^{3+}$, or the $^4F_{3/2} \to {}^4I_{9/2}$, $^4I_{11/2}$, $^4I_{13/2}$ emissions of $Nd^{3+}$ at 870, 1060, and 1350 nm, respectively, upon excitation at 340 nm in the tropolonate absorption band (Zhang et al., 2007c). The nonexponential decays yield lifetimes for the $Yb^{3+}$ in the order of 55 μs and for $Nd^{3+}$ in the order of 5 μs in DMSO solution. Although shorter than in conventional Yb- and Nd-doped $NaYF_4$ nanoparticles these values are much longer than in the corresponding tetrakis Yb and Nd (trop)$_4$ complexes, which demonstrates that the inorganic nanoparticles protect the long-lived character for the NIR emission from the solvent and organic environment quenching.

Interestingly, the functionalization of $Yb^{3+}$/$Er^{3+}$-doped nanoparticles with NIR-based chromophores has been also proved successful for UC. β-$NaYF_4$: 20% Yb, 2% Er capped with IR-dye 806 (4-mercaptobenzoic acid-functionalized IR-780 dye) shows sensitization of the $Yb^{3+}$ and $Er^{3+}$ in the 700–850 nm range. Most importantly, these chromophore-capped particles show sensitized visible emission through ETU upon excitation in the IR-absorbing chromophore, with 3000-fold increase of the excitation with respect to 980 nm excitation as the PL and excitation spectra demonstrate (Zou et al., 2012). This proves that with decreased multiphonon quenching, as guaranteed in the protective inorganic environment of the nanoparticle, external functionalization allows for significant chromophore to lanthanide energy transfer resulting in NIR and visible emissions.

For processability and devices, the sensitized composite zeolites and nanoparticles could be incorporated in polymer matrixes or electrochemical cells for optical and/or optoelectronic applications, which in principle, given the protective function for the inorganic components, would not suppose a decrease of their properties, and could be assimilated as in existing polymer devices doped with NIR-emitting lanthanides-doped $LaF_3$ or $NaYF_4$ nanoparticles (Dekker et al., 2004; Liu et al., 2009; Zhai et al., 2013; Zhang et al., 2007a). Also, the functionalized nanoparticles (and particularly those with upconversion properties) could be employed for biological applications.

## 6.2    Composite Organic Materials

The all-organic alternative to incorporate sensitized highly efficient NIR lanthanides in sensitizing organic environments for amplifying devices at 1.5 μm has been to separate the sensitizing (chromophore) and emitter ($Er^{3+}$ complex) units and combine the two perfluorinated materials in an organic-

based composite. This allows simple direct growth in to thin-film devices. A perfluorinated Zn(II) molecular organic semiconductor [Zn(F-BTZ)$_2$] (F-BTZ = perfluorobenzothiazole) (Li et al., 2013) was employed as a sensitizing unit in the visible range $\lambda_{max} = 480$ nm and [Er(F-tpip)$_3$] was selected as the erbium complex due to its high efficiency and ease of processing. The composite material 70% [Zn(BTZ)$_2$] and 30% [Er(F-tpip)$_3$] was grown as a thin film on SiO$_2$ on silicon at high-vacuum conditions by vapor deposition and with doping control by means of the evaporation rates (Fig. 32). The excitation spectrum of the NIR emission at 1.5 μm follows closely that of the absorption of the Zn(II) complexes, demonstrating outstanding sensitization, as derived from the comparison with the equivalent [Er(F-tpip)$_3$] spectrum.
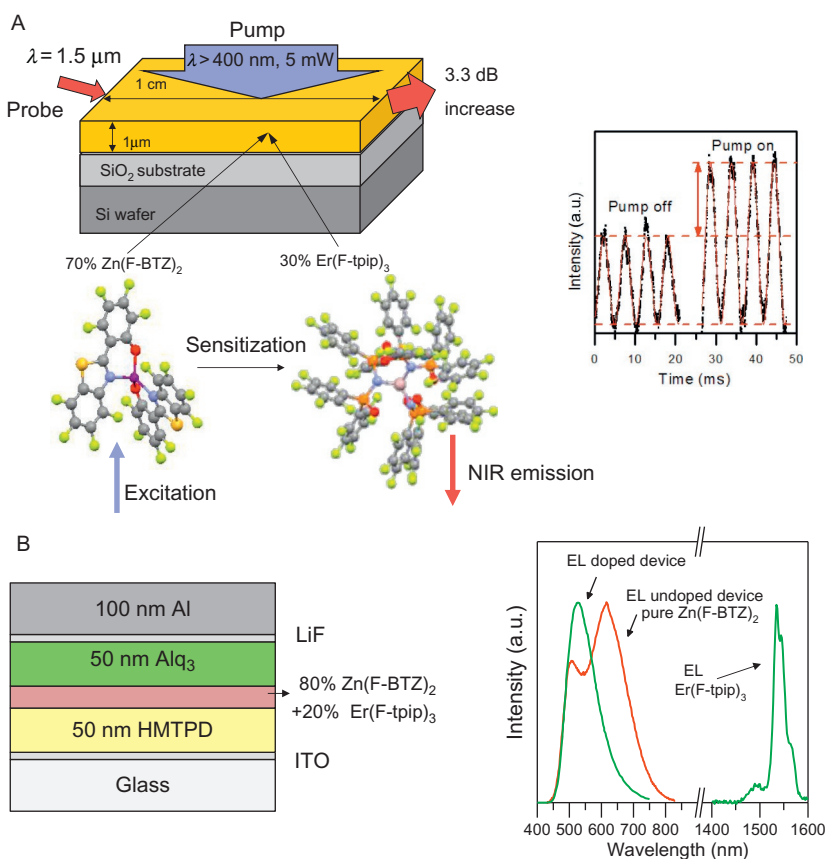


**FIGURE 32** (A) Schematic amplification experiment showing 3.4 dB/cm apparent enhancement of the probe at 1.5 μm upon pumping in the visible, as due to the sensitization of [Er(F-tpip)$_3$] by a Zn$^{2+}$ bis-perfluorobenzothiazole chromophore. (B) Scheme of an OLED and EL in the doped and undoped material, showing NIR emission and the absence of the phosphorescence due to triplet-lanthanide sensitization. *Reproduced with permission from Ye et al. (2014) © Nature Group 2014.*

The $Er^{3+}$ emission lifetime, $\sim$860 µs, is enhanced in the composite with respect to the pure erbium compound as a consequence of the decrease of cross-relaxation and energy transfer mechanisms. Moreover, the semiconducting properties of the material allow for implementation of NIR-emitting OLEDs, the [Er(F-tpip)$_3$]-doped OLEDs, showing NIR emission and extraordinary quenching of the [Zn(F-BTZ)$_3$] phosphorescence (Ye et al., 2014). The spectral overlap of the relaxed singlets and triplets, together with the dynamic analysis of the 1.5 µm emission, suggests that even though singlets do contribute to sensitization, transfer from the relaxed triplet of the [Zn(F-BTZ)$_2$] (peaking at 680 nm) to $Er^{3+}$ resulting in excitation of the $^4F_{9/2}$ states is the most relevant mechanism. This material achieves population inversion at low power pumping, allowing for an $\sim$50% enhancement of a probe signal (Ye et al., 2014) via sensitization of the $Er^{3+}$ complex (Fig. 32).

## 7 CONCLUDING REMARKS

In this report, we have shown that the motivation, fundamentals, and related recent result toward the sensitization of $Nd^{3+}$, $Er^{3+}$, and $Yb^{3+}$ via organic chromophores for advanced applications in the NIR range. We have put the emphasis in explaining the need for very efficient environments near the lanthanide, exclusive of radiationless deactivation channels, and thus requiring high degrees of halogenation. In particular, we have shown the advantages of (per)fluorination and phenomena related with the increased lifetimes, in particular energy transfer and NIR-to-visible UC. New strategies based on composite materials have emerged as potential candidates for taking advantage of organics-mediated sensitization in combination with efficient environments, including an all-organic pathway that exploits sensitization from an additional metal complex-based chromophore of independent nature.

A realistic perspective of the potential of organics-based sensitized NIR-emitting lanthanides for devices and applications must take into account the challenges derived from the organic environment in which the NIR-emitting lanthanides must be immersed for efficient sensitization to take place. Some of them are:

– Lanthanide efficiencies are still typically small due to multiphonon quenching even in the most optimized materials to date, compared to inorganic hosts. Even though for some luminescence and amplification applications the effect of the enhanced pumping obtained if sensitization efficiencies are kept high would allow to balance it for moderate powers, other applications in phosphors and molecular devices may be frustrated. However, it is possible that further research minimizes this issue, and improved performances are not at all unexpected.
– A good matching between absorbed and emitting wavelengths is difficult, and considerable pumping power losses may be in place as a consequence of the downshift. Although applications as phosphors may not necessarily

require this, undesired heating can occur. Redshifts of the organic chromophores will be required with respect to the best instances now available to minimize this, although the nature of the electronic processes involved may result in natural limit due to energy separation requirements for optimal performance.

– The heavy loading of intermediate states with a variety of symmetries and lifetimes may result in bleaching and actual photodegradation or chemodegradation processes of the organics, including oxygen-related degradation. This can be overcome with careful encapsulation of the devices as has been used for OLED displays.

– Highly efficient organics are not free from lanthanide–lanthanide energy transfer interactions resulting in quenching, as in inorganic matrixes. However, they offer an enhanced possibility to control the geometry and concentrations so that these mechanisms are minimized. Moreover, concentration of excited states in the lower-lying levels of the NIR-emitting lanthanides due to the enhanced quenching from higher-lying cases diminishes the number of deexcitation routes. Alternatively, this may allow for UC applications.

– Large absorption coefficients of the organic chromophores may cause excitation difficulties due to the small penetration depth of the pump. Careful selection of the right pumping sources, in terms of wavelength (like polychromatic sources) and device geometry, is to be required to maximize the pumping of the chromophores.

The development of several instances of NIR-emitting lanthanides with advanced properties in organic environments, even for direct excitation and in relatively unoptimized configurations, together with the perspective of successful realization of the sensitization of organic light-harvesting units keeps a moderate optimism toward realizable applications in a number of fields.

## ACKNOWLEDGMENT

## ABBREVIATIONS AND SYMBOLS

| | |
|---|---|
| **acac** | acetylacetonate or 2,4-pentanedionate |
| **bath** | bathophenanthroline |
| **BCP** | bathocuproine |
| **BODIPY** | 4,4-difluoro-4-bora-3*a*,4*a*-diaza-*s*-indacene |
| **CT** | charge transfer |
| **dbm** | 1,3-diphenyl-1,3-propanedionate or dibenzoylmethanate |
| **DMA** | *N*,*N*-dimethylacetamide |
| **DMF** | *N*,*N*-dimethylformamide |
| **dtpa** | diethylene triamine pentaacetic acid |

| | |
|---|---|
| **EBL** | electron transport layer |
| **EIL** | electron injection layer |
| **EL** | electroluminescence |
| **ESA** | excited state absorption |
| **ETL** | electron transport layer |
| **ETU** | energy transfer upconversion |
| **F-tpip** | perfluoro-tetrakisphenyl-imidodiphosphinate |
| **FTPPor** | 5,10,15,20-tetrakis-(pentafluorophenyl)-porphyrin |
| **HBL** | hole-blocking layer |
| **HIL** | hole injection layer |
| **HTL** | hole transport layer |
| **hfa** | hexafluoroacetylacetonate or 1,1,1,5,5,5-hexafluoro-2,4-pentanedionate |
| **HOMO** | highest occupied molecular orbital |
| **ISC** | intersystem crossing |
| **ITO** | indium tin oxide |
| **LED** | light-emitting diode |
| **LUMO** | lowest unoccupied molecular orbital |
| **MOF** | metal organic framework |
| **NIR** | near infrared |
| **NPB** | $N,N'$-di(1-naphthyl)-$N,N'$-diphenyl-(1,1'-biphenyl)-4,4'-diamine |
| **OLED** | organic light-emitting diode |
| **pctrop** | perchlorotropolonate |
| **PEDOT** | poly(3,4-ethylenedioxythiophene) |
| **PFBS** | perfluorobutanesulfonate |
| **PFOS** | perfluorooctanesulfonate |
| **PF2PP** | perfluorobis(phenylphosphinate) |
| **PF3PP** | perfluoro-$p$-phenyl-diphenylphosphinate |
| **PF4PP** | perfluorobis-$p$-diphenylphosphinate |
| **PF2TP** | perfluorobis($p$-tolylphosphinate) |
| **pip** | perfluoro-tetrakisphenyl-imidodiphosphinate |
| **PL** | photoluminescence |
| **PMMA** | polymethyl methacrylate |
| **Porph** | porphirine |
| **PSS** | poly(4-styrenesulfonate) |
| **PVK** | poly(9-vinylcarbazole) |
| **q** | 8-hydroxyquinolinate |
| **SHG** | second harmonic generation |
| **tfa** | trifluoroacetate |
| **tta** | thenoyl-trifluoroacetonate or 4,4,4-trifluoro-1-(thiophen-2-yl)butane-1,3-dionate |
| **TPA** | two-photon absorption |
| **TPD** | $N,N'$-bis(3-methylphenyl)-$N,N'$-diphenylbenzidine |

| TPP | triphenylphosphine |
| **TPPO** | triphenylphosphine oxide |
| **TPPor** | 5,10,15,20-tetraphenylporphyrin |
| **trop** | tropolonate |
| **UC** | upconversion |
| **UV** | ultraviolet |

# REFERENCES

Aboshyan-Sorgho, L., Besnard, C., Pattison, P., Kittilstved, K.R., Aebischer, A., Bünzli, J.C.G., Hauser, A., Piguet, C., 2011. Near-infrared → visible light upconversion in a molecular trinuclear d–f–d complex. Angew. Chem. Int. Ed. Engl. 50, 4108.

Aime, S., Barge, A., Borel, A., Botta, M., Chemerisov, S., Merbach, A.E., Müller, U., Pubanz, D., 1997. A multinuclear NMR study on the structure and dynamics of lanthanide(III) complexes of the poly(amino carboxylate) EGTA4− in aqueous solution. Inorg. Chem. 36, 5104.

Albrecht, M., Osetska, O., Klankermayer, J., Fröhlich, R., Gumy, F., Bünzli, J.C.G., 2007. Enhancement of near-IR emission by bromine substitution in lanthanide complexes with 2-carboxamide-8-hydroxyquinoline. Chem. Commun. 18, 1834–1836.

Albrecht, M., Fiege, M., Osetska, O., 2008. 8-Hydroxyquinolines in metallosupramolecular chemistry. Coord. Chem. Rev. 252, 812.

Artizzu, F., Deplano, P., Marchio, L., Mercuri, M.L., Pilia, L., Serpe, A., Quochi, F., Orrù, R., Cordella, F., Meinardi, F., Tubino, R., Mura, A., Bongiovanni, G., 2005. Structure and emission properties of Er₃Q₉ (Q = 8-quinolinolate). Inorg. Chem. 44, 840.

Artizzu, F., Mercuri, M.L., Serpe, A., Deplano, P., 2011. NIR-emissive erbium–quinolinolate complexes. Coord. Chem. Rev. 255, 2514.

Artizzu, F., Quochi, F., Marchiò, L., Sessini, E., Saba, M., Serpe, A., Mura, A., Mercuri, M.L., Bongiovanni, G., Deplano, P., 2013. Fully efficient direct Yb-to-Er energy transfer at molecular level in a near-infrared emitting heterometallic trinuclear quinolinolato complex. J. Phys. Chem. Lett. 4, 3062.

Atkins, P.W., 1976. Molecular Quantum Mechanics, second ed. Oxford University Press, New York.

Auzel, F., 2004. Upconversion and anti-stokes processes with f and d ions in solids. Chem. Rev. 104, 139.

Babudri, F., Farinola, G.M., Naso, F., Ragni, R., 2007. Fluorinated organic materials for electronic and optoelectronic applications: the role of the fluorine atom. Chem. Commun. 10, 1003.

Bassett, A.P., Van Deun, R., Nockemann, P., Glover, P.B., Kariuki, B.M., Van Hecke, K., Meervelt, L.V., Pikramenou, Z., 2005. Long-lived near-infrared luminescent lanthanide complexes of imidodiphosphinate "shell" ligands. Inorg. Chem. 44, 6140.

Becker, P.C., Olsson, N.A., Simpson, J.R., 1999. Erbium-Doped Fiber Amplifiers, Fundamentals and Technology. Academic Press, London.

Beeby, A., Clarkson, I.M., Dickins, R.S., Faulkner, S., Parker, D., Royle, L., de Sousa, A.S., Willianms, J.A.G., Woods, M., 1999. Non-radiative deactivation of the excited states of europium, terbium and ytterbium complexes by proximate energy-matched OH, NH and CH oscillators: an improved luminescence method for establishing solution hydration states. J. Chem. Soc. Perkin Trans. I 2, 493.

Beeby, A., Dickins, R.S., FitzGerald, S., Govenlock, L.L., Maupin, C.L., Parker, D., Riehl, J.P., Siligardic, G., Williams, J.A.G., 2000. Porphyrin sensitization of circularly polarised near-IR lanthanide luminescence: enhanced emission with nucleic acid binding. Chem. Commun., 13, 1183–1184.

Beeby, A., Burton-Pye, B.P., Faulkner, S., Motson, G.R., Jeffery, J.C., McCleverty, J.A., Ward, M.D., 2002. Synthesis and near-IR luminescence properties of neodymium (III) and ytterbium (III) complexes with poly (pyrazolyl) borate ligands. J. Chem. Soc. Dalton Trans., 9, 1923–1928.

Beer, P.D., Szemes, F., Passaniti, P., Maestri, M., 2004. Luminescent ruthenium (II) bipyridine-calix [4] arene complexes as receptors for lanthanide cations. Inorg. Chem. 43, 3965.

Berger, R., Resnati, G., Metrangolo, P., Weber, E., Hulliger, J., 2011. Organic fluorine compounds: a great opportunity for enhanced materials properties. Chem. Soc. Rev. 40, 3496.

Beverina, L., Crippa, M., Sassi, M., Monguzzi, A., Meinardi, F., Tubino, R., Pagani, G.A., 2009. Perfluorinated nitrosopyrazolone-based erbium chelates: a new efficient solution processable NIR emitter. Chem. Commun., 34, 5103–5105.

Biju, S., Eom, Y.K., Bünzli, J.C.G., Kim, H.K., 2013. Biphenylene-bridged mesostructured organosilica as a novel hybrid host material for Ln III (Ln=Eu, Gd, Tb, Er, Yb) ions in the presence of 2-thenoyltrifluoroacetone. J. Mater. Chem. C 1, 3454–3466.

Binnemans, K., 2005. Rare earth β-diketonate complexes: functionalities and applications. In: Gschneidner, K.A., Bünzli, J.-C.G., Pecharsky, V.K. (Eds.), Handbook on the Physics and Chemistry of Rare Earths, vol. 35. Elsevier, Amsterdam, p. 107 (Chapter 225).

Binnemans, K., 2009. Lanthanide-based luminescent hybrid materials. Chem. Rev. 109, 4283.

Bischof, C., Wahsner, J., Scholten, J., Trosien, S., Seitz, M., 2010. Quantification of C−H quenching in near-IR luminescent ytterbium and neodymium cryptates. J. Am. Chem. Soc. 132, 14334.

Bo, S., Hu, J., Wang, Q., Liu, X., Zhen, Z., 2008. Near-infrared luminescence properties of erbium complexes with the substituted phthalocyaninato ligands. Photochem. Photobiol. Sci. 7, 474.

Bulach, V., Sguerra, F., Hosseini, M.W., 2012. Porphyrin lanthanide complexes for NIR emission. Coord. Chem. Rev. 256, 1468.

Bünzli, J.C., 2004. Luminescent lanthanide probes as diagnostic and therapeutic tools. Met. Ions Biol. Syst. 42, 39.

Bünzli, J.-C.G., Chauvin, A.-S., 2014. Lanthanides in solar energy conversion. In: Bünzli, J.-C.G., Pecharsky, V.K. (Eds.), Handbook on the Physics and Chemistry of Rare Earths, vol. 44. Elsevier, Amsterdam, p. 169 (Chapter 261).

Bünzli, J.-C.G., Eliseeva, S.V., 2013. Intriguing aspects of lanthanide luminescence. Chem. Sci. 4, 1939.

Burroughes, J.H., Bradley, D.D.C., Brown, A.R., Marks, R.N., Mackay, K., Friend, R.H., Burns, P.L., Holmes, A.B., 1990. Light-emitting diodes based on conjugated polymers. Nature 347, 539.

Cantelar, E., Marin-Dobrincic, M., Jardiel, T., Caballero, A.C., Cussó, F., 2014. Judd–Ofelt analysis of powder samples: LiNbO$_3$:Er$^{3+}$ submicron-sized particles as a model case. In: 3rd International Workshop on Photoluminescence in Rare Earths (PRE'14), San Sebastián.

Cantuel, M., Gumy, F., Bünzli, J.C.G., Piguet, C., 2006. Encapsulation of labile trivalent lanthanides into a homobimetallic chromium (III)-containing triple-stranded helicate. Synthesis, characterization, and divergent intramolecular energy transfers. Dalton Trans. 22, 2647.

Carnall, W.T., Fields, P.R., Rajnak, K., 1968. Electronic energy levels in the trivalent lanthanide aquo ions. I. Pr3+, Nd3+, Pm3+, Sm3+, Dy3+, Ho3+, Er3+, and Tm3+. J. Chem. Phys. 49, 4424.

Chatterjee, D.K., Rufaihah, A.J., Zhang, Y., 2008. Upconversion fluorescence imaging of cells and small animals using lanthanide doped nanocrystals. Biomaterials 29, 937.

Chen, R.T., Lee, M., Natarajan, S., Lin, C., Ho, Z.Z., Robinson, D., 1993. Single-mode $Nd^{3+}$-doped graded-index polymer waveguide amplifier. IEEE Photonics Technol. Lett. 5, 1328.

Chen, B., Yang, Y., Zapata, F., Qian, G., Luo, Y., Zhang, J., Lobkovsky, E.B., 2006. Enhanced near-infrared-luminescence in an erbium tetrafluoroterephthalate framework. Inorg. Chem. 45, 8882.

Chen, F.F., Bian, Z.Q., Liu, Z.W., Nie, D.B., Chen, Z.Q., Huang, C.H., 2008. Highly efficient sensitized Red emission from europium (III) in Ir–Eu bimetallic complexes by 3MLCT energy transfer. Inorg. Chem. 47, 2507.

Chen, C., Zhang, D., Li, T., Zhang, D., Song, L., Zhen, Z., 2009. Erbium-ytterbium codoped waveguide amplifier fabricated with solution-processable complex. Appl. Phys. Lett. 94, 041119.

Chen, F.F., Chen, Z.Q., Bian, Z.Q., Huang, C.H., 2010a. Sensitized luminescence from lanthanides in d-f bimetallic complexes. Coord. Chem. Rev. 25, 991.

Chen, Z.Q., Ding, F., Bian, Z.Q., Huang, C.H., 2010b. Efficient near-infrared organic light-emitting diodes based on multimetallic assemblies of lanthanides and iridium complexes. Org. Electron. 11, 369.

Comby, S., Bünzli, J.C.G., 2007. Lanthanide near-infrared luminescence in molecular probes and devices. In: Gschneidner, K.A., Bünzli, J.-C.G., Pecharsky, V.K. (Eds.), Handbook on the Physics and Chemistry of Rare Earths, vol. 37. Elsevier, Amsterdam, p. 217 (Chapter 235).

Comby, S., Tuck, S.A., Truman, L.K., Kotova, O., Gunnlaugsson, T., 2012. New trick for an old ligand! The sensing of Zn (II) using a lanthanide based ternary Yb (III)-cyclen-8-hydroxyquinoline system as a dual emissive probe for displacement assay. Inorg. Chem. 51, 10158.

Coppo, P., Duati, M., Kozhevnikov, V.N., Hofstraat, J.W., De Cola, L., 2005. White-light emission from an assembly comprising luminescent iridium and europium complexes. Angew. Chem. 117, 1840.

Crosby, G.A., Whan, R.E., Alire, R.M., 1961. Intramolecular energy transfer in rare earth chelates. Role of the triplet state. J. Chem. Phys. 34, 743.

Daldosso, N., Navarro-Urrios, D., Melchiorri, M., Pavesi, L., Gourbilleau, F., Carrada, M., Rizk, R., Garcia, C., Pellegrino, P., Garrido, B., Cognolato, L., 2005. Absorption cross section and signal enhancement in Er-doped Si nanocluster rib-loaded waveguides. Appl. Phys. Lett. 86, 261103.

Davies, G.M., Aarons, R.J., Motson, G.R., Jeffery, J.C., Adams, H., Faulkner, S., Ward, M.D., 2005. Structural and near-IR photophysical studies on ternary lanthanide complexes containing poly (pyrazolyl) borate and 1,3-diketonate ligands. Dalton Trans. 8, 1136.

Dehmer, J.L., 1973. Phase-amplitude method in atomic physics. II. Z dependence of spin-orbit coupling. Phys. Rev. A 7, 4.

Dekker, R., Klunder, D.J.W., Borreman, A., Diemeer, M.B.J., Worhoff, K., Driessen, A., Stouwdam, J.W., van Veggel, F.C.J.M., 2004. Stimulated emission and optical gain in LaF3:Nd nanoparticle-doped polymer-based waveguides. Appl. Phys. Lett. 85, 6104.

Di Bartolo, B., 1968. Optical Interactions in Solids. John Wiley & Sons, London.

Dieke, G.H., Crosswhite, H.M., 1963. The spectra of the doubly and triply ionized rare earths. Appl. Opt. 2, 675.

Doffek, C., Alzakhem, N., Bischof, C., Wahsner, J., Güden-Silber, T., Lügger, J., Plata-Iglesias, C., Seitz, M., 2012a. Understanding the quenching effects of aromatic C–H- and C–D-oscillators in near-IR lanthanoid luminescence. J. Am. Chem. Soc. 134, 16413.

Doffek, C., Alzakhem, N., Molon, M., Seitz, M., 2012b. Rigid, perdeuterated lanthanoid cryptates: extraordinarily bright near-IR luminophores. Inorg. Chem. 51, 4539.

Dorenbos, P., 2003. f→d transition energies of divalent lanthanides in inorganic compounds. J. Phys. Condens. Matter 15, 575.

Dorenbos, P., van der Kolk, E., 2008. Location of lanthanide impurity energy levels in the III–V semiconductor $Al_xGa_{1−x}N$ ($0 < x < 1$). Opt. Mater. 30, 1052.

Eckes, F., Bulach, V., Guenet, A., Strassert, C.A., De Cola, L., Hosseini, M.W., 2010. Sensitization of the NIR emission of Nd (III) by the α4 atropisomer of a meso-tetraphenyl porphyrin bearing four 8-hydroxyquinolinylamide chelates. Chem. Commun. 46, 619–621.

Ern, V., Bouchriha, H., Fourny, J., Delacôte, G., 1971. Triplet exciton—trapped hole interaction in anthracene crystals. Solid State Commun. 9, 1201.

Escribano, P., Julián-López, B., Planelles-Aragó, J., Cordoncillo, E., Viana, B., Sánchez, C., 2008. Photonic and nanobiophotonic properties of luminescent lanthanide-doped hybrid organic-inorganic materials. J. Mater. Chem. 18, 23.

Faulkner, S., Pope, S.J.A., 2003. Lanthanide-sensitized lanthanide luminescence: terbium-sensitized ytterbium luminescence in a trinuclear complex. J. Am. Chem. Soc. 125, 10526.

Faulkner, S., Pope, S.J.A., Burton-Pye, B.P., 2005. Lanthanide complexes for luminescence imaging applications. Appl. Spectrosc. Rev. 40, 1.

Fu, L.M., Wen, X.F., Ai, X.C., Sun, Y., Wu, Y.S., Zhang, J.P., Wang, Y., 2005. Efficient two-photon-sensitized luminescence of a europium (III) complex. Angew. Chem. 117, 757.

Fukushima, M., Managaki, N., Fujii, M., Yanagi, H., Hayashi, S., 2005. Enhancement of 1.54-μm emission from Er-doped sol-gel $SiO_2$ films by Au nanoparticles doping. J. Appl. Phys. 98, 024316.

Gao, C., Cui, K., She, J., Hou, C., Guo, H., Zhao, W., Wei, W., Peng, B., 2009. Optical properties of a novel neodymium pentafluoropropionate binuclear complex. Inorg. Chim. Acta 362, 2001.

Geskus, D., Aravazhi, S., García-Blanco, S.M., Pollnau, M., 2012. Giant optical gain in a rare-earth-ion-doped microstructure. Adv. Mater. 24, OP19.

Gillin, W.P., Curry, R.J., 1999. 1.54 μm electroluminescence from erbium(III) tris (8-hydroxyquinoline)(ErQ)-based organic light-emitting diodes. Appl. Phys. Lett. 74, 798.

Glover, P.B., Ashton, P.R., Childs, L.J., Rodger, A., Kercher, M., Williams, R.M., De Cola, L., Pikramenou, Z., 2003. Hairpin-shaped heterometallic luminescent lanthanide complexes for DNA intercalative recognition. J. Am. Chem. Soc. 125, 9918.

Glover, P.B., Bassett, A.P., Nockemann, P., Kariuki, B.M., Van Deun, R., Pikramenou, Z., 2007. Fully fluorinated imidodiphosphinate shells for visible- and NIR-emitting lanthanides: hitherto unexpected effects of sensitizer fluorination on lanthanide emission properties. Chem. Eur. J. 13, 6308.

Gonçalves e Silva, F.R., Malta, O.L., Reinhard, C., Güdel, H.U., Piguet, C., Moser, J.E., Bünzli, J.-C.G., 2002. Visible and near-infrared luminescence of lanthanide-containing dimetallic triple-stranded helicates: energy transfer mechanisms in the SmIII and YbIII molecular edifices. J. Phys. Chem. A 106, 1670.

Görller-Walrand, C., Binnemans, K., Gschneidner Jr., K., Eyring, L., 1998. Spectral intensities of f-f transitions. In: Handbook on the Physics and Chemistry of Rare Earths, vol. 25. Elsevier, Amsterdam, p. 101 (Chapter 167).

Grivas, C., Yang, J., Diemeer, M.B., Driessen, A., Pollnau, M., 2010. Continuous-wave solid-state polymer laser. In: Conference on Lasers and Electro-Optics (CLEO) 2010, San Jose, OSA Technical Digest (CD) (Optical Society of America), Paper CTuU6.

Guo, Z., Xu, H., Su, S., Cai, J., Dang, S., Xiang, S., Qiang, G., Zhang, H., O'Keeffe, M., Chen, B., 2011. A robust near infrared luminescent ytterbium metal–organic framework for sensing of small molecules. Chem. Commun. 47, 5551.

Gurge, R.M., Sarker, A.M., Lahti, P.M., Hu, B., Karasz, F.E., 1997. Light emitting properties of fluorine-substituted poly(1,4-phenylene vinylenes). Macromolecules 30, 8286.

Han, H.-S., Seo, S.-Y., Shin, J.H., 2001. Optical gain at 1.54 μm in erbium-doped silicon nanocluster sensitized waveguide. Appl. Phys. Lett. 79, 4568.

Hanna, D.C., Percival, R.M., Perry, I.R., Smart, R.G., Suni, P.J., Townsend, J.E., Tropper, A.C., 1988. Continuous-wave oscillation of a monomode ytterbium-doped fibre laser. Electron. Lett. 17, 1111.

Harrison, B.S., Foley, T.J., Bouguettaya, M., Boncella, J.M., Reynolds, J.R., Schanze, K.S., Shim, J., Holloway, P.H., Padmanaba, G., Ramakrishnan, S., 2001. Near-infrared electroluminescence from conjugated polymer/lanthanide porphyrin blends. Appl. Phys. Lett. 79, 3770.

Hasegawa, Y., Iwamuro, M., Murakoshi, K., Wada, Y., Arakawa, R., Yamanaka, T., Nakashima, N., Yanagida, S., 1998. Enhanced emission of Nd3+ in liquid systems: formation of symmetrical rigid shells of tightly solvated DMSO molecules and weakly coordinated low-vibrational. BETA.-diketonato ligands. Bull. Chem. Soc. Jpn. 71, 2573.

Hasegawa, Y., Ohkubo, T., Sogabe, K., Kawamura, Y., Wada, Y., Nakashima, N., Yanagida, S., 2000. Luminescence of novel neodymium sulfonylaminate complexes in organic media. Angew. Chem. 112, 365.

Hasegawa, Y., Wada, Y., Yanagida, S., 2004. Strategies for the design of luminescent lanthanide(III) complexes and their photonic applications. J. Photochem. Photobiol. C 5, 183.

Hatanaka, M., Yabushita, S., 2009. Theoretical study on the f−f transition intensities of lanthanide trihalide system. J. Phys. Chem. A 113, 12615.

He, H., Si, L., Zhong, Y., Dubey, M., 2012. Iodized BODIPY as a long wavelength light sensitizer for the near-infrared emission of ytterbium(III) ion. Chem. Commun. 48, 1886.

Hebbink, G.A., Reinhoudt, D.N., van Veggel, F.C., 2001. Increased luminescent lifetimes of Ln3+ complexes emitting in the near-infrared as a result of deuteration. Eur. J. Org. Chem. 21, 4101.

Hebbink, G.A., Klink, S.I., Grave, L., Alink, P.G.B.O., Van Veggel, F.C.J.M., 2002. Singlet energy transfer as the main pathway in the sensitization of near-infrared Nd3+ luminescence by dansyl and lissamine dyes. Chemphyschem 3, 1014.

Hebbink, G.A., Grave, L., Woldering, L.A., Reinhoudt, D.N., Van Veggel, F.C.J.M., 2003. Unexpected sensitization efficiency of the near-infrared Nd3+, Er3+, and Yb3+ emission by fluorescein compared to eosin and erythrosine. J. Phys. Chem. A 107, 2483.

Heer, S., Kömpe, K., Güdel, H.U., Haase, M., 2004. Highly efficient multicolour upconversion emission in transparent colloids of lanthanide-doped NaYF4 nanocrystals. Adv. Mater. 16, 2102.

Hehlen, M.P., Brik, M.G., Krämer, K.W., 2013. 50th anniversary of the Judd-Ofelt theory: an experimentalist's view of the formalism and its application. J. Lumin. 36, 221.

Henderson, B., Imbusch, G.F., 1989. Optical Spectroscopy of Inorganic Solids. Clarendon Press, Oxford.

Hernández, I., Gillin, W.P., 2009. Influence of high hydrostatic pressure on Alq3, Gaq3, and Inq3 (q = 8-hydroxyquinoline). J. Phys. Chem. B 113, 14079.

Hernández, I., Tan, R.H.C., Pearson, J.M., Wyatt, P.B., Gillin, W.P., 2009. Nonradiative de-excitation mechanisms in long-lived erbium (III) organic compounds Er$_x$ Y$_{1-x}$ [(p-CF$_3$-C$_6$F$_4$) 2PO2] 3. J. Phys. Chem. B 113, 7474.

Hernández, I., Pathumakanthar, N., Wyatt, P.B., Gillin, W.P., 2010. Cooperative infrared to visible up conversion in Tb3+, Eu3+, and Yb3+ containing polymers. Adv. Mater. 22, 5356.

Hernández, I., Zheng, Y.X., Motevalli, M., Tan, R.H., Gillin, W.P., Wyatt, P.B., 2013. Efficient sensitized emission in Yb (III) pentachlorotropolonate complexes. Chem. Commun. 49, 1933.

Herrera, J.M., Pope, S.J., Adams, H., Faulkner, S., Ward, M.D., 2006. Structural and photophysical properties of coordination networks combining [Ru (bpy)(CN) 4] 2-or [{Ru (CN) 4} 2 (μ-bpym)] 4-anions (bpym=2,2′-bipyrimidine) with lanthanide (III) cations: sensitized near-infrared luminescence from Yb (III), Nd (III), and Er (III) following Ru-to-lanthanide energy transfer. Inorg. Chem. 45, 3895.

Herrera, J.M., Pope, S.J., Meijer, A.J., Easun, T.L., Adams, H., Alsindi, W.Z., Sun, X.Z., George, M.W., Faulkner, S., Ward, M.D., 2007. Photophysical and structural properties of cyanoruthenate complexes of hexaazatriphenylene. J. Am. Chem. Soc. 129, 11491.

Hoffman, K.R., DeLapp, K., Andrews, H.J., Sprinkle, P., Nickels, M., Norris, B., 1995. Spectroscopic studies of fullerenes doped with rare earth and transition metal ions. J. Lumin. 66, 244.

Horrocks, W.D., Bolender, J.P., Smith, W.D., Supkowski, R.M., 1997. Photosensitized near infrared luminescence of ytterbium(III) in proteins and complexes occurs via an internal redox process. J. Am. Chem. Soc. 119, 5972.

Imbert, D., Cantuel, M., Bünzli, J.C.G., Bernardinelli, G., Piguet, C., 2003. Extending lifetimes of lanthanide-based near-infrared emitters (Nd, Yb) in the millisecond range through Cr(III) sensitization in discrete bimetallic edifices. J. Am. Chem. Soc. 125, 15698.

Ito, Y., Okazaki, T., Okubo, S., Akachi, M., Ohno, Y., Mizutani, T., Nakamura, T., Kitaura, R., Sugai, T., Shinohara, H., 2007. Enhanced 1520 nm photoluminescence from Er3+ ions in di-erbium-carbide metallofullerenes (Er2C2)@ C82 (isomers I, II, and III). ACS Nano 1, 456.

Iwamuro, M., Wada, Y., Kitamura, T., Nakashima, N., Yanagida, S., 2000. Photosensitized luminescence of novel β-diketonato Nd(III) complexes in solution. Phys. Chem. Chem. Phys. 2, 2291.

Jørgensen, C.K., Reisfeld, R., 1983. Judd-Ofelt parameters and chemical bonding. J. Less-Common Met. 93, 107.

Joubert, M.F., 1999. Photon avalanche upconversion in rare earth laser materials. Opt. Mater. 11, 181.

Judd, B., 1963. Configuration interaction in rare earth ions. Proc. Phys. Soc. 82, 874.

Karraker, D.G., 1967. Hypersensitive transitions of six-, seven-, and eight-coordinate neodymium, holmium, and erbium chelates. Inorg. Chem. 6, 1863.

Karve, G., Bihari, B., Chen, R.T., 2000. Demonstration of optical gain at 1.06 μm in a neodymium-doped polyimide waveguide. Appl. Phys. Lett. 9, 1253.

Katkova, M.A., Burin, M.E., Logunov, A.A., Ilichev, V.A., Konev, A.N., Fukin, G.K., Bochkarev, M.N., 2009. Lanthanide imidodiphosphinate complexes: synthesis, structure and new aspects of electroluminescent properties. Synth. Met. 159, 1398.

Katkova, M.A., Pushkarev, A.P., Balashova, T.V., Konev, A.N., Fukin, G.K., Ketkov, S.Y., Bochkarev, M.N., 2011. Near-infrared electroluminescent lanthanide [Pr(III), Nd(III), Ho(III), Er(III), Tm(III), and Yb(III)] N,O-chelated complexes for organic light-emitting devices. J. Mater. Chem. 21, 16611.

Katz, H.E., Lovinger, A.J., Johnson, J., Kloc, C., Siegrist, T., Li, W., Lin, Y.Y., Dodabalapur, A., 2000. A soluble and air-stable organic semiconductor with high electron mobility. Nature 404, 478.

Kawamura, Y., Wada, Y., Hasegawa, Y., Iwamuro, M., Kitamura, T., Yanagida, S., 1999. Observation of neodymium electroluminescence. Appl. Phys. Lett. 74, 3245.

Kawamura, Y., Wada, Y., Iwamuro, M., Kitamura, T., Yanagida, S., 2000. Near-infrared electro-luminescence from ytterbium(III) complex. Chem. Lett. 29, 280.

Kawamura, Y., Wada, Y., Yanagida, S., 2001. Near-infrared photoluminescence and electrolumi-nescence of neodymium(III), erbium(III), and ytterbium(III) complexes. Jpn. J. Appl. Phys. 40, 350.

Kennedy, F., Shavaleev, N.M., Koullourou, T., Bell, Z.R., Jeffery, J.C., Faulkner, S., Ward, M.D., 2007. Sensitised near-infrared luminescence from lanthanide (III) centres using Re(I) and Pt(II) diimine complexes as energy donors in d–f dinuclear complexes based on 2,3-bis (2-pyridyl) pyrazine. Dalton Trans. 15, 1492.

Khreis, O.M., Curry, R.J., Somerton, M., Gillin, W.P., 2000. Infrared organic light emitting diodes using neodymium tris-(8-hydroxyquinoline). J. Appl. Phys. 88, 777.

Khreis, O.M., Gillin, W.P., Somerton, M., Curry, R.J., 2001. 980 nm electroluminescence from ytterbium-tris-8-hydroxyquinoline. Org. Electron. 2, 45.

Klink, S.I., Hebbink, G.A., Grave, L., Veggel, F.C.J.M., Reinhoudt, D.N., Slooff, L.H., Polman, A., Hofstraat, J.W., 1999. Sensitized near-infrared luminescence from polydentate triphenylene-functionalized $Nd^{3+}$, $Yb^{3+}$, and $Er^{3+}$ complexes. J. Appl. Phys. 86, 1181.

Klink, S.I., Keizer, H., van Veggel, F.C., 2000. Transition metal complexes as photosensitizers for near-infrared lanthanide luminescence. Angew. Chem. Int. Ed. Engl. 39, 4319.

Koeppen, C., Yamada, S., Jiang, G., Garito, A.F., Dalton, L.R., 1997. Rare-earth organic com-plexes for amplification in polymer optical fibers and waveguides. J. Opt. Soc. Am. B 14, 15.

Koester, C.J., Snitzer, E., 1964. Amplification in a fiber laser. Appl. Opt. 3, 1182.

Kuriki, K., Kobayashi, T., Imai, N., Tamura, T., Nishihara, S., Tagaya, A., Koike, Y., Okamoto, Y., 2000. Fabrication and properties of polymer optical fibers containing Nd-chelate. IEEE Photonics Technol. Lett. 12, 989.

Kuriki, K., Koike, Y., Okamoto, Y., 2002. Plastic optical fiber lasers and amplifiers containing lanthanide complexes. Chem. Rev. 102, 2347–2356.

Lacovara, P., Choi, H.K., Wang, C.A., Aggarwal, R.L., Fan, T.Y., 1991. Room-temperature diode-pumped Yb:YAG laser. Opt. Lett. 16, 1089.

Landau, L.D., Lifshitz, E.M., 1977. Quantum Mechanics: Nonrelativistic Theory, Course of The-oretical Physics. Butterworth-Heinemann, London.

Lazarides, T., Sykes, D., Faulkner, S., Barbieri, A., Ward, M.D., 2008. On the mechanism of d–f energy transfer in RuII/LnIII and OsII/LnIII dyads: Dexter-type energy transfer over a dis-tance of 20 Å. Chem. Eur. J. 14, 9389.

Le Quang, A.Q., Hierle, R., Zyss, J., Ledoux, I., Cusmai, G., Costa, R., Barberis, A., Pietralunga, S.M., 2006. Demonstration of net gain at 1550 nm in an erbium-doped polymer single mode rib waveguide. Appl. Phys. Lett. 89, 141124.

Lenth, W., Macfarlane, R.M., 1992. Upconversion lasers. Opt. Photon. News 3, 8.

Li, Y.G., Yang, H., He, Z., Liu, L.Y., Wang, W.C., Li, F.Y., Xu, L., 2005. Significant increment of photoluminescence quantum yield by efficiently prohibiting fluorescence quenching in erbium(III) organic complexes. J. Mater. Res. 20, 2940.

Li, Z., Yu, J., Zhou, L., Zhang, H., Deng, R., Guo, Z., 2008. 1.54 μm near-infrared photoluminescent and electroluminescent properties of a new erbium(III) organic complex. Org. Electron. 9, 487.

Li, X.L., Zhang, K.J., Li, J.J., Cheng, X.X., Chen, Z.N., 2010. Dual luminescent dinuclear gold(I) complexes of terpyridyl-functionalized alkyne ligands and their efficient sensitization of EuIII and YbIII luminescence. Eur. J. Inorg. Chem. 22, 3449.

Li, B., Wu, Y.H., Wen, H.M., Shi, L.X., Chen, Z.N., 2012. Gold (I)-coordination triggered multi-step and multiple photochromic reactions in multi-dithienylethene (DTE) systems. Inorg. Chem. 51, 1933.

Li, Z., Dellali, A., Malik, J., Motevalli, M., Nix, R.M., Olukoya, T., Peng, Y., Ye, H., Gillin, W.P., Hernández, I., Wyatt, P.B., 2013. Luminescent zinc(II) complexes of fluorinated benzothiazol-2-yl substituted phenoxide and enolate ligands. Inorg. Chem. 52, 1379.

Lindsey, C.P., Patterson, G.D.J., 1980. Detailed comparison of the Williams–Watts and Cole–Davidson functions. J. Chem. Phys. 73, 3348.

Liu, G.K., Jensen, M.P., Almond, P.M., 2006. Systematic behavior of charge-transfer transitions and energy level variation in soft donor complexes of the trivalent lanthanides. J. Phys. Chem. A 110, 2081.

Liu, X., Chi, Y., Dong, G., Wu, E., Qiao, Y., Zeng, H., Qiu, J., 2009. Optical gain at 1550 nm from colloidal solution of $Er^{3+}$-$yb^{3+}$ codoped NaYF4 nanocubes. Opt. Express 17, 5885.

Ma, H., Jen, A.K.-Y., Dalton, L.R., 2002. Polymer-based optical waveguides: materials, processing and devices. Adv. Mater. 14, 1339.

Ma, X., Tian, J., Yang, H.Y., Zhao, K., Li, X., 2013. 3D rare earth porous coordination frameworks with formamide generated in situ syntheses: crystal structure and down-and up-conversion luminescence. J. Solid State Chem. 201, 172.

Mancino, G., Ferguson, A.J., Beeby, A., Long, N.J., Jones, T.S., 2005. Dramatic increases in the lifetime of the $Er^{3+}$ ion in a molecular complex using a perfluorinated imidodiphosphinate sensitizing ligand. J. Am. Chem. Soc. 127, 524.

Meats, R.J., Reekie, L., Jauncie, I.M., Payne, D.N., 1987. High-gain rare-earth doped fiber amplifier at 1.54 μm. In: Optical Fiber Communication Conference. OSA Technical Digest Series, vol. 3. Optical Society of America, Washington, p. 167.

Mech, A., Monguzzi, A., Meinardi, F., Mezyk, J., Macchi, G., Tubino, R., 2010. Sensitized NIR erbium(III) emission in confined geometries: a new strategy for light emitters in telecom applications. J. Am. Chem. Soc. 132, 4574.

Mehlstäubl, M., Kottas, G.S., Colella, S., De Cola, L., 2008. Sensitized near-infrared emission from ytterbium(III) via direct energy transfer from iridium(III) in a heterometallic neutral complex. Dalton Trans. 18, 2385.

Meruga, J.M., Cross, W.M., May, P.S., Luu, Q., Crawford, G.A., Kellar, J.J., 2012. Security printing of covert quick response codes using upconverting nanoparticle inks. Nanotechnology 23, 395201.

Milián Medina, B., Beljonne, D., Egelhaaf, H.-J., Gierschner, J., 2007. Effect of fluorination on the electronic structure and optical excitations of π-conjugated molecules. J. Chem. Phys. 126, 111101.

Milliez, J., Rapaport, A., Bass, M., Cassanho, A., Jenssen, H., 2006. High-brightness white-light source based on up-conversion phosphors. J. Disp. Technol. 2, 307.

Monguzzi, A., Tubino, R., Meinardi, F., Biroli, A.O., Pizzotti, M., Demartin, F., Quochi, F., Cordella, F., Loi, M.A., 2008. Novel $Er^{3+}$ perfluorinated complexes for broadband sensitized near infrared emission. Chem. Mater. 21, 128.

Monguzzi, A., Milani, A., Lodi, L., Trioni, M.I., Tubino, R., Castiglioni, C., 2009. Vibrational overtones quenching of near infrared emission in $Er^{3+}$ complexes. New J. Chem. 33, 1542.

Montalti, M., Credi, A., Prodi, L., Gandolfi, M.T., 2006. Handbook of Photochemistry. Taylor & Francis, London.

Nah, M.K., Cho, H.G., Kwon, H.J., Kim, Y.J., Park, C., Kim, H.K., Kang, J.G., 2006. Photophysical properties of near-infrared-emitting Ln(III) complexes with 1-(9-anthryl)-4,4,4-trifluoro-1,3-butandione (Ln=Nd and Er). J. Phys. Chem. A 110, 10371.

Nyk, M., Kumar, R., Ohulchanskyy, T.Y., Bergey, E.J., Prasad, P.N., 2008. High contrast in vitro and in vivo photoluminescence bioimaging using near infrared to near infrared up-conversion in $Tm^{3+}$ and $Yb^{3+}$ doped fluoride nanophosphors. Nano Lett. 8, 3834.

Ofelt, G.S., 1962. Intensities of crystal spectra of rare-earth ions. J. Chem. Phys. 37, 511.

O'Riordan, A., O'Connor, E., Moynihan, S., Nockemann, P., Fias, P., Van Deun, R., Cupertino, D., Mackie, P., Redmond, G., 2006. Near infrared electroluminescence from neodymium complex-doped polymer light emitting diodes. Thin Solid Films 497, 299.

O'Riordan, A., Van Deun, R., Mairiaux, E., Moynihan, S., Fias, P., Nockemann, P., Binnemans, K., Redmond, G., 2008. Synthesis of a neodymium-quinolate complex for near-infrared electroluminescence applications. Thin Solid Films 516, 5098.

Peng, Y., Ye, H., Li, Z., Motevalli, M., Hernandez, I., Gillin, W.P., Wyatt, P.B., 2014. Visible-range sensitization of $Er^{3+}$-based infrared emission from perfluorinated 2-acylphenoxide complexes. J. Phys. Chem. Lett. 5, 1560.

Pitois, C., Vestberg, R., Rodlert, M., Malmström, E., Hult, A., Lindgren, M., 2003. Fluorinated dendritic polymers and dendrimers for waveguide applications. Opt. Mater. 21, 499.

Pitois, C., Hult, A., Lindgren, M., 2005. Lanthanide-cored fluorinated dendrimer complexes: synthesis and luminescence characterization. J. Lumin. 111, 265.

Pizzoferrato, R., Francini, R., Pietrantoni, S., Paolesse, R., Mandoj, F., Monguzzi, A., Meinardi, F., 2003. Effects of progressive halogen substitution on the photoluminescence properties of an erbium–porphyrin complex. J. Phys. Chem. A 114, 4163.

Plata-Iglesias, C., Elhabiri, M., Hollenstein, M., Bünzli, J.C.G., Piguet, C., 2000. Effect of a halogenide substituent on the stability and photophysical properties of lanthanide triple-stranded helicates with ditopic ligands derived from bis(benzimidazolyl) pyridine. J. Chem. Soc. Dalton Trans. 13, 2031.

Pollnau, M., Gamelin, D.R., Lüthi, S.R., Güdel, H.U., Hehlen, M.P., 2000. Power dependence of upconversion luminescence in lanthanide and transition-metal-ion systems. Phys. Rev. B 61, 3337.

Pope, M., Swnberg, C., 1982. Electronic Processes in Organic Crystals. Oxford University Press, New York.

Pope, S.J., Coe, B.J., Faulkner, S., Bichenkova, E.V., Yu, X., Douglas, K.T., 2004. Self-assembly of heterobimetallic df hybrid complexes: sensitization of lanthanide luminescence by d-block metal-to-ligand charge-transfer excited states. J. Am. Chem. Soc. 126, 9490.

Pope, S.J., Coe, B.J., Faulkner, S., Laye, R.H., 2005. Metal-to-ligand charge-transfer sensitisation of near-infrared emitting lanthanides in trimetallic arrays M2Ln (M=Ru, Re or Os; Ln=Nd, Er or Yb). Dalton Trans. 8, 1482.

Pushkarev, A.P., Ilichev, V.A., Maleev, A.A., Fagin, A.A., Konev, A.N., Shestakov, A.F., Rumyantzev, R.V., Fukin, G.K., Bochkarev, M.N., 2014. Electroluminescent properties of lanthanide pentafluorophenolates. J. Mater. Chem. C 2, 1532.

Quochi, F., Orru, R., Cordella, F., Mura, A., Bongiovanni, G., Artizzu, F., Deplano, P., Mercuri, M.L., Pilia, L., Serpe, A., 2006. Near infrared light emission quenching in organolanthanide complexes. J. Appl. Phys. 99, 053520.

Quochi, F., Artizzu, F., Saba, M., Cordella, F., Mercuri, M.L., Deplano, P., 2010. Population saturation in trivalent erbium sensitized by organic molecular antennae. J. Phys. Chem. Lett. 1, 141.

Ragni, R., Plummer, E.A., Brunner, K., Hofstraat, J.W., Babudri, F., Farinola, G.M., Naso, F., De Cola, L.J., 2006. Blue emitting iridium complexes: synthesis, photophysics and phosphorescent devices. Mater. Chem. 16, 1161.

Reid, M.F., Richardson, F.S., 1984. Lanthanide 4f–4f electric dipole intensity theory. J. Chem. Phys. 88, 3579.

Reinhard, C., Güdel, H.U., 2002. High-resolution optical spectroscopy of $Na_3[Ln(dpa)_3].13H_2O$ with Ln=$Er^{3+}$, $Tm^{3+}$, $Yb^{3+}$. Inorg. Chem. 41, 1048.

Roh, S.G., Oh, J.B., Nah, M.K., Baek, N.S., Lee, Y., Kim, H.K., Roh, S.G., Oh, J.B., Nah, M.K., Baek, N.S., Lee, Y., Kim, H.K., 2004. Er (III)-chelated prototype complexes based on benzoate and pentafluorobenzoate ligands: synthesis and key parameters for near IR emission enhancement. Bull. Korean Chem. Soc. 25, 1503.

Ronda, C.R. (Ed.), 2007. Luminescence: from theory to applications. John Wiley & Sons.

Ronson, T.K., Lazarides, T., Adams, H., Pope, S.J., Sykes, D., Faulkner, S., Coles, S.J., Hursthouse, M.B., Clegg, W., Harrington, R.W., Ward, M.D., 2006. Luminescent PtII (bipyridyl)(diacetylide) chromophores with pendant binding sites as energy donors for sensitised near-infrared emission from lanthanides: structures and photophysics of PtII/LnIII assemblies. Chem. Eur. J. 12, 9299.

Sakamoto, Y., Suzuki, T., Kobayashi, M., Gao, Y., Fukai, Y., Inoue, Y., Sato, F., Tokito, S., 2004. Perfluoropentacene: high-performance pn junctions and complementary circuits with pentacene. J. Am. Chem. Soc. 126, 8138.

Schwarzer, A., Weber, E., 2008. Influence of fluorine substitution on the crystal packing of N-phenylmaleimides and corresponding phthalimides. Cryst. Growth Des. 8, 2862.

Shavaleev, N.M., Moorcraft, L.P., Pope, S.J., Bell, Z.R., Faulkner, S., Ward, M.D., 2003. Sensitized near-infrared emission from complexes of YbIII, NdIII and ErIII by energy-transfer from covalently attached PtII-based antenna units. Chem. Eur. J. 9, 5283.

She, J., Gao, C., Cui, K., Hou, C., Zhao, W., Wei, W., Peng, B., 2008. Synthesis, crystal structure, and optical properties of a novel rare-earth complex Nd(C2F5COO)3 Phen. Struct. Chem. 19, 905.

Shi, Y.W., Shi, M.M., Huang, J.C., Chen, H.Z., Wang, M., Liu, X.D., Ma, Y.G., Xu, H., Yang, B., 2006. Fluorinated Alq3 derivatives with tunable optical properties. Chem. Commun. 18, 1941.

Sivakumar, S., van Veggel, F.C.M., May, P.S., 2007. Near-infrared (NIR) to red and green up-conversion emission from silica sol-gel thin films made with $La_{0.45}Yb_{0.50}Er_{0.05}F_3$ nanoparticles, hetero-looping-enhanced energy transfer (Hetero-LEET): a new up-conversion process. J. Am. Chem. Soc. 129, 620.

Slooff, L.H., Polman, A., Cacialli, F., Friend, R.H., Hebbink, G.A., van Veggel, F.C.J.M., Reinhoudt, D.N., 2001. Near-infrared electroluminescence of polymer light-emitting diodes doped with a lissamine-sensitized $Nd^{3+}$ complex. Appl. Phys. Lett. 78, 2122.

Smola, S.S., Snurnikova, O.V., Fadeyev, E.N., Sinelshchikova, A.A., Gorbunova, Y.G., Lapkina, L.A., Tsivadze, Y., Rusakova, N.V., 2012. The first example of near-infrared 4f luminescence of sandwich-type lanthanide phthalocyaninates. Macroheterocycles 5, 343.

Song, L., Hu, J., Wang, J., Liu, X., Zhen, Z., 2008. Novel perfluorodiphenylphosphinic acid lanthanide (Er or Er–Yb) complex with high NIR photoluminescence quantum yield. Photochem. Photobiol. Sci. 7, 689.

Song, L.M., Zhen, Z., Liu, X.H., 2010. Erbium ($Er^{3+}$) containing perfluorosulfonic polymer film with high photoluminescence quantum yield. Mater. Lett. 64, 1745–1747.

Sternlicht, H., Nieman, G.C., Robinson, G.W., 1963. Triplet–triplet annihilation and delayed fluorescence in molecular aggregates. J. Chem. Phys. 38, 1326.

Suijver, J.F., 2008. In: Ronda, C. (Ed.), Luminescence: From Theory to Applications. Wiley-VCH, Weinheim, p. 134 (Chapter 6).

Sun, R.G., Wang, Y.Z., Zheng, Q.B., Zhang, H.J., Epstein, A.J., 2000. 1.54 μm infrared photoluminescence and electroluminescence from an erbium organic compound. J. Appl. Phys. 87, 7589.

Sun, C.Y., Zheng, X.J., Chen, X.B., Li, L.C., Jin, L.P., 2009. Assembly and upconversion luminescence of lanthanide–organic frameworks with mixed acid ligands. Inorg. Chim. Acta 362, 325.

Tan, R.H.C., 2008. Synthesis and Characterization of Perfluorinated Lanthanide Complexes for NIR Applications. Ph.D. Thesis, Queen Mary University of London, London.

Tan, R.H., Motevalli, M., Abrahams, I., Wyatt, P.B., Gillin, W.P., 2006. Quenching of IR luminescence of erbium, neodymium, and ytterbium β-diketonate complexes by ligand CH and CD bonds. J. Phys. Chem. B 110, 24476.

Tan, R.H.C., Pearson, J.M., Zheng, Y., Wyatt, P.B., Gillin, W.P., 2008. Evidence for erbium-erbium energy migration in erbium(III) bis(perfluoro-p-tolyl)phosphinate. Appl. Phys. Lett. 92, 103303.

Tanaka, F., Ishibashi, T., 1996. Energy transfer between lanthanide ions in dinuclear complexes. J. Chem. Soc. Faraday Trans. 92, 1105.

Tang, C.W., VanSlyke, S.A., 1987. Organic electroluminescent diodes. Appl. Phys. Lett. 51, 913.

Tart, N.M., Sykes, D., Sazanovich, I., Tidmarsh, I.S., Ward, M.D., 2010. Iridium(III) luminophores as energy donors for sensitised emission from lanthanides in the visible and near-infrared regions. Photochem. Photobiol. Sci. 9, 886.

Torelli, S., Imbert, D., Cantuel, M., Bernardinelli, G., Delahaye, S., Hauser, A., Bünzli, J.C.G., Piguet, C., 2005. Tuning the decay time of lanthanide-based near infrared luminescence from micro- to milliseconds through d→f energy transfer in discrete heterobimetallic complexes. Chem. Eur. J. 11, 3228.

Trupke, T., Green, M.A., Würfel, P., 2002. Improving solar cell efficiencies by up-conversion of sub-band-gap light. J. Appl. Phys. 92, 4117.

van den Hoven, G.N., Koper, R.J.I.M., Polman, A., van Dam, C., van Uffelen, J.W.M., Smit, M.K., 1996. Net optical gain at 1.53 μm in Er-doped $Al_2O_3$ waveguides on silicon. Appl. Phys. Lett. 68, 1886.

Van Deun, R., Fias, P., Driesen, K., Binnemans, K., Görller-Walrand, C., 2003. Halogen substitution as an efficient tool to increase the near-infrared photoluminescence intensity of erbium(III) quinolinates in non-deuterated DMSO. Phys. Chem. Chem. Phys. 5, 2754.

Van Deun, R., Fias, P., Nockemann, P., Schepers, A., Parac-Vogt, T.N., Van Hecke, K., Van Meervelt, L., Binnemans, K., 2004. Rare-earth quinolinates: infrared-emitting molecular materials with a rich structural chemistry. Inorg. Chem. 43, 8461.

Van Deun, R., Fias, P., Nockemann, P., Van Hecke, K., Van Meervelt, L., Binnemans, K., 2006. Visible-light-sensitized near-infrared luminescence from rare-earth complexes of the 9-hydroxyphenalen-1-one ligand. Inorg. Chem. 45, 10416.

Van Dijk, J.M.F., Schuurmans, M.F.H., 1983. On the nonradiative and radiative decay rates and a modified exponential energy gap law for 4f–4f transitions in rare-earth ions. J. Chem. Phys. 78, 5317.

Wada, Y., Okubo, T., Ryo, M., Nakazawa, T., Hasegawa, Y., Yanagida, S., 2000. High efficiency near-IR emission of Nd (III) based on low-vibrational environment in cages of nanosized zeolites. J. Am. Chem. Soc. 122, 8583.

Wang, X., Sun, K., Wang, L., Tian, X., Zhang, Q., Chen, B., 2012. Effect on the fluorescence branching ratio of different synergistic ligands in neodymium complex doped PMMA. J. Non-Cryst. Solids 358, 1506.

Weber, M.J., 1968. Radiative and multiphonon relaxation of rare-earth ions in $Y_2O_3$. Phys. Rev. 171, 283.

Wei, Q.H., Lei, Y.F., Xu, W.R., Xie, J.M., Chen, G.N., 2012. Ru(II) sensitized lanthanide luminescence: synthesis, photophysical properties, and near-infrared luminescent determination of alpha-fetal protein (AFP). Dalton Trans. 41, 11219.

Wei, L., Ye, Y., Zhang, R., 2014. Synthesis, crystal structure and fluorescence properties of $Nd^{3+}$ complex with tetrabromoterephthalic acid. J. Mol. Struct. 1058, 51.

Weissman, S.I., 1942. Intramolecular energy transfer the fluorescence of complexes of europium. J. Chem. Phys. 10, 214.

Werts, M.H.V., Hofstraat, J.W., Geurts, F.A.J., Verhoeven, J.W., 1997. Fluorescein and eosin as sensitizing chromophores in near-infrared luminescent ytterbium(III), neodymium(III) and erbium(III) chelates. Chem. Phys. Lett. 276, 196.

White, K.A., Chengelis, D.A., Zeller, M., Geib, S.J., Szakos, J., Petoud, S., Rosi, N.L., 2009a. Near-infrared emitting ytterbium metal–organic frameworks with tunable excitation properties. Chem. Commun. 30, 4506.

White, K.A., Chengelis, D.A., Gogick, K.A., Stehman, J., Rosi, N.L., Petoud, S., 2009b. Near-infrared luminescent lanthanide MOF barcodes. J. Am. Chem. Soc. 131, 18069.

Winkless, L., Tan, R.H.C., Zheng, Y., Motevalli, M., Wyatt, P.B., Gillin, W.P., 2006. Quenching of Er(III) luminescence by ligand CH vibrations: implications for the use of erbium complexes in telecommunications. Appl. Phys. Lett. 89, 1115.

Wojdak, M., Klik, M., Forcales, M., Gusev, O.B., Gregorkiewicz, T., Pacifici, D., Franzò, G., Priolo, F., Iacona, F., 2004. Sensitization of Er luminescence by Si nanoclusters. Phys. Rev. B 69, 233315.

Wolbers, M.P.O., van Veggel, F.C., Snellink-Ruël, B.H., Hofstraat, J.W., Geurts, F.A., Reinhoudt, D.N., 1998. Photophysical studies of m-terphenyl-sensitized visible and near-infrared emission from organic 1:1 lanthanide ion complexes in methanol solutions. J. Chem. Soc. Perkin Trans. 2, 2141.

Wong, W.K., Liang, H.Z., Wong, W.Y., Cai, Z.W., Li, K.F., Cheah, K.W., 2002. Synthesis and near-infrared luminescence of 3d-4f bi-metallic Schiff base complexes. New J. Chem. 26, 275.

Wong, W.H., Pun, E.Y.B., Chan, K.S., 2004. $Er^{3+}$–$Yb^{3+}$ codoped polymeric optical waveguide amplifiers. Appl. Phys. Lett. 84, 176.

Wong, K.L., Law, G.L., Kwok, W.M., Wong, W.T., Phillips, D.L., 2005a. Simultaneous observation of green multiphoton upconversion and red and blue NLO processes from polymeric terbium(III) complexes. Angew. Chem. Int. Ed. Engl. 117, 3502.

Wong, W.H., Chan, K.S., Pun, E.Y.B., 2005b. Ultraviolet direct printing of rare-earth-doped polymer waveguide amplifiers. Appl. Phys. Lett. 87, 011103.

Xia, G., Lin, Y., Chen, J., Tao, S., 1998. A simple model of erbium-doped fibre amplifiers. J. Opt. 29, 298.

Xiao, X., Haushalter, J.P., Faris, G.W., 2005. Upconversion from aqueous phase lanthanide chelates. Opt. Lett. 30, 1674.

Xiao, F., Chen, R., Shen, Y.Q., Dong, Z.L., Wang, H.H., Zhang, Q.Y., Sun, H.D., 2012. Efficient energy transfer and enhanced infrared emission in Er-doped ZnO-$SiO_2$ composites. J. Phys. Chem. C 116, 13458.

Xiaoya, D., Geng, L., Lascola, R., Wright, J.C., 1997. Site-selective laser spectroscopy and four-wave mixing spectroscopy of fullerenes and Er endohedral fullerenes. J. Lumin. 72, 553.

Xu, H.B., Zhang, L.Y., Chen, X.M., Li, X.L., Chen, Z.N., 2008. Modulation of Pt→Ln energy transfer in $PtLn_2$ (Ln=Nd, Er, Yb) complexes with 2,2′-bipyridyl/2,2′:6′2″-terpyridyl ethynyl ligands. Cryst. Growth Des. 9, 9569.

Xu, H.B., Wen, H.M., Chen, Z.H., Li, J., Shi, L.X., Chen, Z.N., 2010a. Square structures and photophysical properties of $Zn_2Ln_2$ complexes (Ln=Nd, Eu, Sm, Er, Yb). Dalton Trans. 39, 1948.

Xu, H.B., Zhong, Y.T., Zhang, W.X., Chen, Z.N., Chen, X.M., 2010b. Syntheses, structures and photophysical properties of heterotrinuclear $Zn_2Ln$ clusters (Ln=Nd, Eu, Tb, Er, Yb). Dalton Trans. 39, 5676.

Yang, J., Diemeer, M.B.J., Geskus, D., Sengo, G., Pollnau, M., Driessen, A., 2009. Neodymium-complex-doped photodefined polymer channel waveguide amplifiers. Opt. Lett. 34, 473.

Yang, J., Diemeer, M.B.J., Grivas, C., Sengo, G., Driessen, A., Pollnau, M., 2010. Nd-doped polymer waveguide amplifiers. IEEE J. Quantum Electron. 46, 1043.

Ye, H.Q., Peng, Y., Li, Z., Wang, C.C., Zheng, Y.X., Motevalli, M., Wyatt, P., Gillin, W.P., Hernandez, I., 2013a. Effect of fluorination on the radiative properties of $Er^{3+}$ organic complexes: an opto-structural correlation study. J. Phys. Chem. C 117, 23970.

Ye, Y.X., Wei, L.H., Sheng, W.C., Chen, M., Hua, Y.Q., 2013b. Luminescent properties of a new $Nd^{3+}$-doped complex with two different carboxylic acids and pyridine derivative. Rare Met. 32, 490–495.

Ye, H.Q., Li, Z., Peng, Y., Wang, C.C., Li, T.Y., Zheng, Y.X., Sapelkin, A., Adamopoulos, G., Hernández, I., Wyatt, P.B., Gillin, W.P., 2014. Organo-erbium systems for optical amplification at telecommunications wavelengths. Nat. Mater. 13, 382.

Yersin, H. (Ed.), 2008. Highly Efficient OLEDs with Phosphorescent Materials. John Wiley & Sons, London.

Yogo, T., Urano, Y., Ishitsuka, Y., Maniwa, F., Nagano, T., 2005. Highly efficient and photostable photosensitizer based on BODIPY chromophore. J. Am. Chem. Soc. 127, 12162.

Yoshioka, H., Weibo, W., Kuwamitsu, K., Iwasaki, W., Yamashita, Y., Miyadera, N., Oki, Y., 2011. Laser action of Nd-complex-doped-polymer laser based on liquid. Mol. Cryst. Liq. Cryst. 539, 225.

Yoshioka, H., Yamashita, Y., Miyadera, N., Yasui, K., Maeda, D., Oki, Y., 2012. $Nd^{3+}$-TFA: HPDA polymeric microchip laser. In: Conference on Lasers and Electro-Optics (CLEO), San Jose, CLEO., CF1A.3.

Yuan, Y.F., Cardinaels, T., Lunstroot, K., Van Hecke, K., Van Meervelt, L., Görller-Walrand, C., Binnemans, K., Nockemann, P., 2007. Rare-earth complexes of ferrocene-containing ligands: visible-light excitable luminescent materials. Inorg. Chem. 46, 5302.

Zhai, X., Li, J., Liu, S., Liu, X., Zhano, D., Wang, F., Zhang, D., Qin, G., Qin, W., 2013. Enhancement of 1.53 μm emission band in $NaYF_4$:$Er^{3+}$, $Yb^{3+}$, $Ce^{3+}$ nanocrystals for polymer-based optical waveguide amplifiers. Opt. Mater. Express 3, 270.

Zhang, J., Petoud, S., 2008. Azulene-moiety-based ligand for the efficient sensitization of four near-infrared luminescent lanthanide cations: $Nd^{3+}$, $Er^{3+}$, $Tm^{3+}$, and $Yb^{3+}$. Chem. Eur. J. 14, 1264.

Zhang, J., Badger, P.D., Greib, S.J., Petoud, S., 2005. Sensitization of near-infrared-emitting lanthanide cations in solution by tropolonate ligands. Angew. Chem. Int. Ed. Engl. 44, 2508.

Zhang, D., Chen, C., Chen, C., Ma, C., Li, T., Zhang, D., Bo, S., Zhen, Z., 2007a. Optical gain at 1535 nm in $LaF_3$:Er,Yb nanoparticle-doped organic-inorganic hybrid material waveguide. Appl. Phys. Lett. 91, 161109.

Zhang, J., Badger, P.D., Geib, S.J., Petoud, S., 2007b. Synthesis and structural properties of lanthanide complexes formed with tropolonate ligands. Inorg. Chem. 46, 6473.

Zhang, J., Shade, C.M., Chengelis, D.A., Petoud, S., 2007c. A strategy to protect and sensitize near-infrared luminescent $Nd^{3+}$ and $Yb^{3+}$: organic tropolonate ligands for the sensitization of $Ln^{3+}$-doped $NaYF_4$ nanocrystals. J. Am. Chem. Soc. 129, 14834.

Zhang, P., Steelant, W., Kumar, M., Scholfield, M., 2007d. Versatile photosensitizers for photodynamic therapy at infrared excitation. J. Am. Chem. Soc. 129, 4526.

Zhang, D., Li, W., Chu, B., Xiao, L., Han, H., Zhu, J., Li, T., Bi, D., Yang, D., Yan, F., Liu, H., Wang, D., 2008. Sensitized photo- and electroluminescence from Er complexes mixed with IR complex. Appl. Phys. Lett. 92, 093501.

Zheng, Y., Motevalli, M., Tan, R.H., Abrahams, I., Gillin, W.P., Wyatt, P.B., 2008. Near IR luminescent rare earth 3,4,5,6-tetrafluoro-2-nitrophenoxide complexes: synthesis, X-ray crystallography and spectroscopy. Polyhedron 27, 1503.

Zheng, Y., Pearson, J., Tan, R.H.C., Gillin, W.P., Wyatt, P.B., 2009. Erbium bis(pentafluorophenyl)phosphinate: a new hybrid material with unusually long-lived infrared luminescence. J. Mater. Sci. Mater. Electron. 20, S430.

Zhong, Q., Wang, H., Qian, G., Wang, Z., Zhang, J., Qiu, J., Wang, M., 2006. Novel stoichiometrically erbium-ytterbium cocrystalline complex exhibiting enhanced near-infrared luminescence. Inorg. Chem. 45, 4537.

Zhu, X., Wong, W.K., Wong, W.Y., Yang, X., 2011. Design and synthesis of near-infrared emissive lanthanide complexes based on macrocyclic ligands. Eur. J. Inorg. Chem. 30, 4651.

Ziessel, R., Ulrich, G., Charbonnière, L.J., Imbert, D., Scopelliti, R., Bünzli, J.-C.G., 2006. NIR lanthanide luminescence by energy transfer from appended terpyridine–boradiazaindacene dyes. Chem. Eur. J. 12, 5060.

Zou, W., Visser, C., Maduro, J.A., Pshenichnikov, M.S., Hummelen, J.C., 2012. Broadband dye-sensitized upconversion of near-infrared light. Nat. Photonics 6, 560.

# Chapter 270

# Europium Chalcogenide Nanoparticles

**Yasuchika Hasegawa and Takayuki Nakanishi**
*Division of Materials Chemistry, Faculty of Engineering, Hokkaido University, Sapporo, Hokkaido, Japan*

## Chapter Outline

## 1 INTRODUCTION

## 1.1 General Introduction

For the past few decades, considerable attention has been focused on the preparation and properties of magnetic semiconductors from the viewpoints of fundamental condensed matter science and also of practical applications for spintronics and magneto-optic devices (Furdyna, 1988). In order to tune their magnetic and magneto-optic properties, various types of structured magnetic materials have been prepared (Gaj et al., 1978; Jungwirth et al., 1999;

Ohno et al., 1996, 1999). Preparation of semiconductor nanoparticles with magnetic dopants has also been studied, and stochastic control for a number of magnetic dopants in II–VI or III–V semiconductor nanoparticles has been investigated (Wang et al., 1991). However, the characteristic magnetic properties of the semiconductor nanoparticles using transition-metal ions such as Zn(II), Cd(II), and Ti(IV) ions may not have been studied extensively because there are few classes of materials that exhibit both intrinsic magnetic and semiconducting properties (Beaulac et al., 2008; Erwin et al., 2005; Jun et al., 2002; Norberg et al., 2004; Norris et al., 2001; Schwartz et al., 2003; Stowell et al., 2003).

On the other hand, various types of magnetic materials containing lanthanide ions have been reported. The exceptional electronic and spin configuration in 4f orbitals is responsible for distinctive magnetic properties, which in turn allows one to create functional magnetic materials. One of the most important series of intrinsic magnetic semiconductors is europium chalcogenides, EuX (X=O, S, Se, and Te). Europium chalcogenides have localized narrow 4f orbitals that exist as the degeneracy levels between the conduction band and the valence band. In the next sessions, brief histories of EuX bulk and nanomaterials are introduced.

In this chapter, focus is given on magnetic europium chalcogenide nanocrystals and nanoparticles. Their preparation is described along with their electronic, magnetic, photophysical, and magneto-optical properties. The last section concentrates on characteristic structures and nanostructures.

## 1.2 Brief History of Europium Semiconductors

First, a brief history of bulk europium chalcogenides composed of divalent Eu(II) ions (EuX: X=O, S, Se, and Te) is introduced in this section.

The first study on europium oxide (EuO) was reported by Matthias and Bozorth (1961) who were working on ferromagnetic intermetallic rare earth compounds. In their studies, they described that EuO becomes ferromagnetic at 77 K. They suggested the presence of exchange interaction between 4f electrons in EuO to explain its ferromagnetic properties. The ferromagnetism of europium sulfide (EuS), europium selenide (EuSe) and europium telluride (EuTe) were discovered by McGuire in 1962 (MacGuire et al., 1963). The ferromagnetic Curie temperature of an EuS crystal was found to be smaller than that of an EuO crystal. Moruzzi and Teaney reported dominant exchange interaction between nearest neighboring Eu(II) ions in EuS (Moruzzi and Teaney, 1963). The detail magnetic properties of EuSe were also described by Morris in 1964 (Busch et al., 1964). The interaction is not only confined to a single (111) plane, but extends over neighboring (111) planes.

EuSe presents a ferromagnetic coupling in the bulk EuSe lattice. The characteristic magnetic behavior of EuSe results in both ferromagnetic and antiferromagnetic properties. The characteristic parameters for the magnetic phase
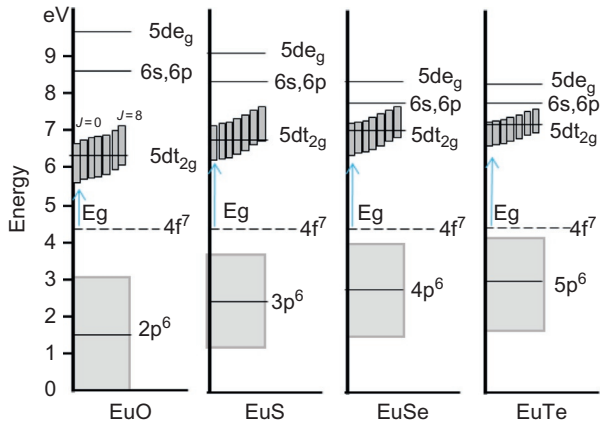
**FIGURE 1** Energy block diagram of the Europium chalcogenides. The origin of the energy scale is the bottom of the valence band of EuO. *Reproduced from Wachter (1972), © 1972 North Holland.*

transition of EuSe were measured on a single crystal by neutron diffraction under low temperature (Fischer et al., 1969). Their large ferromagnetic coupling has been attributed to the NNSS spin structure. NS denotes opposite ferromagnetic order in adjacent (111) planes. Generally, antiferromagnetic spin interaction is generated by NNSS or NSNS spin configuration. Spin configuration in EuSe provides NNSS spin structure, which is including ferrimagnetic NNS spin configuration. Morris also described the antiferromagnetic behavior of EuTe in 1964 (Busch et al., 1964). The general preparation of bulk EuO by thermal reduction of $Eu_2O_3$ above 1000 °C was reported in 1965 (Shafer 1965).

EuX crystals exhibit semiconductor behavior with conduction band and valence band. Europium chalcogenide semiconductors are characterized by narrow 4f orbitals as degenerate levels. The conduction band and the valence band are composed of 5d orbitals of Eu(II) and p orbitals of $O^{2-}$, $S^{2-}$, $Se^{2-}$, or $Te^{2-}$, respectively. The 4f–5d electron transition of EuX crystals leads to unique optical, magnetic, and electronic properties (Fig. 1).

The 4f–5d electronic transitions and the energy gaps of EuX crystals depend on the nature of the chalcogenides. Photoemission studies for unraveling the electronic structure of EuO, EuS, EuSe, and EuTe were described by Eastman in 1969 (Eastman et al., 1969). Then, the optical, electrical, and magnetic properties of EuX were summarized by Wachter in 1972. Crystal-field splitting of the 5d orbitals affects the 4f–5d electronic transitions of EuX crystals. In a simple point charge model, the splitting energy can be expressed by

$$10Dq = \frac{\frac{5}{3}\langle r^4 \rangle}{R^5}, \tag{1}$$

**TABLE 1** Crystal, Magnetic, and Electronic Data for Europium Chalcogenides (Wachter, 1972)

| | $a_0$ (Å) | Magnetic Order | Ionicity (%) | $T_{C,N}$ (K) | Abs. Edge (eV) |
|---|---|---|---|---|---|
| EuO | 5.141 | Ferro | 35 | 64.2 | 1.12 |
| EuS | 5.968 | Ferro | 27 | 16.5 | 1.65 |
| EuSe | 6.195 | Ferro | 25 | 2.8 | 1.80 |
| | | Antiferro | | 4.58 | |
| EuTe | 6.598 | Antiferro | 23 | 9.64 | 2.00 |

$T_{C,N}$, Curie or Néel temperature.

where $r$ and $R$ are the mean radius of the orbitals and the distance to the ligands, respectively. In the europium chalcogenides, the lattice parameter increases from EuO to EuTe. Therefore, the crystal-field splitting is largest in EuO and smallest in EuTe. The fundamental data for EuX bulk crystals are summarized in Table 1.

These europium chalcogenides (EuO, EuS, EuSe, and EuTe) were intensely studied in the 1970s and continue to be of both theoretical and experimental interest. In particular, the 4f–5d electronic transition and spin configuration of EuX crystals lead to specific magneto-optical properties, Faraday and Kerr effects. Greiner and Fan reported effective magneto-optical Kerr effect in EuO and EuS crystals at 12 and 8 K, respectively (Greiner and Fan, 1966). Suits and coworkers also presented magneto-optical properties of EuSe the same year (Suits et al., 1966). The magneto-optical effects of EuX crystals are extremely large. For instance, the Faraday rotation angle of EuSe under 2 T at 4.2 K is $1 \times 10^5$ deg/cm, making it is one the top-choice compound for magneto-optical materials. However, the giant magneto-optical effect is nor operative at room temperature. Enhanced magnetic properties of EuO doped with Gd and Fe ions (Ahn, 1972) were also reported. The Faraday rotation angle of EuO crystal with Gd and Fe ions at 77 K under 0.02 T was estimated to be $1.4 \times 10^5$ deg/cm.

Kasuya and Yanase reported anomalous transport phenomena of EuX crystal in 1968 (Kasuya and Yanase, 1968). The anomalous large negative magneto-resistance and other optical properties were explained by the specific magnetic exciton in which a hole in the 4f conduction band and an electron (for optically active magnetic exciton) in the 5d conduction band combine into a bound state. Molner predicted that the magnetic exciton or magnetic polaron might be expected to form at around the Curie temperature (Molnar and Kasuya, 1970). Study on the bound magnetic polaron and the insulator–metal

transition in EuO were also reported by Torrance (Torrance et al., 1972). The interaction between the specific magnetic exciton and phonons was presented as a magnetic polaron by Takahashi and Kasuya (1983). Presently, the presence of magnetic exciton in EuX crystals continues to stir discussions in the field of physics.

In order to increase the performance temperature of the magneto-optical effect of EuX, various types of EuX with magnetic dopants, e.g., Gd(III) (Kaldis et al., 1971; Mauger et al., 1980), Co(II) (Fumagalli et al., 1996), have been reported. The large Faraday effect of EuO microcrystals in borate glass have also been reported by Tanaka et al. (1997). Electron-spin polarization in the tunneling current in metal-EuS-metal functions, and spin-filter effect of EuS tunnel barriers were observed by Hao et al. (1990). Characteristic magneto-optical properties of EuX crystals are expected to open up new field of spintronic engineering.

## 1.3 Brief History of Europium Chalcogenide Nanoparticles

Presently, there is hefty interest in the synthesis of semiconductor nanoparticles as nanoscale powders dispersible in aqueous or nonaqueous media. The photophysical properties of semiconductor nanoparticles are dominated by their band gaps and their electronic structure related to size, shape, and the environments surrounding the crystals. Such materials have also potential applications including use in displays, biological tagging materials, next-generation photovoltaics, and lasers (Bruchez et al., 1998; Coe et al., 2000; Klimov et al., 2000; Pickett and O'Brien, 2001).

Various types of nanoparticles including lanthanide ions have been reported for several decades during studies on luminescent materials. The first nanocomposites of EuS with cobalt prepared from mechanical alloying of powders of EuS and Co were prepared in 1998 (Tang et al., 1998). In 2000, Chen reported a luminescent EuS nanocluster embedded into zeolite-Y(USY); a similar nanocluster of EuS in zeolite-Y was also prepared by mechanical mixing of the powders of EuS and zeolite (Chen et al., 2000). However, information about particle size and crystallinity of the EuS–Co nanocomposites and EuS–zeolites-Y was not given.

The history of semiconductor nanoparticles containing lanthanide materials such as EuX, starts in 2001. Thongchant and Hasegawa prepared the first EuO single nanoparticles (Thongchant et al., 2001). The EuO nanoparticles displayed spindle-shaped forms (mean length $= 280$ nm, mean width $= 95$ nm). They were synthesized by oxidation of europium metal in liquid ammonia at low-temperature. The superparamagnetic property of spindle-shaped EuO nanoparticles was also described for the first time. Quantum-sized EuO nanoparticles (average diameter $= 3.4$ nm) were obtained the following year by photochemical reaction of europium nitrate with urea in methanol (Hasegawa et al., 2002). Indeed, irradiation of trivalent europium in

methanol in the charge transfer band is known to lead to the formation of Eu(II) (Jørgensen and Brinen, 1963; Kusaba et al., 1992). The quantum-sized EuO nanoparticles showed remarkable blue shift of the absorption and the emission bands due to the quantum-size effect.

Thongchant and Hasegawa also prepared EuS nanoparticles in liquid ammonia by reaction of europium metal with hydrogen sulfide (Thongchant et al., 2003a,b,c). The synthesis of EuS nanoparticles can be improved by starting from an Eu(III) complex as the single-source precursor (Hasegawa et al., 2005; Mirkovic et al., 2005; Regulacio et al., 2005; Zhao et al., 2005). The single-source precursor method has become a standard procedure for the preparation of EuS nanoparticles at the present time. The EuS nanoparticles show effective Faraday rotation in the visible spectral range. For this reason, EuS nanoparticles are promising candidates as optical isolators in the field of next-generation fiber-optic telecommunication systems. EuS nanoparticles doped with Gd ions (Kar et al., 2010; Selinsky et al., 2010) or transition-metal ions (Hasegawa et al. 2013) have been synthesized and characterized by several authors with the aim of obtaining enhanced magnetic and magneto-optical properties, respectively. Alkali metal-doped EuS nanoparticles are also known (Boncher et al., 2012).

The first EuSe nanoparticles were reported by Hasegawa and O'Brien in 2008 (Adachi et al., 2008; Hasegawa et al., 2008). An enhanced Faraday effect for EuSe nanoparticles with an average diameter of 20 nm was observed at around 500 nm. Dickerson reported the first EuTe nanoparticles (average diameter $= 6.5$ nm) having super-antiferromagnetic properties (He et al., 2011). The authors showed that the magnetic properties of EuTe can be tuned by changing the nanoparticle diameter.

Tetravalent Tb ion, Tb(IV), also features 4f–5d electronic transitions under photon irradiation. From this view point, Tb(IV) is expected to form semiconductor materials such as $TbX_2$ (X$=$O, S, Se, and Te). Unfortunately, the Tb(IV) state is unstable under air. Lanthanide semiconductor nanoparticles composed of Tb(IV) ions have not been reported yet. For this reason, it seems that europium chalcogenide nanoparticles, EuO, EuS, EuSe, and EuTe, are the only magnetic semiconductor nanoparticles with 4f-5d electronic transitions.

In Sections 2 and 3 of this chapter, various preparation methods of EuX nanoparticles and nanocrystals are introduced: liquid ammonia method, photochemical reaction, single-source precursor method, electrochemical deposition, vapor phase conversion, preparation of glass materials, among others. The electronic (absorption, emission, and magnetic exciton) and magneto-optical properties of EuX nanoparticles are detailed in Sections 4 and 5. In the last section, characteristic aggregation structures composed of EuX nanoparticles and crystals, nano-aggregation, nano-arrangements, nano-hybrids, and nano-attachments, are presented. These materials are helpful for studying electronic structures and for enhancing magnetic and magneto-optical effects.

## 2 PREPARATION METHODS

### 2.1 Liquid Ammonia Method

Generally, bulk EuO and EuS materials are prepared by solid phase reactions of europium metal (or $Eu_2O_3$) and chalcogenides (oxygen or sulfur sources) at high temperature ($>1000$ °C) (Shafer, 1965). However, chemical and physical instability of their surface constitute an obstacle to the synthesis and isolation of europium chalcogenide nanoparticles. Consequently, liquid phase reactions proved useful for preparing nanoscale semiconductors because the solvent and the surfactant prevent aggregation of the particles and allow a good control of crystal growth (Ahmadi et al., 1996; Manna et al., 2000).

Initially, attempts have been made to prepare EuO and EuS nanoparticles by liquid phase reaction of europium metal in liquid ammonia (Thongchant et al., 2001, 2003a,b,c). In liquid ammonia, the Eu metal is transformed into solvated electrons $\left( e^-_{\text{ammonia}} \right)$ and meta-stable Eu(II) ions. The corresponding equations for the formation of EuO nanoparticles are described in Fig. 2.

Europium metal is added to liquid ammonia under nitrogen atmosphere. The color of the solution turns to deep blue because of the generation of solvated electron (Catteral and Symons, 1965; Warf and Korst, 1956). Oxygen diluted with argon is then introduced into the solution through bubbling. After disappearance of the blue color, the system is warmed to room temperature to remove the excess ammonia. The crude product is washed with HCl solution, deionized water, and methanol, and subsequently dried under vacuum to yield a grayish-white powder.

This preparation method produces spindle-typed EuO nanoparticles (mean length $= 280$ nm, mean width $= 95$ nm). Hasegawa suggested the following reaction mechanism. First, europium metal dissolves in liquid ammonia to give a solvated europium precursor. The strong coordination of ammonia molecules due to the presence of the 5d orbitals of Eu(II) affects the orientation of the solvated precursor so that this compound reacts with oxygen to yield spindle-shaped EuO nanocrystals.

The first preparation of EuS nanoparticles was achieved using the liquid ammonia method with addition of hydrogen sulfide (Thongchant et al., 2003a,b,c). The formation of anionic sulfide by reaction of the latter with liquid ammonia is fast and favored (Fig. 3).

In order to prepare EuS nanoparticles, hydrogen sulfide, $H_2S$, gas is introduced into the liquid ammonia solution containing europium metal through

$$Eu(0) + NH_3 \longrightarrow Eu(II) + 2\ e^-_{\text{ammonia}}$$
$$2e^-_{\text{ammonia}} + 1/2\ O_2 \longrightarrow O^{2-} + 2NH_3 \quad \quad (1)$$
$$Eu(II) + O^{2-} \longrightarrow Eu(II)O$$

**FIGURE 2**   Reaction scheme for the formation of EuO nanoparticles in liquid ammonia.

$$\text{Eu(0)} + \text{NH}_3 \longrightarrow \text{Eu(II)} + 2\,e^-_{\text{ammonia}} \quad (1)$$
$$\text{H}_2\text{S} + \text{NH}_3 \longrightarrow \text{HS}^- + \text{NH}_4^+ \quad (2)$$
$$\text{HS}^- + \text{NH}_3 \longrightarrow \text{S}^{2-} + \text{NH}_4^+ \quad (3)$$
$$\text{NH}_4^+ + e^-_{\text{ammonia}} \longrightarrow 2\text{NH}_3 + 1/2\text{H}_2 \quad (4)$$
$$\text{Eu(II)} + \text{S}^{2-} \longrightarrow \text{Eu(II)S} \quad (5)$$
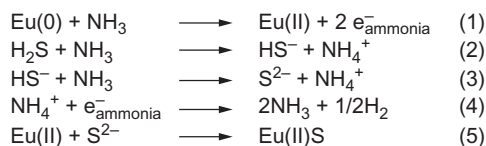
**FIGURE 3**   Reaction scheme for the formation of EuS nanoparticles in liquid ammonia.

bubbling until the color of the solution turns yellow. Liquid ammonia is removed by evaporation at room temperature in 1.5 h. The resulting product is a purple-black powder.

The preparation method using liquid ammonia provided EuS nanoaggregates composed of EuS nanoparticles with various crystal sizes. The average grain size, as estimated from X-ray diffraction (XRD) spectra, was 20 nm. The particle size of EuS nanoparticles synthesized by the liquid ammonia method can be controlled by addition of pyridine (Thongchant et al., 2003a,b,c) or thiourea (Kataoka et al., 2005). The additional molecules bind the Eu(II) ions as ligands and play important role in inhibiting or promoting the growth of the crystal grain. Addition of pyridine leads to an increase in crystal grain from 20 to 36 nm. In contrast, addition of thiourea promotes the inhibition of the crystal growth and the size decreases from 20 to 7 nm.

## 2.2   Photochemical Reactions

An advanced synthetic method for obtaining smaller EuO nanoparticles (average diameter: 3.4 nm) has been reported by Hasegawa et al. (2002). In this protocol, the EuO nanoparticles are synthesized by photochemical reduction of an adduct of europium nitrate with urea in methanol. The corresponding reaction scheme is shown in Fig. 4.

Irradiation into the charge transfer band between an oxygen atom of methanol and the Eu(III) ion induces photoreduction to give Eu(II) and the radical HOCH$_2$ (Jørgensen and Brinen, 1963; Kusaba et al., 1992). The radical intermediate HOCH$_2$ reacts with nitrate to give OH$^-$ and formaldehyde. EuO is formed by dehydrocondensation of Eu(OH)$_2$ (Izaki and Omi, 1997). The growth of EuO nanoparticles is coupled with the polymerization of the coordinated urea with photogenerated formaldehyde to give polyurea-modified EuO nanoparticles. The adduct of Eu(NO$_3$)$_3$ with urea can therefore be regarded as a simple Eu(III) source complex.

A high-pressure mercury arc lamp (500 W) is used for the photochemical crystal growth of EuO nanoparticles; however, this does not result in nanoparticles with clear lattice fringes. Formation of EuO with high crystallinity is desirable for optomagnetic applications. In 1996, molecular crystal growth using laser flash has been reported (Garetz et al., 1996). Crystalline structures can be obtained by irradiating a supersaturated solution with laser light. Hasegawa reported the formation of EuO nanoparticle under ArF laser
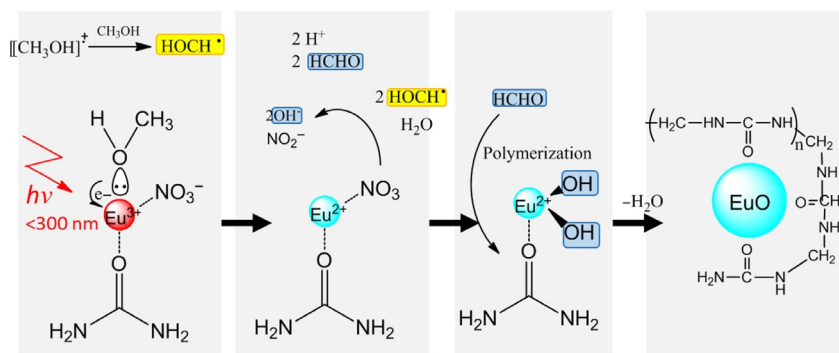
**FIGURE 4** Preparation scheme of EuO nanoparticles using a photochemical reaction. *Reproduced with permission from Hasegawa et al. (2002), © 2002, Wiley-VCH Verlag.*

irradiation ($\lambda_{ex} = 193$ nm, 130 mJ, repetition rate 1 Hz) in 2003 (Hasegawa et al., 2003). Clear lattice fringes of the EuO nanoparticles could successfully be observed. The average size of the EuO nanoparticles was found to be 4.7 nm. Laser irradiation is advantageous in nanocrystal growth. Garetz has reported that laser-induced crystal growth depends on the electric-field-induced effect in saturated solution (Garetz et al., 1996). The laser-induced electric field helps organizing the existing prenucleating cluster, resulting in fast nucleation and growth of the nanoparticles. Crystal growth of EuO nanoparticles does not occur when a KrF excimer laser (248 nm) is employed. These results indicate that direct laser excitation at the charge transfer bands (ca. 195 nm) between the oxygen atom of methanol and the Eu(III) ion is needed to obtain effective reduction of Eu(III) into Eu(II).

Hasegawa also reported EuO nanomaterials with zeolite prepared by photochemical reaction in methanol (Thongchant et al., 2004). In this synthetic procedure, first, europium(II)-exchanged zeolite-X is prepared by ion exchange of NaX with Eu(II), itself obtained by a photochemical reaction. Emission and XPS spectra of Eu(II)X indicated that Eu(II) ions are indeed incorporated into the cavity of zeolite-X. When Eu(II)X is exposed to the atmosphere, EuO crystals having an average size of 4.2 nm form on the outer surface of zeolite-X through oxidation of Eu(II) in the cavities (Fig. 5).

Hasegawa reported that the surface structure of the crystals influenced by the surrounding environments should affect their magnetic properties. Furthermore, photoemission and photoresponse magnetic properties were observed in the EuO nanocrystals.

## 2.3 Single-Source Precursor Method

EuS nanoparticles were also prepared using dithiocarbamate Eu(III) complexes, and the structures of which are shown in Fig. 6. These Eu(III)

$$nEu_{(in)}^{2+} + O_2 \longrightarrow 4Eu_{(in)}^{3+} + 2O^{2-}$$
$$+ (n-6)Eu_{(in)}^{2+} + 2Eu_{(out)}^{2+} \qquad (1)$$



$$2mEu_{(out)}^{2+} + 2mO^{2-} \longrightarrow 2mEuO_{(out)} \qquad (2)$$
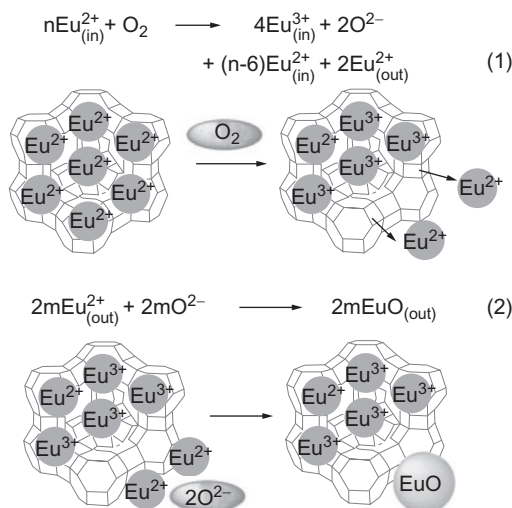


**FIGURE 5** Postulated reaction mechanism for the oxidation of Eu(II)X and the formation of EuO nanocrystals ($Eu_{(in)}^{n+}$ = a europium ion located inside the cavity of zeolite-X, $Eu_{(out)}^{n+}$ = a europium ion on the outer surface of zeolite-X). *Reproduced with permission from Thongchant et al. (2004), © 2004, Chemical Society of Japan.*



$[Eu(S_2CNEt_2)_3](phen)$
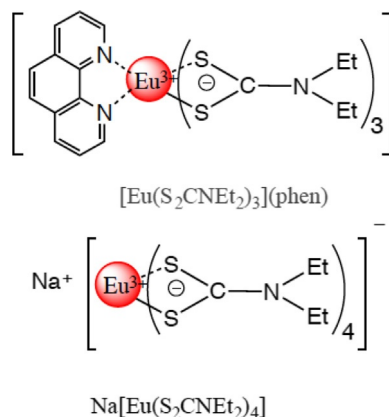
$Na[Eu(S_2CNEt_2)_4]$

**FIGURE 6** Chemical structures of $[Eu(S_2CNEt_2)_3(phen)]$ and $Na[Eu(S_2CNEt_2)_4]$.

complexes are called "single-source precursors (SSP)." They have been utilized for the synthesis of nanoparticles derivatized with a suitable capping reagent (Green and O'Brien, 1998; Revaprasadu et al., 1999).

Stoll and Scholes group reported the formation of EuS nanoparticles by thermal reduction of an Eu(III) dithiocarbamate ternary complex with phenanthroline (phen),[Eu(S₂CNEt₂)₃(phen)] at around 300 °C (Mirkovic et al., 2005; Regulacio et al., 2005; Fig. 6A). The same procedure was used by

Gao (Zhao et al., 2005) who also reported monodisperse cubic-shaped EuS nanoparticles (Zhao et al., 2006a,b). On the other hand, Hasegawa and O'Brien successfully prepared quantum-sized EuS nanoparticles using Na $[Eu(S_2CNEt_2)_4]$ as starting material and photoirradiation; the obtained average particle size was 9 nm (Hasegawa et al., 2005; Fig. 6B).

Hasegawa also reported the crystal growth of EuS nanoparticles starting from Eu(III) dithiocarbamate with tetraphenylphosphonium counterion, $(PPh_4)[Eu(S_2CNEt_2)_4]$ (Fig 7), as precursor and using microwave irradiation (Hasegawa et al., 2006a,b). Indeed, the previous single-source precursor used by Hasegawa, $Na[Eu(S_2CNEt_2)_4]$, causes incorporation of impurity of $Na^+$ cation into EuS, damaging the EuS photophysical properties. Therefore, the SSP has been improved by exchanging the $Na^+$ cation with a bulky organic cation. This single-source precursor provides quantum-sized EuS nanoparticles with clear lattice fringes (average size = 8 nm).

The reaction mechanism postulated by the authors for the thermal reduction of the $Eu(S_2CNEt_2)_n$ unit is described in Fig. 8. The formed EuS nanoparticles might be coordinated by by-products such as organic compounds or the Eu(III) complex itself. Evidence for coordination of organic compounds was supported by IR, FAB-MS, $^1$H- and $^{31}$P-NMR measurements (Hasegawa et al., 2006a,b). The thermal reaction of the SSP gives EuS nanoparticles and the organic radical $(SCN(Et)_2)$ which may react with itself to produce a
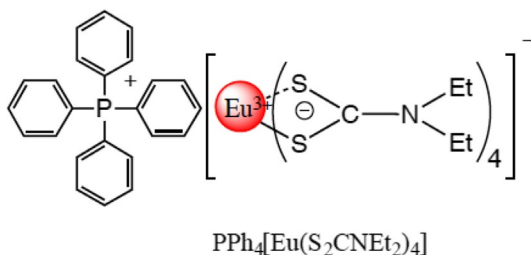


$$PPh_4[Eu(S_2CNEt_2)_4]$$

**FIGURE 7** Chemical structure of $PPh_4[Eu(S_2CNEt_2)_4]$. $PPh_4^+$, tetraphenylphosphonium.
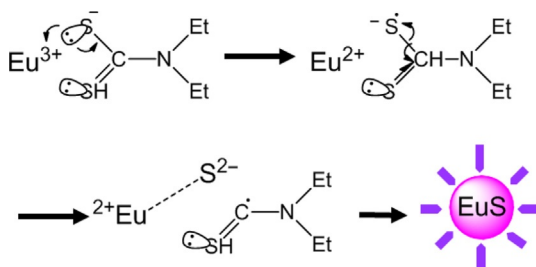


**FIGURE 8** Suggested reaction mechanism for the formation of EuS nanoparticles from the $PPh_4[Eu(S_2CNEt_2)_4]$ precursor. *Reproduced with permission from Hasegawa et al. (2006a,b).* © *2006, American Chemical Society.*

dimer, $(Et)_2NC(S)-(S)CN(Et)_2$ and/or a thiopolymer. The EuS nanoparticle surface might then be covered with the dimer or the polymer.

These synthetic routes open the way to the creation of nanostructures with specific architecture and avoid the use of high temperatures such as a thermal reduction of $Eu_2O_3$ bulk materials. The single-source precursor method for preparing EuS nanoparticles may be used in the fabrication of EuS thin films by decomposing the SSP in a suitable chemical vapor deposition (CVD) process.

EuSe nanoparticles were also prepared by thermal reduction of europium chloride with potassium diphenylphosphinediselenide or tetraphenylphosphonium diphenylphosphinediselenide in hexadecylamine at 330 °C (Fig. 9; Adachi et al., 2008; Hasegawa et al., 2008). EuTe nanoparticles were obtained by the reaction of precursor europium triethanolamine compounds with sodium telluride in ethylene glycol at room temperature, resulting in precipitation of EuTe nanoparticles (He et al., 2011). These preparation methods are based on reactions using europium complexes with organic ligands as precursors.

The single-source precursor method is also adequate to produce europium chalcogenide nanoparticles containing dopant metal ions. Stoll and Jin prepared EuS/Gd nanoparticles using Eu(III) and Gd(III) dithiocarbamate complexes (Kar et al., 2010; Selinsky et al., 2010). Hasegawa described EuS nanoparticles containing transition-metal ions such as Fe(II), Co(II), or Mn(II) and synthesized from dithiocarbamate complexes (Hasegawa et al., 2013; Fig. 10). On the other hand, preparation method of alkali metal-doped EuS nanoparticles cannot be achieved from the single-source precursor method. Mixed powders containing $Eu_2O_3$ and sodium hydroxide are heated at temperature between 350 and 900 °C for 2 h under hydrogen sulfide atmosphere, resulting in $Eu_{1-x}Na_xS$ nanomaterials (Boncher et al., 2012).
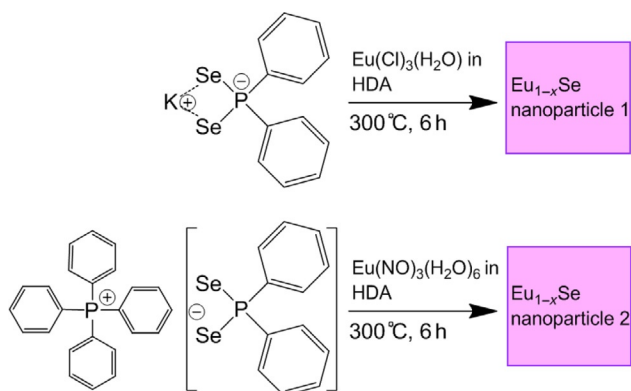


**FIGURE 9**   Reaction schemes for the synthesis of EuSe nanoparticles.
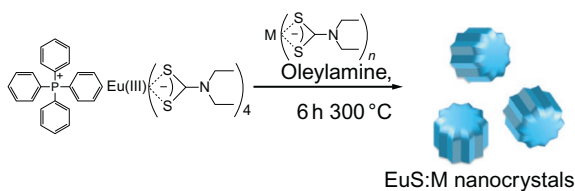
**FIGURE 10** Reaction scheme for the synthesis of transition-metal-doped EuS nanoparticles.
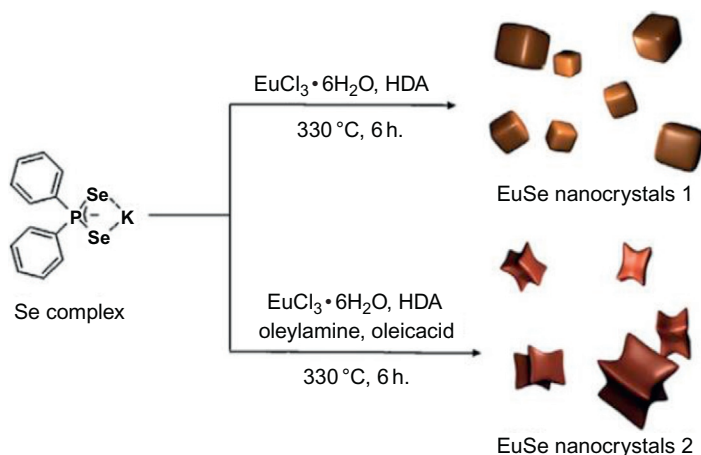


**FIGURE 11** Reaction schemes for the synthesis of EuSe nanocrystals having specific shapes.

Hasegawa also reported on the crystal growth of nano-scaled EuSe crystals by using specific additives, namely oleic acid and oleylamine (Tanaka et al., 2009a,b; Fig. 11). The crystal growth of EuSe nanocrystals 1 was achieved by reacting europium nitrate with an organoselenium compound, n-hexadecylamine (HDA), and the additives. The shape and average particle size were evaluated using transmission electron microscope (TEM) data. The shape of EuSe nanoparticles prepared from $EuCl_3$, HDA, and Se source was cubic, and their average size was found to be 23 nm using TEM, consistent with size determination by XRD (20.5 nm). The characteristic cubic shapes might be due to the NaCl-type fcc-structure of the EuSe lattice. On the other hand, nanoparticles 2 prepared from basic sources with oleic acid and oleylamine sustained anisotropic crystal growth and they had characteristic tetrapod shapes. The average size was found to be 200 nm. These results indicate that the EuSe nanocrystals 2 were built by concentration of EuSe nanocrystal blocks (grain size = 50 nm).

Carboxyl groups of oleic acid play an important role in stabilizing the Eu(III) precursor complexes. The coordination ability of the carboxyl group is stronger than that of HDA. Oleylamine would also support the stabilization of the Eu(III) precursor in HDA. The crystal growth of EuSe nanocrystals 2 is

due to formation of stable Eu(III) precursor complexes as a result of adding oleic acid and oleylamine.

## 2.4 Electrochemical Deposition

Electrochemical deposition by reduction of a single-source precursor, namely an Eu(III) complex, is also a useful method for the preparation of nanostructured EuS thin films. Hasegawa reported on thin films prepared by electrochemical deposition of EuS nanoparticles on a glass electrode using Eu(III) dithiocarbamate complex as single-source precursor, as shown in Fig. 12 (Hasegawa et al., 2012).

The standard reduction potential of Eu(III)/Eu(II) equilibrium in water has been reported to be $E^o = -0.35$ V (SCE), as determined by cyclic voltammetry (Biedermann and Silber, 1973). The reduction potential depends on the solvent and the electron donating ability of the organic ligands in the Eu(III) complex. For the Eu(III) dithiocarbamate complex, an irreversible reduction current was observed during the first cycle around $-1.5$ V (SCE). The irreversible reduction current was assigned to the potential for the reduction of the Eu(III) ion to the Eu(II) ion in the Eu(III) dithiocarbamate complex. The potential shift in the less-noble direction and irreversible current of the Eu(III) dithiocarbamate complex are due to the coordination of dithiocarbamate ligands. The Eu(III) dithiocarbamate complex may be unstable under cathodic polarization, which would lead to decomposition of the ligands. A decrease of the reduction current was observed during the second cycle, which was due to the formation of products with Eu(II) ions on the tin-doped indium oxide (ITO)-coated glass electrode. These results indicate that the ITO-coated glass working electrode is covered with amorphous Eu(II) compounds.

The amorphous thin film composed of Eu and S elements on the ITO electrode was heat-treated to form a crystalline EuS lattice structure. After heat treatment at 300 °C for 3 h in an Ar atmosphere, the color of the thin film changed from white to brown, as shown in the laser scanning microscope image of Fig. 13.

The electron diffraction patterns of EuS tiny nanoparticles obtained by TEM measurements were found to be in good agreement with those of
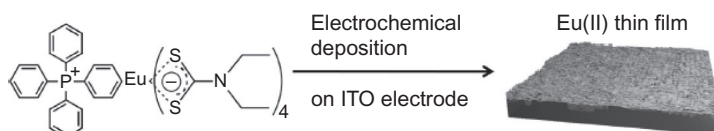


**FIGURE 12** Schematic representation of the synthesis of a EuS nanoparticle thin film on an ITO-coated glass electrode. *Reproduced with permission from Hasegawa et al. (2012),* © 2012, *the American Chemical Society.*
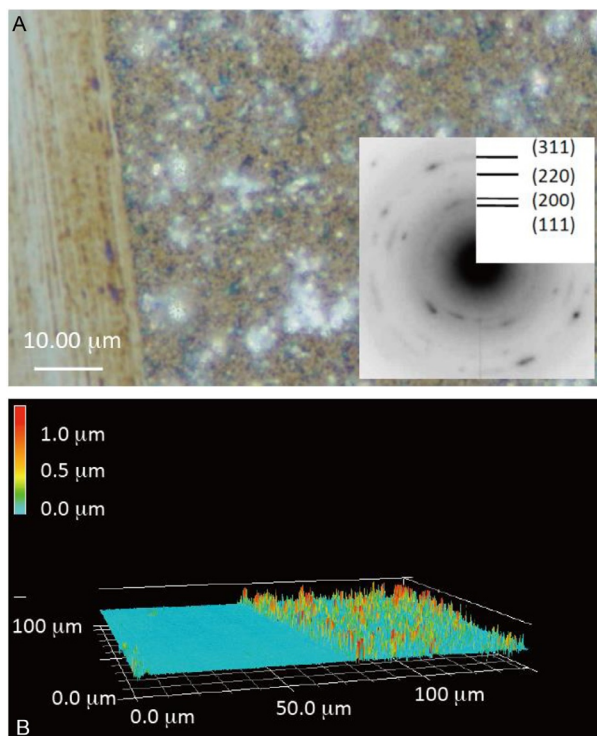
**FIGURE 13** Laser scanning microscope images of an EuS thin film after heat treatment at 300 °C. (A) Color (black and white in the print version) image and (B) three-dimensional image. Inset: electron diffraction pattern image of the thin film using TEM measurement. *Reproduced with permission from Hasegawa et al. (2012), © 2012, the American Chemical Society.*

corresponding (111), (200), (220), and (311) planes of NaCl-type EuS. Hasegawa estimated that the average crystal grain size using TEM and laser scanning microscopy was less than 7 nm. Using electrochemical reduction techniques, EuS nanoparticle thin films with wide band gap and giant Faraday rotation efficiency were successfully prepared on ITO-coated glass electrodes. The Faraday rotation efficiency of the EuS nanoparticle thin film was approximately 10 times larger than that previously reported for EuS nanoparticles. The enhanced magneto-optical efficiency of the EuS thin film is attributed to magnetic interaction between EuS nanoparticles without organic surface stabilizers.

## 2.5 Vapor Phase Conversions

Nano-structural transformation can be an effective synthetic method. Various types of materials synthesized with morphological control such as galvanic replacement, oxidation, diffusion, or cation and anion exchanges have been

reported (Buha et al., 2007; Gao et al., 2003; Hu et al., 2003; Lokhande and Bhosale, 1997; Moon et al., 2011; Son et al., 2004; Vasquez et al., 2008; Yan and Xue, 2006). The morphological transformation is also effective for the formation of nanomaterials with specific sizes and shapes. Dloczil described hexagonal ZnS nanotubes obtained by chemical conversion of crystalline ZnO columns; the ZnS tubes have the same surface morphology as the parent structure (Dloczik et al., 2001).

Stoll reported EuO and EuS nanowires prepared by vapor phase conversion of europium sesquioxide, $Eu_2O_3$ (Boncher et al., 2014). First, they converted $Eu(OH)_3$ single-crystal nanowires to $Eu_2O_3$ single-crystal nanowires. The latter were investigated as a starting material for the controlled-morphology synthesis of EuO, EuS, and EuSe nanoparticles with gas phase reagents.

The transformation method is an important tool for producing europium chalcogenide nanomaterials with characteristic shapes and sizes. In particular, extended studies on the nanorods composed of europium chalcogenides would provide new insights and applications in the field of photo- and magneto-physics, photonics and spintronics, and material sciences.

## 3 GLASS MATERIALS

### 3.1 Polymeric Materials

Europium chalcogenides have characteristic photophysical, magnetic, and magneto-optical properties. Optically transparent thin films or glassy materials such as polymeric thin films containing europium chalcogenide nanoparticles are expected to be useful in applications such as future optical isolators and optomagnetic devices because of their unique photophysical and magnetic properties. From the point of view of opto applications, the EuX/glass hybrid materials are expected to lead to enhancement of the photophysical properties because of effective modification of the EuX surface.

The first report on EuX/polymer hybrid nanomaterials may be EuO/polyurea nanoparticles prepared from the polymerization of urea with photo-generated formaldehyde on EuO surface (Hasegawa et al., 2002). Surface modification with polyurea proved to be effective for enhancing the luminescence properties of the EuO nanoparticles.

Transparent glass materials with EuS nanoparticles were prepared by casting the polymer solutions containing dispersed EuS nanoparticles on glass substrates (Thongchant et al., 2003a,b,c). In order to prepare transparent polymer thin films containing europium chalcogenide nanoparticles, the prepared nanoparticles were added into a 2-propanone (Thongchant et al., 2003a,b,c) or chloroform (Hasegawa et al., 2008) solution of polymethylmethacrylate (PMMA) and well dispersed under ultrasonic treatment for 1 h, giving the colloidal suspension. The PMMA thin films were prepared on a glass substrate from the colloidal suspension via spin-coating or casting methods.

Trindate also reported EuS/polystyrene nanocomposites (Pereira et al., 2008). The EuS polymer nanocomposites were prepared by miniemulsion polymerization of styrene in the presence of the EuS/oleylamine (OA) nanoparticles. As a first step, a stable aqueous miniemulsion was prepared by dispersing the hydrophobe (HD) and the EuS/OA nanocrystals in the styrene droplets. This organic phase was then dispersed in an aqueous solution of surfactant (SDS) and sheared using an ultrasound probe. The polymerization was then carried out under conventional free radical conditions using azobis(isobutyronitrile) (AIBN) or potassium persulfate (KPS) as the initiators and under a nitrogen flow.

Generally, glass transition temperatures of PMMA and polystyrene are approximately 70 and 100 °C, respectively. Polymer thin films containing europium chalcogenides are promising materials for use under room temperature.

## 3.2 Silica Glass Materials

Composite materials with europium chalcogenides thermally stable under 500 °C are expected to be useful for photonic isolators in high-power laser systems. Nakanishi focused on the silica glass materials as the matrix for thermally stable isolators (Nakanishi et al., 2013). Indeed, silica matrixes are thermally stable and optically transparent in the visible spectral range.

Silica glass with EuS nanoparticles was prepared by the sol–gel method with a ligand exchange process. The ligand exchange reaction employed is presented in Fig. 14. In the first step, the initial oleylamine ligands on the EuS nanoparticles (compound A) are exchanged by partially hydrolyzed tetramethylorthosilicate (TMOS, compound B). In this reaction, the EuS nanoparticles silanization is performed in toluene with TMOS. The hydrolysis of TMOS proceeds slowly because of the small amount of water dissolved in toluene. The resulting silanols ($(CH_3-O)_3Si-OH$) obtained by partial hydrolysis of TMOS are coordinated onto the EuS surface. This is because the coordination ability of OH groups is stronger than that of the $NH_2$ groups of oleylamine. In the second step, major residential TMOS are hydrolyzed with EuS/silica particles by the addition of water and ethanol due to formation of monolithic silicate glass (Fig. 14).

The obtained uniform purple gel is slowly dried and used to prepare the EuS/silica nanoglass composite. Silanol modification of the EuS nanoparticles might be a key factor for preparing bulk silica with uniformly dispersed EuS nanoparticles.

The thermal stability of the EuS/silica glass hybrid was evaluated by TG–DTA analysis, as well as its optical properties. Weight losses for the EuS-nanoparticles/PMMA film occur at ca. 100 °C and 290 °C. In contrast, the silica glass exhibits excellent thermal stability (Fig. 15). The surface of the EuS/silica glass hybrid composite was smooth and did not degrade after a thermal resistance test performed at 150 °C for 5 h, whereas the surface of
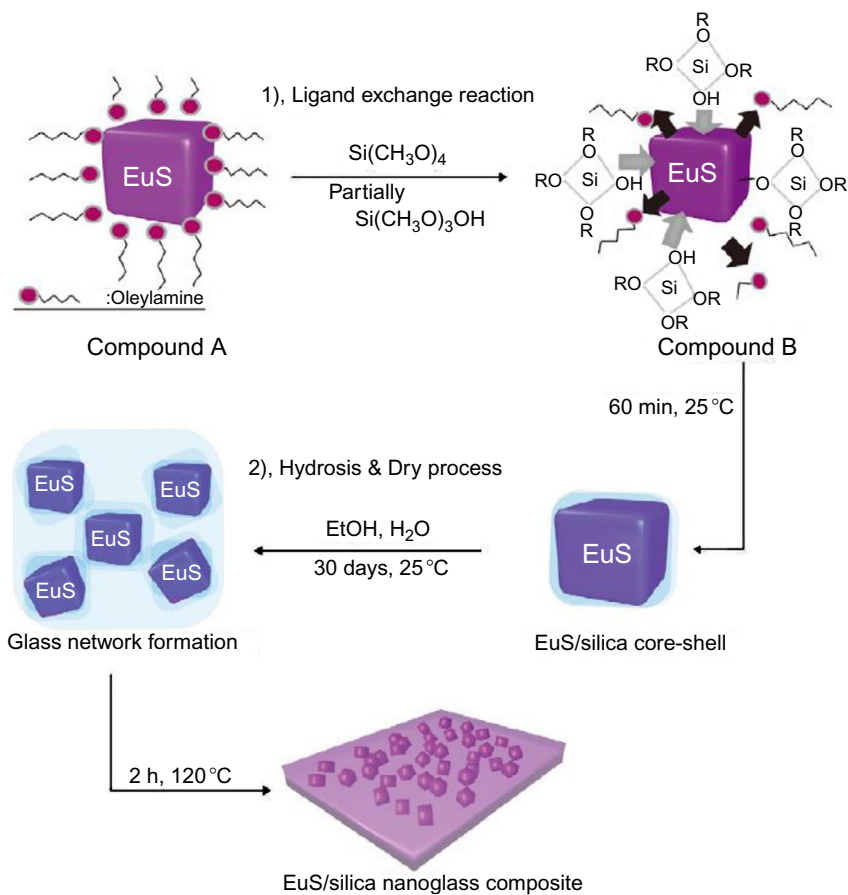
**FIGURE 14** Schematic illustration of the preparation of an EuS/silica nanoglass via two-step reaction with ligand exchange process; Step 1, ligand exchange reaction from alkylamine group (−NH₂) to silanol group (−OH); Step 2, hydrolysis and dry process. *Reproduced with permission from Nakanishi et al. (2013), © 2013 Elsevier B.V.*
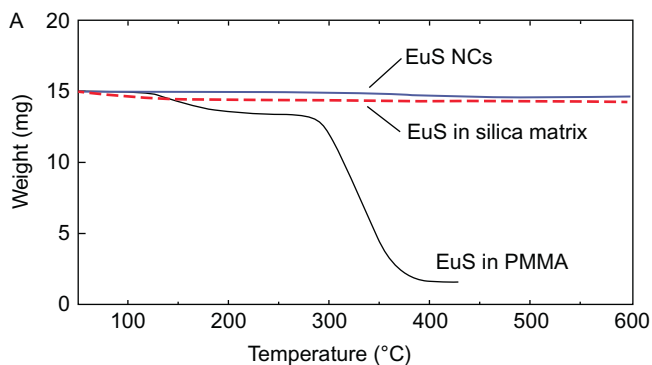


**FIGURE 15** Thermal gravimetric profiles of EuS NCs, EuS NCs/silica nanoglass composite, and EuS NCs in PMMA. *Reproduced with permission from Nakanishi et al. (2013), © 2013 Elsevier B.V.*

the EuS-nanoparticles/PMMA thin film was physically ragged. Excellent transparency was observed in visible spectral range for the EuS/silica glass hybrid (80% transmission at 800 nm). The silica glass phase is an effective matrix for EuS nanoparticles because the tight inorganic framework induces thermal resistance.

# 4 ELECTRONIC AND PHOTOPHYSICAL PROPERTIES

## 4.1 Absorption and Emission Spectra

Europium chalcogenide semiconductors are characterized by narrow 4f levels that are degenerate and lie between the conduction band and the valence band (Wachter, 1972). The electronic transitions between the 4f levels and the conduction band are allowed. The absorption and the emission bands of the lanthanide semiconductor nanoparticles are influenced by the energy gap between 4f levels and the conduction band, the so-called quantum-size effect (Fig. 16).

According to the magnetic polaron model, an electron and a hole are created after the 4f-5d absorption transition; the excited electron lies in the narrow conduction band while the hole is localized in the 4f levels. The electron interacts with the magnetic field (henceforth its name "magnetic polaron") and recombines with the hole, leading to photon emission with a wavelength depending on the band gap. Luminescence enhancement due to quantum-size confinement occurs when the radius of the semiconductor particle becomes close to that of the exciton Bohr radius, $a_0$:

$$a_0 = \frac{\hbar^2 \varepsilon}{e^2} \left( \frac{1}{m_e} + \frac{1}{m_h} \right)$$
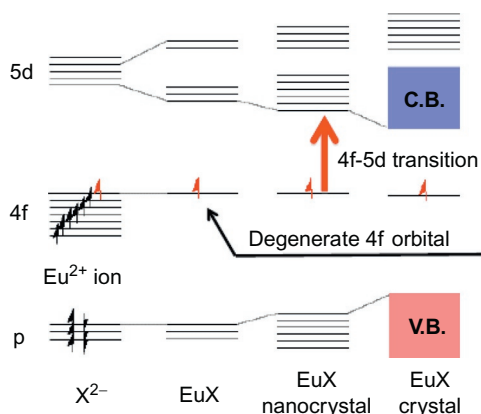


**FIGURE 16** Degenerate 4f level lying between conduction (C.B.) and valence (V.B.) bands in europium chalcogenides. *Reproduced with permission from Hasegawa et al. (2013), © 2013, The Chemical Society of Japan.*

$\varepsilon$ is the dielectric constant, $m_e$ and $m_h$ ($m_h \gg m_e$) the effectives masses of the electron and hole, respectively. For EuS, the effective mass is estimated at 1–2 (Chen et al., 2000). Therefore, the electron Bohr radius is calculated to be 0.75–0.35 nm. EuS nanoparticles with smaller size (diameter $< 2$ nm) would be strongly affected by the quantum-size effect, strongly. The electronic transitions of EuO, EuSe, and EuTe materials are also influenced by the quantum-size effect. Europium chalcogenides with smaller particle size provides larger energy gap, and consequently shorter wavelength of the electronic transition. The absorption spectrum of EuO nanoparticles dispersed in methanol is shown in Fig. 17 (Hasegawa et al., 2002). The particle size using TEM measurements is estimated be 1–4 nm. The band at 280 nm corresponds to the exciton band between the 4f and 5d orbitals. The large Stokes' shift of the exciton bands indicates that the electronic structure or spin state of EuO nanoparticles is significantly different from that of EuO bulk crystals.

When the sample was irradiated at the exciton band, the emission spectrum exhibited a peak at around 357 nm (Fig. 17). The emission quantum yield of the polyurea-modified EuO nanoparticles in methanol was $49 \pm 5\%$ at 300 K (Hasegawa et al. 2002). Interestingly, the quantum yield of EuO nanoparticles without polyurea modification only reached $5 \pm 0.5\%$ at 300 K. These results suggest that the emission quantum yields of the EuO nanoparticles depend on their surface conditions. Wakefield reported that luminescence efficiency of $Eu_2O_3$ composed of Eu(III) ions is increased by a factor of five as the particle size drops below 10 nm related to confinement of the long lifetime Eu(III) excitation in the nanoparticles covered with TOPO molecules (Wakefield et al. 1999). Hasegawa proposed that the presence of
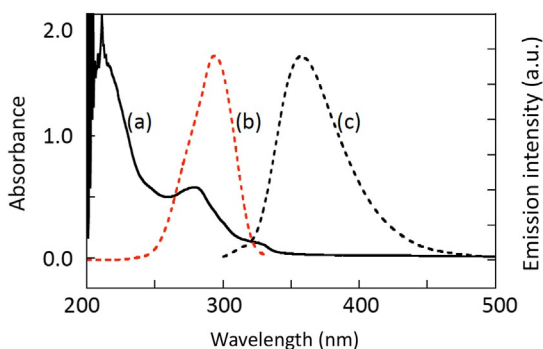


**FIGURE 17** (a) Absorption spectra of EuO nanoparticles in methanol. The absorption below $\lambda = 250$ nm can be assigned to polyurea and methanol, and that above $\lambda = 250$ nm to the exciton band of the EuO nanoparticles. (b) Excitation spectrum of the EuO nanoparticles in methanol, monitored at $\lambda = 340$ nm. (c) Emission spectrum of the EuO nanoparticles in methanol (excitation at $\lambda = 290$ nm). All spectra are corrected for detector sensitivity and lamp emission intensity. *Reproduced with permission from Hasegawa et al. (2002), © 2002 Wiley-VCH Verlag Weinheim.*

polyurea on the quantum-sized EuO surface promotes effective reduction in excitation migration to quenching sites on the EuO surface.

Emission properties of small EuS nanoparticles have been also reported (Hasegawa et al., 2006): nanoparticles with 8-nm size display a blue-shifted spectrum compared with bulk EuS crystals. Their emission quantum yield was found to be $27 \pm 5\%$ at room temperature and their larger energy gap was attributed to the quantum-size effect. An effective blue shift of the emission spectrum of EuS was also reported by Dickerson for nanoparticles with 2-nm size (Redigolo et al., 2007). Band-gap tuning in the strong quantum confinement regime was also described by Fumagalli for EuS thin films (Paulopoulos et al., 2012).

## 4.2 Photo-Induced Magnetic Properties

The 4f–5d electron transition and spin configuration of EuO crystal leads to unique optical-magnetic properties. The photo-magnetic phenomenon was described as "photo-magnetic polaron" (Kasuya and Yanase, 1968) and a theoretical approach to understand the properties of the photo-magnetic polaron was proposed (Takahashi and Kasuya, 1983).

A dramatic increase in magnetization of EuO nanoparticles under UV irradiation at room temperature was observed by photo-magnetic measurements using a superconducting quantum interference device (SQUID) magnetometer fitted with an optical fiber (Hasegawa et al., 2002). The T–$\chi$ curve of the EuO nanoparticles under irradiation was shifted towards high $\chi$ values from that of EuO in darkness. This increase in magnetization under UV irradiation can be explained by the occurrence of a d–f exchange interaction of conductive electrons in the 5d band (Umehara, 1995). Hasegawa suggested that the increase in magnetization may be attributable to the presence of an exciton band in the UV region in agreement with the highly efficient luminescence from the polyurea-modified EuO nanoparticles. The photo-magnetic response of quantum-sized EuO nanoparticles would support the physical theory of the magnetic exciton model with superinteraction between spins in the 5d band and 4f orbitals (Kasuya and Yanase, 1968). The exciton bands should be related to the excited electron in the d orbital and this is in good agreement with the understanding of the photo-magnetic properties. The special interaction between d and f orbitals, i.e., the photo-induced localized magnetic exciton bound by the 4f hole produced in the photoexcitation is an acceptable explanation, as reported for EuTe (Umehara, 1995).

Hasegawa also reported integration curves of EPR signal of EuO nanoparticles under irradiation showing the formation of photoactive species. Evolution of the integration curves with temperature might be linked to an increase in magnetic susceptibility of the EuO nanoparticles under UV irradiation itself due to an exchange interaction of conduction electrons in the 5d band, i.e., to the magnetic exciton (Hasegawa et al., 2006a,b).

## 5 MAGNETIC AND OPTOMAGNETIC PROPERTIES

### 5.1 Magnetic Properties

Bulk europium chalcogenides show ferromagnetic (EuO and EuS) and antiferromagnetic (EuSe and EuTe) properties at low temperature. In this section, magnetic properties of EuX nanoparticles are introduced.

Generally, the spin configuration of paramagnetic metal ions is described with the concept of the effective magnetic moment. First, the effective magnetic moment in Bohr magneton (BM) $p$ is given by

$$p = g[J(J+1)]^{1/2},$$

where the total angular momentum $J$ for the Eu(II) ground electronic configuration is 7/2. If the gyromagnetic ratio $g$ is equal to 2, the theoretical effective magnetic moment for Eu(II) is calculated to be 7.94.

The effective magnetic moment for the EuO nanoparticles was estimated to be 7.98 by SQUID measurements (Hasegawa et al., 2002). Thus, the experimental $p$ for EuO nanoparticles agrees well with the theoretical value estimated for the $4f^7$ configuration of Eu(II). Magnetic properties of europium chalcogenides, Curie or Néel temperatures and hysteresis curves including magnetic moments and coercive fields, are also extracted from SQUID measurements. Spindle-shaped EuO nanoparticles (mean length = 280 nm, mean width = 95 nm) have two magnetically active phases and Curie points were observed at 70 and 150 K (Thongchant et al., 2001). These Curie points were similar to the values reported for EuO films with a thickness between 0.5 and 1 μm and having oxygen vacancies (Borukhovich and Bamburov, 1985). The appearance of a second Curie point at 150 K originates from a large amount of oxygen vacancies that form magnetic impurity states. The number of oxygen vacancies of the described EuO nanoparticles would be as high as in micro-sized EuO films (5–7%) (Borukhovich and Bamburov, 1985; Samokhvalov et al., 1978).

The effective magnetic moment of the EuO nanoparticles was estimated to be 8.27, that is larger than that of Eu(II), 7.94. The correlation between magnetic field and magnetization of the EuO nanocrystals gave a hysteresis curve from which a coercive field $Hc = 8.72 \times 10^{-3}$ T could be calculated.

Hasegawa also found that the EuS nanoparticles turned into the ferromagnetic phase at 16.6 K (Thongchant et al., 2003a,b,c; Fig. 18), consistent with the Curie point of bulk EuS. However, the value of the magnetic moment per Eu(II) ion at 5 K was 4.1 BM, smaller than the expected value of 7.0 BM for the $^8S_{7/2}$ state of Eu(II) at 0 K. Ferromagnetic nanoparticles with diameter in the range of 10–100 nm are usually composed of a single domain structure (Tonomura et al., 1980). A diameter of 20 nm is probably ideal for effectively generating a single domain structure in the EuS nanoparticles. However, the complicated morphology of these nanoparticles is considered
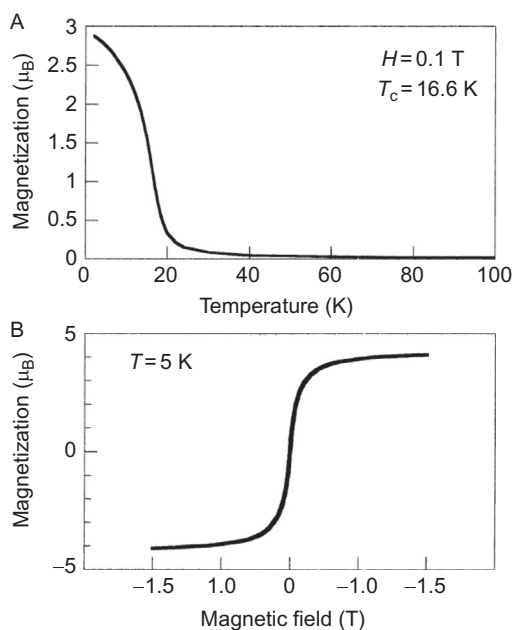
**FIGURE 18**   EuS nanoparticles: (A) Correlation between magnetization ($M$) and temperature ($T$) under magnetic field of 0.1 T, (B) correlation between magnetization ($M$) and magnetic field ($H$) at 5 K. *Reproduced with permission from Thongchant et al. (2003a,b,c), © 2003 the American Chemical Society.*

to affect the magnetic moment value, because the disorderly arrangement of tiny crystals on the surface of the nanoparticles possibly decreases the exchange interaction between Eu(II) ions.

EuSe nanoparticles display antiferromagnetic behavior (Néel point: $T_N = 4.6$ K). (Hasegawa et al., 2008). This Néel point agrees with that of bulk EuSe (Wachter, 1972). The saturation magnetization of EuSe nanoparticles normalized by concentration of EuSe at 1.8 K was found to be 4.6. This value is quite similar to that of corresponding EuS nanoparticles with 36-nm and 21-nm crystal sizes, 4.1 and 2.6 BM, respectively. The experimental effective magnetic moment for the EuSe nanoparticles was found to be 5.58. Note that the EuSe nanoparticles contain organic compounds. The percentages of inorganic Eu compounds in EuSe nanoparticles determined by microwave-induced plasma atomic emission spectrometry (MIP-AES) and energy dispersive X-ray spectrometry (EDX) analyses is estimated to be 70%. Taking this estimation into consideration leads to an effective magnetic moment for inorganic Eu compounds in the nanoparticles is found to be 7.97. Thus, the experimental $p$ for EuSe nanoparticles also agrees perfectly well with the theoretical value for the $4f^7$ configuration of Eu(II).

Magnetic properties of EuTe nanoparticles were reported by Dickerson (He et al., 2011). Nanoparticles with crystal size of 6.5 nm showed a pronounced super-antiferromagnetic transition between 2 and 20 K. The Néel temperature was estimated to be 9.6 K.

Moruzzi and Gambino indicated that the magnetic specific heat of Gd(III) ion doped into EuS bulk microcrystals is shifted to higher temperature (Gambino et al., 1992; Moruzzi et al., 1968). Stoll and Jin have also studied the enhancement of the Curie temperature of nano-sized Gd(III)-doped EuS (Kar et al., 2010; Selinsky et al., 2010). From these reports, Gd(III) ion can be regarded as an effective dopant for enhancing the magnetic properties of EuS nanoparticles.

Hasegawa observed that the coercive field of the EuS nanoparticles is enhanced by the addition of transition-metal ions in the EuS crystal lattice. In particular, the coercive field of the EuS:Mn nanoparticles (70 Oe at 5 K) is approximately three times larger than that of the EuS nanoparticles (25 Oe at 5 K). In the case of semiconductor nanoparticles doped with transition-metal ions, the coercive field is strongly dependent on the ferromagnetic dipole interaction between metal ions. The larger coercive field of observed for EuS nanocrystals doped with transition-metal ions might be due to a strong magnetic dipole interaction between Eu(II) and the transition-metal ions (Hasegawa et al., 2013).

## 5.2 Magneto-Optical Properties

The optical Faraday effect causes rotation of the plane of polarized light, which is linearly proportional to the component of the magnetic field in the direction of propagation (Fig. 19). This effect is important for the construction of optical isolators for fiber-optic telecommunication systems (Furdyna, 1988).

The optical Faraday effect of EuS nanoparticles, was measured in poly(methylmethacrylate) thin films (Thongchant et al., 2003a,b,c). The
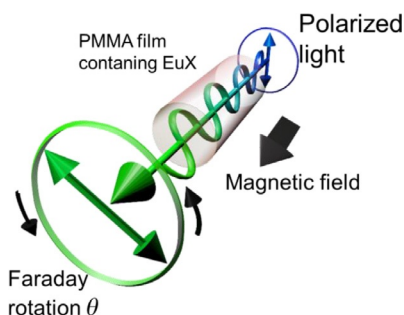


**FIGURE 19** Image of Faraday rotation for fiber-optic telecommunications system. *Reproduced with permission from* Hasegawa et al. (2013), *© 2013 The Chemical Society of Japan.*

PMMA thin films were prepared on a glass substrate from a colloidal suspension via cast method for Faraday rotation measurements. The corresponding Faraday spectrum at room temperature under magnetic field has clear positive and negative peaks as shown in Fig. 20 and arising from contribution of 4f–5d transitions (4f$^7$ ($^8$S$_{7/2}$) → 4f$^6$ ($^7$F$_J$)5d(t$_{2g}$, e$_g$)) of the EuS nanoparticles. The Verdet constant, which indicates the strength of the Faraday rotation efficiency, is estimated by

$$V = \theta/H \times l,$$

where $\theta$, $H$, and $l$ are the Faraday rotation angle (deg), the external magnetic field (15,000 Oe), and the thickness of the thin film (cm), respectively. Veldet constant of PMMA-EuS nanoparticles was estimated to be $1.5 \times 10^{-3}$ deg/cm Oe (concentration of EuS nanoparticles: 5.3 wt%) at 580 nm.

The particle-size dependence of the Faraday rotation peak wavelength is also shown in Fig. 21. The crystal size was determined with help of the Scherrer equation. The EuS sample of smaller particle size showed a blue shift in the Faraday rotation because of the increased energy gap. This physical relationship between the particle size and the peak wavelength of the Faraday rotation can be understood considering the quantum-size effect.
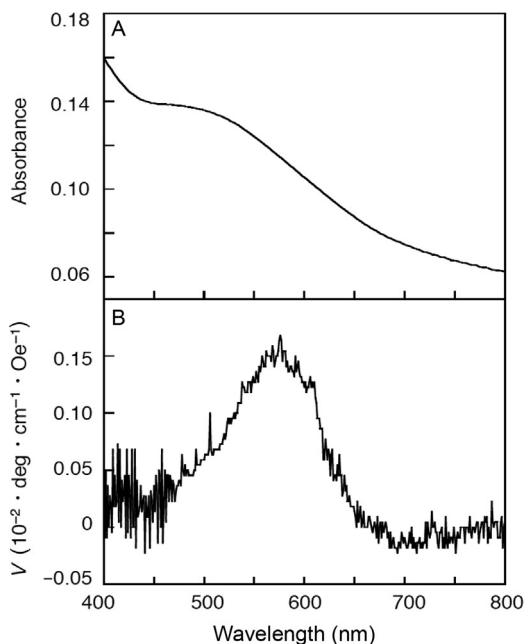


**FIGURE 20**   (A) Absorption spectrum and (B) Faraday rotation spectrum of EuS nanoparticles. *Reproduced with permission from Kataoka et al. (2005), © 2005, The Royal Society of Chemistry.*
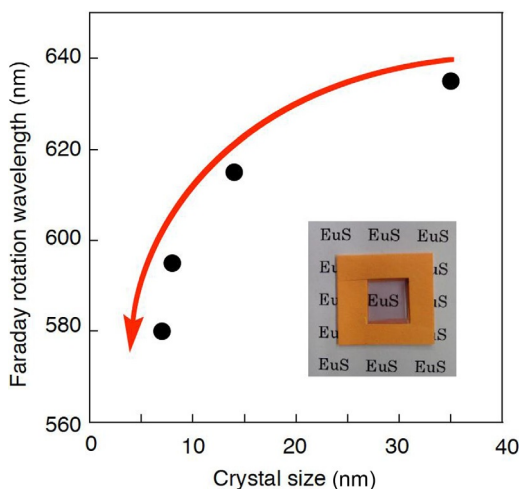
**FIGURE 21** Particle-size dependence of the peak maximum wavelength of the Faraday rotation spectrum recorded for PMMA-EuS film. *Reproduced with permission from Kataoka et al. (2005).* © *2005, The Royal Society of Chemistry.*

The wavelength of Faraday rotation peak of PMMA containing EuSe nanoparticles is the shortest recorded for magneto-optic materials based on europium chalcogenides. The energy gap estimated by the threshold of the Faraday rotation spectrum was found to be 2.0 eV. It clearly shows that PMMA-EuSe is blue shifted in comparison with bulk EuSe crystals (1.8 eV) (Wachter, 1979). The level of the conduction band constructed from 5d orbitals would be affected by the surface compounds through coordination effects (Xavier, 1967). The Verdet constant was found to be $2.4 \times 10^{-3}$ deg/cm Oe, (Hasegawa et al., 2008).

Hasegawa has also carried out calculations of concentration-normalized Verdet constants of PMMA-EuSe nanoparticles for comparison with previous determinations for bulk EuSe crystals and PMMA-EuS nanoparticles. The density of PMMA, EuSe, and EuS is 1.2, 6.5, and 5.7 g/cm$^3$, respectively. The concentration of organic compounds on the EuSe nanoparticle surface was found to be about 1 g/cm$^3$. The volume percentage of the EuSe nanoparticles in PMMA is estimated to be 0.10 vol%. Consideration of the volume percentage of EuSe nanoparticles in PMMA gives large Verdet constants (EuSe nanoparticles, 2.40 deg/cm Oe), which is bigger than the Verdet constant of bulk EuSe (0.16 deg/cm Oe at room temperature) (Suits and Argyle, 1965; Suits et al., 1966). The concentration-normalized Verdet constant of PMMA-EuSe is 5.3 times larger than that of the PMMA-EuS film (0.45 deg/cm Oe). The large Faraday effect of the EuSe nanoparticles might be attributed to their characteristic spin structure. It has been shown that bulk EuSe displays an antiferromagnetic NSNS spin structure at a low temperature ($T < 1.8$ K), ferromagnetic NNS spin

structure (1.8 K $< T <$ 4.6 K), and antiferromagnetic NNSS spin structure close to the Curie-transition temperature $T_c = 4.6$ K (Rumpf et al., 2004). Note that the EuSe nanoparticles possess a wealth of Eu(II) ions on the surface which are capped by organic and inorganic compounds such as $EuSe_2$. We expect that effective magneto-optical properties of EuSe nanoparticles are largely dominated by the special ferromagnetic phase of Eu(II) ions on the surface. It is also proposed that the spin–spin interaction in the EuSe lattice is affected by the Eu(II) ions lying on the nanoparticle surface. Hsu reported that the surface anisotropy dominates the magnetodynamics in the magnetic nanoparticles (Hsu et al., 2005). The surface-modification effect on the EuSe nanoparticles embedded into a PMMA thin film is considered to be an additional factor resulting in a large Faraday effect for this system.

## 6 CHARACTERISTIC STRUCTURES

### 6.1 Aggregations

Construction of superlattice structures (SLSs) by aggregating nanoparticles by means of a self-assembling procedure is effective for enhancing their magnetic properties. Accordingly, enhanced magnetic properties of SLSs composed of FePt, $\gamma$-$Fe_2O_3$, Fe, and $\varepsilon$-Co nanoparticles have been studied (Lisiecki et al., 2007; Nunes et al., 2006; Parker et al., 2007, Sachan et al., 2006). Chaudret and coworkers reported on an electron holography approach for investigating the magnetic properties of cube-shaped magnetic Fe nanoparticles (Snoeck et al., 2008). Their enhanced magnetic properties are due to magnetic dipole interactions between the nanoparticles. Characteristic properties of SLSs assembled with II–VI or III–V semiconductor nanoparticles have also been reported (Talapin and Murray, 2005; Urban et al., 2006). In particular, Urban found that the SLSs composed of semiconductor nanoparticles showed remarkable electronic properties because of characteristic exciton coupling between the nanoparticles (Coe et al., 2000). In view of the peculiar magnetic and electronic properties of SLSs, well-organized SLSs of magnetic semiconductor cube-shaped EuS nanoparticles are thus expected to exhibit enhanced spin polarization and magnetic properties.

Hasegawa has attempted to self-assemble three-dimensional (3D) SLSs composed of EuS nanoparticles with cubic shapes (Tanaka et al., 2009a,b, 2010). SLSs of 3D EuS nanoparticles were prepared by slow evaporation (0.08 mL/h) of a toluene solution with EuS nanoparticles prepared with oleylamine onto the TEM grid substrates and transparent polymer films under room temperature. The fine structures of the 3D SLSs were characterized by TEM and small angle XRD measurements (Fig. 22).

The center-to-center distance between nanoparticles and calculated according to Fitzmaurice's model from 2D fast Fourier transform images corresponds to $d_{100} = 17.0$ nm for SLS of EuS nanoparticles (Korgel et al., 1998).
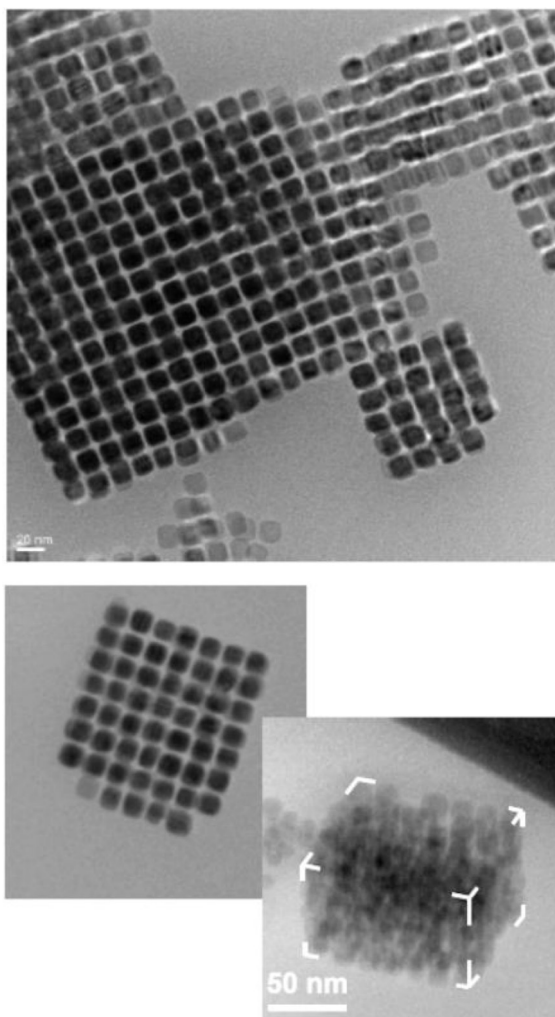
**FIGURE 22** Reconstruction 3D images of transmission electron tomography analysis of EuS nanoparticle SLSs. *Reproduced with permission from Tanaka et al. (2010). © 2010 the American Chemical Society.*

The face-to-face distance between EuS nanoparticles was estimated to be about 3 nm. On the other hand, the length of oleylamine was estimated to be about 2.3 nm by DFT calculations. From these estimations, oleylamines might align in a bilayer manner between the EuS nanoparticles and with some interdigitation. Small-angle XRD analyses also indicated 3D arrangements of EuS nanoparticles on polymer films in cubic superstructure. The magnetic properties of the SLSs on polymer films were investigated and the authors
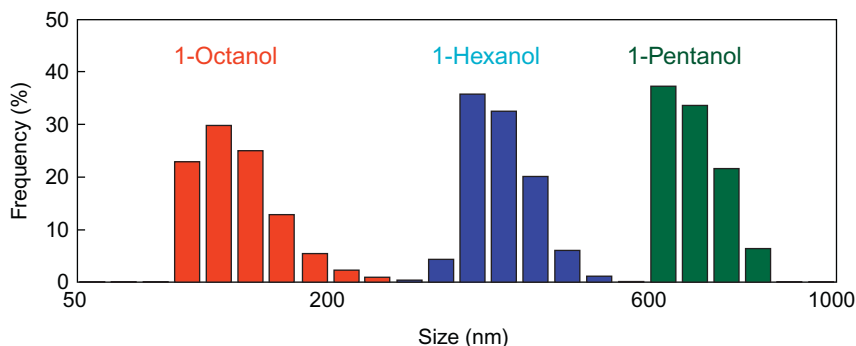
**FIGURE 23** Size distributions of EuS aggregates in alcoholic solutions (1-octanol, 1-hexanol, and 1-pentanol) evaluated with DLS measurements. *Reproduced with permission from Tanaka et al. (2011), © 2011 the American Chemical Society.*

observed that the coercive fields of SLSs on the films were two times larger than those of EuS nanoparticles powder (Korgel et al., 1998).

Stable colloidal particles of aggregated EuS nanoparticles in alcohol solution have also been successfully prepared. The aggregates have cubic-type superlattice structures with tunable aggregation size and interparticle distance, thus, the lattice constant can be adjusted by varying the length of the alkyl chain of alcohols used as solvents (Tanaka et al., 2011; Fig. 23). The molecular structure of the solvent alcohols may influence the structure of the superparticles since an exchange process occurs at the surface of the nanoparticles. The optical band gap and the active wavelength of the magneto-optic properties of EuS nanocrystal-aggregates showed a characteristic red shift with respect to the parent material.

Magneto-optical thin films built by aggregation of europium sulfide (EuS) nanoparticles on a ITO glass electrode have also been reported (Hasegawa et al., 2012). The thin films are prepared by electrochemical reduction of a single-source precursor, an Eu(III) dithiocarbamate complex. The Faraday rotation spectrum indicates that the EuS nanocrystal thin film is blue shifted in comparison with 7-nm diameter EuS nanoparticles (2.2 eV). The Verdet constant of the thin film is 11 m deg/cm Oe at 525 nm, which is approximately 10 times larger than that of previously reported PMMA thin films containing EuS nanoparticles.

## 6.2 Arrangements

The 3D optical manipulation of small particles, such as polystyrene latex spheres (Ashkin et al., 1986; Grier, 2003; Sasaki et al., 1991), metal nanoparticles (Sugiura and Okada, 1998; Sugiura et al., 1997; Svoboda and Block, 1994), semiconductor nanoparticles (Pauzauskie et al., 2006), and biological cells (Ashkin et al., 1987) has been widely studied using laser-trapping

techniques. A number of small nanoparticles can be trapped in the focal zone resulting in the formation of aggregated particles. Masuhara and coworkers have demonstrated light-induced assembling of several polymers and nanoparticles (Hosokawa et al., 2005; Hotta et al., 1996; Ito et al., 2002; Misawa et al., 1991; Yoshikawa et al., 2004).

With respect to lanthanide semiconductor nanoparticles, Hasegawa reported the first demonstration of the manipulation of optomagnetic EuS nanocubes in the aggregated structure using laser-trapping techniques (Tanaka et al., 2007). EuS nanoparticles were prepared by thermal reduction of a single-source precursor, the so-called SSP method. The average size of the EuS nanoparticles was 11.3 nm. The size distribution of the EuS aggregates in methanol was evaluated from dynamic light scattering (DLS) measurement. The distribution of the particle size exhibited a major contribution of about 328 nm. These results indicate that the cubic-shaped EuS nanoparticles form characteristic self-aggregates in methanol.

The EuS self-aggregates of about 330 nm in diameter are expected to be amenable to manipulation by laser trapping because the refractive index of the EuS crystals ($n = 2.43$) (Bachmann and Wachter, 1969) is considerably larger than that of surrounding methanol ($n = 1.33$). A 1064-nm fundamental beam from a Nd:YAG laser was used for the optical trapping. The Nd:YAG laser was introduced into an optical microscope and focused into the suspensions via a microscope objective. The prepared suspensions were dropped into a 1-mm-deep well on a glass slide and covered with a coverslip of 0.17-mm thickness. To observe the laser trapping of the EuS aggregations, a He–Ne laser aligned collinearly with the 1064-nm beam was used for probing light scattering properties. The scattered light from the EuS aggregates trapped at the focal point was detected by a photomultiplier and a charge-coupled device (CCD) camera/video recorder system (Fig. 24).

The typical temporal profile of the scattered light intensity is shown in Fig. 25. The scattering intensity increases with irradiation time and reaches a plateau value, indicating that EuS aggregates of 328-nm diameter are assembled and fill up the focal spot. The stepwise increase in the scattering light intensity was attributed to increase in the number of EuS aggregates in the focal spot. In the temporal profile shown in Fig. 25, the total number of aggregates assembled in the focal spot was estimated to be six.

Hasegawa demonstrated the formation of 3D arrangements of EuS nanoaggregates on glass substrates. The CCD image of these arrangements obtained from laser-trapping experiments is shown in Fig. 26. The assemblies of EuS nanoaggregates were successfully patterned as "E" and "T" shapes on the glass substrate. These results indicate that EuS aggregates in methanol can be independently manipulated using laser-trapping techniques.

3D arrangements of EuS nanoaggregates having optomagnetic properties are expected to open up pioneering fields in microscaled magnetics, optics, and materials science.
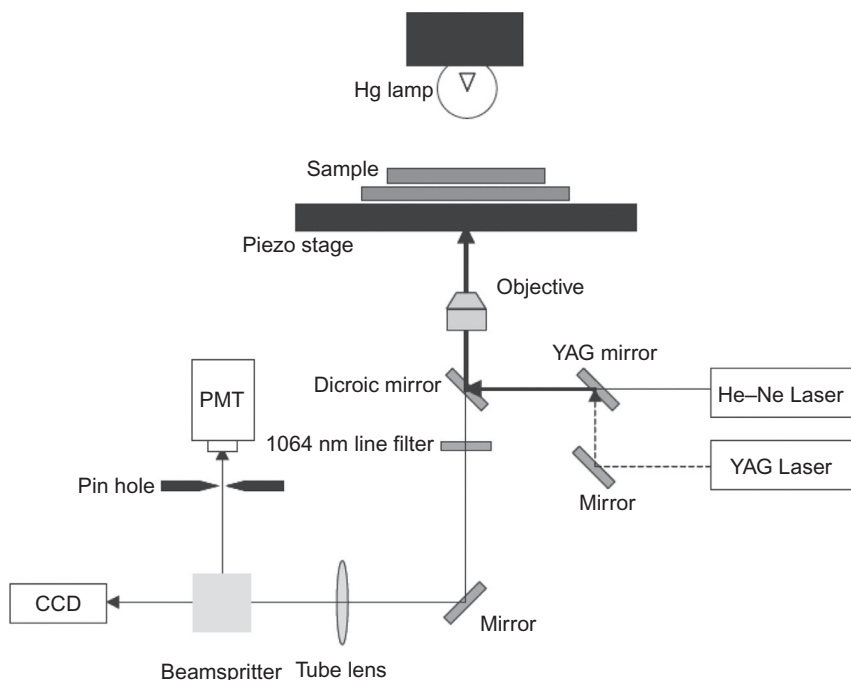
**FIGURE 24** Schematic diagram of experimental setup for laser trapping. *Reproduced with permission from Tanaka et al. (2007), © 2007 the Japan Society of Applied Physics.*
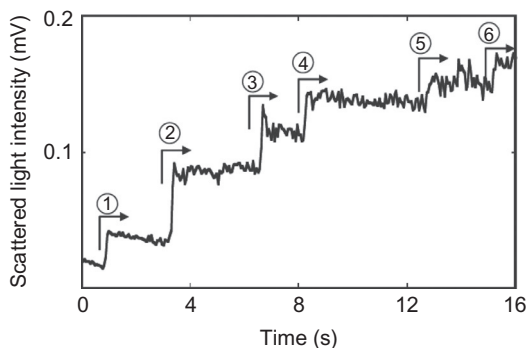


**FIGURE 25** Scattering intensity profile of EuS aggregates in methanol. *Reproduced with permission from Tanaka et al. (2007), © 2007 the Japan Society of Applied Physics.*

## 6.3 Nano-Hybrids

Formation of hetero-nanostructures composed of multiple materials leads to enhancement or modulation of electric, optical, and magnetic properties of nanoparticles (Costi et al., 2010; Donegá, 2011; Nonoguchi et al., 2011; Scholes, 2008; Teranishi et al., 2009).
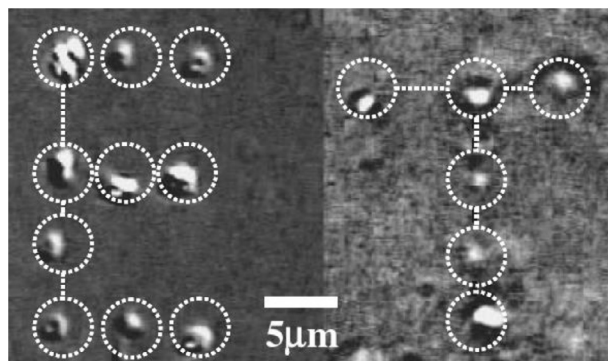
**FIGURE 26** Scattering intensity profile of EuS aggregates in methanol. CCD images of three-dimensional arrangements of EuS aggregates by laser trapping. *Reproduced with permission from Tanaka et al. (2007), © 2007 the Japan Society of Applied Physics.*
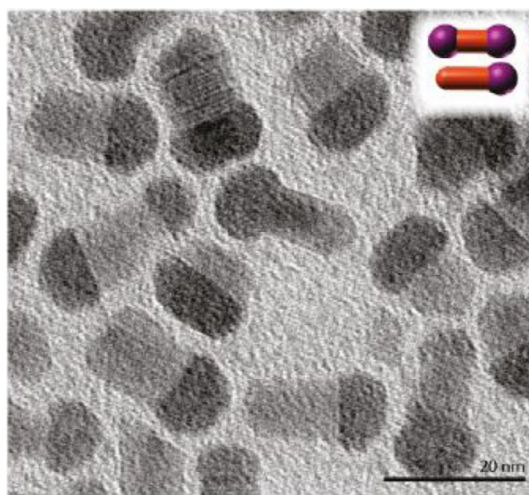


**FIGURE 27** TEM image of EuS nanoparticles formed upon the addition of an EuS precursor to preformed anisotropic CdSe nanocrystals. *Reproduced with permission from Mirkovic et al. (2011), © 2011 the American Chemical Society.*

Scholes and coworkers reported the first integration of magnetic semiconductor EuS nanoparticles with CdS nanoparticle in an attempt to produce a bifunctional nanocomposite with broken band alignment (Mirkovic et al., 2011). EuS–CdSe heterostructures were synthesized via selective deposition of EuS tips on cadmium chalcogenide nanoparticles by thermal decomposition of a single-source precursor. The nanometric heterostructure has broken band alignment, which leads to the quenching of the luminescence of the initial cadmium chalcogenide nanorods following the growth of EuS tips and the formation of the interfacial heterojunction (Fig. 27).
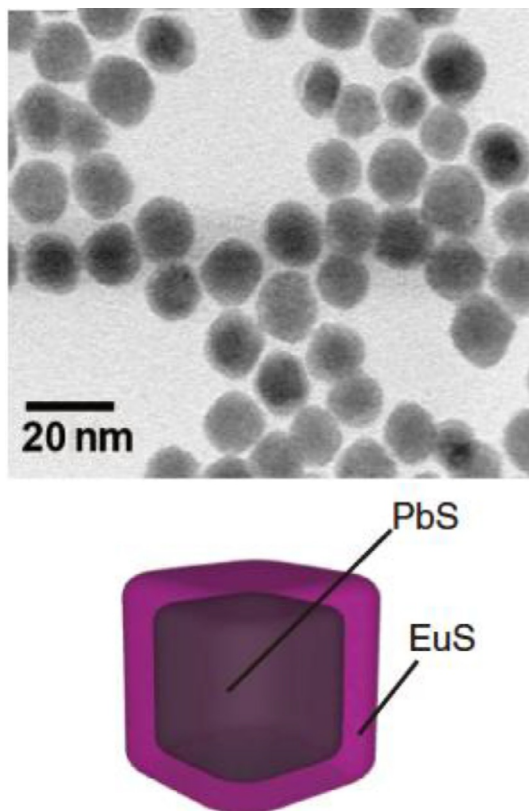
**FIGURE 28**   TEM image of EuS PbS/EuS core/shell nanoparticles. *Reproduced with permission from Nakashima et al. (2012), © 2012 the Chemical Society of Japan.*

Nakashima also reported a PbS/EuS heterostructure obtained by means of the formation of a core/shell configuration (Nakashima et al., 2012). PbS/EuS heterostructures have also been studied as nonmagnetic/magnetic all-semiconductor multilayers (Aharonyan, 2010; Story, 2003). PbS/EuS core/shell nanoparticles were synthesized via the thermal decomposition of a single-source precursor of EuS on the core PbS nanoparticles. The EDS line scan of the nanoparticles clearly demonstrated the core/shell configuration of the heterostructure, and XRD study indicated the epitaxial growth of EuS layer on the PbS core. The magnetic circular dichroism (MCD) spectrum clearly confirmed the formation of the heterostructure and the spin-polarized semiconducting band of EuS shell (Fig. 28).

Gao (Zhao and Gao, 2008; Zhao et al., 2006a,b) and Dickerson (He et al., 2012) reported europium oxysulfide nanoplates and nanorods, respectively. The thermal decomposition of the europium precursor, the Eu(III) dithiocarbamate complex, provided europium and sulfur sources to form $Eu_2O_2S$ (Zhao and Gao, 2008; Zhao et al., 2006a,b). Europium oxysulfide nanorods

were synthesized by hot injection of the sulfur precursor, diethylammonium diethyldithiocarbamate, into a europium oleate, oleylamine, dodecanethiol, and phenanthroline mixture at 320 °C (He et al., 2012). These materials probably contain Eu(III) ions with a small amount of Eu(II) ions. Dickerson observed the superparamagnetic properties of europium oxysulfide nanorods.

Eu(II) ions in semiconductor nanoparticles are also an effective source for luminescent materials. First Eu(II)-doped CaS and SrS nanoparticles were reported by Meijerink (Zhao et al., 2014) in the field of lanthanide phosphors. The EuS material in CaS/SrS nanoparticles plays an important role in bright luminophores for construction of red-emitting solid-state luminescent devices.

## 6.4 Attachments

Optical and magnetic interactions between EuS nanoparticles are based on the formation of nano-assembled structures. In order to analyze the optoelectronic and magnetic interactions in EuS nano-assemblies, linking specific functional molecules with the EuS nanoparticles is required. Hasegawa focused on photo-functional naphthalenedithiol (NpDDT) as a linker for forming the EuS nano-assemblies (Kawashima et al., 2013a; Fig. 29). The naphthalene moiety displays photoluminescence with high emission quantum yield, which is dependent on parameters from the surrounding of this entity, such as the dielectric constant of the matrix (Berlman, 1971). The dithiol unit has often been used as an ideal linker for chemical connection between semiconductor nanoparticles and organic molecules. The NpDDT molecule is therefore expected to be a sensing linker unit for analyzing the optoelectronic properties of EuS nano-assemblies.

EuS nano-assemblies were formed by adding NpDDT dissolved in THF to a solution of oleylamine-capped EuS nanoparticles (EuS–OA) dissolved in THF. After stirring at room temperature for 20 min (EuS–NpDDT-20 min) or 3 h (EuS–NpDDT-3 h), the resulting solution was centrifuged at 4000 rpm for 10 min. The precipitate was added to chloroform and EuS nano-assemblies were obtained. The obtained EuS nano-assemblies were added to a chloroform solution of polymethyl methacrylate and well dispersed under ultrasonic treatment, giving the colloidal suspension. For measurements of photophysical properties, PMMA thin films were prepared on a glass substrate from the colloidal suspension using the drop-cast method.

The emission intensity of the PMMA thin film with EuS–NpDDT-3 h is much smaller than that with corresponding EuS–NpDDT-20 min. The
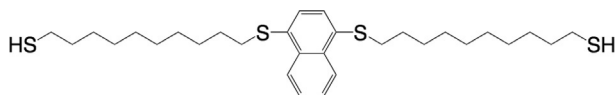


**FIGURE 29** Chemical structure of naphthalenedithiol (NpDDT).

emission quantum yield of NpDDT excited at 330 nm in chloroform was found to be 16%. On the other hand, the emission quantum yields of PMMA thin films with EuS–NpDDT-20 min and EuS–NpDDT-3 h were estimated to be 11% and 6%, respectively. The excited state of naphthalene units in NpDDT may be quenched by adsorption of EuS nanocrystals because of their broad absorption bands at around 400 nm. The emission quantum yield of NpDDT might be related to the size of EuS nano-assemblies. Stoll reported on the properties of EuS nanoparticles functionalized with 1-pyrene carboxylic acid (Kar et al., 2011).

Furthermore, Hasegawa synthesized EuS nanoparticles attached to gold nanoparticles (Kawashima et al., 2013b). The brilliance of gold materials is known to be due to localized surface plasmon resonance (LSPR) leading to unique and unusual photophysical enhancement (Zayats et al., 2005), and has recently been a main focus in the areas of photophysics, materials chemistry, biological science, and advanced photonics, in a quest of improving properties such as enhanced luminescence and photo-catalytic properties (Katz and Willner, 2004; Kulakovich et al., 2002; Lee et al., 2004; Li et al., 2005; Tian and Tatsuma, 2005). Artemyev and coworkers revealed that excitation of the LSPR band of gold nanoparticles promotes efficient luminescence of neighboring CdSe nanoparticles (Kulakovich et al., 2002). Small magneto-optical enhancements in Bi:YIG (YIG: Yttrium Iron Garnet, $Y_3Fe_5O_{12}$) and iron oxide crystals covered with a gold layer or a thin film have also been investigated (Fujikawa et al., 2008; Jain et al., 2009; Li et al., 2005; Ozaki et al., 2009; Wang et al., 2014). In order to analyze and estimate the magneto-optical signal amplification by LSPR, precise control of gold particle size and of the distance between the gold and the magnetic materials is be required.

To construct the EuS–Au nanosystems, cubic EuS, and spherical Au nanoparticles were coupled by a variety of organic linkers, for instance 1,2-ethanedithiol (EDT), 1,6- hexanedithiol (HDT), 1,10-decanedithiol (DDT), 1,4-bisethanethionaphthalene (NpEDT), or 1,4-bisdecanethionaphthalene (NpDDT) (Figs. 30 and 31). The distance between the EuS and Au nanoparticles in EuS–EDT–Au, EuS–HDT–Au, EuS–DDT–Au, EuS–NpEDT–Au, and EuS–NpDDT–Au is estimated to be 0.4, 1.0, 1.5, 1.4, and 3.2 nm, respectively.
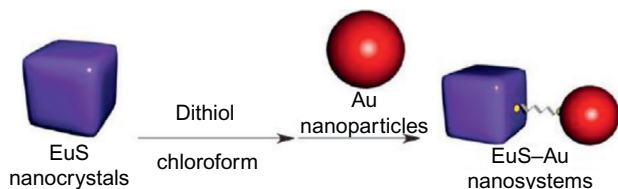


**FIGURE 30** Synthesis of EuS–Au nanosystems. *Reproduced with permission from Kawashima et al. (2013b),* © 2013 Wiley-VCH Verlag.
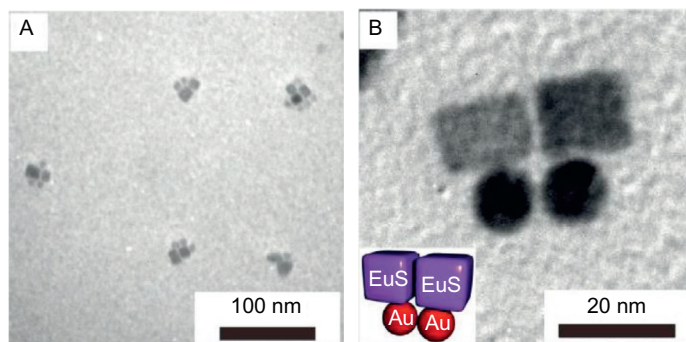
**FIGURE 31** (A) and (B) TEM images of EuS–Au nanosystems. *Reproduced with permission from Kawashima et al. (2013b), © 2013 Wiley-VCH Verlag.*

The magneto-optical properties of the EuS–Au nanosystem were characterized by using Faraday rotation spectroscopy. The Faraday rotation angle of the EuS–Au nanosystem revealed to be dependent on the Au particle size and the distance between EuS and Au nanoparticles (Fig. 32). Enhancement of the Faraday rotation of the EuS–Au nanosystems was also observed. The study and development of magneto-optical enhancement of EuS assisted by LSPR is expected to open up a new field of photophysics and photonic science.

## 7 CONCLUSION AND OUTLOOK

In this chapter, intrinsic magnetic semiconductor nanoparticles containing europium chalcogenides have been presented and discussed. The specific properties of such magnetic semiconductor nanoparticles are now being targeted from the viewpoints of fundamental condensed matter science and also of practical application for spintronics and magneto-optic devices. At the present stage, various types of magnetic dopants in II–VI or III–V semiconductor nanoparticles have been investigated. Europium chalcogenides may become the most popular magnetic semiconductors in the future. The quantum-size and quantum-confinement effects found in europium chalcogenides is indeed providing new photophysics arising from both ferro- and antiferromagnetic spin configurations.

### 7.1 Preparation

Preparation methods of europium chalcogenide nanoparticles are linked to the progress of modern nano-science and technology. They have been dramatically improved by several research groups all over the world. In particular, high-quality nanoscale EuO, EuS, and EuSe materials were successfully prepared by the reaction of an Eu(III) complex used as a single-source
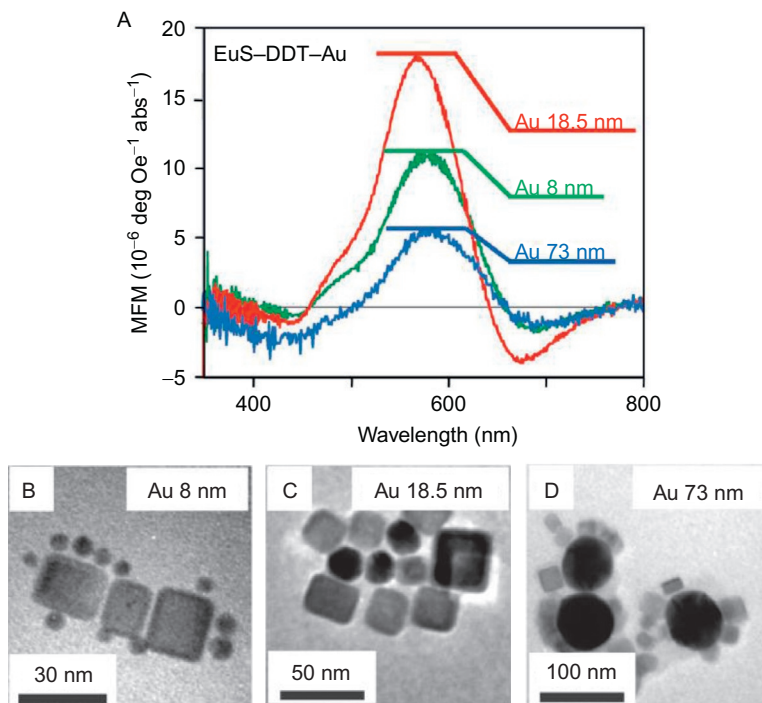
**FIGURE 32**  (A) The calculated magnetic field-microscopy (MFM) constants of polymer thin films containing EuS–DDT–Au nanosystems consisting of the same EuS nanocrystals (particle size: 18.5 nm), but with different particle size of the Au nanoparticles, 8 nm (green (dark gray in the print version)), 18.5 nm (red (gray in the print version)), and 73 nm (blue (black in the print version)). (B)–(D) TEM images of EuSDDT–Au nanosystems consisting of different particle size of Au nanoparticles: (B) 8, (C) 18.5, and (D) 73 nm. *Reproduced with permission from Kawashima et al. (2013b), © 2013 Wiley-VCH Verlag.*

precursor. Electrochemical deposition and vapor phase conversion of EuX nanomaterials are also important for fabricating magneto-optical devices.

## 7.2  Magnetic Properties

Nano-size structures of magnetic semiconductor europium chalcogenides lead to the formation of single domain of magnetic moment in the nanocrystal. Aggregates of sphere-shaped EuX nanoparticles exhibit superparamagnetic and super-antiferromagnetic behaviors. In contrast, enhancement of ferromagnetic properties for aggregates of cube-shaped EuS nanoparticles has been observed. The enhanced magnetic properties may be due to specific magnetic interactions between single-domain EuS nanocrystals. Study on the aggregation of nano-magnetic materials leads to understanding of the formation of magnetization arising from single-domain crystals.

## 7.3 Magneto-Optical Properties

Characteristic photophysical and magneto-optical properties of europium chalcogenide nanoparticles are expected to open up new perspectives in photophysics and chemistry. Quantum-size and quantum-confinement effects of intrinsic semiconductor nanomaterials provide novel aspects and advanced performances for future photo-functional materials. Detailed analysis and understanding of predictable magnetic excitons and polarons in EuX nanoparticles are also important for improving the fabrication of new magneto-optical devices.

Finally, EuX nanoparticles with giant magneto-optical efficiency are expected to be useful in applications such as optical isolators and spintronic devices. Intrinsic magnetic semiconductor nanocrystals containing Eu(II) ions under the form of EuX are therefore promising materials for next-generation photonic devices.

## ABBREVIATIONS

| | |
|---|---|
| **AIBN** | azobis(isobutyronitrile) |
| **BM** | Bohr magneton |
| **CVD** | chemical vapor deposition |
| **DDT** | 1,10-decanedithiol |
| **DFT** | density functional theory |
| **DLS** | dynamic light scattering |
| **EDT** | 1,2-ethanedithiol |
| **HD** | hydrophobe |
| **HDT** | 1,6-hexanedithiol |
| **ITO** | tin-doped indium oxide |
| **MCD** | magnetic circular dichroism |
| **MIP-AES** | microwave-induced plasma atomic emission spectrometry |
| **NpDDT** | 1,4-bisdecanethionaphthalene |
| **NpEDT** | 1,4-bisethanethionaphthalene |
| **OA** | oleylamine |
| **Phen** | phenanthroline |
| **PMMA** | polymethylmethacrylate |
| **PPh$_4$** | tetraphenylphosphonium |
| **S$_2$CNEt$_2$** | diethyldithiocarbamate |
| **SCE** | saturated calomel electrode |
| **SDS** | sodium dodecyl sulfate |
| **SLSs** | superlattice structures |
| **SQUID** | superconducting quantum interference device |
| **SSP** | single-source precursor |
| **TEM** | transmission electron microscope |
| **TMOS** | tetramethylorthosilicate |
| **TOPO** | trioctyl phosphine oxide |
| **XRD** | X-ray diffraction |

# REFERENCES

Adachi, T., Tanaka, A., Hasegawa, Y., Kawai, T., 2008. Preparation of EuSe nanoparticles from Eu(III) complex containing selenides. Thin Solid Films 516, 2460–2462.

Aharonyan, K.H., 2010. Exciton properties of EuS/PbS/EuS finite confining potential quantum well. Phys. E 43, 111–116.

Ahmadi, T.S., Wang, Z.L., Green, T.C., Henglein, A., El-Sayed, M.A., 1996. Shape-controlled synthesis of colloidal platinum nanoparticles. Science 272, 1924–1925.

Ahn, K.Y., 1972. EuO films doped with Fe and Gd. J. Appl. Phys. 43, 231–235.

Ashkin, A., Dziedzic, J.M., Bjorkholm, J.E., Chu, S., 1986. Observation of a single-beam gradient force optical trap for dielectric particles. Opt. Lett. 11, 288–290.

Ashkin, A., Dziedzic, J.M., Yamane, T., 1987. Optical trapping and manipulation of single cells using infrared laser beams. Nature 330, 769–771.

Bachmann, R., Wachter, P., 1969. Effects of magnetic order on refractive index and photoconductivity of europium chalcogenides. J. Appl. Phys. 40, 1326–1327.

Beaulac, R., Archer, P.I., Liu, X., Lee, S., Salley, G.M., Dobrowolska, M., Furdyna, J.K., Gamelin, D.R., 2008. Spin-polarizable excitonic luminescence in colloidal $Mn^{2+}$-doped CdSe quantum dots. Nano Lett. 8, 1197–1201.

Berlman, I.B., 1971. Handbook of Fluorescence Spectra of Aromatic Molecules. Academic Press, New York, NY.

Biedermann, G., Silber, H.B., 1973. On the standard potential of the $Eu^{3+}$–$Eu^{2+}$ couple in 1 M $LiClO_4$ medium. Acta Chem. Scand. 27, 3761–3768.

Boncher, W.L., Gorlich, E.A., Tomala, K., Bitter, J.L., Stoll, S.L., 2012. Valence and magnetic investigations of alkali metal-doped europium sulfide. Chem. Mater. 24, 4390–4396.

Boncher, W.L., Rosa, N., Kar, S., Stoll, S.L., 2014. Europium chalcogenide nanowires by vapor phase conversions. Chem. Mater. 26, 3144–3150.

Borukhovich, A.S., Bamburov, V.G., 1985. Magnetism and magnetic heterogeneity of EuO films. J. Magn. Magn. Mater. 53, 80–82.

Bruchez, M., Moronne Jr., M., Gin, P., Weiss, S., Alivisatos, A.P., 1998. Semiconductor nanocrystals as fluorescent biological labels. Science 281, 2013–2016.

Buha, J., Djerdj, I., Antonietti, M., Niederberger, M., 2007. Thermal transformation of metal oxide nanoparticles into nanocrystalline metal nitrides using cyanamide and urea as nitrogen source. Chem. Mater. 19, 3499–3505.

Busch, G., Junod, P., Morris, R.G., Muhiem, J., Stutius, W., 1964. Low-temperature specific heat measurements of EuSe and EuTe. Phys. Lett. 11, 9–10.

Catteral, R., Symons, M.C.R., 1965. Unstable intermediates. Part XXXI. Solvated electrons: solutions of europium in ammonia. J. Chem. Soc. 3763–3770.

Chen, W., Zhang, X., Huang, Y., 2000. Luminescence enhancement of EuS nanoclusters in zeolite. Appl. Phys. Lett. 76, 2328–2330.

Coe, S., Woo, W., Bawendi, M.G., Bulovic, V., 2000. Electroluminescence from single monolayers of nanocrystals in molecular organic devices. Nature 420, 800–803.

Costi, R., Saunders, A.E., Banin, U., 2010. Colloidal hybrid nanostructures: a new type of functional materials. Angew. Chem. Int. Ed. 49, 4878–4897.

Dloczik, L., Engelhardt, R., Ernst, K., Fiechter, S., Sieber, I., Könenkamp, R., 2001. Hexagonal nanotubes of ZnS by chemical conversion of monocrystalline ZnO columns. Appl. Phys. Lett. 78, 3687–3689.

Donegá, C.M., 2011. Synthesis and properties of colloidal heteronanocrystals. Chem. Soc. Rev. 40, 1512–1546.

Eastman, D.E., Holtzberg, F., Methfessel, S., 1969. Photoemission studies of the electronic structure of EuO, EuS, EuSe, and GdS. Phys. Rev. Lett. 23, 226–229.

Erwin, S.C., Zu, L., Haftel, M.I., Efros, A.L., Kennedy, T.A., Norris, D.J., 2005. Doping semiconductor nanocrystals. Nature 436, 91–94.

Fischer, P., Hälg, W., Yon, W., Wartburg, W.V., Schwob, P., Vogt, O., 1969. Neutron diffraction evidence for magnetic phase transition in Europium selenide. J. Phys. Condens. Mater. 9, 249–259.

Fujikawa, R., Baryshev, A.V., Kim, J., Uchida, H., Inoue, M., 2008. Contribution of the surface plasmon resonance to optical and magneto-optical properties of a Bi:YIG-Au nanostructure. J. Appl. Phys. 103, 07D301.

Fumagalli, P., Schimeisen, A., Gambio, R.J., 1996. Magneto-optic properties and exchange interaction of the macroscopic ferrimagnet $Co_{1-x-y}Tb_x(EuS)_y$. J. Appl. Phys. 79, 5929–5931.

Furdyna, J.K., 1988. Diluted magnetic semiconductors. J. Appl. Phys. 64, R29–R64.

Gaj, J.A., Ginter, J., Galazka, R.R., 1978. Exchange interaction of manganese $3d^5$ states with band electrons in $Cd_{1-x}MnxTe$. Phys. Status Solidi B 89, 655–662.

Gambino, R.J., Fumagalli, P., Ruf, R.R., McGuire, T.R., Bojarczuk, N., 1992. Magneto-optic spectra of EuS-Gd and EuS-Tb films. IEEE Trans. Magn. 28, 2973–2975.

Gao, L., Zhang, Q., Li, J., 2003. Preparation of ultrafine InN powder by the nitridation of $In_2O_3$ or $In(OH)_3$ and its thermal stability. J. Mater. Chem. 13, 154–158.

Garetz, B.A., Aber, J.E., Goddard, N.L., Young, R.G., Myerson, A.S., 1996. Nonphotochemical, polarization-dependent, laser-induced nucleation in supersaturated aqueous urea solutions. Phys. Rev. Lett. 77, 3475–3476.

Green, M., O'Brien, P., 1998. A novel synthesis of cadmium phosphide nanoparticles using the single-source precursor [MeCdPtBu$_2$]$_3$. Adv. Mater. 10, 527–528.

Greiner, J.H., Fan, G.J., 1966. Longitudinal magneto-optical Kerr effect in EuO and EuS. Appl. Phys. Lett. 9, 27–29.

Grier, D.G., 2003. A revolution in optical manipulation. Nature 424, 810–816.

Hao, X., Moodera, J.S., Meservey, R., 1990. Spin-filter effect of ferromagnetic europium sulfide tunnel barriers. Phys. Rev. B Condens. Matter 42, 8235–8243.

Hasegawa, Y., Thongchant, S., Wada, Y., Tanaka, H., Kawai, T., Sakata, T., Mori, H., Yanagida, S., 2002. Enhanced luminescence and photomagnetic properties of surface-modified EuO nanocrystals. Angew. Chem. Int. Ed. 41, 2073–2075.

Hasegawa, Y., Thongchant, S., Kataoka, T., Wada, Y., Yatsuhashi, T., Nakashima, N., Yanagida, S., 2003. EuO nanocrystal formation under ArF laser irradiation. Chem. Lett. 32, 708–709.

Hasegawa, Y., Afzaal, M., O'Brien, P., Wada, Y., Yanagida, S., 2005. A novel method for synthesizing EuS nanocrystals from a single-source precursor under white LED irradiation. Chem. Commun. 14, 242–243.

Hasegawa, Y., Wada, Y., Yanagida, S., 2006a. EPR spectra analysis of photo-magnetic properties of EuO nanocrystals. J. Alloy Compd. 408, 207–211.

Hasegawa, Y., Okada, Y., Kataoka, T., Sakata, T., Mori, H., Wada, Y., 2006b. Synthesis and photophysical properties of EuS nanoparticles from the thermal reduction of single source precursor. J. Phys. Chem. B 110, 9008–9011.

Hasegawa, Y., Adachi, T., Tanaka, A., Afzaal, M., O'Brien, P., Doi, T., Hinatsu, Y., Fujita, K., Tanaka, K., Kawai, T., 2008. Remarkable magneto-optical properties of europium selenide nanoparticles with wide energy gaps. J. Am. Chem. Soc. 130, 5710–5715.

Hasegawa, Y., Kumagai, M., Kawashima, A., Nakanishi, T., Fujita, K., Tanaka, K., Fushimi, K., 2012. First synthesis of EuS nanoparticle thin film with wide energy gap and giant magneto-optical efficiency on glass electrode. J. Phys. Chem. C 116, 19590–19596.

Hasegawa, Y., Maeda, M., Nakanishi, T., Doi, Y., Hinatsu, Y., Fujita, K., Tanaka, K., Koizumi, H., Fushimi, K., 2013. Effective optical Faraday rotations of semiconductor EuS nanocrystals with paramagnetic transition-metal ions. J. Am. Chem. Soc. 135, 2659–2666.

He, W., Somarajan, S., Koktysh, D.S., Dickerson, J.H., 2011. Superantiferromagnetic EuTe nanoparticles: room temperature colloidal synthesis, structural characterization, and magnetic properties. Nanoscale 3, 187–194.

He, W., Osaulski, M.F., Lin, J., Koktysh, D.S., McBride, J.R., Park, J.H., Dickerson, J.H., 2012. Remarkable optical and magnetic properties of ultra-thin europium oxysulfide nanorods. J. Mater. Chem. 22, 16728–16731.

Hosokawa, C., Yoshikawa, H., Masuhara, H., 2005. Cluster formation of nanoparticles in an optical trap studied by fluorescence correlation spectroscopy. Phys. Rev. E 72, 021408.

Hotta, J., Sasaki, K., Masuhara, H., 1996. A single droplet formation from swelled micelles by radiation pressure of a focused infrared laser beam. J. Am. Chem. Soc. 118, 11968–11969.

Hsu, K.H., Wu, J.H., Huang, Y.Y., Wang, L.Y., Lee, H.Y., Lin, J.G., 2005. Critical size effects on the magnetic resonance in $Fe_3O_4$ nanoparticle. J. Appl. Phys. 97, 114322–114324.

Hu, J., Bando, Y., Golberg, D., Liu, Q., 2003. Gallium nitride nanotubes by the conversion of gallium oxide nanotubes. Angew. Chem. Int. Ed. 42, 3493–3497.

Ito, S., Yoshikawa, H., Masuhara, H., 2002. Laser manipulation and fixation of single gold nanoparticles in solution at room temperature. Appl. Phys. Lett. 80, 482–484.

Izaki, M., Omi, T., 1997. Transparent zinc oxide films chemically prepared from aqueous solution. J. Electrochem. Soc. 144, L3–L5.

Jain, P.K., Xiao, Y., Walsworth, R., Cohen, A.E., 2009. Surface plasmon resonance enhanced magneto-optics (SuPREMO): Faraday rotation enhancement in gold-coated iron oxide nanocrystals. Nano Lett. 9, 1644–1650.

Jørgensen, C.K., Brinen, J.S., 1963. Far ultra-violet absorption spectra of cerium(III) and europium(III) aqua ions. Mol. Phys. 6, 629–631.

Jun, Y.W., Jung, Y.Y., Cheon, J.J., 2002. Architectural control of magnetic semiconductor nanocrystals. J. Am. Chem. Soc. 124, 615–619.

Jungwirth, T., Atkinson, W.A., Lee, B.H., MacDonald, A.H., 1999. Interlayer coupling in ferromagnetic semiconductor superlattices. Phys. Rev. B 59, 9818–9822.

Kaldis, E., Schoenes, J., Wachter, P., 1971. Magneto-optical properties of Gd-doped EuO crystals. AIP Conf. Proc. 5, 269–271.

Kar, S., Boncher, W.L., Olszewski, D., Dollahon, N., Ash, R., Stoll, S.L., 2010. Gadolinium doped europium sulfide. J. Am. Chem. Soc. 132, 13960–13962.

Kar, S., Dollahon, N.R., Stoll, S.L., 2011. Dye-coated europium monosulfide. J. Solid State Chem. 184, 1324–1327.

Kasuya, T., Yanase, A., 1968. Anomalous transport phenomena in Eu-chalcogenide alloys. Rev. Mod. Phys. 40, 684–696.

Kataoka, T., Tsukahara, Y., Hasegawa, Y., Wada, Y., 2005. Size-controlled synthesis of quantum-sized EuS nanoparticles and tuning of their Faraday rotation peak. Chem. Commun. (Camb.) 14, 6038–6040.

Katz, E., Willner, I., 2004. Integrated nanoparticle–biomolecule hybrid systems: synthesis, properties, and applications. Angew. Chem. Int. Ed. 43, 6042–6108.

Kawashima, A., Nakanishi, T., Fushimi, K., Hasegawa, Y., 2013a. EuS nano-assembles linked with photo-functional naphthalenedithiols. Mol. Cryst. Liq. Cryst. 579, 69–76.

Kawashima, A., Nakanishi, T., Shibayama, T., Watanabe, S., Fujita, K., Tanaka, K., Koizumi, H., Fushimi, K., Hasegawa, Y., 2013b. Enhanced magneto-optical properties of semiconductor

EuS nanocrystals assisted by surface plasmon resonance of gold nanoparticles. Chem. Eur. J. 19, 14438–14445.

Klimov, V.I., Mikhailovsky, A.A., Xu, S., Malko, A., Hollingsworth, J.A., Leatherdale, C.A., Eisler, H.A., Bawendi, M.G., 2000. Optical gain and stimulated emission in nanocrystal quantum. Science 290, 314–317.

Korgel, B.A., Fullam, S., Connolly, S., Fitzmaurice, D., 1998. Assembly and self-organization of silver nanocrystal superlattices: ordered "soft spheres". J. Phys. Chem. B 102, 8379–8388.

Kulakovich, O., Strekal, N., Yaroshevich, A., Maskevich, S., Gaponenko, S., Nabiev, I., Woggon, U., Artemyev, M., 2002. Enhanced luminescence of CdSe quantum dots on gold colloids. Nano Lett. 2, 1449–1452.

Kusaba, M., Nakashima, N., Kawamura, W., Izawa, Y., Yamanaka, C., 1992. Higher yield of photoreduction from $Eu^{3+}$ to $Eu^{2+}$ with shorter wavelength irradiation. Chem. Phys. Lett. 197, 136–140.

Lee, J., Govorov, A.O., Dulka, J., Kotov, N.A., 2004. Bioconjugates of CdTe nanowires and Au nanoparticles: plasmon-exciton interactions, luminescence enhancement, and collective effects. Nano Lett. 4, 2323–2330.

Li, Y., Zhang, Q., Nurmikko, A.V., Sun, S., 2005. Enhanced magnetooptical response in dumbbell-like Ag-$CoFe_2O_4$ nanoparticle pairs. Nano Lett. 5, 1689–1692.

Lisiecki, I., Parker, D., Salzemann, C., Pileni, M.P., 2007. Face-centered cubic supra-crystals and disordered three-dimensional assemblies of 7.5 nm cobalt nanocrystals: influence of the mesoscopic ordering on the magnetic properties. Chem. Mater. 19, 4030–4036.

Lokhande, C.D., Bhosale, C.H., 1997. Characterization of chemically converted sprayed $Bi_2O_3$ to $Bi_2S_3$ thin films. Mater. Chem. Phys. 49, 46–49.

MacGuire, T.R., Argyle, B.E., Shafer, M.W., Smart, J.S., 1963. Magnetic properties of some divalent europium compounds. J. Appl. Phys. 34, 1345–1346.

Manna, L., Scher, E.C., Alivisatos, A.P., 2000. Synthesis of soluble and processable rod-, arrow-, teardrop-, and tetrapod-shaped CdSe nanocrystals. J. Am. Chem. Soc. 122, 12700–12706.

Matthias, B.T., Bozorth, R.M., 1961. Ferromagnetic interaction in EuO. Phys. Rev. Lett. 7, 160–161.

Mauger, A., Escorner, M., Godart, C., Desfours, J.P., Achard, J., 1980. Magnetic properties of Gd doped EuO single crystals. J. Phys. Colloques 41 (C5), 263–265.

Mirkovic, T., Hines, M.A., Nair, P.S., Scholes, G.D., 2005. Single-source precursor route for the synthesis of EuS nanocrystals. Chem. Mater. 17, 3451–3456.

Mirkovic, T., Rossouw, D., Botton, G.A., Scholes, G.D., 2011. Broken band alignment in EuS-CdS nanoheterostructures. Chem. Mater. 23, 181–187.

Misawa, H., Koshioka, M., Sasaki, K., Kitamura, N., Masuhara, H., 1991. Three-dimensional optical trapping and laser ablation of a single polymer latex particle in water. J. Appl. Phys. 70, 3829.

Molnar, S., Kasuya, T., 1970. Comments on electronic transport in magnetic semiconductors. In: Proceedings of the Xth International Conference on the Physics of Semiconductors, p. 233.

Moon, G.D., Ko, S., Min, Y., Zeng, J., Xia, Y., Jeong, U., 2011. Chemical transformations of nanostructured materials. Nano Today 6, 186–203.

Moruzzi, V.L., Teaney, D.T., 1963. Specific heat of EuS. Solid State Commun. 1, 127–131.

Moruzzi, L.V., Teaney, D.T., Hoeven Jr., B.J.C., 1968. The specific heat of Gd doped EuS. Solid State Commun. 6, 461–464.

Nakanishi, T., Maeda, M., Kawashima, A., Fujita, K., Tanaka, K., Fushimi, K., Hasegawa, Y., 2013. Novel opto-magnetic silicate glass with semiconductor EuS nanocrystals. J. Alloys Compd. 562, 123–127.

Nakashima, T., Nakao, H., Tanaka, A., Hasegawa, Y., Kawai, T., 2012. Synthesis of PbS/EuS core/shell nanocrystals. Chem. Lett. 41, 412–414.

Nonoguchi, Y., Nakashima, T., Tanaka, A., Miyabayashi, K., Miyake, M., Kawai, T., 2011. Oligomerization of cadmium chalcogenide nanocrystals into CdTe-containing superlattice chains. Chem. Commun. 47, 11270–11272.

Norberg, N.S., Kittilstved, K.R., Amonette, J.E., Kukkadapu, R.K., Schwartz, D.A., Gamelin, D.R., 2004. Synthesis of colloidal $Mn^{2+}$:ZnO quantum dots and high-$T_C$ ferromagnetic nanocrystalline thin films. J. Am. Chem. Soc. 126, 9387.

Norris, D.J., Yao, N., Charnock, F.T., Kennedy, T.A., 2001. High-quality manganese-doped ZnSe nanocrystals. Nano Lett. 1, 3–7.

Nunes, W.C., Cebollada, F., Knobel, M., Zanchet, D., 2006. Effects of dipolar interactions on the magnetic properties of $\gamma$-$Fe_2O_3$ nanoparticles in the blocked state. J. Appl. Phys. 99, Art. Nr. 08N705.

Ohno, H., Shen, A., Matsukura, F., Oiwa, A., Endo, A., Katsumoto, S., Iye, Y., 1996. (Ga, Mn)As: a new diluted magnetic semiconductor based on GaAs. Appl. Phys. Lett. 69, 363–365.

Ohno, Y., Young, D.K., Beschten, B., Matsukura, F., Ohno, H., Awschalom, D.D., 1999. Electrical spin injection in a ferromagnetic semiconductor heterostructure. Nature 402, 790–793.

Ozaki, S., Kura, H., Maki, H., Sato, T., 2009. Manipulation of Faraday rotation in Bi-substituted yttrium-iron garnet film using electromagnetic interaction between Au nanoparticles in two-dimensional array. J. Appl. Phys. 106, 123530–123531.

Parker, D., Lisiecki, I., Salzemann, C., Pileni, M.P., 2007. Emergence of new collective properties of cobalt nanocrystals ordered in fcc supracrystals: II, magnetic investigation. J. Phys. Chem. C 111, 12632–12638.

Paulopoulos, P., Lewitz, B., Straub, A., Pappas, S.D., Droulias, S.A., Baskoutas, S., Fumagalli, P., 2012. Band-gap tuning at the strong quantum confinement regime in magnetic semiconductor EuS thin films. Appl. Phys. Lett. 100, Art. Nr. 211910.

Pauzauskie, P.J., Radenovic, A., Trepagnier, E., Shroff, H., Yang, P., Liphordt, J., 2006. Optical trapping and integration of semiconductor nanowire assemblies in water. Nat. Mater. 5, 97–101.

Pereira, A.S., Rauwel, P., Reis, M.S., Silva, N.J.O., Barros-Timmonsa, A., Trindade, T., 2008. Polymer encapsulation effects on the magnetism of EuS nanocrystals. J. Mater. Chem. 18, 4572–4578.

Pickett, N.L., O'Brien, P., 2001. Syntheses of semiconductor nanoparticles using single-molecular precursors. Chem. Rec. 1, 467–479.

Redigolo, M.L., Koktysh, D.S., Rosenthal, S.J., Dickerson, J.H., 2007. Physical properties of quantum-confined europium sulfide nanocrystals. Phys. Status Solidi C 4, 406–408.

Regulacio, M.D., Tomson, N., Stoll, S.L., 2005. Dithiocarbamate precursors for rare-earth sulfides. Chem. Mater. 17, 3114–3121.

Revaprasadu, N., Malik, M.A., O'Brien, P., Wakefield, G., 1999. A simple route to synthesize nanodimensional CdSe–CdS core-shell structures from single molecule precursors. Chem. Commun. 1573–1574.

Rumpf, K., Granitzer, P., Kellner, W., Kirchschlager, R., Janecek, S., Pascher, H., Krenn, H., 2004. SQUID magnetometry and magneto-optics of epitaxial EuSe. Acta Phys. Pol. A 105, 621–629.

Sachan, M., Walrath, N.D., Majetich, S.A., Krycka, K., Kao, C.D., 2006. Interaction effects within Langmuir layers and three-dimensional arrays of $\varepsilon$-Co nanoparticles. J. Appl. Phys. 99, 08C302.

Samokhvalov, A.A., Gunichev, A.F., Gizhevskii, B.A., Loshkareva, N.N., Chebotaev, N.M., Viglin, N.A., 1978. Nonstoichiometric EuO films with increased curie-temperature. Fiz. Tverd. Tela 20, 897.

Sasaki, K., Koshioka, M., Misawa, H., Kitamura, N., Masuhara, H., 1991. Pattern formation and flow control of fine particles by laser-scanning micromanipulation. Opt. Lett. 16, 1463–1465.

Scholes, G.D., 2008. Controlling the optical properties of inorganic nanoparticles. Adv. Funct. Mater. 18, 1157–1172.

Schwartz, D.A., Norberg, N.S., Nguyen, Q.P., Parker, J.M., Gamelin, D.R., 2003. Magnetic quantum dots: synthesis, spectroscopy, and magnetism of $Co^{2+}$- and $Ni^{2+}$-doped ZnO nanocrystals. J. Am. Chem. Soc. 125, 13205–13218.

Selinsky, R.S., Han, J.H., Morales Perez, E.A., Guzei, I.A., Jin, S., 2010. Synthesis and magnetic properties of Gd doped EuS nanocrystals with enhanced Curie temperatures. J. Am. Chem. Soc. 132, 15997–16005.

Shafer, M.W., 1965. Preparation and crystal chemistry of divalent europium compounds. J. Appl. Phys. 36, 1145.

Snoeck, E., Gatel, C., Lacroix, L.M., Blon, T., Lachaize, S., Carrey, J., Respaud, M., Chaudret, B., 2008. Magnetic configurations of 30 nm iron nanocubes studied by electron holography. Nano Lett. 8, 4293–4298.

Son, D.H., Hughes, S.M., Yin, Y., Alivisatos, A.P., 2004. Cation exchange reactions in ionic nanocrystals. Science 306, 1009–1012.

Story, T., 2003. Semiconductor EuS–PbS ferromagnetic multilayers. Phys. Status Solidi B 236, 310–317.

Stowell, C.A., Wiacek, R.J., Saunders, A.E., Korgel, B.A., 2003. Synthesis and characterization of dilute magnetic semiconductor manganese-doped indium arsenide nanocrystals. Nano Lett. 3, 1441–1447.

Sugiura, T., Okada, T., 1998. Near-field scanning optical microscope with an optically trapped metallic Rayleigh particle. Proc. SPIE 3260, 4.

Sugiura, T., Okada, T., Inouye, Y., Nakamura, O., Kawata, S., 1997. Gold-bead scanning near-field optical microscope with laser-force position control. Opt. Lett. 22, 1663–1665.

Suits, J.C., Argyle, B.E., 1965. Paramagnetic Faraday rotation of EuSe. J. Appl. Phys. 36, 1251–1252.

Suits, J.C., Argyle, B.E., Freiser, M.J., 1966. Magneto-optical properties of materials containing divalent europium. J. Appl. Phys. 37, 1391–1397.

Svoboda, K., Block, S.M., 1994. Optical trapping of metallic Rayleigh particles. Opt. Lett. 19, 930–932.

Takahashi, M., Kasuya, T., 1983. Effect of electron–phonon interaction in the magnetic polaron. J. Physical Soc. Japan 52, 3138–3143.

Talapin, D.V., Murray, C.V., 2005. PbSe nanocrystal solids for n- and p-channel thin film field-effect transistors. Science 310, 86–89.

Tanaka, K., Fujita, K., Soga, N., Qiu, J., Hirao, K., 1997. Faraday effect of sodium borate glasses containing divalent europium ions. J. Appl. Phys. 82, 840–843.

Tanaka, A., Sugiura, T., Kawai, T., Hasegawa, Y., 2007. Three-dimensional optical trapping and arrangements of magnetic semiconductor EuS nanoaggregations. Jpn. J. Appl. Phys. 11, L259–L261.

Tanaka, A., Adachi, T., Hasegawa, Y., Kawai, T., 2009a. Crystal growth of nanoscaled europium selenide having characteristic crystal shapes. J. Alloy Compd. 488, 538–540.

Tanaka, A., Hasegawa, Y., Kamikubo, H., Kataoka, M., Kawai, T., 2009b. Self-aggregation of magnetic semiconductor EuS nanocrystals. Thin Solid Films 518, 870–872.

Tanaka, A., Kamikubo, H., Doi, Y., Hinatsu, Y., Kataoka, M., Kawai, T., Hasegawa, Y., 2010. Self-assembly and enhanced magnetic properties of three-dimensional superlattice structures composed of cube-shaped EuS nanocrystals. Chem. Mater. 22, 1776–1781.

Tanaka, A., Kamikubo, H., Kataoka, M., Hasegawa, Y., Kawai, T., 2011. Size-controlled aggregation of cube-shaped EuS nanocrystals with magneto-optic properties in solution phase. Langmuir 27, 104–108.

Tang, J., O'Connor, C.E., Feng, L., 1998. Magnetotransport and antiferromagnetic coupling in nanocomposites EuS-Co. J. Alloys Compd. 275, 606–610.

Teranishi, T., Saruyama, M., Kanehara, M., 2009. Seed-mediated synthesis of metal sulfide patchy nanoparticles. Nanoscale 1, 225–228.

Thongchant, S., Hasegawa, Y., Wada, Y., Yanagida, S., 2001. Spindle-type EuO nanocrystals and their magnetic properties. Chem. Lett. 30, 1274–1275.

Thongchant, S., Hasegawa, Y., Wada, Y., Yanagida, S., 2003a. Liquid phase synthesis of EuS nanocrystals and their physical properties. J. Phys. Chem. B 107, 2193–2196.

Thongchant, S., Hasegawa, Y., Wada, Y., Yanagida, S., 2003b. Size selective synthesis of surface-modified EuS nanocrystals using pyridine and their physical properties. Chem. Lett. 32, 706–707.

Thongchant, S., Hasegawa, Y., Tanaka, K., Fujita, K., Hirao, K., Wada, Y., Yanagida, S., 2003c. First observation of Faraday effect of EuS nanocrystals in polymer thin films. Jpn. J. Appl. Phys. 42, L876–L878.

Thongchant, S., Katagiri, S., Hasegawa, Y., Wada, Y., Watase, S., Nakamoto, M., Sakata, T., Mori, H., Yanagida, S., 2004. Preparation and physical properties of EuO nanocrystals using Eu(II)-exchanged zeolite X as a precursor. Bull. Chem. Soc. Jpn. 77, 807–812.

Tian, Y., Tatsuma, T., 2005. Mechanisms and applications of plasmon-induced charge separation at $TiO_2$ films loaded with gold nanoparticles. J. Am. Chem. Soc. 127, 7632–7637.

Tonomura, A., Matsuda, T., Endo, J., Arii, T., Mihama, K., 1980. Direct observation of fine structure of magnetic domain walls by electron holography. Phys. Rev. Lett. 44, 1430–1432.

Torrance, J.B., Shafer, M.W., McGuire, T.H., 1972. Bound magnetic polarons and the insulator-metal transition in EuO. Phys. Rev. Lett. 29, 1168–1171.

Umehara, M., 1995. Photoinduced localized magnetic polaron and luminescence in Eu chalcogenides, especially in EuTe. Phys. Rev. B Condens. Matter 52, 8140–8143.

Urban, J.J., Talapin, D.V., Shevchenko, E.V., Murray, C.B., 2006. Self-assembly of PbTe quantum dots into nanocrystal superlattices and glassy films. J. Am. Chem. Soc. 128, 3248–3255.

Vasquez, Y., Henkes, A.E., Chris Bauer, J., Schaak, R.E., 2008. Nanocrystal conversion chemistry: a unified and materials-general strategy for the template-based synthesis of nanocrystalline solids. J. Solid State Chem. 181, 1509–1523.

Wachter, P., 1972. CRC Critical Reviews in Solid State Science. North-Holland Publishing Company, pp.189–241.

Wachter, P., 1979. Europium chalcogenides: EuO, EuS, EuSe, and EuTe. In: Gschneidner Jr., K.A., Eyring, L. (Eds.), Handbook on the Physics and Chemistry of Rare Earth, second ed. vol. 2. 509–574, Chapter 19.

Wakefield, G., Keron, H.A., Dobson, P.J., Hutchison, J.L., 1999. Synthesis and properties of sub-50-nm europium oxide nanoparticles. J. Colloid Interface Sci. 215, 179–182.

Wang, Y., Herron, N., Moller, K., Bein, T., 1991. Three-dimensionally confined diluted magnetic semiconductor clusters: $Zn_{1-x}Mn_xS$. Solid State Commun. 77, 33–38.

Wang, L., Clavero, C.S., Huba, Z., Carroll, K.J., Carpenter, E.E., Gu, D., Lukaszew, R.A., 2014. Plasmonics and enhanced magneto-optics in core-shell Co-Ag nanoparticles. Nano Lett. 11, 1237–1240.

Warf, J.C., Korst, W.L., 1956. Solutions of europium and ytterbium metals in liquid ammonia. J. Phys. Chem. 60, 1590–1591.

Xavier, R.M., 1967. On the magnetic properties of divalent europium compounds. Phys. Lett. A 25, 244–245.

Yan, C., Xue, D., 2006. Conversion of ZnO nanorod arrays into ZnO/ZnS nanocable and ZnS nanotube arrays via an in situ chemistry strategy. J. Phys. Chem. B 110, 25850–25855.

Yoshikawa, H., Matsui, T., Masuhara, H., 2004. Reversible assembly of gold nanoparticles confined in an optical microcage. Phys. Rev. E 70, 061406.

Zayats, A.V., Smolyaninov, I.I., Maradudin, A.A., 2005. Nano-optics of surface plasmon polaritons. Phys. Rep. 408, 131–314.

Zhao, F., Gao, S., 2008. Pyrolysis of single molecular precursor for monodisperse lanthanide sulfide/oxysulfide nanocrystals. J. Mater. Chem. 18, 949–953.

Zhao, F., Sun, H.L., Gao, S., Su, G., 2005. Magnetic properties of EuS nanoparticles synthesized by thermal decomposition of molecular precursors. J. Mater. Chem. 15, 4209–4214.

Zhao, F., Zhang, M., Gao, S., 2006a. Monodisperse lanthanide oxysulfide nanocrystals. J. Am. Chem. Soc. 128, 11758–11759.

Zhao, F., Sun, H.L., Su, G., Gao, S., 2006b. Synthesis and size-dependent magnetic properties of monodisperse EuS nanocrystals. Small 2, 244–248.

Zhao, Y., Rabouw, F.T., Puffelen, T., Walree, C.A., Gamelin, D.R., Donega, C.M., Meijerink, A., 2014. Lanthanide-doped CaS and SrS luminescent nanocrystals: a single-source precursor approach for doping. J. Am. Chem. Soc. 136, 16533–16543.

Chapter 271

# Hybrid Materials of the f-Elements Part I: The Lanthanides

**Korey P. Carter and Christopher L. Cahill**

*Department of Chemistry, The George Washington University, Washington, District of Columbia, USA*

## Chapter Outline

## 1 INTRODUCTION

The study of lanthanide-containing hybrid materials has garnered significant interest over the past decade due to their rich structural diversity and distinctive optical and magnetic properties. Hybrid materials may be broadly defined as consisting of both organic and inorganic moieties blended on the molecular scale (Kickelbick, 2007). Hybrid materials are found in a number of different systems that span a wide array of material including highly ordered coordination polymers (CPs), amorphous sol–gel compounds, and materials with or without interactions between the inorganic and organic units. Ln hybrids in particular have presented a range of materials meeting this definition including doped polymers, molecular species, and the rapidly evolving field of CPs and metal–organic frameworks (MOFs). For the purpose of this review, we will focus on crystalline materials only, that is, compounds that crystallize as periodic, ordered arrays for which X-ray crystal structures have been reported. Considering the rate at which these materials continue to appear in

the literature, a comprehensive review would be nearly impossible. Rather, we will highlight representative materials that exemplify some of the key structural features of these classes of materials. Lanthanide CPs and MOFs were previously addressed in this forum in 2004 (Guillou and Daiguebonne, 2004), so we will focus on compounds synthesized in the last 10 years while highlighting earlier works where appropriate. We will also primarily highlight materials made via hydro/solvothermal methods (Rabenau, 1985; Sheets et al., 2006), as it is this synthesis technique that has yielded most of the known lanthanide CPs and MOFs. We will unfortunately not treat cluster materials, defined by Cotton (1966) as a "finite group of metal atoms held together mainly or at least to a significant extent, by bonds directly between metal atoms, even though some non-metal atoms may also be intimately associated with the cluster," as they have been reviewed in this forum by Zheng (2010) and in the literature by Powell and collaborators (Kostakis et al., 2010; Sessoli and Powell, 2009) and others (Andrews et al., 2013; Kremer et al., 2005).

The first group of materials to be discussed—CPs/MOFs can be more clearly defined as assemblies of Ln(III) metal centers (polynuclear or otherwise) polymerized through organic linker molecules to result in diverse topologies of higher dimensionality, making them particularly attractive for applications including sensing (cation, anion, or molecular) (Chen et al., 2008; Cui et al., 2014; Guo et al., 2011), gas storage (He et al., 2013b; Roy et al., 2014; Xue et al., 2013), heterogeneous catalysis (Corma et al., 2010; Gándara et al., 2008; Ren et al., 2011; Vilela et al., 2013), magnetism (Black et al., 2009; Tian et al., 2013; Xu et al., 2013), etc. At this point, we should comment on the distinction between a CP and a MOF. A MOF has been defined as framework-like material displaying permanent porosity by the International Union of Pure and Applied Chemistry (IUPAC; Batten et al., 2013), while a CP refers more generally to extended structures (in one, two, or three dimensions) that continuously extend through coordinative bonds (Batten et al., 2012). Readers may note the overuse of the MOF distinction throughout the literature, as well as some inconsistencies in light of the recent IUPAC definition. We have been guilty of this ourselves and going forward in this contribution, most polymeric species will be CPs, strictly speaking.

CPs and MOFs with d-block metal compositions have been studied and reviewed comprehensively (Devic and Serre, 2014; James, 2003; Janiak, 2003; Kuppler et al., 2009; Li et al., 2013b; Stock and Biswas, 2011; Tranchemontagne et al., 2009; Wang et al., 2013a). One may argue that the chemistry and applications of d-block materials are better developed, perhaps due to a propensity for formation of true MOFs and therefore gas storage/separation and catalytic applications. As such, we point the reader to some of many excellent reviews in this arena, particularly the early pioneering work of Robson and colleagues (Abrahams et al., 1994; Hoskins and Robson, 1989, 1990) that highlights the structural and topological perspectives of these materials. Turning to polymeric materials with lanthanide compositions,

however, a number of recent reviews by Allendorf (Allendorf et al., 2009), Chen (Cui et al., 2012), Almeida Paz (Almeida Paz et al., 2012; Rocha et al., 2011), Müller-Buschbaum (Heine and Müller-Buschbaum, 2013; Meyer et al., 2014), and Bünzli (Bünzli, 2014) as well as the earlier work of Férey (Devic et al., 2005; Férey, 2001), Yaghi and coworkers (Eddaoudi et al., 2001; Ockwig et al., 2005; Reineke et al., 1999; Rosi et al., 2005), Chen (Ye et al., 2005), and our group (De Lill and Cahill, 2008) have captured the "state of the science" with respect to more Ln(III) centric criteria—namely coordination chemistry preferences and luminescent and magnetic properties. In light of these publications, one may ask (fairly): what will be the contribution of this chapter? This will be an admittedly selfish presentation where we utilize the evolution of both materials and mindset within our own group to provide context and a path forward. Presented will be some early examples of materials from our group that served as inspiration for more recent developments. Moreover, we will support our sentiments with examples from other groups that highlight synthetic or structural consistencies. Finally, we note that our own efforts have proceeded (somewhat) in contrast to the evolution of lanthanide chemistry in general. Historically speaking, development of the coordination chemistry of molecular species has preceded efforts targeting polymeric compounds. As we will present, our group began by exploring CPs, yet concluded that there were some challenges regarding control over $Ln^{3+}$ nuclearity in hydrothermally synthesized systems, and that these were perhaps better addressed with some insight from the molecular community. This, coupled with an emergence of the targeted use of noncovalent interactions in crystal engineering (e.g., halogen bonding), has provided a forum for the design of molecular hybrid materials with tunable structural motifs and properties. As such, we present a pathway from polymeric lanthanide hybrids with an overall focus on global topology and influence thereof to an emphasis on controlling the first coordination sphere and directed assembly of molecular species.

## 2 Ln HYBRID MATERIALS

Bonding in lanthanide materials is not directly analogous to that of main group or transition metals and the unique nature of the $Ln^{3+}$ ions is one main reason that lanthanide materials have proven to be a rich topic of study. The 4f orbitals of the lanthanides are shielded from external perturbations by the 5s and 5p orbitals and thus the interactions of the 4f orbitals with ligand orbitals are minimal. This results in bonds (in $Ln^{3+}$ materials) that are only weakly covalent and stereochemistry that is directed by ligand sterics as ligand-field effects are minimal (ligand-field effects for the $Ln^{3+}$ ions are ca. 6 kJ/mol compared to transition metals ca. 120–360 kJ/mol) (Bünzli, 2014). The first coordination sphere of the lanthanide metal centers is spherical in geometry and with little direction provided by anything other than ligand sterics, large

coordination numbers (8–12) are common and the coordination sphere is often completed by binding small molecules or anions (e.g., $H_2O$, $Cl^-$, $OH^-$; Piguet and Bünzli, 1999). Lanthanide cations are considered hard acids and show clear preference for hard bases (i.e., carboxylates; Pearson, 1963, 1990) and these pairings generate strong ionic bonds.

We will first look at the extensive family of lanthanide carboxylate materials due to the known oxophilicity of the $Ln^{3+}$ ions (Chesman et al., 2007). The literature is rich in Ln-carboxylate CPs and MOFs and whereas these materials are limited in their thermal stability as at temperatures $>500\,°C$, they are prone to decomposition (Müller-Buschbaum et al., 2007; compared to say Ln-imidazole CPs), the synthesis of these materials is much more accessible as it can be done via hydro/solvothermal synthesis or at ambient conditions. Overall, these materials can be split into two groups: (1) those that feature aliphatic linkers and (2) those that feature aromatic linkers and we begin with a look into the former. $Ln^{3+}$-aliphatic carboxylate materials are arguably one of the richest systems studied in recent years. For the first part of our discussion (on CPs), we look to GWMOF-1 (Borkowski and Cahill, 2004b; a Nd-adipate three-dimensional (3D) framework) as a material that illustrates many of the structural aspects we intend to highlight and the description of this material will be used as the foundation for further exploration of the rich area of materials that are lanthanide CPs. We note that this is an example on our part of describing a material as a MOF when it only meets the requirements of a CP, yet we will not attempt repair the nomenclature in this review for consistency with the literature.

## 2.1 Ln-O Hybrid Materials: Aliphatic Linkers

GWMOF-1, $[Nd_2(C_6H_8O_4)_3(H_2O)_2]$, is composed of edge-shared $NdO_9$ polyhedra that run along the [100] direction that are further linked by adipic acid chains in the [010] and [001] directions to form a 3D framework (Fig. 1). Around each metal center are nine oxygen atoms, eight from three crystallographically unique adipic acid ligands, and one bound water molecule, which form an overall $NdO_9$ polyhedra. Adipic acid chains in GWMOF-1 coordinate to the $Nd^{3+}$ centers in two different ways: either chelating bridging or a combination of chelating bridging and monodentate coordination (Scheme 1). A polyhedral chain of edge-sharing $NdO_9$ polyhedra propagates in the [100] direction via a series of M–O–M linkages in GWMOF-1, and this result demonstrates that the completion of the lanthanide coordination sphere requires both edge sharing and decoration via solvent molecules.

These results warrant a further discussion of metal cation hydrolysis before proceeding. In the hydrothermal synthesis of lanthanide CPs, 'hydrolysis' in the strictest sense is usually not occurring. By definition, metal-ion hydrolysis involves the formation of a metal–water complex and
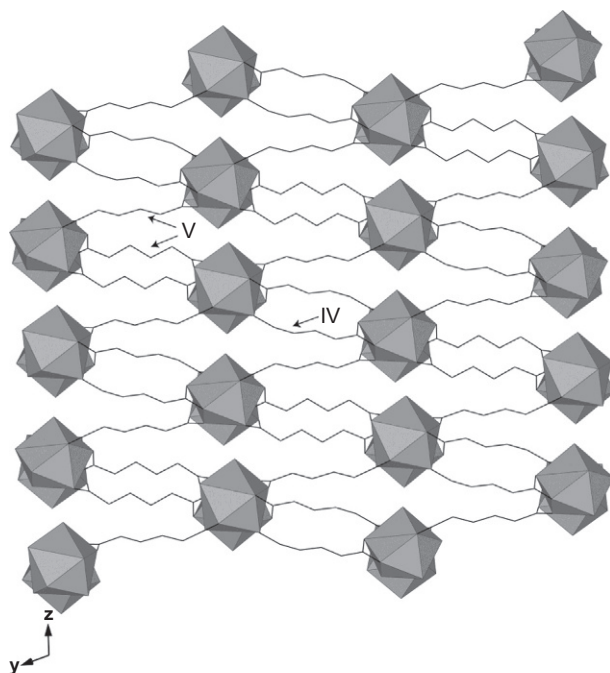
**FIGURE 1**  Polyhedral representation of GWMOF-1. Adipic acid molecules are labeled with their connectivity mode consistent with Scheme 1. Gray polyhedra represent neodymium metal centers, whereas black lines are adipate linkers. *Reproduced with permission from Borkowski and Cahill (2004b). Copyright Elsevier 2004.*
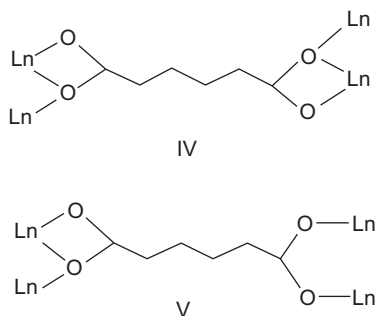


**SCHEME 1**  Coordination modes of adipic acid molecules in GWMOF-1. Labels IV and V are consistent with nomenclature of Duan et al. (2004b). *Reproduced with permission from Borkowski and Cahill (2004b). Copyright Elsevier 2004.*

the subsequent deprotonation of bound water molecules to promote hydroxo-containing polynuclear species as shown in Eq. (1).

$$\left[M(OH_2)_m\right]^{n+} \rightleftharpoons \left[M(OH_2)_{m-h}(OH)_h\right]^{(n-h)+} + hH^+ \tag{1}$$
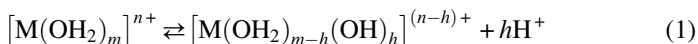
The degree of cation hydrolysis ($h$) in Eq. (1) is principally determined by the cation charge ($n$) to radius ratio and is of course a function of concentration, temperature, pH, etc. Once formed, hydrolyzed polynuclear metal complexes can condense to result in secondary building units (SBUs) in the crystalline solid state. Ln(III) ions exhibit this behavior above pH 6 as shown in Eq. (2) (Baes and Mesmer, 1976), yet complex formation with organic ligands competes with hydrolysis to give rise to either polynuclear SBUs or polynuclear cluster species as recently reviewed in this forum by Zheng (2010). These cluster species often utilize either olation or oxolation pathways to form hydroxo- and oxo-bridges, which are rare in lanthanide hybrid materials, although they are more common in actinide hybrid materials where hydrolysis often occurs at lower pH values (Knope and Soderholm, 2013).

$$Ln^{3+} + H_2O \rightleftharpoons Ln(OH)^{2+} + H^+ \tag{2}$$
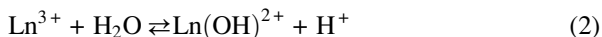
Turning to hydrothermal synthesis of Ln(III) bearing CPs, hydrolysis as described above may contribute to metal-ion speciation and observed building units, yet as we will demonstrate there are likely more complex mechanisms, such as ligand- and crystal-packing influences, at play in the promotion of polynuclear SBUs. Examples of these polynuclear building units include the edge-sharing NdO$_9$ polyhedra of GWMOF-1 and in fact, we will demonstrate that within Ln-aliphatic hybrid materials edge-sharing hydrated polyhedra are the norm, a trend which also continues (for the most part) when we transition to aromatic linkers. This structural motif, edge-sharing LnO$_n$ polyhedra that propagate via M–O–M linkages, exemplifies the general philosophy of CP and MOF construction, which is to assemble metal centers (inorganic building units) into extended architectures through the use of multitopic organic linkers (Cahill et al., 2007).

Another early example of an Ln-MOF from our group featuring the aliphatic carboxylate adipic acid is GWMOF-2: (Borkowski and Cahill, 2004b) [Nd$_2$(C$_6$H$_8$O$_4$)$_3$(H$_2$O)$_2$]·H$_2$O, a material very similar to GWMOF-1 with differences in adipic acid conformation leading to a change in overall topology from GWMOF-1 (see Fig. 2 for a complete depiction of aliphatic linkers). Once again, each Nd(III) center is bound to nine oxygen atoms, one bound water molecule, and eight from adipate anions. The Nd(III) centers polymerize to form chains along the [010], which are cross-linked to again form an overall 3D structure. More recently, Dalai and colleagues (Chowdhuri et al., 2013) have extensively reviewed the topological aspects of several lanthanide-adipate compounds and found that SBUs in this class of materials encompass the one-dimensional (1D) chains seen in GWMOF-1

Oxalic acid

Succinic acid

Adipic acid

Suberic acid

Sebacic acid
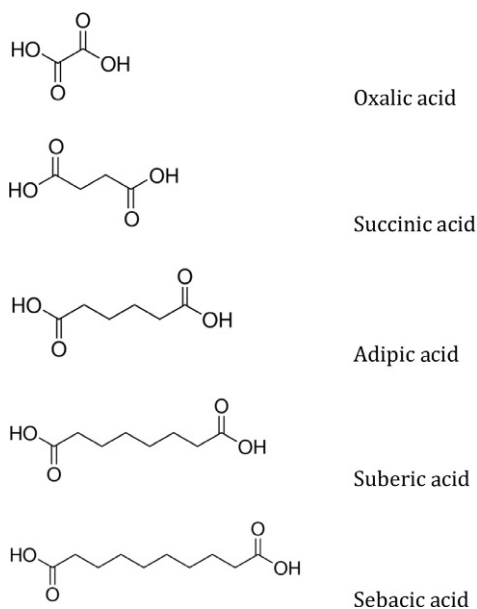
**FIGURE 2** Pictorial representations of the linkers used in the aliphatic-based CPs described in Section 2.1.

(and GWMOF-2), dimers, and two-dimensional (2D) layers of hydrated Ln polyhedra (Fig. 3). A closer look at these SBUs evokes two additional comments: one is that coordinated water molecules seem to fill out the coordination spheres of the larger Ln ions. Interestingly, we do not see adipate species reported for Ln ions smaller than $Er^{3+}$ and therefore hesitate to comment further as to the role of bound water molecules in influencing coordination spheres. Perhaps more interesting, however, is that the chains themselves are oligomerized through varying combinations of bridging carboxylate anions. In other words, there are no hydroxide groups present in the edge sharing of LnO polyhedra.

Following the work that yielded GWMOF-1 and -2, our group continued our exploration of the Ln-adipate system and the first follow-up result was GWMOF-3 ($[Pr_2(C_6H_8O_4)_3(H_2O)_4]\cdot(C_6H_8O_4)\cdot4H_2O$ (De Lill et al., 2005b). The $Ce^{3+}$ analogue of GWMOF-3 had been produced previously via sol–gel synthesis (Sun et al., 2002), yet the potential of this material remained mostly unrealized. A 3D framework made up of 1D chains of $PrO_{10}$ polyhedra that propagate along the [100] direction that are then cross-linked by adipic acid backbones in the [001] and [010] directions, GWMOF-3 shares many structural similarities with both GWMOF-1 and -2 (Fig. 4). The difference between GWMOF-3 and our two earlier results can be found in the channels of the GWMOF-3 framework where there are two water molecules and an intact,
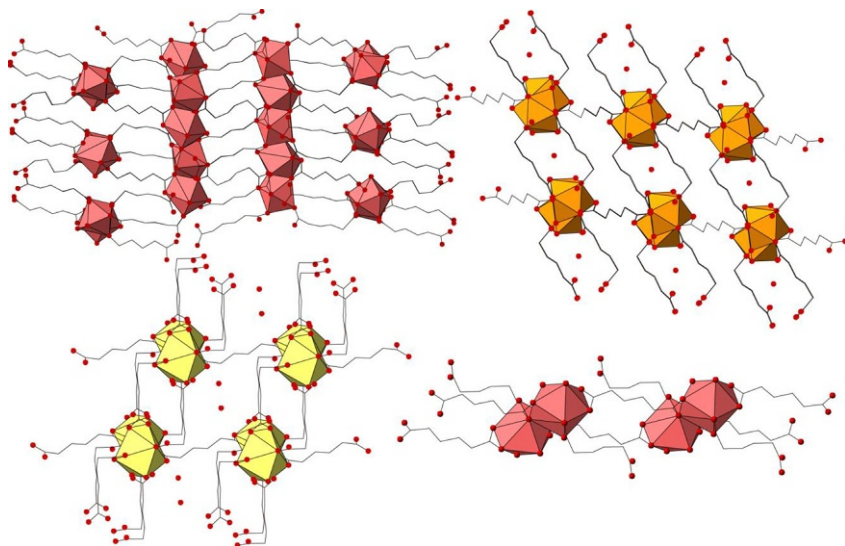
**FIGURE 3** Polyhedral representations highlighting the diversity of Ln-adipate species as delineated by Chowdhuri et al. (2013). Clockwise from top left: 3D structure assembled from two independent 1D Eu-O chains, 3D network composed of 1D chains of $Nd^{3+}$ M–O–M linkages with lattice water molecules included, 2D layer of linked $Eu^{3+}$ dimers, and layered 3D structure of 1D Ce-O chains with lattice water molecules included. Red (gray in the print version) polyhedra represent $Eu^{3+}$ metal centers, whereas orange (light gray in the print version) represent $Nd^{3+}$, and yellow (white in the print version) represent $Ce^{3+}$ metal centers, respectively. Red (dark gray in the print version) spheres represent oxygen atoms and black lines are adipate linkers.
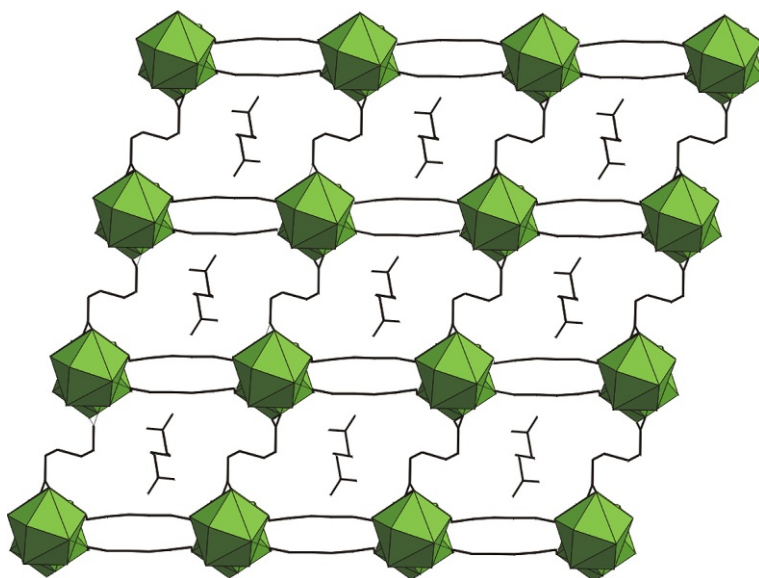


**FIGURE 4** Extended framework structure of GWMOF-3 viewed down the [100] direction. Green (gray in the print version) polyhedra represent $Pr^{3+}$ metal centers, whereas black lines represent adipic acid ligands and guest molecules. *Reproduced with permission from De Lill et al. (2005b). Copyright 2005, American Chemical Society.*

neutral, adipic acid molecule. The protonated adipic acid molecule features bond lengths and angles that are consistent with those in pure adipic acid (Thalladi et al., 2000), yet are markedly kinked as a result of rotation around the C11—C12 bond, presumably as a result of being confined to the channel region. The formation of the GWMOF-3 framework around the adipic acid molecules suggested that these free organic species may be acting as a structure-directing agent and served as the direct inspiration for the GWMOF-6 family of materials that is to be discussed in the following paragraphs.

GWMOF-6, $[Pr_2(C_6H_8O_4)_3(H_2O)_2]\cdot(C_{10}H_8N_2)$, features many of the structural motifs seen in the GWMOF materials discussed thus far, including edge-sharing $PrO_9$ polyhedra that form a 1D chain of M–O–M linkages that are further cross-linked by adipic acid chains to form an overall 3D framework. Design principles are usually retroactively applied to a material when attempting to explain observed structural features (including in GWMOF-3), yet GWMOF-6 marks our first effort to design a material *a priori*. Utilizing the hard–soft acid–base preferences (Pearson, 1963, 1990) of $Ln^{3+}$ cations, 4,4′-bipyridine was selected as a template molecule with the expectation that it would not coordinate to the $Pr^{3+}$ metal centers and would instead remain neutral in the channels and interact with the framework via hydrogen-bonding interactions. A look at GWMOF-6 (Fig. 5) reveals channels which host neutral 4,4′-bipyridine molecules that are interacting with the neutral Pr-adipate framework via O–H···N hydrogen-bonding interactions. These 4,4′-bipyridine molecules act as templating molecules, as anticipated, which direct the formation of the Pr-adipate framework around them.

The concept of templating originates in the zeolite field and has been categorized comprehensively by Davis and Lobo (1992). They define templating in a framework material as "the phenomenon occurring during … the nucleating process whereby the organic species organizes … polyhedra into a geometric topology around itself and thus provides the initial building blocks for a particular structure." Kitagawa and Tanaka have more recently expanded the discussion of templating in MOFs by describing two types of template effects that can take place, either primary or secondary (Tanaka and Kitagawa, 2008). The primary template effect occurs during the synthesis process when an organic guest molecule is self-included into a host framework by noncovalent interactions functioning as placeholder to prevent interpenetration of the framework. The secondary template effect is a dynamic process that only occurs when an appropriate guess molecule acts as a template and induces a reversible phase transformation. In GWMOF-6, 4,4′-bipyridine was chosen and likely operates via the primary template effect. The $Pr^{3+}$ cations in GWMOF-6 coordinate to the adipic acid linkers which allow the 4,4′-bipyridine molecules to remain neutral and uncoordinated (De Lill et al., 2005b). The rigid 4,4′-bipyridine is approximately the same length as an adipic acid chain and the nitrogen atoms at the 4 and 4′-positions hydrogen bond to the coordinated water molecules on the $Pr^{3+}$ cations.
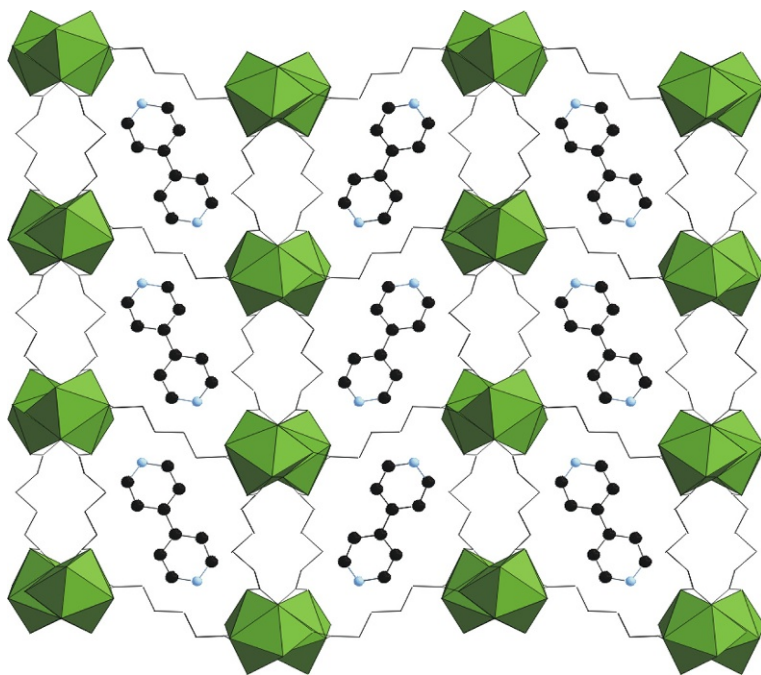
**FIGURE 5** Extended framework structure of GWMOF-6 viewed down the [010] direction. Similar to Fig. 4, green (gray in the print version) polyhedra represent $Pr^{3+}$ metal centers and black lines represent adipic acid ligands. The ball-and-stick figures represent 4,4′-bipyridine (black spheres are carbon and blue (light gray in the print version) spheres are nitrogen). *Reproduced with permission from De Lill et al. (2005b). Copyright 2005, American Chemical Society.*

Templating of a lanthanide MOF as shown in GWMOF-6 is an idea that in our opinion remains underexplored in the lanthanide CP and MOF literature. Further work from our group explored templating with 1,2-bis(4-pyridyl)propane acting as a template for an Nd-adipate framework (GWMOF-9; Cahill et al., 2007), 4,4′-bipyridine again acting as a template, this time within a Pr-suberate framework (GWMOF-10) (Cahill et al., 2007), and 1,2-bis(4-pyridyl)ethane serving as a template in a Pr-adipate framework (GWMOF-11; De Lill and Cahill, 2007; Fig. 6). Common structural features of all these templated materials are neutral frameworks and neutral guests, hydrogen-bonding interactions between nitrogen atoms on the template and bound framework water molecules, and 1D SBUs (of M–O–M linkages) within an overall 3D structure. The importance of the hydrogen-bonding interactions between the template (guest) and framework (host) is apparent in the end product and is likely important during the self-assembly process as well, although this remains a topic that has yet to be explored in depth. Other studies on templated lanthanide CPs and MOFs have focused on alkali metal
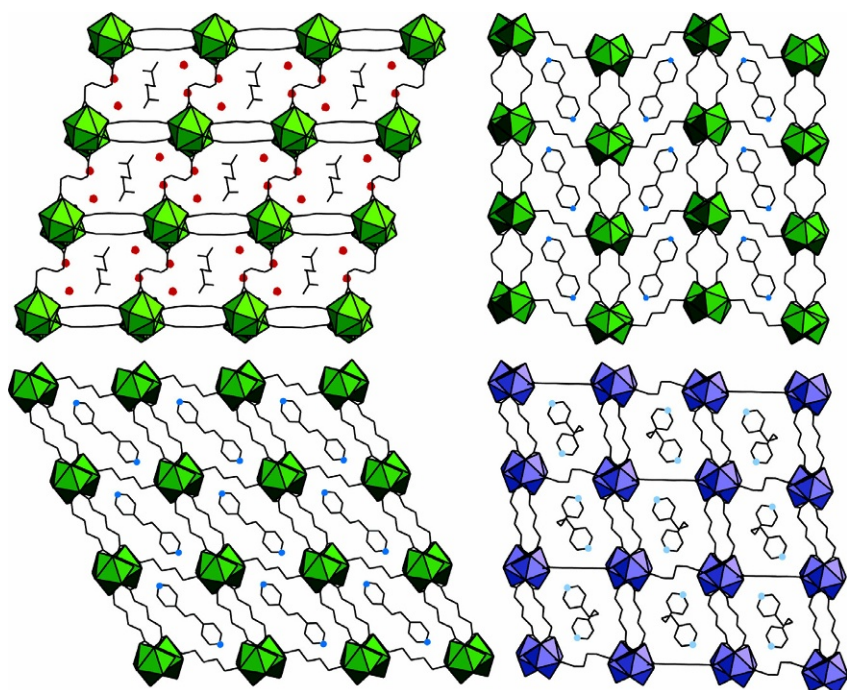
**FIGURE 6** Templated Ln-adipate series. Structures (clockwise from top left): GWMOF-3 with adipic acid and water as template; GWMOF-6 with 4,4′-bipyridine as template; GWMOF-11 with 1,2-bis(4-pyridyl)ethane as template; GWMOF-9 with 1,2-bis(4-pyridyl)propane as template. Green (light gray in the print version) polyhedra represent $Pr^{3+}$ centers while purple (gray in the print version) polyhedra represent $Nd^{3+}$ metal centers. *Reproduced with permission from De Lill and Cahill (2007). Copyright 2007, American Chemical Society.*

cations (Plabst et al., 2010) or small aromatic molecules (i.e., pyridine, toluene, benzene, etc.; Bernini et al., 2011) and similar to our results in the GWMOF series, these other groups have found that a complementary relationship between the template and framework is necessary. Templating appears to rely on the idea of size matching, as the size of the template molecule and the resulting available space (the pores) need to be complementary. This creates favorable interactions that stabilize the structure (i.e., hydrogen bonding), without (these interactions) the templating will not be observed.

The 4,4′-bipyridine template (of GWMOF-6) features a delocalized π-electron system (a result of its aromaticity), which allows for it to serve as a chromophore, in concert with its function as a templating agent. This is of note as each of the 14 lanthanide metals, except lanthanum and lutetium, has a characteristic emission spectrum. The shielding of the 4f orbitals, which affects Ln bonding, as discussed earlier, also manifests in the optical properties of these metals. Intraorbital 4f–4f transitions are only minimally sensitive

to the surrounding chemical environment and the energetic positions of the Ln ground and excited states (and their corresponding transitions) stay consistent in all materials in which they are included. Generally speaking, selection rules render 4f–4f transitions forbidden and the most prominent consequence of this result is that molar absorption coefficients of the $Ln^{3+}$ ions are small. As the 4f wave functions are not completely separate, these selection rules are not strict and thus direct excitation is possible although the characteristic emission of the corresponding $Ln^{3+}$ ions is either minimal or not observed (Binnemans, 2009). Emission of the lanthanide ions ranges from the UV (Gd) to the visible (Sm, Eu, Tb, Dy, Pr, and Tm) to a broad range of the near-IR (NIR) (Pr, Nd, Sm, Dy, Ho, Er, Tm, and Yb) and generally proceeds via indirect excitation (better known today as the antenna effect).

First reported in 1942 (Weissman, 1942), the antenna effect utilizes a ligand that does not suffer from parity-forbidden transitions to absorb incoming light before transferring it to the excited states of an $Ln^{3+}$ ion. As the $^1S^*$ singlet states are often short-lived, it is the $^3T^*$ triplet states of antenna ligands (which have longer lifetimes) that sensitize the lanthanide ions. The first step of the antenna effect involves intersystem crossing between the $^1S^*$ and $^3T^*$ and this process is optimized when the energy gap between the two ligands states is ca. $5000 \, cm^{-1}$ (Scheme 2). The optimal energetic gaps for energy
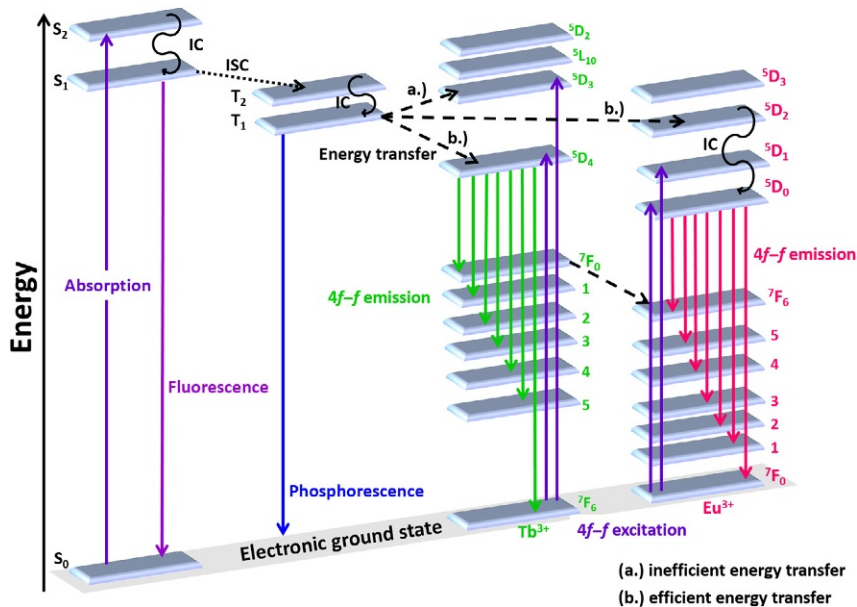


**SCHEME 2** Jablonski diagram showing basic photophysical processes; S, singlet states; T, triplet states; IC, internal conversion; ISC, intersystem crossing (both are nonradiative processes). *Reproduced with permission from Meyer et al. (2014). Copyright 2014, Royal Society of Chemistry.*

transfer between the $^3T^*$ and the lanthanide excited states have been outlined by Latva et al. (1997) and vary depending on the $Ln^{3+}$ ion, yet all fall approximately in the $2000$–$3500\ cm^{-1}$ range. Smaller energy gaps will lead to back-energy transfer, thereby reducing the efficiency of the antenna effect. Luminescent antennas are not limited to organic species, as Ward and colleagues have shown with d-block metal centers as $Ln^{3+}$ sensitizers proving to be especially well suited for sensitization in the NIR region (Lazarides et al., 2008a,b; Shavaleev et al., 2003; Ward, 2007). Further, recent efforts have shown that the use of multiple organic antennas can provide greater enhancement than a single antenna when prudent selection of organic ligands is made (Lima et al., 2013). When selecting antenna ligands or d-block metals, there are two things to avoid as they will lead to diminished luminescence: (1) the number of high-energy oscillators in the first coordination sphere should be minimized (C–H, O–H, N–H, etc.) as they provide means for nonradiative decay and (2) separation of $Ln^{3+}$ metal centers should be increased to prevent energy loss via concentration quenching.

The luminescence of GWMOF-6 was not investigated for $Pr^{3+}$ in the visible region, as this emission, even with an antenna, is not very prominent. Rather, the Eu analogue of GWMOF-6 was synthesized so the luminescent properties of the framework could be investigated. In the case of the GWMOF-6, the 4,4′-bipyridine template molecule also acts as a luminescent antenna and transfers energy to the $Eu^{3+}$ ions (Fig. 7). Luminescence in lanthanide CPs and MOFs is well known (Cui et al., 2012, 2014; Devic et al., 2005; Hasegawa and Nakanishi, 2015; Ma et al., 1999; Reineke et al.,
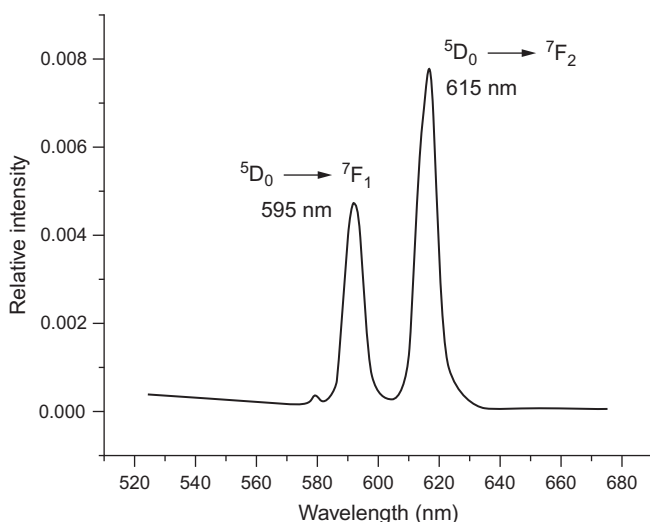


**FIGURE 7** Emission spectrum of europium analogue of GWMOF-6. *Reproduced with permission from De Lill et al. (2005b). Copyright 2005, American Chemical Society.*

1999), but sensitization of an $Ln^{3+}$ ion via template molecule represents a new pathway to achieve luminescence in this class of materials. Utilizing the similar nature of the $Ln^{3+}$ ions has allowed for sensitization of the isomorphous $Tb^{3+}$ GWMOF-6 material (Spencer et al., 2013) and the mixed $Eu^{3+}/Tb^{3+}$ GWMOF-6 material (De Lill et al., 2007) where energy was transferred from the 4,4′-bipyridine to the $Tb^{3+}$ metal center and then onto the $Eu^{3+}$ metal center, although emission from the isomorphous $Sm^{3+}$ GWMOF-6 material was likely hindered by concentration quenching.

As demonstrated in the GWMOF family of materials, an attractive characteristic observed in lanthanide materials is the potential for isomorphous substitution. The International Union of Crystallography defines crystals as isomorphous if they both have the same space group and unit-cell dimensions and the types and the positions of atoms in both are the same except for a replacement of one (or more) atoms in one structure with different types of atoms in the other. As all 14 lanthanide metals feature spherical coordination geometry and are stable in the +3 oxidation state, it is only the ionic radii that vary across the series. This is the well-known lanthanide contraction and the total decrease in size from $La^{3+}$ to $Lu^{3+}$ is ca. 16% (compare that to the ca. 26% difference in ionic radius between $Na^+$ and $K^+$; Shannon, 1976). In the case of the GWMOF-6 family of materials, isomorphous substitution was successful with all lanthanides from cerium to europium (except promethium).

Moving on from adipates to other aliphatic linkers, we begin with the simplest member of this family, the oxalates. Found almost exclusively adopting the bridging bidentate coordination mode, the $C_2O_4^{2-}$ anion promotes a range of topologies. Figure 8 shows an example of a Nd-oxalate CP where monomeric $NdO_9$ polyhedra are polymerized through oxalate linkages to form six-membered rings that are covalently assembled into a neutral, porous sheet (Zhang et al., 2009b). The local $Nd^{3+}$ coordination sphere of this material features three oxalate linkers for every two $Nd^{3+}$ centers with three bound water molecules completing the first coordination sphere of each $Nd^{3+}$ metal center. In this example, we see many of the themes developed in the GWMOF family and like in those materials, isomorphous substitution with a range of $Ln^{3+}$ metal centers was observed (Ollendorff and Weigel, 1969). Similar local geometry with varying topologies and degrees of dimensionality is observed in the many Ln-oxalate materials that populate the literature (Kahwa et al., 1984; Rong-Hua and Han-Guo, 2007; Trombe and Mohanu, 2004; Wang et al., 2013b; Yang et al., 2005).

Increasing the length of the aliphatic carbon chain from two atoms to four yields succinic acid, and the chemistry of lanthanide-succinate materials has proven quite rich. Recent interest in this class of materials began with the synthesis of the $Pr^{3+}$ framework MIL-17 by Serpaggi and Férey (1999a) (Fig. 9) featuring edge-sharing Ln metal centers (similar to the GWMOF family) and has continued as these materials have shown interesting catalytic (Perles et al., 2004), luminescent (Cui et al., 2005), and magnetic properties
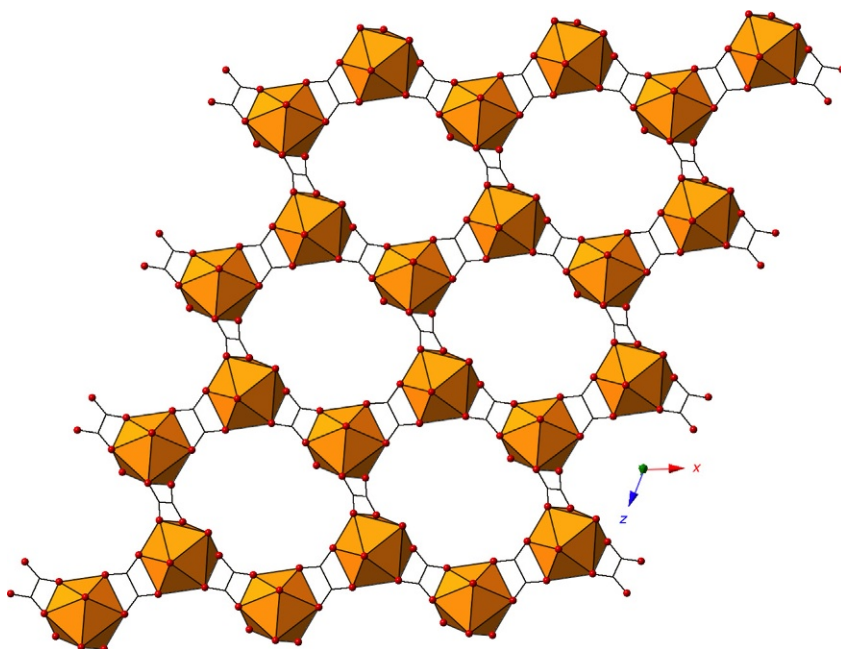
**FIGURE 8** Polyhedral representation of Nd-oxalate sheet from Zhang et al. (2009b) shown in the (101) plane. Interlayer water molecules have been omitted for clarity. Orange (light gray in the print version) polyhedra represent $Nd^{3+}$ metal centers, whereas red (gray in the print version) spheres are oxygen atoms and black lines are oxalate linker species.
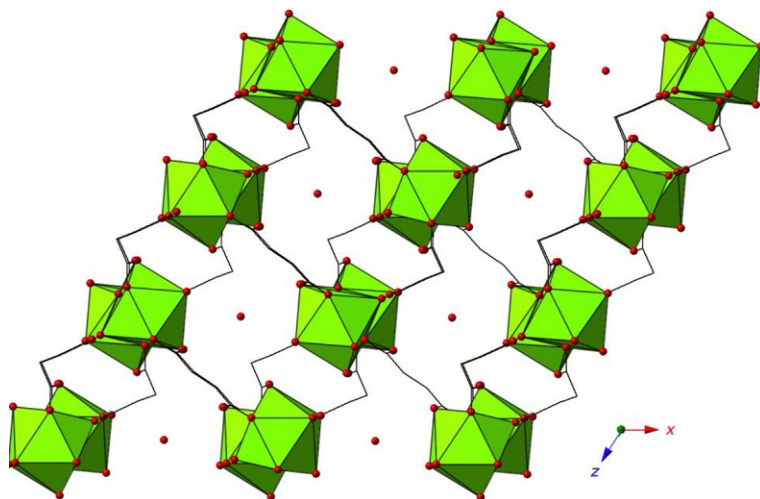


**FIGURE 9** Polyhedral representation of Pr-succinate framework MIL-17 from Serpaggi and Férey (1999a) shown in the (101) plane. Green (light gray in the print version) polyhedra represent $Pr^{3+}$ metal centers, whereas black lines are succinate linker species.

(Manna et al., 2006). Unlike the shorter oxalate anion, which almost exclusively adopts the bridging bidentate coordination mode, succinate linkers can adopt a variety of coordination modes including monodentate, bridging bidentate, and chelating-bridging bidentate.

Aliphatic carboxylates that are longer than adipic acid include suberates and sebacates. Lanthanide CPs with these longer chain aliphatics have not been studied to the same extent as the oxalates, succinates, or adipates yet one can draw parallels between the materials formed with suberic and sebacic acid and those described previously. Lanthanide-sebacates, in particular, are rare with only six known structures (Borkowski and Cahill, 2004a; Wang et al., 2010; Xie et al., 2010) in the Cambridge Structural Database (CSD, v. 5.36, Nov. 2014; Allen, 2002). Polymerization of lanthanide primary building units into multidimensional structures (chains, slabs, frameworks, etc.) is still common as is observed in the isomorphous lanthanum (Benmerad et al., 2004) and praseodymium (Huang et al., 2006) suberate frameworks that feature the characteristic 1D chains of M–O–M linkages first highlighted in our discussion of GWMOF-1. Another result of note can be seen in Fig. 10, which highlights a Eu-suberate CP made in our group (De Lill et al., 2009) where edge-sharing $Eu_2O_{16}$ dimers are tethered together by suberate anions in the [100] and [001] directions to form a 2D sheet. The sheets are
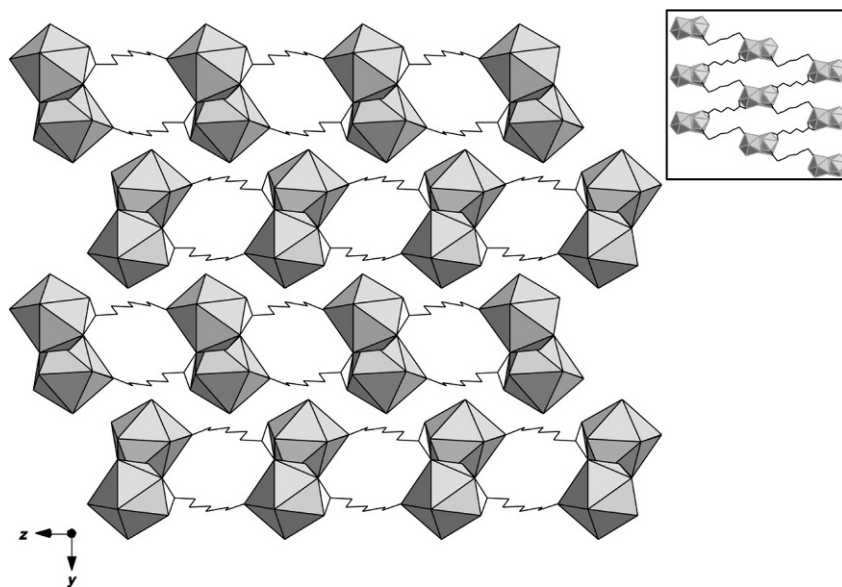


**FIGURE 10** Extended network of Eu(III) suberate CP viewed down the [100] direction. Gray polyhedra represent $(EuO_9)_2$ dimers, the SBU that is polymerized into 2D sheets via suberate anions (black lines). The inset shows the sheet viewed down the [010] direction. *Reproduced with permission from De Lill et al. (2009). Copyright 2009 Elsevier.*

alternatively stacked in an ABAB fashion and this staggered motif is stabilized by strong hydrogen-bonding interaction between bound water molecules and suberate oxygen atoms. Illustrating the similarities between adipates and suberates is the nearly analogous (to the material in Fig. 10) 2D sheet that results from the synthesis of $Dy^{3+}$ and adipic acid (De Lill et al., 2005a).

## 2.2 Ln-O Hybrid Materials: Aromatic Linkers

Ln CPs featuring aromatic carboxylic acids are nearly as diverse of a field as the Ln-aliphatic compounds described previously. This class of materials is dominated by benzene-carboxylate (and related) species, which are attractive linkers due to their planarity, rigidity, and delocalized π-electron rings that allow them to function as antenna ligands for $Ln^{3+}$ sensitization and Fig. 11 contains a depiction of each of the aromatic carboxylates that will be discussed throughout this section. Yaghi and colleagues (Reineke et al., 1999) synthesized one of the first materials featuring $Ln^{3+}$ metal centers and 1,4-benzenedicarboxylic acid (BDC; MOF-6) and since this first result research on these materials (Ln CPs featuring BDC or a BDC derivative) has exploded. In fact, a search of the Cambridge Structural Database (CSD, v. 5.36, Nov. 2014; Allen, 2002) reveals that 462 Ln-BDC CPs have been synthesized in the 15 years since Yaghi and colleagues' initial findings. MOF-6, $[Tb_2(C_8H_4O_4)_3(H_2O)_4]$, features two unique $Tb^{3+}$ metal centers that are each coordinated to six BDC anions and two bound water molecules (Fig. 12). The BDC anions each adopt the bridging bidentate coordination mode and thus each $Tb^{3+}$ metal center is polymerized into non-edge sharing pseudo-chains that propagate along [010]. This material also exhibited promising sorption and catalytic properties while proving to be thermally robust after the removal of the coordinated water molecules.

Manipulating syntheses procedures and functionalizing the BDC ligand have resulted in a diverse array of observed topologies and further allowed for the optimization of properties (including luminescence, sorption, and catalysis) in Ln-BDC CPs. Utilizing the smaller $Er^{3+}$ metal center, instead of $Tb^{3+}$, Zheng and colleagues (Pan et al., 2001) were able to produce two CPs: one that is isomorphous with MOF-6 and a second, $[Er_4(C_8H_4O_4)_6(H_2O)]$, which features four unique $Er^{3+}$ metal centers adopting three unique coordination environments likely due to the additional coordination diversity displayed by the BDC linkers. By extending the synthesis time and increasing the synthesis temperature and pH, Serre and colleagues synthesized MIL-51 (Serre et al., 2002). This 3D structure differs from MOF-6 as it is constructed from 2D inorganic networks that are tethered together by the BDC linkers to create a pillared 3D structure. The 2D inorganic layers are made up of europium polyhedra that face share as a result of $\mu_3$-OH groups, an unusual observation in $Ln^{3+}$ CPs. Metal cation hydrolysis and subsequent condensation can lead to oligomerized products (Baes and Mesmer, 1976),
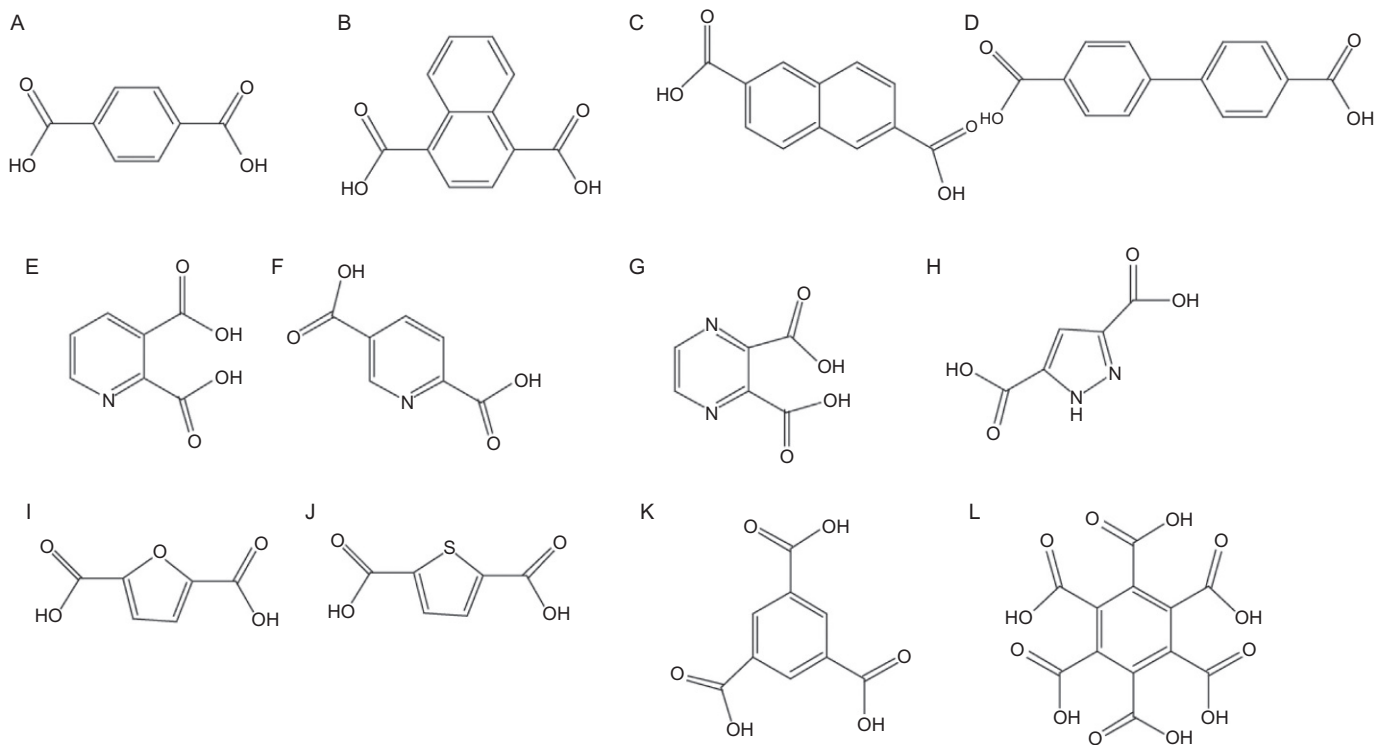
**FIGURE 11** Pictorial representations of the linkers described in the aromatic-based CPs described in Section 2.2. Linkers described are: (A) 1,4-benzenedicarboxylic acid (BDC); (B) 1,4-naphthalenedicarboxylic acid (1,4-NDC); (C) 2,6-naphthalenedicarboxylic acid (2,6-NDC); (D) 4,4'-biphenyldicarboxylic acid (BPDC); (E) 2,3-pyridine dicarboxylic acid (2,3-PYDC); (F) 2,5-pyridine dicarboxylic acid (2,5-PYDC); (G) 2,3-pyrazine dicarboxylic acid (2,3-PZDC); (H) 3,5-pyrazole dicarboxylic acid (3,5-PYZDC); (I) furan-2,5-dicarboxylic acid (FDC); (J) thiophene-2,5-dicarboxylic acid (TDC); (K) benzene-1,3,5-tricarboxylic acid (1,3,5-BTC); (L) mellitic acid.
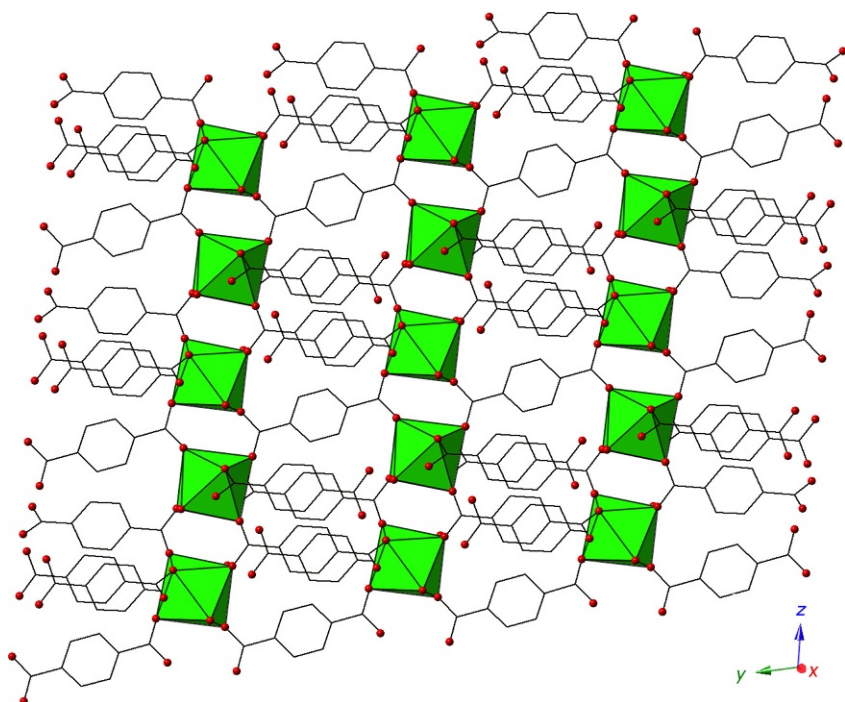
**FIGURE 12** Polyhedral representation highlighting MOF-6 from Reineke et al. (1999) shown in the (011) plane. Green (light gray in the print version) polyhedra represent $Tb^{3+}$ metal centers, whereas red (gray in the print version) spheres are oxygen atoms.

yet this is more often observed in uranyl hybrid materials (Andrews and Cahill, 2013) and lanthanide cluster complexes (Zheng, 2010). Working with a larger $Ln^{3+}$ cation can also lead to a new CP as illustrated by You and colleagues (Han et al., 2010) who were able to produce a new 3D framework, $[Ln_6(C_8H_4O_4)_9(DMF)_6(H_2O)3 \cdot 3DMF]_n$ with La, Ce, and Nd as well as MOF-6 isomorphs with Eu, Dy, and Y. This new material features six unique $Ln^{3+}$ cations that adopt three different coordination numbers: one is seven-coordinate, two are eight-coordinate, and three are nine-coordinate. The material features two different 1D metal-carboxylate SBUs and via cross-linking by additional BDC ligands, these 1D chains are assembled into a 3D framework (Fig. 13). Finally, changing the synthesis medium to an ionic liquid (Cao et al., 2014) yields BDC frameworks that feature very different topologies than those observed for MOF-6 and other materials discussed above.

Functionalization of the BDC linkers with fluorine allows for the optimization of $Ln^{3+}$ luminescent properties in both the visible and near-IR regions as shown by Chen (Chen et al., 2006), Noftle (Macneill et al., 2011), and Ruschewitz (Seidel et al., 2012) by reducing the number of high-energy
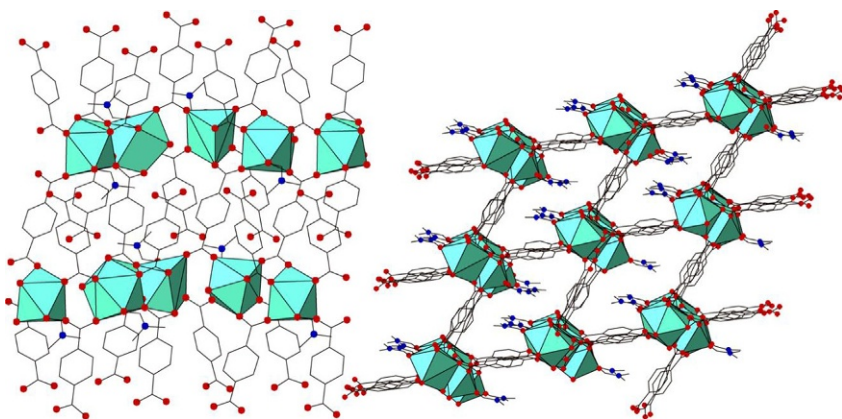
**FIGURE 13** Polyhedral representation of the two independent La$^{3+}$ 1D chain SBUs and resulting 3D network synthesized by Han et al. (2010). Teal polyhedra (light gray in the print version) represent La$^{3+}$ metal centers, whereas blue (black in the print version) spheres represent nitrogen atoms.

oscillators in a material. Halogen-BDC linkers with the larger $X$ atoms (Cl, Br, I) have not been extensively explored, yet the few literature examples have yielded complexes that show promising sorption (Xu et al., 2004) and near-IR luminescent properties (Wei et al., 2014). The use of amino-functionalized BDC linkers in Ln$^{3+}$ CPs has been shown by Reedijk and colleagues (Black et al., 2009) to yield structurally intriguing materials which also happen to show interesting magnetic properties, while additional efforts by both the Reedijk group (Costa et al., 2008) and others (Chen et al., 2005; Haitao et al., 2003; Xu et al., 2003) have shown that the Ln$^{3+}$ hybrids with amino-BDC (and other similar ligands) adopt an array of versatile topologies. Hydroxy-functionalization of the BDC linker results in a very diverse suite of results as illustrated by Liu and colleagues (Wang et al., 2012b) where the 2,5-dihydroxy-BDC ligand adopts 15 different coordination modes in the 6 materials they characterized (Fig. 14). With La$^{3+}$ and Pr$^{3+}$, a 3D framework assembled from a 1D SBU of tubular chains, made of Ln dimers, was observed. Moving to the slightly smaller Nd$^{3+}$ resulted in a 2D-layered network based on Ln dimers. With Eu$^{3+}$ as the lanthanide cation of choice a 1D zigzag chain was observed, while the materials featuring Gd$^{3+}$ and Dy$^{3+}$ are 3D frameworks assembled from 1D chains of M–O–M linkages, the same structural motif we introduced in the GWMOF family.

The addition of conjugation to the BDC linker, in the form of a second benzene ring, yields naphthalenedicarboxylic acid and the two main derivatives of this ligand, 1,4-naphthalenedicarboxylic acid (1,4-NDC) and 2,6-naphthalenedicarboxylic acid (2,6-NDC), have garnered significant interest for use in the construction of lanthanide hybrid materials. Of the two, 2,6-NDC has received the greater share of attention, although both ligands are
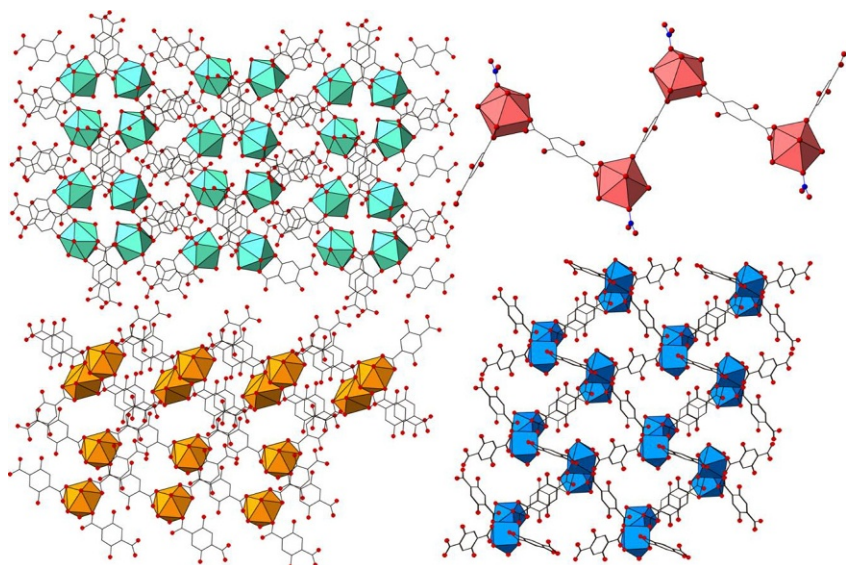
**FIGURE 14** Polyhedral representations highlighting the structural diversity of $Ln^{3+}$-2,5-dihydroxy-BDC materials synthesized by Wang et al. (2012b). Clockwise from top left: $La^{3+}$ 3D framework featuring tubular 1D chain SBUs, 1D zigzag chain of $Eu^{3+}$ metal centers featuring terminating $NO_3^-$ anions, $Dy^{3+}$ 3D network assembled from 1D chains of M–O–M linkages and layered 2D network of $Nd^{3+}$ dimers. Teal (light gray in the print version) polyhedra represent $La^{3+}$ metal centers, whereas red (gray in the print version) represent $Eu^{3+}$, blue (dark gray in the print version) represent $Dy^{3+}$, and orange (light gray in the print version) represent $Nd^{3+}$ metal centers, respectively.

promising for the construction of $Ln^{3+}$ hybrid materials as they are rigid ligands capable of establishing multiple bridges between lanthanide metal centers. The first $Ln^{3+}$ hybrid materials with 2,6-NDC were synthesized by Min and Lee (2002a) and You and colleagues (Wang et al., 2002) in 2002, via hydro- and solvothermal methods, respectively. Soon after these initial results (featuring Eu and Tb), Almeida Paz and Klinowski (2003) synthesized a ytterbium 3D framework with 2,6-NDC that features $Yb^{3+}$ metal centers with coordination numbers of six and seven. The two unique metal centers of this material, CUmof-9, form 1D chains of pseudo paddlewheels that propagate in the [001] direction that are then cross-linked via additional 2,6-NDC linkers (Fig. 15). Jin and colleagues (Zheng et al., 2004a) continued the study of this class of materials and synthesized three similar porous MOFs, with changes as a result of the lanthanide contraction, which remained stable up to 430 °C. Almeida Paz and Klinowski synthesized the $Ho^{3+}$ analogue (Almeida Paz and Klinowski, 2008a) of Jin and collaborators complex **2** (with $Eu^{3+}$) as well as a 2D $Ho^{3+}$ CP that features three bound water molecules in the first coordination sphere (Almeida Paz and Klinowski, 2008b). Loiseau
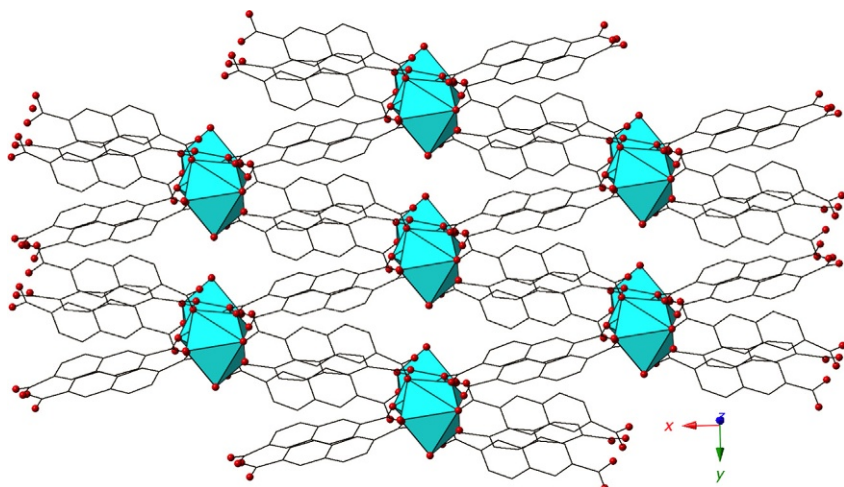
**FIGURE 15** Polyhedral representation of Cumof-9 from Almeida Paz and Klinowski (2003) in the (110) plane. Turquoise (light gray in the print version) polyhedra represent $Yb^{3+}$ metal centers. Lattice water molecules have been omitted for clarity.

and colleagues (Rodrigues et al., 2011) explored a series of $Nd^{3+}$-2,6-NDC CPs, two of which included the additional linkers oxalate and formate. In the CP containing solely 2,6-NDC, there exists both terminal and bridging bound water molecules, and while the oxalate anions partially replace the first coordination sphere water molecules, it is with formate that a water free species is formed. The third phase is then considered for use in the catalytic polymerization of isoprene and shows promising initial results. Finally, recent results from Xie et al. (Lu et al., 2014a) continue to illustrate the rich diversity of this system as small changes to their synthesis procedure, solvothermal synthesis with dimethylacetamide, have yielded five novel 2D networks.

Jin and colleagues also did some of the seminal work on $Ln^{3+}$-1,4-NDC hybrid materials. When they included sodium acetate in their hydrothermal reaction, the result was a 3D framework assembled from the first $[Ln_7(\mu_3\text{-}OH)_8]^{13+}$ clusters, and it was also the first instance of this SBU being observed in a CP structure (Zheng et al., 2004b). Without sodium acetate in the reaction mixture, the result was $[Eu_2(1,4\text{-}NDC)_3(H_2O)_2]\cdot 2H_2O$ (Zheng et al., 2005b), which is a 3D CP made up of $EuO_9$ polyhedra exhibiting 1D chains of M–O–M linkages that propagate along the [001] direction (Fig. 16). Additional 1,4-NDC ligands cross-link the 1D chains to form a 3D CP with square channels, yet these channels are mostly filled by the bulky 1,4-NDC ligands which partially occupy the void space and lattice water molecules that are participating in hydrogen-bonding interactions with the bound water molecules of the framework. Solvothermal synthesis of 2D CPs featuring the lanthanide metal centers $Eu^{3+}$, $Nd^{3+}$, and $La^{3+}$ yielded materials
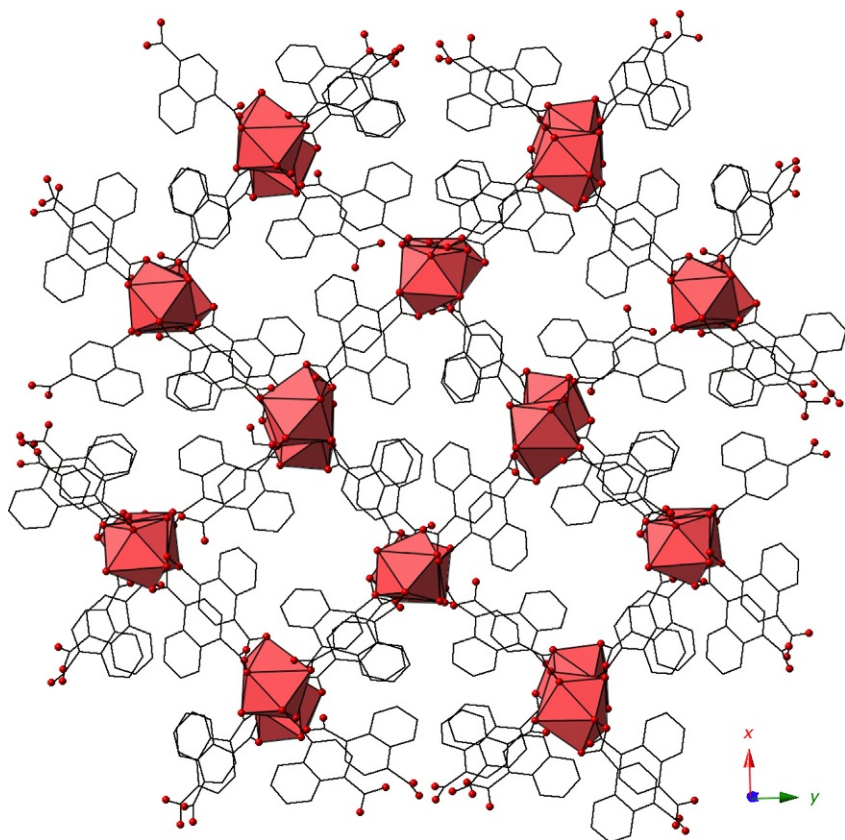
**FIGURE 16**  Polyhedral representation of three-dimensional Eu-1,4-NDC CP from Zheng et al. (2005a) in the (110) plane. Red (gray in the print version) polyhedra represent $Eu^{3+}$ metal centers. Lattice water molecules have been omitted for clarity.

that show interesting upconversion potential (for $Nd^{3+}$) as well as illustrating that 1,4-NDC can function as an efficient sensitizer of both visible and near-IR luminescence (Yang et al., 2006). Finally, changing the synthesis medium to an ionic liquid (Tan et al., 2012), as was explored with BDC previously, yields $Ln^{3+}$-1,4-NDC materials with topologies unlike those observed via other, more traditional methods.

Increasing the distance between carboxylate functional groups, when compared to 1,4-BDC, allows for the use of 4,4′-biphenyldicarboxylic acid (BPDC) and this linker has produced a diverse of array of hybrid materials. Jin and colleagues synthesized some of the first examples of $Ln^{3+}$-BPDC hybrids (Wang et al., 2004c) and the observed 3D topology is generally the norm for this class of materials. A selection of additional examples of $Ln^{3+}$-BPDC hybrids exhibiting 3D topologies can be found in the works of Liu

(Guo et al., 2005), You (Han et al., 2008), Singh-Wilmot (Min et al., 2012), and Hou (Jia et al., 2013). Materials exhibiting other dimensionalities are not unknown as shown by Xie and colleagues (Lu et al., 2014b) who used dimethylacetamide, which functioned as a coordinating solvent, with the net effect of limiting BPDC coordination to only two dimensions. Functionalization of the BPDC linker is not as mature as with 1,4-BDC, yet initial results utilizing BPDC analogues in lanthanide hybrid material synthesis have yielded some very interesting structures which may also show great application potential. One such example was synthesized by Bharadwaj and colleagues (Das et al., 2012) and features tetranitroBPDC (2,2′,6,6′-4,4′-biphenyldicarboxylic acid). With this ligand they synthesized a $Gd^{3+}$ CP, featuring edge-sharing $Ln^{3+}$ dimers that are cross-linked by tetranitroBPDC linkers to form a 3D network highlighted by two unique 1D channels (Fig. 17). The authors found that the Gd-tetranitroBPDC CP was an excellent
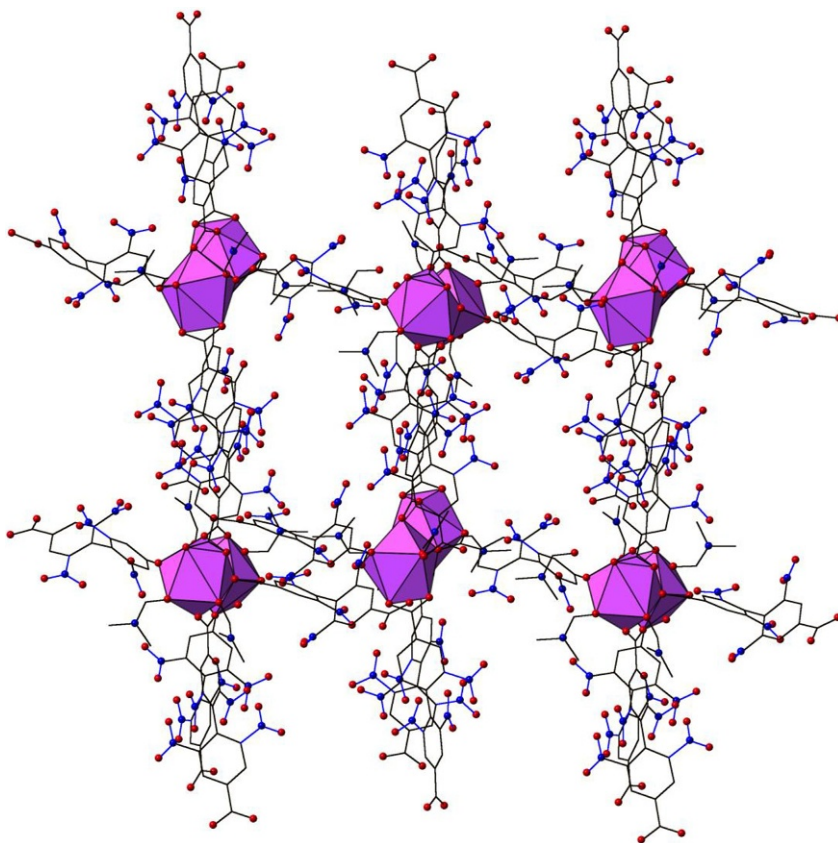


**FIGURE 17** Polyhedral representation of 3D framework of the Gd-tetranitroBPDC material described in Das et al. (2012) shown in the (011) plane. Purple (gray in the print version) spheres represent $Gd^{3+}$ metal centers and lattice water and DMF molecules have been omitted for clarity.

heterogeneous catalyst for the cyanosilylation and Knoevenagel condensation reactions and that when the reactants were put inside the 1D channels of the $Gd^{3+}$ CP they spontaneously underwent both of these reactions at room temperature and atmospheric pressure. Further, these reactions were then monitored via X-ray crystallography as the crystallinity of the Gd-tetranitroBPDC CP was maintained throughout and the results represent one of the first examples of a successful condensation reaction within the pores of a lanthanide CP.

The pyridinedicarboxylic acids are another class of linker molecules that have proven quite effective for use in the construction of hybrid materials. Due to its heterofunctional nature (i.e., the presence of two distinct functional groups: carboxylate and pyridyl), pyridinedicarboxylic acid inclusion in transition metal, lanthanide, and actinide hybrid materials is well known. 2,3-Pyridinedicarboxylic acid (2,3-PYDC) is the least reported of these materials and this may be due to the tendency of 2,3-PYDC to decarboxylate at the 2-position to become nicotinic acid under hydrothermal conditions (Chen et al., 2003). One interesting material featuring 2,3-PYDC was synthesized by de Lill and colleagues (Ramirez et al., 2012) and features edge-sharing Ln dimers that stack in the [100] direction that are further linked by additional 2,3-PYDC linkers to form a 2D sheet. While structurally intriguing, de Lill et al. also found that the 2,3-PYDC is not a very effective luminescent antenna in their material and the combination of this information, along with the tendency of 2,3-PYDC to undergo decarboxylation, may explain the relative scarcity of these hybrid materials in the literature. Similar to 2,3-PYDC, 2,4-pyridinedicarboxylic acid has not been extensively studied in $Ln^{3+}$ hybrid materials (Chang et al., 2013; Min and Lee, 2002b; Shen and Lush, 2012). Instead, the multifunctional 2,4,6-pyridinetricarboxylic acid (2,4,6-PYTC) is preferred as it has the ability to chelate $Ln^{3+}$ metal centers via the pyridine N atom and the carboxylates at the 2- and 6-position while further linking via the carboxylate at 4-position to promote the formation of a higher dimensional CP (Gao et al., 2005; Ghosh and Bharadwaj, 2005; Jin et al., 2012; Li et al., 2008a; Ren et al., 2010; Wang et al., 2007a).

The most widely used pyridinedicarboxylic acid derivative in lanthanide hybrid materials is 2,6-pyridinedicarboxylic acid (2,6-PYDC), which has been shown to form materials of one-, two-, and three-dimensions (Duan et al., 2004a; Gao et al., 2006; Liu et al., 2008; Song et al., 2012; Yang et al., 2011; Zhao et al., 2014). The versatility of 2,6-PYDC, and its ability to form such a diverse suite of materials, is presumably a result of the tridentate, chelating nature of the ligand (like 2,4,6-PYTC), and the many coordination modes it is capable of adapting. The very similar 2,5-pyridinedicarboxylic acid (2,5-PYDC) linker has also garnered extensive attention from researchers, as it, like 2,6-PYDC, is capable of promoting a wide range of SBUs and topologies. Ln-2,5-PYDC CPs have formed from monomeric SBUs (Decadt et al., 2012; Huang et al., 2007; Qin et al., 2005; Wang et al.,

2009; where no metal-ion oligomerization has occurred), dimeric SBUs (Shi et al., 2009; Soares-Santos et al., 2008), and even tetra- (Shi et al., 2009; Silva et al., 2013) and hexameric clusters (Shi et al., 2009; Zhang et al., 2012). Taking a closer look at the lanthanide hybrids featuring tetrameric clusters, we will highlight two materials from the recent work of Almeida Paz and colleagues (Silva et al., 2013). Complex **1** is a 3D framework assembled from heptanuclear $Er^{3+}$ metal clusters, which are in turn a result of the coalescence of two tetranuclear cubane-like $[Er_4(\mu_3\text{-}OH)_4]^{8+}$ clusters. The heptanuclear clusters are interconnected to form a 1D cationic lanthanide hydroxide chain (Fig. 18), and these chains are surrounded by 2,5-PYDC
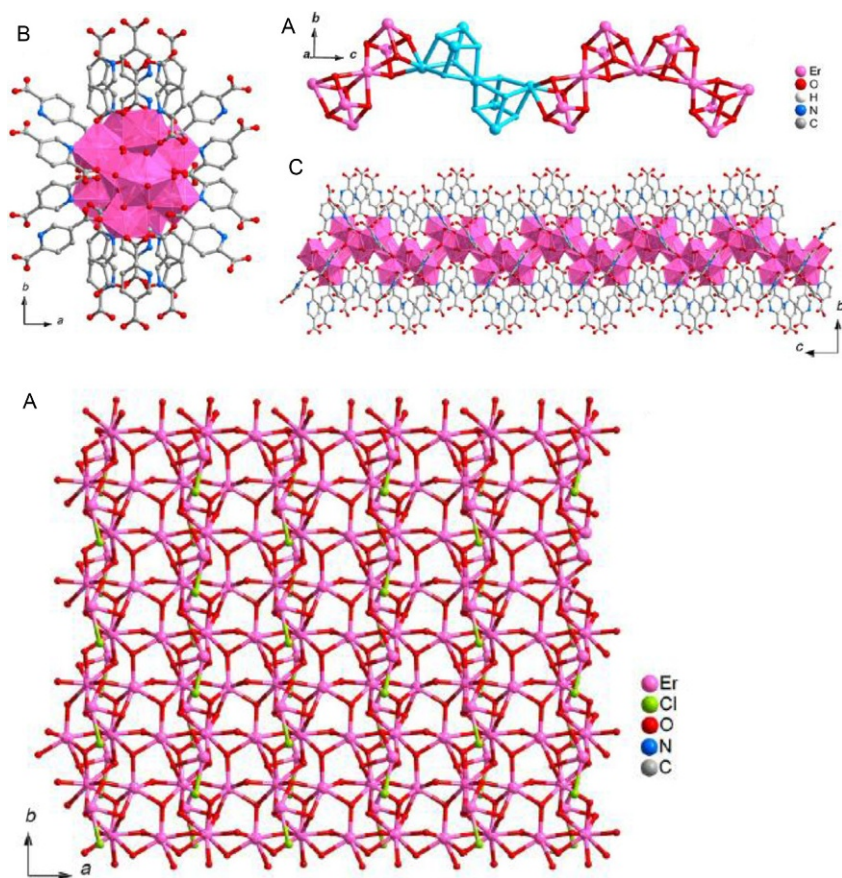


**FIGURE 18** (*Top*) Schematic and polyhedral representation of the heptanuclear cluster of **1** along with polyhedral representation of cationic 1D chain of **1** where hydrogen atoms have been omitted for clarity. (*Bottom*) Ball-and-stick representation of 2D inorganic network of **2**. *Both figures have been adapted with permission from Silva et al. (2013). Copyright 2013 American Chemical Society.*

linkers, which coordinate via three unique coordination modes: bridging, chelating monobridging, and chelating bisbridging. By increasing metal concentration at the time of synthesis, Almeida Paz et al. were able to isolate compound **2**, $[Er_3(OH)_6(2,5\text{-}PYDC)Cl]$, which forms a 2D cationic inorganic network in the (110) plane (Fig. 18). The unique 2,5-PYDC ligand pillars together adjacent 2D layers via coordination to four $Er^{3+}$ metal centers to result in a densely packed 3D framework.

Continuing with heterofunctional linkers that feature both nitrogen atoms and carboxylate functional linkers, we look now at pyrazinedicarboxylic acids, which differ from the pyridinedicarboxylic acids in the number of sites for potential coordination (six vs. five). Increasing linker functionality is a topic of interest as it provides researchers one route to increase the dimensionality of hybrid materials, which then expands the suite of possible applications of the synthesized materials. Transition metal complexes with 2,3-pyrazinedicarboxylic acid (2,3-PZDC) have been well characterized (O'Connor et al., 1982; Smith et al., 1995; Wenkin et al., 1997; Zou et al., 1999), yet it was not until 2002 when Jin and colleagues synthesized the first hybrid material that featured lanthanide cations and 2,3-PZDC (Zheng et al., 2002). A follow-up study, also from Jin and colleagues (Weng et al., 2007), produced three new 2D materials, different from the 3D frameworks synthesized in their first study, and via spectroscopic characterization of these 2D materials the researchers found (when they codoped two $Ln^{3+}$ cations (Yb and Er)) the hybrid network showed promise as an upconversion material. Carlos and collaborators (Soares-Santos et al., 2010) were also interested in the photoluminescent properties of $Ln^{3+}$ hybrid material with 2,3-PZDC and synthesized a series of seven 2D materials, also featuring the oxalate anion that was formed *in situ*, which showed that 2,3-PZDC is an effective antenna for both visible and NIR luminescence. More recently, Liu and colleagues (Yang et al., 2012b) have synthesized the first anionic framework featuring $Ln^{3+}$ cations and the 2,3-PZDC linker, which features charge-balancing ammonium cations in the channels and topology that differs from the neutral $Ln^{3+}$-2,3-PZDC materials that have been characterized previously.

Changing the ring size, while keeping the number of N atoms constant, yields the pyrazoledicarboxylic acid linker, which has not been studied to the same level as the six-membered pyrdine- and pyrazinedicarboxylic acid groups. Li and colleagues were the first to use the asymmetric 3,5-pyrazoledicarboxylic acid (3,5-PYZDC) in the synthesis of lanthanide hybrid materials (Pan et al., 2000). They found that the coordination modes of the 3,5-PYZDC linker could be controlled depending on reaction acidity and by also utilizing the lanthanide contraction. As a result, they synthesized six new materials featuring three unique topologies where 3D frameworks were made of either single- or double layers depending on the size of the $Ln^{3+}$ cation. The structural variability of Ln-35-PYZDC hybrid materials has also been demonstrated by Cheng and colleagues (Xia et al., 2007) who observed
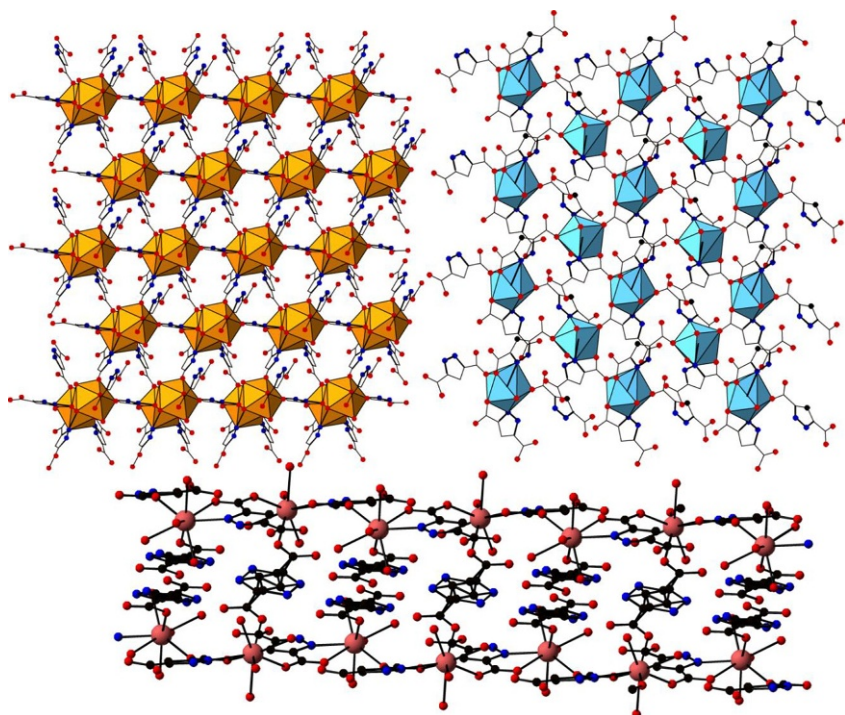
**FIGURE 19** Polyhedral and ball-and-stick representations highlighting structural diversity of Ln-35-PYZDC materials synthesized by Xia et al. (2007). Clockwise from top left: 3D framework assembled from $Nd^{3+}$ dimers, 2D network featuring 1D chains of M–O–M-linked $Ho^{3+}$ metal centers, and 2D $Eu^{3+}$ layer constructed of 1D chain SBUs. Orange (light gray in the print version) polyhedra represent $Nd^{3+}$ metal centers and blue (light gray in the print version) polyhedra represent $Ho^{3+}$ metal centers. Light red (gray in the print version) spheres represent $Eu^{3+}$ metal centers, whereas red (dark gray in the print version) spheres represent oxygen atoms, blue (dark gray in the print version) spheres represent nitrogen atoms, and black spheres represent carbon atoms. Ball-and-stick representation used for the $Eu^{3+}$ material due to disorder in the published CIF.

three unique structure types in the series of nine materials they hydrothermally synthesized (Fig. 19). With the larger lanthanide cations (Pr, Nd, Sm), a 3D framework was observed where $Ln^{3+}$ cations are linked via 3,5-PYZDC ligands and with further dimensionality achieved via coordination of additional 3,5-PYZDC linkers. The second structure type (with Eu, Gd, and Tb) observed by Cheng et al. was a double-decker 2D network where 1D layers are bridged by 3,5-PYZDC linkers to form on overall 2D network. Water molecules in the first coordination sphere along with chelation effects prevent further connectivity in the overall structure. With the smaller $Ln^{3+}$ cations (Dy, Ho, Er), we once again see a 1D chain SBU of M–O–M linkers that are further cross-linked by a second 3,5-PYZDC linker to form an overall 2D structure. The effects of the addition of oxalic acid to the synthesis of

Ln-35-PYZDC hybrid materials were explored recently by Han and collaborators (Zhang et al., 2009a), and they found that this route yielded 3D CPs featuring a unique topology and large, open channels filled with lattice water molecules.

Moving now to five-membered heterofunctional linkers where only the carboxylate groups coordinate, we highlight the furan-2,5-dicarboxylic acid (FDC) and thiophene-2,5-dicarboxylic acid linkers (TDC). The latter has been characterized more extensively, yet we will first look at a few Ln-FDC hybrids to better inform the later discussion of Ln-TDC materials. FDC (and TDC) has two carboxylate groups with a "V-shaped" configuration and is known to adopt a number of coordination modes. One reason that FDC is less utilized than the analogous TDC is that it has a tendency to partially decompose into oxalate under hydrothermal conditions (Shi et al., 2013). When solvothermal conditions are used the 2,5-FDC ligand remains intact (Akerboom et al., 2012; Li et al., 2013a), although both synthesis methods yield exclusively 3D materials. Hu and colleagues synthesized two series of Ln-FDC-oxalate 3D materials that varied with the size of the $Ln^{3+}$ cation and differed slightly in their crystal packing (Wang et al., 2012a). Cheng and collaborators also synthesized a 3D Ln-FDC material (with Tb) and it featured robust 1D honeycomb channels that showed very promising sorption properties, including the selective sorption of $CO_2$ over both $N_2$ and $CH_4$ (Li et al., 2013a).

Since Yaghi and colleagues (Rosi et al., 2005) first synthesized MOF-75, there has been a sustained period of interest in Ln-TDC hybrid materials. In the past decade, 11 papers featuring Ln-TDC hybrid materials have been published (Calderone et al., 2013; Chen et al., 2009; Huang et al., 2009; Macneill et al., 2010; Marques et al., 2012, 2013; Tsai et al., 2013; Wang et al., 2008, 2011; Xu et al., 2011; Zhan et al., 2012) in which 42 new Ln-TDC materials were characterized. All of these materials feature 3D hybrid networks and unlike FDC, 2,5-TDC does not partially decompose to the oxalate anion regardless of the conditions used (hydro-, solvo-, or ionothermal). Su and colleagues (Xu et al., 2011) did include oxalate as a starting material in their work and the result was two very similar 3D materials that varied based on lanthanide ionic radii, a very similar result to that observed by Hu et al. with FDC and an *in situ*-formed oxalate anion (Wang et al., 2012a). While much of the recent interest in Ln-TDC hybrids likely stems from the interesting luminescent (Calderone et al., 2013; Marques et al., 2012, 2013; Wang et al., 2008) and magnetic (Chen et al., 2009; Huang et al., 2009) properties displayed by these materials, it certainly is notable that with the TDC (and FDC) linker there seems to be some sort of propensity for 3D materials. The mechanism for this propensity is one topic that remains underexplored in this class of materials.

Concluding our survey of Ln-O hybrid materials with aromatic linkers, we look now at materials featuring aromatic ligands that feature more than two

carboxylate functional groups. Likely the best-known member of this class of ligands is 1,3,5-benzenetricarboxylic acid (1,3,5-BTC) which was first incorporated into a lanthanide hybrid material by Yaghi and collaborators (MOF-76; Rosi et al., 2005). Solvothermal synthesis (in DMF) by Cheng and colleagues (Wang et al., 2004a) yielded a 2D network with $Nd^{3+}$ and 1,3,5-BTC and showed that while 1,3,5-BTC was a rigid and stable ligand, the dimensionality of the resulting hybrid material was still dependent on the solvent used in synthesis. More recent investigations of Ln-1,3,5-BTC hybrid materials have focused on their great potential for applications including sensing (Chen et al., 2007; Yang et al., 2012a), catalysis (Gustafsson et al., 2010), and gas sorption (Jiang et al., 2010; Xie et al., 2011).

The addition of three more carboxylate moieties to 1,3,5-BTC yields mellitic acid and this ligand is the most functionalized ligand we will discuss. The reactivity of lanthanide cations with mellitic acid has been explored (Chui et al., 2001; Li et al., 2006; Liang Ping et al., 1996; Tang et al., 2008), and throughout these investigations one structure continues to appear. First mentioned by Williams and coworkers (Chui et al., 2001) with $La^{3+}$, then by Yue and colleagues (Tang et al., 2008) with $Nd^{3+}$ and $Ho^{3+}$ and most recently by Loiseau and collaborators (Volkringer et al., 2012; with $Ce^{3+}$), the Ln-mellitate hybrid material features monomeric $LnO_9$ polyhedra that are connected by carboxylate functional groups of the mellitate anions into a narrow MOF with narrow channels that are delimited by terminal water molecules (Fig. 20).

## 2.3 Ln-Phosphonate Hybrid Materials

Phosphonate-containing $Ln^{3+}$ CPs represent an underdeveloped area of lanthanide material synthesis when compared to carboxylate-containing $Ln^{3+}$ CPs. The group of Rocha, Almeida Paz, and others has had some recent success
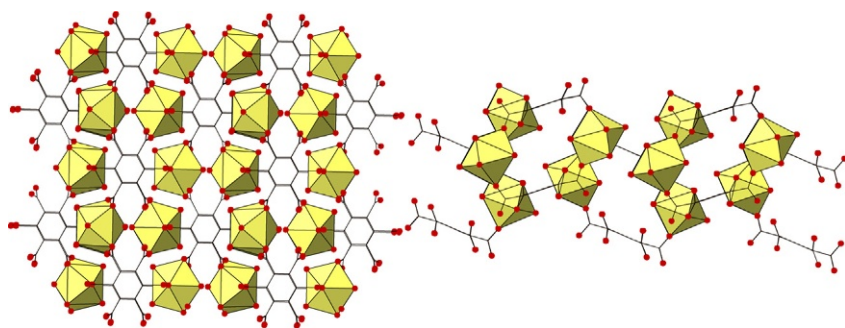


**FIGURE 20** (*Left*) Polyhedral representation of Ce-mellitate hybrid from Volkringer et al. (2012) showing connection of mellitate anions with discrete $Ce^{3+}$ polyhedra. (*Right*) Polyhedral representation of Ce-mellitate hybrid highlighting narrow channels delimited by bound water molecules. Yellow (white in the print version) polyhedra represent $Ce^{3+}$ metal centers.

with the syntheses of these materials, yet their efforts have been tempered by poorly crystalline materials that are the result of a rate of crystal nucleation and growth that may be too fast for single crystal formation (Almeida Paz et al., 2014). As such, much of the structural analysis conducted by Rocha, Almeida Paz, and others has been via full Rietveld refinement from powder X-ray diffraction, which is somewhat uncommon for lanthanide hybrid materials. In fact, these materials may represent a hard-soft acid-base (HSAB) pairing that is *too* good as the 'hard' $Ln^{3+}$ pair so well with the "hard" phosphonate groups that the crystallization process proceeds too quickly. Even with the outlined complications, the nature of the phosphonate group has yielded some very interesting materials as first shown by Serpaggi and Férey (1998, 1999b) in their syntheses of MIL-11 and MIL-19. Following the initial findings of Férey and Serpaggi, Zheng and colleagues (Cao et al., 2005) hydrothermally synthesized a 1D CP with $Gd^{3+}$ and hydroxy(4-pyridyl)methylphosphonic acid that features a $Gd^{3+}$ metal center with a coordination number of six, which is unusual for lanthanide hybrid materials containing O-donor linkers, yet surprisingly common within the Ln-phosphonate class of materials.

Almeida Paz, Rocha, and others stated that their interest in Ln-phosphonate hybrids stems from the phosphonate moiety's ability to chelate a $Ln^{3+}$ cation while also possessing three oxygen atoms in a tetrahedral molecular geometry, which can mimic the building units of zeolites (Silva et al., 2011). Zeolites (and similar materials) possess building units that are capable of anchoring to a wide range of metals and often induce formation of networks with high thermal and mechanical robustness (an important prerequisite for many CP and MOF applications). Using a phosphonate linker very similar to 1,3,5-BTC (benzene-1,3,5-triyltris(methylene)triphosphonic acid{$H_3$bmt}), Almeida Paz and coworkers (Vilela et al., 2012) synthesized four MOFs (with Ln=La—Nd) where chains of edge-sharing $LnO_8$ polyhedra (assembled via M–O–M linkages) are further assembled in three dimensions via multiple phosphonate linkers (Fig. 21). These MOFs are thermally robust, show characteristic luminescence (with the Eu and Tb analogues), and showed promise as a heterogeneous catalyst for the ring opening of styrene oxide with methanol. When using this same phosphonate ligand with smaller $Ln^{3+}$ cations, and slightly different synthesis conditions, Almeida Paz and colleagues (Almeida Paz et al., 2014) were able to synthesize eight isomorphous zeolite-like materials that feature lanthanide cations with a coordination number of six (as seen previously in the 1D CP synthesized by Zheng and collaborators (Cao et al., 2005)). More recently, the same group functionalized the benzene-1,3,5-triyltris(methylene)triphosphonic acid ligand with fluorine to form 2,4,6-trifluorobenzene-1,3,5-triyltris(methylene)triphosphonic acid and the result of including this ligand with $La^{3+}$ was a 2D CP with heptacoordinated $La^{3+}$ cations (Vilela et al., 2014). As these highlights have really only scratched the surface on this burgeoning class of hybrid materials, we point the reader to two excellent reviews from Rocha, Almeida Paz, and others on phosphonate
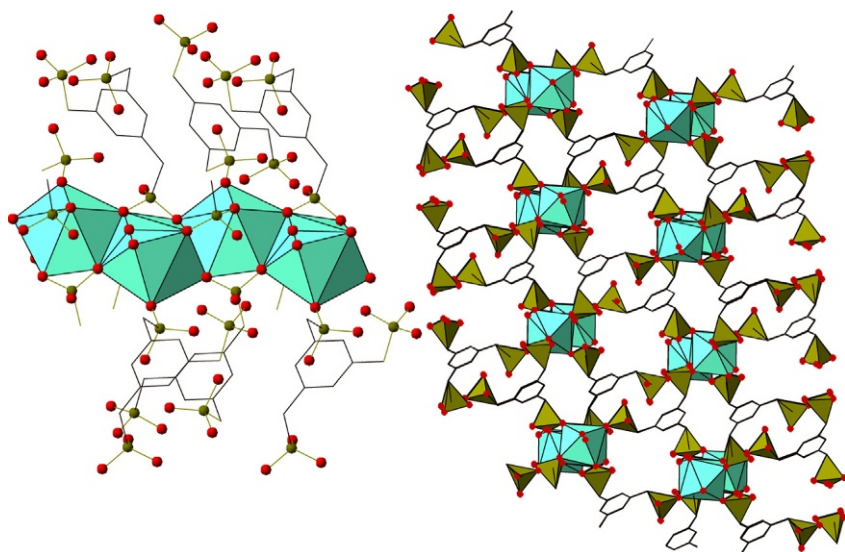
**FIGURE 21** (*Left*) Polyhedral representation of fragment of 1D chain SBU of M–O–M linkages in La-H$_3$bmt material synthesized and characterized by Vilela et al. (2012). (*Right*) Crystal packing of La-H$_3$bmt material shown in the (101) plane. Teal (light gray in the print version) polyhedra represent La$^{3+}$ polyhedra, whereas yellow (dark gray in the print version) polyhedra and spheres represent phosphorus atoms.

ligand design for MOF synthesis (Almeida Paz et al., 2012) as well as the many potential applications of Ln-phosphonates hybrids (Rocha et al., 2011).

## 2.4 Ln-O Hybrid Materials with Chelating Ligands

The use of ancillary ligands in lanthanide CPs serves a twofold purpose. First, it can change the dimensionality of the lanthanide CP by chelating part of the lanthanide first coordination sphere, thereby limiting the space with which linking ligands have to coordinate. Second, the use of an ancillary ligand reduces interpenetration, which results in an increase in pore volume and overall thermal stability. As many of the ideal applications of porous CPs are determined almost exclusively by the porosity and stability of the CP, it is of the utmost importance to control interpenetration, which often leads to partial collapse of the CP upon guest molecule removal, a first step in many of the aforementioned application processes. HSAB preferences are taken into account when selecting a chelating ligand for lanthanide hybrid material synthesis, as one would require a ligand with moderate affinity for Ln$^{3+}$ cation, yet not one with such a strong affinity or sterics hindrance that it will prevent further coordination by O-donor ligands. The best-known example of a chelating ligand that adopts the described role is the bidentate N-donor

1,10-phenanthroline (phen) which has proven over time to be a versatile starting material for inorganic and supramolecular synthesis (more on this later). Phen is a rigid, planar, electron-poor heteroaromatic system with nitrogen atoms ideally placed for binding of large cations (Bencini and Lippolis, 2010; Hancock and Martell, 1989). In aqueous solution, phen behaves as a weak base and displays a moderate affinity for Ln(III) cations likely due to its preorganization (Hancock, 2013). Additionally, phen and other chelating coligands are excellent luminescent antennas, as their delocalized π-electron systems allow for efficient absorption of incident light and corresponding sensitization of the $Ln^{3+}$ excited states via ligand to metal energy transfer.

Jin and colleagues did some of the pioneering work in this area of hybrid material development with the chelating ligand phen and both aliphatic (Huang et al., 2004) and aromatic O-donor linkers (Wan et al., 2003; Zhang et al., 2003; Zheng et al., 2004c, 2005a). Chen and colleagues (Liu et al., 2002) were one of the first groups to utilize 2,2′-bipyridine (2,2′-BPY) in the synthesis of CPs with terbium and characterized two materials, a 2D CP and an MOF, containing the O-donor linker 4,4′-oxy(bis)benzoic acid and 2,2′-BPY with the different materials a result of changing the base used during synthesis. Comparing these results to another work of Jin and coworkers (Wang et al., 2004b) on the synthesis of Ln-4,4-oxy(bis)benzoic acid-phen hybrid materials highlights the differences between 2,2′-BPY and phen as coligands in Ln hybrid material synthesis. The materials characterized by Jin and colleagues are 1D chains that are further assembled into an overall 3D structure via a combination of hydrogen-bonding and π–π stacking interactions that are facilitated by the phen coligands. This same motif is seen in the hybrid materials synthesized by Zheng and collaborators (Li et al., 2009) with 1,3-adamantanedicarboxylic acid and phen and to some extent by Song and colleagues (Song et al., 2008) with 3,4-pyridinedicarboxylic acid and phen, and by Jin and colleagues (Liu et al., 2004) in hybrid materials synthesized from 2-aminoBDC and phen, although in these latter two examples we see further assembly of 2D sheets (Fig. 22). Structural variability based on synthesis conditions was also observed in lanthanide hybrids with 1,3-benzenedicarboxylic acid (1,3-BDC) and 2,2′-BPY that were characterized by Natarajan and collaborators (Thirumurugan and Natarajan, 2006) yet Zhang did not observe similar results when he used a functionalized version of 1,3-BDC and 2,2′-BPY in the synthesis of a novel $Gd^{3+}$ material (Zhang, 2011).

Enhancing the application potential of an Ln hybrid material via the inclusion of a chelating ligand is a topic of continued interest as researchers work to increase the porosity of MOFs by reducing interpenetration, while concurrently enhancing thermal stability. The group of Sun and Zhou (He et al., 2010) solvothermally synthesized Ln MOFs with a similar topology to MOF-6, which featured 1,4-BDC linkers and $H_2O$ and DMF molecules. They then replaced the coordinated solvate molecules with phen ligands to form a
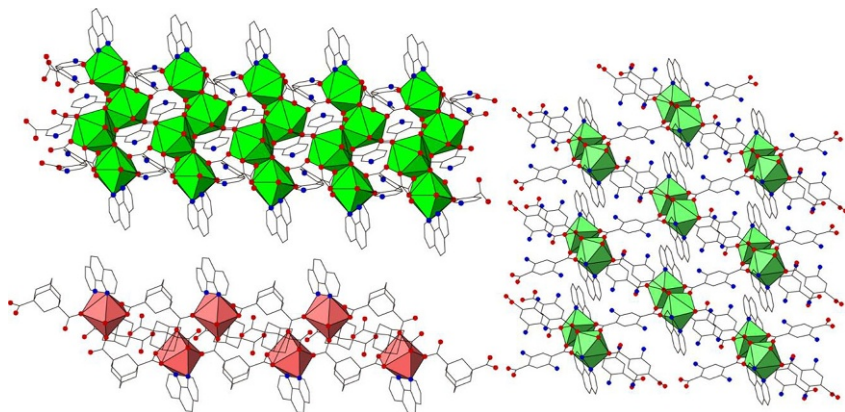
**FIGURE 22** Polyhedral representations highlighting the SBUs of lanthanide hybrid materials featuring both an aromatic O-donor linker and the chelating N-donor phen. Clockwise from top left: 2D sheet of Tb-3, 4-pyridinedicarboxylic acid-phen material from Song et al. (2008), 2D sheet of Er-2aminoBDC-phen material from Liu et al. (2004), 1D chain of Eu-1,3-adamantanedicarboxylic acid-phen material from Li et al. (2009). Green (light gray in the print version) polyhedra represent $Tb^{3+}$ metal centers, whereas light green (gray in the print version) and red (gray in the print version) polyhedra represent $Er^{3+}$ and $Eu^{3+}$ metal centers, respectively.

more stable MOF and then enhanced it further (in terms of reducing interpenetration) by replacing the 1,4-BDC linker with the functionalized 2,3,5,6-tetramethylBDC. The resulting MOF featuring the tetramethylBDC and phen demonstrated adsorption selectivity of $CO_2$ and $H_2$ over $N_2$ and Ar. Further study by Sun and colleagues (He et al., 2013a) on this same system yielded three new MOFs featuring either 1,4-BDC or tetramethylBDC and phen although gas sorption properties of these materials did not show further enhancement from their first study.

Finally, we look at the results of a recent study by Li and collaborators (Cha et al., 2014) on lanthanide hybrid materials featuring 3-fluorophthalic acid and phen. Three isomorphous 2D networks were characterized and they feature nine-coordinate Ln metal centers (La, Eu, Tb) that are chelated by phen moieties and then linked via bridging bidentate 3-fluorophthalic acid ligands (Fig. 23). Beyond the characteristic emission spectra of the Eu and Tb isomorphs, Li and colleagues prepared a doped La complex (with Eu and Tb) that displayed white-light emission upon excitation at the absorption maxima of the phen chromophore.

## 3 MOLECULAR LN MATERIALS

As we have attempted to demonstrate, lanthanide CPs and MOFs represent a rich class of materials featuring a diverse suite of materials highlighted by an array of interesting structural topologies. Whereas the rich structural diversity
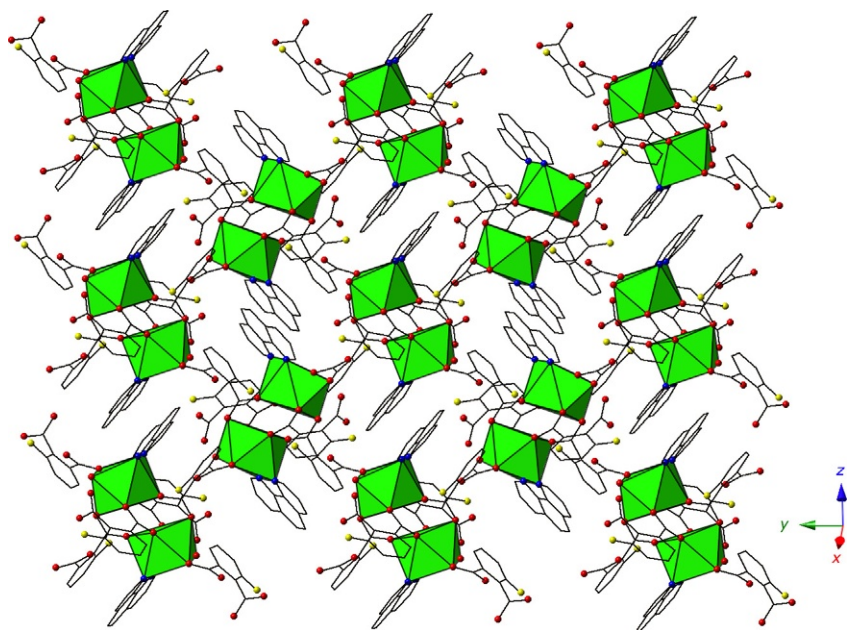
**FIGURE 23** Polyhedral representation of two-dimensional structure of Tb-3-fluorophthlate-phen material from Cha et al. (2014) shown in the (011) plane. Green (gray in the print version) polyhedra represent $Tb^{3+}$ metal centers, whereas yellow (light gray in the print version) spheres represent fluorine atoms. Lattice water molecules have been omitted for clarity.

of these materials has proven fruitful for exploration, the ability to direct the formation of a specific building unit under hydrothermal conditions remains challenging and elusive. Within our GWMOF series, and other similar Ln-aliphatic studies, 1D chains of edge-sharing hydrated polyhedra were found to be a reoccurring SBU, yet when a more rigid linker (i.e. an aromatic carboxylate) is used in Ln hybrid material synthesis, an increased variety of resulting SBUs are observed. These variations can likely be attributed to the limitations of utilizing linkers based on HSAB preferences and the effects of chelation on $Ln^{3+}$ bonding (and extended coordination). Whereas hydrolysis is certainly at play, although not in the strictest sense, the absence of hydroxyl and oxide species so often observed with the uranyl (and other actinide) species (Andrews and Cahill, 2013; Knope and Soderholm, 2013) suggests that lanthanide oligomerization proceeds via a slightly different mechanism. As such, one may look to the extensive work done on the coordination chemistry of *molecular* lanthanide compounds to better understand mechanisms for controlling the first coordination sphere and disrupting oligomerization processes. Motivations for such a strategy in molecular chemistry include the delineation of structure–property relationships so that one may selectively tune the properties of a material such as luminescence via the

reduction of high-energy oscillators (Bischof et al., 2010; Doffek et al., 2012; Wahsner and Seitz, 2013), maximizing magnetic anisotropy of a material (Cucinotta et al., 2012; Hutchings et al., 2014; Yanagida et al., 1998), or lanthanide/minor actinide separations in nuclear waste reprocessing (Drew et al., 2000; Kolarik, 2008). Our own efforts have made use of this approach, yet with a crystal engineering focus, wherein we are also interested in the promotion of extended structures with desired geometries via the use of noncovalent interactions. We will therefore review molecular lanthanide materials through both the traditional coordination chemistry lens, as well as our own mindset where greater attention will be paid to crystal engineering and assembly of molecular species.

The coordination chemistry of lanthanide molecular complexes has been studied rather extensively and we will thus not present an in-depth treatment. Much of the early work in this area has been reviewed quite thoroughly by the Bünzli and Piguet groups (Bünzli, 2006; Bünzli and Piguet, 2002, 2005; Piguet and Bünzli, 1999), and aspects have been reviewed on multiple occasions in this forum (Binnemans, 2005; Comby and Bünzli, 2007; Nief, 2010; Nishioka et al., 2007; Piguet and Bünzli, 2010; Shinoda et al., 2005). Additionally, in-depth treatments of features of Ln coordination chemistry can be found in the more recent works of Bünzli (Bünzli and Piguet, 2002; Bünzli et al., 2010; Eliseeva and Bunzli, 2010), Wong (Wong et al., 2007), Bulach and colleagues (Bulach et al., 2012), Gunnlaugsson (Bradberry et al., 2014), and Bettencourt-Dias (De Bettencourt-Dias, 2007; De Bettencourt-Dias et al., 2014). More recent efforts have also explored the promising applications of molecular lanthanide materials which include electroluminescent materials (Katkova and Bochkarev, 2010; Kido and Okamoto, 2002; Lima et al., 2014), materials displaying nonlinear optical properties (Andraud and Maury, 2009; Sénéchal-David et al., 2006; Tancrez et al., 2005), those used in medical imaging (Bradberry et al., 2014; Bünzli, 2009, 2010; Reddy et al., 2013), and as single-ion and single-molecule magnets (Feltham and Brooker, 2014; Habib and Murugesu, 2013; Luzon and Sessoli, 2012; Woodruff et al., 2013). Precise control over the first coordination sphere is critical for harnessing the aforementioned properties and has also allowed for the study of supramolecular assembly in the lanthanide solid state. Whereas a challenge in the hydrothermal synthesis of CPs and MOFs is largely promoting a single SBU of choice, an analogous challenge for molecular materials is in directing desired arrangements.

Many efforts to control Ln(III) coordination have traditionally incorporated chelating N-donors such as 2,2′-BPY, phen, or 2,2′:6′,2″-terpyridine (terpy). Beyond the structural contributions, these ligands can also function as antennae molecules (Bekiari and Lianos, 2000, 2004; Mürner et al., 2000). With their work on the complexation of $Ln^{3+}$ cations with aliphatic carboxylates and chelating N-donors, White and coworkers (Kepert et al., 1994, 1999; Semenova and White, 1999; Semenova et al., 1999) pioneered

work in this arena and Cotton et al. (2003a,b) continued work in this area by synthesizing Ln molecular complexes featuring terpy and various anions ($NO_3^-$, $SCN^-$). In each of these materials, the authors utilized the strong binding affinity that terpy exhibits for $Ln^{3+}$ cations, which may assist the crystallization process (Hancock, 2013). Our perspective on these results is that the terpy ligands are interrupting oligomerization as the terpy moieties lock up (*cap*) one part of the coordination sphere, which then directs further coordination of additional ligands and solvent molecules. This same behavior is observed in lanthanide molecular coordination complexes with functionalized terpy ligands that have shown great promise for a number of applications (De Bettencourt-Dias et al., 2014).

Moving now to the very similar pyridine-bis(oxazoline) (Pybox) class of chelating ligand, Bettencourt-Dias and colleagues have shown that this heterofunctional N-donor can play a very similar role to terpy. Featuring both oxazoline and pyridine functional groups, the ligands are tridentate, stable, and likely good antenna molecules due to their electronic absorption properties. After first synthesizing a thiophene derivative of Pybox and finding that it was a highly efficient sensitizer of both Eu(III) and Tb(III) (De Bettencourt-Dias et al., 2007), De Bettencourt-Dias et al. (2010) prepared a series of *para*-derivatized Pybox ligands and then used them in the synthesis of a series of new lanthanide complexes. Of note in the resulting materials was complex **3**, [$Eu(C_{11}H_6BrN_3O_2)(NO_3)_3(H_2O)$], which features a 10-coordinate europium metal center bound to a bromo-Pybox ligand as well as three nitrates and a bound water molecule (Fig. 24). The europium units are then assembled via
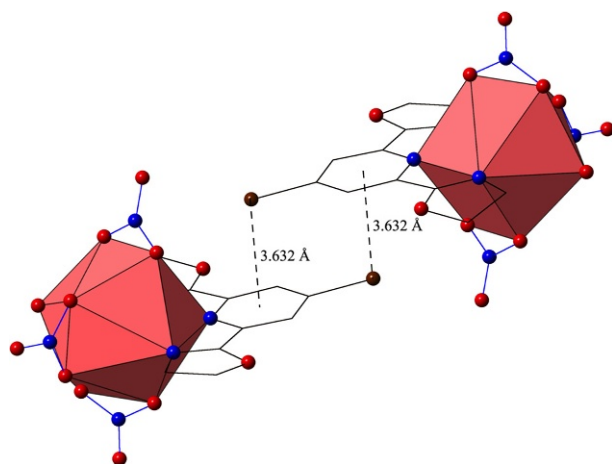


**FIGURE 24** Polyhedral representation of two molecules of complex **3**, [$Eu(C_{11}H_6BrN_3O_2)$ $(NO_3)_3(H_2O)$], from De Bettencourt-Dias et al. (2010) highlighting delocalized Br–π interactions that link neighboring $Eu^{3+}$ monomers. Red (light gray in the print version) polyhedra represent $Eu^{3+}$ metal centers, whereas brown (black in the print version) spheres represent bromine atoms. Hydrogen atoms have been omitted for clarity.

a synergistic combination of hydrogen-bonding and halogen–π interactions. The latter interaction is of note as it is one of the few examples of this supramolecular synthon in a lanthanide molecular complex. The authors then went on to look at the luminescent properties and stability constants of the Pybox derivatives without looking further into the means of assembly they observed. A follow-up from the Bettencourt-Dias group (De Bettencourt-Dias et al., 2012) continued to look at lanthanide complexes with Pybox derivatives, this time with an ethylene glycol ethyl ether functional group, and found that in the resulting materials the Pybox derivative was an efficient sensitizer in both the visible and near-IR regions in a range of solvents. Similar to the terpy complexes discussed previously, Pybox and its derivatives are another class of ligands capable of controlling the lanthanide first coordination sphere. The assembly of the Eu(III) complexes with bromo-Pybox illustrated that with judicious choice of synthons at the periphery of the first coordination sphere, it is also possible to control the lanthanide second coordination sphere.

Whereas the assembly strategies of other researchers discussed thus far are generally implicit as they focus on other properties of the materials they have synthesized, we attempt to make explicit the simultaneous control of the lanthanide first coordination sphere via use of a capping ligand, while judicially placing synthons at the periphery (e.g., halogens) to explore the assembly of molecular structures with desired arrangements. Moreover, we make use of the mindset discussed thus far, wherein hydrothermal synthesis is used to generate oligomerized species and then a chelating N-donor is used to promote a single polynuclear building unit. Once the building unit has been "selected," we build on this by looking into the assembly thereof via noncovalent interactions originating from synthons at the periphery of the coordination sphere. Before we delve into our work on promoting extended molecular structures with desired arrangements, however, a brief discussion of supramolecular assembly and crystal engineering is in order.

Crystal engineering is a branch of supramolecular chemistry that attracts attention from a broad spectrum of chemists. Crystal engineering is concerned with the nature and structural consequences of intermolecular forces and the ways in which these interactions are utilized for controlling the assembly of molecular building blocks into extended architectures. Succinctly summarized by Braga as "making crystals by design" (Braga, 2003), crystal engineering is an understanding of intermolecular interactions in the context of crystal packing and metal–ligand coordination, which can allow for one to address some of the challenges associated with the diverse speciation profile of the lanthanide cations manifested in hydrothermally produced hybrids. The challenge evolves to forming reproducible units (tectons) decorated with appropriate synthons, described by Desiraju (1995) as "structural units within supermolecules which can be formed and/or assembled by known or conceivable synthetic operations involving intermolecular interactions." This is a concept that has been explored for

transition metal chemistry (Alexeev et al., 2010), the actinide series (Andrews and Cahill, 2013; Baker, 2012; although not to the same extent), and by our group with the lanthanide series (Carter et al., 2014a,b).

From our perspective, once a reliable tecton is presented one can then focus on functionalization for supramolecular assembly. More specifically, we have focused on supramolecular assembly via halogen bonding, defined by IUPAC (Desiraju et al., 2013) as "the net attractive interaction between an electrophilic region associated with a halogen atom in a molecular entity and a nucleophilic region in another, or the same, molecular entity." Halogens can participate in a number of favorable acceptor–donor pairings with other halogens, cations, and anions and thus represent a particularly attractive class of synthons. Couple this with the wide array of possible applications of supramolecular assembly in the solid state, which include drug design (Lu et al., 2009; Wilcken et al., 2013), catalysis (Knowles and Jacobsen, 2010; Tang et al., 2013), and nanomaterials (Dinolfo and Hupp, 2001; Kudernac et al., 2009), and one may imagine a field with great potential. In molecular lanthanide systems, most of the attention regarding supramolecular interactions has been focused on hydrogen-bonding and π–π stacking interactions (Bünzli and Piguet, 2002; Liu et al., 2004; Thuéry, 2012; Ye et al., 2008), yet assembly via primarily halogen bonding remains an area that has not been explored as comprehensively. Additionally, as we have mentioned earlier, we have also made explicit the strategy explored implicitly by others where we set out to synthesize materials that would allow for the exploration of the criteria for the promotion of extended structures with desired arrangements.

To highlight this approach, we expanded on four previous one-structure studies (Jin et al., 1996; Li et al., 2008b; Song et al., 2013; Wang et al., 2007b) by synthesizing the complete series of rare earth molecular materials with the organic ligands p-chlorobenzoic acid and phen (Carter et al., 2014b). As we moved across the entire rare-earth series, we observed an evolution in the local structure of the binuclear units that was a result of the lanthanide contraction, which resulted in changes in modes of assembly in the second coordination sphere (Fig. 25). Complex **1**, $[La(C_{12}H_8N_2)(C_7H_4ClO_2)_3(H_2O)]_2$, with lanthanum, featured a nine-coordinate $La^{3+}$ metal cation which was chelated by phen and then further coordinated to p-chlorobenzoic acid ligands adopting three coordination modes: chelating-bridging bidentate, bridging bidentate and monodentate, and a bound water molecule. A pair of moderately strong (Mooibroek et al., 2008) Cl–π interactions between a p-chlorobenzoic ligand on one unit with phen moieties on neighboring units facilitated assembly of the binuclear tectons of **1** into a supramolecular 1D chain. Halogen–π interactions are defined as moderate to strong lone pair–π interactions by Reedijk and collaborators (Mooibroek et al., 2008) based on whether they are less than or equal to the corresponding sum of the van der Waals radii (3.450 Å for chlorine and carbon). Further
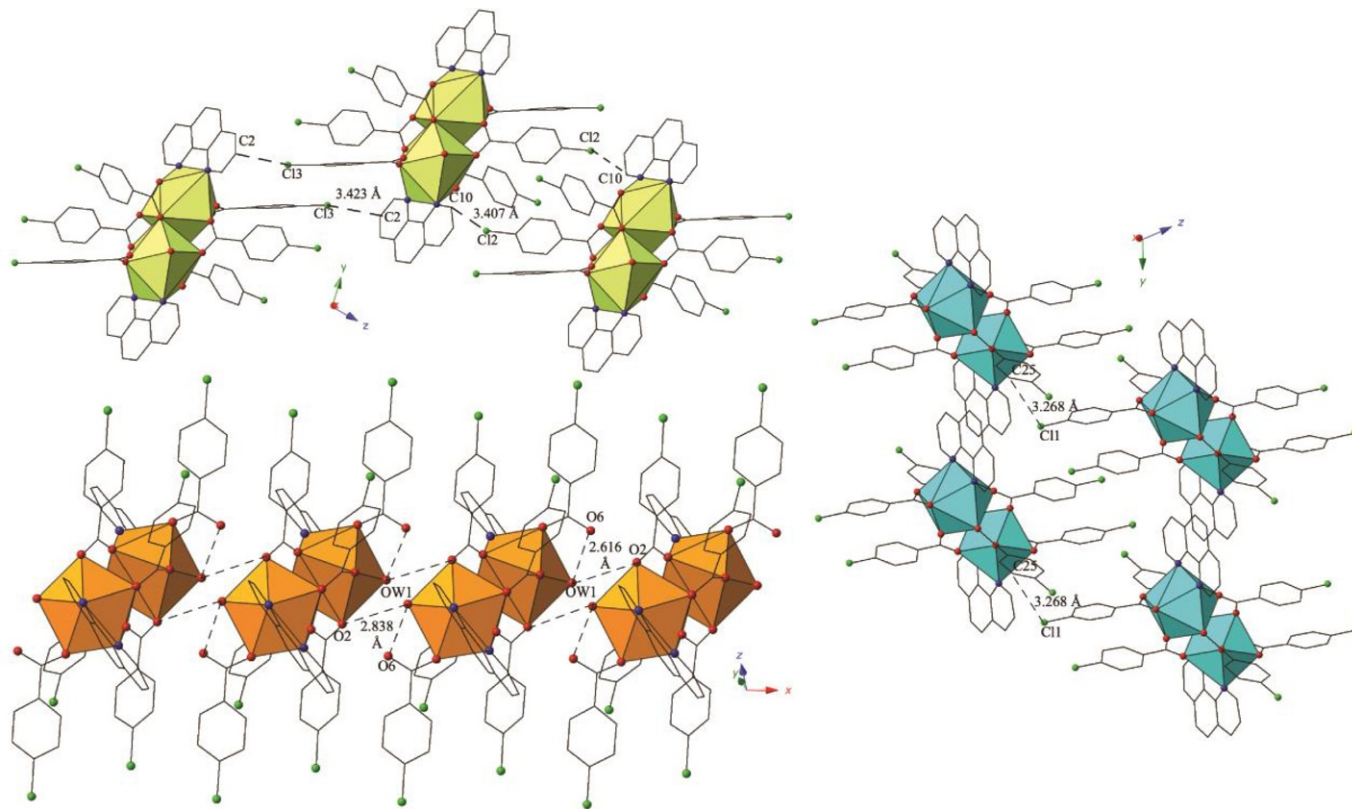
**FIGURE 25** Polyhedral representations of R-*p*-chlorobenzoic acid-phen materials highlighting variations in supramolecular assembly modes structure types I–III. Clockwise from top left, we have 1D chain assembled via combination of Cl–π interactions, 1D chain linked via Cl–π interactions between *p*-chlorobenzoic acid ligands, and 1D chain tethered via bifurcated hydrogen-bonding interactions. Further assembly via slightly offset π–π interactions in all structure types I–III not shown. *Adapted with permission from Carter et al. (2014a). Copyright 2014, Royal Society of Chemistry.*

assembly of **1** into a 2D sheet is a result of slightly offset π–π interactions that are a constant throughout this series. Moving to the right yielded a second binuclear tecton (with Ce-Nd) where the lanthanide cations were chelated by the phen molecules and then coordinated to bridging bidentate and monodentate *p*-chlorobenzoic acid ligands and a bound water molecule. Assembly into a 1D chain was facilitated by bifurcated hydrogen-bonding interactions before slightly offset π–π interactions once again linked the tectons into a 2D sheet (Fig. 25). The third structure type in the series that was observed for the rare-earth cations ranging from $Sm^{3+}$ to $Y^{3+}$ was also a binuclear tecton was very similar to structure type II (with Ce-Nd) except the first coordination sphere was devoid of a coordinated solvent molecule. As the first coordination sphere molecular geometry was now different we once again observed assembly of the binuclear tectons into a 1D chain via halogen–π interactions before the chains were further tethered via slightly offset π–π interactions into a 2D sheet (Fig. 25).

Moving on to a similar series of materials featuring the *p*-chlorobenzoic acid ligand and the tridentate terpy, we saw a similar evolution in modes of supramolecular assembly that was coupled with some variance in lanthanide building unit that is correlated to a decrease in lanthanide ionic radii (Carter et al., 2014a). Binuclear tectons were once again observed with the larger $Ln^{3+}$ cations (Pr-Eu) and these units utilized either slightly offset π–π or type II halogen–halogen interactions for assembly into 1D chains (Fig. 26). Halogen–halogen interactions tend to adopt one of two geometries in order to minimize the overlap of regions of negative charge density (Awwadi et al., 2006; Brammer et al., 2008) and the interactions used to link together the neodymium tectons in Fig. 26 meet the criteria described by Desiraju and collaborators (Desiraju and Parthasarathy, 1989; Mukherjee et al., 2014) for a type II halogen–halogen interaction. Mononuclear tectons were observed with the smaller rare-earth cations (Gd-Y) and were also observed with $Sm^{3+}$ and $Eu^{3+}$ at higher (>150 °C) synthesis temperatures. These mononuclear units were linked via hydrogen-bonding interactions to become supramolecular dimers and then were further assembled via a combination of halogen–π and offset π–π interactions, similar to the Ln-*p*-chloro-phen materials described above, into a 2D sheet (Fig. 26).

The preference for binuclear (or larger) SBUs with larger $Ln^{3+}$ cations seen in our first two works has been confirmed in a series of follow-up studies that are, at present, still ongoing. Additionally, the tendency of phen to promote binuclear tectons has been observed independent of the benzoic acid ligand, yet the mechanism for this result remains elusive. Establishment of a hierarchy of donor–acceptor pairings is also still ongoing and will require additional results before any definitive results can be reported. Halogen bonding does seem to play an important role in lanthanide supramolecular assembly, however, and further understanding of the processes involved will likely be a process that involves both modeling and experiment.
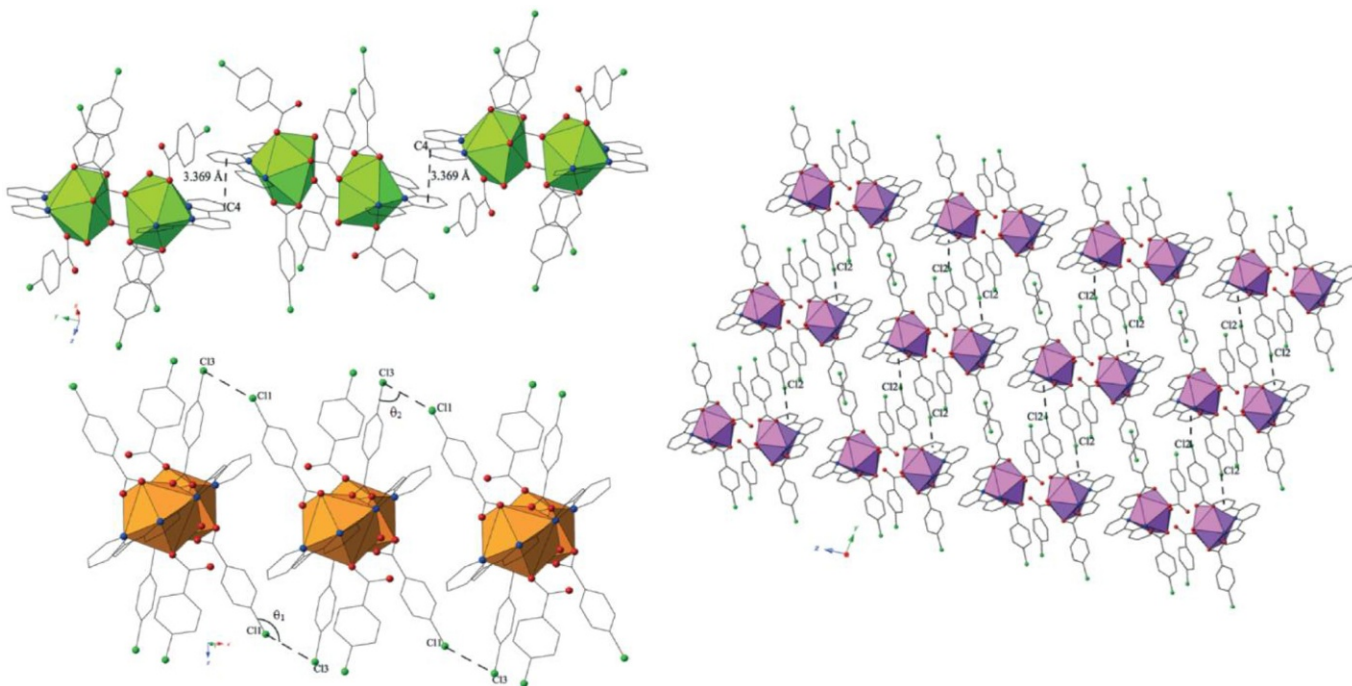
**FIGURE 26** Polyhedral representations of R-*p*-chlorobenzoic acid-TPY materials highlighting variations in supramolecular assembly modes structure types I–III. Clockwise from top left, we have 1D chain assembled via slightly offset π–π interactions, 2D sheet that results from linking via bifurcated hydrogen-bonding interactions and further tethering via delocalized Cl–π interactions between *p*-chlorobenzoic acid and TPY ligands, and 1D chain assembled via type II halogen–halogen interactions. *Adapted with permission from Carter et al. (2014b). Copyright 2014, Royal Society of Chemistry.*

## 4 SUMMARY AND OUTLOOK

The past decade has been a very productive period for the further development of lanthanide hybrid, both extended and molecular materials. Work has moved beyond the serendipitous discoveries that yielded some of the early lanthanide materials to a more crystal engineering centric approach where efforts to rationally design materials with specific topologies and properties are being realized. As both lanthanide hybrid and molecular materials have shown promise in a wide array of applications, research in this area continues to generate excitement and interest.

Significant progress notwithstanding, there is still tremendous potential for further development in both of the main areas of lanthanide materials we have highlighted. Whereas the syntheses of transition metal and main group hybrid materials can for the most part be controlled and predicted, this is still a challenge for the lanthanides as the consistent formation of predictable primary and SBUs remains challenging, even with development of new synthesis techniques (i.e., microwave- and ultrasound-assisted synthesis; Khan and Jhung, 2015). Further, while applications of these materials have shown promise, only gas sorption has really reached an advanced level of understanding. Lanthanide hybrid materials for catalysis require additional study to determine their mechanical stability, long-term stability, and to better elucidate the mechanism of Ln CP-catalyzed reactions (Gascon et al., 2013). Very little is currently known about the mechanical properties of lanthanide hybrid materials, which has implications for catalysis as well as separations where these materials would likely encounter abrasive conditions (Allendorf and Stavila, 2015).

Regarding molecular materials, the challenges going forward in the design of materials primarily of a synthetic origin. Harnessing luminescent and magnetic properties often requires specific metal-ion symmetry and coordination environments so precise control over the first coordination sphere is a matter of the utmost importance. Similar to lanthanide-extended structures, control over the lanthanide coordination sphere remains a challenge, as metal–ligand bonding is dependent on a large number of variables. Two routes are emerging for the synthesis of lanthanide molecular materials with desired properties going forward. Many researchers are focusing on ligand design as a means of synthesizing a lanthanide molecular material of choice, which is a method with promise, although it often does require multistep organic synthesis. The second route, which has been the focus of our group, is to utilize noncovalent interactions, specifically halogen-bonding interactions, as a means of assembling molecular materials. In the organic solid state, this method has shown significant promise (Metrangolo and Resnati, 2012; Meyer and Dubois, 2013; Priimagi et al., 2013) and further efforts within the realm lanthanide materials will hopefully prove equally rewarding.

We have attempted to demonstrate throughout this chapter that synthesis and characterization of lanthanide hybrid materials is a rich field that warrants

further research efforts. Where possible we have highlighted the intriguing structural aspects of these materials and reported on their promise in many different applications. We feel confident in predicting that over the course of the next decade, research efforts in lanthanide hybrid materials chemistry will continue to grow as materials are optimized and many useful applications of this class of materials that have yet to be realized come to fruition so as to require another chapter in this forum.

## ACKNOWLEDGMENTS

## ABBREVIATIONS

| | |
|---|---|
| **1,3,5-BTC** | 1,3,5-benzenetricarboxylic acid |
| **1,3-BDC** | 1,3-benzenedicarboxylic acid |
| **1,4-BDC** | 1,4-benzenedicarboxylic acid |
| **1,4-NDC** | 1,4-naphthalenedicarboxylic acid |
| **1D** | one-dimensional |
| **2,2′-BPY** | 2,2′-bipyridine |
| **2,3-PYDC** | 2,3-pyridinedicarboxylic acid |
| **2,3-PZDC** | 2,3-pyrazinedicarboxylic acid |
| **2,4,6-PYTC** | 2,4,6-pyridinetricarboxylic acid |
| **2,5-PYDC** | 2,5-pyridinedicarboxylic acid |
| **2,6-NDC** | 2,6-naphthalenedicarboxylic acid |
| **2,6-PYDC** | 2,6-pyridinedicarboxylic acid |
| **2D** | two-dimensional |
| **3,5-PYZDC** | 3,5-pyrazoledicarboxylic acid |
| **3D** | three-dimensional |
| **BPDC** | 4,4′-biphenyldicarboxylic acid |
| **CPs** | coordination polymers |
| **FDC** | furan-2,5-dicarboxylic acid |
| **H₃bmt** | benzene-1,3,5-triyltris(methylene)triphosphonic acid |
| **MOFs** | metal–organic frameworks |
| **Phen** | 1,10-phenanthroline |
| **Pybox** | pyridine-bis(oxazoline) |
| **SBUs** | secondary building units |
| **TDC** | thiophene-2,5-dicarboxylic acid |
| **Terpy** | 2,2′:6′,2″-terpyridine |
| **tetranitroBPDC** | 2,2′,6,6′-4,4′-biphenyldicarboxylic acid |

# REFERENCES

Abrahams, B.F., Hoskins, B.F., Michail, D.M., Robson, R., 1994. Assembly of porphyrin building blocks into network structures with large channels. Nature 369, 727–729.

Akerboom, S., Fu, W.T., Lutz, M., Bouwman, E., 2012. Crystal structure and luminescence of complexes of Eu(III) and Tb(III) with furan-2,5-dicarboxylate. Inorg. Chim. Acta 387, 289–293.

Alexeev, Y.E., Kharisov, B.I., García, T.C.H., Garnovskii, A.D., 2010. Coordination motifs in modern supramolecular chemistry. Coord. Chem. Rev. 254, 794–831.

Allen, F., 2002. The Cambridge structural database: a quarter of a million crystal structures and rising. Acta Crystallogr. B 58, 380–388.

Allendorf, M.D., Stavila, V., 2015. Crystal engineering, structure-function relationships, and the future of metal-organic frameworks. CrystEngComm 17, 229–246.

Allendorf, M.D., Bauer, C.A., Bhakta, R.K., Houk, R.J.T., 2009. Luminescent metal-organic frameworks. Chem. Soc. Rev. 38, 1330–1352.

Almeida Paz, F.A., Klinowski, J., 2003. Hydrothermal synthesis of a novel thermally stable three-dimensional ytterbium-organic framework. Chem. Commun., 1484–1485.

Almeida Paz, F.A., Klinowski, J., 2008a. Poly[[[μ]2-aqua-tetraaquahexakis([μ]4-naphthalene-2,6-dicarboxylato)tetraholmium(III)] 1.75-hydrate]. Acta Crystallogr. Sect. E 64, m336–m337.

Almeida Paz, F.A., Klinowski, J., 2008b. Poly[hexaaquabis([μ]3-naphthalene-2,6-dicarboxylato)([μ]2-naphthalene-2,6-dicarboxylato)diholmium(III)]. Acta Crystallogr. Sect. E 64, m140–m141.

Almeida Paz, F.A., Klinowski, J., Vilela, S.M.F., Tome, J.P.C., Cavaleiro, J.A.S., Rocha, J., 2012. Ligand design for functional metal-organic frameworks. Chem. Soc. Rev. 41, 1088–1110.

Almeida Paz, F.A., Vilela, S.M.F., Tomé, J.P.C., 2014. Layered metal–organic frameworks based on octahedral lanthanides and a phosphonate linker: control of crystal size. Cryst. Growth Des. 14, 4873–4877.

Andraud, C., Maury, O., 2009. Lanthanide complexes for nonlinear optics: from fundamental aspects to applications. Eur. J. Inorg. Chem. 2009, 4357–4371.

Andrews, M.B., Cahill, C.L., 2013. Uranyl bearing hybrid materials: synthesis, speciation, and solid-state structures. Chem. Rev. 113, 1121–1136.

Andrews, P.C., Gee, W.J., Junk, P.C., Massi, M., 2013. Variation of structural motifs in lanthanoid hydroxo clusters by ligand modification. New J. Chem. 37, 35–48.

Awwadi, F.F., Willett, R.D., Peterson, K.A., Twamley, B., 2006. The nature of halogen···halogen synthons: crystallographic and theoretical studies. Chem. Eur. J. 12, 8952–8960.

Baes, C.F., Mesmer, R.E., 1976. The Hydrolysis of Cations. John Wiley and Sons, New York, NY.

Baker, R.J., 2012. New reactivity of the uranyl(VI) ion. Chem. Eur. J. 18, 16258–16271.

Batten, S.R., Champness, N.R., Chen, X.-M., Garcia-Martinez, J., Kitagawa, S., Ohrstrom, L., O'Keeffe, M., Suh, M.P., Reedijk, J., 2012. Coordination polymers, metal-organic frameworks and the need for terminology guidelines. CrystEngComm 14, 3001–3004.

Batten, S.R., Champness, N.R., Chen, X.-M., Garcia-Martinez, J., Kitagawa, S., Öhrström, L., O'Keeffe, M., Paik Suh, M., Reedijk, J., 2013. Terminology of metal-organic frameworks and coordination polymers. Pure Appl. Chem. 85, 1715–1724.

Bekiari, V., Lianos, P., 2000. New high-yield luminescent materials obtained by combining terpyridine, metal cations (including lanthanides), and poly(ethylene glycol). Adv. Mater. 12, 1603–1605.

Bekiari, V., Lianos, P., 2004. The unusual luminescence properties of 2,2′,2″-terpyridine-metal ion complexes. Chem. Phys. Lett. 383, 59–61.

Bencini, A., Lippolis, V., 2010. 1,10-Phenanthroline: a versatile building block for the construction of ligands for various purposes. Coord. Chem. Rev. 254, 2096–2180.

Benmerad, B., Guehria-Laidoudi, A., Dahaoui, S., Lecomte, C., 2004. The first suberate lanthanum(III) complex without uncoordinated water. Acta Crystallogr. C 60, m407–m409.

Bernini, M.A.C., Snejko, N., Gutierrez-Puebla, E., Brusau, E.V., Narda, G.E., Monge, M.A.N., 2011. Structure-directing and template roles of aromatic molecules in the self-assembly formation process of 3D holmium–succinate MOFs. Inorg. Chem. 50, 5958–5968.

Binnemans, K., 2005. Rare-earth beta-diketonates. In: Gschneidner, K.A., Bünzli, J.-C.G., Pecharsky, V.K. (Eds.), Handbook on the Physics and Chemistry of Rare Earths. vol. 35. Elsevier, Amsterdam, pp. 107–272, Ch. 225.

Binnemans, K., 2009. Lanthanide-based luminescent hybrid materials. Chem. Rev. 109, 4283–4374.

Bischof, C., Wahsner, J., Scholten, J., Trosien, S., Seitz, M., 2010. Quantification of C−H quenching in near-IR luminescent ytterbium and neodymium cryptates. J. Am. Chem. Soc. 132, 14334–14335.

Black, C.A., Costa, J.S., Fu, W.T., Massera, C., Roubeau, O., Teat, S.J., Aromí, G., Gamez, P., Reedijk, J., 2009. 3-D lanthanide metal-organic frameworks: structure, photoluminescence, and magnetism. Inorg. Chem. 48, 1062–1068.

Borkowski, L.A., Cahill, C.L., 2004a. Poly[[aquaneodymium(III)]-[μ]3-decane-1,10-dicarboxylato-[μ]3-9-carboxynonanecarboxylato]. Acta Crystallogr. C 60, m159–m161.

Borkowski, L.A., Cahill, C.L., 2004b. Two novel three-dimensional Nd-adipates: influence of hydrothermal reaction temperature on framework topology. Inorg. Chem. Commun. 7, 725–728.

Bradberry, S.J., Savyasachi, A.J., Martinez-Calvo, M., Gunnlaugsson, T., 2014. Development of responsive visibly and NIR luminescent and supramolecular coordination self-assemblies using lanthanide ion directed synthesis. Coord. Chem. Rev. 273–274, 226–241.

Braga, D., 2003. Crystal engineering, where from? Where to? Chem. Commun., 2751–2754.

Brammer, L., Minguez Espallargas, G., Libri, S., 2008. Combining metals with halogen bonds. CrystEngComm 10, 1712–1727.

Bulach, V., Sguerra, F., Hosseini, M.W., 2012. Porphyrin lanthanide complexes for NIR emission. Coord. Chem. Rev. 256, 1468–1478.

Bünzli, J.-C.G., 2006. Benefiting from the unique properties of lanthanide ions. Acc. Chem. Res. 39, 53–61.

Bünzli, J.-C.G., 2009. Lanthanide luminescent bioprobes (LLBs). Chem. Lett. 38, 104–109.

Bünzli, J.-C.G., 2010. Lanthanide luminescence for biomedical analyses and imaging. Chem. Rev. 110, 2729–2755.

Bünzli, J.-C.G., 2014. Review: lanthanide coordination chemistry: from old concepts to coordination polymers. J. Coord. Chem. 67, 3706–3733.

Bünzli, J.-C.G., Piguet, C., 2002. Lanthanide-containing molecular and supramolecular polymetallic functional assemblies. Chem. Rev. 102, 1897–1928.

Bünzli, J.-C.G., Piguet, C., 2005. Taking advantage of luminescent lanthanide ions. Chem. Soc. Rev. 34, 1048–1077.

Bünzli, J.-C.G., Chauvin, A.-S., Kim, H.K., Deiters, E., Eliseeva, S.V., 2010. Lanthanide luminescence efficiency in eight- and nine-coordinate complexes: role of the radiative lifetime. Coord. Chem. Rev. 254, 2623–2633.

Cahill, C.L., De Lill, D.T., Frisch, M., 2007. Homo- and heterometallic coordination polymers from the f elements. CrystEngComm 9, 15–26.

Calderone, P.J., Plonka, A.M., Banerjee, D., Nizami, Q.A., Parise, J.B., 2013. Lanthanide metal-organic frameworks based on a thiophenedicarboxylate linker: characterization and luminescence. Solid State Sci. 15, 36–41.

Cao, D.-K., Li, Y.-Z., Song, Y., Zheng, L.-M., 2005. Three-, two-, and one-dimensional metal phosphonates based on [hydroxy(4-pyridyl)methyl]phosphonate: M{(4-C5H4N)CH(OH)

PO3} (H2O) (M = Ni, Cd) and Gd{(4-C5H4N)CH(OH)P(OH)O2}3·6H2O. Inorg. Chem. 44, 3599–3604.

Cao, H.-Y., Liu, Q.-Y., Gao, M.-J., Wang, Y.-L., Chen, L.-L., Liu, Y., 2014. Ionothermal syntheses, crystal structures and luminescence of three three-dimensional lanthanide-1,4-benzenedicarboxylate frameworks. Inorg. Chim. Acta 414, 226–233.

Carter, K.P., Pope, S.J.A., Cahill, C.L., 2014a. A series of Ln-p-chlorobenzoic acid-terpyridine complexes: lanthanide contraction effects, supramolecular interactions and luminescent behavior. CrystEngComm 16, 1873–1884.

Carter, K.P., Zulato, C.H.F., Cahill, C.L., 2014b. Exploring supramolecular assembly and luminescent behavior in a series of RE-p-chlorobenzoic acid-1,10-phenanthroline complexes. CrystEngComm 16, 10189–10202.

Cha, Y.-E., Li, X., Ma, D., Huo, R., 2014. Lanthanide complexes assembled from 3-fluorophthalate and 1,10-phenanthroline: syntheses, crystal structure, photoluminescence, and white-light emission. Eur. J. Inorg. Chem. 2014, 2969–2975.

Chang, Y., Shuai, Q., Pei, Z., 2013. Two luminescent complexes constructed from different metals with pyridine-2,4-dicarboxylic acid (H2PDC). J. Coord. Chem. 66, 3137–3148.

Chen, W., Yuan, H.-M., Wang, J.-Y., Liu, Z.-Y., Xu, J.-J., Yang, M., Chen, J.-S., 2003. Synthesis, structure, and photoelectronic effects of a uranium−zinc−organic coordination polymer containing infinite metal oxide sheets. J. Am. Chem. Soc. 125, 9266–9267.

Chen, X.-Y., Zhao, B., Shi, W., Xia, J., Cheng, P., Liao, D.-Z., Yan, S.-P., Jiang, Z.-H., 2005. Microporous metal−organic frameworks built on a Ln3 cluster as a six-connecting node. Chem. Mater. 17, 2866–2874.

Chen, B., Yang, Y., Zapata, F., Qian, G., Luo, Y., Zhang, J., Lobkovsky, E.B., 2006. Enhanced near-infrared−luminescence in an erbium tetrafluoroterephthalate framework. Inorg. Chem. 45, 8882–8886.

Chen, B., Yang, Y., Zapata, F., Lin, G., Qian, G., Lobkovsky, E.B., 2007. Luminescent open metal sites within a metal–organic framework for sensing small molecules. Adv. Mater. 19, 1693–1696.

Chen, B., Wang, L., Zapata, F., Qian, G., Lobkovsky, E.B., 2008. A luminescent microporous metal−organic framework for the recognition and sensing of anions. J. Am. Chem. Soc. 130, 6718–6719.

Chen, Z., Zhao, B., Cheng, P., Zhao, X.-Q., Shi, W., Song, Y., 2009. A purely lanthanide-based complex exhibiting ferromagnetic coupling and slow magnetic relaxation behavior. Inorg. Chem. 48, 3493–3495.

Chesman, A.S.R., Turner, D.R., Izgorodina, E.I., Batten, S.R., Deacon, G.B., 2007. Homoleptic 12-coordinate lanthanoids with $\eta^2$-nitroso ligands. Dalton Trans., 1371–1373.

Chowdhuri, D.S., Kumar Jana, S., Hazari, D., Zangrando, E., Dalai, S., 2013. Topological aspects of lanthanide–adipate–aqua compounds: close packed and open framework structures. J. Solid State Chem. 203, 128–133.

Chui, S.S.Y., Siu, A., Feng, X., Ying Zhang, Z., Mak, T.C.W., Williams, I.D., 2001. Hydrothermal synthesis of three new 3-D framework rare-earth mellitates. Inorg. Chem. Commun. 4, 467–470.

Comby, S., Bünzli, J.-C.G., 2007. Lanthanide near-infrared luminescence in molecular probes and devices. In: Gschneidner, K.A., Bünzli, J.-C.G., Pecharsky, V.K. (Eds.), Handbook on the Physics and Chemistry of Rare Earths. vol. 37. Elsevier, Amsterdam, pp. 217–470, Ch. 235.

Corma, A., García, H., Llabrés, I., Xamena, F.X., 2010. Engineering metal organic frameworks for heterogeneous catalysis. Chem. Rev. 110, 4606–4655.

Costa, J.S., Gamez, P., Black, C.A., Roubeau, O., Teat, S.J., Reedijk, J., 2008. Chemical modification of a bridging ligand inside a metal–organic framework while maintaining the 3D structure. Eur. J. Inorg. Chem. 2008, 1551–1554.

Cotton, F.A., 1966. Transition-metal compounds containing clusters of metal atoms. Q. Rev. Chem. Soc. 20, 389–401.

Cotton, S.A., Franckevicius, V., How, R.E., Ahrens, B., Ooi, L.L., Mahon, M.F., Raithby, P.R., Teat, S.J., 2003a. Synthesis of complexes of 2,2':6',2''-terpyridine and 1,10-phenanthroline with lanthanide thiocyanates; the molecular structures of [Ln(terpy)$_2$(NCS)$_3$] (Ln=Pr, Nd), [Nd(terpy)$_2$(NCS)$_3$]•2EtOH and [Ln(phen)$_3$(NCS)$_3$]•EtOH (Ln=Pr, Nd). Polyhedron 22, 1489–1497.

Cotton, S.A., Noy, O.E., Liesener, F., Raithby, P.R., 2003b. Unequivocal characterisation of a [Ln(terpy)(NO3)3•(H2O)] complex: the synthesis and structure of [M(terpy)(NO$_3$)$_3$•(H$_2$O)] (M=Eu, Tb); a comparison with the structure of [Eu(bipy)$_2$(NO$_3$)$_3$] and with other europium nitrate complexes {terpy=2,2',:6',2''-terpyridyl; bipy=2,2'-bipyridyl}. Inorg. Chim. Acta 344, 37–42.

Cucinotta, G., Perfetti, M., Luzon, J., Etienne, M., Car, P.-E., Caneschi, A., Calvez, G., Bernot, K., Sessoli, R., 2012. Magnetic anisotropy in a dysprosium/DOTA single-molecule magnet: beyond simple magneto-structural correlations. Angew. Chem. Int. Ed. Engl. 51, 1606–1610.

Cui, G.-H., Li, J.-R., Zhang, R.-H., Bu, X.-H., 2005. Hydrothermal synthesis, crystal structures and luminescent properties of two new Ln(III)–succinate (Ln=Eu, Tb) complexes exhibiting three dimensional networks. J. Mol. Struct. 740, 187–191.

Cui, Y., Yue, Y., Qian, G., Chen, B., 2012. Luminescent functional metal-organic frameworks. Chem. Rev. 112, 1126–1162.

Cui, Y., Chen, B., Qian, G., 2014. Lanthanide metal-organic frameworks for luminescent sensing and light-emitting applications. Coord. Chem. Rev. 273–274, 76–86.

Das, R.K., Aijaz, A., Sharma, M.K., Lama, P., Bharadwaj, P.K., 2012. Direct crystallographic observation of catalytic reactions inside the pores of a flexible coordination polymer. Chem. Eur. J. 18, 6866–6872.

Davis, M.E., Lobo, R.F., 1992. Zeolite and molecular sieve synthesis. Chem. Mater. 4, 756–768.

De Bettencourt-Dias, A., 2007. Lanthanide-based emitting materials in light-emitting diodes. Dalton Trans., 2229–2241.

De Bettencourt-Dias, A., Viswanathan, S., Rollett, A., 2007. Thiophene-derivatized pybox and its highly luminescent lanthanide ion complexes. J. Am. Chem. Soc. 129, 15436–15437.

De Bettencourt-Dias, A., Barber, P.S., Viswanathan, S., De Lill, D.T., Rollett, A., Ling, G., Altun, S., 2010. Para-derivatized pybox ligands as sensitizers in highly luminescent Ln(III) complexes. Inorg. Chem. 49, 8848–8861.

De Bettencourt-Dias, A., Barber, P.S., Bauer, S., 2012. A water-soluble pybox derivative and its highly luminescent lanthanide ion complexes. J. Am. Chem. Soc. 134, 6987–6994.

De Bettencourt-Dias, A., Barber, P.S., Viswanathan, S., 2014. Aromatic N-donor ligands as chelators and sensitizers of lanthanide ion emission. Coord. Chem. Rev. 273–274, 165–200.

Decadt, R., Van Hecke, K., Depla, D., Leus, K., Weinberger, D., Van Driessche, I., Van Der Voort, P., Van Deun, R., 2012. Synthesis, crystal structures, and luminescence properties of carboxylate based rare-earth coordination polymers. Inorg. Chem. 51, 11623–11634.

De Lill, D.T., Cahill, C.L., 2007. Synthesis and characterization of a praseodymium-adipate framework templated with 1,2-bis(4-pyridyl)ethane: host-guest interactions and structural survey. Cryst. Growth Des. 7, 2390–2393.

De Lill, D.T., Cahill, C.L., 2008. Coordination polymers of the lanthanide elements: a structural survey. In: Karlin, K.D. (Ed.), Progress in Inorganic Chemistry. vol. 55. John Wiley & Sons, Inc., Hoboken, NJ, pp. 143–204.

De Lill, D.T., Brennessel, W.W., Borkowski, L.A., Gunning, N.S., Cahill, C.L., 2005a. Poly[([μ]3-n-hexane-1,6-dicarboxylato)dysprosium(III)]. Acta Crystallogr. Sect. E 61, m1343–m1345.

De Lill, D.T., Gunning, N.S., Cahill, C.L., 2005b. Toward templated metal-organic frameworks: synthesis, structures, thermal properties, and luminescence of three novel lanthanide-adipate frameworks. Inorg. Chem. 44, 258–266.

De Lill, D.T., De Bettencourt-Dias, A., Cahill, C.L., 2007. Exploring lanthanide luminescence in metal-organic frameworks: synthesis, structure, and guest-sensitized luminescence of a mixed europium/terbium-adipate framework and a terbium-adipate framework. Inorg. Chem. 46, 3960–3965.

De Lill, D.T., Tareila, A.M., Cahill, C.L., 2009. Synthesis, structure, and luminescence of a two-dimensional lanthanide(III)-suberate coordination polymer resulting from dimeric secondary building units. Inorg. Chem. Commun. 12, 191–194.

Desiraju, G.R., 1995. Supramolecular synthons in crystal engineering—a new organic synthesis. Angew. Chem. Int. Ed. Engl. 34, 2311–2327.

Desiraju, G.R., Parthasarathy, R., 1989. The nature of halogen · halogen interactions: are short halogen contacts due to specific attractive forces or due to close packing of nonspherical atoms? J. Am. Chem. Soc. 111, 8725–8726.

Desiraju, G.R., Ho, P.S., Kloo, L., Legon, A.C., Marquardt, R., Metrangolo, P., Politzer, P., Resnati, G., Rissanen, K., 2013. Definition of the halogen bond (IUPAC recommendations 2013). Pure Appl. Chem. 85, 1711–1713.

Devic, T., Serre, C., 2014. High valence 3p and transition metal based MOFs. Chem. Soc. Rev. 43, 6097–6115.

Devic, T., Serre, C., Audebrand, N., Marrot, J., Férey, G., 2005. MIL-103, a 3-D lanthanide-based metal organic framework with large one-dimensional tunnels and a high surface area. J. Am. Chem. Soc. 127, 12788–12789.

Dinolfo, P.H., Hupp, J.T., 2001. Supramolecular coordination chemistry and functional microporous molecular materials. Chem. Mater. 13, 3113–3125.

Doffek, C., Alzakhem, N., Bischof, C., Wahsner, J., Güden-Silber, T., Lügger, J., Platas-Iglesias, C., Seitz, M., 2012. Understanding the quenching effects of aromatic C–H- and C–D-oscillators in near-IR lanthanoid luminescence. J. Am. Chem. Soc. 134, 16413–16423.

Drew, M.G.B., Iveson, P.B., Hudson, M.J., Liljenzin, J.O., Spjuth, L., Cordier, P.-Y., Enarsson, A., Hill, C., Madic, C., 2000. Separation of americium(III) from europium(III) with tridentate heterocyclic nitrogen ligands and crystallographic studies of complexes formed by 2,2':6',2″-terpyridine with the lanthanides. J. Chem. Soc. Dalton Trans., 821–830.

Duan, L., Li, Y., Liu, F., Wang, E., Wang, X., Hu, C., Xu, L., 2004a. Hydrothermal synthesis and crystal structures of two novel rare earth coordination polymers based on pyridine-2,6-dicarboxylic acid. J. Mol. Struct. 689, 269–274.

Duan, L.-M., Xu, J.-Q., Xie, F.-T., Liu, Y.-B., Ding, H., 2004b. A novel three-dimensional open framework constructed from infinite chains of edge-sharing $CeO_8(H_2O)$ polyhedron: $[Ce_2(ad)_3(H_2O)_2]_n$. Inorg. Chem. Commun. 7, 216–219.

Eddaoudi, M., Moler, D.B., Li, H., Chen, B., Reineke, T.M., O'Keeffe, M., Yaghi, O.M., 2001. Modular chemistry: secondary building units as a basis for the design of highly porous and robust metal−organic carboxylate frameworks. Acc. Chem. Res. 34, 319–330.

Eliseeva, S.V., Bunzli, J.-C.G., 2010. Lanthanide luminescence for functional materials and biosciences. Chem. Soc. Rev. 39, 189–227.

Feltham, H.L.C., Brooker, S., 2014. Review of purely 4f and mixed-metal nd-4f single-molecule magnets containing only one lanthanide ion. Coord. Chem. Rev. 276, 1–33.

Férey, G., 2001. Microporous solids: from organically templated inorganic skeletons to hybrid frameworks · ecumenism in chemistry. Chem. Mater. 13, 3084–3098.

Gándara, F., Andrés, A.D., Gómez-Lor, B., Gutiérrez-Puebla, E., Iglesias, M., Monge, M.A., Proserpio, D.M., Snejko, N., 2008. A rare-earth MOF series: fascinating structure, efficient light emitters, and promising catalysts. Cryst. Growth Des. 8, 378–380.

Gao, H.-L., Yi, L., Ding, B., Wang, H.-S., Cheng, P., Liao, D.-Z., Yan, S.-P., 2005. First 3D Pr(III)−Ni(II)−Na(I) polymer and a 3D Pr(III) open network based on pyridine-2,4,6-tricarboxylic acid. Inorg. Chem. 45, 481–483.

Gao, H.-L., Yi, L., Zhao, B., Zhao, X.-Q., Cheng, P., Liao, D.-Z., Yan, S.-P., 2006. Synthesis and characterization of metal−organic frameworks based on 4-hydroxypyridine-2,6-dicarboxylic acid and pyridine-2,6-dicarboxylic acid ligands. Inorg. Chem. 45, 5980–5988.

Gascon, J., Corma, A., Kapteijn, F., Llabrés, I., Xamena, F.X., 2013. Metal organic framework catalysis: Quo Vadis? ACS Catal. 4, 361–378.

Ghosh, S.K., Bharadwaj, P.K., 2005. Octameric water clusters of staircase structure present in a metal-organic framework built from helical lanthanide coordination polymers. Eur. J. Inorg. Chem. 2005, 4886–4889.

Guillou, O., Daiguebonne, C., 2004. Lanthanide-containing coordination polymers. In: Gschneidner, K.A., Bünzli, J.-C.G., Pecharsky, V.K. (Eds.), Handbook on the Physics and Chemistry of Rare Earths. vol. 34. Elsevier, Amsterdam, pp. 359–404, Ch. 221.

Guo, X., Zhu, G., Fang, Q., Xue, M., Tian, G., Sun, J., Li, X., Qiu, S., 2005. Synthesis, structure and luminescent properties of rare earth coordination polymers constructed from paddle-wheel building blocks. Inorg. Chem. 44, 3850–3855.

Guo, Z., Xu, H., Su, S., Cai, J., Dang, S., Xiang, S., Qian, G., Zhang, H., O'Keeffe, M., Chen, B., 2011. A robust near infrared luminescent ytterbium metal-organic framework for sensing of small molecules. Chem. Commun. 47, 5551–5553.

Gustafsson, M., Bartoszewicz, A., Martín-Matute, B., Sun, J., Grins, J., Zhao, T., Li, Z., Zhu, G., Zou, X., 2010. A family of highly stable lanthanide metal−organic frameworks: structural evolution and catalytic activity. Chem. Mater. 22, 3316–3322.

Habib, F., Murugesu, M., 2013. Lessons learned from dinuclear lanthanide nano-magnets. Chem. Soc. Rev. 42, 3278–3288.

Haitao, X., Nengwu, Z., Xianglin, J., Ruyi, Y., Yonggang, W., Enyi, Y., Zhengquan, L., 2003. Assembly of lanthanide coordination polymers with one dimensional channels. J. Mol. Struct. 655, 339–342.

Han, Y.-F., Zhou, X.-H., Zheng, Y.-X., Shen, Z., Song, Y., You, X.-Z., 2008. Syntheses, structures, photoluminescence, and magnetic properties of nanoporous 3D lanthanide coordination polymers with 4,4'-biphenyldicarboxylate ligand. CrystEngComm 10, 1237–1242.

Han, Y., Li, X., Li, L., Ma, C., Shen, Z., Song, Y., You, X., 2010. Structures and properties of porous coordination polymers based on lanthanide carboxylate building units. Inorg. Chem. 49, 10781–10787.

Hancock, R.D., 2013. The pyridyl group in ligand design for selective metal ion complexation and sensing. Chem. Soc. Rev. 42, 1500–1524.

Hancock, R.D., Martell, A.E., 1989. Ligand design for selective complexation of metal ions in aqueous solution. Chem. Rev. 89, 1875–1914.

Hasegawa, Y., Nakanishi, T., 2015. Luminescent lanthanide coordination polymers for photonic applications. RSC Adv. 5, 338–353.

He, H., Yuan, D., Ma, H., Sun, D., Zhang, G., Zhou, H.-C., 2010. Control over interpenetration in lanthanide-organic frameworks: synthetic strategy and gas-adsorption properties. Inorg. Chem. 49, 7605–7607.

He, H., Ma, H., Sun, D., Zhang, L., Wang, R., Sun, D., 2013a. Porous lanthanide–organic frameworks: control over interpenetration, gas adsorption, and catalyst properties. Cryst. Growth Des. 13, 3154–3161.

He, Y., Furukawa, H., Wu, C., O'Keeffe, M., Chen, B., 2013b. A mesoporous lanthanide-organic framework constructed from a dendritic hexacarboxylate with cages of 2.4 nm. CrystEngComm 15, 9328–9331.

Heine, J., Müller-Buschbaum, K., 2013. Engineering metal-based luminescence in coordination polymers and metal-organic frameworks. Chem. Soc. Rev. 42, 9232–9242.

Hoskins, B.F., Robson, R., 1989. Infinite polymeric frameworks consisting of three dimensionally linked rod-like segments. J. Am. Chem. Soc. 111, 5962–5964.

Hoskins, B.F., Robson, R., 1990. Design and construction of a new class of scaffolding-like materials comprising infinite polymeric frameworks of 3D-linked molecular rods. A reappraisal of the zinc cyanide and cadmium cyanide structures and the synthesis and structure of the diamond-related frameworks $[N(CH_3)_4][Cu^IZn^{II}(CN)_4]$ and $Cu^I[4,4',4'',4'''$-tetracyanotetraphenylmethane]$BF_4.xC_6H_5NO_2$. J. Am. Chem. Soc. 112, 1546–1554.

Huang, L., Zhang, L.-P., Jin, L.-P., 2004. Hydrothermal synthesis and structural characterization of new lanthanide coordination polymers with pimelic acid and 1,10-phenanthroline. J. Mol. Struct. 692, 169–175.

Huang, S.-J., Wei, D.-Y., Zheng, Y.-Q., 2006. Poly[[aquapraseodymium(III)]-[μ]-(8-carboxyoctanoato)-[μ]-octanedioato]. Acta Crystallogr. Sect. E 62, m2482–m2484.

Huang, Y.-G., Jiang, F.-L., Yuan, D.-Q., Wu, M.-Y., Gao, Q., Wei, W., Hong, M.-C., 2007. A prototypical zeolitic lanthanide−organic framework with nanotubular structure. Cryst. Growth Des. 8, 166–168.

Huang, W., Wu, D., Zhou, P., Yan, W., Guo, D., Duan, C., Meng, Q., 2009. Luminescent and magnetic properties of lanthanide-thiophene-2,5-dicarboxylate hybrid materials. Cryst. Growth Des. 9, 1361–1369.

Hutchings, A.-J., Habib, F., Holmberg, R.J., Korobkov, I., Murugesu, M., 2014. Structural rearrangement through lanthanide contraction in dinuclear complexes. Inorg. Chem. 53, 2102–2112.

James, S.L., 2003. Metal-organic frameworks. Chem. Soc. Rev. 32, 276–288.

Janiak, C., 2003. Engineering coordination polymers towards applications. Dalton Trans., 2781–2804.

Jia, L.-N., Hou, L., Wei, L., Jing, X.-J., Liu, B., Wang, Y.-Y., Shi, Q.-Z., 2013. Five sra topological Ln(III)-MOFs based on novel metal-carboxylate/Cl chain: structure, near-infrared luminescence and magnetic properties. Cryst. Growth Des. 13, 1570–1576.

Jiang, H.-L., Tsumori, N., Xu, Q., 2010. A series of (6,6)-connected porous lanthanide−organic framework enantiomers with high thermostability and exposed metal sites: scalable syntheses, structures, and sorption properties. Inorg. Chem. 49, 10001–10006.

Jin, L., Wang, R.-F., Li, L., Lu, S.-Z., 1996. Crystal structure and spectra of the complex $Eu(p\text{-}ClC_6H_4COO)_3C_{12}H_8N_2$. J. Rare Earths 14, 161–166.

Jin, Y.-W., Zhu, H.-L., Wang, J.-F., Zheng, Y.-Q., 2012. Synthesis, structure, photoluminescence and magnetic properties of lanthanide-pyridine-2,4,6-tricarboxylate coordination polymers. Solid State Sci. 14, 682–688.

Kahwa, I.A., Fronczek, F.R., Selbin, J., 1984. The crystal structure and coordination geometry of potassium-catena-μ-oxalato-bis-oxalato aquo lanthanate(III) dihydrates, $K_3[Ln(Ox)_3(OH_2)]\cdot 2H_2O$, (Ln = Nd, Sm, Eu, Gd, Tb). Inorg. Chim. Acta 82, 161–166.

Katkova, M.A., Bochkarev, M.N., 2010. New trends in design of electroluminescent rare earth metallo-complexes for OLEDs. Dalton Trans. 39, 6599–6612.

Kepert, C.J., Weimin, L., Skelton, B.W., White, A.H., 1994. Structural systematics of rare earth complexes. V. The hydrated 1:1 adducts of 2,2':6',2''-terpyridine with the lanthanoid(III) chlorides. Aust. J. Chem. 47, 365–384.

Kepert, C.J., Wei-Min, L., Semenova, L.I., Skelton, B.W., White, A.H., 1999. Structural systematics of rare earth complexes. XII. solvated 1:1 adducts of some lanthanoid (III) carboxylates with 1,10-phenanthroline and 2,2':6',2''-terpyridine. Aust. J. Chem. 52, 481–496.

Khan, N.A., Jhung, S.H., 2015. Synthesis of metal-organic frameworks (MOFs) with microwave or ultrasound: rapid reaction, phase-selectivity, and size reduction. Coord. Chem. Rev. 285, 11–23.

Kickelbick, G., 2007. Introduction to hybrid materials. In: Kickelbick, G. (Ed.), Hybrid Materials. Wiley-VCH Verlag GmbH & Co. KGaA, Weinham, pp. 1–48.

Kido, J., Okamoto, Y., 2002. Organo lanthanide metal complexes for electroluminescent materials. Chem. Rev. 102, 2357–2368.

Knope, K.E., Soderholm, L., 2013. Solution and solid-state structural chemistry of actinide hydrates and their hydrolysis and condensation products. Chem. Rev. 113, 944–994.

Knowles, R.R., Jacobsen, E.N., 2010. Attractive noncovalent interactions in asymmetric catalysis: links between enzymes and small molecule catalysts. Proc. Natl. Acad. Sci. U.S.A. 107, 20678–20685.

Kolarik, Z., 2008. Complexation and separation of lanthanides(III) and actinides(III) by heterocyclic N-donors in solutions. Chem. Rev. 108, 4208–4252.

Kostakis, G.E., Hewitt, I.J., Ako, A.M., Mereacre, V., Powell, A.K., 2010. Magnetic coordination clusters and networks: synthesis and topological description. Philos. Trans. A Math. Phys. Eng. Sci 368, 1509–1536.

Kremer, C., Torres, J., Domínguez, S., Mederos, A., 2005. Structure and thermodynamic stability of lanthanide complexes with amino acids and peptides. Coord. Chem. Rev. 249, 567–590.

Kudernac, T., Lei, S., Elemans, J.A., De Feyter, S., 2009. Two-dimensional supramolecular self-assembly: nanoporous networks on surfaces. Chem. Soc. Rev. 38, 402–421.

Kuppler, R.J., Timmons, D.J., Fang, Q.-R., Li, J.-R., Makal, T.A., Young, M.D., Yuan, D., Zhao, D., Zhuang, W., Zhou, H.-C., 2009. Potential applications of metal-organic frameworks. Coord. Chem. Rev. 253, 3042–3066.

Latva, M., Takalo, H., Mukkala, V.-M., Matachescu, C., Rodríguez-Ubis, J.C., Kankare, J., 1997. Correlation between the lowest triplet state energy level of the ligand and lanthanide(III) luminescence quantum yield. J. Lumin. 75, 149–169.

Lazarides, T., Adams, H., Sykes, D., Faulkner, S., Calogero, G., Ward, M.D., 2008a. Heteronuclear bipyrimidine-bridged Ru-Ln and Os-Ln dyads: low-energy $^3$MLCT states as energy-donors to Yb(III) and Nd(III). Dalton Trans., 691–698.

Lazarides, T., Sykes, D., Faulkner, S., Barbieri, A., Ward, M.D., 2008b. On the mechanism of d–f energy transfer in RuII/LnIII and OsII/LnIII dyads: Dexter-type energy transfer over a distance of 20 Å. Chem. Eur. J. 14, 9389–9399.

Li, Z.-F., Wang, C.-X., Wang, P., Zhang, Q.-H., 2006. Poly[[bis[pentaaquagadolinium(III)]-[μ]4-benzene-1,2,3,4,5,6-hexacarboxylato] tetrahydrate]. Acta Crystallogr. Sect. E 62, m914–m915.

Li, C.-J., Peng, M.-X., Leng, J.-D., Yang, M.-M., Lin, Z., Tong, M.-L., 2008a. Synthesis, structure, photoluminescence and magnetic properties of new 3-D lanthanide-pyridine-2,4,6-tricarboxylate frameworks. CrystEngComm 10, 1645–1652.

Li, Y., Wang, R., Niu, S.-Y., Jin, J., Wang, Z.-L., 2008b. Synthesis crystal structure and photophysical property of series of binuclear rare earth complexes. Chin. J. Inorg. Chem. 24, 1753–1760.

Li, X., Wei, D.-Y., Huang, S.-J., Zheng, Y.-Q., 2009. Syntheses and characterization of novel lanthanide adamantine–dicarboxylate coordination complexes. J. Solid State Chem. 182, 95–101.

Li, H., Shi, W., Zhao, K., Niu, Z., Li, H., Cheng, P., 2013a. Highly selective sorption and luminescent sensing of small molecules demonstrated in a multifunctional lanthanide microporous metal–organic framework containing 1D honeycomb-type channels. Chem. Eur. J. 19, 3358–3365.

Li, M., Li, D., O'Keeffe, M., Yaghi, O.M., 2013b. Topological analysis of metal–organic frameworks with polytopic linkers and/or multiple building units and the minimal transitivity principle. Chem. Rev. 114, 1343–1370.

Liang Ping, W., Munakata, M., Kuroda-Sowa, T., Maekawa, M., Suenaga, Y., 1996. Synthesis, crystal structures and magnetic behavior of polymeric lanthanide complexes with benzenehexacarboxylic acid (mellitic acid). Inorg. Chim. Acta 249, 183–189.

Lima, N.B., Goncalves, S.M., Junior, S.A., Simas, A.M., 2013. A comprehensive strategy to boost the quantum yield of luminescence of europium complexes. Sci. Rep. 3, 2395.

Lima, P.P., Paz, F.A.A., Brites, C.D.S., Quirino, W.G., Legnani, C., Costa e Silva, M., Ferreira, R.A.S., Júnior, S.A., Malta, O.L., Cremona, M., Carlos, L.D., 2014. White OLED based on a temperature sensitive $Eu^{3+}/Tb^{3+}$ β-diketonate complex. Org. Electron. 15, 798–808.

Liu, G.-F., Qiao, Z.-P., Wang, H.-Z., Chen, X.-M., Yang, G., 2002. Synthesis, structures and photoluminescence of three terbium(III) dicarboxylate coordination polymers. New J. Chem. 26, 791–795.

Liu, C.-B., Sun, C.-Y., Jin, L.-P., Lu, S.-Z., 2004. Supramolecular architecture of new lanthanide coordination polymers of 2-aminoterephthalic acid and 1,10-phenanthroline. New J. Chem. 28, 1019–1026.

Liu, M.-S., Yu, Q.-Y., Cai, Y.-P., Su, C.-Y., Lin, X.-M., Zhou, X.-X., Cai, J.-W., 2008. One-, two-, and three-dimensional lanthanide complexes constructed from pyridine-2,6-dicarboxylic acid and oxalic acid ligands. Cryst. Growth Des. 8, 4083–4091.

Lu, Y., Shi, T., Wang, Y., Yang, H., Yan, X., Luo, X., Jiang, H., Zhu, W., 2009. Halogen bonding—a novel interaction for rational drug design? J. Med. Chem. 52, 2854–2862.

Lu, Y.-B., Jin, S., Zhou, Z.-G., Zhang, S.-Y., Lou, G.-T., Xie, Y.-R., 2014a. The syntheses, structures, magnetic and luminescent properties of five new lanthanide(III)–2,6-naphthalenedicarboxylate complexes. Inorg. Chem. Commun. 48, 73–76.

Lu, Y.-B., Jin, S., Zhu, S.-D., Zhang, S.-Y., Lou, G.-T., Xie, Y.-R., 2014b. Four two-dimensional lanthanide(III)-4,4-biphenyldicarboxylate complexes: syntheses, structures, magnetic and luminescent properties. Inorg. Chem. Commun. 49, 120–123.

Luzon, J., Sessoli, R., 2012. Lanthanides in molecular magnetism: so fascinating, so challenging. Dalton Trans. 41, 13556–13567.

Ma, L., Evans, O.R., Foxman, B.M., Lin, W., 1999. Luminescent lanthanide coordination polymers. Inorg. Chem. 38, 5837–5840.

Macneill, C.M., Day, C.S., Gamboa, S.A., Lachgar, A., Noftle, R.E., 2010. Solvothermal and reflux syntheses, crystal structure and properties of lanthanide-thiophenedicarboxylate-based metal-organic frameworks. J. Chem. Crystallogr. 40, 222–230.

Macneill, C.M., Day, C.S., Marts, A., Lachgar, A., Noftle, R.E., 2011. Synthesis, crystal structure and properties of novel isostructural two-dimensional lanthanide-based coordination polymers with 2,3,5,6-tetrafluoro-1,4-benzenedicarboxylic acid. Inorg. Chim. Acta 365, 196–203.

Manna, S.C., Zangrando, E., Bencini, A., Benelli, C., Chaudhuri, N.R., 2006. Syntheses, crystal structures, and magnetic properties of $[Ln^{III}_2(succinate)_3(H_2O)_2] \cdot 0.5H_2O$ [Ln = Pr, Nd, Sm, Eu, Gd, and Dy] polymeric networks: unusual ferromagnetic coupling in Gd derivative. Inorg. Chem. 45, 9114–9122.

Marques, L.F., Dos Santos, M.V., Ribeiro, S.J.L., Castellano, E.E., Machado, F.C., 2012. Terbium(III) and dysprosium(III) 8-connected 3D networks containing 2,5-thiophenedicarboxylate anion: crystal structures and photoluminescence studies. Polyhedron 38, 149–156.

Marques, L.F., Cantaruti Júnior, A.A.B., Ribeiro, S.J.L., Scaldini, F.M., Machado, F.C., 2013. Synthesis, structural characterization and photophysical properties of highly photoluminescent crystals of Eu(III), Tb(III) and Dy(III) with 2,5-thiophenedicarboxylate. Opt. Mater. 35, 2357–2365.

Metrangolo, P., Resnati, G., 2012. Halogen bonding: where we are and where we are going. Cryst. Growth Des. 12, 5835–5838.

Meyer, F., Dubois, P., 2013. Halogen bonding at work: recent applications in synthetic chemistry and materials science. CrystEngComm 15, 3058–3071.

Meyer, L.V., Schonfeld, F., Müller-Buschbaum, K., 2014. Lanthanide based tuning of luminescence in MOFs and dense frameworks—from mono- and multimetal systems to sensors and films. Chem. Commun. 50, 8093–8108.

Min, D., Lee, S.W., 2002a. 3-dimensional terbium coordination polymers: $[Tb_4(NDC)_6(H_2O)_5]$ •$2H_2O$ and $[Tb_2(BPDC)_3(H_2O)_3]$•$H_2O$ (NDC=2,6-naphthalenedicarboxylate; BPDC=2,2'-bipyridine-4,4'-dicarboxylate). Bull. Kor. Chem. Soc. 23, 948–952.

Min, D., Lee, S.W., 2002b. Terbium-oxalate-pyridinedicarboxylate coordination polymers suggesting the reductive coupling of carbon dioxide ($CO_2$) to oxalate ($C_2O_4^{2-}$):$[Tb_2 (3,5-PDC)_2(H_2O)_4 (C_2O_4)]$·$2H_2O$ and $[Tb(2,4-PDC)(H_2O)(C_2O_4)_{0.5}]$ (PDC=pyridinedicarboxylate). Inorg. Chem. Commun. 5, 978–983.

Min, Z., Singh-Wilmot, M.A., Cahill, C.L., Andrews, M., Taylor, R., 2012. Isoreticular lanthanide metal-organic frameworks: syntheses, structures and photoluminescence of a family of 3D phenylcarboxylates. Eur. J. Inorg. Chem. 2012, 4419–4426.

Mooibroek, T.J., Gamez, P., Reedijk, J., 2008. Lone pair-π interactions: a new supramolecular bond? CrystEngComm 10, 1501–1515.

Mukherjee, A., Tothadi, S., Desiraju, G.R., 2014. Halogen bonds in crystal engineering: like hydrogen bonds yet different. Acc. Chem. Res. 47, 2514–2524.

Müller-Buschbaum, K., Gomez-Torres, S., Larsen, P., Wickleder, C., 2007. Crystal engineering of rare earth amides: 3∞ [Tb(Im)3]@NH3, a homoleptic 3D network exhibiting strong luminescence. Chem. Mater. 19, 655–659.

Mürner, H.-R., Chassat, E., Thummel, R.P., Bünzli, J.-C.G., 2000. Strong enhancement of the lanthanide-centred luminescence in complexes with 4-alkylated 2,2':6',2''-terpyridines. J. Chem. Soc. Dalton Trans., 2809–2816.

Nief, F., 2010. Molecular chemistry of the rare-earth elements in uncommon low-valent states. In: Gschneidner, K.A., Bünzli, J.-C.G., Pecharsky, V.K. (Eds.), Handbook on the Physics and Chemistry of Rare Earths. vol. 40. Elsevier, Amsterdam, pp. 241–300, Ch. 246.

Nishioka, T., Fukui, K., Matsumoto, K., 2007. Lanthanide chelates as luminescent labels in biomedical analyses. In: Gschneidner, K.A., Bünzli, J.-C.G., Pecharsky, V.K. (Eds.), Handbook on the Physics and Chemistry of Rare Earths. vol. 37. Elsevier, Amsterdam, pp. 171–216, Ch. 234.

Ockwig, N.W., Delgado-Friedrichs, O., O'Keeffe, M., Yaghi, O.M., 2005. Reticular chemistry: occurrence and taxonomy of nets and grammar for the design of frameworks. Acc. Chem. Res. 38, 176–182.

O'Connor, C.J., Klein, C.L., Majeste, R.J., Trefonas, L.M., 1982. Magnetic properties and crystal structure of (2,3-pyrazinedicarboxylato)copper(II) hydrochloride: a pyrazine bridged ferromagnetic linear chain. Inorg. Chem. 21, 64–67.

Ollendorff, W., Weigel, F., 1969. The crystal structure of some lanthanide oxalate decahydrates, $Ln_2(C_2O_4)_3 \cdot 10H_2O$, with Ln = La, Ce, Pr, and Nd. Inorg. Nucl. Chem. Lett. 5, 263–269.

Pan, L., Huang, X., Li, J., Wu, Y., Zheng, N., 2000. Novel single- and double-layer and three-dimensional structures of rare-earth metal coordination polymers: the effect of lanthanide contraction and acidity control in crystal structure formation. Angew. Chem. Int. Ed. Engl. 39, 527–530.

Pan, L., Zheng, N., Wu, Y., Han, S., Yang, R., Huang, X., Li, J., 2001. Synthesis, characterization and structural transformation of a condensed rare earth metal coordination polymer. Inorg. Chem. 40, 828–830.

Pearson, R.G., 1963. Hard and soft acids and bases. J. Am. Chem. Soc. 85, 3533–3539.

Pearson, R.G., 1990. Hard and soft acids and bases—the evolution of a chemical concept. Coord. Chem. Rev. 100, 403–425.

Perles, J., Iglesias, M., Ruiz-Valero, C., Snejko, N., 2004. Rare-earths as catalytic centres in organo-inorganic polymeric frameworks. J. Mater. Chem. 14, 2683–2689.

Piguet, C., Bünzli, J.-C.G., 1999. Mono- and polymetallic lanthanide-containing functional assemblies: a field between tradition and novelty. Chem. Soc. Rev. 28, 347–358.

Piguet, C., Bünzli, J.-C.G., 2010. Self-assembled lanthanide helicates: from basic thermodynamics to applications. In: Gschneidner, K.A., Bünzli, J.-C.G., Pecharsky, V.K. (Eds.), Handbook on the Physics and Chemistry of Rare Earths. vol. 40. Elsevier, Amsterdam, pp. 301–553, Ch. 247.

Plabst, M., Kohn, R., Bein, T., 2010. The influence of the guest ion on the synthesis and sorption properties of an open framework lanthanide tetrakisphosphonate. CrystEngComm 12, 1920–1926.

Priimagi, A., Cavallo, G., Metrangolo, P., Resnati, G., 2013. The halogen bond in the design of functional supramolecular materials: recent advances. Acc. Chem. Res. 46, 2686–2695.

Qin, C., Wang, X.-L., Wang, E.-B., Su, Z.-M., 2005. A series of three-dimensional lanthanide coordination polymers with rutile and unprecedented rutile-related topologies. Inorg. Chem. 44, 7122–7129.

Rabenau, A., 1985. The role of hydrothermal synthesis in preparative chemistry. Angew. Chem. Int. Ed. Engl. 24, 1026–1040.

Ramirez, A.L., Knope, K.E., Kelley, T.T., Greig, N.E., Einkauf, J.D., De Lill, D.T., 2012. Structure and luminescence of a 2-dimensional 2,3-pyridinedicarboxylate coordination polymer constructed from lanthanide(III) dimers. Inorg. Chim. Acta 392, 46–51.

Reddy, M.L.P., Divya, V., Pavithran, R., 2013. Visible-light sensitized luminescent europium(III)-β-diketonate complexes: bioprobes for cellular imaging. Dalton Trans. 42, 15249–15262.

Reineke, T.M., Eddaoudi, M., Fehr, M., Kelley, D., Yaghi, O.M., 1999. From condensed lanthanide coordination solids to microporous frameworks having accessible metal sites. J. Am. Chem. Soc. 121, 1651–1657.

Ren, Y.-Y., An, B.-L., Xu, Q., 2010. Strong luminescence of novel water-soluble lanthanide complexes sensitized by pyridine-2,4,6-tricarboxylic acid. J. Alloys Compd. 501, 42–46.

Ren, Y.-W., Liang, J.-X., Lu, J.-X., Cai, B.-W., Shi, D.-B., Qi, C.-R., Jiang, H.-F., Chen, J., Zheng, D., 2011. 1,4-Phenylenediacetate-based Ln MOFs—synthesis, structures, luminescence, and catalytic activity. Eur. J. Inorg. Chem. 2011, 4369–4376.

Rocha, J., Carlos, L.D., Paz, F.A.A., Ananias, D., 2011. Luminescent multifunctional lanthanides-based metal-organic frameworks. Chem. Soc. Rev. 40, 926–940.

Rodrigues, I., Mihalcea, I., Volkringer, C., Loiseau, T., Visseaux, M., 2011. Water-free neodymium 2,6-naphthalenedicarboxylates coordination complexes and their application as catalysts for isoprene polymerization. Inorg. Chem. 51, 483–490.

Rong-Hua, Z., Han-Guo, L., 2007. Poly[[triaquasesqui-[μ]2-oxalato-terbium(III)] methanol solvate]. Acta Crystallogr. Sect. E 63, m2925.

Rosi, N.L., Kim, J., Eddaoudi, M., Chen, B., O'Keeffe, M., Yaghi, O.M., 2005. Rod packings and metal−organic frameworks constructed from rod-shaped secondary building units. J. Am. Chem. Soc. 127, 1504–1518.

Roy, S., Chakraborty, A., Maji, T.K., 2014. Lanthanide–organic frameworks for gas storage and as magneto-luminescent materials. Coord. Chem. Rev. 273–274, 139–164.

Seidel, C., Lorbeer, C., Cybińska, J., Mudring, A.-V., Ruschewitz, U., 2012. Lanthanide coordination polymers with tetrafluoroterephthalate as a bridging ligand: thermal and optical properties. Inorg. Chem. 51, 4679–4688.

Semenova, L.I., White, A.H., 1999. Structural systematics of rare earth complexes. XIV. Hydrated 1:1 adducts of lanthanoid(III) nitrates with 2,2':6',2''-terpyridine. Aust. J. Chem. 52, 507–517.

Semenova, L.I., Sobolev, A.N., Skelton, B.W., White, A.H., 1999. Structural systematics of rare earth complexes. XV. Tris(2,2':6',2''-terpyridine)lanthanoid(III) tris(perchlorate) complexes. Aust. J. Chem. 52, 519–529.

Sénéchal-David, K., Hemeryck, A., Tancrez, N., Toupet, L., Williams, J.A.G., Ledoux, I., Zyss, J., Boucekkine, A., Guégan, J.-P., Le Bozec, H., Maury, O., 2006. Synthesis, structural studies, theoretical calculations, and linear and nonlinear optical properties of terpyridyl lanthanide complexes: new evidence for the contribution of f electrons to the NLO activity. J. Am. Chem. Soc. 128, 12243–12255.

Serpaggi, F., Férey, G., 1998. Hybrid open frameworks (MIL-$n$). Part 6 Hydrothermal synthesis and X-ray powder ab initio structure determination of MIL-11, a series of lanthanide organodiphosphonates with three-dimensional networks, $Ln^{III}H[O_3P(CH_2)PO_3]$ ($n$=1-3). J. Mater. Chem. 8, 2749–2755.

Serpaggi, F., Férey, G., 1999a. Hybrid open frameworks (MIL-$n$): synthesis and crystal structure of MIL-17—a rare-earth dicarboxylate with a relatively open framework, $[Pr(H_2O)]_2[O_2C(CH_2)_2CO_2]_3 \cdot H_2O$. Microporous Mesoporous Mater. 32, 311–318.

Serpaggi, F., Férey, G., 1999b. Hybrid organic–inorganic frameworks (MIL-$n$). hydrothermal synthesis of a series of pillared lanthanide carboxyethylphosphonates and x-ray powder ab initio structure determination of MIL-19, $Pr[O_3P(CH_2)_2CO_2]$. Inorg. Chem. 38, 4741–4744.

Serre, C., Millange, F., Marrot, J., Férey, G., 2002. Hydrothermal synthesis, structure determination, and thermal behavior of new three-dimensional europium terephthalates: MIL-51$_{LT, HT}$ and MIL-52 or $Eu_2^n(OH)_x(H_2O)_y(O_2C-C_6H_4-CO_2)_z$ (n = III, III, II; x = 4, 0, 0; y = 2, 0, 0; z = 1, 1, 2). Chem. Mater. 14, 2409–2415.

Sessoli, R., Powell, A.K., 2009. Strategies towards single molecule magnets based on lanthanide ions. Coord. Chem. Rev. 253, 2328–2341.

Shannon, R., 1976. Revised effective ionic radii and systematic studies of interatomic distances in halides and chalcogenides. Acta Crystallogr. A 32, 751–767.

Shavaleev, N.M., Moorcraft, L.P., Pope, S.J.A., Bell, Z.R., Faulkner, S., Ward, M.D., 2003. Sensitised near-infrared emission from lanthanides using a covalently-attached Pt(II) fragment as an antenna group. Chem. Commun., 1134–1135.

Sheets, W.C., Mugnier, E., Barnabé, A., Marks, T.J., Poeppelmeier, K.R., 2006. Hydrothermal synthesis of delafossite-type oxides. Chem. Mater. 18, 7–20.

Shen, F.M., Lush, S.F., 2012. Poly[[hexaaqua([μ]2-oxalato-[κ]4O1, O2:O1', O2')bis([μ]3-pyridine-2,4-dicarboxylato-[κ]4N, O1:O1':O4)dicerium(III)] monohydrate]. Acta Crystallogr. Sect. E 68, m21–m22.

Shi, F.-N., Cunha-Silva, L., Trindade, T., Paz, F.A.A., Rocha, J., 2009. Three-dimensional lanthanide−organic frameworks based on di-, tetra-, and hexameric clusters. Cryst. Growth Des. 9, 2098–2109.

Shi, F.-N., Ananias, D., Yang, T.-H., Rocha, J., 2013. Synthesis and characterization of polymorphs of photoluminescent Eu(III)-(2,5-furandicarboxylic acid, oxalic acid) MOFs. J. Solid State Chem. 204, 321–328.

Shinoda, S., Miyake, H., Tsukube, H., 2005. Molecular recognition and sensing via rare earth complexes. In: Gschneidner, K.A., Bünzli, J.-C.G., Pecharsky, V.K. (Eds.), Handbook on the Physics and Chemistry of Rare Earths. vol. 35. Elsevier, Amsterdam, pp. 273–335, Ch. 226.

Silva, P., Vieira, F., Gomes, A.C., Ananias, D., Fernandes, J.A., Bruno, S.M., Soares, R., Valente, A.A., Rocha, J., Paz, F.A.A., 2011. Thermal transformation of a layered multifunctional network into a metal–organic framework based on a polymeric organic linker. J. Am. Chem. Soc. 133, 15120–15138.

Silva, P., Cunha-Silva, L., Silva, N.J.O., Rocha, J., Paz, F.A.A., 2013. Metal–organic frameworks assembled from erbium tetramers and 2,5-pyridinedicarboxylic acid. Cryst. Growth Des. 13, 2607–2617.

Smith, G., Reddy, A.N., Byriel, K.A., Kennard, C.H.L., 1995. Preparation and crystal structures of the silver(I) carboxylates $[Ag_2\{C_6H_4(CO_2)_2\}$ $(NH_3)_2]$, $[NH_4][Ag_5\{C_6H_3(CO_2)_3\}$ $_2(NH_3)_2$ $(H_2O)_2]\bullet H_2O$ and $[NH_4][Ag\{C_4H_2N_2(CO_2)_2\}]$. J. Chem. Soc. Dalton Trans., 3565–3570.

Soares-Santos, P.C.R., Cunha-Silva, L., Paz, F.A.A., Ferreira, R.A.S., Rocha, J., Trindade, T., Carlos, L.D., Nogueira, H.I.S., 2008. Photoluminescent 3D lanthanide−organic frameworks with 2,5-pyridinedicarboxylic and 1,4-phenylenediacetic acids. Cryst. Growth Des. 8, 2505–2516.

Soares-Santos, P.C.R., Cunha-Silva, L.S., Paz, F.A.A., Ferreira, R.A.S., Rocha, J.O., Carlos, L.S.D., Nogueira, H.I.S., 2010. Photoluminescent lanthanide-organic bilayer networks with 2,3-pyrazinedicarboxylate and oxalate. Inorg. Chem. 49, 3428–3440.

Song, H.-H., Li, Y.-J., Song, Y., Han, Z.-G., Yang, F., 2008. Synthesis, crystal structure and properties of two 1D nano-chain coordination polymers constructed by lanthanide with pyridine-3,4-dicarboxylic acid and 1,10-phenanthroline. J. Solid State Chem. 181, 1017–1024.

Song, S., Shao, C., Zhang, H., Zhang, W., Yang, L., Ren, T., Bu, Z., 2012. A 2D hydrogen-bonded 1D coordination network of Pr(III) with pyridine-2,6-dicarboxylic acid: hydrothermal synthesis, structure, and luminescent properties. Synth. React. Inorg. Metal-Org. Nano-Met. Chem. 43, 169–174.

Song, Y.-M., Luo, F., Zhu, Y., Tian, X.-Z., Sun, G.-M., 2013. Carboxylate-bridged dinuclear $Dy_2$ single-molecule magnets: synthesis, structure, and magnetic studies. Aust. J. Chem. 66, 98–104.

Spencer, E.C., Zhao, J., Ross, N.L., Andrews, M.B., Surbella, R.G., Cahill, C.L., 2013. The influence of pressure on the photoluminescence properties of a terbium-adipate framework. J. Solid State Chem. 202, 99–104.

Stock, N., Biswas, S., 2011. Synthesis of metal-organic frameworks (MOFs): routes to various MOF topologies, morphologies, and composites. Chem. Rev. 112, 933–969.

Sun, Z.-G., Ren, Y.-P., Long, L.-S., Huang, R.-B., Zheng, L.-S., 2002. Guest controlled coordination framework: syntheses, crystal structures and thermal properties of two three-dimensional structures of $[Ce_2(adipate)_3(OH_2)_4]\cdot 6H_2O$ and $[Ce_2(adipate)_3(OH_2)_4]\cdot 4H_2O\cdot(adipic\ acid)$. Inorg. Chem. Commun. 5, 629–632.

Tan, B., Xie, Z.-L., Feng, M.-L., Hu, B., Wu, Z.-F., Huang, X.-Y., 2012. Ionothermal syntheses, crystal structures and properties of three-dimensional rare earth metal-organic frameworks with 1,4-naphthalenedicarboxylic acid. Dalton Trans. 41, 10576–10584.

Tanaka, D., Kitagawa, S., 2008. Template effects in porous coordination polymers. Chem. Mater. 20, 922–931.

Tancrez, N., Feuvrie, C., Ledoux, I., Zyss, J., Toupet, L., Le Bozec, H., Maury, O., 2005. Lanthanide complexes for second order nonlinear optics: evidence for the direct contribution of f electrons to the quadratic hyperpolarizability. J. Am. Chem. Soc. 127, 13474–13475.

Tang, X., Yue, S., Li, P., Wang, N., Liu, Y., 2008. Hydrothermal synthesis and crystal structure study of two novel 3-D mellitates $\{Nd_2[C_6(COO)_6] (H_2O)_6\}$ and $\{Ho_2[C_6(COO)_6](H_2O)_6\}$. J. Rare Earths 26, 800–803.

Tang, W., Johnston, S., Iggo, J.A., Berry, N.G., Phelan, M., Lian, L., Bacsa, J., Xiao, J., 2013. Cooperative catalysis through noncovalent interactions. Angew. Chem. Int. Ed. Engl. 52, 1668–1672.

Thalladi, V.R., Nüsse, M., Boese, R., 2000. The melting point alternation in $\alpha$, $\omega$-alkanedicarboxylic acids. J. Am. Chem. Soc. 122, 9227–9236.

Thirumurugan, A., Natarajan, S., 2006. Assembly of a secondary building unit (SBU) into two- and three-dimensional structures in lanthanide benzenedicarboxylates. Cryst. Growth Des. 6, 983–988.

Thuéry, P., 2012. Supramolecular assemblies built from lanthanide ammoniocarboxylates and cucurbit[6]uril. CrystEngComm 14, 8128–8136.

Tian, J., Li, B., Zhang, X., Li, X., Li, X., Zhang, J., 2013. Three novel 1D lanthanide-carboxylate polymeric complexes: syntheses, crystal structures and magnetic analyses. Dalton Trans. 42, 8504–8511.

Tranchemontagne, D.J., Mendoza-Cortes, J.L., O'Keeffe, M., Yaghi, O.M., 2009. Secondary building units, nets and bonding in the chemistry of metal-organic frameworks. Chem. Soc. Rev. 38, 1257–1283.

Trombe, J.C., Mohanu, A., 2004. Synthesis and crystal structure of three-dimensional open-framework lanthanide oxalates containing either the guanidinium or tetramethylammonium ions. Solid State Sci. 6, 1403–1419.

Tsai, C.-S., Chen, W.-T., Liao, J.-H., 2013. Synthesis, structure and photoluminescence of lanthanide metal-organic frameworks, $Ln_4(TDC)_6(DMF)_4(H_2O)_2$, where $TDC^{2-}$ = thiophene-2,5-dicarboxylate, DMF = N,N-dimethylformamide. J. Chin. Chem. Soc. 60, 755–761.

Vilela, S.M.F., Ananias, D., Gomes, A.C., Valente, A.A., Carlos, L.D., Cavaleiro, J.A.S., Rocha, J., Tome, J.P.C., Almeida Paz, F.A., 2012. Multi-functional metal-organic frameworks assembled from a tripodal organic linker. J. Mater. Chem 22, 18354–18371.

Vilela, S.M.F., Firmino, A.D.G., Mendes, R.F., Fernandes, J.A., Ananias, D., Valente, A.A., Ott, H., Carlos, L.D., Rocha, J., Tome, J.P.C., Almeida Paz, F.A., 2013. Lanthanide-polyphosphonate coordination polymers combining catalytic and photoluminescence properties. Chem. Commun. 49, 6400–6402.

Vilela, S.M.F., Fernandes, J.A., Ananias, D., Carlos, L.D., Rocha, J., Tome, J.P.C., Almeida Paz, F.A., 2014. Photoluminescent layered lanthanide-organic framework based on a novel tri-fluorotriphosphonate organic linker. CrystEngComm 16, 344–358.

Volkringer, C., Henry, N., Grandjean, S., Loiseau, T., 2012. Uranyl and/or rare-earth mellitates in extended organic–inorganic networks: a unique case of heterometallic cation–cation interaction with $U^{VI}$=O–$Ln^{III}$ bonding (Ln = Ce, Nd). J. Am. Chem. Soc. 134, 1275–1283.

Wahsner, J., Seitz, M., 2013. Perdeuterated 2,2′-bipyridine-6,6′-dicarboxylate: an extremely efficient sensitizer for thulium luminescence in solution. Inorg. Chem. 52, 13301–13303.

Wan, Y.-H., Zhang, L.-P., Jin, L.-P., 2003. Three new lanthanide coordination polymers containing isophthalate and 1,10-phenanthroline. J. Mol. Struct. 658, 253–260.

Wang, Z., Jin, C.-M., Shao, T., Li, Y.-Z., Zhang, K.-L., Zhang, H.-T., You, X.-Z., 2002. Syntheses, structures, and luminescence properties of a new family of three-dimensional open-framework lanthanide coordination polymers. Inorg. Chem. Commun. 5, 642–648.

Wang, Q.-L., Liang, M., Liao, D.-Z., Yan, S.-P., Jiang, Z.-H., Cheng, P., 2004a. Structure and magnetic properties of a novel two-dimensional complex from 1, 3, 5-benzenetricarboxylate and neodymium(III)—{[Nd(1, 3, 5-benzenetricarboxylate)(H$_2$O)$_4$]···H$_2$O}$_n$. Z. Anorg. Allg. Chem. 630, 613–616.

Wang, Y., Wang, Z., Yan, C., Jin, L., 2004b. Hydrothermal synthesis and structure of new lanthanide coordination polymers with dicarboxylic acid and 1,10-phenanthroline. J. Mol. Struct. 692, 177–186.

Wang, Y.-B., Zhuang, W.-J., Jin, L.-P., Lu, S.-Z., 2004c. Solvothermal synthesis and structures of lanthanide-organic sandwich coordination polymers with 4,4′-biphenyldicarboxylic acid. J. Mol. Struct. 705, 21–27.

Wang, H.-S., Zhao, B., Zhai, B., Shi, W., Cheng, P., Liao, D.-Z., Yan, S.-P., 2007a. Syntheses, structures, and photoluminescence of one-dimensional lanthanide coordination polymers with 2,4,6-pyridinetricarboxylic acid. Cryst. Growth Des. 7, 1851–1857.

Wang, S.-P., Wang, R.-F., Zhang, J.J., 2007b. Crystal structure and properties of complex [Tb(p-ClBA)$_3$(phen)]$_2$. Chin. J. Inorg. Chem. 23, 862–866.

Wang, J.-G., Huang, C.-C., Huang, X.-H., Liu, D.-S., 2008. Three-dimensional lanthanide thiophenedicarboxylate framework with an unprecedented (4,5)-connected topology. Cryst. Growth Des. 8, 795–798.

Wang, C.-G., Xing, Y.-H., Li, Z.-P., Li, J., Zeng, X.-Q., Ge, M.-F., Niu, S.-Y., 2009. A series of three-dimensional lanthanide-rigid-flexible frameworks: synthesis, structure, and luminescent properties of coordination polymers with 2,5-pyridine dicarboxylic acid and adipic acid. Cryst. Growth Des. 9, 1525–1530.

Wang, Z., Bai, F.-Y., Xing, Y.-H., Xie, Y., Ge, M.-F., Niu, S.-Y., 2010. Synthesis and luminescent properties of the first series of lanthanide complexes based on sebacate and 2,5-pyridine-dicarboxylate. Inorg. Chim. Acta 363, 669–675.

Wang, M.-X., Long, L.-S., Huang, R.-B., Zheng, L.-S., 2011. Influence of halide ions on the chirality and luminescent property of ionothermally synthesized lanthanide-based metal-organic frameworks. Chem. Commun. 47, 9834–9836.

Wang, H., Liu, S.-J., Tian, D., Jia, J.-M., Hu, T.-L., 2012a. Temperature-dependent structures of lanthanide metal–organic frameworks based on furan-2,5-dicarboxylate and oxalate. Cryst. Growth Des. 12, 3263–3270.

Wang, Y.-L., Jiang, Y.-L., Xiahou, Z.-J., Fu, J.-H., Liu, Q.-Y., 2012b. Diversity of lanthanide(III)-2,5-dihydroxy-1,4-benzenedicarboxylate extended frameworks: syntheses, structures, and magnetic properties. Dalton Trans. 41, 11428–11437.

Wang, C., Liu, D., Lin, W., 2013a. Metal–organic frameworks as a tunable platform for designing functional molecular materials. J. Am. Chem. Soc. 135, 13222–13234.

Wang, P., Fan, R.-Q., Liu, X.-R., Wang, L.-Y., Yang, Y.-L., Cao, W.-W., Yang, B., Hasi, W., Su, Q., Mu, Y., 2013b. Two-/three-dimensional open lanthanide-organic frameworks containing rigid/flexible dicarboxylate ligands: synthesis, crystal structure and photoluminescent properties. CrystEngComm 15, 1931–1949.

Ward, M.D., 2007. Transition-metal sensitised near-infrared luminescence from lanthanides in d–f heteronuclear arrays. Coord. Chem. Rev. 251, 1663–1677.

Wei, L., Ye, Y., Zhang, R., 2014. Synthesis, crystal structure and fluorescence properties of Nd$^{3+}$ complex with tetrabromoterephthalic acid. J. Mol. Struct. 1058, 51–55.

Weissman, S.I., 1942. Intramolecular energy transfer the fluorescence of complexes of europium. J. Chem. Phys. 10, 214–217.

Weng, D., Zheng, X., Chen, X., Li, L., Jin, L., 2007. Synthesis, upconversion luminescence and magnetic properties of new lanthanide–organic frameworks with $(4^3)_2(4^6,6^6,8^3)$ topology. Eur. J. Inorg. Chem. 2007, 3410–3415.

Wenkin, M., Devillers, M., Tinant, B., Declercq, J.-P., 1997. Diammine (pyrazine-2,3-dicarboxylato-N, O) palladium(II): synthesis, crystal structure, spectroscopic and thermal properties. Inorg. Chim. Acta 258, 113–118.

Wilcken, R., Zimmermann, M.O., Lange, A., Joerger, A.C., Boeckler, F.M., 2013. Principles and applications of halogen bonding in medicinal chemistry and chemical biology. J. Med. Chem. 56, 1363–1388.

Wong, W.-K., Zhu, X., Wong, W.-Y., 2007. Synthesis, structure, reactivity and photoluminescence of lanthanide(III) monoporphyrinate complexes. Coord. Chem. Rev. 251, 2386–2399.

Woodruff, D.N., Winpenny, R.E.P., Layfield, R.A., 2013. Lanthanide single-molecule magnets. Chem. Rev. 113, 5110–5148.

Xia, J., Zhao, B., Wang, H.-S., Shi, W., Ma, Y., Song, H.-B., Cheng, P., Liao, D.-Z., Yan, S.-P., 2007. Two- and three-dimensional lanthanide complexes: synthesis, crystal structures, and properties. Inorg. Chem. 46, 3450–3458.

Xie, Y., Bai, F.Y., Xing, Y.H., Wang, Z., Pu, Z.F., Ge, M.F., 2010. Lanthanide(III) coordination polymers with longer-spanning flexible ligand: synthesis, crystal structure and luminescence property. J. Inorg. Organomet. Polym. Mater. 20, 258–263.

Xie, L.-H., Wang, Y., Liu, X.-M., Lin, J.-B., Zhang, J.-P., Chen, X.-M., 2011. Crystallographic studies into the role of exposed rare earth metal ion for guest sorption. CrystEngComm 13, 5849–5857.

Xu, H.T., Zheng, N.W., Jin, X.L., Yang, R.Y., Li, Z.Q., 2003. Channel structure of diaquasesqui (2-aminoterephthalato) dysprosium(III) dihydrate. J. Mol. Struct. 646, 197–199.

Xu, H., Liang, J., Zhuang, J., Kou, H., Wang, R., Li, Y., 2004. Microporous-structural rare-earth coordination polymers constructed by 2-bromoterephthalate. J. Mol. Struct. 689, 177–181.

Xu, J., Cheng, J., Su, W., Hong, M., 2011. Effect of lanthanide contraction on crystal structures of three-dimensional lanthanide based metal–organic frameworks with thiophene-2,5-dicarboxylate and oxalate. Cryst. Growth Des. 11, 2294–2301.

Xu, W., Zhou, Y., Huang, D., Xiong, W., Su, M., Wang, K., Han, S., Hong, M., 2013. Crystal structure, multiplex photoluminescence, and magnetic properties of a series of lanthanide coordination polymers based on quinoline carboxylate ligand. Cryst. Growth Des. 13, 5420–5432.

Xue, D.-X., Cairns, A.J., Belmabkhout, Y., Wojtas, L., Liu, Y., Alkordi, M.H., Eddaoudi, M., 2013. Tunable rare-earth fcu-MOFs: a platform for systematic enhancement of $CO_2$ adsorption energetics and uptake. J. Am. Chem. Soc. 135, 7660–7667.

Yanagida, S., Hasegawa, Y., Murakoshi, K., Wada, Y., Nakashima, N., Yamanaka, T., 1998. Strategies for enhancing photoluminescence of $Nd^{3+}$ in liquid media. Coord. Chem. Rev. 171, 461–480.

Yang, Y.-Y., Zai, S.-B., Wong, W.-T., Ng, S.W., 2005. Poly[dimethylammonium aquadi-[µ]-oxalato-europate(III) trihydrate]. Acta Crystallogr. Sect. E 61, m1912–m1914.

Yang, J., Yue, Q., Li, G.-D., Cao, J.-J., Li, G.-H., Chen, J.-S., 2006. Structures, photoluminescence, up-conversion, and magnetism of 2D and 3D rare-earth coordination polymers with multicarboxylate linkages. Inorg. Chem. 45, 2857–2865.

Yang, L.-R., Song, S., Shao, C.-Y., Zhang, W., Zhang, H.-M., Bu, Z.-W., Ren, T.-G., 2011. Synthesis, structure and luminescent properties of two-dimensional lanthanum(III) porous coordination polymer based on pyridine-2,6-dicarboxylic acid. Synth. Met. 161, 925–930.

Yang, H., Wang, F., Tan, Y.-X., Kang, Y., Li, T.-H., Zhang, J., 2012a. Charge matching on designing neutral cadmium–lanthanide–organic open frameworks for luminescence sensing. Chem. Asian. J. 7, 1069–1073.

Yang, K., Luo, J.-H., Liu, Z.-H., 2012b. Synthesis, structures and luminescent property of two lanthanon complexes assembled from 2,3-pyrazinedicarboxylic acid and ammonia. Inorg. Chim. Acta 391, 206–209.

Ye, B.-H., Tong, M.-L., Chen, X.-M., 2005. Metal-organic molecular architectures with 2,2′-bipyridyl-like and carboxylate ligands. Coord. Chem. Rev. 249, 545–565.

Ye, J., Zhang, J., Ning, G., Tian, G., Chen, Y., Wang, Y., 2008. Lanthanide coordination polymers constructed from dinuclear building blocks: novel structure evolution from one-dimensional chains to three-dimensional architectures. Cryst. Growth Des. 8, 3098–3106.

Zhan, C.-H., Wang, F., Kang, Y., Zhang, J., 2012. Lanthanide-thiophene-2,5-dicarboxylate frameworks: ionothermal synthesis, helical structures, photoluminescent properties, and single-crystal-to-single-crystal guest exchange. Inorg. Chem. 51, 523–530.

Zhang, Y.-L., 2011. Poly[[diaquabis(2,2'-bipyridine)bis([µ]3-5-hydroxyisophthalato)([µ]2-5-hydroxyisophthalato)digadolinium(III)] trihydrate]. Acta Crystallogr. Sect. E 67, m1368–m1369.

Zhang, L.-P., Wan, Y.-H., Jin, L.-P., 2003. Hydrothermal synthesis and crystal structure of neodymium(III) coordination polymers with isophthalic acid and 1,10-phenanthroline. Polyhedron 22, 981–987.

Zhang, G.-X., Zhang, W., Han, Z.-B., 2009a. Synthesis, structures, and photoluminescent properties of 3D lanthanide coordination polymers with rare (4,5)-connected topology. Inorg. Chem. Commun. 12, 982–985.

Zhang, X., Xing, Y., Wang, C., Han, J., Li, J., Ge, M., Zeng, X., Niu, S., 2009b. Lanthanide–alkali metals–oxalates coordination polymers: synthesis and structures of $[Nd(C_2O_4)_{1.5}(H_2O)_3]$ •2$H_2O$, $Nd(C_2O_4)(CH_3COO)(H_2O)$, $KLn(C_2O_4)_2(H_2O)_4$ (Ln=Y, Tb). Inorg. Chim. Acta 362, 1058–1064.

Zhang, Q., Wang, X., Wang, S.-T., Liu, C.-B., Che, G.-B., 2012. Poly[[tri-[µ]3-hydroxido-tris([µ] 4-pyridine-2,5-dicarboxylato)trineodymium(III)] monohydrate]. Acta Crystallogr. Sect. E 68, m541–m542.

Zhao, L.-Z., Tian, Y.-Y., Gong, Y.-X., Huang, X.-T., Zhang, F., Rong, J.-X., Cai, X., Li, W.-T., Zeng, R.-H., Lu, D.-S., 2014. 2D $Ln^{III}$(Nd/La)-$Ag^I$ heterometallic and $Tm^{III}$ homometallic coordination polymers based on pyridine dicarboxylate-ligands. Z. Anorg. Allg. Chem. 640, 147–152.

Zheng, Z., 2010. Cluster compounds of rare-earth elements. In: Gschneidner, K.A., Bünzli, J.-C.G., Pecharsky, V.K. (Eds.), Handbook on the Physics and Chemistry of Rare Earths. vol. 40. Elsevier, Amsterdam, pp. 109–239, Ch. 245.

Zheng, X.-J., Jin, L.-P., Lu, S.-Z., 2002. Hydrothermal syntheses, structures, and properties of first examples of lanthanide(III) 2,3-pyrazinedicarboxylates with three-dimensional framework. Eur. J. Inorg. Chem. 2002, 3356–3363.

Zheng, X., Sun, C., Lu, S., Liao, F., Gao, S., Jin, L., 2004a. New porous lanthanide-organic frameworks: synthesis, characterization, and properties of lanthanide 2,6-naphthalenedicarboxylates. Eur. J. Inorg. Chem. 2004, 3262–3268.

Zheng, X.-J., Jin, L.-P., Gao, S., 2004b. Synthesis and characterization of two novel lanthanide coordination polymers with an open framework based on an unprecedented $[Ln_7(µ_3-OH)_8]^{13+}$ cluster. Inorg. Chem. 43, 1600–1602.

Zheng, X.-J., Wang, Z.-M., Gao, S., Liao, F.-H., Yan, C.-H., Jin, L.-P., 2004c. Hydrothermal syntheses, structures, and properties of three 3-D lanthanide coordination polymers that form 1-D channels. Eur. J. Inorg. Chem. 2004, 2968–2973.

Zheng, X.-J., Jin, L.-P., Gao, S., Lu, S.-Z., 2005a. New ternary lanthanide coordination polymers of 1,4-naphthalenedicarboxylate with 1,10-phenanthroline. Inorg. Chem. Commun. 8, 72–75.

Zheng, X.-J., Jin, L.-P., Gao, S., Lu, S.-Z., 2005b. Second ligand-directed self-assembly of lanthanide(III) coordination polymers with 1,4-naphthalenedicarboxylate. New J. Chem. 29, 798–804.

Zou, J.-Z., Xu, Z., Chen, W., Lo, K.M., You, X.-Z., 1999. Synthesis, structure and magnetic properties of new polymeric compounds containing manganese(II)–Pzdc (PzdcH$_2$: 2,3-Pyrazinedicarboxylic acid). Polyhedron 18, 1507–1512.

# Chapter 272

# Microscopic Thermodynamic Descriptors for Rationalizing Lanthanide Complexation Processes

## Claude Piguet

*Department of Inorganic and Analytical Chemistry, University of Geneva, Geneva, Switzerland*

## Chapter Outline

## 1 INTRODUCTION

### 1.1 Coordination Chemistry: f-Block Elements Follow d-Block Elements

At the death of Napoleon the First in 1821, when Chateaubriand wrote *Bonaparte rendit à Dieu le plus puissant souffle de vie qui jamais anima l'argile humaine*, 80% of the natural d-block elements was already discovered (among

the 30 transition metal elements of columns 3–12 of the periodic table, only scandium, technetium, ruthenium, lanthanum, hafnium, and rhenium were missing), while only 11% of the natural f-block elements, i.e., cerium and uranium had been identified (Fig. 1; Weeks, 1960). Because of their reluctance toward reduction, the discovery of the f-block elements is inextricably linked to the separation of "complexes," sometimes referred to as "earths" when combined with oxide or hydroxide anions, a topic which will become relevant to coordination chemistry in the early stage of the twentieth century.

Rare earth coordination chemistry indeed began when Gadolin (1794), a Finnish chemist, separated a novel earth, i.e., a metallic oxide named yttria, by precipitation of the hydrated ions from an acidic solution (Szabadvary, 1988). Using the same strategy, cerium oxide referred to as ceria was discovered in 1804 (Hisinger and Berzelius, 1804; Klaproth, 1804), but it was Mosander (1839), a pupil of Berzelius, that made a major discovery for rare earth coordination chemistry when he reported that lanthanum oxide, a third novel rare earth, was more basic than cerium oxide and was therefore slightly more soluble in cold dilute nitric acid. This crucial report initiated 70 years of intense chemical activity, during which the pH-controlled precipitation and the related fractional crystallization of the double salts and the adducts of rare earth were exploited for the separation of the different elements (Moeller, 1967). However, the formation of coordination complexes was only incidental, and the first planned preparation of a rare earth chelate can be attributed to Urbain (1896), who used acetylacetonates in a separation procedure (Binnemans, 2005). At the same time, Werner (1893) indeed realized that the controversial maximum valency of the carbon atom, eventually fixed to four by Abegg (1904) and Lewis (1916) is not a general trend, and that many other possibilities (in modern language, other coordination numbers, CN) could be found for the various elements of the periodic table. With this concept in mind, coordination chemistry rapidly evolved toward a well-recognized part of chemistry dealing with variable coordination numbers (CN = 2–6), but clearly dominated by octahedral geometry thanks to the discovery of the exceptional stabilities and kinetic inertness of the complexes formed between trivalent d-block cations and (poly)amine ligands (Constable and Housecroft, 2013). Because of their kinetic lability and partial hydrolysis upon reaction with polyamine ligands, the related trivalent rare earth complexes cannot benefit from the isolation of their geometric isomers (Werner, 1893) and the chiral resolution of their diastereoisomeric salts (Werner and Vilmos, 1899) for elucidating their structure. Whereas d-block cations were known to prefer coordination numbers between 4 and 6, the coordination numbers of rare earths was the subject of considerable debate until the number of 9 emerged from the structure of the aqua complex $[R(H_2O)_9]^{3+}$, which was established by X-ray diffraction in the late 1930s for samples of solid ethylsulfates $R(C_2H_5OSO_3)_3 \cdot 9H_2O$ (Ketelaar, 1937) and bromates $Nd(BrO_3)_3 \cdot 9H_2O$ (Helmholz, 1939). Though these hydrates were

**FIGURE 1**  A periodic table showing the date of the discovery of each element. The grayish part highlights the 24 d-block and the 2 f-block elements already isolated in 1821.

found to have a tricapped trigonal prismatic structure, simple molecular mechanics calculation predicts only a marginal destabilization for the alternative capped square antiprism geometry adopted in $[R(H_2O)_8]^{3+}$ (Choppin, 1989). Since the exact structures, thermodynamic and kinetic properties of the hydrated ions were crucial for rationalizing and optimizing separation processes in aqueous solution (Hulet and Bodé, 1972; Powell, 1979), myriad of analytical techniques such as X-ray scattering and absorption, neutron diffraction, ultrasonic absorption, Raman spectra, multinuclear NMR data, and calorimetric titrations (Rizkalla and Choppin, 1991, 1994) were combined with theoretical calculations (D'Angelo and Spezia, 2012) to get a global picture, in which the nine-coordinate and eight-coordinate aquo ions were found to be close in energy and dominate the speciation in aqueous solution along the complete lanthanide series (Ciupka et al., 2010; Kuta and Clark, 2010). A noticeable breakthrough in rare earth coordination chemistry only occurred after the second world war when the chelate effect was recognized as a major contribution to the thermodynamic stability of d-block complexes (Martell, 1966; Motekaitis et al., 1994; Schwarzenbach, 1952). The transfer of this strategy toward trivalent f-block cations resulted in the use of multidentate ligands containing both soft N-donor and hard O-donor atoms such as 2,2′,2″-nitrilotriacetic acid (NTA; Anderegg, 1960), 2,2′,2″,2‴-(ethane-1,2-diyldinitrilo)tetraacetic acid (EDTA; Schwarzenbach, 1957), diethylenetriaminopentaacetic acid (DTPA; Anderegg et al., 1959), or 1,4,7,10-tetraazacyclodoecane-1,4,7,10-tetraacetic acid (DOTA; Bianchi et al., 2000) for the efficient sequestration of rare earths in aqueous solution (Fig. 2). The report by Hoard and his coworkers of the crystal structures of $NH_4La(EDTA)\cdot 8H_2O$ (Lind et al., 1965) and of $HLa(EDTA)\cdot 7H_2O$ (Hoard et al., 1965), whereby lanthanum(III) is, respectively, nine- and ten-coordinated, unambiguously established that valencies beyond six are common for rare earth complexes, an observation which transformed into a rule during the next decade (Moseley, 1975).

## 1.2 Scope of the Review

In this chapter, we identify and highlight some breakthrough or crucial trends in rare earth coordination chemistry which occurred during the past 35 years, i.e., since the seminal review of Thompson (1979) which appeared in the initial set of four volumes of the Handbook. It is worth mentioning here that, in the same set of volumes, Powell (1979) summarized more than a hundred years of intense efforts focused on the separation of rare earths, a procedure which was at the origin of the interest for rare earth coordination chemistry, and Jørgensen (1979) reminded the basis in rare earth theory, with special emphasis on the rational effects produced by local environment on the electronic structures of both the ground state, which controls the magnetic properties of the coordination complexes (Reuben, 1979 and Reuben and Elgavish, 1979) and of the excited states, which induce the optical properties of rare

**A**

NTA$^{3-}$

$+ Gd^{3+}$ $\xrightarrow[298\ K]{H_2O\ /\ 0.1\ M\ KCl}$ [Gd(NTA)]

$\log\left(\beta_{1,1}^{Gd,NTA}\right) = 11.43$

Anderegg (1960)

**B**

EDTA$^{4-}$

$+ Gd^{3+}$ $\xrightarrow[298\ K]{H_2O\ /\ 0.1\ M\ KCl}$ [Gd(EDTA)]$^-$

$\log\left(\beta_{1,1}^{Gd,EDTA}\right) = 16.70$

Wheelwright et al. (1953)

**C**

DPTA$^{5-}$

$+ Gd^{3+}$ $\xrightarrow[298\ K]{H_2O\ /\ 0.1\ M\ KCl}$ [Gd(DPTA)]$^{2-}$

$\log\left(\beta_{1,1}^{Gd,DTPA}\right) = 23.01$

Harder and Chaberek (1959)

**D**

DOTA$^{4-}$

$+ Gd^{3+}$ $\xrightarrow[298\ K]{H_2O\ /\ 0.1\ M\ KCl}$ [Gd(DOTA)]$^-$

$\log\left(\beta_{1,1}^{Gd,DOTA}\right) = 24.0$

Desreux (1979)
Cacheris et al. (1987)
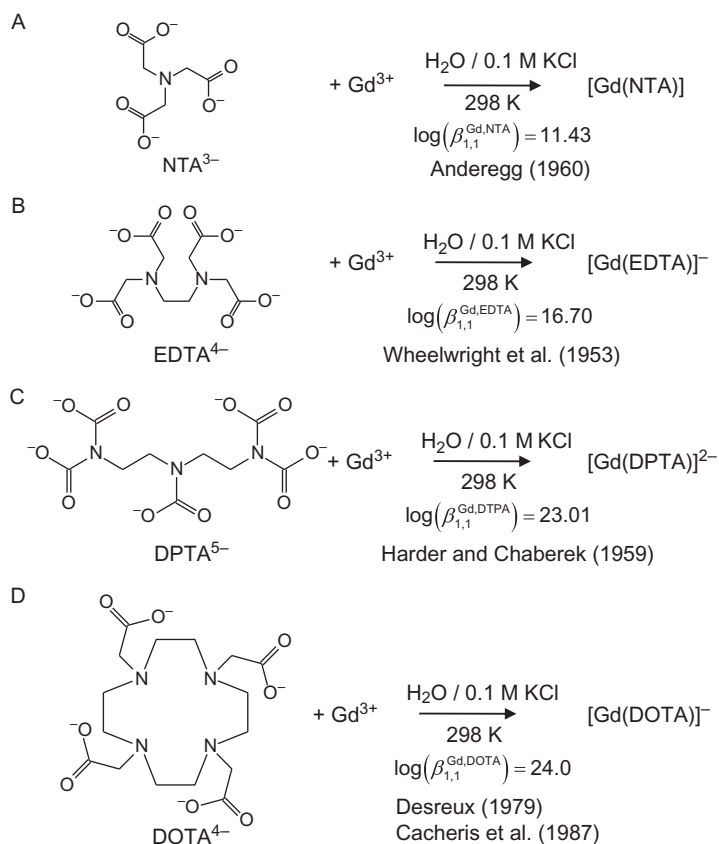
**FIGURE 2** Classical rare earth coordination chemistry at the time of the publication of the first volume of the Handbook on the Physics and Chemistry of Rare Earths dedicated to rare earth non-metallic compounds in 1979.

earth cations in solution (Carnall, 1979). With this in mind, the subsequent exploitation of lanthanide-centered paramagnetism for the design of NMR probes and of contrast agents in solution (Bottrill et al., 2006; Caravan et al., 1999; Forsberg, 1996; Peters et al., 1996; Piguet and Geraldes, 2003; Sharp, 2001; Terreno et al., 2010) together with the recent emergence of intense activities in the design of single-molecular magnets (Feltham and Brooker, 2014; Ishikawa et al., 2003; Rinehart and Long, 2011; Sorace et al., 2011; Woodruff et al., 2013) appears as the straight heritage of these theoretical considerations applied to the modeling of the ground state quadrupolar distribution of the 4f-shell electrons in nonspherical environments (Bleaney, 1972; Helm, 2006; Mironov et al., 2001; Orbach and Stapleton, 1972). Similarly, the yearly report of innumerable lanthanide-centered luminescent complexes undergoing indirect sensitization cannot be considered as

real breakthrough in rare earth coordination chemistry (Comby and Bünzli, 2007; Sabbatini et al., 1996). The stepwise infiltration of the supramolecular semantics, originally initiated by Lehn (1995) for alkaline and alkaline earth complexes into the field of rare earth coordination chemistry, is more intriguing and eventually led to a revolution in the design of sophisticated polynuclear rare earth complexes (dos Santos et al., 2008; Piguet and Bünzli, 2010; Winpenny, 1998). This review therefore aims at highlighting the novel trends brought by the merging of coordination chemistry with supramolecular chemistry using rare earth cations. The first consequence resulted in the report of an impressive amount of thermodynamic data collected in aqueous (Bianchi et al., 2000; Choppin, 1989; Choppin and Rizkalla, 1994; Kremer et al., 2005; Nash, 1994) and in organic solvents (Arnaud-Neu, 1994; Bünzli, 1987; Bünzli and Milicic-Tang, 1995; Di Bernardo et al., 2012; Ishiguro et al., 2002; Kolarik, 2008; Liu et al., 2000; Panak and Geist, 2013) with the ultimate goal of getting an improved understanding of the structure and of the stability exhibited by solvated cations in the presence of multidentate ligands. The second noticeable step is indebted to Choppin (1989), who realized that the biologically famous enthalpy/entropy compensation scheme can be used as a guide for understanding rare earth complexation processes (Liu et al., 2000). Finally, the extension of rare earth coordination chemistry toward multivalency forced coordination chemists to reactivate the concept of thermodynamic cooperativity for rationalizing the formation of polynuclear lanthanide assemblies (Ercolani and Schiaffino, 2011; Piguet, 2010). Please note that the extension of rare earth coordination chemistry toward organometallic compounds (Schumann and Genthe, 1984) and toward lower oxidation state complexes (Evans, 2007; MacDonald et al., 2013; Nief, 2010) is not considered here. For comprehensive reviews of the coordination chemistry of rare earth covering the 1980–2010 period excluding multivalency, the reader should consult the collective works edited by Saez Puche and Caro (1998), Sastri et al. (2003), and Huang (2010).

## 2 THE MAIN STREAM IN RARE EARTH THERMODYNAMICS

### 2.1 The Separation of Rare Earths and Actinides

The first 150 years of rare earth chemistry were dominated by the separation of macroscopic amounts of individual elements by using fractional crystallizations, but the small difference in solubility along the lanthanide series required hundreds or even thousands of repetitions to achieve a satisfying purity for the elements (Moeller, 1963; Powell, 1979). The further need for actinide/lanthanide separation initiated during the second world war led to the rapid development of ion exchange and solvent extraction techniques, which offer the opportunity to exploit a variety of minor chemical effects mainly arising from the well-known ionic radius contraction which

accompanies the increase in their atomic number (Hulet and Bodé, 1972; Nash, 1994). These procedures are built around some standard ligand exchange process (Eq. 1), for which a wide range of empirical solvation/adsorption/affinity effects are exploited to enhance separation (Kolarik, 2008; Panak and Geist, 2013).

$$\left[R(H_2O)_x\right]^{3+} + n\left[L(H_2O)_y\right]^{z-} \rightleftharpoons \left[R(L)_n(H_2O)_{(x+ny-p)}\right]^{(3-nz)} + pH_2O\beta_{1,n}^{R,L} \quad (1)$$
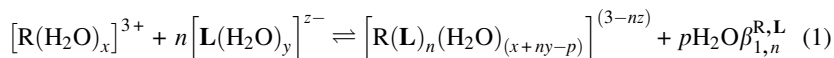
It is important to note that energy differences of only 0.4–1.8 kJ/mol are sufficient for a successful extraction or ion exchange separation process (Nash, 1994), which probably explains the regular publications of thermodynamic data collected along both the lanthanide and actinide series for myriads of different ligands (Kolarik, 2008; Kremer et al., 2005; Panak and Geist, 2013; Sastri et al., 2003). Tables 1–3 and Fig. 3A illustrate such research approach applied to simple multidentate ligands.

Inspired by the success of the ligand-field theory in explaining the thermodynamic Irving–Williams series for transitions metals (Figgis and Hitchman, 2000),

**TABLE 1** Stability Constants $\log(\beta_{1,n}^{R,L})$ of Rare Earth Complexes with 2-Hydroxycyclohepta-2,4,6-Trien-1-on-3 (Tropolone: LH) in Water (Campbell and Moeller, 1969)

| Metal | Ionic Strength | $T$ (°C) | $\log(\beta_{1,1}^{R,L})$ | $\log(\beta_{1,2}^{R,L})$ | $\log(\beta_{1,3}^{R,L})$ |
|---|---|---|---|---|---|
| $La^{3+}$ | 0.1 M KNO$_3$ | 25 | 6.19 | 11.12 | 15.31 |
| $Ce^{3+}$ | 0.1 M KNO$_3$ | 25 | 6.56 | 11.76 | 16.12 |
| $Pr^{3+}$ | 0.1 M KNO$_3$ | 25 | 6.61 | 11.94 | 16.39 |
| $Nd^{3+}$ | 0.1 M KNO$_3$ | 25 | 6.77 | 12.21 | 16.61 |
| $Sm^{3+}$ | 0.1 M KNO$_3$ | 25 | 6.91 | 12.59 | 17.19 |
| $Eu^{3+}$ | 0.1 M KNO$_3$ | 25 | 7.10 | 12.81 | 17.62 |
| $Gd^{3+}$ | 0.1 M KNO$_3$ | 25 | 7.04 | 12.90 | 17.72 |
| $Tb^{3+}$ | 0.1 M KNO$_3$ | 25 | 7.15 | 13.18 | 18.00 |
| $Dy^{3+}$ | 0.1 M KNO$_3$ | 25 | 7.23 | 13.38 | 18.40 |
| $Ho^{3+}$ | 0.1 M KNO$_3$ | 25 | 7.40 | 13.60 | 18.80 |
| $Er^{3+}$ | 0.1 M KNO$_3$ | 25 | 7.54 | 13.91 | 19.15 |
| $Tm^{3+}$ | 0.1 M KNO$_3$ | 25 | 7.60 | 13.99 | 19.39 |
| $Yb^{3+}$ | 0.1 M KNO$_3$ | 25 | 7.85 | 14.35 | 19.83 |
| $Lu^{3+}$ | 0.1 M KNO$_3$ | 25 | 7.69 | 14.33 | 19.77 |

**TABLE 2** Stability Constants $\log(\beta_{1,n}^{R,L})$ of Rare Earth Complexes with 2,6-Pyridinedicarboxylic Acid (Dipicolinic Acid: $LH_2$) in Water (Grenthe, 1961)

| Metal | Ionic Strength | $T$ (°C) | $\log(\beta_{1,1}^{R,L})$ | $\log(\beta_{1,2}^{R,L})$ | $\log(\beta_{1,3}^{R,L})$ |
|---|---|---|---|---|---|
| $La^{3+}$ | 0.5 M $NaClO_4$ | 20 | 7.98 | 13.79 | 18.06 |
| $Ce^{3+}$ | 0.5 M $NaClO_4$ | 20 | 8.34 | 14.42 | 18.8 |
| $Pr^{3+}$ | 0.5 M $NaClO_4$ | 20 | 8.63 | 15.1 | 19.94 |
| $Nd^{3+}$ | 0.5 M $NaClO_4$ | 20 | 8.78 | 15.5 | 20.56 |
| $Sm^{3+}$ | 0.5 M $NaClO_4$ | 20 | 8.86 | 15.88 | 21.23 |
| $Eu^{3+}$ | 0.5 M $NaClO_4$ | 20 | 8.84 | 15.98 | 21.49 |
| $Gd^{3+}$ | 0.5 M $NaClO_4$ | 20 | 8.74 | 16.06 | 21.83 |
| $Tb^{3+}$ | 0.5 M $NaClO_4$ | 20 | 8.68 | 16.11 | 22.03 |
| $Dy^{3+}$ | 0.5 M $NaClO_4$ | 20 | 8.69 | 16.18 | 22.13 |
| $Ho^{3+}$ | 0.5 M $NaClO_4$ | 20 | 8.72 | 16.23 | 22.08 |
| $Er^{3+}$ | 0.5 M $NaClO_4$ | 20 | 8.77 | 16.39 | 22.13 |
| $Tm^{3+}$ | 0.5 M $NaClO_4$ | 20 | 8.83 | 16.54 | 22.04 |
| $Yb^{3+}$ | 0.5 M $NaClO_4$ | 20 | 8.85 | 16.61 | 21.73 |
| $Lu^{3+}$ | 0.5 M $NaClO_4$ | 20 | 9.03 | 16.8 | 21.48 |

**TABLE 3** Stability Constants $\log(\beta_{1,n}^{R,L})$ of Rare Earth Complexes with 2,2′,2″,2‴-(Ethane-1,2-Diyldinitrilo)Tetraacetic Acid (Ethylenediamine Tetraacetic Acid, EDTA: $LH_4$) in Water (Wheelwright et al., 1953)

| Metal | Ionic Strength | $T$ (°C) | $\log(\beta_{1,1}^{R,L})$ |
|---|---|---|---|
| $La^{3+}$ | 0.1 M KCl | 20 | 14.72 |
| $Ce^{3+}$ | 0.1 M KCl | 20 | 15.39 |
| $Pr^{3+}$ | 0.1 M KCl | 20 | 15.75 |
| $Nd^{3+}$ | 0.1 M KCl | 20 | 16.06 |
| $Sm^{3+}$ | 0.1 M KCl | 20 | 16.55 |
| $Eu^{3+}$ | 0.1 M KCl | 20 | 16.69 |
| $Gd^{3+}$ | 0.1 M KCl | 20 | 16.70 |
| $Tb^{3+}$ | 0.1 M KCl | 20 | 17.25 |

**TABLE 3** Stability Constants $\log(\beta_{1,n}^{R,L})$ of Rare Earth Complexes with 2,2',2'',2'''-(Ethane-1,2-Diyldinitrilo)Tetraacetic Acid (Ethylenediamine Tetraacetic Acid, EDTA: LH$_4$) in Water (Wheelwright et al., 1953)—cont'd

| Metal | Ionic Strength | $T$ (°C) | $\log(\beta_{1,1}^{R,L})$ |
|---|---|---|---|
| $Dy^{3+}$ | 0.1 M KCl | 20 | 17.57 |
| $Ho^{3+}$ | 0.1 M KCl | 20 | 17.67 |
| $Er^{3+}$ | 0.1 M KCl | 20 | 17.98 |
| $Tm^{3+}$ | 0.5 M NaClO$_4$ | 20 | 18.83 |
| $Yb^{3+}$ | 0.5 M NaClO$_4$ | 20 | 18.85 |
| $Lu^{3+}$ | 0.5 M NaClO$_4$ | 20 | 19.03 |

similar attempts were made for correlating the minor thermodynamic changes affecting the thermodynamic formation constants along the lanthanide series with the crystal-field effects produced by ligands around the trivalent cations (Sastri et al., 2003).

As a first step toward this goal, the free energy change accompanying the complexation reaction in Eq. (1) was tentatively modeled with Eq. (2), which simply balances the electrostatic energies produced by the replacement of $p$ molecules of water in the aquo-ion $[R(H_2O)_x]^{3+}$ (monopole–dipole interaction: $e$ is the elementary charge, $r_i$ is the ionic radius of the rare earth, $r_w$ is the radius of water, $\mu$ is the dipole moment of water, $N_{Av}$ is Avogadro number) with $n$ molecules of ligand $\mathbf{L}^{z-}$ in $\left[R(\mathbf{L})_n(H_2O)_{(x+ny-p)}\right]^{(3-nz)^+}$ (monopole–monopole interaction: $r_L$ is the ligand radius, $S_p$ is the intramolecular interligand repulsion). The $C$ constant takes into account the changes in solvation energies between the reactants and products (Yatsimirskii and Kostromina, 1964).

$$\frac{\Delta'G_{1,n}^{R,L}}{N_{Av}} = p\frac{3e\mu}{(r_i+r_w)^2} - n\frac{z(3-S_p)e^2}{(r_i+r_L)} - C \qquad (2)$$

Given that the lanthanide contraction is regular along the series, $\Delta'G_{1,n}^{R,L}$ smoothly varies and any deviation of the experimental complexation energies $\Delta G_{1,n}^{R,L} = -2.303RT\log\left(\beta_{1,n}^{R,L}\right)$ is assigned to an extra-stabilization energy $-\Delta E' = 2.303RT\log\left(\beta_{1,n}^{R,L}\right) - \Delta'G_{1,n}^{R,L}$ produced by the crystal field effects (Fig. 3B). Applied to the debatable choice of an octahedral coordination for [Ln(EDTA)]$^-$ complexes, the latter approach eventually estimated crystal field strengths in the 300–600 cm$^{-1}$ range along the lanthanide series (3.6–7.2 kJ/mol, Yatsimirskii and Kostromina, 1964). More realistic treatments
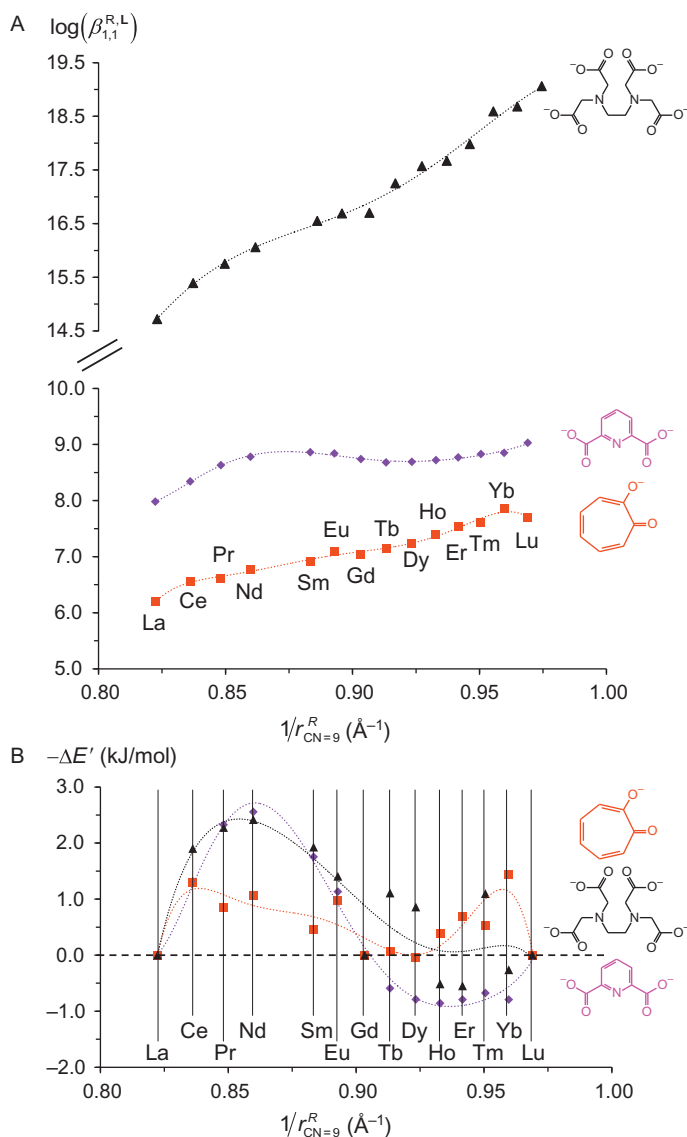
**FIGURE 3** (A) Typical trends for the thermodynamic formation constants $\log\left(\beta_{1,1}^{Ln,L}\right)$ collected for multidentate ligands in water along the lanthanide series (squares, tropolonate; diamond, dipicolinate; triangles, EDTA; Tables 1–3) in function of the inverse of their ionic radii in nine-coordinate complexes, and (B) associated extrastabilization energy $-\Delta E' = 2.303RT \log\left(\beta_{1,1}^{Ln,L}\right) - \Delta'G_{1,1}^{Ln,L}$ (see text). The dotted traces are only guides for the eyes.

of the lanthanide coordination spheres using larger coordination numbers indeed showed that these effects are often dominated by spin-pairing energies (Johnson, 1982), which require a deeper insights into the electronic distribution in the 4f-orbitals for being quantitatively modeled (Jørgensen, 1973). Consequently, the specific thermodynamic trends reported for various ligands along the lanthanide series usually escapes rationalization with the standard tools used with d-block transition metals (Sastri et al., 2003). We, however, note that the consequent lack of planning for the design of thermodynamic stabilities was not considered as a severe handicap when profitable lanthanide/actinide separations and extractions are foreseen, and several thousands of stability constants and/or separation coefficients were carefully collected along the last three decades for overcoming the theoretical limitations (Kolarik, 2008; Panak and Geist, 2013). In the modern context of the treatment of contaminated nuclear wastes which requires some selective two-phase aqueous/organic extraction processes, uncharged ligands with low affinities for trivalent lanthanides or actinides have found a renewal of interest when used in anhydrous organic solvents (Ishiguro et al., 2002; Drew et al., 2004). Consequently, some impressive tabulations of thermodynamic formation constants collected for simple ligands (Bünzli and Milicic-Tang, 1995) or for sophisticated podands and macro(poly) cylic receptors (Arnaud-Neu, 1994; Bünzli, 1987; Di Bernardo et al., 2012; Liu et al., 2000) with trivalent cations in alcohol, in acetonitrile, in $N,N'$-dimethylformamide, in dimethylsulfoxide, and in propylene carbonate now complete the original set of data collected in water.

## 2.2 Solvation and Hydrolysis

Since the formation constants, i.e., the free energy change, cannot be rationalized in terms of simplistic factors, the close examination of the thermodynamic origin of the free energy changes accompanying the complexation reaction $\Delta G_{1,n}^{\mathrm{R,L}} = -RT \ln\left(\beta_{1,n}^{\mathrm{R,L}}\right) = \Delta H_{1,n}^{\mathrm{R,L}} - T\Delta S_{1,n}^{\mathrm{R,L}}$ in terms of enthalpy ($\Delta H_{1,n}^{\mathrm{R,L}}$) and entropy ($\Delta S_{1,n}^{\mathrm{R,L}}$) changes was thought to bring crucial clues to this challenge. Since most of the systems studied implied aqueous solution, initial efforts were focused on the rationalization of the rare earth hydration process as shown in Eq. (3) (Rizkalla and Choppin, 1991), which is considered as one of the most simple coordination processes leading to the formation of rare earth–ligand dative bonds (Ciupka et al., 2010).

$$R_{(g)}^{3+} \xrightarrow{\mathrm{H_2O}} R_{(aq)}^{3+} \quad \Delta G_{\mathrm{hyd}}^{\mathrm{R}} = \Delta H_{\mathrm{hyd}}^{\mathrm{R}} - T\Delta S_{\mathrm{hyd}}^{\mathrm{R}} \tag{3}$$
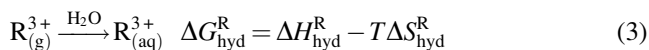
Since Eq. (3) violates the principle of electroneutrality (Johnson, 1982), the thermodynamic hydration energies are not experimentally accessible and only the global hydration processes involving ion pairs in Eq. (4) can be approached by using a thermodynamic cycle, which combines the oxidation energies of rare earths by halides ($\Delta G_{\mathrm{ox}}^{\mathrm{R,X}}$) and the electrode potentials
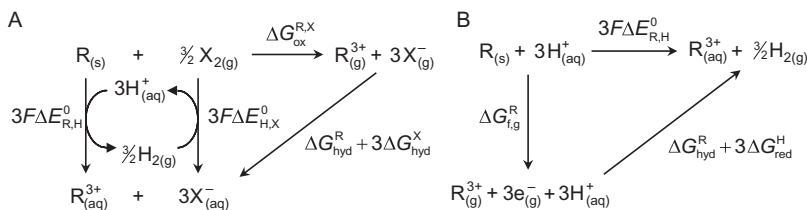
**FIGURE 4** Born–Haber thermochemical cycles used for estimating (A) the experimentally measurable free energy of hydration of rare earth halides and (B) the calculated single-ion hydration energies of trivalent rare earths. $F$ is the Faraday constant and the gaseous halides are taken in the standard state.

monitored for the electrochemical cells $R_{(s)}\left|R^{3+}_{(aq)}\right|\left|H^{+}_{(aq)}\right|H_{2(g)}$ ($\Delta E^{0}_{R,H}$) and $H_{2(g)}\left|H^{+}_{(aq)}\right|\left|X_{2(g)}\right|X^{-}_{(aq)}$ ($\Delta E^{0}_{H,X}$) (Fig. 4A and Eq. 5).

$$R^{3+}_{(g)} + 3X^{-}_{(g)} \rightarrow R^{3+}_{(aq)} + 3X^{-}_{(aq)} \quad \Delta G^{R}_{hyd} + 3\Delta G^{X}_{hyd} \tag{4}$$

$$\Delta G^{R}_{hyd} + 3\Delta G^{X}_{hyd} = -\Delta G^{R,X}_{ox} - 3F\left(\Delta E^{0}_{R,H} + \Delta E^{0}_{H,X}\right) \tag{5}$$
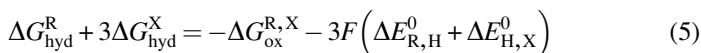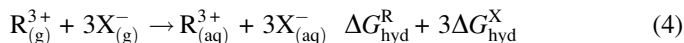
The precise constancy of the figures for RF-RCl, i.e., $\left(\Delta G^{R}_{hyd} + 3\Delta G^{F}_{hyd}\right) - \left(\Delta G^{R}_{hyd} + 3\Delta G^{Cl}_{hyd}\right)$, as R varies indeed justifies the assignment of a unique $\Delta G^{R}_{hyd}$ to each individual ion as expressed in Eq. (3), according to that an absolute values can be attributed to a reference cation. This limitation is closely related to the use of the reduction of $H^{+}_{(aq)}$ (Eq. 6) as a reference for the electrochemical series, and the associated free energy change $\Delta G^{H}_{red}$ was similarly selected for arbitrarily fixing the zero scale of the hydration energies (Johnson, 1982).

$$H^{+}_{(aq)} + e^{-}_{(g)} \rightarrow \frac{1}{2}H_{2(g)} \Delta G^{H}_{red} \tag{6}$$
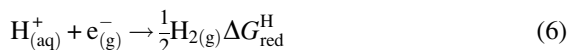
Since the experimental free energy of oxidation of $R_{(s)}$ in acidic medium to give $R^{3+}_{(g)}$ ($\Delta G^{R}_{f,gas}$) and $R^{3+}_{(aq)} + {}^{3}/_{2}H_{2(g)}$ ($3F\Delta E^{0}_{R,H}$) is experimentally accessible, the single ion hydration energies $\Delta G^{R}_{hyd}$ can be deduced from the thermodynamic cycle depicted in Fig. 4B and summarized in Eq. (7) (Johnson, 1982).

$$\Delta G^{R}_{hyd} = 3F\Delta E^{0}_{R,H} - \Delta G^{R}_{f,g} - 3\Delta G^{H}_{red} \tag{7}$$
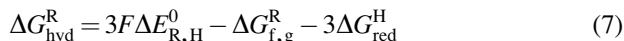
Many attempts have been made to obtain reliable values for $\Delta G^{H}_{red}$, but all of them involve assumptions that cannot be unambiguously substantiated, and we will refer to $\Delta G^{H}_{red} = -458$ kJ/mol reported by Gomer and Tryson (1977) for computing the hydration free energies $\Delta G^{R}_{hyd}$ illustrated in Fig. 5. Similar reasoning applies for the calculation of the hydration enthalpies changes $\Delta H^{R}_{hyd}$, from which the entropic contributions can be deduced $T\Delta S^{R}_{hyd} = \Delta H^{R}_{hyd} - \Delta G^{R}_{hyd}$ (Marcus, 1994). The free energies and the enthalpies of hydration of the
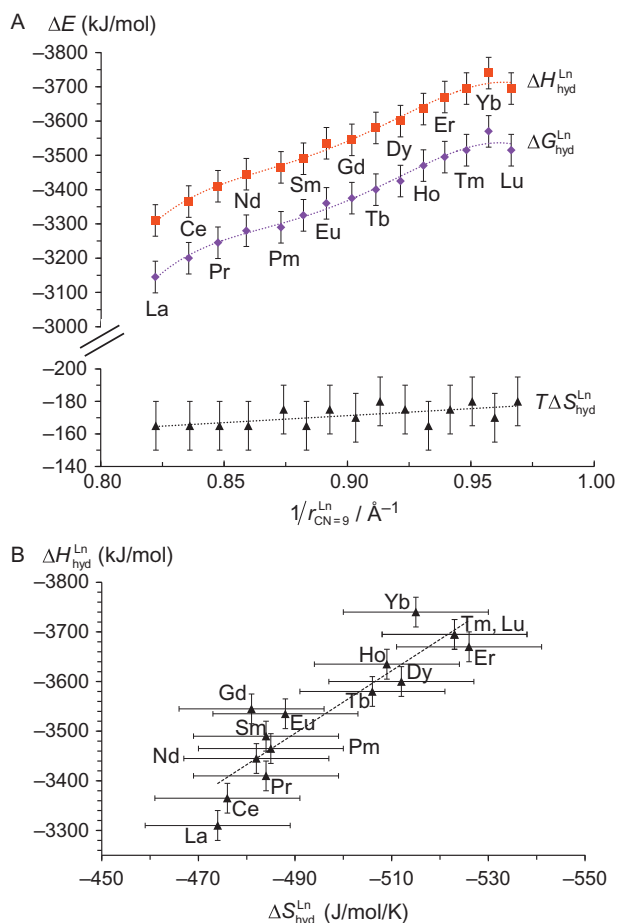
**FIGURE 5** (A) Standard molar single-ion hydration free energies $\Delta G_{hyd}^{Ln}$, enthalpies $\Delta H_{hyd}^{Ln}$, and entropies $T\Delta S_{hyd}^{Ln}$ reported for trivalent lanthanides (Marcus, 1994) and (B) entropy–enthalpy plot for which $\Delta S_{hyd}^{Ln}$ refers to aqueous solutions at infinite dilutions (Marcus, 1994).

trivalent lanthanides have an approximately linear dependence with the inverse of the ionic radii, a trend in line with a pure electrostatic model. The two minor bumps in the Ce-Nd and Er-Tm regions have been attributed to a combination of crystal-field and spin pairing energies (Morss, 1971). The solvation enthalpy change dominates the hydration process, while the entropy contribution only counts for 3–5% of the overall free energy change (Fig. 5A). It is worth noting that (i) $\Delta H_{hyd}^{R} < 0$ are favorable whereas $-T\Delta S_{hyd}^{R} > 0$ fight against the lanthanide solvation process and (ii) the latter two opposite contributions are roughly linearly correlated within experimental errors (Fig. 5B). The latter behavior has been reported for innumerable intermolecular association processes occurring in chemistry (Leung et al., 2008; Searle et al., 1995) and in biology (Williams

et al., 2004), and it is referred to as enthalpy/entropy compensation (Piguet, 2011). Its justification relies on the straightforward and easy-to-accept concept that the unfavorable change in dynamics accompanying a simple intermolecular association between partners A and B $\left(-T\Delta S_{\text{asso}}^{\text{A,B}} > 0\right)$ is correlated with the strength in bonding $\left(\Delta H_{\text{asso}}^{\text{A,B}} < 0\right)$. Applied to hydration process, the lack of countable water molecules (i.e., of ligands) directly bound to the metallic center in $R_{(\text{aq})}^{3+}$ represents a severe handicap for the molecular interpretation of the energy changes accompanying this reaction, which is usually limited to the application of the Born equation (Johnson, 1982) or some modified versions of it (D'Angelo and Spezia, 2012; Kumar, 1992; Murakami et al., 2014). Interestingly, major efforts were focused during the last three decades of the twentieth century for addressing the composition, structure, and lability of rare earth cations in solution (Billard, 2003; David et al., 2001; Helm and Merbach, 2005; Richens, 2005; Rizkalla and Choppin, 1991, 1994). A common picture slowly emerged for $R_{(\text{aq})}^{3+}$ as being made primarily of inner sphere $\left[R(OH_2)_n\right]^{3+}$ complexes surrounded by more or less organized outer sphere interactions. The coordination number stepwise decreases from $n = 9$ for the larger rare earth cations adopting a tricapped trigonal prismatic geometry toward $n = 8$ for the smaller rare earth cations adopting a square antiprismatic geometry. In the middle of the series, noninteger coordination numbers reflect rapid dynamic equilibria between the two extreme values of $n$. The exact mechanism of water exchange processes was at the origin of intense debates, but, as far as thermodynamic is concerned, the introduction of the concept of localized Ln—O bonds existing in a defined molecular entity $\left[R(OH_2)_n\right]^{3+}$ is sufficient to roughly interpret the hydration process in Eq. (8).

$$R_{(g)}^{3+} + nH_2O_{(l)} \rightarrow \left[R(OH_2)_n\right]^{3+} \quad \Delta G_{\text{hyd}}^{\text{R}} = \Delta H_{\text{hyd}}^{\text{R}} - T\Delta S_{\text{hyd}}^{\text{R}} \tag{8}$$

Assuming a thermodynamic equilibrium for Eq. (8), the associated stability constants $\beta_{1,n}^{\text{R,H}_2\text{O}} = \exp\left(-\Delta G_{\text{hyd}}^{\text{R}}/RT\right)$ can be broken down into a statistical factor $K_{1,n,\text{stat}}^{\text{R,H}_2\text{O}}$, which takes into account the change in rotational entropy between the reactants and products (Ercolani et al., 2007), and a chemical factor $K_{1,n,\text{chem}}^{\text{R,H}_2\text{O}}$ measuring the electronic and bonding reorganization produced by the chemical reaction (Piguet, 2010). $K_{1,n,\text{stat}}^{\text{R,H}_2\text{O}}$ is estimated by using the symmetry number method (Benson, 1958) and only slightly varies in going from the tricapped trigonal prismatic $\left[R(OH_2)_9\right]^{3+}$ $\left(K_{1,9,\text{stat}}^{\text{R,H}_2\text{O}} = 1/6\right)$ to the square antiprismatic $\left[R(OH_2)_8\right]^{3+}$ $\left(K_{1,8,\text{stat}}^{\text{R,H}_2\text{O}} = 1/4\right)$. Consequently, the more negative free energy of hydration observed along the lanthanide series reflects the increase in the sum of the Ln—O bond energies in $\left[Ln(OH_2)_n\right]^{3+}$. Using the simple relationship $\Delta G_{\text{hyd}}^{\text{Ln}} = -RT \ln\left(\beta_{1,n,\text{chem}}^{\text{Ln,H}_2\text{O}}\right) \approx -RT \ln\left(K_{1,n,\text{chem}}^{\text{Ln,H}_2\text{O}}\right)$, one can assign "bonding energies" of $-440$ (Ln = Lu) $\leq \Delta G_{\text{hyd}}^{\text{R}}/n \leq -350$ kJ/mol (Ln = La)

for the Ln–OH$_2$ interaction. Once the affinity for water has been established, the same concept can be deduced for other monodentate ligands by using the thermodynamic transfer functions $\Delta G_{tr}^R$ and $\Delta H_{tr}^R$ of the ions from a solvent to another (Di Bernardo et al., 2012). Experimental data for lanthanides in organic solvents are scarce and scattered, but a nearly complete dataset has been reported for the transfer of trivalent lanthanide from water to DMSO showing $\Delta H_{tr, water \to DMSO}^R \ll 0$ and the preference of Ln$^{3+}$ for binding the oxygen atom of a DMSO molecule rather than that of a water molecule (Clark and Bear, 1969). Because of their importance in separation processes, the hydrolysis of $\left[ R(OH_2)_n \right]^{3+}$ shown in Eq. (9) was the subject of several thermodynamic investigations (Rizkalla and Choppin, 1991, 1994). However, the extreme complexity of the speciation of polynuclear polyhydroxo complexes (Zheng, 2001) prevents thermodynamic modeling, which limits this field to the systematic reports of hydrolysis constants explored under different conditions for each identified $\left[ R_q(OH_2)_{n-p}(OH)_p \right]^{(3-p)^+}$ complex.

$$q\left[R(OH_2)_n\right]^{3+} \rightleftharpoons \left[R_q(OH_2)_{n-p}(OH)_p\right]^{(3-p)^+} + pH^+ \quad \beta_{q,p}^{R,OH} \qquad (9)$$
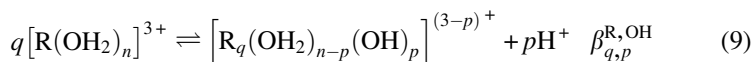
## 2.3 Complexation Using Monodentate and Multidentate Ligands

The strong rare earth–water interactions measured by the hydration free energies combined with their quasi-linear dependence on the inverse of the ionic radii are evidence that rare earth complexation in aqueous solution can be interpreted in terms of an electrostatic model. In other words, trivalent rare earth cations behave as typical "hard" acids and interact preferentially with hard bases such as fluorides, carboxylates, or phosphates rather than with softer bases such as amines or phosphines. Since complex formation in aqueous solution most frequently involves the replacement of R—O(water) bonds with R—O(ligand) bonds (Eq. 1), the minor degree of covalency present in the two types of bonds would be likely to be about the same and the energy balance driving the thermodynamic process arises from the differences in the electrostatic interactions and in the interligand steric constraints (Choppin, 1989). Reminding that the H$_{(aq)}^+$ cation is included among the hard acid species, straightforward correlations are therefore expected and indeed observed (Fig. 6) between the affinity of the hydrogen ion for the ligand measured by its acid constants ($\beta_{1,1}^{H,L} = 1/K_a^1$, Eq. 10) and by its formation constant with the trivalent rare earth cations ($\beta_{1,1}^{R,L}$, Eq. 11).

$$H_{(aq)}^+ + L \rightleftharpoons [LH]^+ \quad \beta_{1,1}^{H,L} = 1/K_a^1 \qquad (10)$$

$$R_{(aq)}^{3+} + L \rightleftharpoons [LR]^{3+} \quad \beta_{1,1}^{R,L} \qquad (11)$$
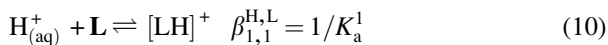
Large deviations from the electrostatic trend are thus considered as the signature of additional effects, which cannot be taken into account by the
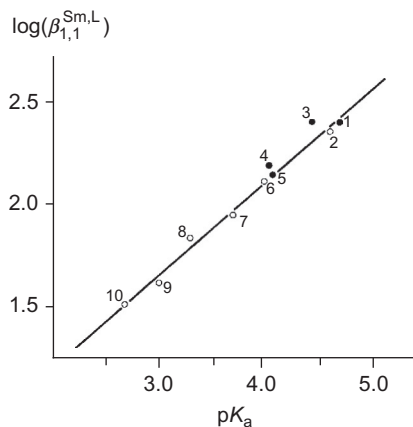
**FIGURE 6** Relationship between the stability constants $\log(\beta_{1,1}^{Sm,L})$ for the formation of $[SmL]^{2+}$ and the acid constants $pK_a^1 = \log\left(\beta_{1,1}^{H,L}\right)$ of **LH**: (1) propionic acid, (2) acetic acid, (3) 4-hydroxybenzoic acid, (4) benzoic acid, (5) 3-hydroxybenzoic acid, (6) 4-fluorobenzoic acid, (7) 3-fluorobenzoic acid, (8) 3-nitrobenzoic acid, (9) chloroacetic acid, and (10) iodoacetic acid. *Redrawn from Choppin (1989), copyright Elsevier 1989.*
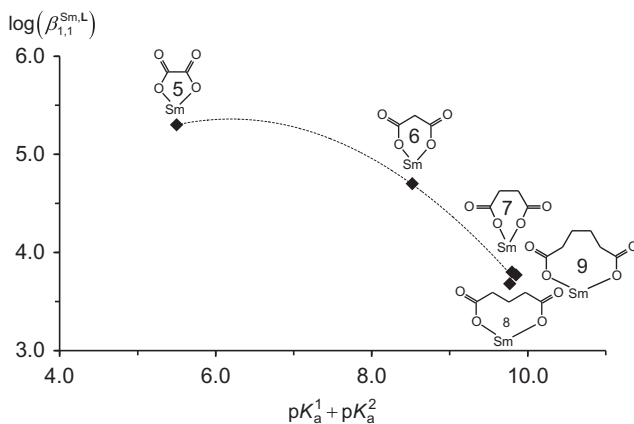


**FIGURE 7** Relationship between the stability constants $\log(\beta_{1,1}^{Sm,L})$ for the formation of $[SmL]^+$ and the sum of the acid constants $pK_a^1 + pK_a^2 = \log\left(\beta_{1,1}^{H,L}\right) + \log\left(\beta_{2,1}^{H,L}/\beta_{1,1}^{H,L}\right)$ of $LH_2$: oxalic acid ($n=5$), malonic acid ($n=6$), succinic acid ($n=7$), glutaric acid ($n=8$), adipic acid ($n=9$). $n$ indicates the size of the chelate ring in the $[SmL]^+$ complexes and the dotted trace is only a guide for the eyes.

simple electrostatic model. Figure 7 illustrates this point for the chelate complexation of dicarboxylic acids, in which an intermolecular binding process is replaced with its intramolecular counterpart. In this case, the formation of five-membered chelate rings is well known to be preferred for large cations such as trivalent lanthanides (Motekaitis et al., 1994). Consequently, modern sophisticated multidentate ligands designed for the implementation of fashionable magnetic or optical properties in the resulting polycyclic lanthanide
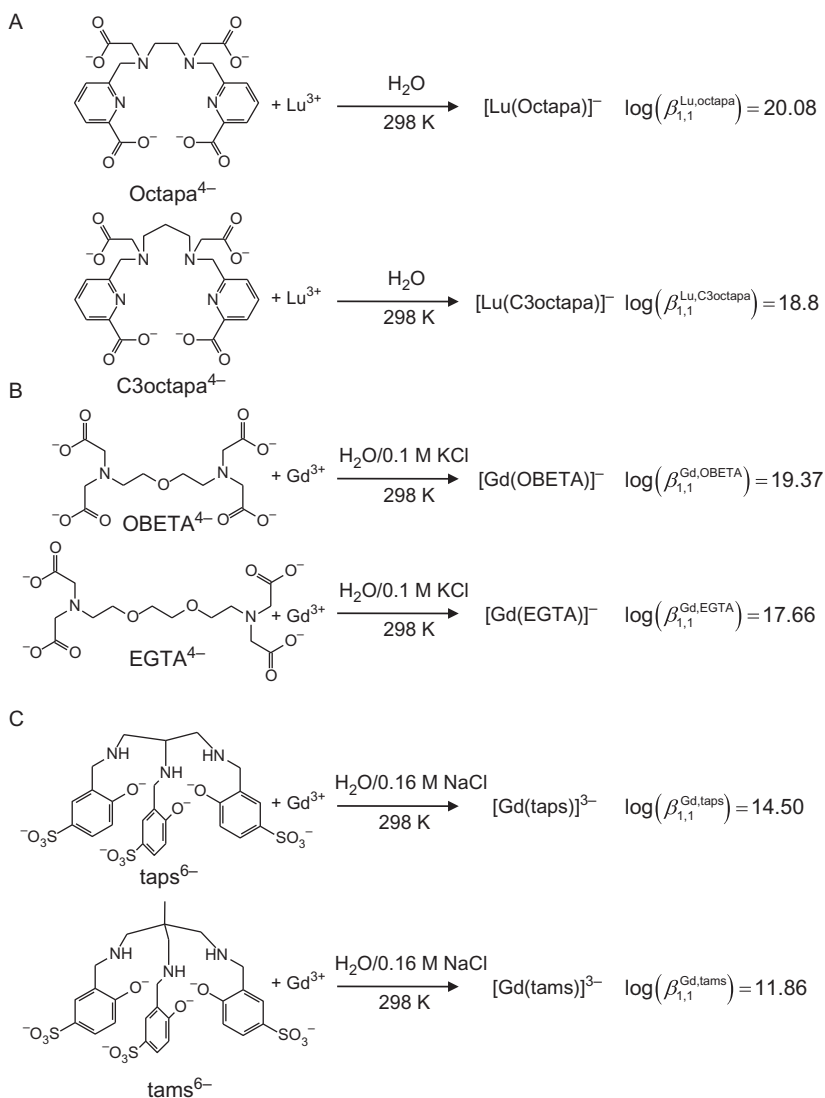
**FIGURE 8** Structure–stability relationships reported for the complexation of multidentate ligands with trivalent lanthanides in water upon an increase of (A) the size of the central chelate ring (Price et al., 2014), (B) the number of central chelate rings (Negri et al., 2014), and (C) the length of the bridges in the covalent tripod (Lowe et al., 1998).

complexes usually do not follow the electrostatic trend and standard thermo-dynamic discussions are usually restricted to some comparisons between the formation constant of the novel complex and those recorded for structurally related receptors (Fig. 8). In the absence of reliable theoretical modeling catching the origins of the deviations from the simple electrostatic trend, the thermodynamic characterization relies on the systematic determinations of

equilibrium constants of novel multidentate ligands with the trivalent cation along the lanthanide series (Martell and Smith, 1989; Sastri et al., 2003).

# 3  ENTHALPY–ENTROPY CORRELATION

## 3.1  Two-Step Choppin's Model for Rare Earth Coordination

In aqueous solutions (Choppin, 1989), but more generally speaking in polar solvents (Liu et al., 2000), the complexation reaction summarized in Equilibrium 12 (S is a solvent molecule) surprisingly displays linear enthalpy–entropy correlations (Fig. 9), whereas this behavior is intuitively expected
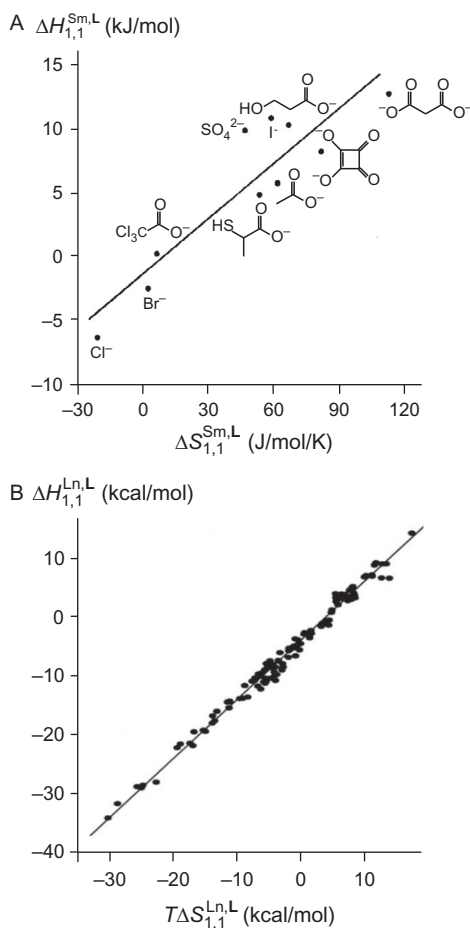


**FIGURE 9**  Enthalpy–entropy compensation plots for the formation of 1:1 complexes (A) of Sm(III) with simple anions in water and (B) of light lanthanides with crown ethers in acetonitrile. *Panel A redrawn from Choppin (1989) and panel B redrawn from Liu et al. (2000).*

only for a simple intermolecular association process occurring in the absence of solvent expulsion as depicted in Eq. (13) (Searle et al., 1995).

$$\left[R(S)_x\right]^{3+} + \left[L(S)_y\right]^{z-} \rightleftharpoons \left[R(L)(S)_p\right]^{(3-z)^+} + (x+y-p)S\,\beta_{1,1}^{R,L} \qquad (12)$$

$$\left[R(S)_x\right]^{3+} + \left[L(S)_y\right]^{z-} \rightleftharpoons \left[R(L)(S)_{x+y}\right]^{(3-z)^+} \qquad \beta_{asso}^{R,L} \qquad (13)$$
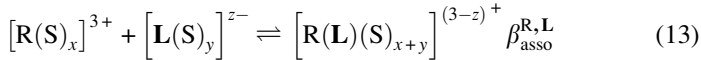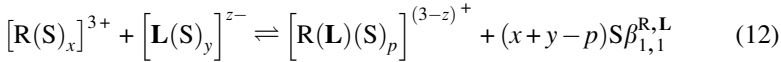
Beyond the justified Jencks' claim that the entropic cost $\left(-T\Delta S_{asso}^{R,L}\right)$ accompanying the decrease in translational degrees of freedom for an intermolecular association involving two independent partners is a constant fraction of 50–60 kJ/mol within a series of similar binding processes (Jencks, 1981), further modulations link a strong bonding between the metal and the ligand characterized by $\Delta H_{asso}^{R,L} \ll 0$ in $\left[R(L)(S)_{x+y}\right]^{(3-z)^+}$ with a decrease in the randomness of the system $\Delta S_{asso}^{R,L} \ll 0$ (Williams et al., 1993). Though theoretically justified when dealing with the isobaric–isothermal treatment of hidden thermodynamic cycles (Starikov, 2013; Starikov and Norden, 2007), the recurrent observation of innumerable linear positive correlations between $\Delta H_{asso}^{R,L}$ and $\Delta S_{asso}^{R,L}$ ($\alpha > 0$ in Eq. 14) supports the latter chemically intuitive statement, which is often referred to as $H/S$ compensation since the addition of opposite contributions tends to minimize changes in $\Delta G_{asso}^{R,L}$ along the series (Ford, 2005a).

$$\Delta H_{asso}^{R,L} = \alpha \cdot \Delta S_{asso}^{R,L} + \beta \qquad (14)$$

The slope of each correlation has Kelvin units and is called the compensation temperature $\alpha = T_{asso}^{comp}$ (Leffler, 1955). At this temperature, any variation in the standard enthalpy of association $\Delta H_{asso}^{R,L}$ across the series of investigated compounds is balanced by an exact compensating variation in the standard entropy $\Delta S_{asso}^{R,L}$, thus leading to complexation processes displaying the same exergonicities, which are given by the intercepts of the linear correlations $\beta = \Delta G_{asso}^{comp}$. However, Choppin (1989) unambiguously pointed out that the complexation of ligands to solvated rare earth cations as written in Eq. (12) indeed combines two successive processes. Firstly, the partners undergo partial desolvation (Eq. 15) followed by their bimolecular association (Eq. 16).

$$\left[R(S)_x\right]^{3+} + \left[L(S)_y\right]^{z-} \rightleftharpoons \left[R(S)_{x-p}\right]^{3+} + \left[L(S)_{y-q}\right]^{z-} + (p+q)S\,\Delta G_{desolv}^{R,L} \quad (15)$$

$$\left[R(S)_{x-p}\right]^{3+} + \left[L(S)_{y-q}\right]^{z-} \rightleftharpoons \left[R(L)(S)_{x+y-p-q}\right]^{(3-z)^+} \Delta G_{asso}^{R,L} \qquad (16)$$
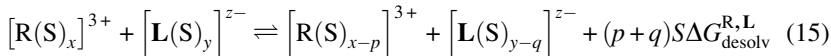
Since each step corresponds to a simple intermolecular breaking (Eq. 15) or binding (Eq. 16) process, opposite enthalpic and entropic contributions are intuitively expected for each reaction with $\Delta H_{desolv}^{R,L} > 0$ and $\Delta S_{desolv}^{R,L} > 0$

for the dissociation process (Eq. 15) and $\Delta H_{\text{asso}}^{\text{R,L}} < 0$ and $\Delta S_{\text{asso}}^{\text{R,L}} < 0$ for the binding process. The free energy change controlling the global complexation process $\Delta G_{1,1}^{\text{R,L}}$ corresponds to Eq. (17), in which both enthalpic and entropic contributions are the balances of two opposite trends.

$$\Delta G_{1,1}^{\text{R,L}} = \Delta G_{\text{desolv}}^{\text{R,L}} + \Delta G_{\text{asso}}^{\text{R,L}} = \left( \Delta H_{\text{desolv}}^{\text{R,L}} + \Delta H_{\text{asso}}^{\text{R,L}} \right) - T \left( \Delta S_{\text{desolv}}^{\text{R,L}} + \Delta S_{\text{asso}}^{\text{R,L}} \right) \quad (17)$$

For outer-sphere complexes, the primary solvation sphere is minimally perturbed, a situation characterized by a global exothermic enthalpy $\Delta H_{1,1}^{\text{R,L}} < 0$ $\left( \left| \Delta H_{\text{desolv}}^{\text{R,L}} \right| \ll \left| \Delta H_{\text{asso}}^{\text{R,L}} \right| \right)$ and a negative entropy $\Delta S_{1,1}^{\text{R,L}} < 0$ $\left( \left| \Delta S_{\text{desolv}}^{\text{R,L}} \right| \ll \left| \Delta S_{\text{asso}}^{\text{R,L}} \right| \right)$ resulting from the predominance of the association process (Khalili et al., 1988). This reasoning assigned an outer-sphere character to the formation of $[\text{RL}]^{2+}$ complexes with $\text{L} = \text{Cl}^-$, $\text{Br}^-$, $\text{I}^-$, $\text{ClO}_3^-$, $\text{NO}_3^-$, $\text{RSO}_3^-$ in water (Choppin and Rizkalla, 1994). For inner-sphere complexes, the desolvation process dominates, particularly in water, and the global complexation reaction is endothermic $\Delta H_{1,1}^{\text{R,L}} > 0$ $\left( \left| \Delta H_{\text{desolv}}^{\text{R,L}} \right| \gg \left| \Delta H_{\text{asso}}^{\text{R,L}} \right| \right)$ and entropically driven $\Delta S_{1,1}^{\text{R,L}} > 0$ $\left( \left| \Delta S_{\text{desolv}}^{\text{R,L}} \right| \gg \left| \Delta S_{\text{asso}}^{\text{R,L}} \right| \right)$, as observed for the formation of $[\text{RL}]^{2+}$ complexes with $\text{L} = \text{F}^-$, $\text{IO}_3^-$, and $\text{SO}_4^{2-}$. Choppin (1989) eventually suggested that $H/S$ compensation observed in water (Fig. 9A) indeed originated from a negligible free energy change $\Delta G_{\text{desolv}}^{\text{R,L}} \simeq 0$, which lets the bimolecular association characterized by $\Delta G_{\text{asso}}^{\text{R,L}} = \Delta H_{\text{asso}}^{\text{R,L}} - T\Delta S_{\text{asso}}^{\text{R,L}}$ as the only decisive factors controlling the global free energy of the complexation process. This intuition also justified the emergence of the electrostatic trend for a given ligand along the lanthanide series because the minor variation expected for $\Delta S_{\text{asso}}^{\text{R,L}}$ in going from one lanthanide to its neighbor along the series will be dominated by the enthalpic change $\Delta H_{\text{asso}}^{\text{R,L}}$ produced by the contraction of the trivalent cations $\text{R}^{3+}$ (Fig. 3A). Taken linear $H/S$ compensation (Eq. 14) as granted for the dissociation and association processes depicted in Eqs. (15) and (16), Piguet (2011) wrote

$$\Delta H_{\text{desolv}}^{\text{R,L}} = T_{\text{desolv}}^{\text{comp}} \cdot \Delta S_{\text{desolv}}^{\text{R,L}} + \Delta G_{\text{desolv}}^{\text{comp}} \quad (18)$$

$$\Delta H_{\text{asso}}^{\text{R,L}} = T_{\text{asso}}^{\text{comp}} \cdot \Delta S_{\text{asso}}^{\text{R,L}} + \Delta G_{\text{asso}}^{\text{comp}} \quad (19)$$

The introduction of Eqs. (18) and (19) into Eq. (17) yielded

$$\Delta H_{1,1}^{\text{R,L}} = T_{\text{asso}}^{\text{comp}} \Delta S_{1,1}^{\text{R,L}} + \Delta S_{\text{desolv}}^{\text{R,L}} \left( T_{\text{desolv}}^{\text{comp}} - T_{\text{asso}}^{\text{comp}} \right) + \left( \Delta G_{\text{desolv}}^{\text{comp}} + \Delta G_{\text{asso}}^{\text{comp}} \right) \quad (20)$$

A close scrutiny at Eq. (20) indicates that the operation of a linear $H/S$ correlation for the global complexation process in solution occurs when $\Delta S_{\text{desolv}}^{\text{R,L}} = $ constant along the series of reactions under investigation. Compared with intuitive Choppin's suggestion claiming that $\Delta H_{\text{desolv}}^{\text{R,L}} \approx -T\Delta S_{\text{desolv}}^{\text{R,L}}$ and which lacks of theoretical support, the latter requirement has deep physical roots (Matyushov, 2004; Onsager, 1936) and it is usually obeyed for limited

perturbations affecting the complexation process along the series (Jensen et al., 2010).

## 3.2 Ford's Model of Enthalpy–Entropy Compensation

In order to rationalize $H/S$ correlations characterizing bimolecular association processes, Ford (2005b) followed the formalism of molecular association proposed by Luo and Sharp (2002) that is traced back to Bjerrum's model. Let us fix the rare earth cation $R^{3+}$ at the origin while the ligand **L** is approaching at a distance $r$ and with an angle $\Omega$ (Fig. 10).

The equilibrium constant $K_{asso}^{R,L}$ for the association process leading to [**RL**] is given by Eq. (21), whereby $\beta = (k_b T)^{-1}$ is the thermal factor with $k_b$ being Boltzmann's constant and $T$ being the temperature, $\omega$ is the potential mean force between R and **L**, and $H(r, \Omega)$ is a bonding function that is $H(r, \Omega) = 1$ when complex [**RL**] exists and $H(r, \Omega) = 0$ otherwise (Ford, 2005b). The reference concentration of the standard state ($c^\theta$) takes into account that the number of particles decreases for a bimolecular association process (Munro, 1977).

$$K_{asso}^{R,L} = \frac{|[\mathbf{RL}]|}{|\mathbf{R}||\mathbf{L}|} = \frac{c^\theta}{8\pi^2} \int H(r, \Omega) \cdot e^{-\beta\omega(r, \Omega)} dr d\Omega \qquad (21)$$

Neglecting any specific internal structure and considering $R^{3+}$ and **L** as purely spherical, the potential mean force simplifies to $\omega(r, \Omega) = u(r)$ and only depends on the scalar distance $r$ between the centers of mass. Moreover, Ford (2005b) assumes that $u(r) = u_{min}^{R,L} + (\kappa^{R,B}/2)r^2$ is a straightforward harmonic potential with the energy minimum $u_{min}^{R,L}$ located at $r = 0$ (Fig. 10) and with a force constant $\kappa^{R,L}$. Following Luo and Sharp (2002), $H(r, \Omega) = 1$ over all space since the Boltzmann's factor $e^{-\beta\left(u_{min}^{R,L} + \left(\kappa^{R,B}/2\right)r^2\right)}$ in Eq. (21) will vanish for high-energy configurations anyway (i.e., unbound states with large $r$ distance). With these assumptions, the integral in Eq. (21) can be solved to give (Ford, 2005b)

$$K_{asso}^{R,L} = c^\theta \left(\frac{2\pi}{\beta\kappa^{R,L}}\right)^{3/2} e^{-\beta u_{min}^{R,L}} \qquad (22)$$

The use of the *van't Hoff* equation transforms the association constant into its associated free energy ($N_{Av}$ is Avogadro number).
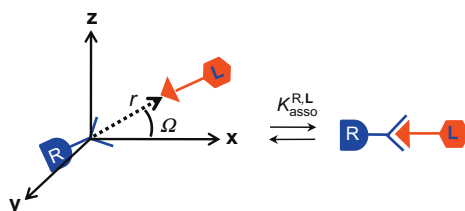


**FIGURE 10** Schematic illustration of *Bjerrum*'s model for the intermolecular association process involving a rare earth cation ($R^{3+}$) and a ligand (**L**).

$$\frac{\Delta G_{\mathrm{asso}}^{\mathbf{R},\mathbf{L}}}{N_{\mathrm{Av}}} = -k_{\mathbf{b}}T \ln\left(K_{\mathrm{asso}}^{\mathbf{R},\mathbf{L}}\right) = -\frac{1}{\beta} \ln\left[c^{\theta}\left(\frac{2\pi}{\beta\kappa^{\mathbf{R},\mathbf{L}}}\right)^{3/2} e^{-\beta u_{\mathrm{min}}^{\mathbf{R},\mathbf{L}}}\right]$$

$$= u_{\mathrm{min}}^{\mathbf{R},\mathbf{L}} - k_{\mathbf{b}}T \ln\left[c^{\theta}\left(\frac{2\pi}{\beta\kappa^{\mathbf{R},\mathbf{L}}}\right)^{3/2}\right] \tag{23}$$

Taking into account the change in the number of translational degrees of freedom accompanying the association process, application of the *Gibbs–Helmholtz* relationship to Eq. (23) yields

$$\frac{\Delta H_{\mathrm{asso}}^{\mathbf{R},\mathbf{L}}}{N_{\mathrm{Av}}} = u_{\mathrm{min}}^{\mathbf{R},\mathbf{L}} + \frac{3}{2}k_{\mathbf{b}}T \tag{24}$$

$$\frac{\Delta S_{\mathrm{asso}}^{\mathbf{R},\mathbf{L}}}{N_{\mathrm{Av}}} = k_{\mathbf{b}} \ln\left[c^{\theta}\left(\frac{2\pi e}{\beta\kappa^{\mathbf{R},\mathbf{L}}}\right)^{3/2}\right] \tag{25}$$

In complete agreement with chemical intuition, the enthalpic contribution $\Delta H_{\mathrm{asso}}^{\mathbf{R},\mathbf{L}}$ only depends on the well depth of the interaction ($u_{\mathrm{min}}^{\mathbf{R},\mathbf{L}}$ in Eq. 24), while the entropic contribution $\Delta S_{\mathrm{asso}}^{\mathbf{R},\mathbf{L}}$ depends on the original choice of the standard state ($c^{\theta}$ in Eq. 25) and on the stiffness of the intercomponent connection as measured by its force constant ($\kappa^{\mathbf{R},\mathbf{L}}$ in Eq. 25). The emergence of *H/S* correlations further requires some dependence of well depth $u_{\mathrm{min}}^{\mathbf{R},\mathbf{L}}$ on the force constant $\kappa^{\mathbf{R},\mathbf{L}}$ or vice versa. If a perturbation is applied to the molecular [RL] pairs such that $u_{\mathrm{min}}^{\mathbf{R},\mathbf{L}}$ and $\kappa^{\mathbf{R},\mathbf{L}}$ move in the opposite direction, for instance, $u_{\mathrm{min}}^{\mathbf{R},\mathbf{L}}$ becomes more negative while $\kappa^{\mathbf{R},\mathbf{L}}$ increases, the result will be *H/S* compensation with, in this specific case, $\Delta H_{\mathrm{asso}}^{\mathbf{R},\mathbf{L}}$ and $\Delta S_{\mathrm{asso}}^{\mathbf{R},\mathbf{L}}$ both decreasing. When $u_{\mathrm{min}}^{\mathbf{R},\mathbf{L}}$ and $\kappa^{\mathbf{R},\mathbf{L}}$ move in the same direction, anticompensation occurs. To the best of our knowledge, there is however no fundamental or *a priori* principle of weak interactions that dictates the relative dependence of well depth $u_{\mathrm{min}}^{\mathbf{R},\mathbf{L}}$ and force constant $\kappa^{\mathbf{R},\mathbf{L}}$, hence justifying a special thermodynamic relationship between $\Delta H_{\mathrm{asso}}^{\mathbf{R},\mathbf{L}}$ and $\Delta S_{\mathrm{asso}}^{\mathbf{R},\mathbf{L}}$. The next step of the reasoning establishes a relationship between the physical forces responsible for the formation of the molecular [RL] pair (derived from a simple harmonic potential) and the use of a Lennard–Jones (12,6) potential $V_{\mathrm{LJ}}$ for modeling the chemical intermolecular interaction (Atkins and De Paula, 2010; Fig. 11). The intermolecular interaction therefore resorts to only two parameters: (i) the absolute minimum of the attractive well depth $\varepsilon$ and (ii) the minimum intermolecular R⋯L distance $r_0$ at which the potential of the interaction is zero and which fixes the minimum of the curve for $r_{\mathrm{min}} = 2^{1/6}r_0$ (Eq. 26 and Fig. 11).

$$V_{\mathrm{LJ}}(r) = 4\varepsilon\left[\left(r_0/r\right)^{12} - \left(r_0/r\right)^{6}\right] \tag{26}$$

The superimposition of the harmonic and Lennard–Jones potentials describing the interaction in [RL] provides a trivial correlation between the well depth and the harmonic potential: $\varepsilon = -u_{\mathrm{min}}^{\mathbf{R},\mathbf{L}}$ (Fig. 11). Application of
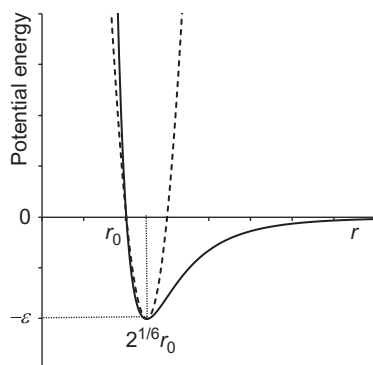
**FIGURE 11** Representation of a Lennard–Jones (12,6) potential (full trace) with the interpretation of $\varepsilon$ and $r_0$ parameters, and its harmonic approximation modeling the intermolecular interactions responsible for the formation of a [RL] complex. *Reproduced with permission © 2011, The Royal society of Chemistry 2011. Reproduced from Piguet (2011) with permission from The Royal Society of Chemistry.*

the *Hooke*'s law for a special extension $A = r_0 - r_{min} = r_0\left(1 - 2^{1/6}\right)$ of the intermolecular interaction provides an extra energy $\kappa^{R,L}A^2/2$ which exactly matches the potential depth $\varepsilon$ (Eq. 27 and Fig. 11).

$$\varepsilon = \frac{\kappa^{R,L}A^2}{2} = \frac{\kappa^{R,L}\left[r_0\left(1 - 2^{1/6}\right)\right]^2}{2} \Rightarrow \kappa^{R,L} = \frac{2}{\left(1 - 2^{1/6}\right)^2} \cdot \frac{\varepsilon}{(r_0)^2} \qquad (27)$$

Equation (27) eventually transforms into Eq. (28) if we remind that $\varepsilon = -u_{min}^{R,L}$.

$$\kappa^{R,L} = -\frac{2}{\left(1 - 2^{1/6}\right)^2 (r_0)^2} \cdot u_{min}^{R,L} = -f \cdot u_{min}^{R,L} \quad \text{with} \quad f = \frac{2}{\left(1 - 2^{1/6}\right)^2 (r_0)^2} > 0 \qquad (28)$$

For a minor structural perturbation affecting a series of R and **L** partners, the minimum contact distance $r_0$ is constant within the resulting [R**L**] pairs and Ford's model (Eq. 28) predicts that the force constants $\kappa^{R,L}$ (that affect the entropy changes, Eq. 25) are linearly correlated with the potential well depths $u_{min}^{R,L}$ (that measure the enthalpy change, Eq. 24). Since the coefficient $f = 2/\left(1 - 2^{1/6}\right)^2(r_0)^2$ is positive, a larger cohesive energy between R and **L** in the [R**L**] pair, i.e., $u_{min}^{R,L}$ and $\Delta H_{asso}^{R,L}$ become more negative, produces an increase in the force constant $\kappa^{R,L}$ and hence a larger vibration frequency in the deeper potential. Since $\Delta S_{asso}^{R,L}/N_{Av} \propto -3/2 \ln\left[\kappa^{R,L}\right]$ in Eq. (25), larger values of $\kappa^{R,L}$ induce more negative association entropies and *H/S* compensation occurs. This model is nothing but the Einstein model for crystals (Einstein, 1907; Rogers, 2005), from which Lindemann (1910) postulated that the melting of a solid occurs when the amplitude of the atomic thermal

vibrations reaches some critical fraction of the equilibrium lattice spacing. Introducing Eq. (28) into Eq. (24) provides a simple correlation between the enthalpy change of the association process and the force constant in the bound state (Eq. 29; $R = k_b N_{Av}$ is the ideal gas constant). Further introduction into Eq. (25) gives the searched (logarithmic) dependence between $\Delta H_{asso}^{R,L}$ and $\Delta S_{asso}^{R,L}$ (Eq. 30).

$$\frac{\Delta H_{asso}^{R,L}}{N_{Av}} = \frac{-\kappa^{R,L}}{f} + \frac{3}{2}k_b T \Rightarrow \kappa^{R,L} = \frac{f}{N_{Av}}\left(\frac{3}{2}RT - \Delta H_{asso}^{R,L}\right) \tag{29}$$

$$\Delta S_{asso}^{R,L} = R\left[\ln\left(c^\theta\right) + \frac{3}{2}\ln\left(\frac{2\pi e RT}{f}\right) - \frac{3}{2}\ln\left(\frac{3}{2}RT - \Delta H_{asso}^{R,L}\right)\right] \tag{30}$$

For a series of similar complexes, the force constant $\kappa^{R,L}$ does not span a large domain and it can be approximated by a first-order Taylor series around its average magnitude $\kappa_0^{R,L}$. Consequently, $\ln\left(\frac{3}{2}RT - \Delta H_{asso}^{R,L}\right)$ in Eq. (30) can be replaced with $\ln\left(\frac{3}{2}RT - \Delta H_{asso,0}^{R,L}\right) + \left(\Delta H_{asso,0}^{R,L} - \Delta H_{asso}^{R,B}\right)/\left(\frac{3}{2}RT - \Delta H_{asso,0}^{R,L}\right)$, where $\Delta H_{asso,0}^{R,L}$ is the average association enthalpy in the series (Dutronc et al., 2014). Linear H/S eventually results, while larger perturbation requires higher-order Taylor series (Searle et al., 1995).

We are now in a position to reconsider the two-step Choppin's model (Eqs. 15 and 16) with more pertinent theoretical tools. Since both steps, i.e., desolvation and association reactions, correspond to simple intermolecular connection processes, the linear H/S correlations proposed in Eqs. (18) and (19) are justified as long that each process is characterized by a constant value for the minimal contact distances $r_0$ separating the partners in the $[R(S)_x]^{3+}$, $[L(S)_y]^{z-}$, and $[R(L)(S)_{x+y-p-q}]^{(3-z)+}$ complexes. These conditions are easily fulfilled when one selected metal reacts with various ligands of the same family as illustrated in Fig. 9, but the situation is less obvious when a given ligand interacts with different rare earth cations of variable sizes although the total 15% contraction along the complete series remains small (see Section 3.3). Finally, the conditions fixing $r_0$ for both desolvation and association steps must be combined with the third criteria emerging from Eq. (20), i.e., $\Delta S_{desolv}^{A,S} = $ constant. The very minor variation of $\Delta S_{hyd}^{R}$ detected along the lanthanide series (Fig. 5A) subscribes to this requirement, a trend further substantiated by the small change in free energies, hence in entropies, accompanying the desolvation of large neutral ligands (Matyushov, 2004).

## 3.3 Dimerization in Rare Earth Complexes

The dimerization of lipophilic 1:1 complexes $[Ln(L1^{a-j})(NO_3)_3]$ occurring in dichloromethane (Equilibrium 31 and Fig. 12) has been intentionally designed by Jensen et al. (2010) for testing the pertinence of Ford's model for rationalizing a simple complexation process within the frame of the two-step
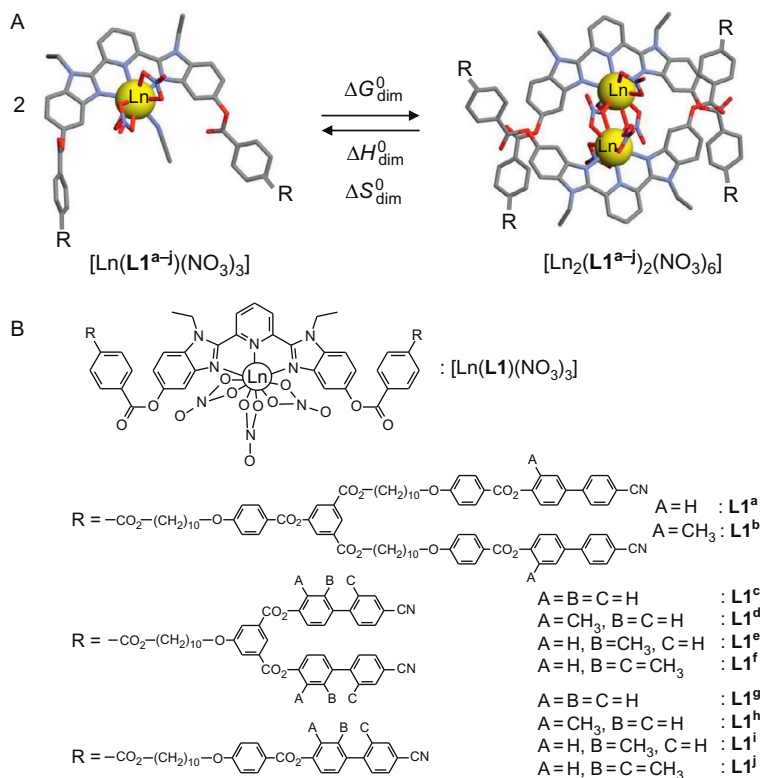
**FIGURE 12** (A) Schematic dimerization of $[Ln(\mathbf{L1^{a-j}})(NO_3)_3]$ occurring in dichloromethane (Eq. 31) and (B) chemical structures of the pseudodendrimeric complexes $[Ln(\mathbf{L1^{a-j}})(NO_3)_3]$ (Jensen et al., 2010).

Choppin's model summarized in Eq. (20). During the dimerization reaction, the metallic coordination number increases by one unit with the formation of a novel lanthanide—O(nitrate) bond and the perturbations applied to the series involve peripheral ligand substitutions on one hand and changes in the lanthanide ionic radii (Ln=Pr, Eu) on the other hand.

$$2\left[Ln\left(\mathbf{L1^{a-j}}\right)(NO_3)_3\right] \rightleftharpoons \left[Ln_2\left(\mathbf{L1^{a-j}}\right)_2(NO_3)_6\right] \quad \Delta G_{dim}^{Ln,\mathbf{L1^x}} \quad (31)$$
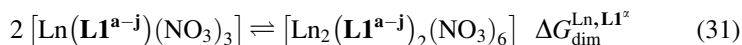
The classical Onsager's approach predicts that the solvation free energy change $\Delta G_{solv}$ produced by a neutral dipolar molecule in a solvent with a relative dielectric permittivity $\varepsilon_r$ depends on both the solute dipole moment $\mu_{dip}$ and its molecular volume $V_{mol}$ (Eq. 32; Matyushov, 2004; Onsager, 1936).

$$\Delta G_{solv}^0 = -\frac{N_{av}}{\varepsilon_0} \cdot \frac{\mu_{dip}^2}{V_{mol}^3} \cdot \left(\frac{\varepsilon_r - 1}{2\varepsilon_r + 1}\right) \quad (32)$$

Since no drastic variations in dipole moments or in molecular volumes are expected for solvation processes within the series of compounds collected in Fig. 12B, one can reasonably assume that the change in desolvation entropies $\Delta S_{desolv}^{Ln,L1^{\alpha}}$ for the dimerization reaction is constant whatever the ligand for a given metal. The emergence of $H/S$ compensation therefore only depends on the global invariance of the minimal contact distances $r_0$ separating the interacting partners in the dimers $[Ln_2(L1^{a-j})_2(NO_3)_6]$ (Eq. 28).

The thermodynamic data collected for the dimerization of $[Ln(L6^{a-j})(NO_3)_3]$ (Fig. 13) indeed display exact $H/S$ compensations along the complete series of ligands in agreement with Eq. (20), but with different slopes for each specific metal (Ln = Pr, Eu; Fig. 13). Since the slopes of the $\Delta H_{dim}^{Ln,L1^{\alpha}}$ versus $\Delta S_{dim}^{Ln,L1^{\alpha}}$ correlation plots correspond to the compensation temperature $T_{asso}^{comp}$ (Eq. 20), a parameter which can be theoretically rationalized by using Ford's model as $T_{asso}^{comp} = \left(1 - 2^{1/6}\right)^2 (r_0)^2 \kappa_0/3k_b$ (Eq. 30; Piguet, 2011), we deduce that the observed trend $T_{asso,\,Ln=Pr}^{comp} = 329(17)K > T_{asso,\,Ln=Eu}^{comp} = 278(7)K$ can be assigned to a logical decrease of the minimum intermolecular contact distance $r_0$ for the smaller europium(III) cation. It is worth noting here that the peripheral structural changes imposed by the ligand strands have no detectable impact on the $H/S$ compensation along each series because they do not affect the inter-component contact distance in the dimers. However the different substituents in the complexes $[Ln(L1^{a-j})(NO_3)_3]$ provide $\left\langle \Delta S_{dim}^{Ln,L1^{\alpha}}; \Delta H_{dim}^{Ln,L1^{\alpha}} \right\rangle$ couples dispersed over a considerable domain with $-60 \leq \Delta H_{dim}^{Ln,L1^{\alpha}} \leq 0$ kJmol$^{-1}$ and $-170 \leq S_{dim}^{Ln,L1^{\alpha}} \leq 50$ Jmol$^{-1}$K$^{-1}$ (Fig. 13).
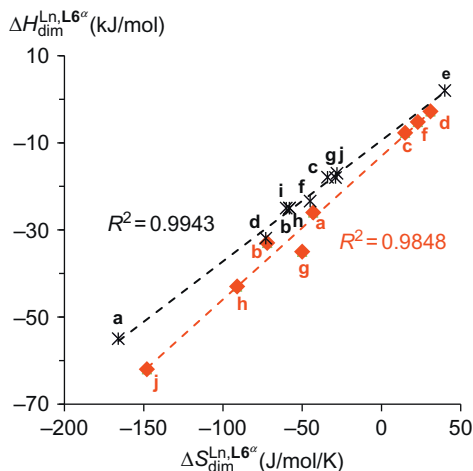


**FIGURE 13** $\Delta H_{dim}^{Ln,L1^{\alpha}}$ versus $\Delta S_{dim}^{Ln,L1^{\alpha}}$ correlation plots for the dimerization of $[Pr(L6^{a-j})(NO_3)_3]$ (red (light gray in the print version) diamonds and red trace) and $[Eu(L6^{a-j})(NO_3)_3]$ (black stars and black trace) in dichloromethane.

## 4 THE METALLOSUPRAMOLECULAR REVOLUTION

According to the principle of maximum site occupancy (Lehn and Eliseev, 2001), the combination of a rare earth cation R possessing $n$ binding sites with a ligand **L** possessing $m$ binding sites produces a saturated complex $[R_{pm}L_{pn}]$ (Eq. 33), where $p$ is a coefficient, often referred to as the complexity of the assembly, needed to account for the stoichiometry of R and **L** in the complex (Ercolani, 2003).

$$pmR + pnL \rightleftharpoons [R_{pm}L_{pn}] \beta_{pm,pn}^{R,L} \tag{33}$$
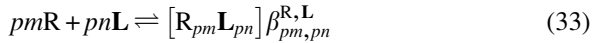
The final complex $[R_{pm}L_{pn}]$ contains $N = pm + pn$ components joined by $B = pmn$ connections, among which $N - 1 = pm + pn - 1$ are intermolecular and $B - (N - 1) = pmn - pm - pn + 1$ are intramolecular (Fig. 14). The associated cumulative stability constant $\beta_{pm,pn}^{R,L}$ is given in Eq. (34), whereby each pair of parallel vertical lines refers to molar concentrations and $c^{\theta}$ is the reference molar concentration in the standard state (Motekaitis et al., 1994).

$$\beta_{pm,pn}^{R,L} = \frac{\left(\left|[R_{pm}L_{pn}]\right|/c^{\theta}\right)}{(|R|/c^{\theta})^{pm} \cdot (|L|/c^{\theta})^{pn}} = \frac{\left|[R_{pm}L_{pn}]\right|}{|R|^{pm} \cdot |L|^{pn}} \cdot \left(c^{\theta}\right)^{(pm+pn-1)} \tag{34}$$

The application of the *van't Hoff* equation $\Delta G^0 = -RT \ln(\beta)$ gives Eq. (35).

$$\begin{aligned}
\Delta G^{\circ R,L}_{pm,pn} &= -RT \ln\left(\beta_{pm,pn}^{R,L}\right) \\
&= -RT \ln\left(\frac{\left|[R_{pm}L_{pn}]\right|}{|R|^{pm} \cdot |L|^{pn}}\right) - RT(pm + pn - 1) \ln\left(c^{\theta}\right) \tag{35}
\end{aligned}$$

Usually, coordination chemists implicitly refer to the convenient one molar standard state (i.e., $c^{\theta} = 1$ M), a choice that we will obviously adopt for the rest of our discussions, but one should keep in mind that the latter choice arbitrarily fixes a specific reference for the absolute entropy change $-T\Delta S^{\circ R,L}_{pm,pn}$ contributing to $\Delta G^{\circ R,L}_{pm,pn} = -RT \ln\left(\beta_{pm,pn}^{R,L}\right)$ (Munro, 1977).

Once $\beta_{pm,pn}^{R,L}$ has been estimated by using Eq. (34) with the help of the experimental speciation obtained under thermodynamic equilibrium, its transformation into free energy with Eq. (35) is at the origin of the additive free energy model proposed by Ercolani (2003), who assigned single-event free energy contributions $\Delta g_{inter}^{R,L} = -RT \ln\left(f_{inter}^{R,L}\right)$ and $\Delta g_{intra}^{R,L} = -RT \ln\left(f_{intra}^{R,L}\right)$ to each type of heterocomponent connection (Eqs. 36 and 37 and Fig. 14).

$$\begin{aligned}
\Delta G^{\circ R,L}_{pm,pn} &= -RT \ln\left(\omega_{pm,pn}^{R,L}\right) - (pm + pn - 1)RT \ln\left(f_{inter}^{R,L}\right) \\
&\quad - (pmn - pm - pn + 1)RT \ln\left(f_{intra}^{R,L}\right) \tag{36}
\end{aligned}$$

$$\beta_{pm,pn}^{R,L} = \omega_{pm,pn}^{R,L} \left(f_{inter}^{R,L}\right)^{pm+pn-1} \left(f_{intra}^{R,L}\right)^{pmn-pm-pn+1} \tag{37}$$

A

$pm\,[R(CH_3CN)_9]^{3+} + pn$ 〔**L2** structure〕 $\xrightarrow[\substack{p=1\\m=1\\n=3}]{\beta_{1,3}^{R,L2}}$ $[R(\mathbf{L2})_3]^{3+}$ $+9pm\,CH_3CN$

R      **L2**

$D_{3h}$      $C_{2v}$      $\sigma_{tot}^S = 3$

$\sigma_{tot}^R = 6\cdot 3^9$      $\sigma_{tot}^{L2} = 2\cdot 2^2\cdot 3^4$

$N = 1\cdot 1 + 1\cdot 3 = 4$ components

$[R(\mathbf{L2})_3]^{3+}$
$D_3$

$\sigma_{tot}^{R(L2)3} = \tfrac{1}{2}\cdot 6\cdot 3^{18}\cdot 2^6$

$B = 1\cdot 1\cdot 3 = 3$ connections $\left\{\begin{array}{l} N-1 = 3 \text{ intermolecular} \\ B-(N-1) = 0 \text{ intramolecular} \end{array}\right\}$ Noncyclic

$$\beta_{1,3}^{R,L2} = 16\left(f_{inter}^{R,L2}\right)^3$$

B

$pm\,[R(CH_3CN)_9]^{3+} + pn$ 〔**L3** structure〕 $\xrightarrow[\substack{p=1\\m=2\\n=3}]{\beta_{2,3}^{R,L3}}$ $[R_2(\mathbf{L3})_3]^{6+}$ $+9pm\,CH_3CN$

R      **L3**

$D_{3h}$      $C_{2v}$      $\sigma_{tot}^S = 3$

$\sigma_{tot}^R = 6\cdot 3^9$      $\sigma_{tot}^{L3} = 2\cdot 2^2\cdot 3^6$

$N = 1\cdot 2 + 1\cdot 3 = 5$ components

$[R_2(\mathbf{L3})_3]^{6+}$
$D_3$

$\sigma_{tot}^{R2(L3)3} = \tfrac{1}{2}\cdot 6\cdot 3^{18}\cdot 2^6$

$B = 1\cdot 2\cdot 3 = 6$ connections $\left\{\begin{array}{l} N-1 = 4 \text{ intermolecular} \\ B-(N-1) = 2 \text{ intramolecular} \end{array}\right\}$ Macrobicyclic

$$\beta_{2,3}^{R,L3} = 96\left(f_{inter}^{R,L3}\right)^4\left(f_{intra}^{R,L3}\right)^2 = 96\left(f_{inter}^{R,L3}\right)^6\left(EM_{2,2}^{R,L3}\right)\left(EM_{2,3}^{R,L3}\right)$$

**FIGURE 14** Distribution of inter- and intramolecular heterocomponent connections joining the $N = pm + pn$ components in saturated $[R_{pm}L_{pn}]$ complexes. Note that each metal–ligand interaction is considered as a single connection point. Formation of (A) a three-bladed propeller (Renaud et al., 1997) and (B) a binuclear triple-stranded helicate (Martin et al., 1998).

Let us stress here that $\Delta g_{inter}^{R,L}$ corresponds to the desolvation/association balance previously modeled with Eqs. (15) and (16), and for which $H/S$ compensation is expected according to Eq. (20). $\Delta g_{intra}^{R,L}$ refers to the same process according to that the entering cation is already bound to the receptor by a second connection point (chelate effect). Both intermolecular $f_{inter}^{R,L}$ and intramolecular binding $f_{intra}^{R,L}$ affinities involve similar bond breaking (desolvation) and bond formation (association) events, but the intramolecular character of the latter process limits the spatial exploration (entropic contribution) and induces internal constraints (enthalpic contribution) with respect to the closely related intermolecular association (Mandolini, 1986). Whereas the

consequences on the entropic contribution produced by an intramolecular binding event can be theoretically approached for a freely joint chain linking the two connecting atoms (Jacobson and Stockmayer, 1950; Kuhn, 1934), the enthalpic benefit/penalty intimately depends on the specific molecular structures, and one therefore prefers to introduce the concept of effective molarity (EM) which empirically correlates $f_{inter}^{R,L}$ and $f_{intra}^{R,L}$ with the help of Eq. (38) (Piguet, 2010).

$$f_{intra}^{R,L} = f_{inter}^{R,L} \cdot \left( \frac{EM}{c^\theta} \right) \tag{38}$$

EM has thus molar concentration unit and its effect on the free energy changes accompanying the replacement of an intermolecular binding process with its intramolecular counterpart $\Delta g_{conn}^{R,L} = \Delta g_{intra}^{R,L} - \Delta g_{inter}^{R,L} = -RT \ln \left( EM/c^\theta \right)$ depends on the choice of the $c^\theta$, a phenomenon at the origin of lively debates during the 1960s when attempting to define some absolute chelate effects in coordination chemistry (Motekaitis et al., 1994; Schwarzenbach, 1952). Finally, the initial factor $\omega_{pm,pn}^{R,L}$ in Eq. (37) takes into account the pure statistical (i.e., entropic) contribution due to the change in the molecular rotational degeneracies (Lin, 1996) occurring when the reactants are transformed into products (Ercolani et al., 2007). Once the point groups of each partner contributing to the self-assembly are at hand, $\omega_{pm,pn}^{R,L}$ can be calculated with Eq. (39) by using their symmetry numbers $\sigma_{tot}$ (Bailey and Monahan, 1978; Benson, 1958).

$$\omega_{pm,pn}^{R,L} = \frac{\left( \sigma_{tot}^R \right)^{pm} \left( \sigma_{tot}^L \right)^{pn}}{\left( \sigma_{tot}^{R_{pm}L_{pn}} \right)} \tag{39}$$

The external symmetry number $\sigma_{ext}$ of a molecule is defined as the total number of permutations of identical atoms than can be arrived at by simple rotations of the entire molecule (excluding improper axis) or by rotations about single bond within a molecule. If a species is chiral and present as a racemic mixture, the symmetry number must be multiplied by $\sigma_{chir} = 1/2$ to account for the entropy of mixing of the two enantiomers (Ercolani et al., 2007). Let us illustrate this method for the calculation of the symmetry number associated with a tricapped trigonal prismatic $[R(CH_3CN)_9]^{3+}$ cation displaying $D_{3h}$ symmetry (Fig. 14). Because of the existence of a principal threefold axis with three perpendicular twofold axes, there are $\sigma_{ext} = 3 \cdot 2 = 6$ possible simple rotations of the entire molecule which simply permute identical atoms. Since the molecule is not chiral, $\sigma_{chir} = 1$. We, however, notice that each methyl group of the acetonitrile molecules can rotate along the C—C bond according to local threefold axes, thus leading to the additional concept of an internal symmetry number. For $[R(CH_3CN)_9]^{3+}$, there are $\sigma_{int} = 3^9$ possible internal rotations which do not affect the geometry of the molecule. The global symmetry number for $[R(CH_3CN)_9]^{3+}$ can be computed as

$\sigma_{tot} = \sigma_{ext} \cdot \sigma_{int} \cdot \sigma_{chir} = 6 \cdot 3^9 \cdot 1 = 118'098$. Applying this technique to each part-
ner of the assembly followed by their introduction into Eq. (39) provides
the statistical factors gathered in Fig. 14. In conclusion, any complexation
constant, even that associated with the sophisticated assembly process
depicted in Fig. 15 (Hamacek et al., 2008), can be modeled with the resort
to two microscopic thermodynamic descriptors $f_{inter}^{R,L}$ and $f_{intra}^{R,L}$, and one statis-
tical factor as proposed by Ercolani (2003).



$pm \ [R(CH_3CN)_9]^{3+} + pn$

R

$D_{3h}$

$\sigma_{tot}^R = 6 \cdot 3^9$

L4

$C_{3v}$

$\sigma_{tot}^{L4} = 3 \cdot 2^3 \cdot 3^7$

$p = 4/3$
$m = 3$
$n = 3$

$\beta_{4,4}^{R,L4}$

$+9pm \ CH_3CN$

$\sigma_{tot}^S = 3$

$[R_4(L4)_4]^{12+}$

$T$

$\sigma_{tot}^{R4(L4)4} = \frac{1}{2} \cdot 12 \cdot 3^{28} \cdot 2^{12}$

$N = 4/3 \cdot 3 + 4/3 \cdot 3 = 8$ components

$B = 4/3 \cdot 3 \cdot 3 = 12$ connections $\left\{ \begin{array}{l} N-1 = 7 \text{ intermolecular} \\ B-(N-1) = 5 \text{ intramolecular} \end{array} \right\}$ Macropentacyclic

$$\beta_{4,4}^{R,L4} = 17496 \left( f_{inter}^{R,L4} \right)^7 \left( f_{intra}^{R,L4} \right)^5 = 17496 \left( f_{inter}^{R,L4} \right)^{12} \left( EM^{R,L4} \right)^5$$
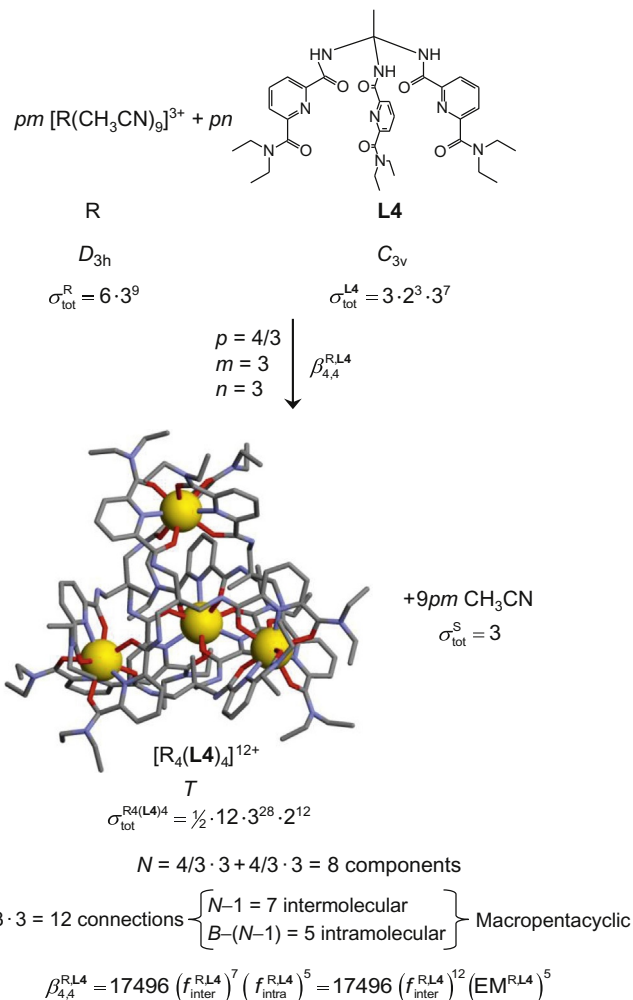
**FIGURE 15** Assembly of a tetrahedral $[R_4(L4)_4]^{12+}$ pentacyclic cluster illustrating the distribu-
tion of inter- and intramolecular heterocomponent connections joining the $N = pm + pn$ compo-
nents (Hamacek et al., 2008).

## 4.1 Intermolecular Affinities and the Allosteric Cooperativity

The simple complexation of three successive terdentate neutral ligands **L2** with a trivalent lanthanide cation in acetonitrile is summarized in Eq. (40) (for the sake of clarity, we only consider nine-coordinate lanthanide centers) and the associated cumulative stability constants are collected in Fig. 16A (Renaud et al., 1997).

$$\left[Ln(CH_3CN)_9\right]^{3+} + n\mathbf{L2} \rightleftharpoons \left[Ln(\mathbf{L2})_n(CH_3CN)_{9-3n}\right]^{3+} + 3nCH_3CN \quad \beta_{1,n}^{Ln,\mathbf{L2}} \quad (40)$$

The modeling of the associated thermodynamic formation constants with the help of Ercolani's model (Eq. 37) leads to Eqs. (41)–(43), which are ideally suited for extracting a specific intermolecular affinity $f_{inter}^{Ln,\mathbf{L2}}$ for each trivalent cation along the series by using linear least-square processes (Escande et al., 2009). Expressed as free energy changes $\Delta g_{inter}^{Ln,\mathbf{L2}} = -RT \ln\left(f_{inter}^{Ln,\mathbf{L2}}\right)$ in Fig. 16B (left), these data confirm the operation of the electrostatic trend suggested by Choppin's model with a stepwise larger affinity for cations of decreasing sizes.

$$\beta_{1,1}^{Ln,\mathbf{L2}} = 6f_{inter}^{Ln,\mathbf{L2}} \quad (41)$$

$$\beta_{1,2}^{Ln,\mathbf{L2}} = 12\left(f_{inter}^{Ln,\mathbf{L2}}\right)^2 \quad (42)$$

$$\beta_{1,3}^{Ln,\mathbf{L2}} = 16\left(f_{inter}^{Ln,\mathbf{L2}}\right)^3 \quad (43)$$

The excellent match between the experimental formation constants and those recalculated using Eqs. (41)–(43) agrees with the operation of a statistical binding of **L2** to the various trivalent lanthanides. On the contrary, the same approach applied to the successive fixation of dipicolinate dianions $[\mathbf{L5}\text{-}2H]^{2-}$ to trivalent lanthanides in water (Eq. 44; Grenthe, 1961) essentially fails as ascertained by the large uncertainties affecting $\Delta g_{inter}^{Ln,\mathbf{L5}\text{-}2H}$ along the series (Fig. 16B, right) and by the poor match between experimental and recalculated stability constants (Fig. 16C, right).

$$\left[Ln(H_2O)_9\right]^{3+} + n[L5\text{-}2H]^{2-} \rightleftharpoons \left[Ln(L5\text{-}2H)_n(H_2O)_{9-3n}\right]^{(3-2n)+} + 3nH_2O \quad \beta_{1,n}^{Ln,L5-2H}$$

$$(44)$$
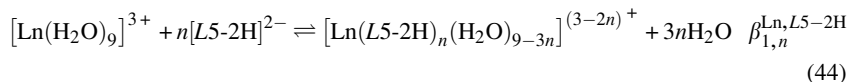
A careful inspection of the correlation shown in Fig. 16C right shows that the computed formation constants for the successive binding of dipicolinate dianions to the trivalent cation are severely underestimated for $\beta_{1,1}^{Ln,\mathbf{L5}\text{-}2H}$, they are slightly better for $\beta_{1,2}^{Ln,\mathbf{L5}\text{-}2H}$, and overestimated for $\beta_{1,3}^{Ln,\mathbf{L5}\text{-}2H}$. In other words, the absolute affinity $f_{inter}^{Ln,\mathbf{L5}\text{-}2H}$ of the ligand for the metallic center decreases upon the successive fixation of dipicolinate ligands to the metal ion, a phenomenon known as allosteric cooperativity, which can be quantitatively
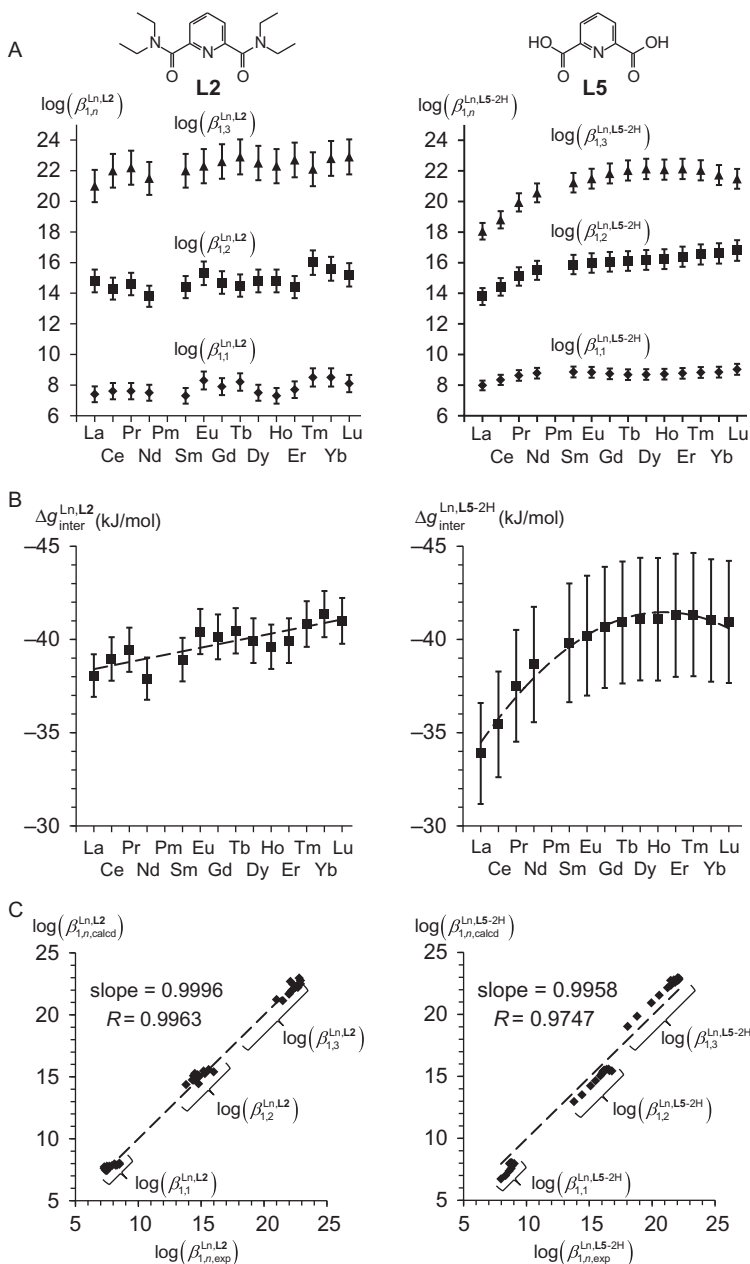
**FIGURE 16** (A) Experimental thermodynamic cumulative formation constants for the triple-helical $[Ln(\mathbf{L2})_3]^{3+}$ (left, Renaud et al., 1997) and $[Ln(\mathbf{L5}\text{-}2H)_3]^{3-}$ complexes (right, Grenthe, 1961), (B) intermolecular affinities $\Delta g_{inter}^{Ln,L} = -RT \ln\left(f_{inter}^{Ln,L}\right)$ fitted with Eqs. (41)–(43) (the dashed traces are guides for the eyes), and (C) thermodynamic constants recomputed using Eqs. (41)–(43) with respect to the experimental data (the dashed traces are linear correlations).

defined as the ratio $\alpha_n$ of the absolute affinities for the $n$th binding event with respect to the first binding process taken as the noncooperative reference (Eq. 45, Ercolani and Schiaffino, 2011).

$$\alpha_n = \frac{f_{\text{inter},\,n}^{\text{Ln},\mathbf{L}}}{f_{\text{inter},\,1}^{\text{Ln},\mathbf{L}}} \tag{45}$$

The introduction of the concept of allosteric cooperativity (Eq. 45) within the frame of successive intermolecular binding events transforms Eqs. (41)–(43) into

$$\beta_{1,1}^{\text{Ln},\mathbf{L5}\text{-}2H} = 6f_{\text{inter},1}^{\text{Ln},\mathbf{L5}\text{-}2H} \tag{46}$$

$$\beta_{1,2}^{\text{Ln},\mathbf{L5}\text{-}2H} = 12\alpha_2 \left(f_{\text{inter},1}^{\text{Ln},\mathbf{L5}\text{-}2H}\right)^2 \tag{47}$$

$$\beta_{1,3}^{\text{Ln},\mathbf{L5}\text{-}2H} = 16\alpha_2\alpha_3 \left(f_{\text{inter},1}^{\text{Ln},\mathbf{L5}\text{-}2H}\right)^3 \tag{48}$$

For each set of three cumulative constants measured for a given lanthanide cation, Eqs. (46)–(48) assign a noncooperative intermolecular affinity $f_{\text{inter},1}^{\text{Ln},\mathbf{L5}\text{-}2H}$ (Fig. 17A), which is further modulated by the empirical allosteric factors $\alpha_2$ and $\alpha_3$ characterizing the free energy penalty, i.e, negative cooperativity ($\alpha_2 < 1$ and $\alpha_3 \ll 1$, Fig. 17B) accompanying the coordination of the second and the third dianionic dipicolinate ligand, respectively. Obviously, the stability constants recomputed with Eqs. (46)–(48) exactly match the
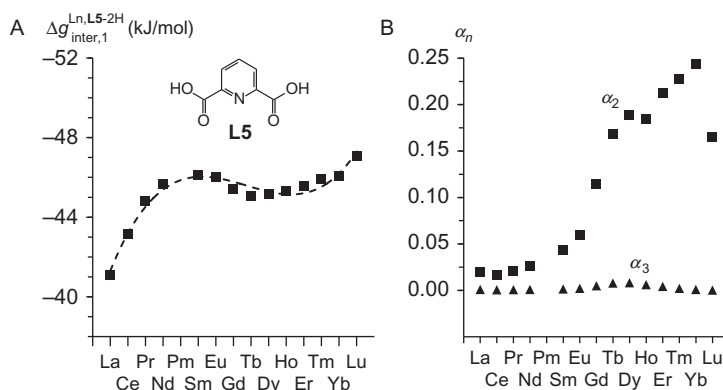


**FIGURE 17** (A) Experimental noncooperative intermolecular affinities $\Delta g_{\text{inter},1}^{\text{Ln},\mathbf{L5}\text{-}2H} = -RT \ln\left(f_{\text{inter},1}^{\text{Ln},\mathbf{L5}\text{-}2H}\right)$ and (B) allosteric cooperativity factors $\alpha_n$ fitted with Eqs. (46)–(48) for the successive complexation of dipicolinate dianions $[\mathbf{L5}\text{-}2H]^{2-}$ to trivalent lanthanides in water. The dashed trace is only a guide for the eyes. The abrupt decrease of $\alpha_2$ for the smallest lanthanide cation $Lu^{3+}$ is associated with an abrupt increase of its affinity $\Delta g_{\text{inter},1}^{\text{Lu},\mathbf{L5}\text{-}2H}$, a trend in line with a more compact arrangement around the metal produced by a decrease of the coordination number.

experimental data (three equations for three parameters!), but the physical origin of the allosteric cooperativity remains elusive.

This limitation has been overcome with the help of the site-binding model, which was developed for rationalizing multiple protonation reactions operating in proteins and polyelectrolytes (Borkovec et al., 2001; Koper and Borkovec, 2010) or metal loadings of polymeric receptors (Borkovec et al., 2004; Koper and Borkovec, 2001). Applied to lanthanide coordination chemistry, the site-binding model aims at modeling the successive intermolecular metal–ligand binding process summarized in Eq. (49) and Fig. 18 with the help of two parameters: the noncooperative affinity of site $i$ for intermolecular association $f_{inter,i}^{Ln,L}$ and the free energy of interaction occurring when two adjacent sites $i$ and $j$ are occupied $\Delta E_{i,j}^{Ln,Ln}$ (Borkovec et al., 2006). Obviously, the labels for metal and ligands can be exchanged, and the same model can be used for the loading of a multisite ligand **L** with lanthanide cations (Eq. 49 and Fig. 18A) or for the loading of a multisite lanthanide metals with several ligands (Eq. 50 and Fig. 18B).

$$mLn^{3+} + L \rightleftharpoons [Ln_mL]^{3m+} \quad \beta_{m,1}^{Ln,L} \tag{49}$$

$$Ln^{3+} + nL \rightleftharpoons [LnL_n]^{3+} \quad \beta_{1,n}^{Ln,L} \tag{50}$$
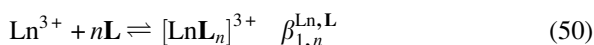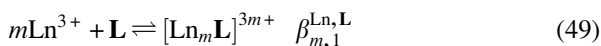
Any macrospecies $[Ln_mL]^{3m+}$ is composed of numerous microspecies $\{s_i\}-[Ln_mL]^{3m+}$, all possessing the same number $m$ of metals bound to the receptor, but differing on their exact location in the various sites as described by the state vector $\{s_i\}$ for which each element $s_i = 1$ indicates that a metal is
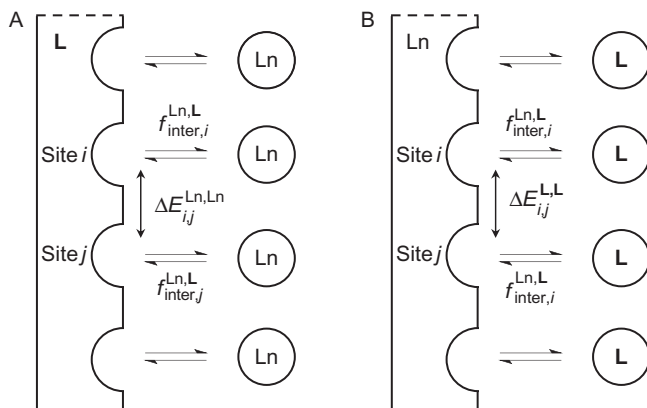


**FIGURE 18** Thermodynamic models for the successive intermolecular connections of (A) lanthanides Ln to a multisite receptor **L** and (B) ligands **L** to a multisite lanthanide Ln. $f_{inter,i}^{Ln,L}$ and $\Delta g_{inter,i}^{Ln,L} = -RT \ln\left(f_{inter,i}^{Ln,L}\right)$ are the (noncooperative) intrinsic affinity, respectively, free energy of connection between the site $i$ and the metal, while $\Delta E_{i,j}^{Ln,Ln}$ and $\Delta E_{i,j}^{L,L}$ are the free energy of interaction occurring when two adjacent sites $i$ and $j$ are occupied.

bound to site $i$ and $s_i = 0$ when no metal is coordinated. The Lenz-Ising model limited to nearest-neighbor interactions associates a binding free energy $\Delta G_{m,1}^{\text{Ln},\mathbf{L}}\{s_i\}$ (Eq. 51) and thus a stability microconstant $\beta_{m,1}^{\text{Ln},\mathbf{L}}\{s_i\}$ (Eq. 52) to each $\{s_i\}-[\text{Ln}_m\mathbf{L}]^{3m+}$ microspecies for a ligand $\mathbf{L}$ possessing a total of $N$ available binding sites.

$$\Delta G_{m,1}^{\text{Ln},\mathbf{L}}\{s_i\} = -RT\sum_{i=1}^{N}\ln\left(f_{\text{inter},i}^{\text{Ln},\mathbf{L}}\right)s_i + \frac{1}{2}\cdot\sum_{i=1}^{N}\sum_{i\neq j}^{N}\Delta E_{i,j}^{\text{Ln},\text{Ln}}s_i s_j \qquad (51)$$

$$\beta_{m,1}^{\text{Ln},\mathbf{L}}\{s_i\} = \prod_{i=1}^{N}\left(f_{\text{inter},i}^{\text{Ln},\mathbf{L}}\right)^{s_i}\cdot\sqrt{\prod_{i=1}^{N}\prod_{j\neq i}^{N}\left[\exp\left(-\frac{\Delta E_{i,j}^{\text{Ln},\text{Ln}}}{RT}\right)\right]^{s_i s_j}} \qquad (52)$$

Application of Eq. (52) to the formation of $[\text{Ln}(\mathbf{L5}\text{-2H})_n(\text{H}_2\text{O})_{9-3n}]^{(3-2n)+}$ ($n = 1$–3, Eq. 44) leads to Eqs. (53)–(55), where $u_{\text{Ln}}^{\mathbf{L5}\text{-2H},\mathbf{L5}\text{-2H}} = e^{-\Delta E_{\text{Ln}}^{\mathbf{L5}\text{-2H},\mathbf{L5}\text{-2H}}/RT}$ is known as the *Boltzmann* factor accounting for the interaction operating between two adjacent ligands bound to the same lanthanide (Escande et al., 2009).

$$\beta_{1,1}^{\text{Ln},\mathbf{L5}\text{-2H}} = 6f_{\text{inter},1}^{\text{Ln},\mathbf{L5}\text{-2H}} \qquad (53)$$

$$\beta_{1,2}^{\text{Ln},\mathbf{L5}\text{-2H}} = 12\left(f_{\text{inter},1}^{\text{Ln},\mathbf{L5}\text{-2H}}\right)^2 u_{\text{Ln}}^{\mathbf{L5}\text{-2H},\mathbf{L5}\text{-2H}} \qquad (54)$$

$$\beta_{1,3}^{\text{Ln},\mathbf{L5}\text{-2H}} = 16\left(f_{\text{inter},1}^{\text{Ln},\mathbf{L5}\text{-2H}}\right)^3\left(u_{\text{Ln}}^{\mathbf{L5}\text{-2H},\mathbf{L5}\text{-2H}}\right)^3 \qquad (55)$$

The comparison of Eqs. (53)–(55) with Eqs. (46)–(48) immediately assigns any cooperative effects to homocomponent interactions (Piguet, 2010). A fit of the experimental stability constants (Fig. 19A) to the site-binding model (Eq. 53–55) satisfyingly reproduces the data (Fig. 19C) with the help of the intermolecular affinities and homocomponent interactions gathered in Fig. 19A and B. Again, the noncooperative free energies of complexation $\Delta g_{\text{inter},1}^{\text{Ln},\mathbf{L}} = -RT\ln\left(f_{\text{inter},1}^{\text{Ln},\mathbf{L}}\right)$ follow the electrostatic trend along the lanthanide series (Fig. 19A), but the successive fixation of negatively charged dipicolinate dianions $[\mathbf{L5}\text{-2H}]^{2-}$ to any $\text{Ln}^{3+}$ cation in water is anticooperative with a drift in free energy of $5 \leq \Delta E_{\text{Ln}}^{\mathbf{L5}-2\text{H},\mathbf{L5}-2\text{H}} \leq 10$ kJ/mol for each additional interligand interactions operating in the first coordination sphere of the metal (Fig. 19B).

The extension of this approach to similar complexation processes involving the terdentate neutral ligands $\mathbf{L2}$, $\mathbf{L6}$, and $\mathbf{L7}$ in acetonitrile shows a decrease of both intermolecular affinities and interligand interactions by a few kJ/mol compared with $[\mathbf{L5}\text{-2H}]^{2-}$, but the successive binding of the ligands remains systematically (weakly) anticooperative (Fig. 20). On the contrary, the successive loading of multisite ligands $\mathbf{L8}$ or $\mathbf{L9}$ with the neutral lanthanide carriers $\text{Ln}(\text{NO}_3)_3$ or $\text{Ln}(\text{hexafluoroacetylacetonate})_3$ ($\text{Ln}(\text{hfac})_3$)
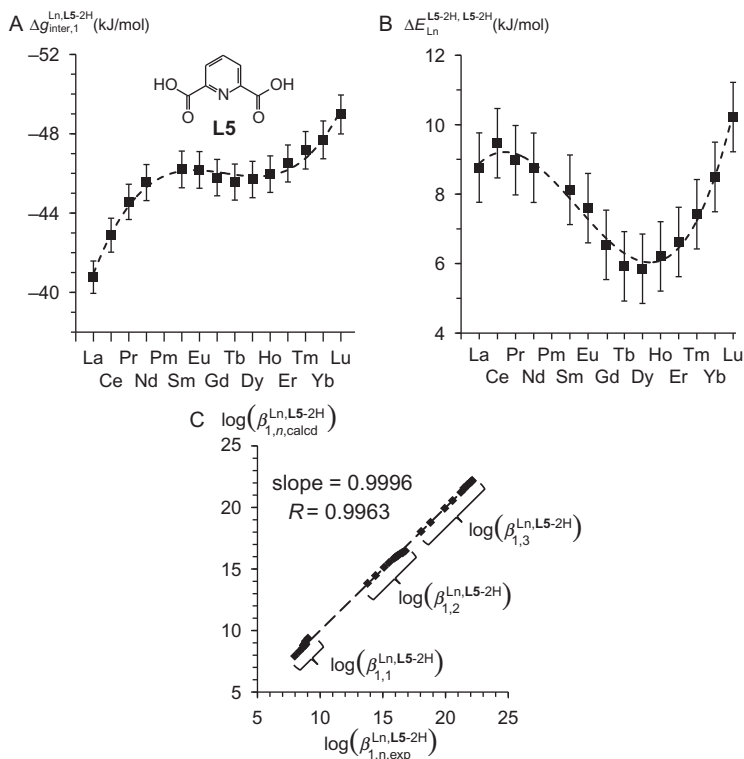
**FIGURE 19** (A) Experimental noncooperative intermolecular affinities $\Delta g_{inter,1}^{Ln,\mathbf{L5}-2H} = -RT \ln\left(f_{inter,1}^{Ln,\mathbf{L5}-2H}\right)$ and (B) interligand interactions $\Delta E^{\mathbf{L5}-2H,\mathbf{L5}-2H} = -RT \ln\left(u^{\mathbf{L5}-2H,\mathbf{L5}-2H}\right)$ fitted with Eqs. (53)–(55) for the successive complexation of dipicolinate dianions $[\mathbf{L5}-2H]^{2-}$ to trivalent lanthanides in water (the dashed traces are a guide for the eyes). (C) Thermodynamic constants recomputed using Eqs. (53)–(55) with respect to the experimental data (the dashed trace is a linear correlation).

displays variable allosteric cooperativities, which strongly depend on the nature of the counteranions and on the intersite distances (Fig. 21).

A rational programming of allosteric cooperativity is required for the control of the facial $(fac)$-$[\mathbf{ML}_3] \leftrightarrow mer$-$[\mathbf{ML}_3]$ isomerization process, which is crucial for implementing predetermined physicochemical properties (volatility, optical response) in pseudo-octahedral d-block complexes where $\mathbf{L}$ is an unsymmetrical bidentate chelate ligands (Katakura and Koide, 2006).

Its counterpart in lanthanide coordination chemistry has been addressed only once for the $fac$-$[\mathrm{Lu}(\mathbf{L}k)_3]^{3+} \leftrightarrow mer$-$[\mathrm{Lu}(\mathbf{L}k)_3]^{3+}$ ($\mathbf{L}k = \mathbf{L10}$–$\mathbf{L12}$) isomerization process involving nonsymmetrical terdentate chelates of increasing bulkiness (Fig. 22A, Le Borgne et al., 2004). Application of the site-binding model (Eq. 52) to the $fac \leftrightarrow mer$ equilibrium constant $K_{fac \rightarrow mer}^{\mathrm{Lu},\mathbf{L}}$ gives (Fig. 22B)

$\Delta g^{Eu,L2}_{inter} = -42(1)$ kJ/mol

$\Delta E^{L2,L2}_{Eu} = 2(1)$ kJ/mol

$[Eu(L2)_3]^{3+}$    Piguet and Bünzli (2009)

$\Delta g^{Eu,L6}_{inter} = -39(2)$ kJ/mol

$\Delta E^{L6,L6}_{Eu} = 6(2)$ kJ/mol

$[Eu(L6)_3]^{3+}$    Escande et al. (2009)

$\Delta g^{Eu,L7}_{inter} = -41(2)$ kJ/mol

$\Delta E^{L7,L7}_{Eu} = 4(2)$ kJ/mol

$[Eu(L7)_3]^{3+}$    Escande et al. (2009)
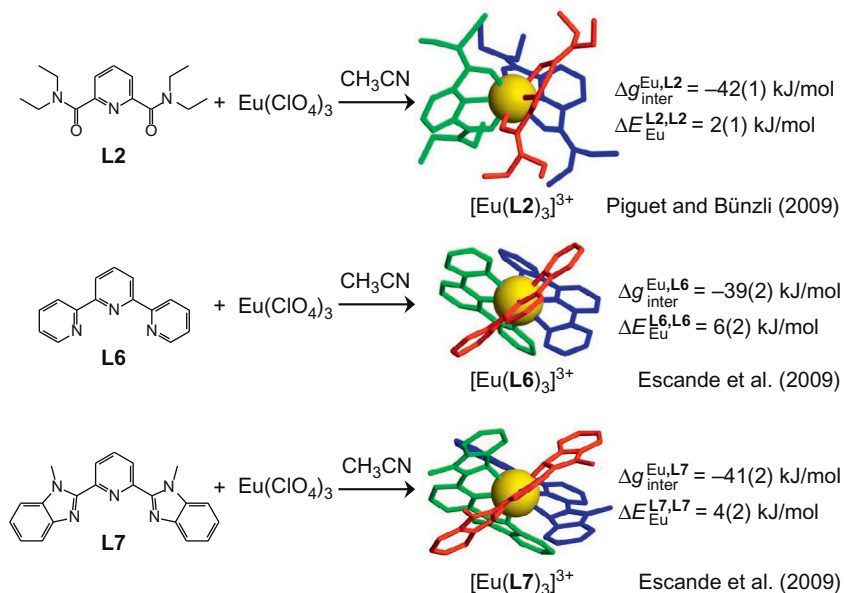
**FIGURE 20** Application of the site-binding model to the successive complexation of neutral terdentate ligands to Eu(ClO$_4$)$_3$ in acetonitrile.

$$K^{Lu,L}_{fac \to mer} = 3 \left( \frac{u^{L,L}_{cis,mer}}{u^{L,L}_{cis,fac}} \right)^2 \tag{56}$$

where $\Delta E^{L,L}_{cis,fac} = -RT \ln \left( u^{L,L}_{cis,fac} \right)$ and $\Delta E^{L,L}_{cis,mer} = -RT \ln \left( u^{L,L}_{cis,mer} \right)$ are the free energy of interligand interactions operating between two adjacent ligands adopting either head-to-head ($\Delta E^{L,L}_{cis,fac}$) or head-to-tail orientations ($\Delta E^{L,L}_{cis,mer}$). When $\Delta E^{L,L}_{cis,fac} = \Delta E^{L,L}_{cis,mer}$, the binding of a ligand **L** to the central lanthanide is isoenergetic whatever its relative orientation, and a statistical constant of $K^{Lu,L}_{fac \to mer} = 3$ is expected (Aboshyan-Sorgho et al., 2014). Minor deviations from the statistical 75% mer-[Lu(**L**k)$_3$]$^{3+}$/25% fac-[Lu(**L**k)$_3$]$^{3+}$ speciation were indeed observed in acetonitrile leading to $K^{Lu,L10}_{fac \to mer} = 10.4$, $K^{Lu,L11}_{fac \to mer} = 4.9$, and $K^{Lu,L12}_{fac \to mer} = 4.0$ at room temperature in acetonitrile. Applying the van't Hoff equation to Eq. (56) provides $-1.5 \leq \left( \Delta E^{L,L}_{cis,mer} - \Delta E^{L,L}_{cis,fac} \right) \leq -0.4$ kJ/mol, which can be summarized by a cooperativity process at room temperature favoring the formation of the meridional (mer) isomer ($\Delta E^{L,L}_{cis,mer} < \Delta E^{L,L}_{cis,fac}$; Le Borgne et al., 2004). Interestingly, the enthalpic and entropic contributions deduced from the dependence of $K^{Lu,L}_{fac \to mer}$ on the temperature obey H/S compensation despite the
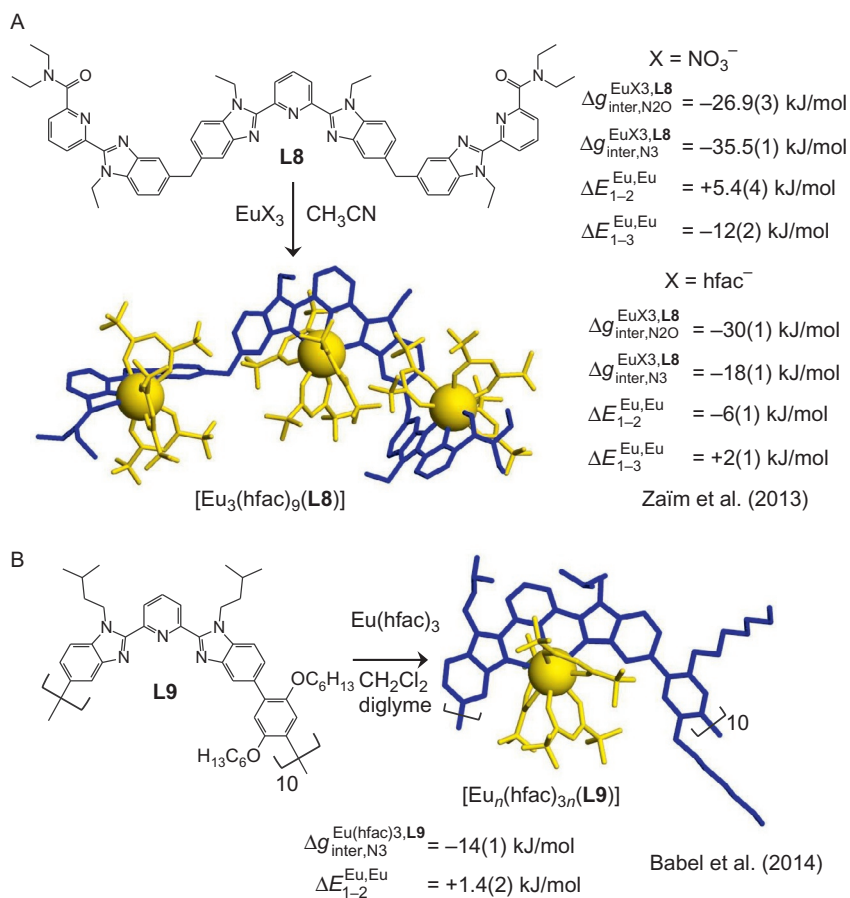
FIGURE 21 Application of the site-binding model to the successive complexation of neutral lanthanide carriers Eu(NO₃)₃ or Eu(hfac)₃ to the linear multiterdentate receptors **L8** and **L9** in organic solvents.

completely different behavior observed for the bulky **L12** ligand, for which the meridional isomer $mer$-[Lu($\mathbf{L}k$)₃]³⁺ is affected by a large enthalpic penalty of $\Delta H^{Lu,\mathbf{L12}}_{fac \to mer} = 21(2)$ kJ/mol due to some unfavorable intramolecular interligand packing (Fig 22C, Le Borgne et al., 2004).

## 4.2 Intramolecular Connections and the Chelate Cooperativity

The different nature of intermolecular (modeled with $f^{R,L}_{inter}$) and intramolecular (modeled with $f^{R,L}_{intra}$) binding events is related to each other with the help of the EM (Eq. 38), which is commonly defined as $EM = f^{R,L}_{intra}/f^{R,L}_{inter}$ upon

A



**L10**        **L11**        **L12**

B



$K_{fac \to mer}^{Lu,L10}$

$CH_3CN$

$fac$-$[Lu(Lk)_3]^{3+}$        $mer$-$[Lu(Lk)_3]^{3+}$

C $\Delta H_{fac \to mer}^{Lu,L}$ (kJ/mol)



$\Delta S_{fac \to mer}^{Lu,L}$ (J/mol/K)
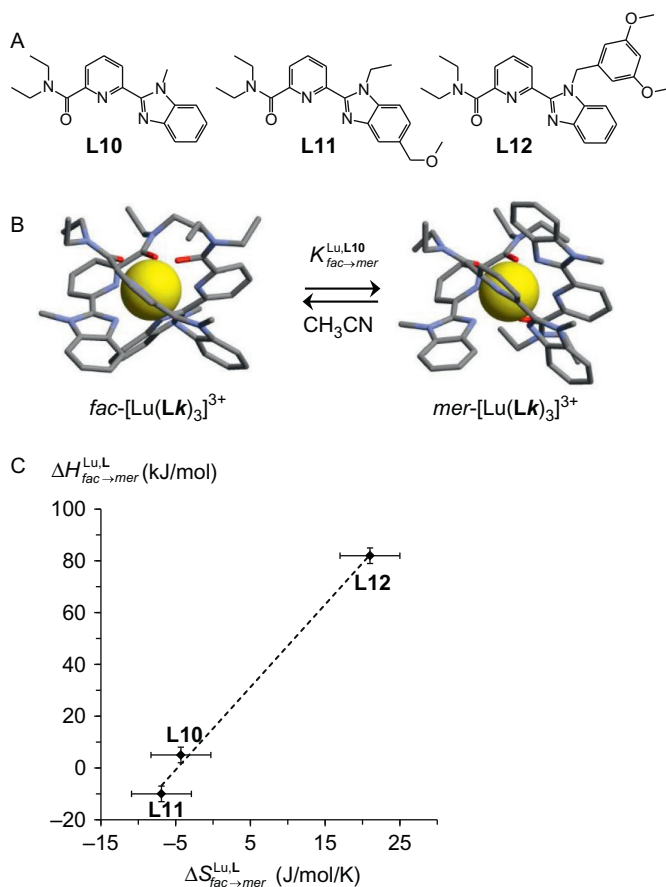
**FIGURE 22** (A) Chemical structures of ligands **L10–L12**, (B) schematic $fac$-$[Lu(Lk)_3]^{3+}$ $\leftrightarrow mer$-$[Lu(Lk)_3]^{3+}$ isomerization process, and (C) $\Delta H_{fac \to mer}^{Lu,L}$ versus $\Delta S_{fac \to mer}^{Lu,L}$ plot for the isomerization reaction occurring in acetonitrile (Le Borgne et al., 2004).

fixing $c^\theta = 1$ M for the concentration of the reference standard state (Mandolini, 1986). It is thus tempting to assume that in the absence of chelate cooperativity EM = 1 M, whereas EM > 1 M and EM < 1 M would indicate positive, respectively, negative cooperativity brought by the intramolecular process (Calderone and Williams, 2001; Mammen et al., 1998). However, this assumption is inconsistent since EM has units of concentration and its numerical value depends on the choice of the standard state. Hunter and Anderson (2009) proposed the product $f_{inter}^{R,L} EM = f_{intra}^{R,L}$ as a measure of chelate cooperativity, but (i) its identification with a single intramolecular binding interaction whereas cooperativity factor is necessarily a ratio of two equilibrium constants, (ii) its independence on the ligand concentration, and (iii) its limiting

value of zero instead of one in the absence of chelate cooperativity precludes its further consideration. An elegant and adequate derivation of the chelate cooperativity based on the competition between intra- and intermolecular complexation processes has been reported by Ercolani and Schiaffino (2011). It is illustrated in Fig. 23 for bidentate ligands reacting with metal ion possessing two binding sites.

In the absence of chelate cooperativity, the fixation of the second ligand is strictly intermolecular (Fig. 23, right) and the equilibrium constant is given by

$$K_{\text{noncooperative}} = \frac{\left|[\mathbf{ML_2}]\right|}{\left|[\mathbf{ML}]_{\text{open}}\right|\left|[\mathbf{L}]\right|} = \omega_{\text{inter}}^{\mathbf{M,L}} f_{\text{inter}}^{\mathbf{M,L}} \tag{57}$$

In the presence of chelate cooperativity, the saturation of the receptor results either from the chelate-binding process leading to $[\mathbf{ML}]_{\text{closed}}$ or from the intermolecular reaction leading to $[\mathbf{ML_2}]$, a reaction summarized by the apparent constant $K_{\text{cooperative}}$ for the formation of the saturated receptor starting from the partially bound open complex $[\mathbf{ML}]_{\text{open}}$.

$$\begin{aligned}
K_{\text{cooperative}} &= \frac{\left|[\mathbf{ML_2}]\right| + \left|[\mathbf{ML}]_{\text{closed}}\right|}{\left|[\mathbf{ML}]_{\text{open}}\right|\left|[\mathbf{L}]\right|} = \omega_{\text{inter}}^{\mathbf{M,L}} f_{\text{inter}}^{\mathbf{M,L}} + \omega_{\text{intra}}^{\mathbf{M,L}} f_{\text{inter}}^{\mathbf{M,L}} \frac{EM}{\left|[\mathbf{L}]\right|} \\
&= \omega_{\text{inter}}^{\mathbf{M,L}} f_{\text{inter}}^{\mathbf{M,L}} \left(1 + \frac{\omega_{\text{intra}}^{\mathbf{M,L}}}{\omega_{\text{inter}}^{\mathbf{M,L}}} \frac{EM}{\left|[\mathbf{L}]\right|}\right) = K_{\text{noncooperative}} \left(1 + \frac{\omega_{\text{intra}}^{\mathbf{M,L}}}{\omega_{\text{inter}}^{\mathbf{M,L}}} \frac{EM}{\left|[\mathbf{L}]\right|}\right)
\end{aligned} \tag{58}$$
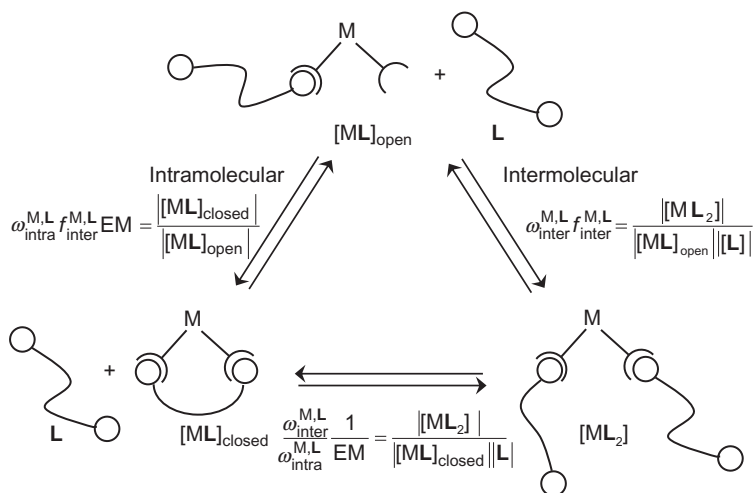


**FIGURE 23** Competition between intermolecular and intramolecular complexation processes in the formation of coordination complexes.

The factor $\beta' = 1 + \dfrac{\omega_{\text{intra}}^{\mathbf{M},\mathbf{L}}}{\omega_{\text{inter}}^{\mathbf{M},\mathbf{L}}} \dfrac{\text{EM}}{|[\mathbf{L}]|} = \dfrac{K_{\text{cooperative}}}{K_{\text{noncooperative}}}$ corresponds to the searched cooperativity index. It tends to $\beta' = 1$ in the absence of chelate effect ($\text{EM} = 0$) or in large excess of ligand ($|[\mathbf{L}]| \to \infty$). Moreover, $\beta' \geq 1$ and chelate cooperativity can only be positive as far as the overall binding is concerned. According to Fig. 23 (bottom), the factor $\beta = \dfrac{\omega_{\text{intra}}^{\mathbf{M},\mathbf{L}}}{\omega_{\text{inter}}^{\mathbf{M},\mathbf{L}}} \dfrac{\text{EM}}{|[\mathbf{L}]|} = \dfrac{|[\mathbf{ML}]_{\text{closed}}|}{|[\mathbf{ML}_2]|}$ is the contribution of the intramolecular pathway to the cooperativity factor $\beta'$. It therefore measures the benefit/drawback produced by the chelate interaction with respect to the intermolecular binding. When the concentration of the bidentate ligand is equal to $|[\mathbf{L}]| = \left(\omega_{\text{intra}}^{\mathbf{M},\mathbf{L}} / \omega_{\text{inter}}^{\mathbf{M},\mathbf{L}}\right) \text{EM}$, the chelate interaction is noncooperative ($\beta = 1$) and produces equal amounts of $[\mathbf{ML}]_{\text{closed}}$ and $[\mathbf{ML}_2]$ complexes. Positive ($\beta > 1$), respectively, negative ($\beta < 1$) chelate cooperativity results when $|[\mathbf{L}]| < \left(\omega_{\text{intra}}^{\mathbf{M},\mathbf{L}} / \omega_{\text{inter}}^{\mathbf{M},\mathbf{L}}\right) \text{EM}$, respectively, $|[\mathbf{L}]| > \left(\omega_{\text{intra}}^{\mathbf{M},\mathbf{L}} / \omega_{\text{inter}}^{\mathbf{M},\mathbf{L}}\right) \text{EM}$. Obviously, the higher the value of the EM, the larger the ligand concentration range over which positive chelate cooperativity operates. The successive fixation of three nonsymmetrical terdentate binding units similar to **L7**, but held together by a covalent tripod in **L13**, to trivalent rare earth cations to give $[\text{Ln}(\mathbf{L13})]^{3+}$ are good candidates for investigating chelate cooperativity in lanthanide coordination complexes because the initial intermolecular association process ($K_{\text{inter}}^{\text{Ln},\mathbf{L13}}$) is followed by two related, but intramolecular binding events ($K_{\text{intra},1}^{\text{Ln},\mathbf{L13}}$ and $K_{\text{intra},2}^{\text{Ln},\mathbf{L13}}$ in Fig. 24, Canard et al., 2008).

The cumulative thermodynamic constants for the formation of $[\text{Ln}(\mathbf{L13})]^{3+}$ (Eq. 59) is the only experimentally accessible data, whereas its modeling within the frame of the site-binding model requires three parameters: the noncooperative Ln-terdentate binding unit affinity $f_{\text{inter}}^{\text{Ln},\mathbf{N3}}$, the allosteric cooperativity brought by interligand interaction $u_{\text{Ln}}^{\mathbf{N3},\mathbf{N3}} = \exp\left(-\Delta E_{\text{Ln}}^{\mathbf{N3},\mathbf{N3}} / RT\right)$, and the $\text{EM}_{\text{Ln}}$ measuring the chelate cooperativity (Eq. 60)

$$\mathbf{L13} + \text{Ln}^{3+} \rightleftharpoons [\text{Ln}(\mathbf{L13})]^{3+} \quad \beta_{1,1}^{\text{Ln},\mathbf{L13}} \tag{59}$$
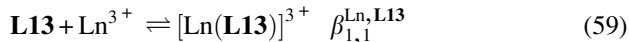
$$\beta_{1,1}^{\text{Ln},\mathbf{L13}} = 12\left(f_{\text{inter}}^{\text{Ln},\mathbf{N3}}\right)^3 (\text{EM}_{\text{Ln}})^2 \left(u_{\text{Ln}}^{\mathbf{N3},\mathbf{N3}}\right)^3 \tag{60}$$

A satisfying approximation assumes that the set of thermodynamic parameters $f_{\text{inter}}^{\text{Ln},\mathbf{N3}}$ and $u_{\text{Ln}}^{\mathbf{N3},\mathbf{N3}}$ also holds for modeling the successive fixation of the terdentate side arms **L7** to $\text{Ln}^{3+}$ to give $[\text{Ln}(\mathbf{L7})_n]^{3+}$ (Fig. 19 and Eqs. 53–55). The simultaneous consideration of four thermodynamic constants $\beta_{1,1}^{\text{Ln},\mathbf{L13}}$, $\beta_{1,1}^{\text{Ln},\mathbf{L7}}$, $\beta_{1,2}^{\text{Ln},\mathbf{L7}}$, and $\beta_{1,3}^{\text{Ln},\mathbf{L7}}$ eventually provides a complete set of three microscopic parameters $\Delta g_{\text{inter}}^{\text{Ln},\mathbf{N3}} = -RT \ln\left(f_{\text{inter}}^{\text{Ln},\mathbf{N3}}\right)$, $\Delta E_{\text{Ln}}^{\mathbf{N3},\mathbf{N3}} = -RT \ln\left(u_{\text{Ln}}^{\mathbf{N3},\mathbf{N3}}\right)$, and $\text{EM}_{\text{Ln}}$ for each lanthanide by using linear least-squares techniques (Table 4, Canard et al., 2008).

**FIGURE 24** Successive complexation reactions leading to the formation of $[Ln(\mathbf{L13})]^{3+}$ in acetonitrile and associated thermodynamic constants deduced by using the site-binding model (Canard et al., 2008). The point groups considered for the calculation of the statistical factors are mentioned; S stands for solvent ($=CH_3CN$).

**TABLE 4** Microscopic Thermodynamic Parameters Obtained for the Successive Complexation of 2,6-Bis(Benzimidazol-2-yl)Pyridine Units to $Ln^{3+}$ to Give $[Ln(L7)_n]^{3+}$ and $[Ln(L13)]^{3+}$ in Acetonitrile (0.1 M $^nBu_4ClO_4$; Canard et al., 2008)

| Microscopic Parameters | La | Eu | Lu |
|---|---|---|---|
| $\Delta g_{inter}^{Ln,N3}$ kJ/mol | $-35(1)$ | $-49(2)$ | $-51.3(5)$ |
| $\Delta g_{intra}^{Ln,N3} = \Delta g_{inter}^{Ln,N3} - RT \ln(EM_{Ln})$ kJ/mol | $-8(1)$ | $-8(1)$ | $-8.5(4)$ |
| $\Delta E_{Ln}^{N3,N3}$ kJ/mol | $5(1)$ | $10(2)$ | $9.8(5)$ |
| $EM_{Ln}$ M | $10^{-4.8(2)}$ | $10^{-7.3(3)}$ | $10^{-7.63(8)}$ |

The monotonous decrease of $\Delta g_{\text{inter}}^{\text{Ln,N3}}$ along the lanthanide series is reminiscent of the expected electrostatic effect, a trend minimized by the operation of both negative allosteric cooperativity $\left(0 < \Delta E_{\text{La}}^{\text{N3,N3}} < \Delta E_{\text{Eu}}^{\text{N3,N3}} \approx \Delta E_{\text{Lu}}^{\text{N3,N3}}\right)$ and unfavorable chelate interaction $(\text{EM}_{\text{Lu}} \ll \text{EM}_{\text{Eu}} < \text{EM}_{\text{La}} < 10^{-4.8}\ \text{M}$, Table 4). According to the competitive reaction pathway proposed by Ercolani and Schiaffino (2011, Fig. 23) for the thermodynamic rationalization of chelate cooperativity, positive chelate cooperativity operates for the formation of $[\text{Ln}(\textbf{L13})]^{3+}$ when $\beta_{\text{Ln}} = \dfrac{\omega_{\text{intra}}^{\textbf{M,L}}}{\omega_{\text{inter}}^{\textbf{M,L}}} \dfrac{\text{EM}_{\text{Ln}}}{|[\textbf{L13}]|} = \dfrac{2}{3}\dfrac{\text{EM}_{\text{Ln}}}{|[\textbf{L13}]|} > 1$ (Fig. 25). In other words, minute free ligand concentrations $|[\textbf{L13}]| < (2/3)\text{EM}_{\text{Ln}}$, i.e., smaller than $10^{-5}$ M for $[\text{La}(\textbf{L13})]^{3+}$ and smaller than $10^{-8}$ M for $[\text{Lu}(\textbf{L13})]^{3+}$, are required for the intramolecular chelate pathway to become dominant for saturating the central cation, thus leading to the preferred formation of the mononuclear macrobicyclic complexes $[\text{Ln}(\textbf{L13})]^{3+}_{\text{closed}}$. Translated for a stoichiometric 1:1 mixing of **L13** and $\text{Ln}^{3+}$, positive chelate cooperativity only occurs for total ligand concentrations smaller than $4 \cdot 10^{-3}$ M (Ln = La) and $2 \cdot 10^{-8}$ M (Ln = Lu) in acetonitrile.

The extreme reluctance of $[\text{Ln}(\textbf{L13})]^{3+}$ for intramolecular macrocyclization was assigned by Ryan et al. (2009) to severe constraints occurring within the sulfur-containing organic tripod. This drawback can be turned into an advantage for the selective complexation of lanthanide cations with different sizes in the same molecular complex $[\text{Ln}_2(\textbf{L14})]^{6+}$ (Eq. 61 and Fig. 26, Ryan et al., 2012).

$$\textbf{L14} + m\text{Ln}^{3+} \rightleftharpoons [\text{Ln}_m(\textbf{L14})]^{3m+} \qquad \beta_{m,1}^{\text{Ln,L14}} \tag{61}$$
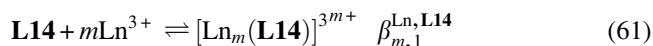
In the absence of interannular cooperativity (see Section 4.3), the thermodynamic modeling of the cumulative formation constants leading to the podates $[\text{Ln}(\textbf{L14})]^{3+}$ and $[\text{Ln}_2(\textbf{L14})]^{6+}$ can be summarized with Eqs. (62) and (63) (Fig. 26).

$$\beta_{1,1}^{\text{Ln,L14}} = 12\left(f_{\text{inter}}^{\text{Ln,N3}}\right)^3 \left(u_{\text{Ln}}^{\textbf{N3,N3}}\right)^3 \left(\text{EM}_{\text{Ln}}^{\text{prox}}\right)^2 + 12\left(f_{\text{inter}}^{\text{Ln,N2O}}\right)^3 \left(u_{\text{Ln}}^{\textbf{N2O,N2O}}\right)^3 \left(\text{EM}_{\text{Ln}}^{\text{dist}}\right)^2 \tag{62}$$

$$\beta_{2,1}^{\text{Ln,L14}} = 72\left(f_{\text{inter}}^{\text{Ln,N3}}\right)^3 \left(f_{\text{inter}}^{\text{Ln,N2O}}\right)^3 \left(u_{\text{Ln}}^{\textbf{N3,N3}}\right)^3 \left(u_{\text{Ln}}^{\textbf{N2O,N2O}}\right)^3 \left(\text{EM}_{\text{Ln}}^{\text{prox}}\right)^2 \left(\text{EM}_{\text{Ln}}^{\text{dist-2}}\right)^2 u^{\text{Ln,Ln}} \tag{63}$$

No fewer than eight microscopic thermodynamic parameters are required in Eqs. (61) and (62), while only two experimental stability constants are available. However, the successive complexation processes leading to $[\text{Ln}(\textbf{L7})_3]^{3+}$ and $[\text{Ln}(\textbf{L10})_3]^{3+}$ are easily modeled with Eqs. (53)–(55) and they can be used for independently estimating $f_{\text{inter}}^{\text{Ln,N3}}$ and $f_{\text{inter}}^{\text{Ln,N2O}}$ (Fig. 27B) as well as $u_{\text{Ln}}^{\textbf{N3,N3}}$ and $u_{\text{Ln}}^{\textbf{N2O,N2O}}$ (Fig. 27D). Among the three different effective molarities required to model the formation of $[\text{Ln}(\textbf{L14})]^{3+}$ and $[\text{Ln}_2(\textbf{L14})]^{6+}$, that associated with the macrocyclization process involving the $\text{N}_3$ binding
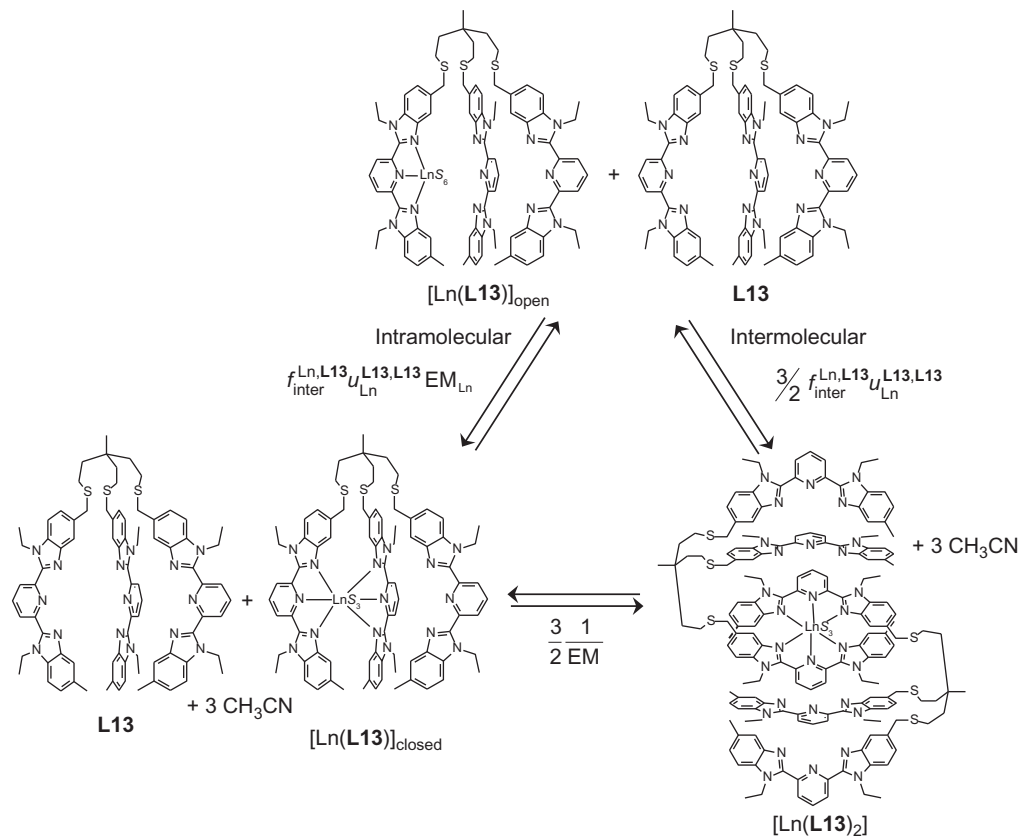
**FIGURE 25** Competition between intermolecular and intramolecular complexation processes in the formation of podate [Ln(**L13**)]$^{3+}$.

**L14** $C_{3v}$

$+ 2\,[Ln(CH_3CN)_9]^{3+}$
$D_{3h}$

$12\left(f_{inter}^{Ln,N3}\right)^3 \left(u_{Ln}^{N3,N3}\right)^3 \left(EM_{Ln}^{prox}\right)^2$

$12\left(f_{inter}^{Ln,N2O}\right)^3 \left(u_{Ln}^{N2O,N2O}\right)^3 \left(EM_{Ln}^{dist}\right)^2$

$[Ln(CH_3CN)_9]^{3+}$
$+$
$9\,CH_3CN$

$[Ln(CH_3CN)_9]^{3+}$
$+$
$9\,CH_3CN$

Ln $\quad C_3$
proximal-$[Ln(\mathbf{L14})]^{3+}$

Ln $\quad C_3$
distal-$[Ln(\mathbf{L14})]^{3+}$

$6\left(f_{inter}^{Ln,N2O}\right)^3 \left(u_{Ln}^{N2O,N2O}\right)^3 \left(EM_{Ln}^{dist-2}\right)^2 u^{Ln,Ln}$

$6\left(f_{inter}^{Ln,N3}\right)^3 \left(u_{Ln}^{N3,N3}\right)^3 \left(EM_{Ln}^{prox-2}\right)^2 u^{Ln,Ln}$

Ln $\quad$ Ln $\quad + 18\,CH_3CN$

7 Å $\quad$ 9 Å
$C_3$
$[Ln_2(\mathbf{L14})]^{6+}$
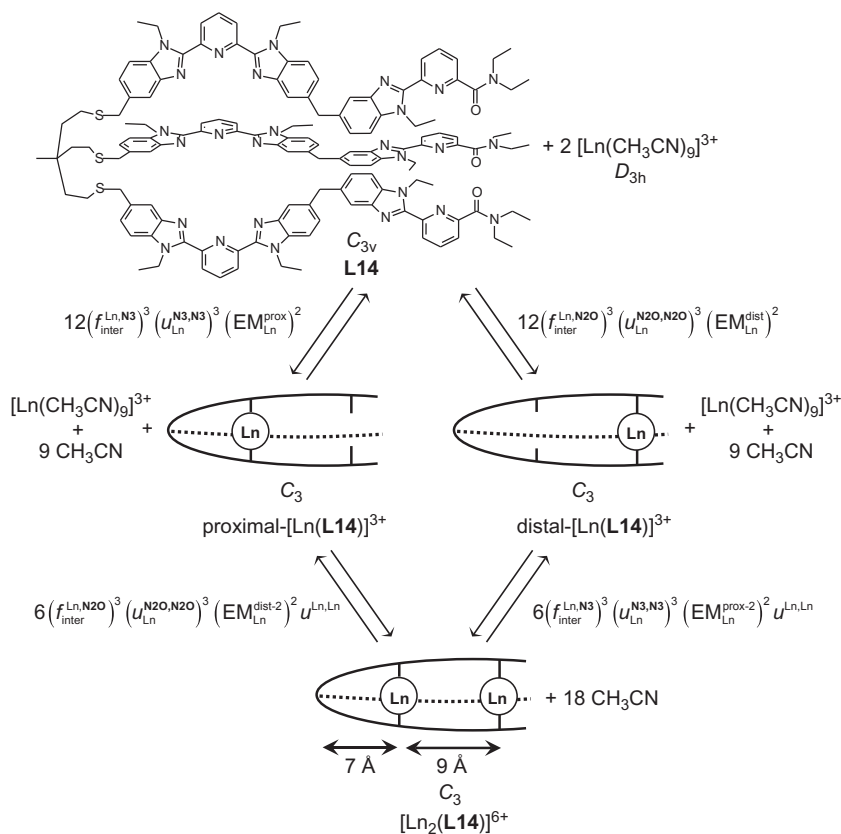
**FIGURE 26** Complexation reactions leading to the formation of $[Ln(\mathbf{L14})]^{3+}$ and $[Ln_2(\mathbf{L14})]^{6+}$ in acetonitrile and associated thermodynamic constants deduced by using the site-binding model (Ryan et al., 2012). The point groups considered for the calculation of the statistical factors are mentioned.

units in $[Ln(\mathbf{L14})]^{3+}$, $EM_{Ln}^{prox}$ is closely related to $EM_{Ln}$ observed for $[Ln(\mathbf{L13})]^{3+}$ (Eq. 60) and three unknown parameters remain to be fitted: $EM_{Ln}^{dist}$ and $EM_{Ln}^{dist-2}$, which are the effective molarities for the macrocyclization involving the terminal $N_2O$ binding units in the absence, respectively, in the presence of a lanthanide cation in the proximal $N_9$ coordination site and $u^{Ln,Ln} = \exp(-\Delta E^{Ln,Ln}/RT)$, which represents the intermetallic interaction operating in $[Ln_2(\mathbf{L14})]^{6+}$. An ultimate approximation considers that each ligand strand in the tripod ligand $\mathbf{L14}$ acts as a freely joint chain of length $d$ bridging the two units bound to the same metal. In this context, Kuhn's theory predicts that $EM \propto d^{-3/2}$ (Kuhn, 1934; Piguet, 2010) and a simple inspection of the molecular structures shown in Fig. 26 (bottom) implies that $EM_{Ln}^{prox}$ is correlated with an end-to-end distance of $d = 2 \times 7 = 14$ Å, $EM_{Ln}^{dist-2}$ corresponds to $d = 2 \times 9 = 18$ Å, whereas $EM^{dist}_{Ln}$ involves a much larger separation
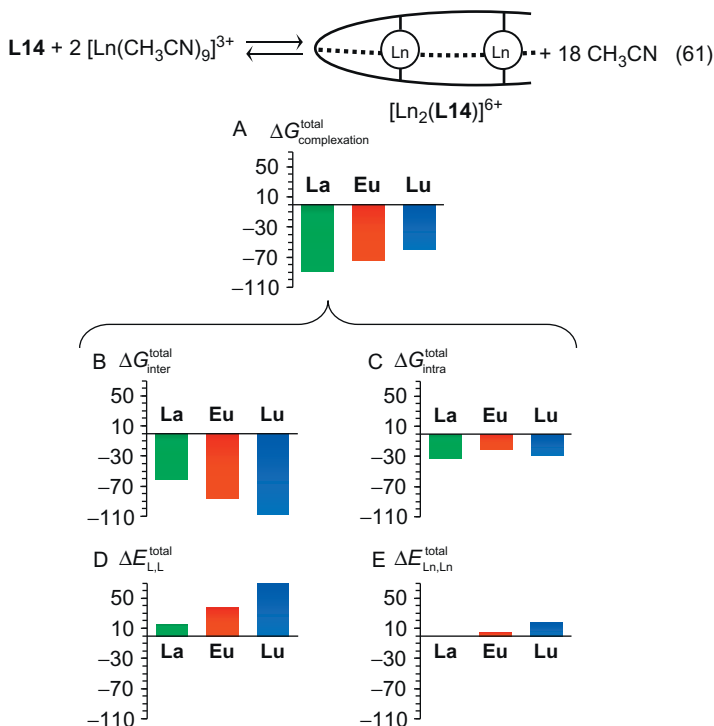
**FIGURE 27** Thermodynamic contributions in kJ/mol accompanying the complexation process leading to $[Ln_2(\mathbf{L14})]^{6+}$. (A) Global free energy change, (B) sum of the two Ln–ligand intermolecular connections, (C) sum of the four intramolecular Ln–ligand connections, (D) sum of the six interligand interactions (allosteric cooperativity), and (E) intermetallic interaction (Ln = La, Eu, Lu; $CH_3CN/CH_2Cl_2$ (9:1) + $10^{-2}$ M $NBu_4ClO_4$, 298 K, Ryan et al., 2012).

of $d = 2 \times (7 + 9) = 32$ Å. Altogether, the missing effective molarities can be therefore deduced from $EM_{Ln}^{prox}$ since $EM_{Ln}^{dist\text{-}2}/EM_{Ln}^{prox} = (18/14)^{-3/2} = 0.69$ and $EM_{Ln}^{dist}/EM_{Ln}^{prox} = (32/14)^{-3/2} = 0.29$ and the contributions of the various intramolecular processes to the formation of $[Ln_2(\mathbf{L14})]^{6+}$ become accessible (Fig. 27C). Finally, the intermetallic interaction can be deduced with Eq. (63) (Fig. 27E).

The global complexation reaction leading to $[Ln_2(\mathbf{L14})]^{6+}$ exhibits an unusual antielectrostatic trend along the lanthanide series (Fig. 27A), which result from the operation of a standard electrostatic trend found for the intermolecular intercomponent affinity (Fig. 27B), which is overcome by an opposite increase in the interligand (Fig. 27D) and intermetallic (Fig. 27E) repulsions for the smallest cations (i.e., negative allosteric cooperativities). The reluctance of these tripods for macrocyclization with trivalent lanthanides is confirmed by the (very) limited contributions of the intramolecular binding to the overall complexation process (Fig. 27C), but its global invariance along

the series makes these complexes good candidates for the size-selective complexation of trivalent lanthanides. The latter set of microscopic thermodynamic parameters can be used for predicting the stability of the two heterometallic microspecies for the La/Lu pair, where La(III) either occupies the proximal $N_9$ coordination site in [LaLu(**L14**)]$^{6+}$ (Eq. 64 and Fig. 28, top center) or the distal $N_6O_3$ coordination site in [LuLa(**L14**)]$^{6+}$ (Eq. 65 and Fig. 28, bottom center).

$$\beta_{1,1,1}^{La,Lu,L14} = 72 \left( f_{inter}^{La,N3} \right)^3 \left( f_{inter}^{Lu,N2O} \right)^3 \left( u_{La}^{N3,N3} \right)^3 \left( u_{Lu}^{N2O,N2O} \right)^3$$
$$(EM_{La}^{prox})^2 (EM_{Lu}^{prox})^2 (0.69)^2 u^{La,Lu} \tag{64}$$

$$\beta_{1,1,1}^{Lu,La,L14} = 72 \left( f_{inter}^{Lu,N3} \right)^3 \left( f_{inter}^{La,N2O} \right)^3 \left( u_{Lu}^{N3,N3} \right)^3 \left( u_{La}^{N2O,N2O} \right)^3$$
$$(EM_{La}^{prox})^2 (EM_{Lu}^{prox})^2 (0.69)^2 u^{Lu,La} \tag{65}$$

Following the concept of the mixing rule (Borkovec et al., 2004), the intermetallic interaction operating in the heterometallic complexes can be estimated as the arithmetic mean $\Delta E^{La,Lu} = \Delta E^{Lu,La} = (1/2)(\Delta E^{La,La} + \Delta E^{Lu,Lu})$. This translates into $u^{La,Lu} = u^{Lu,La} = e^{-(\Delta E^{Lu,La}/RT)} = \sqrt{u^{La,La}u^{La,La}} = 0.059$ for the heterometallic *Boltzmann* factors, which are finally introduced into Eqs. (64) and (65) in order to predict $\log \left( \beta_{1,1,1}^{La,Lu,L9} \right) = 14.36$ for [LaLu (**L14**)$_3$]$^{6+}$ and $\log \left( \beta_{1,1,1}^{Lu,La,L9} \right) = 12.20$ for [LuLa(**L14**)$_3$]$^{6+}$. The speciation computed in solution at millimolar concentrations for the competitive filling
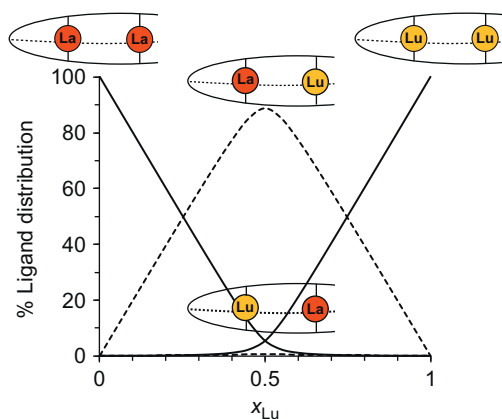


FIGURE 28 Predicted ($\Delta E_{mix} = 2\Delta E^{Lu,La} - (\Delta E^{Lu,La} + \Delta E^{Lu,La}) = 0$) ligand distributions in the microspecies [La$_x$Lu$_{2-x}$(**L14**)]$^{6+}$ during the titration of **L14** with La$^{3+}$ and Lu$^{3+}$ in the absence of ligand dissociation (lutetium mole fractions $x_{Lu} = |Lu|_{tot}/(|La|_{tot} + |Lu|_{tot}) = 0 - 1$).

of the two sites of **L14** with the $La^{3+}/Lu^{3+}$ pair shows the predominance ($>90\%$) of the $[LaLu(L14)]^{6+}$ isomer for an equimolar mixture of the two cations (Fig. 28), a prediction in line with the detection of a single heterobimetallic complex in the experimental NMR spectra (Ryan et al., 2009).

## 4.3 Multivalency and the Interannular Cooperativity

Interannular cooperativity is a logical consequence of multivalency (Mulder et al., 2004), since it arises from the interplay of two or more intramolecular binding interactions (Ercolani and Schiaffino, 2011). This phenomenon can be illustrated by the reactions of a single-stranded receptor $[M_2L]$ with an excess of chelating ligands to successively give the double-stranded $[M_2L_2]$ and triple-stranded $[M_2L_3]$ complexes (Fig. 29).

The first ligand molecule **L** binds to form a ring in $[M_2L_2]$ that hampers internal rotation. The connection of a second ligand to give the macrobicyclic complex $[M_2L_3]$ may benefit or suffer from the freezing in internal rotation (entropic contribution) and/or some preorganization of the two remaining binding sites (enthalpic + entropic contributions), thus leading to either positive or negative cooperativity. This type of cooperativity is not due to an increase/decrease of the affinity of the binding site measured by the interligand interactions parameter $\Delta E_M^{L,L}$ (i.e., allosteric cooperativity), but it is the result from an increase/decrease of the EM controlling the closure of the second ring with respect to that of the first ring. When the ratio $\gamma = EM_2/EM_1 = 1$, no
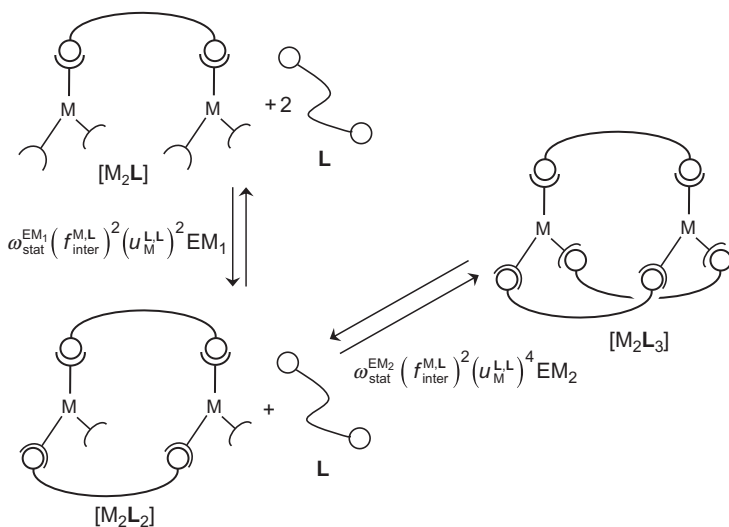


**FIGURE 29** Binding of a divalent ligand **L** to a tetravalent metallic receptors for highlighting the operation of interannular cooperativity ($EM_1 \neq EM_2$). The associated thermodynamic constants are deduced by using the site-binding model.

interannular cooperativity occurs, but $EM_2/EM_1 > 1$ or $EM_2/EM_1 < 1$ corresponds to positive, respectively, negative interannular cooperativity.

The formation of the polynuclear lanthanide triple-stranded helicates $[Ln_2(L15)_3]^{6+}$ (Piguet et al., 1993), $[Ln_2(L16)_3]^{6+}$ (Ryan et al., 2013), and $[Ln_2(L17\text{-}2H)_3]$ (Terazzi et al., 2009) is ideally suited for exploring the emergence of interannular cooperativity since the thermodynamic data systematically show the formation of an intermediate double-stranded helicate (a macrocyclic edifice characterized by $EM_1$), followed by that of the final triple-stranded helicate (a macrobicyclic edifice characterized by $EM_1 \cdot EM_2$, Fig. 30). The fit of the thermodynamic stability constants collected for the complexation of **L15**, **L16**, and $[L17\text{-}2H]^{2-}$ with $Lu(CF_3SO_3)_3$ shows that
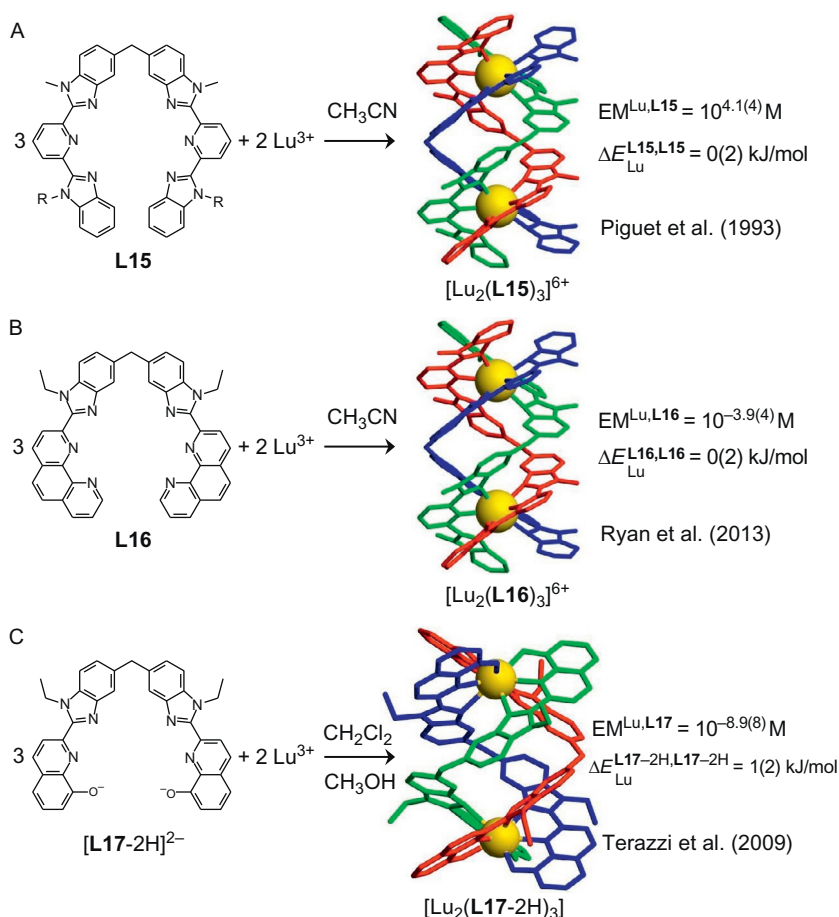


**FIGURE 30** Application of the site-binding model to the successive complexation of bis-terdentate ligands to $Lu^{3+}$ to give binuclear triple-stranded helicates in the absence of interannular cooperativities ($\gamma = EM_2/EM_1 \approx 1$).

the ratio $\gamma = EM_2/EM_1$ is close to 1.0, and no evidence for interannular cooperativity could be detected whatsoever the changes in the rigidity of the ligand strand (**L16** and **L17**) or the choice of the solvent (Fig. 30). It is worth stressing here that the removal of the covalent tripod found in **L14** to give **L15** significantly favors the macrocyclization processes since the EM measured for $[Lu_2(\mathbf{L14})]^{6+}$ ($EM_{Lu}^{\mathbf{L14}} = 10^{-8.0(4)}$ M, Ryan et al., 2012) increases by four orders of magnitude in the helicate $[Lu_2(\mathbf{L15})_3]^{6+}$ ($EM_{Lu}^{\mathbf{L15}} = 10^{-4.1(4)}$ M, Riis-Johannessen et al., 2009).

The situation drastically changes when a rigid aromatic phenyl ring separates the two terdentate binding unit in **L18** instead of the methylene bridge used in ligands **L15**–**L17** (Fig. 31, Lemonnier et al., 2010). Titration of **L18** with $Lu(CF_3SO_3)_3$ shows the exclusive formation of the macrocyclic binuclear double-stranded helicate $[Ln_2(\mathbf{L18})_2]^{6+}$ (crystallized as the cation $[Ln_2(\mathbf{L18})_2(CF_3SO_3)_4]^{2+}$, Fig. 31), in which the EM amounts to $EM_{Lu,1}^{\mathbf{L18}} = 10^{-5.5(3)}$ M. The extreme reluctance of $[Ln_2(\mathbf{L18})_2]^{6+}$ to bind an additional ligand to give $[Ln_2(\mathbf{L18})_3]^{6+}$ at millimolar concentration implies that $EM_{Lu,2}^{\mathbf{L18}} \leq 10^{-12.9}$ M, which leads to an impressive anticooperative index of $\gamma \leq 10^{-12.9}/10^{-5.5} = 10^{-7.4}$ (Lemonnier et al., 2010). A thorough analysis of the crystal structure observed for the binuclear helicate $[Ln_2(\mathbf{L18})_2(CF_3SO_3)_4]^{2+}$ suggests that the addition of a third ligand would require severe steric constraints within the bridges, which are not compatible with the rigid phenyl spacers.
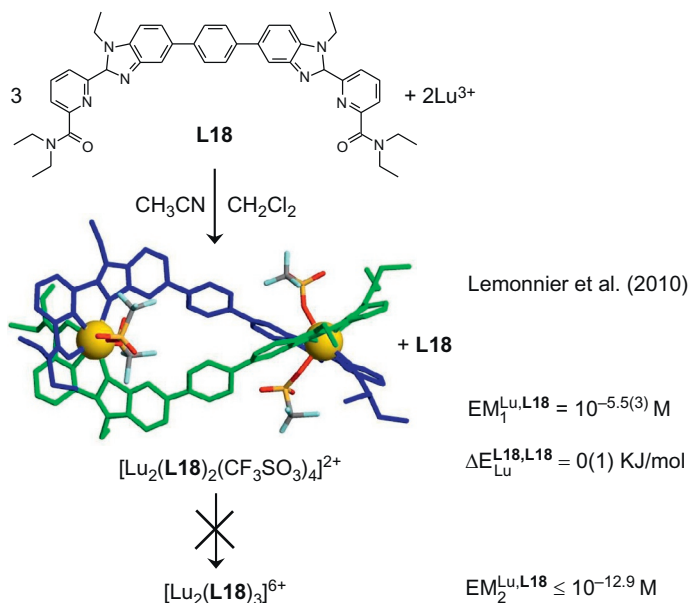


**FIGURE 31** The successive complexation of two terdentate ligands **L18** with $Lu^{3+}$ gives the binuclear helicate $[Lu_2(\mathbf{L18})_2]^{6+}$ with negative interannular cooperativity ($\gamma \leq 10^{-12.9}/10^{-5.5} = 10^{-7.4}$, Lemonnier et al., 2010).

## 5  CONCLUSIONS AND PERSPECTIVES

There is no doubt that the large majority of thermodynamic contributions to lanthanide coordination chemistry corresponds to main stream activity, in which stability constants are collected for novel multidentate ligands and compared with closely related partners displaying minor structural/electronic variations. Systematic measurements along the complete lanthanide series are often tedious and time consuming and nowadays scarcely published in broad-scope journals. According that the profitable aspects linked with technological applications in medicine, in bioanalytical chemistry, and in separation sciences require precise and accurate knowledge of the thermodynamic behaviors, the methical determination of lanthanide formation constants in complicated mixtures still remains very active in lanthanide coordination chemistry. Interpretation of the data is usually limited to the consideration of the electrostatic trend, and any deviation is analyzed in terms of molecular specificities, which may be *a posteriori* justified by theoretical calculations within the frame of *ab initio* or DFT methods (Petit et al., 2007). The consideration of the complexation reaction as a two-step process (desolvation followed by association) in Choppin's model, combined with the estimation of both enthalpic and entropic contributions to each process (Eqs. 15–17), represents an important milestone for rationalizing coordination reactions, especially in rare earth chemistry where covalent effects are limited. Its main support arises from the myriad of stability constants empirically gathered by main stream research, but a theoretical justification to the remarkable axiomatic intuition fixing some exact $H/S$ compensation for the desolvation process was delayed for more than a decade (Ford, 2005a,b; Piguet, 2011; Starikov, 2013; Starikov and Norden, 2007), while its experimental demonstration by Castellano and Eggers (2013) is only available for the formation of $[Ca(EDTA)]^{2-}$ in water ($\Delta G_{\text{desolv}}^{\text{Ca,EDTA}} = 1354 - 3.637T$ in kJ/mol, where $T$ is the absolute temperature in Kelvin). To make a long story short, let us say that any bimolecular complexation process involving a rare earth carrier (solvated cations, unsaturated complex, etc.) and a ligand binding unit is expected to display $H/S$ compensation as long as (i) the desolvation entropy is constant and (ii) the minimum contact distance between the interacting partners (the rare earth–solvent and the rare earth–ligand pairs) is constant along the imposed perturbation. The most obvious consequence in lanthanide coordination chemistry concerns the recurrent minor changes in complexation free energies (i.e., in stability constants) obtained when (chelate) ligands are reacted with the trivalent cations along the lanthanide series. A breakthrough in coordination chemistry arose with the emergence of multistep complexation processes, which were thought to shake up classical thermodynamics (Pfeil and Lehn, 1992). Thanks to Ercolani (2003), the different energetic contributions to multistep metal–ligand assembly processes (statistics, intermolecular, and intramolecular binding) could be judiciously

addressed, thus leading to the implementation of the extended site-binding model (Hamacek et al., 2005a,b), which was expanded during the following years (Hamacek and Piguet, 2006; Hamacek et al., 2006; Piguet, 2010; Steed and Atwood, 2009). Some deviations from statistical binding rapidly emerged, but clear-cut concepts rationalizing the different sources of cooperative effects brought by multivalency in supramolecular assembly only appeared in 2011 (Ercolani and Schiaffino, 2011). The manipulation of the EM proved to be attractive for controlling both selectivity and molecularities over large energy domains. Its common roots with the chelate effects should greatly help coordination chemists to exploit the EM for the design of sophisticated assemblies. On the other hand, the allosteric cooperativity produced by interligand ($\Delta E^{\mathbf{L},\mathbf{L}}$) and/or by intermetallic ($\Delta E^{\mathrm{M,M}}$) interactions in solution is currently underexploited because (i) of its limited magnitude (Babel et al., 2014) and (ii) of its counterintuitive correlation with classical coulombic trends (Fig. 32A, Dalla Favera et al., 2010). The use of Born–Haber thermodynamic cycles for rationalizing the reorganization of the multinuclear triple-stranded helicates $[\mathrm{Lu}_m(\mathbf{L19})_3]^{3m+}$ (Fig. 32B) shows that $\Delta E^{\mathrm{M,M}}$ indeed corresponds to a delicate balance between coulombic repulsion and favorable solvation effects (Eqs. 66–68 where $e$ is the elementary charge, $N_{\mathrm{Av}}$ is Avogadro number, and $\varepsilon_0$ is vacuum permittivity), which are either globally favorable $\left(\Delta E^{\mathrm{Lu,Lu}}_{1-3}\right)$ or unfavorable ($\Delta E^{\mathrm{Lu,Lu}}_{1-2}$ and $\Delta E^{\mathrm{Lu,Lu}}_{1-4}$, Fig. 32A, Riis-Johannessen et al., 2009).

$$\Delta E^{\mathrm{Lu,Lu}}_{1-2} = \frac{N_{\mathrm{Av}}9e^2}{4\pi\varepsilon_0} \cdot \frac{1}{d^{\mathrm{Lu,Lu}}_{1-2}} - 2\Delta_{\mathrm{solv}}G^0_{\mathrm{Lu}(\mathbf{L19})_3} + \Delta_{\mathrm{solv}}G^0_{\mathrm{Lu}_2(\mathbf{L19})_3} + 3\Delta_{\mathrm{solv}}G^0_{\mathbf{L19}}$$

(66)

$$\Delta E^{\mathrm{Lu,Lu}}_{1-3} = \frac{N_{\mathrm{Av}}9e^2}{4\pi\varepsilon_0\varepsilon_{\mathrm{r}}} \cdot \frac{1}{d^{\mathrm{Lu,Lu}}_{1-3}} - 2\Delta_{\mathrm{solv}}G^0_{\mathrm{Lu}_2(\mathbf{L19})_3} + \Delta_{\mathrm{solv}}G^0_{\mathrm{Lu}_3(\mathbf{L19})_3} + \Delta_{\mathrm{solv}}G^0_{\mathrm{Lu}(\mathbf{L19})_3}$$

(67)

$$\Delta E^{\mathrm{Lu,Lu}}_{1-4} = \frac{N_{\mathrm{Av}}9e^2}{4\pi\varepsilon_0\varepsilon_{\mathrm{r}}} \cdot \frac{1}{d^{\mathrm{Lu,Lu}}_{1-4}} - 2\Delta_{\mathrm{solv}}G^0_{\mathrm{Lu}_3(\mathbf{L19})_3} + \Delta_{\mathrm{solv}}G^0_{\mathrm{Lu}_4(\mathbf{L19})_3} + \Delta_{\mathrm{solv}}G^0_{\mathrm{Lu}_2(\mathbf{L19})_3}$$

(68)

Building on these results, attempts to modulate $\Delta E^{\mathrm{Ln,Ln}}$ in the related heterometallic complexes $[\mathrm{La}_{4-x}\mathrm{Lu}_x(\mathbf{L19})_3]^{12+}$ displayed deviations from statistics since the geminal heterometallic La···Lu interaction was found to be less repulsive than the average of the homometallic ones ($\Delta E^{\mathrm{La,Lu}}_{1-2} - \left(\Delta E^{\mathrm{La,La}}_{1-2} + \Delta E^{\mathrm{Lu,Lu}}_{1-2}\right)/2 = 2\ \mathrm{kJ/mol}$, Dalla Favera et al., 2007). Its amplification with an increasing number of metallic cations in the tetranuclear helicate favored the alternating filling of the binding sites to give LaLu-LaLu and LaLuLuLa as the most stable species for a $\mathbf{L19}$:$\mathrm{La}^{3+}$:$\mathrm{Lu}^{3+} = 3$:1:1 stoichiometric mixture in acetonitrile.
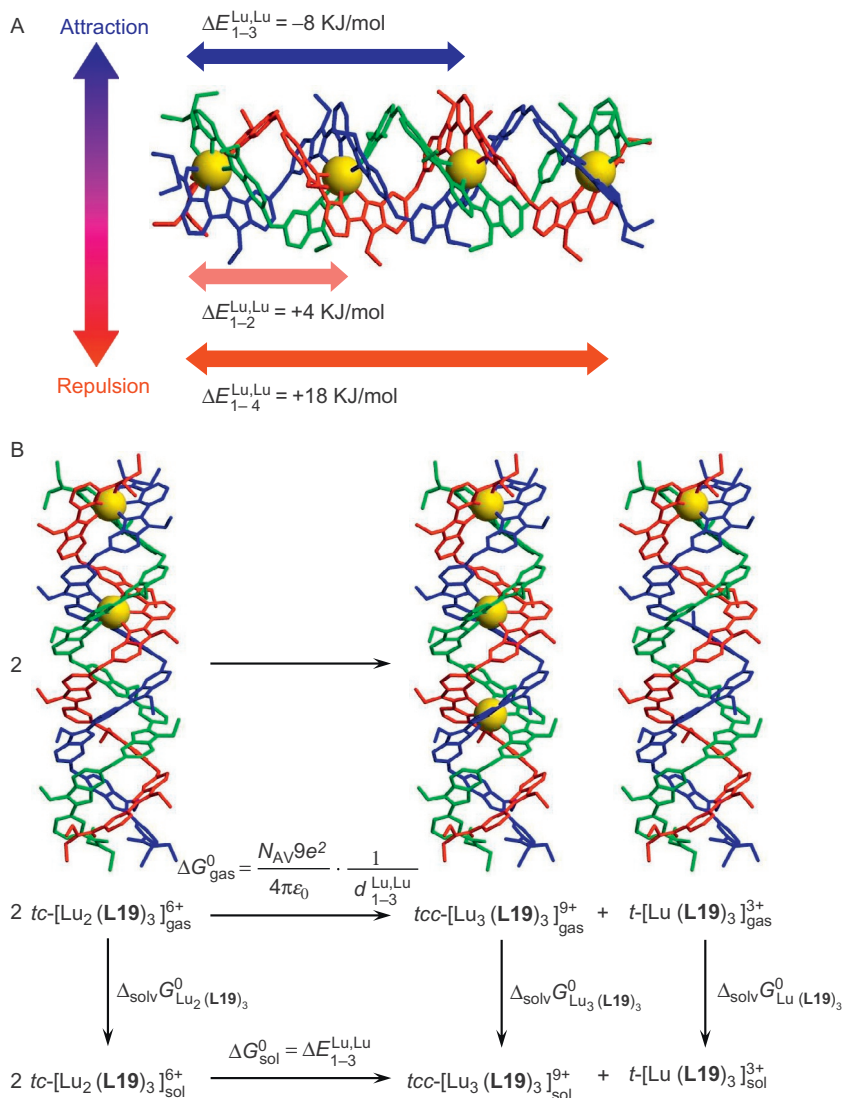
**FIGURE 32** (A) Intermetallic interactions $\Delta E^{Lu,Lu}$ measured for the tetranuclear helicate $[Lu_4(\mathbf{L19})_3]^{12+}$ in acetonitrile and (B) Born–Haber cycle highlighting the physical origin of $\Delta E^{Lu,Lu}_{1-3}$ (Riis-Johannessen et al., 2009).

As far as thermodynamics is concerned, the metallosupramolecular revolution successfully gathered together different aspects which were previously addressed separately. The concept of EM is indebted to polymer and material sciences, while allosteric cooperativity has deep roots in biochemistry and chelate effects is well known in coordination chemistry. Applied to lanthanide

coordination chemistry, the metallosupramolecular approach paves the way for the rational design of sophisticated discrete objects such as the helicates, wheels, and clusters. We also note that the minor energy differences produced by cooperativity in supramolecular assemblies have been exploited for preparing dynamic combinatorial libraries, in which several microspecies rapidly interconvert under thermodynamic equilibrium conditions (Albrecht, 2000; Cougnon and Sanders, 2012; Li et al., 2013; Smulders et al., 2013). The selection of one particular species via the introduction of a minor thermodynamic drift is reminiscent of the biological assembly of superstructures (Greig and Philp, 2001) and this concept is thought by Lehn (2015) as a major issue for the development of adaptive chemistry. Lanthanide coordination chemistry is currently not concerned by this perspective, but the kinetically fast exchange processes combined with the large variety of controllable cooperative effects which can be implemented are fully compatible with a possible evolution of the field along this line.

## ABBREVIATIONS

| | |
|---|---|
| $c^{\theta}$ | reference concentration of the standard state |
| **DFT** | density functional theory |
| **DOTA** | 1,4,7,10-tetraazacyclodoecane-1,4,7,10-tetraacetic acid |
| **DTPA** | diethylenetriaminopentaacetic acid |
| $E$ | elementary electrostatic charge |
| **EDTA** | 2,2′,2″,2‴-(ethane-1,2-diyldinitrilo)tetraacetic acid |
| **EM** | effective molarity |
| *fac* | facial |
| $k_{b}$ | Boltzmann's constant |
| *mer* | meridional |
| $N_{Av}$ | Avogadro number |
| **NTA** | 2,2′,2″-nitrilotriacetic acid |
| $R$ | ideal gas constant |
| $\varepsilon_{r}$ | relative permittivity or dielectric constant |
| $\varepsilon_{0}$ | vacuum permittivity |

## REFERENCES

Abegg, R., 1904. Die Valenz und das periodische System. Versuch einer Theorie der Molekular-verbindungen. Z. Anorg. Chem. 39, 330.

Aboshyan-Sorgho, L., Lathion, T., Guénée, L., Besnard, C., Piguet, C., 2014. Thermodynamic N-donor trans influence in labile pseudo-octahedral zinc complexes: a delusion? Inorg. Chem. 53, 13093.

Albrecht, M., 2000. From molecular diversity to template-directed self-assembly—new trends in metallosupramolecular chemistry. J. Incl. Phenom. Macrocycl. Chem. 36, 127.

Anderegg, G., 1960. Komplexone XXXII. Die 1: 2-Komplexe der Kationen der Seltenen Erden mit Nitrilotriacetat (NTE). Helv. Chim. Acta 43, 825.

Anderegg, G., Nägeli, P., Müller, F., Schwarzenbach, G., 1959. Komplexone XXX. Diathylentriamin-pentaessigsaure (DTPA). Helv. Chim. Acta 42, 827.

Arnaud-Neu, F., 1994. Solution chemistry of lanthanide macrocyclic complexes. Chem. Soc. Rev. 23, 235.

Atkins, P., De Paula, J., 2010. Physical Chemistry, ninth ed. Oxford University Press, Oxford. pp. 642–643.

Babel, L., Hoang, T.N.Y., Nozary, H., Salamanca, J., Guénée, L., Piguet, C., 2014. Lanthanide loading of luminescent multi-tridentate polymers under thermodynamic control. Inorg. Chem. 53, 3568.

Bailey, W.F., Monahan, A.S., 1978. Statistical effects and the evaluation of entropy differences in equilibrium processes. J. Chem. Educ. 55, 489.

Benson, S.W., 1958. Statistical factors in the correlation of rate constants and equilibrium constants. J. Am. Chem. Soc. 80, 5151.

Bianchi, A., Calabi, L., Corana, F., Fontana, S., Losi, P., Maiocchi, A., Paleari, L., Valtancoli, B., 2000. Thermodynamic and structural properties of Gd(III) complexes with polyamino-polycarboxylic ligands: basic compounds for the development of MRI contrast agents. Coord. Chem. Rev. 204, 309.

Billard, I., 2003. Lanthanide and actinide solution chemistry studied by time-resolved emission spectroscopy. In: Gschneidner Jr., K.A., Bünzli, J.-C.G., Pecharsky, V.K. (Eds.), Handbook on the Physics and Chemistry of Rare Earths, vol. 33. Elsevier B.V, pp. 465–514.

Binnemans, K., 2005. Rare earth beta-diketonates. In: Gschneidner Jr., K.A., Bünzli, J.-C.G., Pecharsky, V.K. (Eds.), In: Handbook on the Physics and Chemistry of Rare Earths, vol. 35. Elsevier B.V, pp. 107–272.

Bleaney, B.J., 1972. Nuclear magnetic resonance shifts in solution due to lanthanide ions. Magn. Reson. 8, 91.

Borkovec, M., Jönsson, B., Koper, G.J.M., 2001. Ionization processes and proton binding in polyprotic systems: small molecules, proteins, interfaces and polyelectrolytes. Colloid Surf. Sci. 16, 99.

Borkovec, M., Hamacek, J., Piguet, C., 2004. Statistical mechanical approach to competitive binding of metal ions to multi-center receptors. Dalton Trans. 4096–4105.

Borkovec, M., Koper, G.J.M., Piguet, C., 2006. Ion binding to polyelectrolytes. Curr. Opin. Colloid Interface Sci. 11, 280.

Bottrill, M., Kwok, L., Long, N.J., 2006. Lanthanides in magnetic resonance imaging. Chem. Soc. Rev. 35, 557.

Bünzli, J.-C.G., 1987. Complexes with synthetic ionophores. In: Gschneidner Jr., K.A., Eyring, L. (Eds.), Handbook on the Physics and Chemistry of Rare Earths, vol. 9. Elsevier Science B. V, pp. 321–394.

Bünzli, J.-C.G., Milicic-Tang, A., 1995. Solvation and anion interaction in organic solvents. In: Gschneidner Jr., K.A., Eyring, L. (Eds.), Handbook on the Physics and Chemistry of Rare Earths, vol. 21. Elsevier Science B. V, pp. 306–366.

Cacheris, W.P., Nickle, S.K., Sherry, A.D., 1987. Thermodynamic study of lanthanide complexes of 1,4,7-triazacyclononane-N, N′, N″-triacetic acid and 1,4,7,10-tetraazacyclododecane-N, N′, N″, N‴-tetraacetic acid. Inorg. Chem. 26, 958.

Calderone, C.T., Williams, D.H., 2001. An enthalpic component in cooperativity: the relationship between enthalpy, entropy and non-covalent structures in weak associations. J. Am. Chem. Soc. 123, 6262.

Campbell, D.L., Moeller, T., 1969. Observations on the rare earths MLXXXI formation constants of tropolone chelates of the tripositive ions at 25°. J. Inorg. Nucl. Chem. 31, 1077.

Canard, G., Koeller, S., Bernardinelli, G., Piguet, C., 2008. Effective concentration as a tool for quantitatively addressing preorganization in multicomponent assemblies: application to the selective complexation of lanthanide cations. J. Am. Chem. Soc. 130, 1025.

Caravan, P., Ellison, J.J., McMurry, T.J., Lauffer, R.B., 1999. Gadolinium(III) chelates as MRI contrast agents: structure, dynamics and applications. Chem. Rev. 99, 2293.

Carnall, W.T., 1979. The absorption and fluorescence spectra of rare earth ions in solution. In: Gschneidner Jr., K.A., Eyring, L. (Eds.), Handbook on the Physics and Chemistry of Rare Earths, vol. 3. North-Holland Publishing Company, pp. 81–109. Chapter 24.

Castellano, B.M., Eggers, D.K., 2013. Experimental support for a desolvation energy term in governing equations for binding equilibria. J. Phys. Chem. B 117, 8180.

Choppin, G.R., 1989. Chemical properties of the rare earth elements. In: Bünzli, J.-C.G., Choppin, G.R. (Eds.), Lanthanide Probes in Life, Chemical and Earth Science. Elsevier, Amsterdam, pp. 1–42.

Choppin, G.R., Rizkalla, E.N., 1994. Solution chemistry of actinides and lanthanides. In: Gschneidner Jr., K.A., Eyring, L., Choppin, G.R., Lander, G.H. (Eds.), Handbook on the Physics and Chemistry of Rare Earths, vol. 18. Elsevier Science B.V, pp. 559–589. Chapter 128.

Ciupka, J., Cao-Dolg, X., Wiebke, J., Dolg, M., 2010. Computational study of lanthanide(III) hydration. Phys. Chem. Chem. Phys. 12, 13215.

Clark, M.E., Bear, J.L., 1969. Some lanthanide ion enthalpies of transfer from water to dimethyl-sulfoxide. J. Inorg. Nucl. Chem. 31, 2619.

Comby, S., Bünzli, J.-C.G., 2007. Lanthanide near-infrared luminescence in molecular probes and devices. In: Gschneidner Jr., K.A., Bünzli, J.-C.G., Pecharsky, V.K. (Eds.), Handbook on the Physics and Chemistry of Rare Earths, vol. 37. Elsevier Science B. V, pp. 217–470. Chapter 235.

Constable, E.C., Housecroft, C.E., 2013. Coordination chemistry: the scientific legacy of Alfred Werner. Chem. Soc. Rev. 42, 1429.

Cougnon, F.B.L., Sanders, J.K.M., 2012. Evolution of dynamic combinatorial chemistry. Acc. Chem. Res. 45, 2211.

D'Angelo, P., Spezia, R., 2012. Hydration of lanthanoids(III) and actinoids(III). An experimental/theoretical saga. Chem. Eur. J. 18, 11162.

Dalla Favera, N., Hamacek, J., Borkovec, M., Jeannerat, D., Ercolani, G., Piguet, C., 2007. Tuneable intramolecular intermetallic interactions as a new tool for programming linear heterometallic 4f-4f complexes. Inorg. Chem. 46, 9312.

Dalla Favera, N., Kiehne, U., Bunzen, J., Hyteballe, S., Lützen, A., Piguet, C., 2010. Intermetallic interactions within solvated polynuclear complexes: a misunderstood concept. Angew. Chem. Int. Ed. Engl. 49, 125.

David, F., Vokhim, V., Ionova, G., 2001. Water characteristics depend on the ionic environment. Thermodynamic and modelisation of the aquo ions. J. Mol. Liq. 90, 45.

Desreux, J.F., 1979. Complexing of lanthanides by macrocycles. Bull. Cl. Sci. Acad. Belg. 64, 814.

Di Bernardo, P., Melchior, A., Tolazzi, M., Zanonato, P.L., 2012. Thermodynamics of lanthanide(III) complexation in non-aqueous solvents. Coord. Chem. Rev. 256, 328.

dos Santos, C.M.G., Harte, A.J., Quinn, S.J., Gunnlaugsson, T., 2008. Recent development in the field of supramolecular lanthanide luminescent sensors and self-assemblies. Coord. Chem. Rev. 252, 2512.

Drew, M.G.B., Hill, C., Hudson, M.J., Iveson, P.B., Madic, C., Youngs, T.G.A., 2004. Solvent extraction and lanthanide complexation studies with new terdentate ligands containing two 1,3,5-triazine moieties. Dalton Trans. 244.

Dutronc, T., Terazzi, E., Piguet, C., 2014. Melting temperatures deduced from molar volumes: a consequence of enthalpy-entropy compensation with linear cohesive free-energy densities. RSC Adv. 4, 15740.

Einstein, A., 1907. Die Plancksche Theorie der Strahlung und die Theorie der spezifischen Wärme. Ann. Phys. 22, 180.

Ercolani, G., 2003. Assessment of cooperativity in self-assembly. J. Am. Chem. Soc. 125, 16097.

Ercolani, G., Schiaffino, L., 2011. Allosteric, chelate, and intermolecular cooperativity: a mise au point. Angew. Chem. Int. Ed. Engl. 50, 1762.

Ercolani, G., Piguet, C., Borkovec, M., Hamacek, J., 2007. Symmetry numbers and statistical factors in self-assembly and multivalency. J. Phys. Chem. B 111, 12195.

Escande, A., Guénée, L., Buchwalder, K.-L., Piguet, C., 2009. Complexation of trivalent lanthanides with planar tridentate aromatic ligands tuned by counteranions and steric constraints. Inorg. Chem. 48, 1132.

Evans, W.J., 2007. The importance of questioning scientific assumptions: some lessons from f element chemistry. Inorg. Chem. 46, 3435.

Feltham, H.L.C., Brooker, S., 2014. Review of purely 4f and mixed-metal nd-4f single-molecule magnets containing only one lanthanide ion. Coord. Chem. Rev. 276, 1.

Figgis, B.M., Hitchman, M.A., 2000. Ligand Field Theory and Its Applications. Wiley-VCH, New York.

Ford, D.M., 2005a. Probing the origins of linear free energy relationships with molecular theory and simulation. Adsorption 11, 271.

Ford, D.M., 2005b. Enthalpy-entropy compensation is not a general feature of weak association. J. Am. Chem. Soc. 127, 16167.

Forsberg, J.H., 1996. NMR studies of paramagnetic lanthanide complexes and shift reagents. In: Gschneidner Jr., K.A., Eyring, L. (Eds.), Handbook on the Physics and Chemistry of Rare Earths, vol. 23. Elsevier Science B. V, pp. 1–68.

Gadolin, J., 1794. Undersökning af en svart tung Stenart ifran Ytterby Stenbrott I Roslagen. Kong. Svensk. Vetenskap. Acad. Handl. 15, 137.

Gomer, R., Tryson, G., 1977. An experimental determination of absolute half-cell emf's and single ion free energies of solvation. J. Chem. Phys. 66, 4413.

Greig, L.M., Philp, D., 2001. Applying biological principles to the assembly and selection of synthetic superstructures. Chem. Soc. Rev. 30, 287.

Grenthe, I., 1961. Stability relationships among the rare earth dipicolinates. J. Am. Chem. Soc. 83, 360.

Hamacek, J., Piguet, C., 2006. How to adapt Scatchard plot for graphically addressing cooperativity in multicomponent self-assemblies. J. Phys. Chem. B 110, 7783.

Hamacek, J., Borkovec, M., Piguet, C., 2005a. A simple thermodynamic model for quantitatively addressing cooperativity in multicomponent self-assembly processes-Part 1: theoretical concepts and application to monometallic coordination complexes and bimetallic helicates possessing identical binding sites. Chem. Eur. J. 11, 5217.

Hamacek, J., Borkovec, M., Piguet, C., 2005b. A simple thermodynamic model for quantitatively addressing cooperativity in multicomponent self-assembly processes-Part 2: extension to multimetallic helicates possessing different binding sites. Chem. Eur. J. 11, 5227.

Hamacek, J., Borkovec, M., Piguet, C., 2006. Simple thermodynamics for unravelling sophisticated self-assembly processes. Dalton Trans. 1473.

Hamacek, J., Bernardinelli, G., Filinchuk, Y., 2008. Tetrahedral assembly with lanthanides: toward discrete polynuclear complexes. Eur. J. Inorg. Chem. 3419.

Harder, R., Chaberek, S., 1959. Interaction of rare earth ions with diethylenetriaminepentaacetic acid. J. Inorg. Nucl. Chem. 11, 197.

Helm, L., 2006. Relaxivity in paramagnetic systems: theory and mechanisms. Prog. Nucl. Magn. Reson. Spectrosc. 49, 45.

Helm, L., Merbach, A.E., 2005. Inorganic and bioinorganic solvent exchange mechanisms. Chem. Rev. 105, 1923.

Helmholz, L., 1939. The crystal structure of neodymium bromate enneahydrate, $Nd(BrO_3)_3 \cdot 9H_2O$. J. Am. Chem. Soc. 61, 1544.

Hisinger, W., Berzelius, J.J., 1804. Cerium, ein neues Metall aus einer Schwedischen Steinart Bastnaes Tungstein genannt. Gehlens J. Chem. 2, 355.

Hoard, J.L., Lee, B., Lind, M.D., 1965. On the structure-dependent behavior of ethylenediaminetetraacetato complexes of the rare earth $Ln^{3+}$ ions. J. Am. Chem. Soc. 87, 1612.

Huang, C. (Ed.), 2010. Rare Earth Coordination Chemistry, Fundamentals and Applications. John Wiley & Sons, Singapore.

Hulet, E.K., Bodé, D.D., 1972. Separation chemistry of the lanthanides and transplutonium actinides. In: Bagnall, K.W. (Ed.), Inorganic Chemistry Series One, vol. 7. Butterworths, London, pp. 1–45.

Hunter, C.A., Anderson, H.L., 2009. What is cooperativity? Angew. Chem. Int. Ed. Engl. 48, 7488.

Ishiguro, S., Umebayashi, Y., Komiya, M., 2002. Thermodynamic and structural aspects on the solvation steric effect of lanthanide(III)—dependence on the ionic size. Coord. Chem. Rev. 226, 103.

Ishikawa, N., Sugita, M., Ishikawa, T., Koshihara, S.-Y., Kaizu, Y., 2003. Lanthanide double-decker complexes functioning as magnets at the single-molecular level. J. Am. Chem. Soc. 125, 8694.

Jacobson, H., Stockmayer, W.H., 1950. Intramolecular reaction in polycondensations. I. The theory of linear systems. J. Chem. Phys. 18, 1600.

Jencks, W.P., 1981. On the attribution and additivity of binding energies. Proc. Natl. Acad. Sci. U.S.A. 78, 4046.

Jensen, T.B., Terazzi, E., Buchwalder, K., Guénée, L., Nozary, H., Schenk, K., Heinrich, B., Donnio, B., Guillon, D., Piguet, C., 2010. Dimerization of dendrimeric lanthanide complexes: thermodynamic, thermal and liquid-crystalline properties. Inorg. Chem. 49, 8601.

Johnson, D.A., 1982. Some Thermodynamic Aspects of Inorganic Chemistry, second ed. Cambridge University Press, Cambridge London New York New Rochelle Melbourne Sydney.

Jørgensen, C.K., 1973. The inner mechanism of rare earths elucidated by photo-electron spectra. In: Dunitz, J.D., Hemmerich, P., Ibers, J.A., Jorgensen, C.K., Neilands, J., Nyholm, R.S., Reinen, D., Williams, R.J.P. (Eds.), In: Structure and Bonding, vol. 13. Springer, Berlin, pp. 199–253.

Jørgensen, C.K., 1979. Theoretical chemistry of rare earths. In: Gschneidner Jr., K.A., Eyring, L. (Eds.), Handbook on the Physics and Chemistry of Rare Earths, vol. 3. North-Holland Publishing Company, pp. 111–170. Chapter 23.

Katakura, R., Koide, Y., 2006. Configuration-specific synthesis of the facial and meridional isomers of tris(8-hydroxyquinolinate)aluminum (Alq3). Inorg. Chem. 45, 5730.

Ketelaar, J.A.A., 1937. The crystal structure of the ethyl sulphates of the rare earths and yttrium. Physica 4, 619.

Khalili, F.I., Choppin, G.R., Rizkalla, E.N., 1988. The nature of U(VI) complexation by halates and chloroacetates. Inorg. Chim. Acta 143, 131.

Klaproth, H.M., 1804. Chemische Untersuchung des Ochroïts. Gehlens J. Chem. 2, 303.

Kolarik, Z., 2008. Complexation and separation of lanthanide(III) and actinides(III) by heterocyclic N-donors in solutions. Chem. Rev. 108, 4208.

Koper, G.J.M., Borkovec, M., 2001. Binding of metal ions to polyelectrolytes and their oligomeric counterparts: an application of a generalized Potts model. J. Phys. Chem. B 105, 6666.

Koper, G.J.M., Borkovec, M., 2010. Proton binding by linear, branched, and hyperbranched polyelectrolytes. Polymer 51, 5649.

Kremer, C., Torres, J., Dominguez, S., Mederos, A., 2005. Structure and thermodynamic stability of lanthanide complexes with amino acids and peptides. Coord. Chem. Rev. 249, 567.

Kuhn, W., 1934. The shape of fibrous molecules in solutions. Kolloid Z. 68, 2.

Kumar, A., 1992. A modified Born equation for solvation energy of ions. J. Phys. Soc. Jpn. 61, 4247.

Kuta, J., Clark, A.E., 2010. Trends in aqueous hydration across the 4f period assessed by reliable computational methods. Inorg. Chem. 49, 7808.

Le Borgne, T., Altmann, P., André, N., Bünzli, J.-C.G., Bernardinelli, G., Morgantini, P.-Y., Weber, J., Piguet, C., 2004. Tuning facial-meridional isomerisation in monometallic nine-coordinate lanthanide complexes with unsymmetrical tridentate ligands. Dalton Trans. 723.

Leffler, J.E., 1955. The enthalpy-entropy relationship and its implication for organic chemistry. J. Org. Chem. 20, 1202.

Lehn, J.-M., 1995. Supramolecular Chemistry, Concepts and Perspectives. VCH, Weinheim.

Lehn, J.-M., 2015. Perspectives in chemistry—aspects of adaptative chemistry and materials. Angew. Chem. Int. Ed. Engl. 54, 3276.

Lehn, J.-M., Eliseev, A.V., 2001. Dynamic combinatorial chemistry. Science 291, 2331.

Lemonnier, J.-F., Guénée, L., Bernardinelli, G., Vigier, J.-F., Bocquet, B., Piguet, C., 2010. Planned failure from the principle of maximum site occupancy in lanthanide helicates. Inorg. Chem. 49, 1252.

Leung, D.H., Bergman, R.G., Raymond, K.N., 2008. Enthalpy-entropy compensation reveals solvent reorganization as a driving force for supramolecular encapsulation in water. J. Am. Chem. Soc. 130, 2798.

Lewis, G.N., 1916. The atom and the molecule. J. Am. Chem. Soc. 38, 762.

Li, J., Nowak, P., Sijbren, O., 2013. Dynamic combinatorial libraries: from exploring molecular recognition to systems chemistry. J. Am. Chem. Soc. 135, 9222.

Lin, S.-K., 1996. Correlation of entropy with similarity and symmetry. J. Chem. Inf. Comput. Sci. 36, 367.

Lind, M.D., Lee, B., Hoard, J.L., 1965. Structure and bonding in a ten-coordinate lanthanum(III) chelate of ethylenediaminetetraacetic acid. J. Am. Chem. Soc. 87, 1611.

Lindemann, F.A., 1910. The calculation of molecular vibration frequencies. Physik. Z. 11, 609.

Liu, Y., Han, B.-H., Chen, Y.-T., 2000. The complexation thermodynamics of light lanthanides by crow ethers. Coord. Chem. Rev. 200–202, 53.

Lowe, M.P., Caravan, P., Rettig, S.J., Orvig, C., 1998. Tightening the hydrophobic belt: effects of backbone and donor group variation on podand ligand complexes of the lanthanides. Inorg. Chem. 37, 1637.

Luo, H.B., Sharp, K., 2002. On the calculation of absolute macromolecular binding free energies. Proc. Natl. Acad. Sci. U.S.A. 99, 10399.

MacDonald, M.R., Bates, J.E., Ziller, J.W., Furche, F., Evans, W.J., 2013. Completing the series of +2 ions for the lanthanide elements: synthesis of molecular complexes of Pr(II), Gd(II), Tb(II) and Lu(II). J. Am. Chem. Soc. 135, 9857.

Mammen, M., Choi, S.-K., Whitesides, G.M., 1998. Polyvalent interactions in biological systems: implication for design and use of multivalent ligands and inhibitors. Angew. Chem. Int. Ed. Engl. 37, 2754.

Mandolini, L., 1986. Intramolecular reactions of chain molecules. Adv. Phys. Org. Chem. 22, 1.

Marcus, Y., 1994. A simple empirical model describing the thermodynamics of hydration of ions of widely varying charges, sizes, and shapes. Biophys. Chem. 51, 111.

Martell, A.E., 1966. The chelate effect. Adv. Chem. Ser. 62, 272.

Martell, A.E., Smith, R.M., 1989. Critical Stability Constants. Plenum Press, New York, London.

Martin, N., Bünzli, J.-C.G., McKee, V., Piguet, C., Hopfgartner, G., 1998. Self-assembled dinuclear helicates: substantial luminescence enhancement upon replacing terminal benzimidazole groups by carboxamide binding units. Inorg. Chem. 37, 577.

Matyushov, D.V., 2004. Dipole solvation in dielectrics. J. Chem. Phys. 120, 1375.

Mironov, V.S., Galyametdinov, Y.G., Ceulemans, A., Görller-Walrand, C., Binnemans, K., 2001. Influence of crystal-field perturbation on the room-temperature magnetic anisotropy of lanthanide complexes. Chem. Phys. Let. 345, 132.

Moeller, T., 1963. The Chemistry of the Lanthanides. Reinhold, New York.

Moeller, T., 1967. Coordination chemistry of the lanthanide elements—one hundred years of development and understanding. In: Kaufmann, G. (Ed.), Werner CentennialAmerican Chemical Society, Washington, p. 306.

Morss, L.R., 1971. Thermochemistry of some chlorocomplex compounds of the rare earths. Third ionization potentials and hydration enthalpies of the trivalent ions. J. Phys. Chem. 75, 392.

Mosander, G.C., 1839. Lanthan ein neues metal. Pogg. Ann. 46, 648, and 47, 207.

Moseley, P.T., 1975. Aspects of the structural chemistry of lanthanides and actinide compounds. In: Bagnall, K.W. (Ed.), MTP International Review of Science Series 2, vol. 7. 65.

Motekaitis, R.J., Martell, A.E., Hancock, R.D., 1994. Factors affecting stabilities of chelate, macrocyclic and macrobicyclic complexes in solution. Coord. Chem. Rev. 133, 39.

Mulder, A., Huskens, J., Reinhoudt, D.N., 2004. Multivalency in supramolecular chemistry and nanofabrication. Org. Biomol. Chem. 2, 3409.

Munro, D., 1977. Misunderstandings over the chelate effect. Chem. Brit. 13, 100.

Murakami, W., Eda, K., Yamamoto, M., Osakai, T., 2014. A non-Bornian analysis of the Gibbs energy of ion hydration. Bull. Chem. Soc. Jpn. 87, 403.

Nash, K.L., 1994. Separation chemistry for lanthanides and trivalent actinides. In: Gschneidner Jr., K.A., Eyring, L., Choppin, G.R., Lander, G.H. (Eds.), Handbook on the Physics and Chemistry of Rare Earths, vol. 18. Elsevier Science B.V, pp. 559–589.

Negri, R., Baranyai, Z., Tei, L., Giovenzana, G.B., Platas-Iglesias, C., Benyei, A.C., Bodnar, J., Vagner, A., Botta, M., 2014. Lower denticity leading to higher stability: structural and solution studies of Ln(III)-OBETA complexes. Inorg. Chem. 53, 12499.

Nief, F., 2010. Molecular chemistry of the rare-earth elements in uncommon low-valent states. In: Gschneidner Jr., K.A., Bünzli, J.-C.G., Pecharsky, V.K. (Eds.), Handbook on the Physics and Chemistry of Rare Earths, vol. 40. Elsevier Science B. V, pp. 241–300. Chapter 247.

Onsager, L., 1936. Electric moments of molecules in liquids. J. Am. Chem. Soc. 58, 1486.

Orbach, R., Stapleton, H.J., 1972. Electron-spin lattice relaxation. In: Geschwind, S. (Ed.), Electron Paramagnetic Resonance. Plenum Press, New York, pp. 112–216.

Panak, P.J., Geist, A., 2013. Complexation and extraction of trivalent actinides and lanthanides by triazinylpyridine N-donor ligands. Chem. Rev. 113, 1199.

Peters, J.A., Huskens, J., Raber, D.J., 1996. Lanthanide induced shifts and relaxation rate enhancements. Prog. NMR Spectrosc. 28, 283.

Petit, L., Daul, C., Adamo, C., Maldivi, P., 2007. DFT modeling of the relative affinity of nitrogen ligand for trivalent f elements: an energetic point of view. New J. Chem. 31, 1738.

Pfeil, A., Lehn, J.-M., 1992. Helicate self-organisation: positive cooperativity in the self-assembly of double-helical metal complexes. J. Chem. Soc. Chem. Commun. 838.

Piguet, C., 2010. Five thermodynamic describers for addressing serendipity in the self-assembly of polynuclear complexes in solution. Chem. Commun. 46, 6209.

Piguet, C., 2011. Enthalpy-entropy correlations as chemical guides to unravel self-assembly processes. Dalton Trans. 40, 8059.

Piguet, C., Bünzli, J.-C.G., 2010. Self-assembled lanthanide helicates: from basic thermodynamics to applications. In: Gschneidner Jr., K.A., Bünzli, J.-C.G., Pecharsky, V.K. (Eds.), Handbook on the Physics and Chemistry of Rare Earths, vol. 40. Elsevier Science B. V, pp. 301–553. Chapter 247.

Piguet, C., Geraldes, C.F.G.C., 2003. Paramagnetic NMR lanthanide induced shifts for extracting solution structures. In: Gschneidner Jr., K.A., Bünzli, J.-C.G., Pecharsky, V.K. (Eds.), Handbook on the Physics and Chemistry of Rare Earths, vol. 33. Elsevier Science B. V, pp. 353–464. Chapter 215.

Piguet, C., Bünzli, J.-C.G., Bernardinelli, G., Hopfgartner, G., Williams, A.F., 1993. Self-assembly and photophysical properties of lanthanide dinuclear triple-helical complexes. J. Am. Chem. Soc. 115, 8197.

Powell, J.E., 1979. Separation chemistry. In: Gschneidner Jr., K.A., Eyring, L. (Eds.), Handbook on the Physics and Chemistry of Rare Earths, vol. 3. North-Holland Publishing Company, pp. 81–109. Chapter 22.

Price, E.W., Zeglis, B.M., Cawthray, J.F., Lewis, J.S., Adam, M.J., Orvig, C., 2014. What a difference a carbon makes: H4octapa versus H4C3octapa ligands for In-111 and Lu-177 radiochemistry. Inorg. Chem. 53, 10412.

Renaud, F., Piguet, C., Bernardinelli, G., Bünzli, J.-C.G., Hopfgartner, G., 1997. In search for mononuclear helical lanthanide building blocks with predetermined properties: triple-stranded helical complexes with N, N, N′, N′-tetraethylpyridine-2,6-dicarboxamide. Chem. Eur. J. 3, 1646.

Reuben, J., 1979. Bioinorganic chemistry: lanthanides as probes in systems of biological interest. In: Gschneidner Jr., K.A., Eyring, L. (Eds.), Handbook on the Physics and Chemistry of Rare Earths, vol. 4. North-Holland Publishing Company, pp. 515–552. Chapter 39.

Reuben, J., Elgavish, G.A., 1979. Shift reagents and NMR paramagnetic lanthanide complexes. In: Gschneidner Jr., K.A., Eyring, L. (Eds.), Handbook on the Physics and Chemistry of Rare Earths, vol. 4. North-Holland Publishing Company, pp. 483–514. Chapter 38.

Richens, D.T., 2005. Ligand substitution reactions at inorganic centers. Chem. Rev. 105, 1961.

Riis-Johannessen, T., Dalla Favera, N., Todorova, T.K., Huber, S.M., Gagliardi, L., Piguet, C., 2009. Understanding, controlling and programming cooperativity in self-assembled polynuclear complexes in solution. Chem. Eur. J. 15, 12702.

Rinehart, J.D., Long, J.R., 2011. Exploiting single-ion anisotropy in the design of f-element single-molecule magnets. Chem. Sci. 2, 2078.

Rizkalla, E.N., Choppin, G.R., 1991. Hydration and hydrolysis of lanthanides. In: Gschneidner Jr., K.A., Eyring, L. (Eds.), Handbook on the Physics and Chemistry of Rare Earths, vol. 15. Elsevier Science Publishers, pp. 393–442.

Rizkalla, E.N., Choppin, G.R., 1994. Lanthanides and actinides hydration and hydrolysis. In: Gschneidner Jr., K.A., Eyring, L., Choppin, G.R., Lander, G.H. (Eds.), Handbook on the Physics and Chemistry of Rare Earths, vol. 18. Elsevier Science B.V, pp. 529–558. Chapter 127.

Rogers, D.W., 2005. Einstein's Other Theory, the Plank-Bose-Einstein Theory of Heat Capacity. Princeton University Press, Princeton, NJ.

Ryan, P.E., Guénée, L., Canard, G., Gumy, F., Bünzli, J.-C.G., Piguet, C., 2009. Structural, spectroscopic, and thermodynamic consequences of anti-chelate effect in nine-coordinate lanthanide podates. Inorg. Chem. 48, 2549.

Ryan, P.E., Canard, G., Koeller, S., Bocquet, B., Piguet, C., 2012. Allosteric effects in binuclear homo- and heterometallic triple-stranded lanthanide podates. Inorg. Chem. 51, 10012.

Ryan, P.E., Guénée, L., Piguet, C., 2013. Monitoring helical twists and effective molarities in dinuclear triple-stranded lanthanide helicates. Dalton Trans. 42, 11047.

Sabbatini, N., Guardigli, M., Manet, I., 1996. Antenna effect in encapsulation complexes of lanthanide ions. In: Gschneidner Jr., K.A., Eyring, L. (Eds.), Handbook on the Physics and Chemistry of Rare Earths, vol. 23. Elsevier Science B. V, pp. 69–119.

Saez Puche, R., Caro, P.A. (Eds.), 1998. Rare Earths. Editorial Complutense, Madrid.

Sastri, V.S., Bünzli, J.-C.G., Ramachandra Rao, V., Rayudu, G.V.S., Perumareddi, J.R., 2003. Modern Aspects of Rare Earths and Their Complexes. Elsevier B. V, Amsterdam.

Schumann, H., Genthe, W., 1984. Organometallic compounds of the rare earths. In: Gschneidner Jr., K.A., Eyring, L. (Eds.), Handbook on the Physics and Chemistry of Rare Earths, vol. 7. Elsevier Science Publishers B. V, pp. 445–571.

Schwarzenbach, G., 1952. Der Chelateffeckt. Helv. Chim. Acta 35, 39.

Schwarzenbach, G., 1957. Complexometric Titrations. Chapman & Hall, London.

Searle, M.S., Westwell, M.S., Williams, D.H., 1995. Application of a generalized enthalpy/entropy relationship to binding cooperativity and weak associations in solution. J. Chem. Soc. Perkin Trans. 2, 141–151.

Sharp, R.R., 2001. Paramagnetic NMR. Nucl. Magn. Res. 30, 477.

Smulders, M.M.J., Riddell, I.A., Browne, C., Nitschke, J.R., 2013. Building on architectural principles for three-dimensional metallosupramolecular construction. Chem. Soc. Rev. 42, 1728.

Sorace, L., Benelli, C., Gatteschi, D., 2011. Lanthanides in molecular magnetism: old tools in a new field. Chem. Soc. Rev. 40, 3092.

Starikov, E.B., 2013. Valid entropy-enthalpy compensation: its true physical-chemical meaning. J. Appl. Sol. Chem. Model. 2, 240.

Starikov, E.B., Norden, B., 2007. Enthalpy-entropy compensation: a phantom of something useful? J. Phys. Chem. B 111, 14431.

Steed, J.W., Atwood, J.L., 2009. Supramolecular Chemistry. John Wiley & Sons Ltd., Chichester. pp. 604–619.

Szabadvary, F., 1988. The history and the discovery and separation of the rare earths. In: Gschneidner Jr., K.A., Eyring, L. (Eds.), Handbook on the Physics and Chemistry of Rare Earths, vol. 11. Elsevier Science Publishers, pp. 33–80. Chapter 73.

Terazzi, E., Guénée, L., Bocquet, B., Lemonnier, J.-F., Dalla Favera, N., Piguet, C., 2009. A simple chemical tuning of the effective concentration: selection of single-, double-, and triple-stranded binuclear lanthanide helicates. Chem. Eur. J. 15, 12719.

Terreno, E., Delli Castelli, D., Viale, A., Aime, S., 2010. Challenges for molecular magnetic resonance imaging. Chem. Rev. 110, 3019.

Thompson, L.C., 1979. Complexes. In: Gschneidner Jr., K.A., Eyring, L. (Eds.), Handbook on the Physics and Chemistry of Rare Earths, Vol. 3. North-Holland Publishing Company, pp. 209–297.

Urbain, G., 1896. Contribution à l'étude du thorium. Bull. Soc. Chim. Paris 15, 347.

Weeks, M.E., 1960. Discovery of the Elements, sixth ed. Journal of Chemical Education Press, Easton, PA.

Werner, A., 1893. Beitrag zur Konstitution anorganischer Verbindungen. Z. Anorg. Chem. 3, 267.

Werner, A., Vilmos, A., 1899. Beitrag zur Konstitution anorganischer Verbindungen. XVII. Mitteilung. Über Oxalatodiäthylendiaminkobaltisalze. Z. Anorg. Chem. 21, 45.

Wheelwright, E.J., Spedding, F.H., Scharzenbach, G., 1953. The stability of the rare earth complexes with ethylenediaminetetraacetic acid. J. Am. Chem. Soc. 75, 4196.

Williams, D.H., Searle, M.S., Mackay, J.P., Gerhard, U., Maplestone, R.A., 1993. Toward an estimation of binding constants in aqueous solution: studies of associations of vancomycin group antibiotics. Proc. Natl. Acad. Sci. U.S.A. 90, 1172.

Williams, D.H., Stephens, E., O'Brien, D.P., Zhou, M., 2004. Understanding noncovalent interactions: ligand binding energy and catalytic efficiency from ligand-induced reductions in motion within receptors and enzymes. Angew. Chem. Int. Ed. Engl. 43, 6596.

Winpenny, R.E.P., 1998. The structure and magnetic properties of complexes containing 3d- and 4f-metals. Chem. Soc. Rev. 27, 447.

Woodruff, D.N., Winpenny, R.E.P., Layfield, R.A., 2013. Lanthanide single-molecule magnets. Chem. Rev. 113, 5110.

Yatsimirskii, K.B., Kostromina, N.A., 1964. Effect of the ligand field on the properties of compounds of rare earth elements. Zh. Neorg. Khim. 9, 1793.

Zaïm, A., Dalla Favera, N., Guénée, L., Nozary, H., Hoang, T.N.Y., Eliseeva, S.V., Petoud, S., Piguet, C., 2013. Lanthanide hexafluoroacetylacetonate vs nitrates for the controlled loading of luminescent polynuclear single-stranded oligomers. Chem. Sci. 4, 1125.

Zheng, Z., 2001. Ligand-controlled self-assembly of polynuclear lanthanide-oxo/hydroxo complexes: from synthetic serendipity to rational supramolecular design. Chem. Commun, 2521.

Chapter 273

# Near-IR Triggered Photon Upconversion: Imaging, Detection, and Therapy

**Diana C. Rodriguez Burbano\***, **Rafik Naccache**[†]
and **John A. Capobianco\***

*Department of Chemistry and Biochemistry and Centre for NanoScience Research, Concordia University, Montreal, Quebec, Canada*
[†]*Institut National de la Recherche Scientifique—Énergie, Matériaux et Télécommunications, Université du Québec, Varennes, Quebec, Canada*

## Chapter Outline

## 1 INTRODUCTION

Fluorescent probes are classically defined as molecules, which emit a specific spectroscopic response following stimulus with irradiation of a specific wavelength of light. In recent years, this definition has been expanded to include nanomaterials and nanoparticles that can serve the same role. The aim of the fluorescent probe is to detect a specific target, which is typically quantified by photometry, or qualitatively visualized through microscopy (Johnson, 1998). Although organisms are known to contain endogenous fluorophores, such as NADH, flavins, and porphyrins to name but a few (Brandes and

**273**

Bers, 1996), they are not necessarily ideal for most situations. In fact, the potential of detection or imaging of any given method is, to a great extent, determined by the physicochemical properties of the fluorophore used (Waggoner, 2006). Thus, the design, synthesis, and application of exogenous fluorescent probes have become a research area that has garnered significant interest in the past few decades.

In the design and selection of exogenous fluorescent probes, several criteria must be addressed, particularly taking biological systems and related applications into consideration (Johnson, 1998; Resch-Genger et al., 2008):

- *Delivery*: the probe has to be biocompatible in chemical nature and size with the target and must be dispersible and stable in buffers, cell culture media, and bodily fluids. It must also be introduced without damaging the structural and physiological conditions of the target or harming its integrity.
- *Targeting*: the probe must interact selectively with the targeted entity; therefore, it is required to possess functional groups for site-specific labeling allowing for the discrimination of the region of interest versus the surrounding environment.
- *Detectability*: the probe must be conveniently excitable, without simultaneous excitation of the biological matrix, which would otherwise induce autofluorescence. It must also be detectable with conventional instrumentation.
- *Fluorescence response*: the emission of the probe must possess a high molar absorption coefficient at the excitation wavelength and a high fluorescence quantum yield. Interaction with the target must be detectable either by imaging or via a spectroscopic response, such as a fluorescence intensity change or a spectral shift.

There exists a number of fluorescent probes that offer nanometer scale resolution and which can address some or most of the requirements outlined above. We discuss these fluorescent probes in detail in the next section.

## 1.1 Luminescent Probes

### 1.1.1 Organic Fluorophores

Organic fluorophores are molecules that absorb light of a specific wavelength and emit light of a different, typically longer, wavelength (a process known as fluorescence). Examples of organic fluorophores are:

- Molecular systems with a defined chemical structure such as small organic dyes including rhodamine, fluorescein, and indocyanine green (Waggoner, 2006; Zhang et al., 2002)
- Fluorophores of biological origin like phycobiliproteins and genetically encoded fluorescent proteins (Shaner et al., 2005)

The optical properties of the organic fluorophores such as the organic dyes depend on the electronic transitions involved (Table 1; Resch-Genger et al.,

**TABLE 1** Comparison of the Optical Properties of Organic Dyes and QDs

| Property | Organic Dyes | QDs[a] |
|---|---|---|
| Absorption spectra | Discrete bands, FWHM[b] 35 nm[c] to 80–100 nm[d] | Steady increase toward UV wavelengths starting from absorption onset; enables free selection of excitation wavelength |
| Molar absorption coefficient | $2.5 \times 10^4$–$2.5 \times 10^5$ $M^{-1}$ $cm^{-1}$ (at long wavelength absorption maximum) | $10^5$–$10^6$ $M^{-1}$ $cm^{-1}$ at first excitonic absorption peak, increasing toward UV; larger (longer wavelengths) QDs generally have higher absorption |
| Emission spectra | Asymmetric, often tailing to long-wavelength side; FWHM, 35 nm[c] to 70–100 nm[d] | Symmetric, Gaussian profile; FWHM 30–90 nm |
| Stokes shift | Normally <50 nm[c], up to >150 nm[d] | Typically <50 nm for visible - emitting QDs |
| Quantum yield | 0.5–1.0 (visible[e]), 0.05–0.25 (NIR[e]) | 0.1–0.8 (visible), 0.2–0.7 (NIR) |
| Fluorescence lifetimes | 1–10 ns, mono-exponential decay | 10–100 ns, typically multi-exponential decay |
| Two-photon action cross section | $1 \times 10^{-52}$–$5 \times 10^{-48}$ $cm^4$ s $photon^{-1}$ (typically about $1 \times 10^{-49}$ $cm^4$ s $photon^{-1}$) | $2 \times 10^{-47}$–$4.7 \times 10^{-46}$ $cm^4$ s $photon^{-1}$ |

[a]*Emission wavelength regions for QDs (approximate): CdSe, 470–660 nm; CdTe, 520–750 nm; InP, 620–720 nm; PbS> 900 nm; and PbSe> 1000 nm.*
[b]*FWHM, full width at half height of the maximum.*
[c]*Dyes with resonant emission such as fluoresceins, rhodamines, and cyanines.*
[d]*CT dyes.*
[e]*Definition of spectral regions used here: visible, 400–700 nm; and NIR, >700 nm (Resch-Genger et al., 2008).*

2008). The emission may originate from an optical transition delocalized over the whole chromophore (resonant dyes), or from intramolecular charge transfer transitions (CT dyes) (Resch-Genger et al., 2008). Resonant dyes such as the fluorescein, rhodamine, 4,4′-difluoro-4-bora-3a,4a-diaza-s-indacenes, and cyanine families are typically characterized by several distinct features including a slightly structured features where the absorption and emission bands are considered to be comparatively narrow. They also possess a small Stokes shift that is insensitive to the solvent polarity. These dyes have a typically high molar absorption coefficient and a moderate/high quantum yield

associated with their fluorescence. In contrast, CT dyes, such as those belonging to the coumarin family, show well separated but broader absorption and emission bands in polar solvents. These features are also structureless. A large Stokes shift is also observed and is sensitive to the solvent polarity impacting their spectroscopic properties. Their quantum yield is moderate or high although CT dyes absorbing or emitting in the near-infrared (NIR) region of the spectrum typically have low fluorescence quantum yields.

Organic fluorophores have been widely used as fluorescent probes for *in vitro* assays and *in vivo* imaging (Yuste, 2005). Green fluorescent proteins have allowed systematic imaging studies of protein localization in living cells and the structures and the functions of subcellular components (Tsien, 1998). Rhodamine, fluorescein, cyanine, and dipyrroylmethane have been used as core structures in tracking changes in intracellular pH or ions (e.g., $Ca^{2+}$ and $Zn^{2+}$) (Han and Burgess, 2009). Although organic dyes have been and continue to be used successfully, many significant limitations persist (Chen et al., 2014b).

Dye-based imaging is usually limited in its detection power due to a process known as autofluorescence, whereby both the analyte and the surrounding environment are concomitantly excited resulting in multiple emissions and limited detection sensitivity. Another significant problem related to the use of organic dyes lies in the fact that organic molecules tend to undergo photobleaching (or photodegradation) over a period of time due to the interaction with the excitation radiation (typically UV or visible light). As the organic fluorophore degrades with time (over the course of the analysis), its optical response deteriorates resulting in decreased detection sensitivity and reliability, as well as in the decrease of the signal-to-noise ratio. Moreover, most small organic dyes, such as fluorescein isothiocyanate for example, are strongly phototoxic, and produce reactive oxygen species in the excitation process, which in turn can result in the unwanted oxidation of several biological components in the system under study. Moreover, the large majority of these organic fluorophores are hydrophobic. As such, dispersibility and transport in aqueous media is very challenging. This problem may be addressed via the use of hydrophilic fluorophores; however, these dyes may still demonstrate a poor ability in crossing cellular membranes. Finally, with respect to targeting and drug delivery, organic fluorophores lack the structure necessary to develop a scaffold system capable of multimodal functionalities for targeting (example with antibodies, peptides, or nucleic acids), diagnostics, and therapeutics. The chemical modification and purification may thus become relatively sophisticated.

### 1.1.2 Quantum Dots

With the emergence of nanomaterials, much of the work over the last two decades has focused on alternatives to organic dye-fluorescent labels and principally on QDs. Quantum dots are inorganic semiconductors with electronic

properties that are deemed to fall in between the bulk and molecular phases. These nano-scaled inorganic materials are typically composed of groups II–VI or III–V elements (CdSe or CdTe for example) (Alivisatos, 1996). They possess unique optical properties, which stem from the fact that their physical dimensions (typically 2–10 nm) are smaller than the exciton Bohr radius (the distance between an electron in the conduction band and the hole it leaves behind in the valence band) (Han and Burgess, 2009). Excitation using a photon promotes some of the electrons, in the valence band, to higher excited energy states, in the conduction band. Following de-excitation and the return of an electron to its ground state, a photon of a frequency equivalent to the band gap is emitted. As the QD size changes so does the band gap, meaning that the optical properties are directly related to the QD size (Table 1). This is known as the quantum confinement effect (Han and Burgess, 2009). The fluorescence emission of QDs can be tuned from near ultraviolet to near infrared by varying their size and composition.

QDs possess broad excitation profiles yet show relatively narrow emission spectra in comparison to organic dyes. They also possess large Stokes shifts that reduce autofluorescence and increase sensitivity (useful for multiplexing analysis under excitation of single wavelength) (Han et al., 2001). These QDs also show a very high quantum yield and are $\sim 10–20 \times$ brighter than organic dyes. They are highly resistant to photobleaching due to their stable inorganic composition. Finally, their surfaces may be modified relatively easily, allowing for the introduction of additional functionality exploiting the surficial chemical groups available from capping ligands or on the surface of a silica shell for example (Chan and Nie, 1998).

Owing to their optical properties, QDs have attracted considerable attention, as fluorescent probes, for *in vitro* and *in vivo applications*, in engineered biosensor development, as photodynamic therapy agents or sensitizers and in theranostic platforms (Biju et al., 2010; Ho and Leong, 2010; Zrazhevskiy et al., 2010). For example, Gao et al. reported a clinically translatable fluorescent nanoprobe for tumor imaging in living mice with targeting peptide $RGD_2$-modified Dendron-coated InP/ZnS core/shell QDs. The nanoprobe featured NIR emission, good biocompatibility and stability, reasonable size, and renal clearance. This nanoprobe fulfilled most of the requirements for clinical translation; so, it was recommended as a potentially useful nanoplatform for preclinical biomedical research (Gao et al., 2011). *In vivo* imaging of the gastrointestinal tract of living mice was performed using poly(lactic-co-glycolic acid) (PLGA) microparticle-encapsulated $CuInSe_xSe_{2-x}/ZnS$ QDs as a distinct visible fluorescent marker (Panthani et al., 2013). This assembly was conjugated with an oral vaccine and applied in mice for tracking.

Advances in the development of QDs have made possible the synthesis of QDs with emission in the NIR-I (750–900 nm) to NIR-II (1100–1400 nm) regions of the spectrum allowing scientists to image in the first and second biological optical windows, respectively. As a consequence, the imaging

depth has been improved down to 10–100 μm (Dong et al., 2013). Per-fluorocarbon (PFC)/[CdSe/ZnS QDs] nanocomposite emulsions were used by Lim et al. as biomarkers to label immunotherapeutic cells for detection and localization of labeled cells in living mice. It was demonstrated that a combination of optical/magnetic resonance imaging (MRI) leads to the differential visualization of macrophages, dendritic cells, and T cells (Lim et al., 2009).

For single-particle imaging and tracking applications, QDs are superior to most organic fluorophores due to photostability, which allows single-fluorophore tracking for much longer times than with organic fluorophores (Resch-Genger et al., 2008); the intermittence in emission (also referred as "blinking") before considered a drawback for single-molecule applications was addressed by Ren et al. The authors demonstrated that by controlling the structure and concentration of thiol ligands on the surface of QDs, the blinking may be eliminated. This elimination is attributed to the suppression of QDs surface traps by thiol ligands (Dong et al., 2014).

One of the main concerns in using QDs is the toxicity of the heavy metal ions that comprise this type of nanoparticles. In this regard, a significant body of research has been dedicated to the potential degradation and breakdown of the QDs and possible leakage of these elements from the nanocrystals over time, upon illumination or oxidation (Hoshino, 2004; Ma, 2006; Zhang et al., 2006b). Moreover, the chemical toxicity of the QD itself is not the only aspect in question. Safety concerns need to be addressed regarding the ligands, coatings, or capping agents used as they may as well contribute to undesirable effects and could increase the cytotoxicity of the QD probe (Lewinski et al., 2008). It is noteworthy that in the latter case, the concern for potential toxicity of the molecules functionalized onto the surface could probably be extended to all nanoparticle systems.

### 1.1.3 Lanthanide-Doped Nanoparticles

In the past decade, lanthanide-doped nanoparticles have emerged as an attractive alternative to current imaging probes. Unlike organic dyes, they do not suffer from photobleaching; hence, the optical signal measured throughout the course of an analysis remains constant. Unlike semiconducting QDs, lanthanide-doped inorganic nanoparticles are insulators implying that they possess an extremely wide band gap and hence the quantum confinement effect is not observed in contrast to QDs (Hecht, 1993).

A change in size of these lanthanide-doped nanoparticles does not impart drastic changes in their luminescence behavior, which typically yields a varying spectrum of emission colors in QDs. Instead, size-related effects result in changes to the crystal phase, morphology, or the extent of surface defects (Suljoti et al., 2008). The luminescent behavior can be tailored to emit from the UV to the IR region of the electromagnetic spectrum via dopant selection and concentration.

Generally, luminescent probes rely on single photon excitation using UV light (high energy light) resulting in emissions at lower energies (Stokes emission). Multiphoton excitation may be possible with dyes or QDs; however, it requires a very high photon density as opposed to lanthanide ions. The latter can be excited using NIR light (low energy) and emit in the UV, VIS, or NIR regions (higher energy light known as anti-Stokes emission) using low power densities (Auzel, 2004). This multiphoton process is known as upconversion. With respect to biologically oriented, and especially *in vivo*, applications, upconversion is highly interesting (Chatterjee et al., 2008; Lim et al., 2005, 2009; Wang and Li, 2006) as it can circumvent the requirement for UV or visible light as principle source of excitation of the optical probe. In addition, NIR light does not excite the surroundings virtually eliminating autofluorescence. Furthermore, in contrast to UV light, NIR light offers significantly better penetration depth in tissue systems (König, 2000), does not impart damage to the sample under study, and is less prone to scattering. Unlike most other two-photon absorption (TPA) materials where emission occurs via "virtual" excited states, excitation of $Ln^{3+}$ ions such as $Er^{3+}$ or $Tm^{3+}$ proceeds via "real" electronic states of long lifetimes and thus high power, ultrafast lasers are not required for efficient excitation. In fact, excitation can be carried out using commercially available cheap continuous wave NIR diodes. Lanthanide-doped nanoparticles therefore offer a significant advantage relative to current imaging probes and may offer a succinct advantage in biologically oriented applications (Chen et al., 2015; Zheng et al., 2015).

## 1.2 Upconversion

The fundamentals of the studies in upconversion began in 1959 through the work of Bloembergen, who proposed the idea to construct a device capable of detecting and counting IR photons using an upconverting material in a solid matrix (Bloembergen, 1959). During 1960s, Auzel extensively studied upconversion processes and proposed a mechanism, which occurs via energy transfers between excited state ions. Auzel reported a detailed review on the history and fundamentals of upconverting materials in 2004 (Auzel, 2004).

Conventionally, lanthanide luminescence, in both micro- and nano-sized materials, is observed upon direct excitation into an excited state followed by emission and return of the excited ion to its ground state. A suitable excitation source such as a laser, of a wavelength resonant with the energy gap separating the ground and excited states, is required. High energy light emanating from the excitation source (UV or visible for example) is therefore converted to UV, visible, NIR, or IR light, light of lower energy than the source. This process is shown for the erbium ion in Fig. 1. A 488 nm excitation source (an argon gas laser for example) is used to excite the erbium ion and promote it to the $^4F_{7/2}$ excited state after which a non-radiative decay to the lower lying $^2H_{11/2}$ and $^4S_{3/2}$ energy states occurs, which is followed by green emission
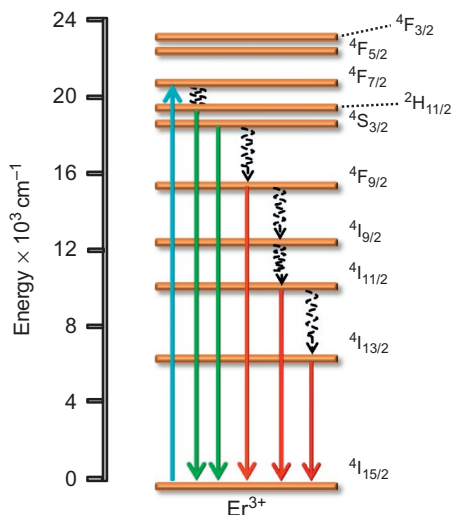
**FIGURE 1** Erbium ion emission following direct excitation into the $^4F_{7/2}$ energy level (single photon absorption) using an excitation wavelength of 488 nm.

upon relaxation of the ion to the ground state. This non-radiative decay is mediated by phonons (lattice vibrations). A second possibility involves further non-radiative decay to the lower lying $^4F_{9/2}$ state resulting in red visible emission. Additional non-radiative decay pathways may result in the population of the $^4I_{11/2}$ and $^4I_{13/2}$ states and subsequent NIR and IR emissions, respectively.

An alternative method to achieve lanthanide emission is through a process known as upconversion. In its simplest definition, upconversion is a process where low energy light such as NIR is converted to higher energy light such as UV, visible, or even NIR (with a wavelength shorter than the excitation source). Hence, following excitation, a system relaxes via the emission of photons of higher energy than those absorbed through the excitation process (Auzel, 1966a, 1973, 2004; Scheps, 1996). It is a multiphoton process involving at least two photons. Unlike other multiphoton processes, absorption of the photons is sequential and not simultaneous. One of the most important requirements is the presence of a metastable absorbing state, located between the ground and emitting states, that acts as a population reservoir (Scheps, 1996).

Upconversion offers an interesting alternative to conventional direct excitation for a myriad of reasons. First, upconversion luminescence may be achieved using highly compact, commercially available, and cheap semiconductor diodes. In fact, in some cases, upconversion may be observed using sub 20 mW cm$^{-2}$ surficial powered diodes similar to those found in laser pointing devices. Second, in order to achieve upconversion, a NIR source is typically used. The use of NIR light to generate emission spanning the

UV-NIR region of the electromagnetic spectrum is of great interest and importance as it opens up novel avenues in multiple research areas. One such area is in the field of display devices where upconverting nanophosphors can be used to replace their conventional micro-sized counterparts. The requirement for compact diode sources for excitation provides the advantage of the miniaturization of the technology rendering possible thinner and lighter displays and resulting in a significant reduction of materials required for manufacturing. It can also potentially render the research and development, production and recycling/recovery processes more "green" and ecologically oriented.

There are four major mechanisms by which upconversion may occur, namely, excited state absorption, energy transfer upconversion, cooperative upconversion, and photon avalanche upconversion. These mechanisms may occur alone or simultaneously and have been widely studied (Auzel, 2004; Gamelin and Gudel, 2001).

### 1.2.1 Excited State Absorption

Excited state absorption (ESA) involves the sequential absorption of two or more photons promoting an ion from the ground to an excited state (Bloembergen, 1959; Scheps, 1996). This process results in upconversion following the radiative relaxation of the ion back to its ground state. In Fig. 2, ion X is in its ground state. An incoming pump photon of a wavelength resonant with the energy gap separating ground state G and excited state $E_1$ will promote the ion to this excited state (step ①). A second incoming pump photon promotes the ion to a higher excited state, $E_2$ (step ②), followed by emission (green for example) and relaxation of the ion to its ground state. Assuming the energy gap separating $G \rightarrow E_1$ and $E_1 \rightarrow E_2$ are equal, the same pump wavelength may be used otherwise multi-pumping sources are required.
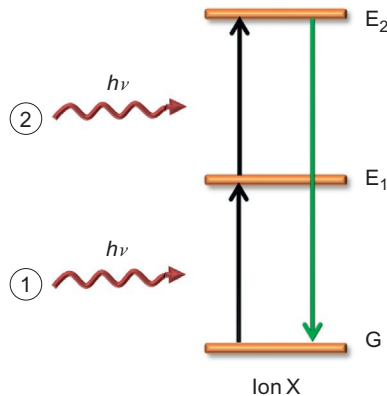


**FIGURE 2**   A general mechanism for excited state absorption upconversion.

In this case, there may be requirements to mitigate certain issues pertaining to beam alignment and differing pump efficiencies. The rate equation for ESA can be summarized as follows:

$$W_{G,E_1} n_G = W_{E_1,E_2} n_{E_1} + \frac{n_{E_1}}{\tau_{E_1}} \tag{1}$$

where $W_{G,E_1}$ and $W_{E_1,E_2}$ are the pump rate coefficients from the G to $E_1$ and $E_1$ to $E_2$ levels, respectively. The terms $n_G$ and $n_{E_1}$ are the populations of the ground state, G, and the intermediate excited state, $E_1$, respectively. Finally, $\tau_{E_1}$ is the lifetime of the $E_1$ energy level. In the case of fixed pump intensities, the metastable state ($E_1$ in this case) population caries directly with the meta-stable state lifetime (Scheps, 1996).

ESA is considered to be the least efficient among the four major mechan-isms (Auzel, 2004); however, Chen et al. demonstrated the obtention of a lumi-nescence quantum yield of approximately 1.2% in $LiYF_4$:$Er^{3+}$ upconverting nanoparticles. A value comparable to those exhibited by $Er^{3+}$/$Yb^{3+}$ co-doped materials (Chen et al., 2011a).

### 1.2.2 Energy Transfer Upconversion

Energy transfer upconversion (ETU) occurs via the transfer of energy between a neighboring pair of ions where one ion acts as a donor of energy, while the second acts as an acceptor of energy. The donor ion concentration usually ranges from 10X to 50X that of the acceptor concentration. This upconversion process requires only a single pump wavelength and hence alignment and pump efficiency issues are not relevant. The existence of a metastable state is very important in ETU processes as the intermediate energy levels act as population reservoirs. A simplified mechanism of energy transfer upconver-sion is summarized in Fig. 3.

In this upconversion process, an incoming pump photon, corresponding to the energy gap separating states G and $E_1$, promotes both donor ions Y (usually an ion with a high absorption cross section) to the intermediate excited state $E_1$ (step ①). In the second step (step ②), a non-radiative energy transfer from the donor ion Y to the acceptor ion X results in the promotion of the latter to its excited state $E_1$ after which a second energy transfer promotes the acceptor ion to excited state $E_2$ (step ③). This non-radiative energy transfer may occur in two ways:

(a) If the energy difference between the G and $E_1$ states of the donor is reso-nant with the $E_1$ to $E_2$ transition of the acceptor, then the energy transfer occurs before the donor relaxes radiatively to its ground state G.

(b) If there is an energy mismatch between G and $E_1$ and $E_1$ as well as $E_2$, then the energy transfer must be phonon-assisted in order to meet the res-onance absorption condition.

Following the energy transfer, the donor ion relaxes to their ground state while the acceptor ion, now in $E_2$, undergoes a radiative decay with emission
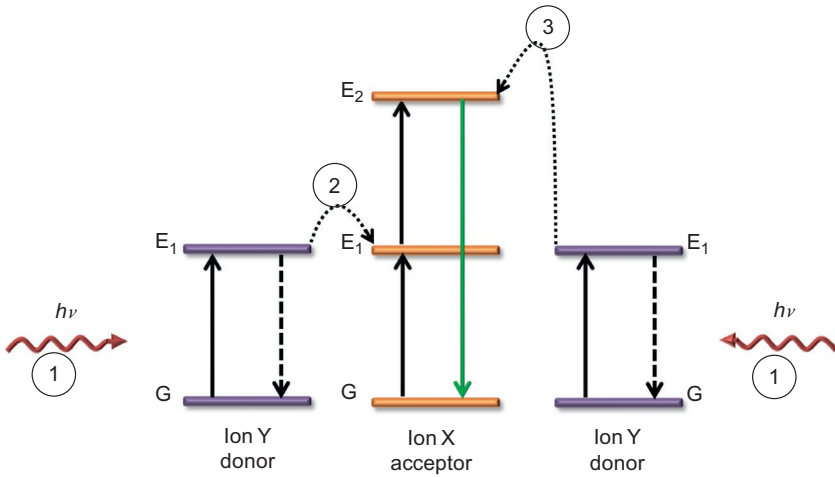
**FIGURE 3**  A general mechanism for energy transfer upconversion.

and returns to its ground state. The upconversion emission rate in ETU can be expressed as follows:

$$2\gamma n_{E_1}^2 + \frac{n_{E_1}}{\tau_{E_1}} = W_{G,E_1} n_G \tag{2}$$

where $\gamma$ is the ion pair cooperative upconversion rate coefficient, and $n_{E_1}$ and $\tau_{E_1}$ are the population density and lifetime of the $E_1$ intermediate energy level, respectively. The factor of 2 in Eq. (2) accounts for the fact that two energy quanta from intermediate excited state $E_1$ are required to produce an ion in level $E_2$. For a given pump intensity, the emission rate of the ETU process increases with an increase in the metastable transition lifetime (Scheps, 1996).

The energy transfer in this mechanism occurs through dipole–dipole interactions and can occur as long as there is a columbic overlap between the two electronic systems. This is dependent on the overall dopant ion concentration due to the increased proximity of neighboring ion pairs that facilitate the energy transfer process. In fact, the energy transfer rate varies as $r^{-6}$, where $r$ is the separation distance between two ions.

The ETU mechanism efficiency is also influenced by the choice of donor and acceptor ions, as well as their respective concentrations (Auzel, 1966a,b; Scheps, 1996). This not only affects the upconversion process efficiency, but can also serve to tailor the optical signature of the materials. This was documented earlier in the past decade. For example, varying the concentrations of the dopant ion pairs, $Er^{3+}$ and $Yb^{3+}$, in $Y_2O_3$ nanoparticles could be used to fine-tune the green to red emission ratio in erbium (Capobianco et al., 2002). This work was also reported in colloids where the blue, red, or NIR emissions of $LiYF_4$ co-doped with $Tm^{3+}/Yb^{3+}$ could be modulated by design to enhance certain transitions at the expense of others (Mahalingam et al., 2009).

The ETU mechanism is prominent in co-doped systems; however, ESA cannot be completely ruled out. In fact in many cases, both mechanisms may be operative with a strong emphasis on ETU in co-doped materials. Upconversion through ETU will result in an appearance of a rise time attributed to the non-radiative energy transfer between donor and acceptor in time-resolved measurements.

### 1.2.3 Cooperative Upconversion

Cooperative upconversion, a mechanism distinguished by second-order electronic transitions, occurs between a pair of ions and a third, single ion in an upconverting material (Fig. 4). In this process, two ions Y are both excited from the G to the $E_1$ excited energy level (step ①). In the second step ②, a non-radiative energy transfer occurs between ions Y and X due to their close proximity, causing ion X to be excited to $E_1$ and ion Y to be de-excited to the ground state non-radiatively. Then, the second Y ion still in its excited state can simultaneously transfer its energy causing the excitation of ion X to the $E_2$ energy level (step ③), followed by a radiative emission from the latter in the visible region. This mechanism is observable only when the pump intensity is as high as $10^5$ W cm$^{-2}$ by using a cw laser confining the light in an optical waveguide with a 1–10 μm mode diameter (Sivakumar and Veggel, 2007).

### 1.2.4 Photon Avalanche

This mechanism is characterized by three nonlinear behaviors: transmission, emission, and rise time. Photon avalanche upconversion is dependent on the pump power and shows slow response times (Joubert, 1999; Scheps, 1996).
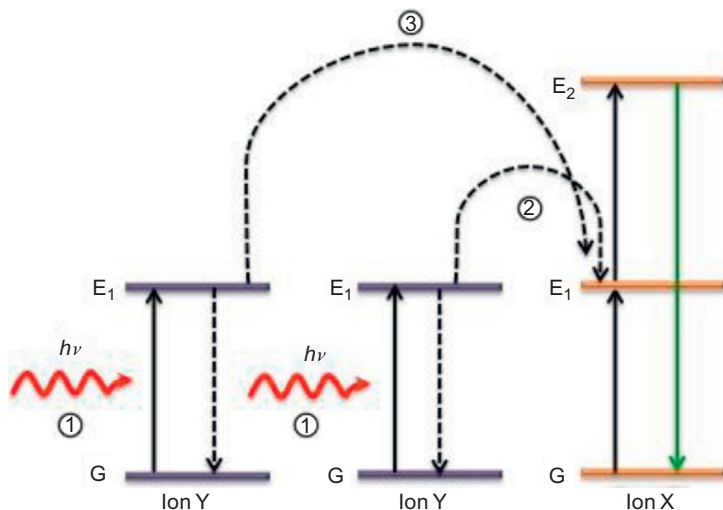


**FIGURE 4** A general mechanism for cooperative upconversion.
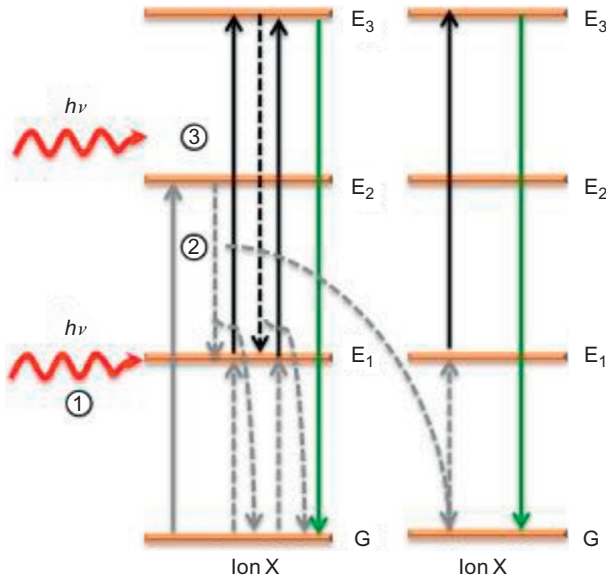
**FIGURE 5** A general mechanism scheme for photon avalanche.

Figure 5 shows the diagram for the general mechanism. In this process, an electron of ion X is promoted from the ground state G to the second metastable excited state, $E_2$ (step ①). In the second step (step ②), a relaxation of this electron from $E_2$ to $E_1$ results in: (i) excitation of an electron in G to the $E_1$ state in the same ion or (ii) the excitation of an electron from G to $E_1$ in a neighboring ion X via ion pair relaxation energy transfer processes. The energy of the irradiation is absorbed by the electrons populating the $E_1$ energy level resulting in the promotion to the $E_3$ level, followed by a non-radiative relaxation and a ion pair relaxation energy transfer, promoting electrons from the G to $E_1$ in the same or in the neighbor ion (step ③). This latter process of excitation is repeated, resulting in an exponential increase of the population of the $E_3$ energy level and a radiative relaxation from the $E_3$ to the G state (Auzel, 2004). The basic underlying principle of this mechanism is the production of two ions due to photon absorption and subsequent energy transfer, by one ion in the metastable state. Two ions will produce 4 ions and 4 ions will produce 8 ions and so on resulting in an avalanche of photons. It is noteworthy to mention that the avalanche process requires a power threshold below which the mechanism cannot be observed. The emission rate for this process can be described as follows:

$$W_{E_1,E_3}^{th} = \frac{W_{E_1,G}(k_q + W_{E_3})}{k_q - xW_{E_3}} \tag{3}$$

where $k_q$ is the cross relaxation coefficient and $W_{E_1,E_3}^{th}$ is the threshold rate coefficient. A low threshold in the avalanche mechanism is associated with

high ion pair relaxation rate coefficients and a long metastable state lifetime. Due to its unusual nature, the presence of an operative photon avalanche mechanism is usually easily verified and is observed as a threshold in the upconversion emission intensity at one specific pump power. A pump power-upconversion emission study would also show a change in the upconversion luminescence intensity with a break in the slope and a quadratic increase.

## 2 UPCONVERTING NANOPARTICLES

Upconverting nanoparticles (UCNPs) are lanthanide-doped nano-sized crystals that possess the unique optical property of converting low energy light (NIR) into a higher energy counterpart (UV or visible) through the sequential absorption of multiple photons or via energy transfer processes. The agents responsible for this conversion are predominantly lanthanide ions introduced as dopants in inorganic hosts (Auzel, 2004).

## 2.1 The Choice of Host and Lanthanide Dopant Ions

### 2.1.1 Choice of Host

The host plays a very important role in the upconversion (UC) process, particularly as it can dictate the luminescence efficiency. In fact, an ideal host needs to possess high chemical stability in order to ensure that the physical integrity of the nanomaterial is preserved. It should ideally possess low lattice phonon energies in order to minimize non-radiative processes including non-radiative decay and return to the ground state, while maximizing the radiative emission component (Wang and Liu, 2009). To date, UC processes at the nanoscale have been studied in a myriad of host matrices including fluorides (e.g., $NaYF_4$, $NaYbF_4$, $NaGdF_4$, $NaLaF_4$, $LaF_3$), oxyfluorides (e.g., GdOF), oxides (e.g., $La_2O_3$, $Lu_2O_3$, $Y_2O_3$), halides (e.g., $BaCl_2$, $CsCdBr_3$, $Cs_3Y_2I_9$), oxysulfides (e.g., $Y_2O_2S$), phosphates (e.g., $YPO_4$), and vanadates (e.g., $YVO_4$) (Güdel and Pollnau, 2000; Zhang et al., 2010c; Zhou et al., 2012). Upon comparison of the aforementioned matrices, chloride, bromide, and iodide hosts exhibit very low phonon energies ($\sim 300\ cm^{-1}$), which is ideal for higher efficiencies of the UC process; however, they are chemically unstable. As such, they are not generally regarded as suitable hosts. Moreover, being prone to chemical degradation suggests that these hosts may not be suitable in display and lighting applications, or in biology. In contrast to the halides, oxides exhibit high chemical stability accompanied with phonon energies larger than $500\ cm^{-1}$, a phonon energy that is considered to be relatively high. Fluoride hosts offer an acceptable compromise. They possess low phonon energies ($\sim 350\ cm^{-1}$) and high chemical stability. It is in this regard that the fluorides have garnered significant attention particularly in biological applications of UCNPs (Chen et al., 2015; Zhang et al., 2014; Zhou et al., 2012).

Heer et al. reported the dependence of the UC emission efficiency in $NaYF_4$ on the crystal phase of the host matrix. Hexagonal $NaYF_4$ was shown to exhibit UC efficiency emission of about one order of magnitude greater than cubic $NaYF_4$ (Heer et al., 2004). This dependece was addressed by Renero-Lecuna et al. The authors stated that the symmetry reduction from cubic to hexagonal host, offers a more highly disorder structure accompanied by a vast site distribution, that favours the electronic coupling between 4f energy levels and higher electronic configuration. Thus, increasing f-f transition probabilities of dopant ions. (Renero-Lecuna et al., 2011)

Core–shell systems using fluoride hosts significantly increase the UC efficiency. Huang et al reported the synthesis of $LiLuF_4:Ln^{3+}@LiLuF_4$ core–shell upconverting nanoparticles with values of quantum yields of 5% and 7.6% for $Er^{3+}$ and $Tm^{3+}$, respectively. This higher UC efficiency is attributed to the isolation of the active emissive centers using a shell (Huang et al., 2014).

### 2.1.2 Single Ion Dopant

Lanthanide ions such as $Er^{3+}$, $Tm^{3+}$, and $Ho^{3+}$ have multiple metastable excited energy levels that favor UC processes (Fig. 6) (Wang and Liu, 2009)). In order to generate UC emission, the following conditions need to be met:

**(a)** The ion must have almost equally spaced energy levels to facilitate excited state absorption (ESA) (see Section 1.2.1). Wang et al. discussed an example that facilitates the understanding of this requirement. The energy level diagram of $Er^{3+}$ is shown in Fig. 6. It can be estimated that the energy difference between the $^4I_{11/2}$ and $^4I_{15/2}$ ground state in $Er^{3+}$ amounts to $\sim 10350 \ cm^{-1}$. This energy gap is almost equal to the energy gap separating the upper excited state, $^4F_{7/2}$, and the intermediate state, $^4I_{11/2}$ ($\sim 10370 \ cm^{-1}$). Thus, upon 970-nm excitation, it is possible to excite the ion from the ground state to the intermediate level via ESA, followed by a second photon absorption, which will further excite the ion to the $^4F_{7/2}$ followed by radiative UC emission (Wang and Liu, 2009).

**(b)** To have a low probability of non-radiative multiphonon relaxation transitions. This process is represented by dotted arrows in Fig. 6. The rate of these non-radiative transitions ($k_{nr}$) is a parameter that depends on an empirical constant of the host ($\beta$), the energy gap between the populated level and the next low-lying energy level of $Ln^{3+}$ ($\Delta E$), and the highest vibrational energy mode of the host lattice ($\hbar\omega_{max}$) as expressed in Eq. (4) (Van Dijk and Schuurmans, 1983).

$$k_{nr} \cong e^{\left(-\beta\frac{\Delta E}{\hbar\omega_{max}}\right)} \tag{4}$$

Thus, based on this equation, the multiphonon relaxation rate decreases exponentially with increasing energy gap. Among the lanthanides, both $Er^{3+}$ and $Tm^{3+}$ possess relatively large gaps separating intermediate or excited states from the ground state thus lowering the probability of
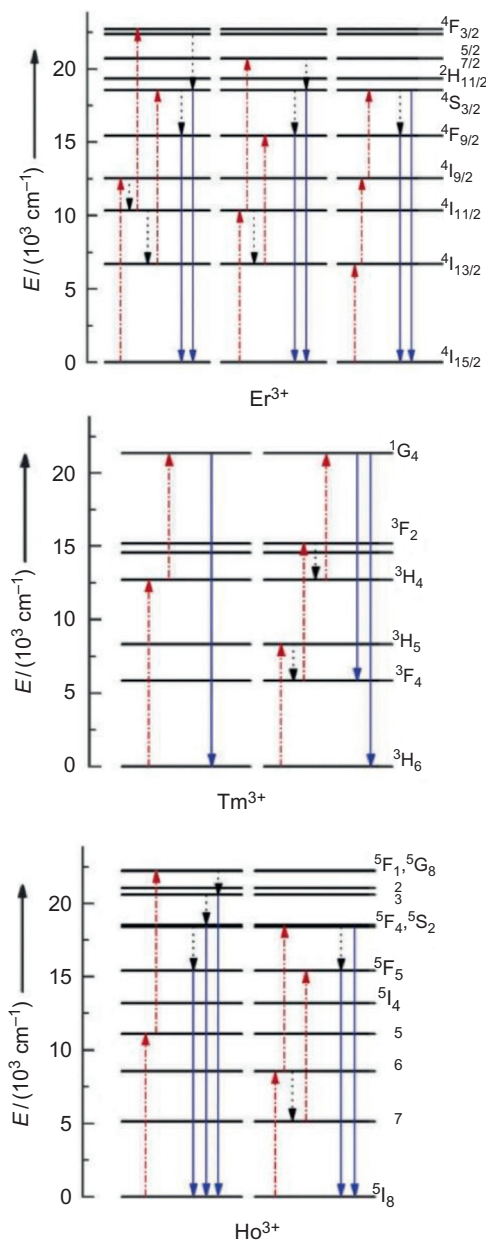
**FIGURE 6** Schematic energy-level diagrams showing UC process for $Er^{3+}$, $Tm^{3+}$, and $Ho^{3+}$. The dashed-dotted, dotted, and full arrows represent excitation, multiphonon relaxation, and emission processes, respectively. *Reproduced with permission from Wang and Liu (2009), © 2009 Royal Society of Chemistry.*

non-radiative transitions. As a result, both ions are typically incorporated as dopants in the host matrix (Wang and Liu, 2009).

**(c)** To maintain low concentration of the dopant ion. This is necessary in order to control the distance separating neighboring ions to avoid cross-relaxation processes that may occur, and which are non-radiative in nature. These processes are typically responsible for emission quenching and ultimately a decrease in the UC efficiency (Wang and Liu, 2009).

### 2.1.3 Multiple Ion Doping: The Activator–Sensitizer System

The majority of the lanthanide ions exhibit low absorption cross sections and consequentially, they do not show high pump efficiency. Thus, the overall UC efficiency for singly doped nanocrystals is generally low (Wang and Liu, 2009). In order to enhance the UC efficiency, co-doping with a second ion in the host crystal is generally utilized. In this case, this second ion must have a high absorption cross section that will allow it to build a population reservoir, which can be used for energy transfer processes to the other ion. The ion with the high absorption cross section will act as a sensitizer, while the emitting center to which the energy transfer will act as the activator. Co-doping favors the more efficient ETU mechanism (see Section 1.2.2) due to the necessary energy transfer that must occur from the sensitizer to the activator. Among the lanthanides, the $Yb^{3+}$ ion has an absorption band with a high absorption cross section (largest among the lanthanide ions) at approximately 980 nm and corresponding to the $^2F_{7/2} \rightarrow {}^2F_{5/2}$ transition.

The $^2F_{7/2} \rightarrow {}^2F_{5/2}$ transition is the only one in $Yb^{3+}$ and as such there exist no other transitions where non-radiative decay can play a major role. The energy gap separating the two levels of ytterbium is resonant with the f–f transition of many activator ions (e.g., $Er^{3+}$ and $Tm^{3+}$). In Fig. 7, the visible and NIR emissions that can be obtained following UC, via an ETU process, using $Yb^{3+}$ as the sensitizer ion and $Er^{3+}$ and $Tm^{3+}$ as activator ions are shown. It is important to remark that both ion couples show the highest upconversion efficiency when introduced in hexagonal phase $NaYF_4$. The concentration of the sensitizer is typically selected to be between 18 and 25 mol% and it is usually 10–50$\times$ higher than the concentration of the activator (0.5–2 mol%) (Haase and Schafer, 2011; Wang and Liu, 2009).

Other approaches to enhance the UC efficiency such as core–shell structures, the introduction of other dopants such as Gd or Lu, and the use of metal plasmonic materials have been reported and are addressed in Section 3.

## 2.2 Synthesis

Various synthetic methods have been developed in order to prepare lanthanide-doped UCNPs with the aim of obtaining high luminescence efficiencies. Indeed, great efforts have been oriented to optimize the synthesis procedures for UCNPs that would allow for their integration in biological
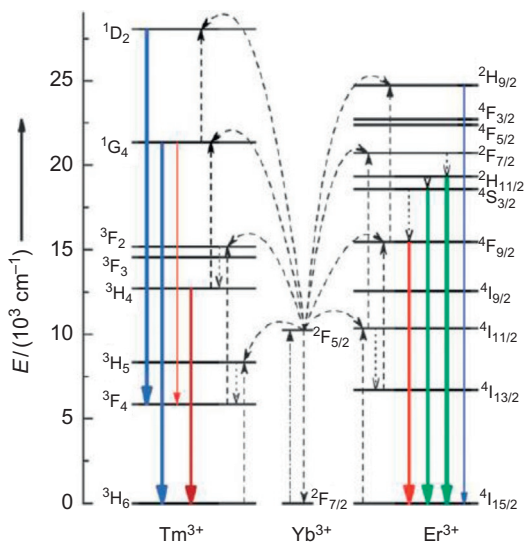
**FIGURE 7** Energy transfer upconversion mechanisms for ion couples $Er^{3+}/Yb^{3+}$ and $Tm^{3+}/Yb^{3+}$ upon 980-nm excitation. The dashed-dotted, dashed, dotted, and full arrows represent photon excitation, energy transfer, multiphonon relaxation, and emission processes, respectively. *Reproduced with permission of* Wang and Liu (2009), *© 2009 Royal Society of Chemistry.*

applications. UCNPs used in this type of applications (e.g., *in vitro* and *in vivo* imaging, drug delivery, therapeutics) must fulfill certain requirements such as being mono-dispersed, possessing a narrow size distribution, be monophasic, and finally be dispersible in aqueous media (e.g., water, saline solution, phosphate-buffered saline (PBS)).

Among the synthetic routes for preparing UCNPs, the most widely used methods are thermal decomposition, hydro(solvo) thermal, and coprecipitation. These aforementioned syntheses are discussed in detail in Sections 2.2.1–2.2.3. We also discuss some of the other synthetic routes previously reported. For the sake of brevity, a general overview is provided in Table 2 (Dacosta et al., 2014), and a list of the advantages and disadvantages of the nanomaterials is prepared using other not so common synthetic approaches.

## 2.2.1 Thermal Decomposition Method

This method is one of the most commonly used procedures for the preparation of alkali lanthanide tetrafluoride UCNPs such as $NaYF_4$ (Boyer et al., 2006, 2007), $NaGdF_4$ (Vetrone et al., 2009), $NaLuF_4$ (Liu et al., 2011b), $LiYF_4$ (Liu et al., 2013b), and $KGdF_4$ (Wong et al., 2011).

The general procedure for the preparation of alkali lanthanide tetrafluoride UCNPs starts by the preparation of lanthanide trifluoroacetate precursors from the reaction between lanthanide oxides and trifluoroacetic acid. The alkali

**TABLE 2** General Overview of Some Synthetic Methods of Lanthanide-Doped UCNPs (Dacosta et al., 2014)

| Synthetic Strategy | Process | Advantages | Disadvantages | Materials Prepared |
|---|---|---|---|---|
| Arrested precipitation | Poorly soluble; product precipitated within a template or confined space | Simple and fast reaction, cost-effective, does not require high temperatures or pressure | Little control over particle shape and size, aggregation is typical, high temperature post reaction annealing/calcinations step required resulting in aggregation | $LuPO_4$<br>$YbPO_4$<br>$NaYF_4$<br>$BaYF_5$<br>$Y_3Al_5O_{12}$<br>$Y_2O_3$<br>$LaPO_4$<br>$NaGdF_4$ |
| Microwave-assisted synthesis | Uses 0.3–300 GHz microwave irradiation to heat reaction mixtures | Increased reaction rates, milder reaction conditions, decreased energy consumption, high reproducibility | Requires specialized microwave irradiators, limited solvent choice (must be effectively heated by microwaves) | $Y_2O_3$<br>InGaP<br>InP<br>$M_2O_3$ (M=Pr, Nd, Sm, Eu, Gd, Tb, Dy)<br>$NaYF_4$<br>$LiYF_4$<br>$GdF_3$ |
| Microemulsion or reverse micelle method | Uses the interior aqueous environments of reverse micelles in organic solvents as nano-scale reactors | Very versatile, reproducible, produces homogeneous monodisperse materials, control over size, and morphology of produced materials | Organic solvents being used, very limited production capacity since relying on amount of aqueous phase that can be solubilized, and precursor concentrations | $NaYF_4$<br>$Y_2O_3$<br>$Gd_2O_3$<br>$YVO_4$<br>$XO_2$ (X=Ce, Sn, Zr)<br>$SrTiO_3$<br>$Sr_2TiO_4$<br>$Ba_2TiO_4$<br>$XZrO_3$ (X=Sr, Ba, Pb) |

trifluoroacetate is dispersed in a mixture of a high boiling point solvent (1-octadecene containing the capping ligand, oleic acid, or oleylamine). The resulting solution is then heated to approximately 150 °C under vacuum with stirring for 30 min to remove residual water and oxygen. The temperature of the mixture is then increased under a flow of argon to reach a value slightly above the decomposition temperature (>300 °C). Simultaneously, the lanthanide precursors, which are well dispersed in the same mixture of organic solvents, are heated to 125 °C and injected at a constant rate to the previously described solution (Boyer et al., 2006). Once the lanthanide trifluoroacetate precursors are injected, a rapid nucleation burst occurs due to the fast decomposition of the precursors with temperature (Dacosta et al., 2014). The growth kinetics mechanism of the UCNPs follows LaMer mechanism, which implies that delayed nucleation occurs first; subsequently, the nanoparticles start to grow by monomer supply. This is followed by the dissolution of the nanoparticles resulting in size reduction and finally aggregation to produce the final material (Fig. 8) (Mai et al., 2007; Wang and Liu, 2009).

The presence of the capping ligand (oleic acid or oleylamine) assists in the dispersion of the growing nanoparticles via coordination of the polar heads toward the surface through electrostatic interactions while the hydrophobic chain interacts with the solvent molecules. Thus, the ligand prevents aggregation through repulsive interactions and controls the growth of the UCNPs (Lin et al., 2012). The ligand dictates the hydrophobicity or hydrophilicity of the UCNP dispersion. Hence, UCNPs capped with oleic acid or oleylamine are typically hydrophobic.

Other parameters such as temperature, rate of injection of the lanthanide trifluoroacetate precursors, and reaction time also need to be controlled in order to control the growth of the nanocrystals and to obtain high quality mono-disperse UCNPs of narrow size distribution (Boyer et al., 2007). Once the reaction is complete, the UCNPs are precipitated by the addition of hexane/acetone and isolated via centrifugation. In order to purify the particles, the UCNPs are washed several times with ethanol, dispersed in a minimum amount of chloroform, and precipitated again with excess ethanol. The collected UCNPs exhibit nonpolar dispersibility and colloidal stability for prolonged periods (Boyer et al., 2007).
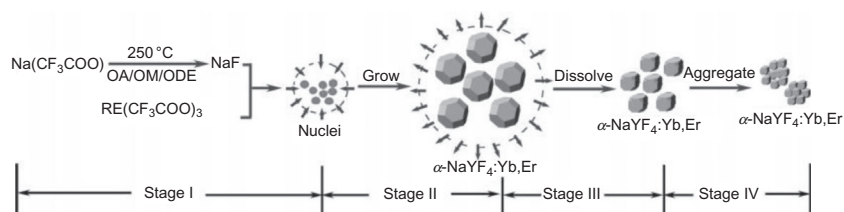


**FIGURE 8** Schematic illustration of the growth stages of cubic $NaYF_4:Er^{3+}/Yb^{3+}$ nanoparticles. *Reproduced with permission from Mai et al. (2007), © 2007 American Chemical Society.*

Mai et al., first reported the synthesis of NaReF$_4$ nanoparticles (Re = Pr to Lu, Y) co-doped with Er$^{3+}$/Yb$^{3+}$ and Tm$^{3+}$/Yb$^{3+}$. They demonstrated that they could obtain high quality cubic phase NaNdF$_4$, NaEuF$_4$, NaYF$_4$, and NaYbF$_4$ (Fig. 9) and the hexagonal phase of NaYF$_4$, NaNdF$_4$, NaEuF$_4$, and NaHoF$_4$ nano-sized materials (Fig. 10) (Mai et al., 2006). Boyer et al. further improved this procedure and they reported a synthetic procedure with few preparatory steps toward obtaining pure cubic phase NaYF$_4$ nanoparticles with an average particle size of 25 nm (Boyer et al., 2007). Later on, Ostrowski et al. reported the synthetic conditions necessary to prepare hexagonal phase NaYF$_4$ with an average particle size of 10 nm (Ostrowski et al., 2012). Clearly, controlling the reaction parameters allows for tailoring the particle size, morphology, and crystal phase of the synthesized UCNPs.

Generally, the thermal decomposition method requires high reaction temperatures, organic solvents, air-sensitive precursors, and inert atmosphere. This method provides control over particle size and yields high-quality
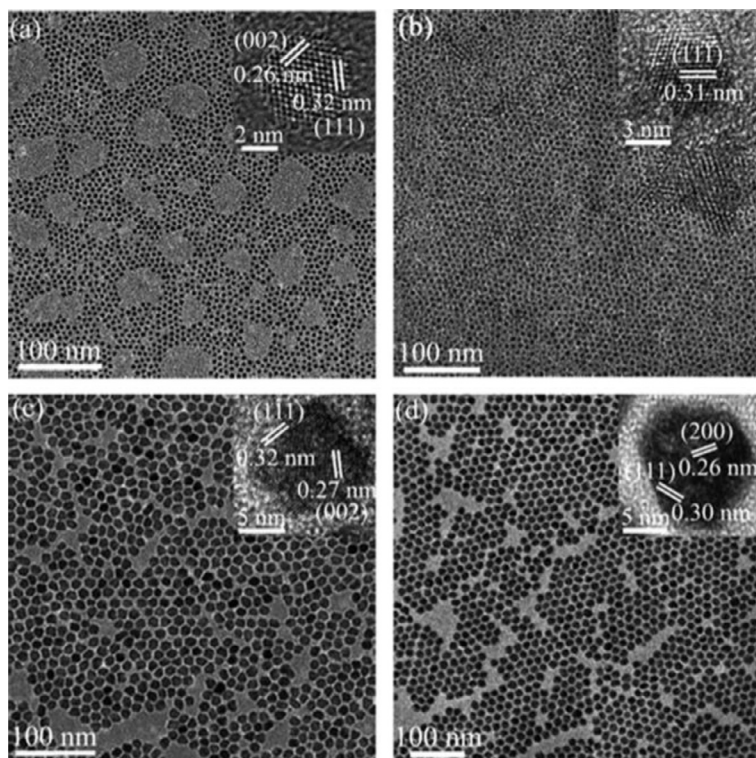


**FIGURE 9** Transmission electron microscopy (TEM) and high-resolution transmission electron microscopy (HRTEM) images of cubic phase of (A) NaNdF$_4$, (B) NaEuF$_4$, (C) NaYF$_4$, and (D) NaYF$_4$ nanocrystals. *Reproduced with permission from Mai et al. (2006), © 2006 American Chemical Society.*
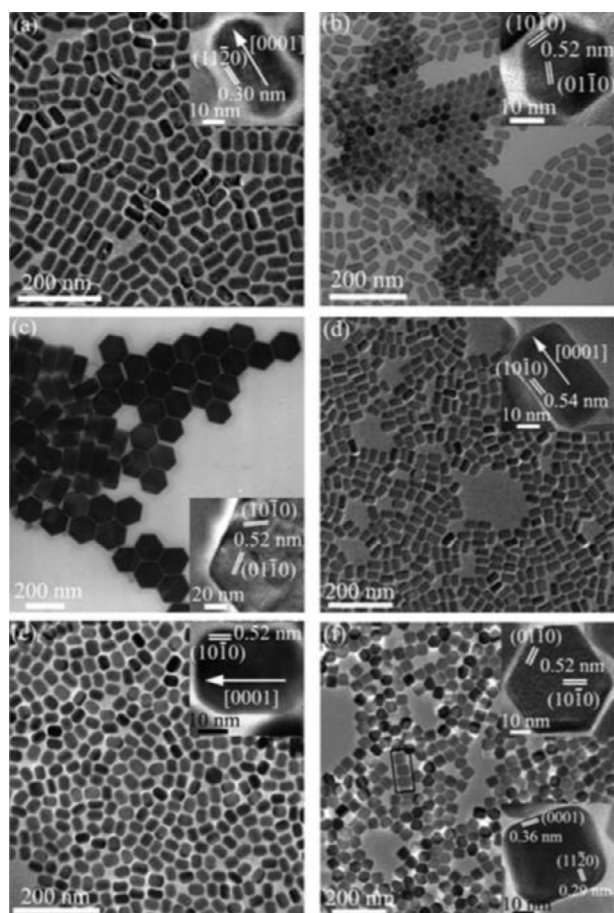
**FIGURE 10** TEM and HRTEM of hexagonal phase of (A) NaYF$_4$ nanorods in 1:1 toluene/hexane and in (B) 1:1:0.48 toluene:hexane:ethanol, (C) NaYF$_4$ nanoplates, (D) NaNdF$_4$ nanorods, (E) NaEuF$_4$ nanorods and (F) TEM and HRTEM (inset, upper: lying flat on the face; lower: standing on the side face from the highlighted square) images of hexagonal phase NaHoF$_4$. *Reproduced with permission from Mai et al. (2006), © 2006 American Chemical Society.*

mono-dispersed nano-sized materials. However, the obtained nanocrystals require further surface modification for biological applications. These methods are discussed in Section 2.3.

### 2.2.2 Hydro(solvo)thermal Method

The hydro(solvo)thermal method is a solution-based approach that operates at pressures and temperatures above the critical point of the solvent (Chen et al., 2012b; Dacosta et al., 2014; Wang and Liu, 2009). By using supercritical solvents, the solubility of the precursors is increased and therefore it favors the

rate at which the nanoparticles grow. The experimental setup is based on a reaction vessel embedded into a thick steel walled construction, hermetic seals, and protective inserts made of Teflon® or titanium to avoid corrosion brought about by the use of certain solvents (Lin et al., 2012).

Li et al. extensively studied the synthesis of hexagonal phase $NaYF_4$: $Er^{3+}/Yb^{3+}$ by the hydro(solvo)thermal method. Solvents such as distilled water, acetic acid, and ethanol along with mediator capping ligands including cetyltrimethylammonium bromide (CTAB), ethylenediamine tetraacetic acid (EDTA), and trisodium citrate ($cit^{3-}$) were evaluated as parameters to tune the morphology and size of UCNPs. The authors found that using water as solvent and by varying the pH conditions, most of the particles obtained showed needle morphology; however, no particle size control could be achieved (Fig. 11) (Li et al., 2007).
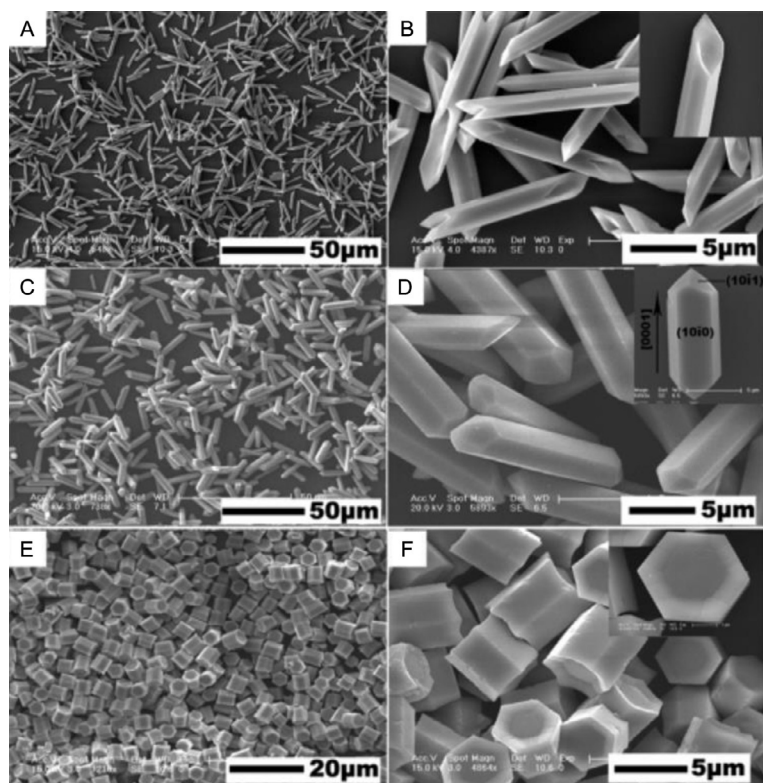


**FIGURE 11** Influence of pH values on the morphology of $NaYF_4$ microcrystals with $NH_4F$ as fluoride source. (A and B) pH 3, (C and D) pH 7, and (E and F) pH 10. These samples were hydrothermally treated at 180 °C for 24 h (1:1 molar ratio for trisodium citrate:$Y^{3+}$). *Reproduced with permission from Li et al. (2007), © 2007 American Chemical Society.*

Later on, the same group found that the morphology and size of the nano-particles may be tuned by controlling $cit^{3-}/Ln^{3+}$ ratio. Low ratios promoted the formation of larger particles and conversely high ratios resulted in the formation of smaller crystals (Fig. 12) (Mai et al., 2007).

Wang et al. reported a one-step hydro(solvo)thermal synthesis method to prepare water-soluble $NaYF_4$:$Er^{3+}/Yb^{3+}$ nanoparticles that are surface functionalized with organic polymers. The reaction uses $Ln^{3+}$ stearates (($C_{17}H_{35}COO^{-})_3Ln^{3+}$), NaF, and biocompatible polymers such as polyvinylpyrrolidone (PVP), poly-ethylene glycol (PEG), polyethylenimine (PEI), and polyacrylic acid (PAA). A mixture of water (10 ml)/ethanol (15 ml) was used with a reaction time of 24 h at 180 °C. The authors demonstrated that under these conditions, the hex-agonal phase of $NaYF_4$ could be obtained with an average particle size of 40 nm. Using PAA and PEI opens the possibility for further functionalization of the UCNP surface with covalently bonded targeting ligands by the introduction of carboxylic or amine terminal groups (Wang et al., 2009b).
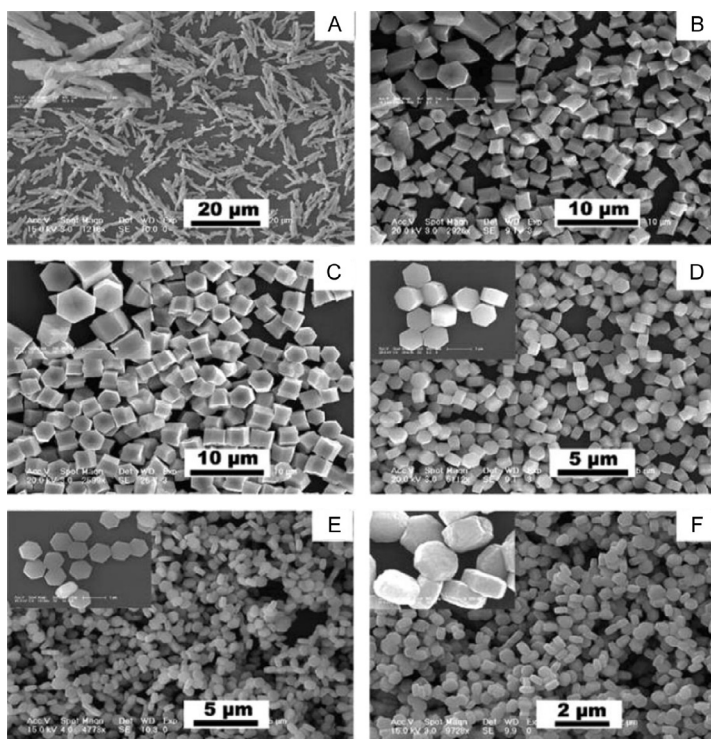


**FIGURE 12** Scanning electron microscopy (SEM) images of hexagonal phase of $NaYF_4$:$Tb^{3+}$ samples prepared with different molar ratios of $cit^{3-}/Tb^{3+}$. (A) Without $cit^{3-}$ (B) 1:2, (C) 1:1, (D) 2:1, (E) 4:1, and (F) 8:1. All of the samples were hydrothermally treated at 180 °C for 24 h. Insets are higher magnification images for the corresponding samples. *Reproduced with permission from Mai et al. (2007),* © *2007 American Chemical Society.*

In order to favor the formation of the more efficient hexagonal crystal phase by solvothermal method, Zhang et al. demonstrated that the introduction of $Gd^{3+}$ (3 mol%) ions favors the transition from cubic to hexagonal phase (Zhang et al., 2012b).

## 2.2.3 Coprecipitation Method

Although this method employs significantly less complicated experimental assemblies, it is mostly used to prepare ultra small UCNPs with a particle size of 2–10 nm (Liu et al., 2013b; Wang and Liu, 2009). In contrast, thermal decomposition and hydro(solvo)thermal syntheses are commonly used to prepare NPs in the size range of 10–100 nm.

Van Veggel pioneered the use of the coprecipitation method to synthesize $LaF_3:Ln^{3+}$ ($Ln^{3+} = Eu^{3+}$, $Er^{3+}$, $Nd^{3+}$, and $Ho^{3+}$) nanoparticles. In the synthesis procedure reported by the authors, di-*n*-octadecyldithiophosphate was used as the capping ligand as it had previously been shown to control the particle growth and favor the production of monodispersed nanoparticles. The authors report the formation of single crystals without ideal spherical morphology and diameters between 5 and 10 nm (Stouwdam and Van Veggel, 2002). Later on, optimization of the reaction conditions to obtain hexagonal phase $LaF_3:Ln^{3+}/Yb^{3+}$ ($Ln^{3+} = Er^{3+}$, $Tm^{3+}$ and $Ho^{3+}$) with an average particle size of $5.4 \pm 0.9$ nm was reported by Yi and Chow (2005).

Heer et al. first reported the synthetic procedure for obtaining cubic phase $NaYF_4:Er^{3+}/Yb^{3+}$ and $Tm^{3+}/Yb^{3+}$ nanoparticles by the coprecipitation method. They demonstrated by TEM that UCNPs could be obtained with a broad particle size distribution (5–30 nm) (Heer et al., 2004). Subsequently, Yi et al. reported significant improvements to the synthesis. The optimized procedure involved the fast injection of $Ln^{3+}$–EDTA complexes into a vigorously stirred aqueous solution of NaF in order to induce the homogeneous formation of spherical $NaYF_4$ nuclei with an average size diameter of approximately 40 nm. The generation of nanoparticles by the coprecipitation method also follows the LaMer growth mechanism model. The key point in the achievement to produce monodispersed nanoparticles with narrow size distribution is the separation of the nucleation and growth steps (Fig. 8). The chelation of $Ln^{3+}$ by EDTA facilitates the particle growth without incurring further nucleation events. Therefore, the synthesis of the UCNPs may be tuned by varying the concentration of EDTA. The authors demonstrate that a low EDTA/$Ln^{3+}$ molar ratio resulted in large $NaYF_4:Er^{3+}/Yb^{3+}$ nanoparticles and when the EDTA/$Ln^{3+}$ ratio is above 1, the size of the nanoparticles was not significantly affected (Yi et al., 2004). Polymers such as polyols (glycol, diethylene glycol, and glycerol), PEI, and PVP have also been employed as stearic barriers to control the nanocrystal growth. Polymers adsorb and desorb dynamically during the crystal growth, providing simultaneous stabilization and steric repulsion. The higher the steric hindrance obtained the smaller the nanoparticle's average size obtained (Wang and Liu, 2008; Wang et al., 2006; Wei et al., 2008).

The low crystallinity of the final product is the principal disadvantage of using this synthetic method. Therefore, most of the procedures are complemented with high temperature heat treatments such as annealing or calcination (400–700 °C) (Dacosta et al., 2014; Wang and Liu, 2009). In the quest of improving the crystallinity of the final product, reducing the particle size distribution, and increasing the luminescence efficiency, Wang et al. proposed a "high-temperature coprecipitation method" using 1-octadecene as the solvent and oleic acid as the capping ligand. In this procedure, small amorphous $NaYF_4$ crystals were produced at room temperature conditions. An increase in temperature to ~300 °C was used in order to facilitate particle growth and generate monodisperse nanocrystals via Ostwald ripening mechanism. The authors reported the production of $NaYF_4:Er^{3+}/Yb^{3+}$ and $Tm^{3+}/Yb^{3+}$ where the morphology and size were tuned by varying the concentration of oleic acid used in the reaction (Wang and Liu, 2008). Zhang et al. further modified the procedure to synthesize hexagonal phase $NaYF_4.Ln^{3+}@NaYF_4$ core–shell with an average particle size range of 25–30 nm (Li and Zhang, 2008). Other core–shell nanosystems based on hosts such as $NaGdF_4$, $NaTbF_4$, and $CaF_2$ have been synthesized using this modified coprecipitation method (Chen et al., 2012b; Gai et al., 2012).

## 2.2.4 Sol–Gel Method

The sol–gel synthesis is a wet chemical technique used for the synthesis of micro and nanocrystals, especially oxides, which are useful in thin film coatings and glass materials applications. This method is usually carried out in two steps. The first step is the hydrolysis and polycondensation of metal alkoxide (or halide)-based precursors. This step provides a homogeneous material that will be further calcinated. In the second step, at high temperatures in order to improve the crystallinity of the product allowing for an increase in the luminescence efficiency (Li and Zhang, 2015). Patra et al. developed a modified sol–gel method that uses reverse micelles formed in emulsions. These micelles act as reactors to grow $ZrO_2:Er^{3+}$ nanocrystals (Patra et al., 2002). Other upconverting nanocrystals such as $BaTiO_3:Er^{3+}$ (Patra et al., 2003), $ZnO:Er^{3+}$ (Wang et al., 2004), $Lu_3Gd_5O_{12}:Er^{3+}$ (Venkatramu et al., 2008), $NaNbO_3: Tm^{3+}/Er^3$ $^+/Yb^{3+}$ (Kumar et al., 2012), and $SrMO_4: Ho^{3+}/Tm^{3+}/Yb^{3+}$ (Fig. 13) (Li et al., 2013b) have also been synthesized by the coprecipitation method. Nanocrystals suitable for biological applications are not generally synthesized using this method due to lack of particle size control and high degree of aggregation brought about by the heat treatment step (Li and Zhang, 2015).

## 2.2.5 Combustion Method

This is a rapid synthesis method based on oxidation–reduction reactions occurring through a series of controlled explosions, forming nano and micro upconverting particles (Vennerberg and Lin, 2011).
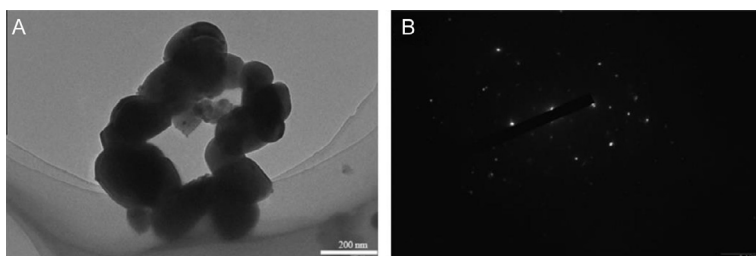
**FIGURE 13** (A) TEM image and (B) Selected Area Electron Diffraction (SAED) pattern of $SrMO_4$: 0.2 mol% $Ho^{3+}$/0.3 mol% $Tm^{3+}$/2 mol% $Yb^{3+}$ nanocrystals. *Reproduced with permission from Li et al. (2013b) © 2013 Elsevier B.V.*
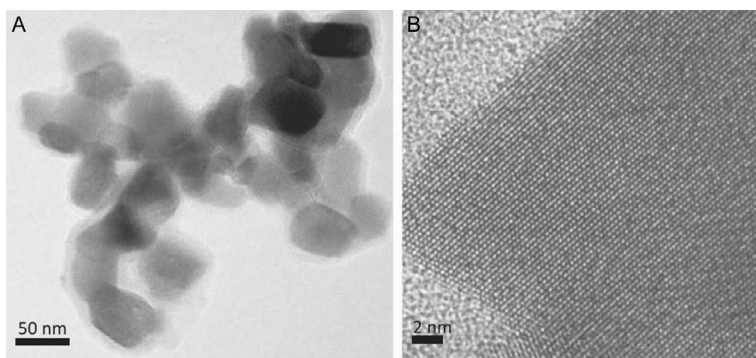


**FIGURE 14** (A) TEM image of $Y_2O_3$: 2 mol% $Er^{3+}$/1 mol% $Yb^{3+}$ nanocrystals prepared via combustion method and (B) HRTEM image. The interplanar distance (0.330 nm) corresponds to the (2 2 2) crystal plane. *Reproduced with permission from Martín-Rodríguez et al. (2009) © 2009 Elsevier B.V.*

Metal and rare-earth nitrates are used as oxidizing agents, and organic compounds such as urea or glycine are used as reducing agents, as well as fuel (Chang et al., 2014). Usually, an organic solvent such as ethanol is introduced as an assistant fuel. Its role is to dissolve the nitrates, therefore facilitating the rapid formation of the host (Luo et al., 2006). Oxide and oxysulfide upconverting nanomaterials such as $Y_2O_3$:$Er^{3+}$/$Yb^{3+}$ (Fig. 14) (Martín-Rodríguez et al., 2009; Vetrone et al., 2004), $Y_2O_2S$:$Eu^{3+}$ (Luo et al., 2006), $Gd_3Ca_5O_{12}Tm^{3+}$/$Yb^{3+}$ (Pandozzi et al., 2005), and $G_2O_3$:$Er^{3+}$ (Xu et al., 2008) have been synthesized via the combustion method.

## 2.2.6 Flame Synthesis

This method is almost exclusively limited to the production of oxide-based upconverting nanomaterials. The flame synthesis method offers several advantages including high production rates, short reaction times, broad temperature controllability, and low cost (Chang et al., 2014). The procedure

consists of the use of a precursor-evaporating chamber, where precursors are dissolved; a co-flow burner and a combustion chamber where nuclei formation occurs; an electrostatic precipitator where particles grow; and a cooling and filtering system (Qin et al., 2007). The synthesis of $Y_2O_3$: $Er^{3+}/Yb^{3+}$ by flame synthesis has been reported by Qin et al. (2007). Later on, the same group used the same method to synthesize $Re_2O_3$: $Er^{3+}/Yb^{3+}$ (Re = La, Gd) (Kong et al., 2010). Mangiarini et al. reported the synthesis of $Re_2O_3$: $Er^{3+}$ where the final product showed greater uniformity and less aggregation suggesting that these particles may be used in field display applications (Mangiarini et al., 2010).

## 2.3 Surface Modification of Ln-Doped Upconversion Nanoparticles

In many cases, the synthetic methods that yield high-quality nanoparticles with high monodispersibility and crystallinity, as well as good luminescence efficiency, also possess the disadvantage of producing nanoparticles that are hydrophobic (see Section 2.2.1). This is the case with the thermal decomposition synthesis for example. In order to use UCNPs for biological applications, such as bioimaging, these nano-sized materials must show high luminescence efficiency, biocompatibility, sub-100 nm sizes, a narrow size distribution and dispersibility, and compatibility in biologically relevant media (Chang et al., 2014).

Different strategies have been developed in order to render UCNPs hydrophilic and biocompatible along with efforts to maintain or enhance the upconversion luminescence efficiency in aqueous environments. These strategies are ligand oxidation and ligand removal (Sections 2.3.1 and 2.3.2), ligand exchange (Section 2.3.2), silane coupling agents (Section 2.3.3), and polymer coating (Section 2.3.4).

### 2.3.1 Ligand Oxidation and Ligand Removal

This technique is based on the oxidation of the unsaturated carbon–carbon bonds present in the capping ligands of hydrophobic UCNPs. Oxidizing agents such as the Lemieux-von Rudloff reagent (Chen et al., 2008) and ozone (Zhou et al., 2009) are among those typically used as they generate terminal carboxylic acid groups. The presence of these functional groups renders UCNPs dispersible in aqueous media and provides reactive sites that facilitate the coupling of biological molecules to the UCNP surface (Chang et al., 2014).

Chen et al. demonstrated the conversion of hydrophobic UCNPs into water-dispersible, carboxylic acid-functionalized nanoparticles by directly oxidizing the oleate ligands using the Lemieux-von Rudloff reagent. The oxidation caused the generation of hydrophilic nanoparticles, which were surface functionalized with azelaic acid (Fig. 15). Additionally, it was shown that the oxidation process does not impact the morphology, crystal phase, and
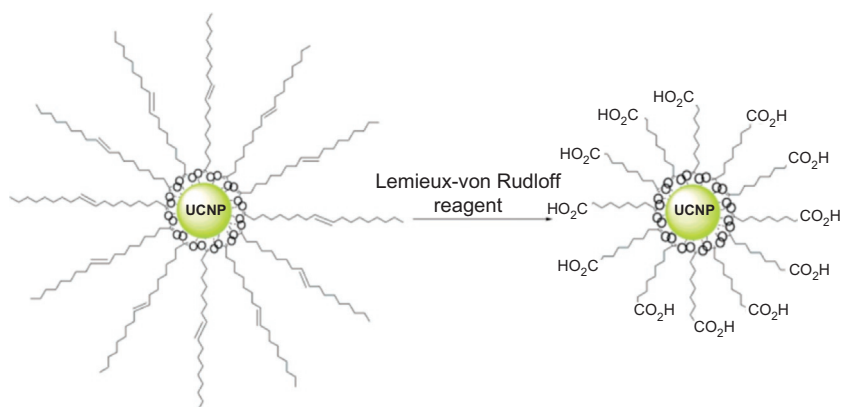
**FIGURE 15** Scheme of the synthesis of carboxylic acid-functionalized UCNPs from oleate-capped UCNPs. *Reproduced with permission from Chen et al. (2008) © 2008 American Chemical Society.*

chemical composition of the nanocrystals. Furthermore, functionalization with a DNA sensor based on streptavidin was reported by the authors (Chen et al., 2008) relying on UCNPs prepared using this approach.

Capobianco and colleagues showed that water-dispersible and ligand-free UCNPs can be obtained by tuning the pH. After inducing the protonation of the oleate ligands, the surface of the Ln-OA (OA: oleate) is modified to Ln-OH. Different acids such as HCl, HF, and $H_3PO_4$ were studied, showing an enhancement of the red emission at low pH (Fig. 16) (Bogdan et al., 2011).

One modified approach to this surface modification method was developed by Hu et al. The authors reported an epoxidation strategy and further coupling with polyethylene glycol monomethyl (mPEG) ether to convert hydrophobic UCNPs into amphiphilic mPEG-UCNP. The authors demostrated low cytotoxicity, good cell membrane permeability, and dispersibility in polar and non-polar media (Hu et al., 2008).

### 2.3.2 Ligand Exchange

In this method, the hydrophobic capping ligands of the UCNPs are displaced by other ligands that possess a stronger coordination to the surface-lying lanthanide ions. Among the most used hydrophobic ligands are oleic acid ($-COOH$) and oleylamine ($-NH_2$). The carboxylic and amine chemical functions coordinate with the $Ln^{3+}$ ions of the surface. In order to render the UCNPs water dispersible, the nanocrystals are dispersed in the presence of a hydrophilic ligand with a much higher affinity for the $Ln^{3+}$ ions (Yang, 2014). Chow and coworkers demonstrated the production of water-dispersible $NaYF_4:Er^{3+}/Yb^{3+}$ and $Tm^{3+}/Yb^{3+}$ nanoparticles. The nanoparticles were initially capped with oleylamine ligands. They were further modified via ligand exchange with polyethylene glycol diacid (MW $= 600$) (Yi and Chow, 2006b).
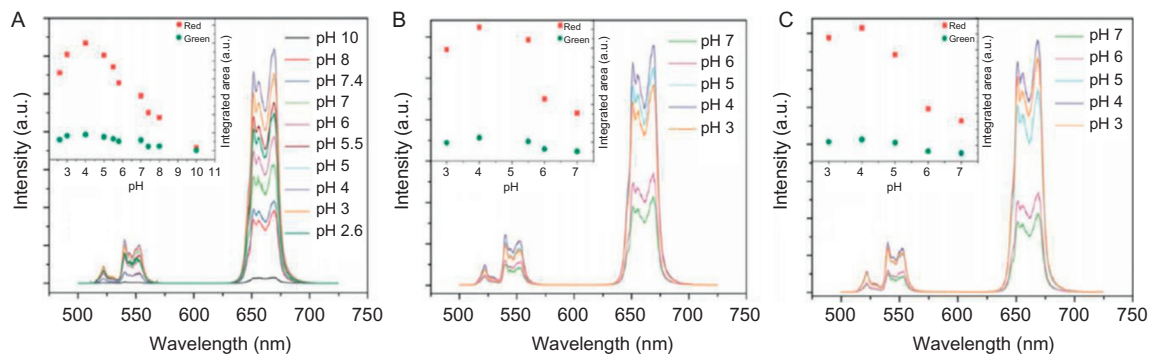
**FIGURE 16** Effect of pH on the upconversion luminescence of the oleate-free UCNPs. The acidic solutions were prepared in (A) HCl, (B) HF, and (C) $H_3PO_4$ ($\lambda_{exc}=980$ nm). *Reproduced with permission from Bogdan et al. (2011) © 2011 American Chemical Society.*
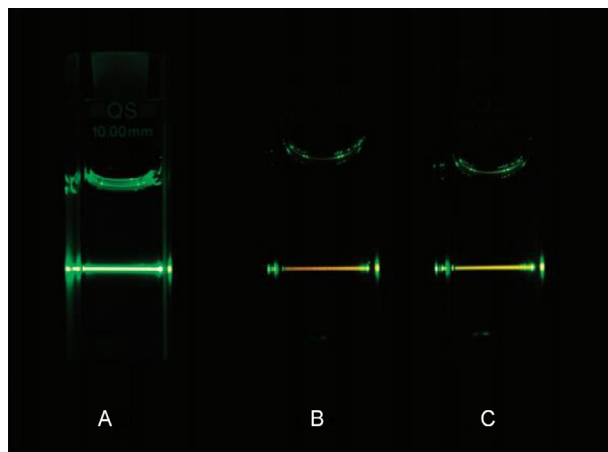
**FIGURE 17** Upconversion emission of NaGdF$_4$:Ho$^{3+}$/Yb$^{3+}$ nanoparticles (A) dispersed in ethanol, (B) dispersed in water following oxidation of oleic acid, and (C) dispersed in water following exchange of oleic acid ligand with PAA ($\lambda_{exc} = 980$ nm). *Reproduced with permission from Naccache et al. (2009) © 2009 American Chemical Society.*

Naccache et al. reported a ligand-exchange procedure using PAA (MW = 1800). The hydrophilic nanoparticles produce a clear and transparent solution in water (1 wt%) with moderate upconversion emission, slightly brighter in comparison with hydrophilic nanoparticles obtained via ligand oxidation (Fig. 17) (Naccache et al., 2009).

Boyer et al. reported that NaYF$_4$:Er$^{3+}$/Yb$^{3+}$ and Tm$^{3+}$/Yb$^{3+}$ nanoparticles capped with PEG phosphate could be synthesized following ligand exchange. The authors described quenching of the luminescence intensity of the hydrophilic nanoparticles when dispersed in water; therefore, they developed a core/shell system to enhance the upconverting luminescence (Boyer et al., 2009).

Other ligands, such as hexanedioic acid (Wang et al., 2009b), dimercaptosuccinic acid (Chen et al., 2011c), mercaptosuccinic acid (Chen et al., 2011c), citrate (Zhou et al., 2011), poly(amidoamine) (Bogdan et al., 2010), polyethylenimine (Yi et al., 2011), thioglycollic acid (Zhang et al., 2010b), and maleimide-PEG-COOH (Raphaela et al., 2012), also render hydrophobic UCNPs hydrophilic via ligand exchange.

### 2.3.3 Surface Silanization

This is one of the most important and often used surface functionalization methods. It involves the growth of an amorphous silica shell on the surface of UCNPs via hydrolysis and condensation of siloxane monomers (Feng et al., 2006). Silica is considered to be an attractive coating due to its biocompatibility, chemical stability, and optical transparency. Moreover, its chemistry and reactivity are well understood (Vennerberg and Lin, 2011).

The most often used procedures to graft uniform silica shell on the surface of UCNPs are the Stöber and the microemulsion methods. In the Stöber-type reactions, the silica coating is grown directly on the surface by the hydrolysis of tetraalkoxysilanes. The microemulsion method uses a silane-coupling agent, such as tetraethyl orthosilicate (TEOS), that first disperses the nanoparticles in an aqueous media, followed by the hydrolysis and controlled growth of the silica shell (Li and Zhang, 2008).

One of the most important advantages of using silica shells is the possibility of grafting various modified silanes such as aminopropyl trimethoxysilane (Zako et al., 2009) and (3-aminopropyl) triethoxysilane (Wang et al., 2009b) to the surface of the UCNPs. This facilitates the conjugation of other molecules, especially biological molecules that may have some reactivity toward carboxylates, amines, or thiols.

Feng et al. reported the grafting of a silica shell on the surface of PVP-stabilized $NaYF_4:Er^{3+}/Yb^{3+}$ and $Tm^{3+}/Yb^{3+}$, as well as the parameters to control the thickness of the shell in the range of 2–10 nm (Feng et al., 2006). This group also reported the synthesis of monodisperse $SiO_2$-coated UCNPs by using a microemulsion method (Li and Zhang, 2008). Silanization of TEOS conjugated to PEG linkers with NHS ester-activated carboxylic acid and functionalities on the terminal end affords a biocompatible surface useful to the conjugation of proteins to UCNPs as it was demonstrated by Wolfbeis and colleagues (Wilhelm et al., 2013).

### 2.3.4 Polymer Coating

Another approach to render hydrophobic UCNPs hydrophilic is through the adsorption of an amphiphilic polymer onto the surface of the nanoparticles through the hydrophobic–hydrophobic attraction between the hydrophobic ligand and the hydrocarbon chains of the polymer (Sperling and Parak, 2010).

Chow used PAA to prepare water-dispersible $NaYF_4:Er^{3+}$ $(Tm^{3+})/Yb^{3+}/$ $Yb^{3+}@NaYF_4$ core–shell nanoparticles (Yi and Chow, 2006a). Wang et al. modified the surface of the UCNPs with PEG. The pegylated UCNPs were loaded with a chemotherapy therapeutic agent, doxorubicin (DOX), by physical adsorption via a supramolecular chemistry approach for intracellular imaging and drug delivery (Fig. 18) (Wang et al., 2011a). Other block copolymers that have been used include PEG-block-poly(caprolactone), PEG-block-polylactic-coglycolic acid, octylamine-modified, PAA and PEG–phospholipids in order to coat the surface of the nanoparticles and improve the UCNP water dispersibility (Dacosta et al., 2014).

## 3 ENHANCING UPCONVERSION

UCNPs have been touted as useful and efficient luminescent probes in biological applications owing to their attractive optical properties. UCNPs show large anti-Stokes shift, high photostability, finely tuned multicolor
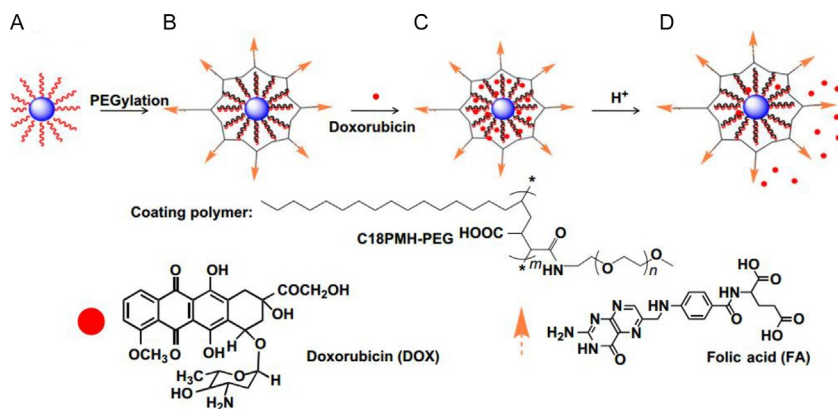
**FIGURE 18** Scheme of a polymer-coated UCNP-based drug delivery system: (A) oleate-capped UCNPs, (B) C18PMH-PEG-FA-functionalized UCNPs, (C) DOX loading, and (D) release of DOX from UCNPs triggered by decreasing pH. *Reproduced with permission from Wang et al. (2011a) © 2011 Elsevier B.V.*

emissions, and narrow absorption and emission bands (Yang, 2014). However, UCNPs do not offer high luminescence quantum yield (LQY). LQY is defined as the ratio of photons absorbed to photons emitted. Higher values of LQY translate into an improvement of the signal-to-noise ratio in the optical imaging technique and allow for ease in detection and lower detection limits (Zhou et al., 2012). van Veggel and colleagues reported LQYs in the range of 0.005–0.3% for $NaYF_4:Er^{3+}$ (2 mol%)/$Yb^{3+}$ (20 mol%) nanoparticles with particle sizes ranging from 10 to 100 nm. These LQYs are considerably low in comparison with the LQY of 3% of bulk samples (Boyer and Van Veggel, 2010).

The low LQY is related to two effects: (i) the non-radiative decay of the surface emitting centers by the presence of surface defects and (ii) vibrational deactivation from solvents and capping ligands when UCNPs are dispersed in solution. As the size of the nanoparticles is decreased, there is a significant increase of the surface area, as well as an increase in the number of surface defects and higher number of capping ligand molecules, causing the decrease in the luminescence efficiency. This was demonstrated by Wang et al. in the study of the surface quenching effect observed in different sizes (10, 15, and 25 nm) of $NaGdF_4:Tm^{3+}/Yb^{3+}$ nanoparticles (Wang et al., 2010b). Larger size nanoparticles offer higher efficiencies; however, they are no longer suitable for *in vivo* imaging.

The highest upconversion efficiencies have been reported for the hexagonal-phase $NaYF_4$ host. Different approaches to induce transformation of the cubic phase to the hexagonal counterpart have been reported based on the control of the temperature, reaction time, or annealing treatments (Mai et al., 2006; Wei et al., 2006; Zhang et al., 2009). An alternative

technique to induce the phase transition from cubic to the hexagonal structure is through the introduction of $Gd^{3+}$ and $Ti^{4+}$ dopant ions that disrupt the symmetry and favor the hexagonal crystal growth (Wang et al., 2010a; Zhang et al., 2011). Other efforts have focused on the development of nano-sized upconverting hosts. For example, Prasad and colleagues demonstrated that $NaYbF_4:Tm^{3+}$ nanoparticles showed NIR upconversion with an intensity $3.6 \times$ higher (per nanoparticle) than the analogue in size $NaYF_4:Tm^{3+}/Yb^{3+}$ nanoparticles due to the larger number of donor ions ($Yb^{3+}$) (Wang et al., 2010a).

## 3.1 Core–Shell Structures

As previously mentioned, emitting centers located at the surface of the nanoparticle are quenched through non-radiative decay pathways via the high vibrational phonons of the capping ligands and solvent molecules, as well as by the presence of surface defects. It was demonstrated by Ghosh et al. that by using a shell to cover the surface emitting ions, this type of quenching is significantly decreased (Ghosh et al., 2008).

Several methods have been developed for the preparation of core–shell nanostructures in the efforts to enhance luminescence efficiency of the UCNP emissions:

**(a)** Seed-mediated shell growth

In this method, a homogeneous inorganic shell is grown onto core nanoparticles. In order for this core–shell growth process to occur, core "seed-particles", which are isotropic in geometry, must have a small lattice mismatch with the shell material. In contrast, if the lattice mismatch is too large, non-epitaxial growth will occur resulting in hybrid structures, also referred to as nanocomposite materials (Feng et al., 2013). The limitation of this method is related to independent nucleation events. The shell may present an anisotropic growth (Liu et al., 2013b).

**(b)** Self-focusing by Ostwald ripening

This epitaxial growth technique is based on the physical phenomenon of ripening in colloids to grow shells. In this method, small sacrificial nanocrystals (SNC, $\sim 5$ nm) are injected as shell precursors into a hot solution of larger core nanocrystals ($>15$ nm). The rapid dissolution of the SNCs favors the rapid deposition of material on the larger core particles (self-focusing) and the yield of core–shell nanostructures. Shell thickness may be tuned via optimization of the concentration of SNCs (Johnson et al., 2012).

**(c)** Shell formation via surface cation exchange

van Veggel and colleagues first reported the use of this method to synthesize $GdF_3/LnF_3$ ($Ln = La^{3+}$, $Eu^{3+}$) core–shell structures. The process is based on the exchange of $Gd^{3+}$ in $GdF_3$ with $Ln^{3+}$ cations present in the reaction solution. This process is favorable for $Ln^{3+}$ ions since they have

high hydration energies and the diffusion of $Ln^{3+}$ in the fluoride hosts is almost inhibited due to the high lattice energies of the lanthanide fluorides. This method offers the possibility to generate shells in the range of a monolayer thickness (Dong and Veggel, 2009).

Subsequently, the same group introduced improvements to the procedure. The authors reported the synthesis of multifunctional $NaYF_4:Tm^{3+}/Yb^{3+}@NaGdF_4$ core–shell nanoparticles that exhibit upconverting and magnetic properties with a shell thickness that is tunable to sub-nanometer dimensions (Johnson et al., 2012).

### 3.1.1 Homogeneous Core@Shell

A homogeneous core@shell nanostructure consists of an undoped shell surrounding a doped upconverting core. Both core and shell are prepared with the same material (Dacosta et al., 2014). Lezhnina et al. reported the synthesis of $LnF_3:Ho^{3+}$, $Yb^{3+}$ ($Ln=La^{3+}$, $Gd^{3+}$, $Lu^{3+}$)@$LaF_3/La_{0.8}Yb_{0.2}F_3$ and demonstrated the conservation of the luminescence properties in the presence of the shell (Lezhnina et al., 2006).

Chow and colleagues developed $NaYF_4:(Er^{3+}/Tm^{3+}),Yb^{3+}@NaYF_4$ core@shell nanoparticles with an average particle size of 11 nm and a shell thickness of 1.5 nm on average. It was demonstrated that an enhancement effect by a factor of 7.4 was observed in co-doped $Er^{3+}/Yb^{3+}$ NPs. This enhancement factor increased to 29.6 for $Tm^{3+}/Yb^{3+}$ co-doped particles (Yi and Chow, 2006a). The LQY of the $NaYF_4:Er^{3+}/Yb^{3+}@NaYF_4$ core–shell (30 nm) NPs was determined to be 0.3%, following 980 nm excitation (150 W/cm$^2$), approximately $3\times$ higher than the value observed for the core-only NPs (Boyer and Van Veggel, 2010).

Typically, the formation of core–shell structures is characterized by an increase in the size distribution by TEM and dynamic light scattering (DLS), enhancement of the absolute intensity, and longer decay times (Chen et al., 2014a).

### 3.1.2 Heterogeneous Core@Shell

A heterogeneous core–shell nanostructure consists of an undoped shell and a doped core. Moreover, the core and the shell comprised different materials. In order to grow a heterogeneous layer, the shell host matrix requires having a small lattice mismatch with the core host matrix (Chen et al., 2014a).

Using heterogeneous core–shell nanostructures opens the possibility to carry out two types of imaging modalities such as MRI and optical imaging (OI) using the same core@shell luminescent probe as, for example, in the case of $NaYF_4:Er^{3+}$ ($Tm^{3+}$)/$Yb^{3+}@NaGdF_4$. The doped core provides the capability to carry out luminescence for OI purposes, while the large number of $Gd^{3+}$ present on the shell surface can be used in MRI imaging (Chen et al., 2011b; Johnson et al., 2012).
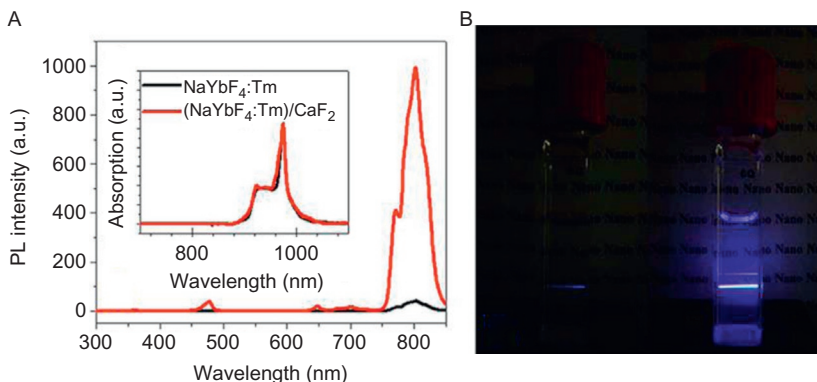
**FIGURE 19** (A) Emission spectra of NaYbF$_4$:Tm$^{3+}$ and NaYbF$_4$:Tm$^{3+}$/CaF$_2$ under 975-nm irradiation. Inset: absorption spectra normalized to the $^2$F$_{7/2}$→$^2$F$_{5/2}$ transition of Yb$^{3+}$ ion. (B) Photography of luminescence of (left) core NaYbF$_4$:Tm$^{3+}$ and (right) NaYbF$_4$:Tm$^{3+}$/CaF$_2$ in hexane under 975-nm irradiation. *Reproduced with permission from Xu et al. (2012), © 2012 MDPI AG.*

Xu et al. reported the enhancement of the luminescence of NaYbF$_4$:Tm$^{3+}$ (Ho$^{3+}$) using CaF$_2$ as a shell host matrix (Fig. 19) (Xu et al., 2012). It was found that using CaF$_2$ results in higher upconverting emissions as the shell provides better separation from aqueous media.

This type of core–shell structure can be characterized by TEM due to the difference in contrast given by the heterogeneity of the materials comprising the core and the shell.

### 3.1.3 Active-Core@Active-Shell

Another approach to enhance upconversion luminescence is by introducing lanthanide dopant ions in the shell layer. The most common dopant ion used for this purpose is Yb$^{3+}$. Using a doped shell not only minimizes the non-radiative deactivation brought about by surface defects, but also enhances the luminescence via energy transfer from the dopant ions in the shell as was demonstrated by Capobianco and colleagues, who reported the synthesis of NaGdF$_4$:Er$^{3+}$/Yb$^{3+}$@NaGdF$_4$:Yb$^{3+}$ active-core@active-shell nanoparticles. A significant enhancement of the luminescence was achieved in comparison with NaGdF$_4$:Er$^{3+}$, Yb$^{3+}$@NaGdF$_4$ (active-core/inert shell) and NaGdF$_4$:Er$^{3+}$, Yb$^{3+}$ nanoparticles (Fig. 20) (Vetrone et al., 2009).

Other systems such as LaPO$_4$:Er$^{3+}$@LaPO$_4$:Yb$^{3+}$ nanorods (Ghosh et al., 2008), BaGdF$_5$: Er$^{3+}$, Yb$^{3+}$@BaGdF$_5$: Yb$^{3+}$ (Yang et al., 2011), and BaF$_2$: Ln$^{3+}$@ SrF$_2$: Ln$^{3+}$ (Ln$^{3+}$ = Tm$^{3+}$, Yb$^{3+}$, Nd$^{3+}$, Gd$^{3+}$) (Chen et al., 2012a) nanoparticles have been investigated showing significant enhancement of upconversion luminescence due to the active shell doping approach.
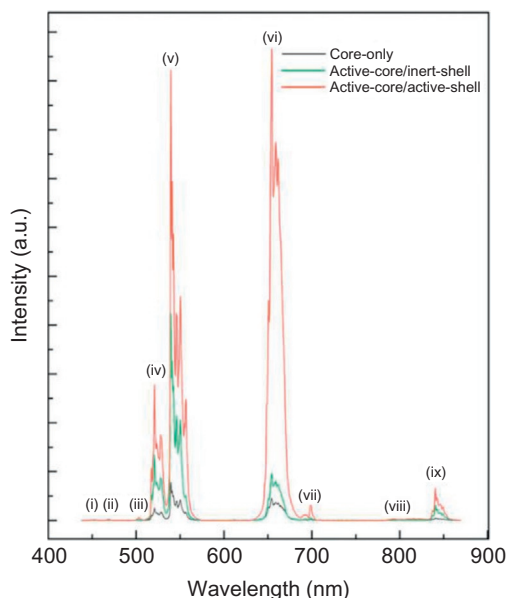
**FIGURE 20** Upconversion luminescence spectra of $NaGdF_4:Er^{3+}$, $Yb^{3+}$ (Core-Only), $NaGdF_4$: $Er^{3+}$, $Yb^{3+}$@ $NaGdF_4$ (active-core@inert-shell), and $NaGdF_4:Er^{3+}$, $Yb^{3+}$@$NaGdF_4$: $Yb^{3+}$ (active-core@active-shell) nanoparticles dispersed in toluene ($\lambda_{exc} = 980$ nm). Labeled emissions: (i) $^4F_{5/2} \rightarrow {}^4I_{15/2}$, (ii) $^4P_{3/2} \rightarrow {}^4I_{11/2}$, (iii) $^4F_{7/2} \rightarrow {}^4I_{15/2}$, (iv) $^2H_{11/2} \rightarrow {}^4I_{15/2}$, (v) $^4S_{3/2} \rightarrow {}^4I_{15/2}$, (vi) $^4F_{9/2} \rightarrow {}^4I_{15/2}$, (vii) $^2H_{9/2} \rightarrow {}^4I_{11/2}$, (viii) $^4I_{9/2} \rightarrow {}^4I_{15/2}$, and (ix) $^4S_{3/2} \rightarrow {}^4I_{13/2}$. *Reproduced with permission from Vetrone et al. (2009), © 2009 Wiley VCH.*

## 3.2 Metal Enhancement

The use of surface plasmon resonance (SPR) effects present in nano-sized metallic structures has been proposed to enhance the upconversion luminescence of UCNPs. SPR is the collective oscillation of electrons at the interface of metallic structures produced by the electromagnetic interaction of the metal with an incident light of a specific wavelength (Jain et al., 2008). SPR is a small particle effect and is not observed in single metal atoms or in their bulk forms. SPR of metallic nanoparticles give rise to strong electromagnetic fields that when coupled with UCNPs may be boost the efficiency of the upconversion process (Darvill et al., 2013; Han et al., 2014).

Three approaches have been reported to achieve enhancement of upconversion luminescence:

**(a)** Lanthanide-doped UCNPs have been deposited on metallic films, dense metal nanoparticles (Ag or Au), or on 3D plasmonic antennas. By using these deposition methods, the upconversion luminescence may be enhanced by a factor of 5 to 310 (Paudel et al., 2011; Saboktakin et al., 2012; Zhang et al., 2011).

**(b)** Covalently bonded or self-assembled metallic nanoparticles onto the surface of lanthanide-doped UCNPs have also been investigated (Kannan et al., 2013; Zhang et al., 2010b; Zhao et al., 2012). Schietinger et al. demonstrated that coupling of $NaYF_4:Er^{3+}/Yb^{3+}$ with Au nanoparticles resulted in an enhancement of $3.8\times$ of the absolute luminescence intensity (Schietinger et al., 2010).

**(c)** Development of metallic/silica/UCNPs or UCNPs/silica/metallic core/shell/shell nanoparticle systems resulted in enhancement of the overall intensity amounting to 4- to 10-fold may be observed (Ge et al., 2013; Xu et al., 2012; Zhang et al., 2010a). Plasmon-induced enhancement is attributed to the increase of the radiative rate and/or the excitation intensity of the surface plasmon resonance. However, there are reports of plasmon-induced quenching due to resonance energy transfer and/or the absorption by the metallic nanoparticle of the light emitted by the UCNP. This quenching is mostly observed when both nanostructures are in direct contact or are within a critical distance apart, less than 5 nm. Therefore, the introduction of a spacer, such as a silica shell, and the control of the distance separating the UCNP and the metallic nanoparticle are required (Dulkeith et al., 2002).

## 4 BIOASSAYS AND BIOSENSING

The excellent upconversion luminescence properties observed upon NIR irradiation of lanthanide-doped nanoparticles have attracted the attention of different research fields including biology, biochemistry, and medicine. UCNPs have been proposed as optical sensors since the luminescence is activated at excitation wavelengths that do not induce the fluorescence of other biological species in tissue and organs (Fig. 21), hence circumventing the autofluorescence phenomenon. This facilitates the identification of biochemical entities and molecular targets, as well as the monitoring of fundamental physiological process that may be targeted by UCNPs.

## 4.1 Biosensing

UCNPs have been investigated as biosensors in order to detect change-based variation of the luminescence intensity in biological environments. This was carried out in samples at different temperatures, or via Förster resonance energy transfer (FRET) mechanisms occurring between UCNPs and indicator dyes conjugated to biochemical entities such as enzymes, antibodies, or polynucleotides (Chen et al., 2014a).

### 4.1.1 Nanothermometry: Sensing the Temperature of Cells

As mentioned above, UCNP luminescence properties are sensitive to temperature, as in the case of $Er^{3+}$, a commonly used activator ion. The intensity ratio between the $^2H_{11/2} \rightarrow {}^4I_{15/2}$ (centered at $\sim$520 nm) to the $^4S_{3/2} \rightarrow {}^4I_{15/2}$
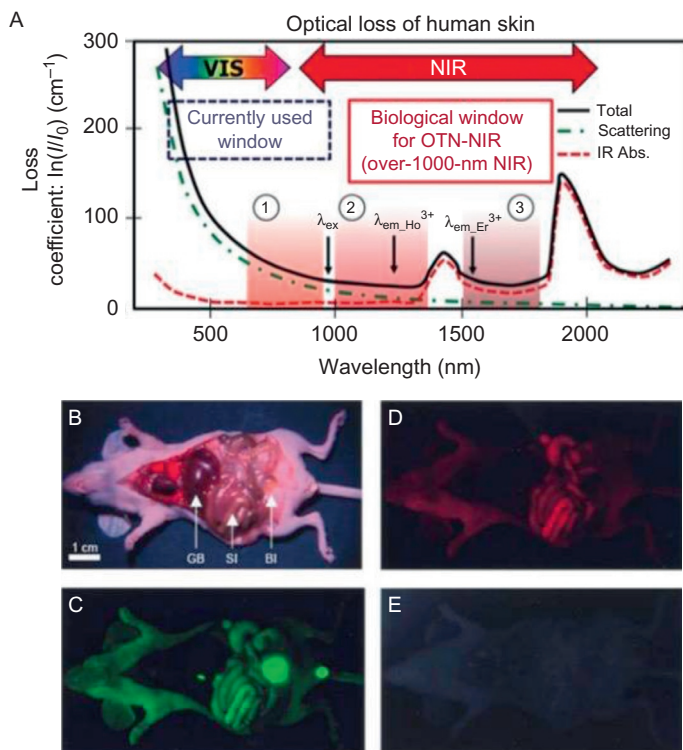
**FIGURE 21** (A) Absorption spectrum of human skin. It shows the first, second, and third biological window and potential NIR excitation (980 nm) and NIR emission wavelength ranges ($Ho^{3+}$:1.2 μm, $Er^{3+}$: 1.55 μm). (B) Image of the viscera of an athymic nude mouse taken immediately after sacrifice. The arrows indicate the location of gall bladder (GB), small intestine (SI), and bladder (Bl). Tissue autofluorescence was imaged using three different excitation/emission filter sets; (C) (460–500/505–560 nm); (D) (525–555/590–650 nm); and (E) Near-infrared (NIR) (725–775/790–830 nm). *Panel (A) reproduced with permission from Hemmer et al. (2013) © 2013 Royal Society of Chemistry. Panels (B–E) reproduced with permission from Frangioni (2003) © 2003 Elsevier B.V.*

(centered at ∼550 nm) transitions is highly sensitive to changes in temperature. The relation governing the $I_{520}/I_{550}$ intensities ratio and the temperature is given in Eq. (5), where $k_B$ is the Boltzmann constant, $\Delta E$ is the energy gap between the two excited levels, and A is a constant that depends on the lifetimes of both levels.

$$\frac{I_{520}}{I_{550}} = Ae^{\left(-\frac{\Delta E}{k_B T}\right)} \tag{5}$$

Vetrone et al. first reported on the use of UCNPs as nanothermometers based on the ratiometric relationship between these two levels in the erbium

ion. PEI-coated $NaYF_4$:$Er^{3+}$/$Yb^{3+}$ nanoparticles were incubated with HeLa cervical cells. The authors showed that it was possible to determine the internal temperature of cancer cells, through spectroscopic measurements, in the biological range of 25–45 °C (Vetrone et al., 2010b).

Wolfbeis and colleagues showed that core–shell $NaYF_4$: (2 mol%) $Er^{3+}$/ (20 mol%) $Yb^{3+}$@$NaYF_4$ can also be used as a temperature sensor with higher brightness and the capacity to resolve temperature differences lower than 0.5 °C in the same biological range (Sedlmeier et al., 2012).

### 4.1.2 Detection of Metal Ions

Due to the availability of a large number of ligands for surface modification to the UCNPs, conjugation of organic dyes to the UCNPs can be carried out and opens up the possibility for imaging and detection of metal ions such as $Hg^{2+}$ for example. This detection capacity is based on a FRET mechanism between UCNPs (donor) and an ion-detector organic dye (acceptor). In the presence of the targeted ion, the upconversion luminescence intensity will change due to the energy transfer to the organic dye (Chen et al., 2014a).

Mercuric ion, $Hg^{2+}$, is the most stable form of mercury that is converted by microbial biomethylation into methylmercury in aquatic sediments. This toxic heavy metal is then included in the food chain, and its accumulation in the human body has been proved to cause damage to the central nervous system (Cotton et al., 1999). Liu et al. reported the conjugation of ruthenium complex N719 ($C_{58}H_{86}N_8O_8RuS_2$) to the surface of $NaYF_4$: (0.4 mol%) $Tm^{3+}$/(1.6 mol%) $Er^{3+}$/(20 mol%) $Yb^{3+}$ to detect and image $Hg^{2+}$ in aqueous solutions and in living cells, reporting a level of detection as low as 1.95 ppb. This achieved limit of detection is lower than the maximum level (2 ppb) of $Hg^{2+}$ established by the U.S. EPA (Liu et al., 2011a).

The development of sensors based on UCNPs for the detection of ions is illustrated by many examples: $Cr^{3+}$, in urine, as a biological marker to environmental exposure (Liu et al., 2013a), $Cu^{2+}$ as essential trace element for many biological processes and a significant environmental pollutant (Zhang et al., 2012a), and ions with important roles in biological functions such as $Na^+$ and $Ca^{2+}$ (Xie et al., 2012).

## 4.2 Bioassays

Bioassays are biochemical tests that are used to detect the presence and measure the concentration of biomolecules. Different organic dyes have been used for the development of these bioassays; however, they do not offer the same advantages as offered by upconversion luminescence in UCNPs. Using the latter, the signal of the background luminescence is greatly reduced, offering lower limits of detection (Chen et al., 2014a; Dacosta et al., 2014).

There are two types of assays (Chen et al., 2014a):

**(a)** Heterogeneous assays: In this type of assay, biofunctionalized capture molecules are immobilized on a solid substrate. They involve multiple steps, namely, analyte addition, washing, and separation steps.
**(b)** Homogeneous assays: These assays are prepared by mixing the analytes and receptors in the same solution; this approach, based on FRET, is considered to be faster and simpler.

### 4.2.1 Heterogeneous Assays

These assays are subdivided into two categories (Chen et al., 2014a):

**(a)** Noncompetitive or "sandwich" assays: The immobilized capture molecules are able to detain the analyte, followed by the conjugation with functionalized UCNPs present in the solution. Following removal of all free non-captured species, measurement of the luminescence intensity may be related to the concentration of UCNPs coupled with the analyte and hence the concentration of the analyte (Fig. 22A). The optical response is therefore proportional to the concentration of the analyte.
**(b)** Competitive assays: In these protocols, competition between free analytes and UCNPs conjugated with analytes is initiated. Based on a calibration curve reflecting the intensity of the upconversion luminescence versus the concentration of the analyte, the concentration of the latter can be determined (Fig. 22B). The optical response is inversely proportional to the concentration of the analyte.
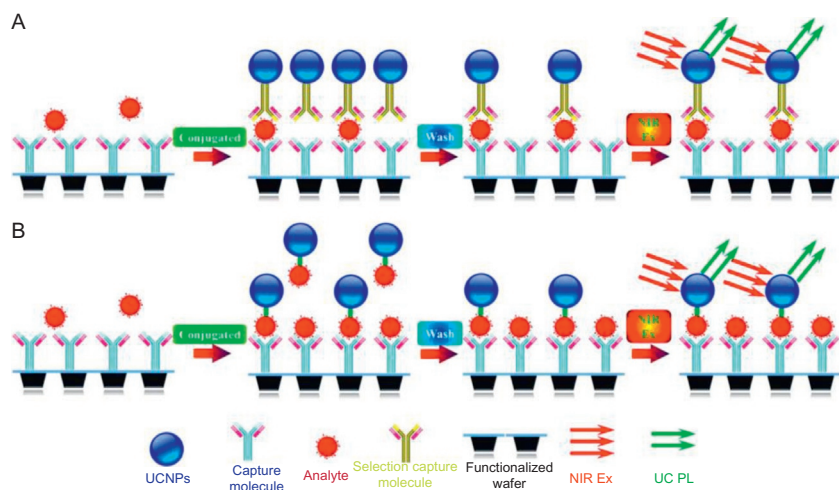


**FIGURE 22** Scheme of heterogeneous assays based on UCNPS: (A) noncompetitive assay and (B) competitive assay schema. *Reproduced with permission from Chen et al. (2014a) © 2014 American Chemical Society.*

Submicrometer-sized upconverting particles were first used to develop hetero-geneous assays for the detection of biomolecules such as prostate-specific antigen (Zijlmans et al., 1999), human chorionic gonadotropin (Hampl et al., 2001), DNA (Corstjens et al., 2001), and nucleic acids (Rijke et al., 2001). Later on, Li reported the use of sub 50-nm $NaYF_4:Er^{3+}/Yb^{3+}$ for the detection of DNA with a limit of detection of 10 nM without polymerase chain reaction (PCR) amplification (Wang and Li, 2006).

Duan et al. reported the detection of *Salmonella typhimurium* and *Staphy-lococus aureos* with limits of detection of 5 and 8 cfu mL$^{-1}$ respectively, using $NaYF_4$ UCNPs and amine-functionalized $Fe_3O_4$ nanoparticles. The authors reported that with magnetic separation and concentration effect of $Fe_3O_4$ nanoparticles, as well as the high sensitivity of UCNPs and the differ-ent emission lines, this method had higher sensitivity and selectivity for the two types of bacteria in comparison with the currently used plate-counting method (Duan et al., 2012).

### 4.2.2 Homogeneous Assays

Homogeneous assays operate on a distance-dependent FRET mechanism between the capture-conjugated UCNP energy donor and an acceptor mole-cule for detection of analytes in solution. When both species are located within a distance greater than 10nm, no detectable FRET signal can be observed. Upon entering in close proximity (distances < 10 nm), the FRET mechanism is favored, and the optical signal can be related to the identifica-tion and concentration of the analytes in solution (Chen et al., 2014a).

First, homogeneous arrays made use of micro-sized upconverting particles (Kuningas et al., 2005). However, this system was not stable in aqueous envir-onments and particles were observed to precipitate during analysis. Zhang et al. showed that the use of small-sized oligonucleotide modified UCNPs to detect DNA can be successfully carried out with a reported limit of detec-tion of 1.3nM (Zhang et al., 2006a).

Kumar et al. reported an improved homogeneous assay for the detection of DNA hybridization based on $NaYF_4:Tm^{3+}/Yb^{3+}$ and an intercalating dye SYBR Green I. Detection of perfectly matched target DNA with a detection limit of 20 fmol could be achieved, as well as the ability to distinguish targets with single-nucleotide variations (Kumar and Zhang, 2009).

## 5 APPLICATIONS IN IMAGING

### 5.1 Imaging

Imaging is an important biomedical tool that has been shown to be useful for early detection, screening, and image-guided therapies of various types of dis-eases (Prasad, 2003). UCNPs offer multiple advantages over other available luminescent probes previously discussed. The excitation wavelengths of

UCNPs lie within the first biological optical transparency window— 650–1000 nm (see Fig. 21A) allowing deeper light penetration, reduced light scattering, and lower autofluorescence in tissues (Chen et al., 2014a,b; Dacosta et al., 2014). Due to these attractive properties, an increase in the number of UCNP publications and review articles has been observed, particularly in areas concerned with cellular and whole animal body imaging (Chen et al., 2014a,c, 2015; Han et al., 2014; Lim et al., 2015; Liu et al., 2014a,b; Sun et al., 2014; Van Veggel, 2014; Wang and Zhang, 2014; Wei et al., 2014; Zhang et al., 2014; Zhou et al., 2015).

### 5.1.1   In vitro *Imaging*

*In vitro* imaging of living cells is dependent on the cellular uptake of the UCNPs by the cells. There are three active processes in which nanoparticles may be uptaken by living cells, namely, phagocytosis, pinocytosis, and caveolin-dependent endocytosis, also referred as clathrin-mediated endocytosis (Zhu et al., 2013). The latter is most commonly reported as the main cellular uptake mechanism observed (Chen et al., 2014a).

The cellular uptake of nanoparticles is dependent on their physicochemical properties including their charge, size, and the nature of the capping ligands (He et al., 2010). Since the cellular membrane has a net negative charge, the uptake of nanoparticles with positively charged surfaces is usually favored. In terms of size, nanoparticles smaller than 50nm are usually uptaken in a more efficient manner (Jin et al., 2008). In addition, the nature of the ligand may also facilitate cellular uptake. The use of peptides, aptamers, affibodies and antibodies favor receptor-mediated endocytosis. Other factors such as purity, chemical composition, aggregation, nanoparticles–protein interactions, nanoparticles–cell incubation conditions, cell types, and cell treatment need to be taken into account in the studies of cellular uptake of nanoparticles (Chen et al., 2014b).

In addition, one must consider that once the nanoparticles trespass the membrane barrier, the capping ligands need to possess chemical characteristics that prevent the nanoparticles from being discarded in the lysosomes, the waste disposal systems of eukaryotic cells. This can be achieved by using ligands such as cationic polymers, transcriptional activators, and amphiphilic peptides for example (Varkouhi et al., 2011).

Chatterjee et al. were pioneers in demonstrating the potential of UCNPs as *in vitro* luminescent probes with the aim of carrying out cellular imaging. The authors used PEI-coated $NaYF:Er^{3+}/Yb^{3+}$ nanoparticles conjugated with folic acid to target HT29 adenocarcinoma cells and human OVCAR3 ovarian carcinoma cells. Both cancer cell lines possess significantly higher numbers of folate receptors on the cellular membrane. The authors demonstrated high fluorescent detection sensitivity of the nanoparticles using continuous-wave infrared laser stimulation (Chatterjee et al., 2008).

UCNPs with no targeting functionalization have also been used to image breast cancer cells (SKBR-3 and MCF-7) (Park et al., 2009), HeLa cells (Cao et al., 2010; Vetrone et al., 2010a), AB12 mouse mesothelioma (Shan et al., 2008), HUH-7 liver cancer cells (Hirotada et al., 2010), and MB49 bladder cancer cells (Zhengquan et al., 2010), which all reported cellular uptake of UCNPs via endocytosis. However, Jin et al. demonstrated that cellular uptake efficiency is improved by using positively charged PEI-coated UCNPs due to the higher charge affinity to the cellular membrane (Fig. 23) (Jin et al., 2011).

Later on, targeted functionalized UCNPs were reported for imaging of different cancer cell lines. UCNPs functionalized with bimolecular recognition moieties such as folic acid were used to image human HT29 adenocarcinoma cells, human cancer colon cells, HeLa cells, and OVCAR3 ovarian carcinoma cells (Chatterjee and Yong, 2008; Liu et al., 2012b; Wang et al., 2011a; Xiong et al., 2009b). Other target moieties used were rabbit anti-CEA8 antibodies for carcinoembryonic antigen and HeLa cells (Wang et al., 2009a) and RGD peptide for human glioblastoma (Zako et al., 2009). These approaches represent a great potential in the improvement of the early detection of cancer in living subjects.
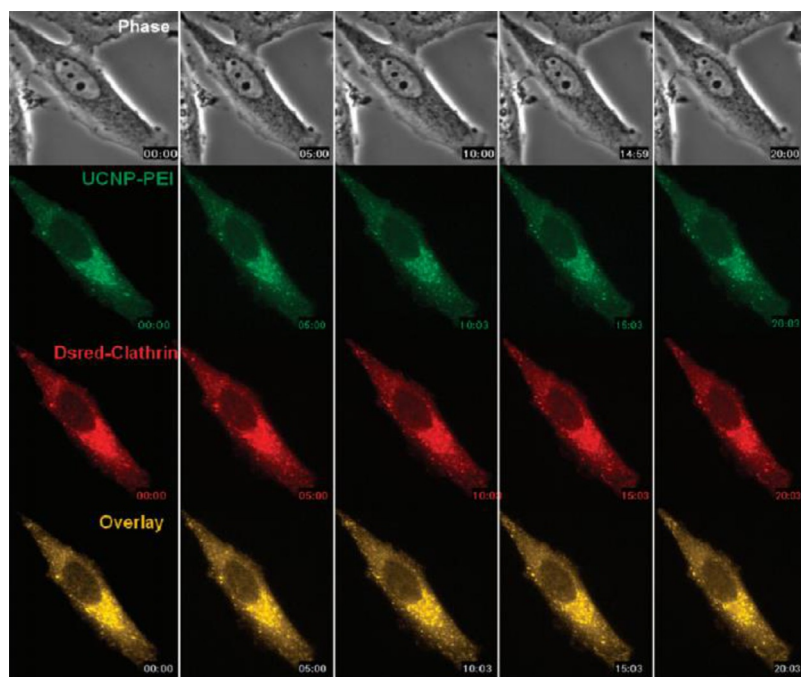


**FIGURE 23** UCNP-PEI (FITC-labeled) uptake through clathrin-mediated endocytosis. HeLa cells transfected with RFP-tagged clathrin for 24 h. After transfection, UCNP-PEI was added subsequently to the culture, and live-cell imaging was started on the motorized stage of the Zeiss Axiovert microscope. *Reproduced with permission from Jin et al. (2011) © 2011 American Chemical Society.*
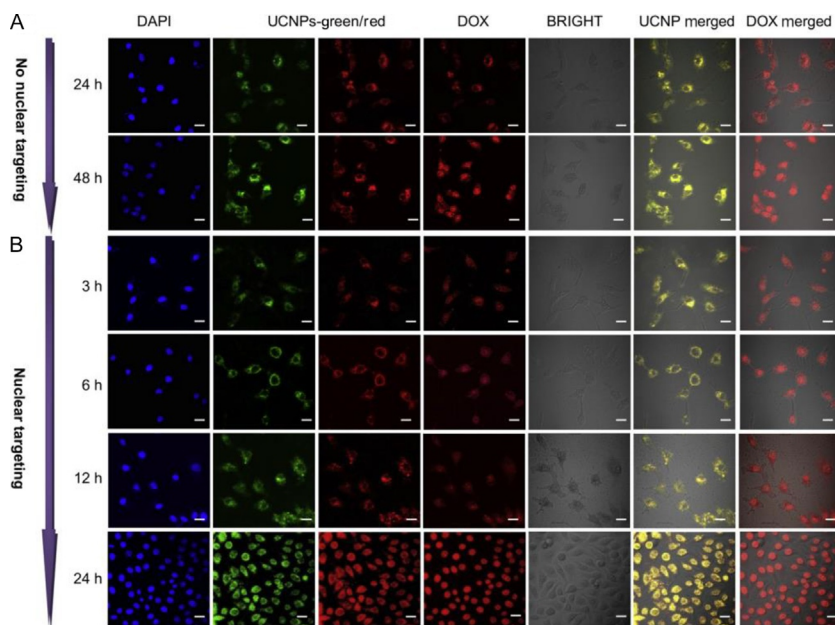
**FIGURE 24** *In vitro* confocal observations of UCNPs and DOX in HeLa cells incubated with DOX-UCNPs-PEG (A) and DOX-UCNPs-PEG/TAT (B) for varied time durations. The blue (gray in the print version) fluorescence is from DAPI used to stain the nuclei. The green (light gray in the print version) and red (dark gray in the print version) emissions (second and third column from the left) are from UCNPs under 980-nm laser excitation, while DOX emits red (gray in the print version) fluorescence (fourth column from the left) under 488-nm laser excitation. DOX loadings are 5 mg/ml for all the particles. Scale bar: 20 μm. *Reproduced with permission from Liu et al. (2012a) © 2012 Elsevier B.V.*

Liu et al. developed multifunctional PEG-NaYF$_4$:Er$^{3+}$, Yb$^{3+}$/NaGdF$_4$ nanoparticles possessing a surface modified with TAT peptide (transactivator of transcription of human immunodeficiency virus) and loaded with DOX, an anticancer drug that targets the cancer cellular nucleus, and proved the possibility of DOX delivery to the nucleus. The authors showed simultaneous magnetic resonance (MRI) and upconversion fluorescence imaging (Fig. 24) (Liu et al., 2012a). For DOX-UCNPs-PEG, UCNPs could be found within the cytoplasm, but not in the nucleus, and DOX accumulated mostly within the cytoplasm with a negligible DOX fluorescence within nuclei in 24 h of incubation. Only after further incubation for another 24 h, DOX could be found diffused into the cell nuclei from the cytoplasm where it is released. For DOX-UCNPs-PEG/TAT, the fluorescence microscopic images show the significant internalization of UCNPs by HeLa cells in 12 h and strong fluorescent emissions from both UCNPs and DOX can be found mostly emanating from the nuclei in 24 h, indicating the effective internalization of the NPs into the cell nucleus.

## 5.1.2 In vivo *Imaging*

The optical properties of UCNPs have attracted considerable attention in the development of novel applications and therapeutic approaches in medicine and biology where they have been principally studied as luminescent probes for *in vivo* imaging. Cheng et al. found that although water-dispersible QDs show quantum yields in the order of 40%, the *in vivo* lowest limit of detection is only 5 nM due to the auto-fluorescence background from biological tissues following excitation with visible light (Cheng et al., 2010). *In vivo* imaging using UCNPs as luminescent probes is typically oriented toward the small animal model. Several studies have made use of mice and rat models to study tumor-targeted imaging, lymphatic and vascular imaging, as well as cell tracking (Zhou et al., 2012).

One important parameter to consider when using UCNPs for *in vivo* imaging is the biodistribution of the luminescent probes inside the body. Austin and colleagues were pioneers in reporting UCNPs as biocompatible luminescent probes. The authors used $Y_2O_3:Er^{3+}/Yb^{3+}$ UCNPs (50–150 nm) to inoculate live nematode *C. elegans* worms. Two photon images show the UCNPs visible in the intestines, pharynx, and the rectum (Fig. 25) (Lim et al., 2005).
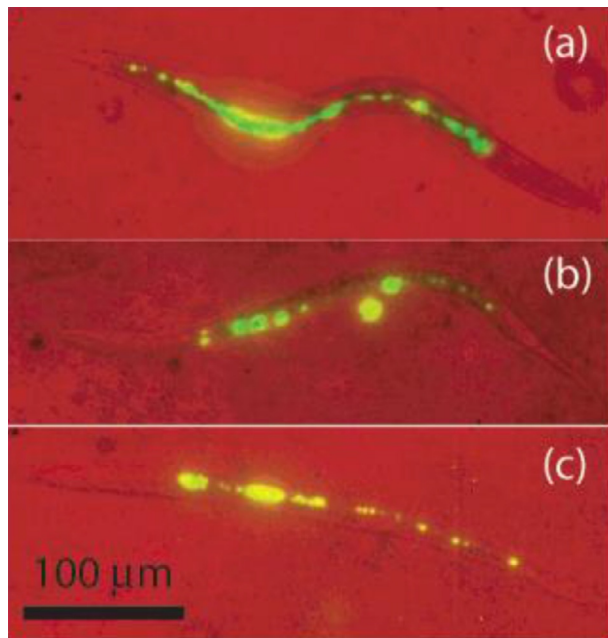


**FIGURE 25** *In vivo* images of *C. elegans*. Red (dark gray in the print version) represents the bright field and green (light gray in the print version) the phosphor emission. Images taken at (A) 0 h, (B) 4 h, and (C) 24 h. *Reproduced with permission from Lim et al. (2005)* © 2005 *American Chemical Society.*

Xiong et al. reported the long-term *in vivo* distribution of PAA-coated NaYF$_4$: Tm$^{3+}$/Yb$^{3+}$ upconverting nanoparticles (PAA-UCNPs $\approx$ 11.5 nm) in athymic nude mice. A concentration of 15 mg/kg body weight of PAA-UCNPs was injected through the tail vain. The results obtained showed that PAA-UCNPs were mostly uptaken and retained in the liver and the spleen. The mice survived up to 115 days without any adverse effect to their health. A slow rate of excretion from the body was also noted. Histological, hematological, and biochemical analysis proved no overt toxicity due to PAA-UCNPs in mice even after the long UCNPs, administration periods (Xiong et al., 2010).

UCNPs have also played a major role in the development of luminescent probes for tumor diagnostics and therapy. Advances in targeted imaging have led to the surface modification of UCNPs with folic acid (FA), antibodies, and peptides. FA is one of the most reported ligands to target tumors. This acid is highly stable, has a non-immunogenic character and may be conjugated with a wide variety of molecules. Moreover, it has been reported that folate receptors are overexpressed in many types of cancer cells (see Section 5.1.1) (Zhou et al., 2012).

Xiong et al. used FA to functionalize 6-aminohexanoic acid-coated NaYF$_4$:Er$^{3+}$/Yb$^{3+}$ nanoparticles through EDC chemistry (EDC: 1-ethyl-3-(3-dimethylaminopropyl)carbodiimide). Folic acid and non-FA-functionalized nanoparticles were injected in athymic nude mice bearing HeLa tumors (tumor size: 0.4–0.6 cm, doses: 160 μg of nanoparticles per animal) through a tail vein injection. After 24 h, a strong upconversion signal was observed following 980 nm irradiation at the tumor site, whereas no obvious signal was observed in the control mouse injected with non-functionalized FA-UCNPs (Xiong et al., 2009b).

The argentine-glycine-aspartic acid (RGD) peptide has a high affinity for the $\alpha_v\beta_3$ integrin receptor. This receptor has been related to tumor angiogenesis (Chen et al., 2004). Li and colleagues conjugated RGD to the surface of PEG-modified NaYF$_4$: Tm$^{3+}$ (0.2 mol%)/Er$^{3+}$ (1.8 mol%)/Yb$^{3+}$ (20 mol%) nanoparticles to image a nude mouse inoculated with human glioblastoma U87MG tumors that overexpress $\alpha_v\beta_3$. The authors reported the detection of an upconversion signal 1 h post injection of the probes and an achievement of a tumor signal-to-noise ratio of 24 (Xiong et al., 2009a). Antibodies such as antiHer2 and rabbit CEA8 have also been conjugated to UCNPs@SiO$_2$ and proved to be good targeting and imaging agents of HeLa cells (Shan et al., 2009; Wang et al., 2009c).

An important route for the metastasis of cancer cells is the local lymphatic drainage. It has been postulated that the identification and blocking of sentinel lymph nodes could lead to the prevention of cancer metastasis (Fidler, 2003). Kobayashi et al. demonstrated two-color imaging of mouse lymph nodes without autofluorescence using CTAB and PEG surface-functionalized NaYF$_4$:Er$^{3+}$ (Tm$^{3+}$)/Yb$^{3+}$, revealing the potential of the UCNPs to identify

only affected lymph nodes (Kobayashi et al., 2009). UCNPs have also been used for vascular imaging. Vascular abnormalities are associated with cardiovascular, kidney, and pulmonary disease (Carmeliet, 2003). To prove the potential of UCNPs for imaging the vascular system, Idris et al. reported the use of $NaYF_4:Er^{3+}/Yb^{3+}@SiO_2$ to track live myoblast cells for the imaging of mouse ear blood vessels (Idris et al., 2009).

## 5.2 Multimodal Imaging

Clinical imaging is a noninvasive tool used for the diagnosis of diseases, characterization of damaged tissues, and the evaluation of treatment efficiencies (Naumova et al., 2014). The following are currently approved and commonly used clinical approaches where UCNPs can find integration and potentially have a strong impact both as luminescent probes and contrast agents (Naumova et al., 2014):

- MRI: uses magnetic fields (0.5–7 T) to polarize the hydrogen nuclei of water molecules in human tissues. Using time-varying gradient magnetic fields and radio frequency pulses is possible to map the spatial distribution of the protons and construct multidimensional images.
- Positron emission tomography (PET): produces images through the detection of biologically active positron-emitting radio tracers (for example: $^{18}$F) conjugated to low-molecular-weight biocompatible molecules.
- X-ray computed tomography (CT): uses computer-processed X-rays to produce tomographic images.

In Table 3, a summary of these aforementioned applications, their respective contrast agents, main characteristics, depth of penetration, sensitivity, resolution, and disadvantages are presented (Naumova et al., 2014).

### 5.2.1 Upconversion Luminescence and MRI

Multimodal imaging agents are developed in order to combine the advantages of two or more imaging techniques. The use of UCNPs for optical imaging offers high sensitivity but poor tissue penetration depth. In contrast, MRI, an approved clinical imaging technique, offers moderate sensitivity but a limitless penetration depth and high spatial resolution. Based on this, imaging research efforts have been oriented toward the development of nano-sized probes that show both upconverting and magnetic properties. These probes are touted as being advantageous for obtaining simultaneous MRI/optical images (Zhou et al., 2012).

Two types of contrast agents are used in MRI: $T_1$-weighted agents that change the spin–lattice relaxation of the protons of water in tissues, usually appearing in images as white zones (positive contrast). In this case, the

**TABLE 3** Characteristics of Clinical Imaging Modalities (Naumova et al., 2014)

| Modality | Applications | Contrast Agents | Main Characteristics | Depth of Penetration | Sensitivity | Image Resolution (voxel size) | Disadvantages |
|---|---|---|---|---|---|---|---|
| MRI | Anatomy, pathology, metabolism, chemical exchange, physiology, function, intervention, cellular, molecular | Iron oxide nanoparticles, $Gd^{3+}$ chelates, Microcapsules with fluorine sodium carbon, Ferritin, Lysine-rich protein, protamine | Versatile, high soft tissue contrast, metabolite concentrations, perfusion, characterization of the microenvironment, short- and medium-term cell tracking, graft size | No limit | Moderate | <1–3 mm$^3$ | Not compatible with patients with implants. Acoustic noise. Specialized coils (^{19}F, [23]Na, ^{13}C) |
| PET | Metabolism Physiology Function Cellular Molecular | [18]FDG, [18]FHBG, [18]FDOPA | Graft proliferation, tissue viability, inducible cell death, longitudinal serial imaging, and differentiation possibilities. | No limit | High | 3–5 mm$^3$ | Ionizing radiation, bio-hazardous labels |
| CT | Anatomy Pathology Intervention Vascular delivery Biopsy | Microcapsules, Barium, Gold Nanoparticles | Multimodal paring with PET, SPECT, bone, lung | No limit | High | <1 mm$^3$ | Ionizing radiation, not suitable for soft tissue imaging |

intensity is dependent on the concentration of water molecules. The second class of agents is $T_2$-weighted agents that change the spin–spin relaxation time. This is observed in MRI images as darkened zones (negative contrast).

The importance of $Gd^{3+}$ ions in MRI imaging is evident through the fact that several $Gd^{3+}$chelates have been developed for imaging in the hospital and clinical settings. In order to develop $T_1$-weighted MRI/optical imaging agents, three strategies have been proposed:

**(a)** Use of $Gd^{3+}$-based hosts

While the host provides the magnetic properties, dopants such as $Er^{3+}$ and $Tm^{3+}$ offer the optical emission centers. Das et al. reported the synthesis of upconverting $Gd_2O_3:Er^{3+}/Tm^{3+}/Yb^{3+}$ nanorods with $T_1$ and specific relaxivity, $r_1$ of 665 ms and 1.5 $s^{-1}$ $mM^{-1}$, respectively. The authors report a good $T_1$-weighted MRI contrast, comparable to the $T_1$ contrast agents commercially available (Das et al., 2010).

Naccache et al. reported the synthesis of water-dispersible small ($\approx 25$ nm) and ultra-small (<5 nm, US) citrate-capped $NaY(Gd)F_4:Tm^{3+}/Yb^{3+}$ nanoparticles. The authors demonstrated that US-NaY(Gd) $F_4:Tm^{3+}/Yb^{3+}$ show superior properties for MRI imaging due to lower relaxometric ratios $r_2/r_1 = 1.18$. US-NaY(Gd)$F_4:Tm^{3+}/Yb^{3+}$ also evidenced long blood retention time in mice (>90 min) and they were eliminated from the body through the reticuloendothelial and urinary systems (Naccache et al., 2013).

**(b)** $Gd^{3+}$ as dopant

Kumar et al. showed that $NaYF_4:Gd^{3+}/Tm^{3+}/Yb^{3+}$ nanoparticles not only possess upconverting luminescence properties but magnetic properties as well that are suitable for MRI. The authors reported a specific relaxivity $r_1 = 0.14$ $s^{-1}$ $mM^{-1}$ (Kumar et al., 2009).

Optimization of the concentration of $Gd^{3+}$ dopant ion in $NaYF_4:Gd^{3+}/Er^{3+}/Yb^{3+}$ was carried out and the authors reported an $r_1$ value of 0.41 $s^{-1}$ $mM^{-1}$ when using 60 mol% of the $Gd^{3+}$ dopant ion (Zhou et al., 2011)

**(c)** Core/$Gd^{3+}$-based shell nanoparticles

Different core/$Gd^{3+}$-based shell nanoparticles have been reported as luminescent probes for optical imaging. Using a $Gd^{3+}$-based shell also provides the required magnetic properties to use these probes as MRI contrast agents. Examples of MRI/Optical hybrid imaging probes are $NaGdF_4:Er^{3+}/Yb^{3+}@NaGdF_4$ ($r_1 = 1.05–1.40$ $s^{-1}$ $mM^{-1}$) (Park et al., 2009), $NaYF_4:Er^{3+}/Yb^{3+}@NaGdF_4$ ($r_1 = 0.48$ $s^{-1}$ $mM^{-1}$) (Hai et al., 2010), and $NaYbF_4:Tm^{3}@NaGdF_4$ ($r_1 = 2.6$ $s^{-1}$ $mM^{-1}$) (Chen et al., 2011b).

In terms of the second class of MRI contrast agents ($T_2$-weighted), the coupling of superparamagnetic iron oxide nanoparticles with UCNPs has opened up the possibility to develop $T_2$-weigthed MRI/optical imaging agents. Chen and colleagues reported a facile approach for synthesizing

$Fe_3O_4$(18.4 nm)@$SiO_2$@$Y_2O_3$: $Er^{3+}$/$Yb^{3+}$ (3.3 nm) nanoparticles with a saturation magnetization of 7.22 emu g$^{-1}$, $r_2$ value of 186.2 s$^{-1}$ mM$^{-1}$, and upconversion luminescence. The amorphous silica shell provides water dispersibility to the iron oxide core maintaining its robust magnetic responsive properties (Yu et al., 2011). Other core–shell systems developed as $T_2$-weigthed MRI/optical imaging agents include NaYF$_4$:$Er^{3+}$/ $Yb^{3+}$@$Fe_3O_4$@Au (Cheng et al., 2011) and $Fe_3O_4$/NaLuF$_4$: $Tm^{3+}$/$Er^{3+}$/ $Yb^{3+}$ (Zhu et al., 2012).

## 5.2.2 Upconversion Luminescence and PET

PET is a nuclear medicine-based imaging technique for the detection of γ-rays emitted indirectly by a positron-emitting radionuclide usually conjugated to small organic molecules. The most used radionuclide is $^{18}$F. PET produces three-dimensional images of the whole body with detection sensitivity below the picomolar range. However, it offers low spatial resolution (∼mm) (Hoff et al., 1996). UCNPs could offer the needed improvement in resolution for getting more anatomical and physiological details (Dacosta et al., 2014; Park et al., 2015; Zhou et al., 2012). The synthetic procedure is based on the inorganic reaction between rare earth cations and fluoride ions. The $^{18}$F-NaYF$_4$:$Tm^{3+}$/$Yb^{3+}$ nanoparticles were evaluated using PET imaging monitoring their *in vivo* distribution as well being able to carry out lymph imaging. The authors state that this facile $^{18}$F-labeling method overthrows the conventional $^{18}$F-labeling methods (Sun et al., 2011).

## 5.2.3 Upconversion Luminescence and X-ray CT

CT is an imaging technique based on computer-processed X-rays to produce tomographic images of specific areas of the body. The use of lanthanide-based nanoparticles as X-ray contrast agents may result in improving the X-ray attenuation coefficient to enhance CT images, due to their higher atomic numbers and K-edge values within the X-ray spectrum (Chen et al., 2014a).

Sun et al. reported the synthesis of US water-dispersible NaGdF$_4$: $Er^{3+}$($Tm^{3+}$,$Ho^{3+}$)/$Yb^{3+}$ (∼5 nm) using a two-phase system via an ionic liquid-based reaction. These nanoparticles proved to be effective contrast agents for *in vivo* optical/CT imaging (Sun et al., 2011). The same group developed FA-conjugated silica-modified LaF$_3$:$Tm^{3+}$/$Yb^{3+}$ nanoparticles for simultaneous targeted optical/CT imaging (Ma et al., 2012).

$Yb^{3+}$-based UCNPs have K-edge energies (∼61 keV) located at the higher intensity edge of the X-ray spectrum at the commonly used voltage in clinical CT (120 KVp) (Chen et al., 2014a). The same group developed folic acid-conjugated, silica-modified LaF$_3$: $Tm^{3+}$/$Yb^{3+}$ nanoparticles for simultaneous targeted optical/CT imaging (Ma et al., 2012). They also demonstrated that PEG-NaYbF$_4$:$Er^{3+}$ has higher X-ray absorption in comparison to Lobitridal and Au-, Pt-, Bi-, or Ta-based nanoparticles (Liu et al., 2012c).

## 5.3 Drug Delivery and Release

### 5.3.1 Chemotherapy

The international Agency for Research on Cancer (IARC) has estimated that by 2030 the number of new cases of cancer reported each year will be around 21.4 million and the number of cancer-related deaths will amount to about 13.2 million (Allen and Cullis, 2004). Nowadays, one of the most used treatments of cancer is chemotherapy. This method employs synthetic molecules and natural products as anticancer agents.

Despite the considerable advances that have been realized in the development of efficient chemotherapeutic agents, challenges still exist concerning drug delivery and release to the body. The main drawbacks of chemotherapeutic agents are their rapid clearance and short blood circulation half-life. As a consequence, the concentration of the agents in the tumors cannot be maintained for long durations (Iyer et al., 2013). Reports have also shown that anticancer drugs lack selectivity to tumor tissues and cells following administration as the drugs diffuse across all types of blood vessels irrigating healthy and tumor tissues causing undesired side effects (Hortobagyi, 1997).

The aforementioned drawbacks underscore the need to develop targeted delivery systems that offer full protection against degradation of chemotherapy agents in the blood stream. The use of UCNPs has been proposed as a potential avenue to explore improved approaches toward drug delivery. There are two major methods of UCNP-mediated drug delivery: (i) Change in pH medium and (ii) bond cleavage by UV light produced *in situ* by the emission of UCNPs (Shanmugam et al., 2014).

In the first method, the chemotherapeutic drug is accommodated on the surface of the UCNPs or encapsulated inside a mesoporous silica shell grafted on the surface of the nanoparticles. The drug is retained by the interaction with the surface ligand capping the UCNPs. Through a change in pH (especially to low pH), the drug can be protonated, and consequently released. Thus, UCNPs can be used as the drug carrier and drug delivery can be monitored and its release image-guided (Dong et al., 2011; Hou et al., 2011; Li et al., 2013a; Tian et al., 2012). Some examples of this drug release approach are described below.

Tian et al. reported the synthesis of $NaYF_4$: $Er^{3+}/Mn^{2+}/Yb^{3+}$. Introducing $Mn^{2+}$ resulted in enhancing the red emission of $Er^{3+}$ due to changes in the surroundings of the rare-earth ion and in the cross-relaxation energy between $Er^{3+}$ and $Mn^{2+}$. Thus, they improved the imaging ability of the upconverting nanoparticles. $NaYF_4$: $Er^{3+}/Mn^{2+}/Yb^{3+}$ UCNPs were loaded with Doxorubicin (DOX), a chemotherapy drug, through hydrophobic interaction with the oleate-capped UCNPs and coated with poly(ethylene glycol)-conjugated phospholipid (DSPE-PEG 2000) in order to render them water dispersible. The nanoparticles were injected into mice and *in vivo* imaging was
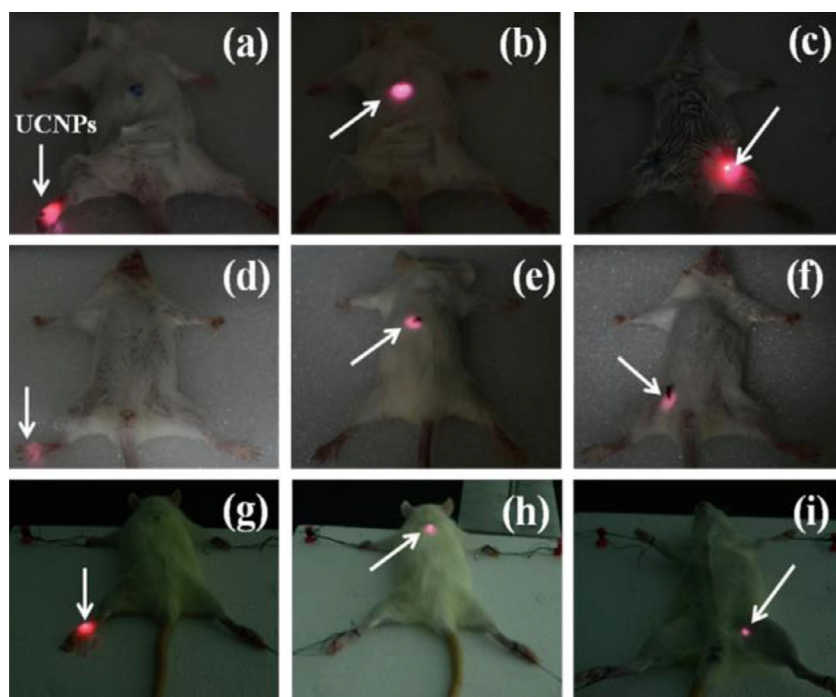
**FIGURE 26** *In vivo* imaging study using DSPE-PEG-DOX-NaYF$_4$: Er$^{3+}$/Mn$^{2+}$/Yb$^{3+}$. The nanoparticles were injected in (A, D, E) translucent foot; (B, E, H) below skin of back and (C, F, G) thigh muscle of mice. Images (A–C) correspond to Kunming mouse with 100 μL of 2.0-mg/mL-modified UCNP; images (D–F) correspond to Kunming mouse with 100 μL of 0.5-mg/mL-modified UCNPs; images (G–I) correspond to S.D. rat with 100 μL of 2.0-mg/mL-modified-UCNPs. *Reproduced with permission from Tian et al. (2012) © 2012 Wiley VCH.*

demonstrated (Fig. 26). Drug release experiments were conducted, *in vitro*, under two pH conditions. For the simulation of the intracellular cancer cell environment, a pH of 5 was used while a pH of 7.4 was used for the healthy cell counterpart. A slow DOX release of approximately 19.1% was observed after 48 h at pH 7.4, whereas a release of 50.5% was measured at pH 5. Finally, A549 cells were treated with DOX-loaded NaYF$_4$: Er$^{3+}$/Mn$^{2+}$/Yb$^{3+}$ nanoparticles. The cells exhibited 10% viability while the survival rate was 30% for the administered free DOX (Tian et al., 2012).

Wang et al. reported the loading of DOX on PEGylated NaYF$_4$:Er$^{3+}$/Yb$^{3+}$ for simultaneous imaging and therapy. They reported the loading of DOX by physical adsorption and its release under slightly acidic pH conditions (Wang et al., 2011a). The same group described the encapsulation of UCNPs together with iron oxide nanoparticles and fluorescent dye and/or DOX via a microemulsion method relying on an amphiphilic block copolymer, poly(styrene-block-allyl alcohol) (PS$_{16}$-b-PAA$_{10}$). Using this multifunctional

nanocomposite system, upconversion luminescence/down-conversion fluorescence and MRI *in vitro* and *in vivo*, as well as, *in vivo* cancer cell tracking in mice were demonstrated (Xu et al., 2011; Zhang et al., 2011).

In the second method, the chemotherapy drug is bonded to a photocleavable group. The drug release is carried out via bond cleavage by the *in situ* UV emission from the UCNPs. The main advantage of this method is that it eliminates the direct exposure to UV light and the photocleavable molecule is used to mask the therapeutic agent preventing unwanted early release and possible side effects (Dacosta et al., 2014; Fan et al., 2012).

Paudel et al. reported the proof-of-concept release of a hydrophobic group by the use of the UV emission (360 nm) of $NaYF_4:Tm^{3+}/Yb^{3+}$ nanoparticles. They demonstrated the photoinduction of the cleavage of *o*-nitrobenzyl group from poly(ethylene oxide)-block-poly(4,5-dimethoxy-2-nitrobenzyl methacrylate) upon 980 irradiation (Paudel et al., 2011). Similarly, Carling et al. described the release of a hydrophilic group (acetic acid) from 3′,5′-di(carboxymethoxy) benzoin cage by using the UV emission of $NaYF_4:Tm^{3+}/Yb^{3+}$-$NaYF_4$ core–shell nanocrystals. The core–shell nanocrystals were surface functionalized with 3′,5′-di(carboxymethoxy) benzoin cage. This cage exhibits an absorption maximum at 282 nm. The authors demonstrated the release of acetic acid following 980 nm irradiation via UV generation *in situ* from the nanocrystals and by using direct 313 nm UV irradiation (Carling et al., 2010).

In another study, $SiO_2$ and 3-aminopropyltriethoxysilane (APTES) coated $NaYF4:Tm^{3+}/Yb^{3+}$ nanoparticles were synthesized. The terminal amine groups were conjugated with a homobifunctional PEG(HOOC-PEG-COOH) and thiolated DOX using *N*-succinimidyl 3-(2-pyridyldithio)-propionate (SPDP) to form a DOX-PEGylatedUCNP@$SiO_2$ nanocomposite. In order to include a targeting ligand, the carboxyl groups in folic acid were masked using the photosensitive cage 2-nitrobenzylamine to form caged folates. Furthermore, the terminal amines of the cages were conjugated with DOX-PEGylatedUCNP@-$SiO_2$ to obtain the caged folate-DOX-PEGlyted UCNP@$SiO_2$. The uptake of the nanosystem was evaluated with HeLa cells (folate receptor-positive) and A549 (folate receptor-negative). The authors demonstrated that by using 980 nm irradiation with a power density of 11 W cm$^{-2}$, the uptake of the nanosystem in HeLa cells was $2.5\times$ greater than in A549. *In vitro* chemotherapy tests showed HeLa cell apoptosis occurred when treated in presence of the nanosystem upon 980-nm excitation. When no irradiation was administered, the cell viability was maintained above 90% (Fig. 27). Finally, the nanosystem was tested *in vivo* following a tail vein injection in mice bearing HeLa cell tumors. A decrease in tumor size was observed in the treated mice after light exposure in comparison with nonirradiated mice (Chien et al., 2013).

### 5.3.2 Photodynamic Therapy

Photodynamic therapy (PDT) is a clinical therapeutic modality that causes the death of cancer cells by producing lethal singlet oxygen species *in situ*. This
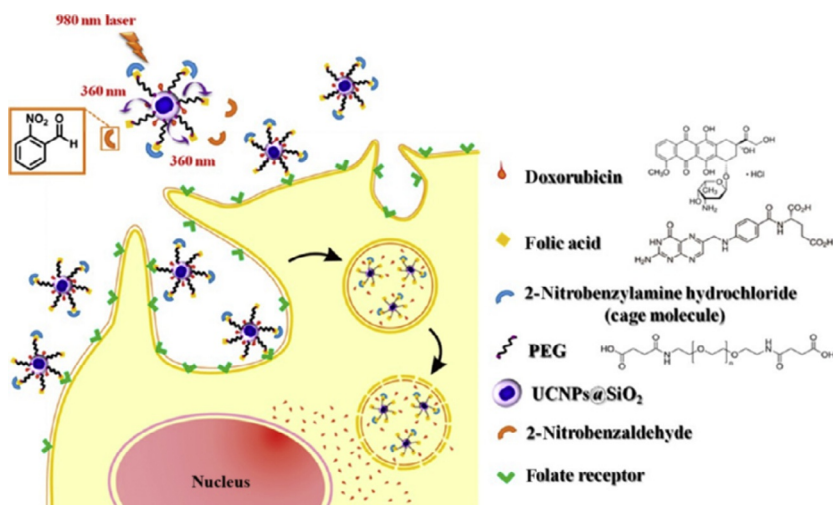
**FIGURE 27** Scheme of the uptake of caged folate-DOX-PEGlyted UCNP@SiO$_2$ by HeLa cells (folate—receptor-positive). The targeting folic acid groups were masked by a UV photocleavable 2-nitrobenzylamine cage to enable the nanosystem to enter into the cells after 980-nm irradiation. *Reproduced with permission from Chien et al. (2013) © 2013 American Chemical Society.*

highly reactive species is generated as a consequence of the excitation of a photosensitizer (PS) with high-energy light such as UV light. Four types of photosensitizers have been approved by the U.S. Food and Drug Administration for clinical use: (i) porphyrin derivatives, (ii) chlorins, (iii) phthalocyanines, and (iv) porphycenes. However, this therapeutic approach method is limited to superficial pathologies due to the poor tissue penetration depth of UV light (Koo et al., 2007; Lucky et al., 2015; Wang et al., 2011b; Yang, 2014).

Significant attention has been directed toward the development of PDT-capable nanoplatforms based on lanthanide-doped UCNPs. Different methods to conjugate PDT agents to UCNPs have been proposed and include the use of (i) electrostatic interactions between carboxyl ligands and the positively charged surface of the UCNPs; (ii) coating a mesoporous silica shell; (iii) -alpha-cyclodextrin; (iv) PEI or PEG adsorbed onto the surface of UCNPs; and (v) chitosan derivatives (Yang, 2014).

Capobianco and colleagues reported the development of nanoconstructs built from LiYF$_4$:Tm$^{3+}$/Yb$^{3+}$ UCNPs and a chlorine-based photosensitizer 5,10,15,20-tetra(m-hydroxyphenyl)-chlorin4–6 (m-THPC, Foscans, Temporfin) conjugated via electrostatic interactions (Fig. 28B). The authors demonstrated the generation of singlet oxygen using the blue light emitted following NIR excitation of the UCNPs. *In vitro* analysis was carried out in HeLa carcinoma cells to confirm the effect of the nanoconstruct on the cells in the absence and presence of irradiation at 980 nm (Fig. 28A). It was found that the nanoconstruct was not toxic towards cells not exposed to light;
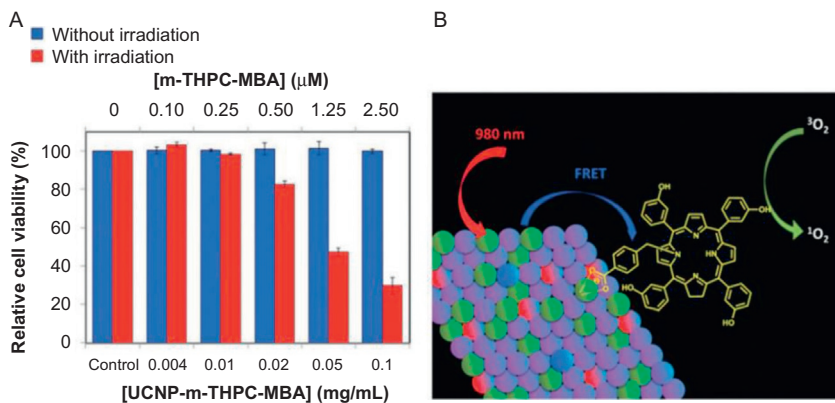
**FIGURE 28** (A) Viability of HeLa cancer cells following incubation with the nanoconstructs and in the presence and absence of NIR irradiation (1-h irradiation; bottom *x*-axis: concentration of the nanoconstruct; top *x*-axis: equivalent concentration with respect to the photosensitizer) (B) schematic illustration of the nanoconstruct. *Reproduced with permission from Yu et al. (2014) © 2014 The Royal Society of Chemistry.*

however, upon 980-nm excitation, the nanoconstruct caused cell death up to 70% (Yu et al., 2014).

Similarly, Wang et al. conjugated β-carboxyphthalocyanince zinc PS to LiYF$_4$:Er$^{3+}$/Yb$^{3+}$. The authors demonstrated an energy transfer efficiency of 96.3% accompanied by a high production rate of singlet oxygen species upon 26 min of NIR irradiation at a power density of 1 W cm$^{-2}$. They also demonstrated the efficiency of this nanoconstruct to inhibit tumor growth *in vitro* and *in vivo* (Wang et al., 2014).

The major disadvantage of using electrostatic interactions between UCNPs and PS are associated with the low number of PS molecules on the surface and the usually easy release from the surface along with PS degradation in the body prior to reaching the targeting site. Zhang and colleagues proposed the encapsulation of PS in a mesoporous silica shell (mSiO$_2$) grafted on the surface of NaYF$_4$:Er$^{3+}$/Yb$^{3+}$. The shell provides protection for the PS and allows for a higher loading of PS molecules. The multicolor emission of UCNPs activates the PS contained in the mSiO$_2$ shell, resulting in enhanced generation of singlet oxygen. *In vivo* studies in melanoma tumor-bearing mice revealed that PS-mSiO$_2$-NaYF$_4$:Er$^{3+}$/Yb$^{3+}$ nanoparticles caused tumor growth inhibition in PDT-treated mice by direct injection of the nanoparticles into melanoma tumors and by intravenous injection of FA-PS-mSiO$_2$-NaYF$_4$:Er$^{3+}$/Yb$^{3+}$ nanoparticles (Idris et al., 2012). Qian et al. reported the synthesis of mSiO$_2$-NaYF$_4$ nanoparticles. The mSiO$_2$ shell had a large surface area of approximately 770 m$^2$ g$^{-1}$ with an average pore size of 2 nm. This shell was used to encapsulate zinc phthalocyanine. The authors demonstrated the efficient production of singlet oxygen as evidenced that the PS loaded was not released from the mSiO$_2$ at any point of the irradiation process (Qian et al., 2009).
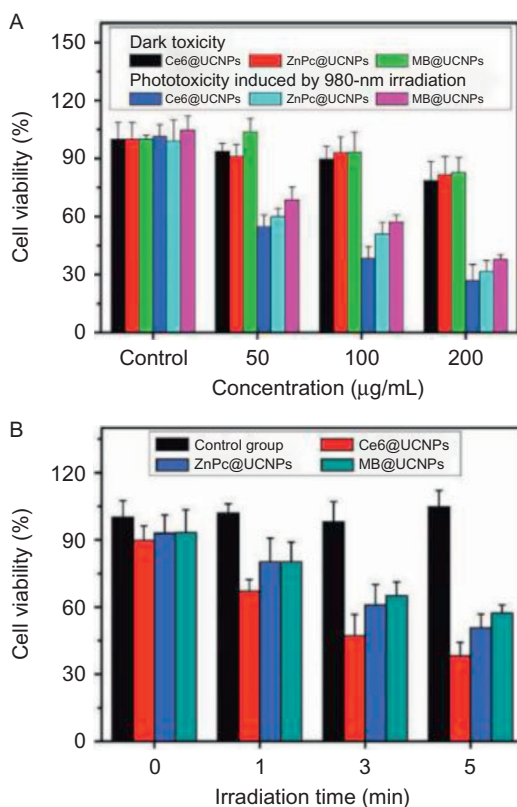
**FIGURE 29** Results of the *in vitro* studies: (A) concentration-dependent cell viability of A-549 cancer cells incubated with Ce6/ZnPc/MB-α cyclodextrin UCNPs (power density: 1 W cm$^{-2}$; irradiation time: 5 min); (B) viability of A-549 cells incubated with Ce6/ZnPc/MB-α cyclodextrin-UCNPs as a function of irradiation time intervals (power density: 1 W cm$^{-2}$; concentration: 100 μg mL$^{-1}$). *Reproduced with permission from Tian et al. (2013) © 2013 Wiley VCH.*

The use of α-cyclodextrin-modified NaYF$_4$:Er$^{3+}$/Yb$^{3+}$ has been proposed for loading chlorine e6 (Ce6), zinc phthalocyanine (ZnPc), and methylene blue (MB). *In vitro* studies demonstrated efficient generation of singlet oxygen upon NIR irradiation via resonance energy transfer from the nanoparticles to the PS (Fig. 29). Furthermore, the authors proposed the use of this system as a combination therapeutic approach with DOX and Ce6 (Tian et al., 2013).

Another approach for the conjugation of photosensitizers to UCNPs involves the use of polymers such as PEI and PEG. These polymers are biocompatible, may be chemically modified, provide water dispersibility, and allow the penetration of O$_2$ and diffusion of singlet oxygen (Ungun et al., 2009). For instance, poly(ethylene glycol-bock-(DL)tartaric acid) block copolymer-coated NaYF$_4$:Er$^{3+}$/Yb$^{3+}$ nanoparticles conjugated to meso-tetraphenyl

porphyrin (TPP) showed efficient HeLa cervical cancer cell-killing activity upon 980 irradiation (Shan et al., 2011).

Finally, chitosan derivatives are also good candidates as linkers between PS and UCNPs due to their good biocompatibility and the resultant water dispersibility. Cui et al. used folate-modified amphiphilic chitosan to coat the surface of $NaYF_4:Er^{3+}/Yb^{3+}$ for anchoring ZnPc. *In vivo* studies demonstrated efficient tumor targeting and therapeutic efficacy with a tumor inhibition rate 50% higher than visible-light-activated PDT (Cui et al., 2013).

### 5.3.3 Photothermal Therapy

This type of therapy is based on heat-generating probes after being exposed to light irradiation. The local temperatures generated reach values as high as 80 °C, the temperature at which tissue ablation occurs. This has been used for thermal ablation of cancer cells.

UCNPs possess a low extinction coefficient, therefore low capability to generate heat. However, by coupling UCNPs with metallic nanostructures, it is possible to develop nanosystems for theranostics proposes in photothermal therapy (PTT; Chen et al., 2014a).

For instance, $NaYF_4:Er^{3+}/Yb^{3+}@Ag$ nanoparticles were incubated with HepG2 cells from human hepatic cancer and BCap-37 cells from human breast cancer. After 980 nm, irradiation-induced death of the cancer cells was observed (Dong et al., 2011) demonstrating the ability of these UCNPs as PTT agent.

Cheng et al. proposed a core@shell@shell system using $NaYF_4:Er^{3+}/Yb^{3+}$ as a core, $Fe_3O_4$ (IONP) as a shell, and an Au layer as the outer shell. The UCNP@IONP@Au nanoparticles were coated with PEG to improve the biocompatibility of the system in physiological solutions. The authors demonstrated *in vivo* dual modal optical/MRI imaging of $4T_1$ tumor-bearing Balb/c nude mice, after injection of PEG-coated UCNP@IONP@Au. Total tumor elimination was reported following NIR laser irradiation (Cheng et al., 2012).

Moreover, the synthesis of $NaYbF_4:Er^{-3+}/Gd^{3+}@SiO_2-NH_2$ nanoparticles decorated with CuS nanoparticles was developed for synergistic PTT and radiotherapy. Following injection of the nanoparticles in $4T_1$ tumor-bearing Balb/c nude mice, and upon 980-nm irradiation, the tumors were eradicated without visible recurrence in 120 days (Xiao et al., 2013).

## 6 CONCLUSIONS AND PERSPECTIVES

The past decades have seen an exponential increase in the number of publications in the field of upconverting nanomaterials attesting to the importance that the research community has placed on this area. The potential for integration in a broad range of applications, specifically in nanomedicine, has stoked the allure. In this chapter, we have provided an account of

lanthanide-doped upconverting nanoparticles with a focus on the mechanisms of upconversion, the choice of the host material and the lanthanide-dopant ions, the various synthetic approaches for their preparation, the different strategies to achieve surface modifications to accomplish hydrophilicity, and finally targeting of specific diseases. We have also presented some innovative examples that have been developed to enhance upconversion including core/ shell architectures.

Lanthanide-doped upconverting nanoparticles offer significant advantages in bioscience and nanomedicine due to their unique ability to convert NIR light to higher energy light such as UV, visible, or even NIR (with a wavelength shorter than the excitation source). Upconversion is a multiphoton process involving the sequential absorption of at least two photons unlike other multiphoton processes that require the simultaneous absorption of two photons. This has an effect on the efficiency of upconversion. For example, in lanthanide-doped nanomaterials, the efficiency is of the order of $10^{-3}$ for ETU and $10^{-5}$ for ESA, whereas for two-photon absorption, it is of the order of $10^{-13}$. Also, it can be achieved using commercially available cheap continuous wave NIR diodes versus high power, ultrafast lasers, which are required for excitation in two photon absorption experiments. In addition, lanthanide-doped upconverting nanoparticles show excellent photo and chemical stability, sharp f–f absorption, and emission peaks with distinguishable fingerprints, non-blinking, non-bleaching, and optical properties that are not sensitive to size. These properties and the use of NIR excitation, which allows for deeper tissue penetration, minimized autofluorescence and reduced photodamage in comparison to UV excitation makes them highly promising candidates for applications in bioscience and nanomedicine. Due to the aforementioned properties, lanthanide-doped upconverting nanoparticles have found widespread integration in novel applications including bioassays, biosensing, optical multimodal bioimaging, light-triggered photoactivation and drug release, photodynamic, as well as PTT. However, there exist a number of challenges before they develop into serious contenders and become an alternative option to the traditionally used organic fluorophores and quantum dots.

Fluoride hosts such as $NaYF_4$, $NaGdF_4$, $LiYF_4$, $CaF_2$, $BaF_5$, and others have been synthesized using a variety of synthesis routes, namely, thermal decomposition, hydro(solvo)thermal, coprecipitation, microwave-assisted ionic liquids, and microemulsion. Although in the more recent publications, excellent progress has been made to provide detailed reaction mechanisms and understanding and insight into the role that solvents, reaction time, and temperature have on the morphology, many questions persist. Challenges with respect to size, shape, surface chemistry, and optical properties need to be addressed before lanthanide-doped upconverting nanoparticles become the premiere choice in biomedical applications.

At the nanometer scale, the surface is a very important parameter that cannot be ignored since the majority of atoms lie there. Therefore, an

understanding of the surface interactions with biological molecules is required since this may not only determine the fate of the nanoparticles in the body but also their efficiency in potential biomedical applications. The low efficiency of the upconversion process must be addressed since this has a direct effect on their luminescence intensity. Therefore, the synthesis of new host materials is required with more efficient upconversion than $NaYF_4$ or $NaGdF_4$. This is not an easy task since it is well known that changes in the local environment of lanthanide ions have very little effect on their extinction coefficient. Other approaches such as interactions with plasmonic nanoparticles (e.g., gold NPs) and energy transfer from organic dyes should be studied. Moreover, the community must forge ahead in the use of theoretical models and methods in order to provide a more critical analysis of the upconversion processes in nanomaterials.

There has also been a flurry of activity in the development of multimodal bioimaging probes based on the combination of different types of imaging modalities (upconversion luminescence/PET/MRI/CT). Multimodal imaging probes provide a number of advantages over a single modality since each probe brings specific advantages and benefits that improve resolution, penetration depth in tissues, and detection limits. Multimodality is not restricted to the use of different imaging techniques since nanoparticles may be modified with multiple molecules on the surface to carry out multiple functions such as detection and therapeutics. Upconverting nanoparticles have also been developed for light-trigged drug release and the important focus has been on tuning the upconversion emission to induce the required *in situ* photochemical reaction to release the drug.

Notwithstanding the many reports on the possible applications of upconverting nanoparticles, the impact of upconverting nanoparticles on health and the environment remains a challenge that must be addressed, one that is often overlooked (Gnach et al., 2015). There are a plethora of other parameters, which may act alone or in concert such as, chemical composition, hydrodynamic size, size heterogeneity, redox properties, tendency for aggregation, surface modifications and surfactants, chemical and colloidal stability, biodegradability, and unknown interactions with other engineered nanoparticles or behavior under electromagnetic field exposure (e.g. heating, photoactivation etc.), which need to be studied.

The combination of different imaging probes, targeting and detection of specific disease, and therapeutics could propel upconverting nanoparticles at the forefront of nanomaterials to become a versatile platform for the generation of nanotheranostic tools in nanomedicine. With the continuously evolving development of novel imaging and detection instrumentation, we are optimistic that upconverting nanoparticles can soon offer high resolution imaging beyond the cellular level. We envision that like MRI and CT, it may also be used for whole organ imaging with high resolutions that would allow for early detection and a greater chance of therapeutic success.

## ACKNOWLEDGMENTS

## LIST OF SYMBOLS

| | |
|---|---|
| $W_{G,Ei}$ | pump rate coefficient |
| $n_G$ | population of the ground state |
| $n_{Ei}$ | population of the $i$-th excited state |
| $\tau_{Ei}$ | lifetime of the $i$-th energy level |
| $\gamma$ | ion pair cooperative upconversion rate coefficient |
| $k_q$ | cross relaxation coefficient |
| $W_{E1,E3}^{th}$ | threshold rate coefficient |
| $k_{nr}$ | rate of non-radiative transition |
| $\hbar\omega_{max}$ | highest vibrational mode |
| $k_B$ | Boltzmann's constant |

## ACRONYMS AND ABBREVIATIONS

| | |
|---|---|
| **cfu** | colony-forming unit |
| **cit$^{3-}$** | trisodium citrate |
| **CT** | charge transfer |
| **CTAB** | cetyltrimethylammonium bromide |
| **DLS** | dynamic light scattering |
| **EDTA** | ethylenediamine tetraacetic acid |
| **ESA** | excited state absorption |
| **ETU** | energy transfer upconversion |
| **FRET** | Förster resonance energy transfer |
| **FWHM** | Full width at half height of the maximum |
| **IR** | infrared |
| **Ln$^{3+}$** | trivalent lanthanide ion |
| **LQY** | luminescence quantum yield |
| **mPEG** | polyethylene glycol monomethyl |
| **MRI** | magnetic resonance imaging |
| **NIR** | near infrared |
| **OI** | optical imaging |
| **PAA** | polyacrylic acid |
| **PBS** | phosphate-buffered saline |
| **PEG** | polyethylene glycol |
| **PEI** | polyethylenimine |
| **PFC** | perfluorocarbon |

| | |
|---|---|
| **PLGA** | poly(lactic-co-glycolic acid) |
| **PS** | photosensitizer |
| **PVP** | polyvinylpyrrolidone |
| **QDs** | quantum dots |
| **SNC** | small sacrificial nanocrystals |
| **SPR** | surface plasmon resonance |
| **TEM** | transmission electron microscopy |
| **TEOS** | tetraethyl orthosilicate |
| **TPA** | two-photon absorption |
| **UC** | upconversion |
| **UCNPs** | upconverting nanoparticles |
| **US** | ultrasmall |
| **UV** | ultraviolet |

# REFERENCES

Alivisatos, A.P., 1996. Semiconductor clusters, nanocrystals, and quantum dots. Science 271 (5251), 933–937.

Allen, T.M., Cullis, P.R., 2004. Drug delivery systems: entering the mainstream. Science 303 (5665), 1818–1822.

Auzel, F., 1966a. C. R. Acad. Sci. (Paris) 262, 1016–1019.

Auzel, F., 1966b. C. R. Acad. Sci. (Paris) 263, 819–822.

Auzel, F., 1973. Materials and devices using double-pumped phosphors energy transfer. Proc. IEEE 61, 758–786.

Auzel, F., 2004. Upconversion and anti-stokes processes with f and d ions in solids. Chem. Rev. 104 (1), 139–174.

Biju, V., Itoh, T., Ishikawa, M., 2010. Delivering quantum dots to cells: bioconjugated quantum dots for targeted and nonspecific extracellular and intracellular imaging. Chem. Soc. Rev. 39 (8), 3031–3056.

Bloembergen, N., 1959. Infrared quantum cutters. Phys. Rev. Lett. 2, 84–85.

Bogdan, N., Vetrone, F., Roy, R., Capobianco, J.A., 2010. Carbohydrate-coated lanthanide-doped upconverting nanoparticles for lectin recognition. J. Mater. Chem. 20 (35), 7543–7550.

Bogdan, N., Vetrone, F., Ozin, G.A., Capobianco, J.A., 2011. Synthesis of ligand-free colloidally stable water dispersible brightly luminescent lanthanide-doped upconverting nanoparticles. Nano Lett. 11 (2), 835–840.

Boyer, J.-C., Van Veggel, F.C.J.M., 2010. Absolute quantum yield measurements of colloidal NaYF$_4$: Er$^{3+}$, Yb$^{3+}$ upconverting nanoparticles. Nanoscale 2 (8), 1417–1419.

Boyer, J.C., Vetrone, F., Cuccia, L.A., Capobianco, J.A., 2006. Synthesis of colloidal upconverting NaYF$_4$ nanocrystals doped with Er$^{3+}$, Yb$^{3+}$ and Tm$^{3+}$, Yb$^{3+}$ via thermal decomposition of lanthanide trifluoroacetate precursors. J. Am. Chem. Soc. 128 (23), 7444–7445.

Boyer, J.-C., Cuccia, L.A., Capobianco, J.A., 2007. Synthesis of colloidal upconverting NaYF$_4$: Er$^{3+}$/Yb$^{3+}$ and Tm$^{3+}$/Yb$^{3+}$ monodisperse nanocrystals. Nano Lett. 7 (3), 847–852.

Boyer, J.-C., Manseau, M.-P., Murray, J.I., Van Veggel, F.C.J.M., 2009. Surface modification of upconverting NaYF$_4$ nanoparticles with PEG−phosphate ligands for NIR (800 nm) biolabeling within the biological window. Langmuir 26 (2), 1157–1164.

Brandes, R., Bers, D.M., 1996. Increased work in cardiac trabeculae causes decreased mitochondrial NADH fluorescence followed by slow recovery. Biophys. J. 71 (2), 1024–1035.

Cao, T., Yang, T., Gao, Y., Yang, Y., Hu, H., Li, F., 2010. Water-soluble NaYF$_4$:Yb/Er upconversion nanophosphors: synthesis, characteristics and application in bioimaging. Inorg. Chem. Commun. 13 (3), 392–394.

Capobianco, J.A., Vetrone, F., Boyer, J.C., Speghini, A., Bettinelli, M., 2002. Enhancement of red emission ($^4$F$_{9/2}$ → $^4$I$_{15/2}$) via upconversion in bulk and nanocrystalline cubic Y$_2$O$_3$:Er$^{3+}$. J. Phys. Chem. B 106 (6), 1181–1187.

Carling, C.-J., Nourmohammadian, F., Boyer, J.-C., Branda, N.R., 2010. Remote-control photorelease of caged compounds using near-infrared light and upconverting nanoparticles. Angew. Chem. Int. Ed. 49 (22), 3782–3785.

Carmeliet, P., 2003. Angiogenesis in health and disease. Nat. Med. 9 (6), 653–660.

Chan, W.C.W., Nie, S., 1998. Quantum dot bioconjugates for ultrasensitive nonisotopic detection. Science 281 (5385), 2016–2018.

Chang, H., Xie, J., Zhao, B., Liu, B., Xu, S., Ren, N., Xie, X., Huang, L., Huang, W., 2014. Rare earth ion-doped upconversion nanocrystals: synthesis and surface modification. Nanomaterials 5 (1), 1–25.

Chatterjee, D.K., Yong, Z., 2008. Upconverting nanoparticles as nanotransducers for photodynamic therapy in cancer cells. Nanomedicine 3 (1), 73–82.

Chatterjee, D.K., Rufaihah, A.J., Zhang, Y., 2008. Upconversion fluorescence imaging of cells and small animals using lanthanide doped nanocrystals. Biomaterials 29 (7), 937–943.

Chen, X., Park, R., Shahinian, A.H., Tohme, M., Khankaldyyan, V., Bozorgzadeh, M.H., Bading, J.R., Moats, R., Laug, W.E., Conti, P.S., 2004. 18F-labeled RGD peptide: initial evaluation for imaging brain tumor angiogenesis. Nucl. Med. Biol. 31 (2), 179–189.

Chen, Z., Chen, H., Hu, H., Yu, M., Li, F., Zhang, Q., Zhou, Z., Yi, T., Huang, C., 2008. Versatile synthesis strategy for carboxylic acid − functionalized upconverting nanophosphors as biological labels. J. Am. Chem. Soc. 130 (10), 3023–3029.

Chen, G., Ohulchanskyy, T.Y., Kachynski, A., Ågren, H., Prasad, P.N., 2011a. Intense visible and near-infrared upconversion photoluminescence in colloidal LiYF$_4$:Er$^{3+}$ nanocrystals under excitation at 1490 nm. ACS Nano 5 (6), 4981–4986.

Chen, G., Ohulchanskyy, T.Y., Law, W.C., Agren, H., Prasad, P.N., 2011b. Monodisperse NaYbF$_4$: Tm$^{3+}$/NaGdF$_4$ core/shell nanocrystals with near-infrared to near-infrared upconversion photoluminescence and magnetic resonance properties. Nanoscale 3 (5), 2003–2008.

Chen, Q., Wang, X., Chen, F., Zhang, Q., Dong, B., Yang, H., Liu, G., Zhu, Y., 2011c. Functionalization of upconverted luminescent NaYF$_4$: Yb/Er nanocrystals by folic acid-chitosan conjugates for targeted lung cancer cell imaging. J. Mater. Chem. 21 (21), 7661–7667.

Chen, D., Yu, Y., Huang, F., Lin, H., Huang, P., Yang, A., Wang, Z., Wang, Y., 2012a. Lanthanide dopant-induced formation of uniform sub-10 nm active-core/active-shell nanocrystals with near-infrared to near-infrared dual-modal luminescence. J. Mater. Chem. 22 (6), 2632–2640.

Chen, G., Ohulchanskyy, T.Y., Liu, S., Law, W.C., Wu, F., Swihart, M.T., Argen, H., Prasad, P.N., 2012b. Core/shell NaGdF$_4$:Nd($^{3+}$)/NaGdF$_4$ nanocrystals with efficient near-infrared to near-infrared downconversion photoluminescence for bioimaging applications. ACS Nano 6, 2969–2977.

Chen, G., Qiu, H., Prasad, P.N., Chen, X., 2014a. Upconversion nanoparticles: design, nanochemistry, and applications in theranostics. Chem. Rev. 114 (10), 5161–5214.

Chen, M., He, X., Wang, K., He, D., Yang, X., Shi, H., 2014b. Inorganic fluorescent nanoprobes for cellular and subcellular imaging. Trends Anal. Chem. 58, 120–129.

Chen, X., Liu, Y., Tu, D., 2014c. Lanthanide-Doped Luminescent Nanomaterials. Springer Verlag, Berlin.

Chen, Z., Zheng, W., Huang, P., Tu, D., Zhou, S., Huang, M., Chen, X., 2015. Lanthanide-doped luminescent nano-bioprobes for the detection of tumor markers. Nanoscale 7 (10), 4274–4290.

Cheng, L., Yang, K., Zhang, S., Shao, M., Lee, S., Liu, Z., 2010. Highly-sensitive multiplexed in vivo imaging using pegylated upconversion nanoparticles. Nano Res. 3 (10), 722–732.

Cheng, L., Yang, K., Li, Y., Chen, J., Wang, C., Shao, M., Lee, S.-T., Liu, Z., 2011. Facile preparation of multifunctional upconversion nanoprobes for multimodal imaging and dual-targeted photothermal therapy. Angew. Chem. Int. Ed. 50 (32), 7385–7390.

Cheng, L., Yang, K., Li, Y., Zeng, X., Shao, M., Lee, S.-T., Liu, Z., 2012. Multifunctional nanoparticles for upconversion luminescence/MR multimodal imaging and magnetically targeted photothermal therapy. Biomaterials 33 (7), 2215–2222.

Chien, Y.-H., Chou, Y.-L., Wang, S.-W., Hung, S.-T., Liau, M.-C., Chao, Y.-J., Su, C.-H., Yeh, C.-S., 2013. Near-infrared light photocontrolled targeting, bioimaging, and chemotherapy with caged upconversion nanoparticles in vitro and in vivo. ACS Nano 7 (10), 8516–8528.

Corstjens, P., Zuiderwijk, M., Brink, A., Li, S., Feindt, H., Niedbala, R.S., Tanke, H., 2001. Use of up-converting phosphor reporters in lateral-flow assays to detect specific nucleic acid sequences: a rapid, sensitive DNA test to identify human papillomavirus type 16 infection. Clin. Chem. 47 (10), 1885–1893.

Cotton, F.A., Willkinson, G., Murillo, C.A., Bochmann, M., 1999. Advanced Inorganic Chemistry. Wiley, New York, NY.

Cui, S., Yin, D., Chen, Y., Di, Y., Chen, H., Ma, Y., Achilefu, S., Gu, Y., 2013. In vivo targeted deep-tissue photodynamic therapy based on near-infrared light triggered upconversion nanoconstruct. ACS Nano 7 (1), 676–688.

Dacosta, M.V., Doughan, S., Han, Y., Krull, U.J., 2014. Lanthanide upconversion nanoparticles and applications in bioassays and bioimaging: a review. Anal. Chim. Acta 832, 1–33.

Darvill, D., Centeno, A., Xie, F., 2013. Plasmonic fluorescence enhacement by metal nanostructures: shaping the future of bionanotechnology. Phys. Chem. Chem. Phys. 15 (38), 15709–15726.

Das, G.K., Heng, B.C., Ng, S.-C., White, T., Loo, J.S.C., D'silva, L., Padmanabhan, P., Bhakoo, K.K., Selvan, S.T., Tan, T.T.Y., 2010. Gadolinium oxide ultranarrow nanorods as multimodal contrast agents for optical and magnetic resonance imaging. Langmuir 26 (11), 8959–8965.

Dong, C., Veggel, F.C.J.M.V., 2009. Cation exchange in lanthanide fluoride nanoparticles. ACS Nano 3 (1), 123–130.

Dong, B., Xu, S., Sun, J., Bi, S., Li, D., Bai, X., Wang, Y., Wang, L., Song, H., 2011. Multifunctional NaYF$_4$: Yb$^{3+}$, Er$^{3+}$@Ag core/shell nanocomposites: integration of upconversion imaging and photothermal therapy. J. Mater. Chem. 21 (17), 6193–6200.

Dong, B., Li, C., Chen, G., Zhang, Y., Zhang, Y., Deng, M., Wang, Q., 2013. Facile synthesis of highly photoluminescent Ag$_2$Se quantum dots as a New fluorescent probe in the second near-infrared window for in vivo imaging. Chem. Mater. 25 (12), 2503–2509.

Dong, C., Liu, H., Zhang, A., Ren, J., 2014. Controllable blinking-to-nonblinking behavior of aqueous CdTeS alloyed quantum dots. Chem. Eur. J. 20 (7), 1940–1946.

Duan, N., Wu, S., Zhu, C., Ma, X., Wang, Z., Yu, Y., Jiang, Y., 2012. Dual-color upconversion fluorescence and aptamer-functionalized magnetic nanoparticles-based bioassay for the simultaneous detection of Salmonella typhimurium and Staphylococcus aureus. Anal. Chim. Acta 723, 1–6.

Dulkeith, E., Morteani, A.C., Niedereichholz, T., Klar, T.A., Feldmann, J., Levi, S.A., Van Veggel, F.C.J.M., Reinhoudt, D.N., Möller, M., Gittins, D.I., 2002. Fluorescence quenching of dye molecules near gold nanoparticles: radiative and nonradiative effects. Phys. Rev. Lett. 89 (20), 203002.

Fan, N.-C., Cheng, F.-Y., Ho, J.-A., Yeh, C.-S., 2012. Photocontrolled targeted drug delivery: photocaged biologically active folic acid as a light-responsive tumor-targeting molecule. Angew. Chem. Int. Ed. 51 (35), 8806–8810.

Feng, W., Dev, K.C., Zhengquan, L., Yong, Z., Xianping, F., Minquan, W., 2006. Synthesis of polyethylenimine/NaYF$_4$ nanoparticles with upconversion fluorescence. Nanotechnology 17 (23), 5786.

Feng, W., Han, C., Li, F., 2013. Upconversion-nanophosphor-based functional nanocomposites. Adv. Mater. 25 (37), 5287–5303.

Fidler, I.J., 2003. The pathogenesis of cancer metastasis: the 'seed and soil' hypothesis revisited. Nat. Rev. Cancer 3 (6), 453–458.

Frangioni, J.V., 2003. In vivo near-infrarred fluorescence imaging. Curr. Opin. Chem. Biol. 7 (5), 626–634.

Gai, S., Yang, G., Li, X., Li, C., Dai, Y., He, F., Yang, P., 2012. Facile synthesis and up-conversion properties of monodisperse rare earth fluoride nanocrystals. Dalton Trans. 41, 11716–11724.

Gamelin, D.R., Gudel, H.U., 2001. Transition Metal and Rare Earth Compounds. Chapter 1, Springer, Springer-Verlag Berlin Heidelberg.

Gao, J., Chen, K., Luong, R., Bouley, D.M., Mao, H., Qiao, T., Gambhir, S.S., Cheng, Z., 2011. A novel clinically translatable fluorescent nanoparticle for targeted molecular imaging of tumors in living subjects. Nano Lett. 12 (1), 281–286.

Ge, W., Zhang, X.R., Liu, M., Lei, Z.W., Knize, R.J., Lu, Y., 2013. Distance dependence of gold-enhanced upconversion luminescence in Au/SiO$_2$/Y$_2$O$_3$:Yb$^{3+}$, Er$^{3+}$ nanoparticles. Theranostics 3 (4), 282–288.

Ghosh, P., Oliva, J., Rosa, E.D.L., Haldar, K.K., Solis, D., Patra, A., 2008. Enhancement of upconversion emission of LaPO$_4$:Er@Yb core−shell nanoparticles/nanorods. J. Phys. Chem. C 112 (26), 9650–9658.

Gnach, A., Lipinski, T., Bednarkiewicz, A., Rybka, J., Capobianco, J.A., 2015. Upconverting nanoparticles: assessing the toxicity. Chem. Soc. Rev. 44 (6), 1561–1584.

Güdel, H.U., Pollnau, M., 2000. Near-infrared to visible photon upconversion processes in lanthanide doped chloride, bromide and iodide lattices. J. Alloy. Compd. 303–304, 307–315.

Haase, M., Schafer, H., 2011. Upconverting nanoparticles. Angew. Chem. Int. Ed. 50, 5808–5829.

Hai, G., Zhengquan, L., Haisheng, Q., Yong, H., Idris Niagara, M., 2010. Seed-mediated synthesis of NaYF$_4$:Yb, Er/NaGdF$_4$ nanocrystals with improved upconversion fluorescence and MR relaxivity. Nanotechnology 21 (12), 125602.

Hampl, J., Hall, M., Mufti, N.A., Yao, Y.-M.M., Macqueen, D.B., Wright, W.H., Cooper, D.E., 2001. Upconverting phosphor reporters in immunochromatographic assays. Anal. Biochem. 288 (2), 176–187.

Han, J., Burgess, K., 2009. Fluorescent indicators for intracellular pH. Chem. Rev. 110 (5), 2709–2728.

Han, M., Gao, X., Su, J.Z., Nie, S., 2001. Quantum-dot-tagged microbeads for multiplexed optical coding of biomolecules. Nat. Biotechnol. 19, 631–635.

Han, S., Deng, R., Xie, X., Liu, X., 2014. Enhancing luminescence in lanthanide- doped upconversion nanoparticles. Angew. Chem. Int. Ed. 53 (44), 11702–11715.

He, C., Hu, Y., Yin, L., Tang, C., Yin, C., 2010. Effects of particle size and surface charge on cellular uptake and biodistribution of polymeric nanoparticles. Biomaterials 31 (13), 3657–3666.

Hecht, J., 1993. Understanding Lasers: An Entry-Level Guide, second ed. Wiley-IEEE Press, Piscataway, NJ.

Heer, S., Kömpe, K., Güdel, H.U., Haase, M., 2004. Highly efficient multicolour upconversion emission in transparent colloids of lanthanide-doped NaYF$_4$ nanocrystals. Adv. Mater. 16 (23–24), 2102–2105.

Hemmer, E., Venkatachalam, N., Hyodo, H., Hattori, A., Ebina, Y., Kishimoto, H., Soga, K., 2013. Upconverting and NIR emitting rare earth based nanostructures for NIR bioimaging. Nanoscale 5, 11339–11361.

Hirotada, A., Kimikazu, T., Hiroko, O., Kohei, S., Fumio, T., 2010. Application of liposome-encapsulated ceramic phoshpors for cancer cell imaging under near infrared excitation. J. Phys. Conf. Ser. 232 (1), 012001.

Ho, Y.-P., Leong, K.W., 2010. Quantum dot-based theranostics. Nanoscale 2 (1), 60–68.

Hoff, J.V.D., Burchert, W., Wolpers, H.G., Meyer, G.J., Hundeshagen, H., 1996. A kinetic model for cardiac PET with [1-carbon-11]-acetate. J. Nucl. Med. 37, 521–529.

Hortobagyi, G.N., 1997. Anthracyclines in the treatment of cancer. An overview. Drugs. 54 (Suppl. 4), 1–7.

Hoshino, A., 2004. Physicochemical properties and cellular toxicity of nanocrystal quantum dots depend on their surface modification. Nano Lett. 4, 2163–2169.

Hou, Z., Li, C., Ma, P., Li, G., Cheng, Z., Peng, C., Yang, D., Yang, P., Lin, J., 2011. Electrospinning preparation and drug-delivery properties of an up-conversion luminescent porous NaYF$_4$:Yb$^{3+}$, Er$^{3+}$@silica fiber nanocomposite. Adv. Funct. Mater. 21 (12), 2356–2365.

Hu, H., Yu, M., Li, F., Chen, Z., Gao, X., Xiong, L., Huang, C., 2008. Facile epoxidation strategy for producing amphiphilic up-converting rare-earth nanophosphors as biological labels. Chem. Mater. 20 (22), 7003–7009.

Huang, P., Zheng, W., Zhou, S., Tu, D., Chen, Z., Zhu, H., Li, R., Ma, E., Huang, M., Chen, X., 2014. Lanthanide-doped LiLuF$_4$ upconversion nanoprobes for the detection of disease biomarkers. Angew. Chem. Int. Ed. 53 (5), 1252–1257.

Idris, N.M., Li, Z., Ye, L., Wei Sim, E.K., Mahendran, R., Ho, P.C.-L., Zhang, Y., 2009. Tracking transplanted cells in live animal using upconversion fluorescent nanoparticles. Biomaterials 30 (28), 5104–5113.

Idris, N.M., Gnanasammandhan, M.K., Zhang, J., Ho, P.C., Mahendran, R., Zhang, Y., 2012. In vivo photodynamic therapy using upconversion nanoparticles as remote-controlled nanotransducers. Nat. Med. 18 (10), 1580–1585.

Iyer, A.K., Singh, A., Ganta, S., Amiji, M.M., 2013. Role of integrated cancer nanomedicine in overcoming drug resistance. Adv. Drug Deliv. Rev. 65, 1784–1802.

Jain, P.K., Huang, X., El-Sayed, I.H., El-Sayed, M.A., 2008. Noble metals on the nanoscale: optical and photothermal properties and some applications in imaging, sensing, biology, and medicine. Acc. Chem. Res. 41 (12), 1578–1586.

Jin, Y., Lohstreter, S., Pierce, D.T., Parisien, J., Wu, M., Hall, C., Zhao, J.X., 2008. Silica nanoparticles with continuously tunable sizes: synthesis and size effects on cellular contrast imaging. Chem. Mater. 20 (13), 4411–4419.

Jin, J., Gu, Y.-J., Man, C.W.-Y., Cheng, J., Xu, Z., Zhang, Y., Wang, H., Lee, V.H.-Y., Cheng, S.-H., Wong, W.-T., 2011. Polymer-coated NaYF$_4$:Yb$^{3+}$, Er$^{3+}$ upconversion nanoparticles for charge-dependent cellular imaging. ACS Nano 5 (10), 7838–7847.

Johnson, I., 1998. Review: fluorescent probes for living cells. Histochem. J. 30 (3), 123–140.

Johnson, N.J.J., Korinek, A., Dong, C., Van Veggel, F.C.J.M., 2012. Self-focusing by Ostwald ripening: a strategy for layer-by-layer epitaxial growth on upconverting nanocrystals. J. Am. Chem. Soc. 134 (27), 11068–11071.

Joubert, M.-F., 1999. Photon avalanche upconversion in rare earth laser materials. Opt. Mater. 11 (2–3), 181–203.

Kannan, P., Abdul Rahim, F., Chen, R., Teng, X., Huang, L., Sun, H., Kim, D.-H., 2013. Au nanorod decoration on NaYF$_4$:Yb/Tm nanoparticles for enhanced emission and wavelength-dependent biomolecular sensing. ACS Appl. Mater. Interfaces 5 (9), 3508–3513.

Kobayashi, H., Kosaka, N., Ogawa, M., Morgan, N.Y., Smith, P.D., Murray, C.B., Ye, X., Collins, J., Kumar, G.A., Bell, H., Choyke, P.L., 2009. In vivo multiple color lymphatic imaging using upconverting nanocrystals. J. Mater. Chem. 19 (36), 6481–6484.

Kong, W., Shan, J., Ju, Y., 2010. Flame synthesis and effects of host materials on Yb$^{3+}$/Er$^{3+}$ co-doped upconversion nanophosphors. Mater. Lett. 64 (6), 688–691.

König, K., 2000. Multiphoton microscopy in life sciences. J. Microsc. 200 (2), 83–104.

Koo, Y.-E.L., Fan, W., Hah, H., Xu, H., Orringer, D., Ross, B., Rehemtulla, A., Philbert, M.A., Kopelman, R., 2007. Photonic explorers based on multifunctional nanoplatforms for biosensing and photodynamic therapy. Appl. Opt. 46 (10), 1924–1930.

Kumar, M., Zhang, P., 2009. Highly sensitive and selective label-free optical detection of DNA hybridization based on photon upconverting nanoparticles. Langmuir 25 (11), 6024–6027.

Kumar, R., Nyk, M., Ohulchanskyy, T.Y., Flask, C.A., Prasad, P.N., 2009. Combined optical and MR bioimaging using rare earth Ion doped NaYF$_4$ nanocrystals. Adv. Funct. Mater. 19 (6), 853–859.

Kumar, K., Upendra, K., Vijaya, N., Oliva, J., Jacinto, C., Rosa, E.D.L., Jayasankar, C.K., 2012. Multicolor upconversion emission and color tunability in Tm$^{3+}$/Er$^{3+}$/Yb$^{3+}$ tri-doped NaNbO$_3$ nanocrystals. Mater. Express 2 (4), 294–302.

Kuningas, K., Rantanen, T., Ukonaho, T., Lövgren, T., Soukka, T., 2005. Homogeneous assay technology based on upconverting phosphors. Anal. Chem. 77 (22), 7348–7355.

Lewinski, N., Colvin, V., Drezek, R., 2008. Cytotoxicity of nanoparticles. Small 4, 26–49.

Lezhnina, M.M., Jüstel, T., Kätker, H., Wiechert, D.U., Kynast, U.H., 2006. Efficient luminescence from rare-earth fluoride nanoparticles with optically functional shells. Adv. Funct. Mater. 16 (7), 935–942.

Li, Z., Zhang, Y., 2008. An efficient and user-friendly method for the synthesis of hexagonal-phase NaYF$_4$:Yb, Er/Tm nanocrystals with controllable shape and upconversion fluorescence. Nanotechnology 19 (34), 345606–345611.

Li, X., Zhang, F., 2015. "Wet" chemical synthesis and manipulation of upconversion nanoparticles. In: Zhang, F. (Ed.), Photon Upconversion Nanomaterials. Springer, Berlin, pp. 21–71.

Li, C., Yang, J., Quan, Z., Yang, P., Kong, D., Lin, J., 2007. Different microstructures of β-NaYF$_4$ fabricated by hydrothermal process: effects of pH values and fluoride sources. Chem. Mater. 19 (20), 4933–4942.

Li, C., Yang, D., Ma, P.A., Chen, Y., Wu, Y., Hou, Z., Dai, Y., Zhao, J., Sui, C., Lin, J., 2013a. Multifunctional upconversion mesoporous silica nanostructures for dual modal imaging and in vivo drug delivery. Small 9 (24), 4150–4159.

Li, D., Wang, Y., Zhang, X., Shi, G., Liu, G., Song, Y., 2013b. White upconversion emission in Yb$^{3+}$/Tm$^{3+}$/Ho$^{3+}$ doped SrMoO$_4$ nanocrystals by high excited state energy transfer. J. Alloy. Compd. 550, 509–513.

Lim, S.F., Riehn, R., Ryu, W.S., Khanarian, N., Tung, C.-K., Tank, D., Austin, R.H., 2005. In vivo and scanning electron microscopy imaging of upconverting nanophosphors in caenorhabditis elegans. Nano Lett. 6 (2), 169–174.

Lim, Y.T., Noh, Y.-W., Cho, J.-H., Han, J.H., Choi, B.S., Kwon, J., Hong, K.S., Gokarna, A., Cho, Y.-H., Chung, B.H., 2009. Multiplexed imaging of therapeutic cells with multispectrally encoded magnetofluorescent nanocomposite emulsions. J. Am. Chem. Soc. 131 (47), 17145–17154.

Lim, E.-K., Kim, T., Paik, S., Haam, S., Huh, Y.-M., Lee, K., 2015. Nanomaterials for theranostics: recent advances and future challenges. Chem. Rev. 115 (1), 327–394.

Lin, M., Zhao, Y., Wang, S., Liu, M., Duan, Z., Chen, Y., Li, F., Xu, F., Lu, T., 2012. Recent advances in synthesis and surface modification of lanthanide-doped upconversion nanoparticles for biomedical applications. Biotechnol. Adv. 30 (6), 1551–1561.

Liu, Q., Peng, J., Sun, L., Li, F., 2011a. High-efficiency upconversion luminescent sensing and bioimaging of Hg(II) by chromophoric ruthenium complex-assembled nanophosphors. ACS Nano 5 (10), 8040–8048.

Liu, Q., Sun, Y., Yang, T., Feng, W., Li, C., Li, F., 2011b. Sub-10 nm hexagonal lanthanide-doped $NaLuF_4$ upconversion nanocrystals for sensitive bioimaging in vivo. J. Am. Chem. Soc. 133 (43), 17122–17125.

Liu, J.-N., Bu, W., Pan, L.-M., Zhang, S., Chen, F., Zhou, L., Zhao, K.-L., Peng, W., Shi, J., 2012a. Simultaneous nuclear imaging and intranuclear drug delivery by nuclear-targeted multifunctional upconversion nanoprobes. Biomaterials 33 (29), 7282–7290.

Liu, K., Liu, X., Zeng, Q., Zhang, Y., Tu, L., Liu, T., Kong, X., Wang, Y., Cao, F., Lambrechts, S.A., Aalders, M.C.G., Zhang, H., 2012b. Covalently assembled NIR nanoplatform for simultaneous fluorescence imaging and photodynamic therapy of cancer cells. ACS Nano 6 (5), 4054–4062.

Liu, Y., Ai, K., Lu, L., 2012c. Nanoparticulate X-ray computed tomography contrast agents: from design validation to in vivo applications. Acc. Chem. Res. 45 (10), 1817–1827.

Liu, B., Tan, H., Chen, Y., 2013a. Upconversion nanoparticle-based fluorescence resonance energy transfer assay for Cr(III) ions in urine. Anal. Chim. Acta 761, 178–185.

Liu, Y., Tu, D., Zhu, H., Chen, X., 2013b. Lanthanide-doped luminescent nanoprobes: controlled synthesis, optical spectroscopy, and bioapplications. Chem. Soc. Rev. 42 (16), 6924–6958.

Liu, C., Hou, Y., Gao, M., 2014a. Are rare-earth nanoparticles suitable for in vivo applications? Adv. Mater. 26 (40), 6922–6932.

Liu, Q., Feng, W., Li, F., 2014b. Water-soluble lanthanide upconversion nanophosphors: synthesis and bioimaging applications in vivo. Coord. Chem. Rev. 273–274, 100–110.

Lucky, S.S., Soo, K.C., Zhang, Y., 2015. Nanoparticles in photodynamic therapy. Chem. Rev. 115 (4), 1990–2042.

Luo, X., Cao, W., Xing, M., 2006. Preparation of nano $Y_2O_2S$:Eu phosphor by ethanol assisted combustion synthesis method. J. Rare Earths 24 (1), 20–24.

Ma, J., 2006. Photostability of thiol-capped CdTe quantum dots in living cells: the effect of photooxidation. Nanotechnology 17, 2083–2089.

Ma, J., Huang, P., He, M., Pan, L., Zhou, Z., Feng, L., Gao, G., Cui, D., 2012. Folic acid-conjugated $LaF_3$:Yb, Tm@$SiO_2$ nanoprobes for targeting dual-modality imaging of upconversion luminescence and X-ray computed tomography. J. Phys. Chem. B 116 (48), 14062–14070.

Mahalingam, V., Vetrone, F., Naccache, R., Speghini, A., Capobianco, J.A., 2009. Colloidal $Tm^{3+}/Yb^{3+}$−doped $LiYF_4$ nanocrystals: multiple luminescence spanning the UV to NIR regions via low-energy excitation. Adv. Mater. 21 (40), 4025–4028.

Mai, H.-X., Zhang, Y.-W., Si, R., Yan, Z.-G., Sun, L.-D., You, L.-P., Yan, C.-H., 2006. High-quality sodium rare-earth fluoride nanocrystals: controlled synthesis and optical properties. J. Am. Chem. Soc. 128 (19), 6426–6436.

Mai, H.-X., Zhang, Y.-W., Sun, L.-D., Yan, C.-H., 2007. Size- and phase-controlled synthesis of monodisperse NaYF$_4$:Yb, Er nanocrystals from a unique delayed nucleation pathway monitored with upconversion spectroscopy. J. Phys. Chem. C 111 (37), 13730–13739.

Mangiarini, F., Naccache, R., Speghini, A., Bettinelli, M., Vetrone, F., Capobianco, J.A., 2010. Upconversion in Er$^{3+}$ – doped Gd$_2$O$_3$ nanocrystals prepared by propellant synthesis and flame spray pyrolysis. Mater. Res. Bull. 45 (8), 927–932.

Martín-Rodríguez, R., Valiente, R., Pesquera, C., González, F., Blanco, C., Potin, V., Marco De Lucas, M.C., 2009. Optical properties of nanocrystalline-coated Y$_2$O$_3$:Er$^{3+}$, Yb$^{3+}$ obtained by mechano-chemical and combustion synthesis. J. Lumin. 129 (9), 1109–1114.

Naccache, R., Chevallier, P., Lagueux, J., Gossuin, Y., Laurent, S., Vander Elst, L., Chilian, C., Capobianco, J.A., Fortin, M.-A., 2013. High relaxivities and strong vascular signal enhancement for NaGdF$_4$ nanoparticles designed for dual MR/optical imaging. Adv. Healthc. Mater. 2 (11), 1478–1488.

Naccache, R., Vetrone, F., Mahalingam, V., Cuccia, L.A., Capobianco, J.A., 2009. Controlled synthesis and water dispersibility of hexagonal phase NaGdF$_4$:Ho$^{3+}$/Yb$^{3+}$ Nanoparticles. Chem. Mater. 21 (4), 717–723.

Naumova, A.V., Modo, M., Moore, A., Murry, C.E., Frank, J.A., 2014. Clinical imaging in regenerative medicine. Nat. Biotechnol. 32 (8), 804–818.

Ostrowski, A.D., Chan, E.M., Gargas, D.J., Katz, E.M., Han, G., Schuck, P.J., Milliron, D.J., Cohen, B.E., 2012. Controlled synthesis and single-particle imaging of bright, sub-10 nm lanthanide-doped upconverting nanocrystals. ACS Nano 6 (3), 2686–2692.

Pandozzi, F., Vetrone, F., Boyer, J.-C., Naccache, R., Capobianco, J.A., Speghini, A., Bettinelli, M., 2005. A spectroscopic analysis of blue and ultraviolet upconverted emissions from Gd$_3$Ga$_5$O$_{12}$:Tm$^{3+}$, Yb$^{3+}$ nanocrystals. J. Phys. Chem. B 109 (37), 17400–17405.

Panthani, M.G., Khan, T.A., Reid, D.K., Hellebusch, D.J., Rasch, M.R., Maynard, J.A., Korgel, B.A., 2013. In vivo whole animal fluorescence imaging of a microparticle-based oral vaccine containing (CuInSe$_x$S$_{2-x}$)/ZnS core/shell quantum dots. Nano Lett. 13 (9), 4294–4298.

Park, Y.I., Kim, J.H., Lee, K.T., Jeon, K.-S., Na, H.B., Yu, J.H., Kim, H.M., Lee, N., Choi, S.H., Baik, S.-I., Kim, H., Park, S.P., Park, B.-J., Kim, Y.W., Lee, S.H., Yoon, S.-Y., Song, I.C., Moon, W.K., Suh, Y.D., Hyeon, T., 2009. Nonblinking and nonbleaching upconverting nanoparticles as an optical imaging nanoprobe and T1 magnetic resonance imaging contrast agent. Adv. Mater. 21 (44), 4467–4471.

Park, Y.I., Lee, K.T., Suh, Y.D., Hyeon, T., 2015. Upconverting nanoparticles: a versatile platform for wide-field two-photon microscopy and multi-modal in vivo imaging. Chem. Soc. Rev. 44 (6), 1302–1317.

Patra, A., Friend, C.S., Kapoor, R., Prasad, P.N., 2002. Upconversion in Er$^{3+}$:ZrO$_2$ nanocrystals. J. Phys. Chem. B 106 (8), 1909–1912.

Patra, A., Friend, C.S., Kapoor, R., Prasad, P.N., 2003. Fluorescence upconversion properties of Er$^{3+}$ – doped TiO$_2$ and BaTiO$_3$ nanocrystallites. Chem. Mater. 15 (19), 3650–3655.

Paudel, H.P., Zhong, L., Bayat, K., Baroughi, M.F., Smith, S., Lin, C., Jiang, C., Berry, M.T., May, P.S., 2011. Enhancement of near-infrared-to-visible upconversion luminescence using engineered plasmonic gold surfaces. J. Phys. Chem. C 115 (39), 19028–19036.

Prasad, P.N., 2003. Introduction to Biophotonics. Wiley-Interscience, Hoboken, NJ.

Qian, H.S., Guo, H.C., Ho, P.C.-L., Mahendran, R., Zhang, Y., 2009. Mesoporous-silica-coated up-conversion fluorescent nanoparticles for photodynamic therapy. Small 5 (20), 2285–2290.

Qin, X., Yokomori, T., Ju, Y., 2007. Flame synthesis and characterization of rare-earth (Er$^{3+}$, Ho$^{3+}$, and Tm$^{3+}$) doped upconversion nanophosphors. Appl. Phys. Lett. 90 (7), 073104.

Raphaela, B.L., Tero, S., Otto, S.W., Hans, H.G., 2012. Maleimide activation of photon upconverting nanoparticles for bioconjugation. Nanotechnology 23 (48), 485103.

Renero-Lecuna, C., Martín-Rodríguez, R., Valiente, R., González, J., Rodríguez, F., Krämer, K.W., Güdel, H.U., 2011. Origin of the high upconversion green luminescence efficiency in β-NaYF4:2%Er3+,20%Yb3+. Chem. Mater. 23 (15), 3442–3448.

Resch-Genger, U., Grabolle, M., Cavaliere-Jaricot, S., Nitschke, R., Nann, T., 2008. Quantum dots versus organic dyes as fluorescent labels. Nat. Methods 5 (9), 763–775.

Rijke, F.V.D., Zijlmans, H., Li, S., Vail, T., Raap, A.K., Niedbala, R.S., Tanke, H.J., 2001. Up-converting phosphor reporters for nucleic acid microarrays. Nat. Biotechnol. 19, 273–276.

Saboktakin, M., Ye, X., Oh, S.J., Hong, S.-H., Fafarman, A.T., Chettiar, U.K., Engheta, N., Murray, C.B., Kagan, C.R., 2012. Metal-enhanced upconversion luminescence tunable through metal nanoparticle–nanophosphor separation. ACS Nano 6 (10), 8758–8766.

Scheps, R., 1996. Upconversion laser processes. Prog. Quant. Electron. 20, 271–358.

Schietinger, S., Aichele, T., Wang, H.-Q., Nann, T., Benson, O., 2010. Plasmon-enhanced upconversion in single NaYF$_4$:Yb$^{3+}$/Er$^{3+}$ codoped nanocrystals. Nano Lett. 10 (1), 134–138.

Sedlmeier, A., Achatz, D.E., Fischer, L.H., Gorris, H.H., Wolfbeis, O.S., 2012. Photon upconverting nanoparticles for luminescent sensing of temperature. Nanoscale 4 (22), 7090–7096.

Shan, J., Chen, J., Meng, J., Collins, J., Soboyejo, W., Friedberg, J.S., Ju, Y., 2008. Biofunctionalization, cytotoxicity, and cell uptake of lanthanide doped hydrophobically ligated NaYF$_4$ upconversion nanophosphors. J. Appl. Phys. 104, 094308 (094301–094307).

Shan, J., Yong, Z., Kian Meng, L., Eugene, K.W.S., Lei, Y., 2009. NIR-to-visible upconversion nanoparticles for fluorescent labeling and targeted delivery of siRNA. Nanotechnology 20 (15), 155101.

Shan, J., Budijono, S.J., Hu, G., Yao, N., Kang, Y., Ju, Y., Prud'homme, R.K., 2011. Pegylated composite nanoparticles containing upconverting phosphors and meso-tetraphenyl porphine (TPP) for photodynamic therapy. Adv. Funct. Mater. 21 (13), 2488–2495.

Shaner, N.C., Steinbach, P.A., Tsien, R.Y., 2005. A guide to choosing fluorescent proteins. Nat. Methods 2 (12), 905–909.

Shanmugam, V., Selvakumar, S., Yeh, C.-S., 2014. Near-infrared light-responsive nanomaterials in cancer therapeutics. Chem. Soc. Rev. 43 (17), 6254–6287.

Sivakumar, S., Veggel, F.C.J.M.V., 2007. Red, green and blue light through cooperative upconversion in sol–gel thin films made with Yb$_{0.80}$La$_{0.15}$Tb$_{0.05}$F$_3$ and Yb$_{0.80}$La$_{0.15}$Eu$_{0.05}$F$_3$ nanoparticles. J. Disp. Technol. 3 (2), 176–183.

Sperling, R.A., Parak, W.J., 2010. Surface modification, functionalization and bioconjugation of colloidal inorganic nanoparticles. Phil. Trans. R. Soc. A 368 (1915), 1333–1383.

Stouwdam, J.W., Van Veggel, F.C.J.M., 2002. Near-infrared emission of redispersible Er$^{3+}$, Nd$^{3+}$, and Ho$^{3+}$ doped LaF$_3$ nanoparticles. Nano Lett. 2 (7), 733–737.

Suljoti, E., Nagasono, M., Pietzsch, A., Hickmann, K., Trots, D.M., Haase, M., Wurth, W., Föhlisch, A., 2008. Geometric and electronic structure of lanthanide orthophosphate nanoparticles determined with X-rays. J. Chem. Phys. 128, 134706-1–134706-9.

Sun, Y., Yu, M., Liang, S., Zhang, Y., Li, C., Mou, T., Yang, W., Zhang, X., Li, B., Huang, C., Li, F., 2011. Fluorine-18 labeled rare-earth nanoparticles for positron emission tomography (PET) imaging of sentinel lymph node. Biomaterials 32 (11), 2999–3007.

Sun, L.-D., Wang, Y.-F., Yan, C.-H., 2014. Paradigms and challenges for bioapplication of rare earth upconversion luminescent nanoparticles: small size and tunable emission/excitation spectra. Acc. Chem. Res. 47 (4), 1001–1009.

Tian, G., Gu, Z., Zhou, L., Yin, W., Liu, X., Yan, L., Jin, S., Ren, W., Xing, G., Li, S., Zhao, Y., 2012. $Mn^{2+}$ dopant-controlled synthesis of $NaYF_4$:Yb/Er upconversion nanoparticles for in vivo imaging and drug delivery. Adv. Mater. 24 (9), 1226–1231.

Tian, G., Ren, W., Yan, L., Jian, S., Gu, Z., Zhou, L., Jin, S., Yin, W., Li, S., Zhao, Y., 2013. Red-emitting upconverting nanoparticles for photodynamic therapy in cancer cells under near-infrared excitation. Small 9 (11), 1929–1938.

Tsien, R.Y., 1998. The green fluorescent protein. Annu. Rev. Biochem. 67 (1), 509–544.

Ungun, B., Prud'homme, R.K., Budijon, S.J., Shan, J., Lim, S.F., Ju, Y., Austin, R., 2009. Nanofabricated upconversion nanoparticles for photodynamic therapy. Opt. Express 17 (1), 80–86.

Van Dijk, J.M.F., Schuurmans, M.F.H., 1983. On the nonradiative and radiative decay rates and a modified exponential energy gap law for 4f–4f transitions in rare-earth ions. J. Chem. Phys. 78 (9), 5317–5323.

Van Veggel, F.C.J.M., 2014. Upconversion of $Ln^{3+}$ – based nanoparticles for optical bio-imaging. In: Ana de Bettencourt-Dias, (Ed.), Luminescence of lanthanide Ions in Coordination Compounds and Nanomaterials. John Wiley & Sons Ltd, The Atrium, Southern Gate, Chichester, West Sussex, United Kingdom, p. 269.

Varkouhi, A.K., Scholte, M., Storm, G., Haisma, H.J., 2011. Endosomal escape pathways for delivery of biologicals. J. Control. Release 151 (3), 220–228.

Venkatramu, V., Falcomer, D., Speghini, A., Bettinelli, M., Jayasankar, C.K., 2008. Synthesis and luminescence properties of $Er^{3+}$ – doped $Lu_3Ga_5O_{12}$ nanocrystals. J. Lumin. 128 (5–6), 811–813.

Vennerberg, D., Lin, Z., 2011. Upconversion nanocrystals: synthesis, properties, assembly and applications. Sci. Adv. Mater. 3, 26–40.

Vetrone, F., Boyer, J.-C., Capobianco, J.A., Speghini, A., Bettinelli, M., 2004. Significance of $Yb^{3+}$ concentration on the upconversion mechanisms in codoped $Y_2O_3$:$Er^{3+}$, $Yb^{3+}$ nanocrystals. J. Appl. Phys. 96 (1), 661–667.

Vetrone, F., Naccache, R., Mahalingam, V., Morgan, C.G., Capobianco, J.A., 2009. The active-core/active-shell approach: a strategy to enhance the upconversion luminescence in lanthanide-doped nanoparticles. Adv. Funct. Mater. 19 (18), 2924–2929.

Vetrone, F., Naccache, R., Juarranz De La Fuente, A., Sanz-Rodriguez, F., Blazquez-Castro, A., Rodriguez, E.M., Jaque, D., Sole, J.G., Capobianco, J.A., 2010a. Intracellular imaging of HeLa cells by non-functionalized $NaYF_4$: $Er^{3+}$, $Yb^{3+}$ upconverting nanoparticles. Nanoscale 2 (4), 495–498.

Vetrone, F., Naccache, R., Zamarrón, A., Juarranz De La Fuente, A., Sanz-Rodríguez, F., Martinez Maestro, L., Martín Rodriguez, E., Jaque, D., García Solé, J., Capobianco, J.A., 2010b. Temperature sensing using fluorescent nanothermometers. ACS Nano 4 (6), 3254–3258.

Waggoner, A., 2006. Fluorescent labels for proteomics and genomics. Curr. Opin. Chem. Biol. 10 (1), 62–66.

Wang, L., Li, Y., 2006. Green upconversion nanocrystals for DNA detection. Chem. Commun. 24, 2557–2559.

Wang, F., Liu, X., 2008. Upconversion multicolor fine-tuning: visible to near-infrared emission from lanthanide-doped $NaYF_4$ nanoparticles. J. Am. Chem. Soc. 130 (17), 5642–5643.

Wang, F., Liu, X., 2009. Recent advances in the chemistry of lanthanide-doped upconversion nanocrystals. Chem. Soc. Rev. 38 (4), 976–989.

Wang, R., Zhang, F., 2014. NIR luminescent nanomaterials for biomedical imaging. J. Mater. Chem. B 2, 2422–2443.

Wang, X., Kong, X., Shan, G., Yu, Y., Sun, Y., Feng, L., Chao, K., Lu, S., Li, Y., 2004. Luminescence spectroscopy and visible upconversion properties of $Er^{3+}$ in ZnO nanocrystals. J. Phys. Chem. B 108 (48), 18408–18413.

Wang, F., Chatterjee, D.K., Li, Z., Zhang, Y., Fan, X., Want, M., 2006. Synthesis of polyethylenimine/$NaYF_4$ nanoparticles with upconversion fluorescence. Nanotechnology 17 (23), 5786–5791.

Wang, M., Mi, C., Zhang, Y., Liu, J., Li, F., Mao, C., Xu, S., 2009a. NIR-responsive silica-coated $NaYbF_4$:Er/Tm/Ho upconversion fluorescent nanoparticles with tunable emission colors and their applications in immunolabeling and fluorescent imaging of cancer cells. J. Phys. Chem. C 113 (44), 19021–19027.

Wang, M., Mi, C.-C., Liu, J.-L., Wu, X.-L., Zhang, Y.-X., Hou, W., Li, F., Xu, S.-K., 2009b. One-step synthesis and characterization of water-soluble $NaYF_4$:Yb, Er/polymer nanoparticles with efficient up-conversion fluorescence. J. Alloy. Compd. 485 (1–2), L24–L27.

Wang, M., Mi, C.-C., Wang, W.-X., Liu, C.-H., Wu, Y.-F., Xu, Z.-R., Mao, C.-B., Xu, S.-K., 2009c. Immunolabeling and NIR-excited fluorescent imaging of HeLa cells by using $NaYF_4$:Yb, Er upconversion nanoparticles. ACS Nano 3 (6), 1580–1586.

Wang, F., Han, Y., Lim, C.S., Lu, Y., Wang, J., Xu, J., Chen, H., Zhang, C., Hong, M., Liu, X., 2010a. Simultaneous phase and size control of upconversion nanocrystals through lanthanide doping. Nature 463, 1061–1065.

Wang, F., Wang, J., Liu, X., 2010b. Direct evidence of a surface quenching effect on size-dependent luminescence of upconversion nanoparticles. Angew. Chem. Int. Ed. 49 (41), 7456–7460.

Wang, C., Cheng, L., Liu, Z., 2011a. Drug delivery with upconversion nanoparticles for multifunctional targeted cancer cell imaging and therapy. Biomaterials 32 (4), 1110–1120.

Wang, S., Fan, W., Kim, G., Hah, H.J., Lee, Y.-E.K., Kopelman, R., Ethirajan, M., Gupta, A., Goswami, L.N., Pera, P., Morgan, J., Pandey, R.K., 2011b. Novel methods to incorporate photosensitizers into nanocarriers for cancer treatment by photodynamic therapy. Lasers Surg. Med. 43 (7), 686–695.

Wang, M., Chen, Z., Zheng, W., Zhu, H., Lu, S., Ma, E., Tu, D., Zhou, S., Huang, M., Chen, X., 2014. Lanthanide-doped upconversion nanoparticles electrostatically coupled with photosensitizers for near-infrared-triggered photodynamic therapy. Nanoscale 6, 8274–8282.

Wei, Y., Lu, F., Zhang, X., Chen, D., 2006. Synthesis of oil-dispersible hexagonal-phase and hexagonal-shaped $NaYF_4$:Yb, Er nanoplates. Chem. Mater. 18 (24), 5733–5737.

Wei, Y., Lu, F., Zhang, X., Chen, D., 2008. Polyol-mediated synthesis and luminescence of lanthanide-doped $NaYF_4$ nanocrystal upconversion phosphors. J. Alloy. Compd. 455 (1–2), 376–384.

Wei, L., Doughan, S., Han, Y., Dacosta, M.V., Krull, U.J., Ho, D., 2014. The intersection of CMOS microsystems and upconversion nanoparticles for luminescence bioimaging and bioassays. Sensors 14 (9), 16829–16855.

Wilhelm, S., Hirsch, T., Patterson, W.M., Scheucher, E., Mayr, T., Wolfbeis, O.S., 2013. Multicolor upconversion nanoparticles for protein conjugation. Theranostics 3 (4), 239–248.

Wong, H.T., Vetrone, F., Naccache, R., Chan, H.L.W., Hao, J., Capobianco, J.A., 2011. Water dispersible ultra-small multifunctional $KGdF_4$:$Tm^{3+}$, $Yb^{3+}$ nanoparticles with near-infrared to near-infrared upconversion. J. Mater. Chem. 21 (41), 16589–16596.

Xiao, Q., Zheng, X., Bu, W., Ge, W., Zhang, S., Chen, F., Xing, H., Ren, Q., Fan, W., Zhao, K., Hua, Y., Shi, J., 2013. A core/satellite multifunctional nanotheranostic for in vivo imaging and tumor eradication by radiation/photothermal synergistic therapy. J. Am. Chem. Soc. 135 (35), 13041–13048.

Xie, L., Qin, Y., Chen, H.-Y., 2012. Polymeric optodes based on upconverting nanorods for fluorescent measurements of pH and metal ions in blood samples. Anal. Chem. 84 (4), 1969–1974.

Xiong, L., Chen, Z., Tian, Q., Cao, T., Xu, C., Li, F., 2009a. High contrast upconversion luminescence targeted imaging in vivo using peptide-labeled nanophosphors. Anal. Chem. 81 (21), 8687–8694.

Xiong, L.-Q., Chen, Z.-G., Yu, M.-X., Li, F.-Y., Liu, C., Huang, C.-H., 2009b. Synthesis, characterization, and in vivo targeted imaging of amine-functionalized rare-earth up-converting nanophosphors. Biomaterials 30 (29), 5592–5600.

Xiong, L., Yang, T., Yang, Y., Xu, C., Li, F., 2010. Long-term in vivo biodistribution imaging and toxicity of polyacrylic acid-coated upconversion nanophosphors. Biomaterials 31 (27), 7078–7085.

Xu, L., Yu, Y., Li, X., Somesfalean, G., Zhang, Y., Gao, H., Zhang, Z., 2008. Synthesis and upconversion properties of monoclinic $Gd_2O_3$:$Er^{3+}$ nanocrystals. Opt. Mater. 30 (8), 1284–1288.

Xu, H., Cheng, L., Wang, C., Ma, X., Li, Y., Liu, Z., 2011. Polymer encapsulated upconversion nanoparticle/iron oxide nanocomposites for multimodal imaging and magnetic targeted drug delivery. Biomaterials 32 (35), 9364–9373.

Xu, W., Chen, B., Yu, W., Zhu, Y., Liu, T., Xu, S., Min, X., Bai, X., Song, H., 2012. The up-conversion luminescent properties and silver-modified luminescent enhancement of $YVO_4$:$Yb^{3+}$, $Er^{3+}$ NPs. Dalton Trans. 41 (43), 13525–13532.

Yang, Y., 2014. Upconversion nanophosphors for use in bioimaging, therapy, drug delivery and bioassays. Microchim. Acta 181, 263–294.

Yang, D., Li, C., Li, G., Shang, M., Kang, X., Lin, J., 2011. Colloidal synthesis and remarkable enhancement of the upconversion luminescence of $BaGdF_5$:$Yb^{3+}$/$Er^{3+}$ nanoparticles by active-shell modification. J. Mater. Chem. 21 (16), 5923–5927.

Yi, G.-S., Chow, G.-M., 2005. Colloidal $LaF_3$:Yb, Er, $LaF_3$:Yb, Ho and $LaF_3$:Yb, Tm nanocrystals with multicolor upconversion fluorescence. J. Mater. Chem. 15 (41), 4460–4464.

Yi, G.-S., Chow, G.-M., 2006a. Water-soluble $NaYF_4$:Yb, Er(Tm)/$NaYF_4$/polymer core/shell/shell nanoparticles with significant enhancement of upconversion fluorescence. Chem. Mater. 19 (3), 341–343.

Yi, G.S., Chow, G.M., 2006b. Synthesis of hexagonal-phase $NaYF_4$:Yb, Er and $NaYF_4$:Yb, Tm nanocrystals with efficient up-conversion fluorescence. Adv. Funct. Mater. 16 (18), 2324–2329.

Yi, G., Lu, H., Zhao, S., Ge, Y., Yang, W., Chen, D., Guo, L.-H., 2004. Synthesis, characterization, and biological application of size-controlled nanocrystalline $NaYF_4$:Yb, Er infrared-to-visible up-conversion phosphors. Nano Lett. 4 (11), 2191–2196.

Yi, G., Peng, Y., Gao, Z., 2011. Strong red-emitting near-infrared-to-visible upconversion fluorescent nanoparticles. Chem. Mater. 23 (11), 2729–2734.

Yu, X., Shan, Y., Li, G., Chen, K., 2011. Synthesis and characterization of bifunctional magnetic-optical $Fe_3O_4$@$SiO_2$@$Y_2O_3$: $Yb^{3+}$, $Er^{3+}$ near-infrared-to-visible up-conversion nanoparticles. J. Mater. Chem. 21 (22), 8104–8109.

Yu, Q., Rodriguez, E.M., Naccache, R., Forgione, P., Lamoureux, G., Sanz-Rodriguez, F., Scheglmann, D., Capobianco, J.A., 2014. Chemical modification of temoporfin—a second generation photosensitizer activated using upconverting nanoparticles for singlet oxygen generation. Chem. Commun. 50 (81), 12150–12153.

Yuste, R., 2005. Fluorescence microscopy today. Nat. Methods 2 (12), 902–904.

Zako, T., Nagata, H., Terada, N., Utsumi, A., Sakono, M., Yohda, M., Ueda, H., Soga, K., Maeda, M., 2009. Cyclic RGD peptide-labeled upconversion nanophosphors for tumor cell-targeted imaging. Biochem. Biophys. Res. Commun. 381 (1), 54–58.

Zhang, J., Campbell, R.E., Ting, A.Y., Tsien, R.Y., 2002. Creating new fluorescent probes for cell biology. Nat. Rev. Mol. Cell Biol. 3 (12), 906–918.

Zhang, P., Rogelj, S., Nguyen, K., Wheeler, D., 2006a. Design of a highly sensitive and specific nucleotide sensor based on photon upconverting particles. J. Am. Chem. Soc. 128 (38), 12410–12411.

Zhang, Y., He, J., Wang, P.-N., Chen, J.-Y., Lu, Z.-J., Lu, D.-R., Guo, J., Wang, C.-C., Yang, W.-L., 2006b. Time-dependent photoluminescence blue shift of the quantum dots in living cells: effect of oxidation by singlet oxygen. J. Am. Chem. Soc. 128 (41), 13396–13401.

Zhang, F., Li, J., Shan, J., Xu, L., Zhao, D., 2009. Shape, size, and phase-controlled rare-earth fluoride nanocrystals with optical up-conversion properties. Chem. Eur. J. 15 (41), 11010–11019.

Zhang, F., Braun, G.B., Shi, Y., Zhang, Y., Sun, X., Reich, N.O., Zhao, D., Stucky, G., 2010a. Fabrication of $Ag@SiO_2@Y_2O_3$:Er nanostructures for bioimaging: tuning of the upconversion fluorescence with silver nanoparticles. J. Am. Chem. Soc. 132 (9), 2850–2851.

Zhang, H., Li, Y., Ivanov, I.A., Qu, Y., Huang, Y., Duan, X., 2010b. Plasmonic modulation of the upconversion fluorescence in $NaYF_4$:Yb/Tm hexaplate nanocrystals using gold nanoparticles or nanoshells. Angew. Chem. Int. Ed. 49 (16), 2865–2868.

Zhang, Y.-M., Li, Y.-H., Li, P., Hong, G.-Y., Yu, Y.-N., 2010c. Preparation and upconversion luminescence of $YVO_4$:Er$^{3+}$, Yb$^{3+}$. Int. J. Miner. Metall. Mater. 17 (2), 225–228.

Zhang, H., Xu, D., Huang, Y., Duan, X., 2011. Highly spectral dependent enhancement of upconversion emission with sputtered gold island films. Chem. Commun. 47 (3), 979–981.

Zhang, J., Li, B., Zhang, L., Jiang, H., 2012a. An optical sensor for Cu(ii) detection with upconverting luminescent nanoparticles as an excitation source. Chem. Commun. 48 (40), 4860–4862.

Zhang, J., Mi, C., Wu, H., Huang, H., Mao, C., Xu, S., 2012b. Synthesis of $NaYF_4$:Yb/Er/Gd up-conversion luminescent nanoparticles and luminescence resonance energy transfer-based protein detection. Anal. Biochem. 421 (2), 673–679.

Zhang, Y., Wei, W., Das, G.K., Yang Tan, T.T., 2014. Engineering lanthanide-based materials for nanomedicine. J. Photochem. Photobiol. C 20, 71–96.

Zhao, P., Zhu, Y., Yang, X., Fan, K., Shen, J., Li, C., 2012. Facile synthesis of upconversion luminescent mesoporous $Y_2O_3$:Er microspheres and metal enhancement using gold nanoparticles. RSC Adv. 2 (28), 10592–10597.

Zheng, W., Tu, D., Huang, P., Zhou, S., Chen, Z., Chen, X., 2015. Time-resolved luminescent biosensing based on inorganic lanthanide-doped nanoprobes. Chem. Commun. 51 (20), 4129–4143.

Zhengquan, L., Huichen, G., Haisheng, Q., Yong, H., 2010. Facile microemulsion route to coat carbonized glucose on upconversion nanocrystals as high luminescence and biocompatible cell-imaging probes. Nanotechnology 21 (31), 315105.

Zhou, H.-P., Xu, C.-H., Sun, W., Yan, C.-H., 2009. Clean and flexible modification strategy for carboxyl/aldehyde-functionalized upconversion nanoparticles and their optical applications. Adv. Funct. Mater. 19 (24), 3892–3900.

Zhou, J., Yu, M., Sun, Y., Zhang, X., Zhu, X., Wu, Z., Wu, D., Li, F., 2011. Fluorine-18-labeled Gd$^{3+}$/Yb$^{3+}$/Er$^{3+}$ co-doped $NaYF_4$ nanophosphors for multimodality PET/MR/UCL imaging. Biomaterials 32 (4), 1148–1156.

Zhou, J., Liu, Z., Li, F., 2012. Upconversion nanophosphor for small animal imaging. Chem. Soc. Rev. 41, 1323–1349.

Zhou, J., Liu, Q., Feng, W., Sun, Y., Li, F., 2015. Upconversion luminescent materials: advances and applications. Chem. Rev. 115 (1), 395–465.

Zhu, X., Zhou, J., Chen, M., Shi, M., Feng, W., Li, F., 2012. Core–shell $Fe_3O_4$@$NaLuF_4$:Yb, Er/Tm nanostructure for MRI, CT and upconversion luminescence tri-modality imaging. Biomaterials 33 (18), 4618–4627.

Zhu, M., Nie, G., Meng, H., Xia, T., Nel, A., Zhao, Y., 2013. Physicochemical properties determine nanomaterial cellular uptake, transport, and fate. Acc. Chem. Res. 46 (3), 622–631.

Zijlmans, H.J., Bonnet, J., Burton, J., Kardos, K., Vail, T., Niedbala, R.S., Tanke, H.J., 1999. Detection of cell and tissue surface antigens using up-converting phosphors: a new reporter technology. Anal. Biochem. 267 (1), 30–36.

Zrazhevskiy, P., Sena, M., Gao, X., 2010. Designing multifunctional quantum dots for bioimaging, detection, and drug delivery. Chem. Soc. Rev. 39 (11), 4326–4354.

# Index

Note: Page numbers followed by "*f*" indicate figures.